

AD-A014 361

NONDESTRUCTIVE TESTING OF DIFFUSION BONDED TITANIUM  
ALLOYS FOR ENGINE AND AIRFRAME COMPONENTS

John A. Regalbuto, et al

General Dynamics

Prepared for:

Air Force Materials Laboratory

May 1975

DISTRIBUTED BY:

**NTIS**

National Technical Information Service  
U. S. DEPARTMENT OF COMMERCE

258073

**AFML-TR-74-215**

AD A014361

**NONDESTRUCTIVE TESTING OF DIFFUSION  
BONDED TITANIUM ALLOYS FOR  
ENGINE AND AIRFRAME COMPONENTS**

*FORT WORTH DIVISION  
GENERAL DYNAMICS CORPORATION*

TECHNICAL REPORT AFML-TR-74-215

MAY 1975

Approved for public release; distribution unlimited.


**AIR FORCE MATERIALS LABORATORY  
AIR FORCE SYSTEMS COMMAND  
WRIGHT-PATTERSON AIR FORCE BASE, OHIO 45433**

Reproduced by  
NATIONAL TECHNICAL  
INFORMATION SERVICE  
US Department of Commerce  
Springfield, VA. 22151

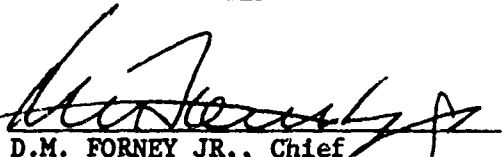
# NOTICE

When Government drawings, specifications, or other data are used for any purpose other than in connection with a definitely related Government procurement operation, the United States Government thereby incurs no responsibility nor any obligation whatsoever; and the fact that the government may have formulated, furnished, or in any way supplied the said drawings, specifications, or other data, is not to be regarded by implication or otherwise as in any manner licensing the holder or any other person or corporation, or conveying any rights or permission to manufacture, use, or sell any patented invention that may in any way be related thereto.

This technical report has been reviewed and is approved:

  
JAMES A. HOLLOWAY  
Project Engineer

FOR THE COMMANDER

  
D.M. FORNEY JR., Chief  
Nondestructive Evaluation Branch  
Metals and Ceramics Division

Copies of this report should not be returned unless return is required by security considerations, contractual obligations, or notice on a specific document.

AIR FORCE/56780/31 July 1975 - 500

ADDRESS ON 10	
NTIS	
DOC	
2	
1	
A	

UNCLASSIFIED

SECURITY CLASSIFICATION OF THIS PAGE (When Data Entered)

REPORT DOCUMENTATION PAGE		READ INSTRUCTIONS BEFORE COMPLETING FORM
1. REPORT NUMBER AFML-TR-74-215	2. GOVT ACCESSION NO. 67364.0	3. RECIPIENT'S CATALOG NUMBER
4. TITLE (and Subtitle) Nondestructive Testing of Diffusion Bonded Titanium Alloys for Engine and Airframe Components		5. TYPE OF REPORT & PERIOD COVERED Final Technical Report 30 June 1972-30 June 1974
7. AUTHOR(s) John A. Regalbuto, D. E. Gordon, B. O. McCauley, J. S. Kunselman, R. H. McDaniel, R. J. Jones, J. W. Hagemeyer, A. D. Crowe		6. PERFORMING ORG. REPORT NUMBER
9. PERFORMING ORGANIZATION NAME AND ADDRESS General Dynamics Corporation Fort Worth Division Fort Worth, Texas 76101		8. CONTRACT OR GRANT NUMBER(s) F33615-72-C-1705
11. CONTROLLING OFFICE NAME AND ADDRESS Air Force Materials Laboratory Air Force Systems Command, USAF Wright-Patterson Air Force Base, Ohio 45433		10. PROGRAM ELEMENT, PROJECT, TASK AREA & WORK UNIT NUMBERS 7351/735109
14. MONITORING AGENCY NAME & ADDRESS (if different from Controlling Office)		12. REPORT DATE MAY 1975
		13. NUMBER OF PAGES 385
		15. SECURITY CLASS. (of this report) Unclassified
16. DISTRIBUTION STATEMENT (of this Report) Approved for public release; distribution unlimited.		15a. DECLASSIFICATION/DOWNGRADING SCHEDULE
17. DISTRIBUTION STATEMENT (of the abstract entered in Block 20, if different from Report)		
18. SUPPLEMENTARY NOTES		
19. KEY WORDS (Continue on reverse side if necessary and identify by block number) Diffusion bonding; solid state welding; Ti6Al-4V alloy; non-destructive testing; ultrasonics; blue etch-anodize, signal averaging; acoustic emission monitoring; ultrasonic attenuation; computer-automated inspection; materials testing.		
20. ABSTRACT (Continue on reverse side if necessary and identify by block number) The development and evaluation of ultrasonic instrumentation for the nondestructive testing of diffusion bonded titanium alloy components is described. Results of a survey to define potential diffusion bonding deficiencies are given. A signal-averaging pulse-echo system developed to increase defect signal-to-grain noise ratio is described. The AFML Computer-Automated Ultrasonic Inspection System was used to evaluate displaced and angularized		

DD FORM 1 JAN 73 1473

EDITION OF 1 NOV 65 IS OBSOLETE

UNCLASSIFIED

SECURITY CLASSIFICATION OF THIS PAGE (When Data Entered)



UNCLASSIFIED

SECURITY CLASSIFICATION OF THIS PAGE(When Data Entered)

bond planes. The fabrication of 600 diffusion bonded specimens containing intentional deficiencies such as voids, inclusions, lack of deformation, and grain size variations is described. Diffusion bonded internal defect specimens were evaluated by blue-etch-anodize, fluorescent penetrant, signal-averaged pulse-echo, and Delta-Scan techniques. Ultrasonic attenuation measurements versus grain size are reported.

Static tensile and axial fatigue data are reported and correlated with nondestructive evaluation and fractographic results. Acoustic emission behavior of parent material specimens is compared with that of internal defect specimens.

Results are documented of the nondestructive evaluation of a large diffusion bonded titanium structure utilizing blue-etch-anodize, fluorescent penetrant, signal-averaged pulse-echo, Delta-Scan, and variable tilt-multiple scan pulse-echo techniques. Defect data resulting from sectioning the large structure are documented.

UNCLASSIFIED

SECURITY CLASSIFICATION OF THIS PAGE(When Data Entered)

## FOREWORD

This Final Technical Report covers the Nondestructive Testing Techniques for Diffusion Bonded Titanium effort pursued under Contact F33615-72-C-1705 Project 7351 "Metallic Materials," Task No. 735109 "Nondestructive Methods." The work was performed in the period 30 June 1972 to 30 June 1974. The Air Force Project Engineer is Mr. J. A. Holloway of the Air Force Materials Laboratory (LLP), Air Force Systems Command, Wright-Patterson Air Force Base, Ohio. Two interim progress reports and one interim technical report were published during this period.

The program was performed in the Applied Research Laboratory, Fort Worth Division, General Dynamics Corporation, Fort Worth, Texas, with Dr. J. A. Regalbuto as Program Manager. Valued participants in this program and in the preparation of this report are: J. S. Kunselman, D. E. Gordon, A. H. Gardner, A. D. Crowe, J. W. Hagemeyer, Dr. B. G. W. Yee, Dr. F. H. Chang, B. O. McCauley, R. H. McDaniel, R. L. Jones and Dr. M. Featherby (San Diego).

Acknowledgment is gratefully extended to the principals of Contract No. F33615-72-C-1828, "Computer-Automated Ultrasonic Inspection System for Aircraft Forgings," Lt. John Allison, Program Monitor and Dr. B. G. W. Yee, Program Manager. The computer-automated inspection system under development in this program demonstrated its versatility in the evaluation of the large diffusion bonded titanium structure and the provision of permanent inspection records.

This report was submitted by the author in July 1974.

## TABLE OF CONTENTS

<u>Section</u>	<u>Page</u>
1 SUMMARY	1
2 INTRODUCTION	2
3 DIFFUSION BONDING SURVEY	3
3.1 Diffusion Bonding Considerations	3
3.1.1 Potential Deficiencies	3
3.2 Survey Goals and Results	4
4 INSTRUMENTATION DEVELOPMENT	9
4.1 Signal Processing System	9
4.1.1 Grain Structure Noise	9
4.1.2 Signal-Averaging System	10
4.1.3 System Operation	13
4.2 Displacement and Angularization System	16
4.2.1 Multiple Transducer Array Systems	16
4.2.2 AFML Computer-Automated Ultrasonic Inspection System	18
5 FEASIBILITY STUDIES	30
5.1 Acoustic Emission Monitoring	
5.1.1 Experimental Setup and Procedures	31
5.1.2 Results	35
5.1.3 Conclusions	75

## TABLE OF CONTENTS (Cont'd)

<u>Section</u>	<u>Page</u>
5.2 Grain Size Variations vs. Attenuation	78
5.2.1 Attenuation Theory	78
5.2.2 Attenuation Measurement Technique	79
5.2.3 Experimental Setup	80
5.2.4 Experimental Measurements	80
5.2.5 Other Titanium Alloys	84
6 BOND TESTING	87
6.1 Sample Preparation	87
6.1.1 Diffusion Bonding Procedures	88
6.1.2 Production of Intentional Deficiencies	91
6.1.3 Verification of Defects	122
6.2 Nondestructive Evaluation	124
6.2.1 Blue Etch-Anodize Process	134
6.2.2 Fluorescent Penetrant Inspection	146
6.2.3 Ultrasonic Inspection	153
7 MECHANICAL TESTING	181
7.1 Specimen Configuration, Equipment, and Procedures	181
7.1.1 Test Specimen Configurations	181
7.1.2 Test Equipment and Procedures	181
7.2 Mechanical Properties Data	187
7.2.1 Parent and Heat-Cycled Ti-6Al-4V Fatigue and Tensile Data	189
7.2.2 Single-Bond/Single-Axis Ti-6Al-4V Fatigue and Tensile Data	193
7.2.3 Double-Bond/Single-Axis Ti-6Al-4V Fatigue and Tensile Data	201

## TABLE OF CONTENTS (Cont'd)

<u>Section</u>		<u>Page</u>
	7.2.4 Multiple-Bond/Two-Axes Ti-6Al-4V Fatigue and Tensile Data	209
	7.2.5 Multiple-Bond/Three-Axes Ti-6Al-4V Fatigue and Tensile Data	217
	7.2.6 Fracture Toughness and Stress Corrosion Data for Diffusion Bonded Ti-6Al-4V	225
8	CORRELATION OF NDE DATA, MECHANICAL PROPERTIES, AND FRACTOGRAPHY	229
	8.1 Tensile Properties	229
	8.1.1 Effects of Intentional Defects on Tensile Properties	229
	8.1.2 Correlation of NDE Data with Tensile Properties	230
	8.2 Axial Fatigue Properties	234
	8.2.1 Effects of Intentional Defects on Fatigue Properties	234
	8.2.2 Correlations of NDE Data with Fatigue Properties	235
	8.3 Fracture Analysis	242
	8.3.1 Scanning Electron Microscope Fractography	242
	8.3.2 Optical Fractography	258
	8.3.3 Microstructural Analysis of Intentional-Defect Initiated Fatigue Failures	307
9	LARGE STRUCTURE EVALUATION	314
	9.1 Blue Etch-Anodize (BEA) Inspection	314
	9.1.1 Inspection Results	317
	9.1.2 Verification of Defects	317

## TABLE OF CONTENTS (Cont'd)

<u>Section</u>	<u>Page</u>
9.2 Fluorescent Penetrant Inspection	317
9.2.1 Inspection Results	317
9.2.2 Verification of Defects	322
9.3 Ultrasonic Inspection	322
9.3.1 Delta-Scan	322
9.3.2 Variable Tilt-Multiple Scan	330
9.3.3 Contact Signal-Averaged Pulse-Echo	335
9.3.4 Defect Verification	335
10 CONCLUSIONS AND RECOMMENDATIONS	344
REFERENCES	347
APPENDICES -	349
A. Material Characterization	349
B. Blue Etch-Anodize Procedure	358

## LIST OF ILLUSTRATIONS

<u>Figure</u>		<u>Page</u>
3.1	Longitudinal Section Micrographs through Bond Plane of Ti-6Al-4V Specimens with Parent Metal Tensile Properties	5
4.1	Signal Averaging System	11
4.2	Laboratory Setup of Signal Averaging System	12
4.3a	Location of Signal-Averaged Data Points on Diffusion Bonded Specimens	15
4.3ab	Transducer Manipulator	15
4.4	Reflectoscope, Sampling Oscilloscope, and Waveform Educator Outputs	17
4.5	Proposed Displacement and Angularization System	20
4.6	System Block Diagram	21
4.7	Block Diagram of AFML Computer-Automated Ultrasonic Inspection System	22
4.8	Block Diagram of Scanner System	24
4.9	AFML Computer-Automated Ultrasonic Inspection System	25
4.10	Transducer Gimbal Assembly	26
4.11	Geometry of Reference Block	28
4.12	Pulse-Echo Record of Reference Block at 0° Transducer Inclination	28

<u>Figure</u>		<u>Page</u>
4.13	Pulse-echo Records of Reference Block at 2°, 4°, 6° and 8° Transducer Inclina- tions	29
5.1	Block Diagram of Experimental Setup for Acoustic Emission Monitoring	31
5.2	Sensor Mounting for Phase II Test	32
5.3	AEM Characteristics of Tensile Specimen D1-2	38
5.4	AEM Characteristics of Tensile Specimen Y1A-3	39
5.5	AEM Characteristics of Tensile Specimen Z1C-5	40
5.6	Amplitude Distribution of Emission Sig- nals for Specimen D1-2	41
5.7	Amplitude Distribution of Emission Sig- nals for Specimen Y1A-3	42
5.8	Amplitude Distribution of Emission Sig- nals for Specimen Z1C-5	43
5.9	AEM Characteristics of Tensile Specimen A2-3	45
5.10	AEM Characteristics of Tensile Specimen B2-3	46
5.11	AEM Characteristics of Tensile Specimen D2-1	47
5.12	Amplitude Distribution of Emission Signals for Specimen D2-1	48



<u>Figure</u>		<u>Page</u>
5.13	Amplitude Distribution of Emission Signals for Specimen B2-3	49
5.14	Amplitude Distribution of Emission Signals for Specimen A2-3	50
5.15	AEM Characteristics of Tensile Specimen E1-2	52
5.16	Amplitude Distribution of Emission Signals for Specimen E1-2	53
5.17	AEM Characteristics of Tensile Specimen F1-1	54
5.18	Amplitude Distribution of Emission Signals for Specimen F1-1	55
5.19	AEM Characteristics of Tensile Specimen A3-2	56
5.20	Amplitude Distribution of Emission Signals for Specimens A3-2	57
5.21	AEM Characteristics of Tensile Specimen B3-2	58
5.22	Amplitude Distribution of Emission Signals for Specimen B3-2	60
5.23	AEM Characteristics of Tensile Specimen I3-3	61
5.24	Amplitude Distribution of Emission Signals for Specimen I3-3	62
5.25	AEM Characteristics of Tensile Specimen E3-3	63

<u>Figure</u>		<u>Page</u>
5.26	AEM Characteristics of Tensile Specimen F3-1	64
5.27	Amplitude Distribution of Emission Signals for Specimen E3-3	65
5.28	Amplitude Distribution of Emission Signals for Specimen F3-1	66
5.29	AEM Characteristics of Tensile Specimen A6-1	68
5.30	Amplitude Distribution of Emission Signals for Specimen A6-1	69
5.31	AEM Characteristics of Tensile Specimen H6-3	70
5.32	Amplitude Distribution of Emission Signals for Specimen H6-3	71
5.33	AEM Characteristics of Tensile Specimen K6-3	72
5.34	Amplitude Distribution of Emission Signals for Specimen K6-3	73
5.35	AEM Characteristics of Tensile Specimen D3-3	76
5.36	Amplitude Distribution of Emission Signals for Specimen D3-3	77
5.37	Reflection Diagram for Buffer Rod System	81
5.38	Experimental Setup for Attenuation Measurements	81
5.39	Power Output vs Frequency for a 2.25 MHz/.375 Dia. Transducer	82

<u>Figure</u>		<u>Page</u>
5.40	Attenuation vs Primary Alpha Grain Size	83
5.41	Attenuation vs Frequency	85
6.1a	Preparation of Single-Bond Tensile and Fatigue Specimens	89
6.1b	Preparation of Single Axis Multiple Bond Tensile and Fatigue Specimens	89
6.2a	Preparation of 2-Axes Multiple Bond Tensile and Fatigue Specimens	90
6.2b	Preparation of 3-Axes Multiple Bond Tensile and Fatigue Specimens	90
6.3	Wedge Tooling for 2-Axes Diffusion Bonded Specimens	92
6.4	Wedge Tooling for 3-Axes Diffusion Bonded Specimens	93
6.5	Photomicrographs of Center of 1-inch Ti-6Al-4V Plate, Annealed, Longitudinal Direction	102
6.6	Photomicrograph of 1-inch Ti-6Al-4V Plate, Heated at 1735 <sup>C</sup> F for 6 Hours	103
6.7	Photomicrograph of 1-inch Ti-6Al-4V Plate, Heated at 1775 <sup>O</sup> F for 6 Hours	104
6.8	Photomicrographs of Central Interior of ½-inch Ti-6Al-4V Plate, Annealed	105
6.9	Photomicrographs of ½-inch Ti-6Al-4V Plate, Condition Lab R A per NAR Spec STO-170-LBO-032 Rev. E	106
6.10	Location of Voids in Single-Bond/ Single-Axis Joints	108

<u>Figure</u>		<u>Page</u>
6.11	Location of Voids in Double-Bond/Single-Axis Joints	108
6.12	Location of Voids in Multiple Bond/2-Axes Joints	109
6.13	Location of Chamfered Corner Voids in Multiple Bond/3-Axes Joints	113
6.14	Microhardness vs Depth Below an Exposed Surface	115
6.15	Location of Alpha Case Layer in Multiple Bond/2-Axes Joints	118
6.16	Location of Inclusions in Multiple Bond/2-Axes Joints	121
6.17	Photomicrographs at Bond Plane of DB Specimen M-4B	124
6.18	Photomicrographs at Bond Plane of DB Specimen B-3	125
6.19	Photomicrographs at Bond Plane of DB Specimen C-3	126
6.20	Photomicrographs at Bond Plane of DB Specimen P-4B	127
6.21	Photomicrographs at Bond Plane of DB Specimen Q-4B	128
6.22	Photomicrographs at Bond Plane of DB Specimen R-4B	129
6.23	Photomicrographs at Bond Plane of DB Specimen H-4	130

<u>Figure</u>		<u>Page</u>
6.24	Photomicrographs at Bond Plane of DB Specimen J-4	131
6.25	Photomicrographs at Bond Plane of DB Specimen K-3	132
6.26	Photomicrographs at Bond Plane of DB Specimen L-3	133
6.27	Photograph showing Alpha Case Layer at Bondline in Specimen V5-A	138
6.28	Microhardness vs Distance from Bondline	139
6.29	Blue Etch-Anodize Records of Specimens T4-A and V4-B	141
6.30	Blue Etch-Anodize Records of Specimens N5-B and O5-A	142
6.31	Blue Etch-Anodize Records of Specimens L5 and P5-A	143
6.32	Blue Etch-Anodize Record of Specimen J5 (Alpha Case Layer in Bond Planes)	144
6.33	Blue Etch-Anodize Records of Specimens J5 and V6-A	145
6.34	Fluorescent Penetrant Record of Diffusion Bonded Specimen with No Defects	148
6.35	Fluorescent Penetrant Record of Diffusion Bonded Specimen with Surface Gouge	149

<u>Figure</u>		<u>Page</u>
6.36	Delta-Scan Applied to Distorted Bond Plane	154
6.37	Laboratory Setup of Delta/C-Scan System	155
6.38	Diffusion Bonded Ultrasonic Reference Standard	156
6.39	Optimized Delta-Scan Configuration	158
6.40	Ultrasonic Delta-Scan Record of Reference Standard	160
6.41	Delta-Scan Reference Standard for Multiple-Bond Specimens	161
6.42	Delta/C-Scan Record of Specimen S3-B	164
6.43	Delta/C-Scan Record of Specimen T3-A	165
6.44	Delta/C-Scan Record of Specimen U4-A	166
6.45	Delta/C-Scan Records of Specimens N6-B and M6-A	169
6.46	Delta/C-Scan Records of Specimens C6 and O5-B	170
6.47	Delta/C-Scan Records of Specimens H5 and U5-A	171
6.48	Delta/C-Scan Records of Specimens H6 and S6-B	172
6.49	Delta/C-Scan Records of Specimens V6-A and K5	173
6.50	Delta/C-Scan Record of Specimen X5-A	174
6.51	Delta/C-Scan Record of Specimen X6-B	175
6.52	Single and Averaged Waveforms from Bond Plane of Specimen Q6-A (ASTM Grain Size No. 8)	177

<u>Figure</u>		<u>Page</u>
6.53	Single and Averaged Waveforms from 3/64-in. Flat Bottom Hole Reference Standard	178
6.54	Statistical Analysis of Signal-Averaged Waveforms for Specimen G6	179
7.1	Configuration of Tensile Test Specimen-Collet Grip	182
7.2	Configuration of Fatigue Test Specimen, $K_t = 1$ , Collet Grip	183
7.3	Configuration of Fatigue Test Specimen, Double Diffusion Bond, $K_t = 1$ , Collet Grip	184
7.4	Configuration of Compact Tension Fracture Toughness Specimen	185
7.5	Configuration of Constant Deflection Specimen	186
7.6	Axial Fatigue Properties of Single-Bond/Single-Axis Diffusion Bonded Specimens as Affected by Bonding Anomalies	194
7.7	Axial Fatigue Properties of Double-Bond/Single-Axis Specimens as Affected by Bonding Anomalies	202
7.8	Axial Fatigue Properties of Multiple-Bond/2-Axes Specimens as Affected by Bonding Anomalies	210
7.9	Axial Fatigue Properties of Multiple-Bond/3-Axes Specimens as Affected by Bonding Anomalies	218
8.1	Reduction of Area vs. Defect Amplitude/AA for Diffusion Bonded Tensile Specimens	232
8.2	Statistical Analysis of Reduction of Area vs. Defect Amplitude/AA for Diffusion Bonded Tensile Specimens	233

<u>Figure</u>		<u>Page</u>
8.3	Fatigue Life vs. Defect Amplitude/AA for Diffusion Bonded Specimens with Internally-Initiated Failures (Stress Level = 110 KSI)	236
8.4	Fatigue Life vs. Defect Amplitude/AA for Diffusion Bonded Specimens with Surface-Initiated Failures (Stress Level = 110 KSI)	237
8.5	Fatigue Life vs. Defect Amplitude/AA for Diffusion Bonded Specimens with Internally-Initiated Failures (Stress Level = 80 KSI)	238
8.6	Fatigue Life vs. Defect Amplitude/AA for Diffusion Bonded Specimens with Surface-Initiated Failures (Stress Level = 80 KSI)	239
8.7	Statistical Analysis of Fatigue Life vs. Defect Amplitude/AA (Stress Level = 110 KSI)	240
8.8	Statistical Analysis of Fatigue Life vs. Defect Amplitude/AA (Stress Level = 80 KSI)	241
8.9	Scanning Electron Micrographs of Two Ti-6Al-4V Fracture Surfaces with Different Thermal Histories (10X)	243
8.10	Scanning Electron Micrographs of Two Ti-6Al-4V Fracture Surfaces with Different Thermal Histories (10X)	244
8.11	Scanning Electron Micrographs of Two Ti-6Al-4V Fracture Surfaces (1000X)	245
8.12	Scanning Electron Micrographs Showing Fracture Surfaces of Two Ti-6Al-4V Diffusion Bonded Specimens Containing Good Bonds	246
8.13	Scanning Electron Micrographs Showing Fracture Surfaces of Two Ti-6Al-4V Diffusion Bonded Specimens with Different Primary Alpha Grain Sizes	247



<u>Figure</u>		<u>Page</u>
8.14	Scanning Electron Micrographs Showing the Fracture Surface of a Diffusion Bonded Specimen Having a Bad Bond	248
8.15	SEM Fractographs of Diffusion Bonded Specimen S4B3 Containing a Cylindrical Void of 0.0065 in. Diameter	249
8.16	SEM Fractographs of Diffusion Bonded Specimen U3B1 Containing a Cylindrical Void of 0.020 in. Diameter	250
8.17	SEM Fractographs of Diffusion Bonded Specimen T4A1 Containing Four Cylindrical Voids of 0.010 in. Diameter	251
8.18	SEM Fractographs of Diffusion Bonded Specimen S5A1 Containing a Void in the Form of a Chamfer	252
8.19	SEM Fractographs of Diffusion Bonded Specimen T5B1 Containing a Void in the Form of a Chamfer	253
8.20	SEM Fractographs of Diffusion Bonded Specimen V5A1 Containing an Alpha Case Layer	255
8.21	SEM Fractographs of Diffusion Bonded Specimen W3-A2 Containing Stainless Steel Powder Inclusions	256
8.22	SEM Fractographs of Diffusion Bonded Specimen Containing SiO <sub>2</sub> Powder Inclusions	257
8.23	Fracture Surfaces of Failed Fatigue Specimens	259
through	↑ ↓	↑ ↓
8.70	Fracture Surfaces of Failed Fatigue Specimens	306
8.71	Microstructure of Diffusion Bonded Ti-6Al-4V Specimen S3B2 Containing a 0.0065 in. Dia. Electric Discharge Formed Hole	308

<u>Figure</u>		<u>Page</u>
8.72	Microstructure of Diffusion Bonded Ti-6Al-4V Fatigue Specimen U3B1 Containing Drilled 0.020 in. Dia. Void	309
8.73	Microstructure of Diffusion Bonded Ti-6Al-4V Fatigue Specimen V3A3 Containing an Alpha Case Defect	310
8.74	Microstructure of Diffusion Bonded Ti-6Al-4V Specimen W3B2 Containing 304S.S. Powder Defect at the Bond Plane	311
8.75	Microstructure of Diffusion Bonded Ti-6Al-4V Specimen X3A1 Containing SiO <sub>2</sub> Powder in Drilled 0.013 in. Dia. Hole	312
8.76	Microprobe X-ray Analysis of Diffusion Bonded Ti-6Al-4V Containing 304 S.S. Powder Defect, Specimen W3B2	313
9.1	Large Diffusion Bonded Structure Details	315
9.2	Sectioning and Numbering Diagram	316
9.3	Blue Etch-Anodize Record of Part #1 Showing Surface-Connected Segregation	318
9.4	Blue Etch-Anodize Record of Part #2 Indicating Color Discontinuities at Fillets	319
9.5	Blue Etch-Anodize Record of Part #3 Showing Surface-Connected Segregation	320
9.6	Photomicrograph of Contaminated Surface Layer in Part #1 (80X)	321
9.7	Fluorescent Penetrant Record of Part #2 with Location of Flaw Indication	323
9.8	Fluorescent Penetrant Records of Part #3 Showing Flaw Indications and Locations	324

<u>Figure</u>		<u>Page</u>
9.9	Photographs of Flaw in Fillet of Part #3 Detected by Fluorescent Penetrant Inspection	325
9.10	Orientation of Reference Holes in Part #1	326
9.11	Delta/C-Scan Record of Part #1	327
9.12	Delta/C-Scan Record of Part #1 (90° Rotation)	328
9.13	Orientation of Part #1 with Respect to Scanner Coordinate System	330
9.14	Flaw Display in Reference Hole Area of Part #1 (Transducer Inclinations, -8° and -6°)	331
9.15	Flaw Display in Reference Hole Area of Part #1 (Transducer Inclinations, -2° and 0°)	333
9.16	Flaw Display of Part #1 (-8°, -6° Tilt; 0° Rotate)	335
9.17	Flaw Display of Part #1 (0°, +4° Tilt; 0° Rotate)	336
9.18	Flaw Display of Part #1 (-8° Tilt; -90° Rotate)	337
9.19	Signal-Averaged Pulse-Echo Record (X = 5.5 in., Y = 4.6 in.)	338
9.20	Signal-Averaged Pulse-Echo Record (X = 1.1 in.; Y = 1.5 in.)	339
9.21	Photomicrographs of Microstructural Anomalies in Bond Plane of Part #1 at X = 8.3 in., Y = 4.8 in.	340
9.22	Microhardness Variations Across Elliptic Area in Rib Intersection of Part #1	342

## LIST OF TABLES

<u>Table</u>	<u>Page</u>
3.1      Summary of DB Survey Results	7
3.2      Deficiency Catalogue	8
5.1      Tensile Properties of Annealed Ti 6Al-4V Plate, 1" Thick	37
5.2      Ultrasonic Attenuation in Diffusion Bonded and Parent Heat Cycled Ti 6Al-4V Specimens with Different Rolling Orientations and Primary Alpha Grain Sizes	86
6.1      Test Specimen Parameter Matrix and Quantities	94
6.2      Bonding Parameter Variations in Single- Bond/Single Axis and Double-Bond/ Single-Axis Joints	95
6.3      Bonding Parameter Variations in Multiple-Bond/2-Axes Joints	96
6.4      Bonding Parameter Variations in Multiple-Bond/3-Axes Joints	97
6.5      Grain Size and Orientation Variations	99
6.6      Size of Voids in Single-Bond/Single- Axis and Double-Bond/Single-Axis Joints	110
6.7      Size of Voids in Multiple-Bond/2-Axes Joints	111
6.8      Size of Voids in Multiple-Bond/3-Axes Joints	114

<u>Table</u>		<u>Page</u>
6.9	Forms and Size of Contamination in Single-Bond/Single-Axis and Double-Bond/Single-Axis Joints	117
6.10	Forms and Size of Contamination in Multiple-Bond/2-Axes Joints	119
6.11	Blue Etch-Anodize (BEA) Results on Selected Single-Bond/Single-Axis and Double-Bond/Single-Axis Diffusion Bonded Specimens	135
6.12	Blue Etch-Anodize (BEA) Results on Selected Multiple-Bond/2-Axes Specimens	136
6.13	Blue Etch-Anodize (BEA) Results on Selected Multiple-Bond/3-Axes Specimens	137
6.14	Fluorescent Penetrant Inspection Results	147
6.15	Fluorescent Penetrant Results on Selected Multiple-Bond/2-Axes Specimens	151
6.16	Fluorescent Penetrant Results on Selected Multiple-Bond/3-Axes Specimens	152
6.17	Ultrasonic Delta-Scan Flaw Indication Results for Single-Axis Specimens	162
6.18	Ultrasonic Delta-Scan Indication Results for Multiple-Bond/2-Axes Specimens	167
6.19	Ultrasonic Delta-Scan Indication Results for Multiple-Bond/3-Axes Specimens	168
7.1	Tensile Properties of Annealed Ti-6Al-4V Plate, 1 in. Thick	190
7.2	Axial Fatigue Properties of 1-in. Thick Ti-6Al-4V, $K_t = 1.0$ , $R = 0.1$	191
7.3	Statistical Analysis of Axial Fatigue Data, Single-Bond/Single-Axis, $K_t = 1$ , $R = 0.1$	195

<u>Table</u>		<u>Page</u>
7.4	Effect of Bonding Parameter Variations on Axial Fatigue Properties, Single-Bond/Single-Axis, $K_t = 1$ , $R = 0.1$	196
7.5	Effect of Grain Size Variations on Axial Fatigue Properties, Single-Bond/Single Axis, $K_t = 1$ , $R = 0.1$	197
7.6	Effect of Voids on Axial Fatigue Properties, Single-Bond/Single-Axis, $K_t = 1$ , $R = 0.1$	198
7.7	Effect of Contamination on Axial Fatigue Properties, Single-Bond/Single-Axis, $K_t = 1$ , $R = 0.1$	199
7.8	Tensile Properties of Single-Bond/Single-Axis Specimens	200
7.9	Statistical Analysis of Axial Fatigue Data, Double-Bond/Single-Axis, $K_t = 1$ , $R = 0.1$	203
7.10	Effect of Bonding Parameter Variations on Axial Fatigue Properties, Double-Bond/Single-Axis, $K_t = 1$ , $R = 0.1$	204
7.11	Effect of Grain Size Variations on Axial Fatigue Properties, Double-Bond/Single-Axis, $K_t = 1$ , $R = 0.1$	205
7.12	Effect of Voids on Axial Fatigue Properties, Double-Bond/Single-Axis, $K_t = 1$ , $R = 0.1$	206
7.13	Effect of Contaminants on Axial Fatigue Properties, Double-Bond/Single-Axis, $K_t = 1$ , $R = 0.1$	207
7.14	Tensile Properties of Double-Bond/Single-Axis Specimens	208

<u>Table</u>		<u>Page</u>
7.15	Statistical Analysis of Axial Fatigue Data, Double-Bond/2-Axis, $K_t = 1$ , $R = 0.1$	211
7.16	Effect of Bonding Parameter Variations on Axial Fatigue Properties, Double-Bond/2-Axis, $K_t = 1$ , $R = 0.1$	212
7.17	Effect of Grain Size Variations on Axial Fatigue Properties, Double-Bond/2-Axes, $K_t = 1$ , $R = 0.1$	213
7.18	Effect of Chamfered Edge Voids on Axial Fatigue Properties, Double-Bond/2-Axes, $K_t = 1$ , $R = 0.1$	214
7.19	Effect of Contamination on Axial Fatigue Properties, Double-Bond/2-Axes, $K_t = 1$ , $R = 0.1$	215
7.20	Tensile Properties of Double-Bond/2-Axes Specimens	216
7.21	Statistical Analysis of Axial Fatigue Data, Multiple-Bond/3-Axes, $K_t = 1$ , $R = 0.1$	219
7.22	Effect of Bonding Parameter Variations on Axial Fatigue Properties, Multiple-Bond/3-Axes, $K_t = 1$ , $R = 0.1$	220
7.23	Effect of Grain Size Variations on Axial Fatigue Properties, Multiple-Bond/3-Axes, $K_t = 1$ , $R = 0.1$	221
7.24	Effect of Chamfered Corner Voids on Axial Fatigue Properties, Multiple-Bond/3-Axes, $K_t = 1$ , $R = 0.1$	222
7.25	Effect of Contamination on Axial Fatigue Properties, Multiple-Bond/3-Axes, $K_t = 1$ , $R = 0.1$	223
7.26	Tensile Properties of Multiple-Bond/3-Axes Specimens	224
7.27	Compact Tension Fracture Toughness of Diffusion Bonded Ti-6Al-4V Plate, L-T Directions, 1" Thick	226

<u>Table</u>		<u>Page</u>
7.28	Results of Stress Corrosion Cracking Tests on Bonded and Unbonded Ti-6Al-4V	228
9.1	Reflection Mode Data Report	332



## 1. SUMMARY

The development and testing described in this report indicate the importance of a multiple-technique approach to the evaluation of diffusion bonded titanium alloy structures. The types of deficiencies revealed by the diffusion bonding survey are sufficiently different in character that no one technique is adequate.

Alpha case surfaces and emergent oxygen-rich bond planes were readily detected by the blue etch-anodize process. Fluorescent penetrant was effective only for detection of low deformation diffusion bonds resulting in surface-connected porosity. Optimized Delta/C-scan proved capable of detecting 0.010-in. voids and inclusions in thin (1 in.) sections.

Feasibility of utilizing acoustic emission monitoring to detect flaws before failure and even yielding was shown. Ultrasonic attenuation was shown to increase measurably with grain size and especially the degree of beta processing.

Signal-averaged pulse-echo measurements were related to tensile and fatigue properties by normalizing defect signal amplitudes by the arithmetic average (AA) of the corresponding grain noise waveforms. Reduction in area of tensile specimen decreased as the defect amplitude/AA ratio increased. Fatigue properties were poor for defect amplitude/AA ratios greater than 30. Large standard deviations in cycles to failure vs. defect amplitude ratios less than 30 lessened the correlation of fatigue life in that range.

The AFML Computer-Automated Ultrasonic Inspection System was shown to operate efficiently in the variable-tilt/multiple-scan mode used to inspect a large diffusion bonded titanium structure. Correlation of the variable tilt, Delta/C-scan and contact pulse-echo inspection results was used to identify a potential flawed area within the structure. Sectioning at the indicated location revealed an anomaly in the form of an elliptic area of decreased hardness compared to the matrix. Blue etch-anodize indications of surface contamination were also verified by sectioning and metallographic examination.

## 2. INTRODUCTION

Joining titanium alloy materials with diffusion bonding techniques has been pursued extensively by various industries because titanium has been used successfully as an aerospace structural material, and it forms a homogeneous solid-state bond more easily than other metal combinations. Titanium diffusion bonded laminated sections should have superior properties to heavy section forgings, since the fine, uniform grain of the sheet stock material is retained in the laminate structure. This laminated structure inherent in diffusion bonded parts can present, however, large fractions of the part plan area as potential defect sites. Rigid process controls for cleanliness, etc., are necessary but not sufficient conditions for confidence in the structural integrity of the diffusion bonded structure.

Advanced nondestructive evaluation techniques are required to establish the desired level of confidence in critical titanium structures fabricated by diffusion bonding. Thus, the major objectives of this program are:

- . To develop advanced ultrasonic instrumentation capable of determining bond quality and the spatial location of discontinuities,
- . To evaluate the instrumentation on a series of test specimens by correlation between nondestructive data, observed mechanical properties, and failure analyses,
- . To optimize defect signals from a structure containing displaced and angularized multiple bonds, and
- . To generate a procedural document for incorporation into NDT specifications.

This report describes the major accomplishments made during this program at the Fort Worth Division of General Dynamics. It covers the diffusion bonding survey, instrumentation development, specimen preparation, nondestructive evaluation, mechanical testing and fractography.

### 3. DIFFUSION BONDING SURVEY

#### 3.1 Diffusion Bonding Considerations

Solid-state diffusion bonding is here defined as a process by which a joint is formed between similar or dissimilar metals in intimate contact under controlled conditions of time, temperature, and pressure. The metal parts to be bonded are placed together in the desired configuration, heated, and pressure is applied to the parts after the desired temperature is reached. After plastic flow occurs in the area adjacent to the surfaces, diffusion of atoms, recrystallization and grain growth across the interface takes place, then bonding is considered to be complete. No melting occurs during this solid-state process, in sharp contrast to brazing and welding joining techniques. Ideally, this method produces a joint which has parent metal properties but does not contain discontinuities which are often the cause of embrittlement and fatigue in a part joined by fusion welding.

In order to obtain the ultimate joint efficiencies using this process, stringent process controls are necessary to keep the bond area from becoming a potential defect site. These process controls are necessary but not sufficient conditions for confidence in the structural integrity of the diffusion bonded structure.

##### 3.1.1 Potential Deficiencies

In general, deficiencies in diffusion bonded joints may arise from:

- (a) Prebonding shortcomings in the mating surfaces (i.e., particulate and chemical contamination, surface finish anomalies, etc.);
- (b) Failure to achieve the desired bonding parameters in localized areas of the bonding plane, resulting in less than a totally homogeneous solid-state bond.

Process controls are normally sufficient to overcome the defects produced by item (a). The localized disbonding of item (b) is more insidious, however.

Ashton, et al. (Ref. 1) in a diffusion bonding parameter study with Ti 6Al-4V showed that localized disbond or contaminated areas can exist in specimens which exhibit parent material tensile properties. Figure 3.1 presents longitudinal section micrographs at the bondline of two diffusion bonded tensile specimens which failed completely away from the bond area and exhibited parent metal (heat-cycled) static test properties.

The specimens above were also inspected ultrasonically in the pulse-echo mode (reflectoscope) with no identifiable flaw indications. The implication, then, is that minute flaws can be masked by grain noise enhanced by the diffusion-bonding heat cycle. The effect of these flaws on static test properties is undetectable. The effect of this type of flaw on fatigue and fracture toughness properties of titanium will be a secondary goal of this program.

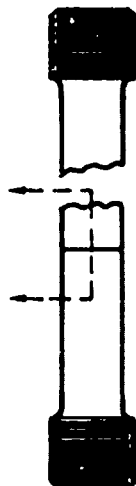
### 3.2 Survey Goals and Results

The goal of this survey was to establish the geometry, size, type, and composition of typical probable defects for inclusion in a series of diffusion bonded tensile and tensile-fatigue specimens. The survey was conducted among facilities actively engaged in the utilization of diffusion bonded components in real systems and/or with a history of significant research and development in diffusion bonding. Data was collected by personal contact and questionnaire.

To be as complete as possible, the entire diffusion bonding process was examined for interactions which may result in undesirable deficiencies, e.g., initial material procurement, pre-bonding procedures, bonding environment and parameters, and post-bonding treatments.

The responses of the various companies contacted (either by visit or questionnaire) varied, depending on the particular diffusion bonding technique practiced at a particular facility. Some potential problem areas suggested follow:

- . Localized variance of bonding parameters (e.g., fitup tolerance buildup, thermal gradients)
- . Particulate contamination (e.g., alumina, silica, airborne particles, parting agents, etc.)
- . Chemical contamination (e.g.,  $O_2$ ,  $N_2$ , hydrocarbons from oily shop atmosphere)

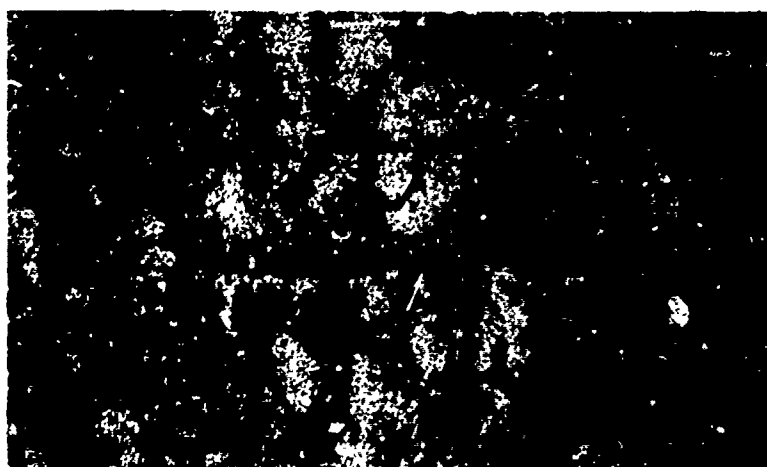


LONGITUDINAL SECTIONS AT BONDLINE  
OF TENSILE SPECIMENS WHICH BROKE  
OUTSIDE OF THE BOND AREA AND HAD  
PARENT METAL TENSILE PROPERTIES



(825X)

- UTS = 141.3 ksi
- YIELD = 131.6 ksi
- RED A = 26.8 %
- ELONG = 15.0 %



(825X)

- UTS = 141.5 ksi
- YIELD = 132.4 ksi
- RED A = 27.0 %
- ELONG = 13.0 %

Figure 3.1 Longitudinal Section Micrographs through Bond Plane of  
Ti6Al-4V Specimens with Parent Metal Tensile Properties

- . Gas entrapment between faying surfaces (e.g., argon, air)
- . Surface finish defects (e.g., scratches, out-of-spec surface roughness, impact damage)
- . Grain size differences between mating parts (e.g., sheet joined to forgings)
- . Grain orientation differences between mating parts (e.g., perpendicular orientation of rolling directions)
- . Metallurgical changes at the bond plane (e.g., transformed beta, intermetallics)
- . Alpha stringers from surface to interior along bond plane
- . Voids from excessive chamfers on corners of details which meet to form two- or three-axis joints.

A summary of the responses follows in Table 3.1. The three problem areas considered most pertinent by each facility are listed generally in descending order of importance. Particulate and chemical contamination appear most frequently in the summary. When frequency of occurrence is weighted by degree of importance, particulate and chemical contamination still rank first, followed by void defects, grain size and orientation effects, and localized variation of bonding parameters, in that order.

Table 3.2 presents the specimen parameter matrix with the intentional deficiencies defined. Defect sizes are based on metallurgical considerations and theoretical limits imposed by acoustic theory.

<u>Company "A"</u>	<u>Company "B"</u>	<u>Company "C"</u>	<u>Company "D"</u>
<ul style="list-style-type: none"> <li>- Localized variance of bonding parameters (incomplete diffusion &amp; recrystallization)</li> <li>- Particulate &amp; chemical contamination</li> <li>- Voids from joint fitup &amp; microporosity at bond plane</li> </ul>	<ul style="list-style-type: none"> <li>- Metallurgical changes at bond plane</li> <li>- Particulate contamination</li> <li>- Surface finish defects</li> </ul>	<ul style="list-style-type: none"> <li>- Localized variance of bonding parameters (incomplete diffusion &amp; recrystallization)</li> <li>- Grain size differences &amp; texture orientation</li> <li>- Chemical contamination</li> </ul>	<ul style="list-style-type: none"> <li>- Grain size differences &amp; texture orientations</li> <li>- Chemical contamination (alpha stringers)</li> <li>- Particulate contamination</li> </ul>
<u>Company "E"</u>	<u>Company "F"</u>	<u>Company "G"</u>	<u>Company "H"</u>
<ul style="list-style-type: none"> <li>- Chemical contamination</li> <li>- Voids from joint fitup</li> <li>- Particulate contamination</li> </ul>	<ul style="list-style-type: none"> <li>- "Mechanical defects" (i.e., voids from fitup tolerance buildup surface finish defects)</li> <li>- "Processing defects" (particulate &amp; chemical contamination)</li> <li>- "Metallurgical differences" (grain size &amp; orientation differences)</li> </ul>	<ul style="list-style-type: none"> <li>- Chemical contamination (alpha stringers)</li> <li>- Particulate contamination</li> <li>- Voids due to insufficient deformation</li> </ul>	<ul style="list-style-type: none"> <li>- Localized variance of bonding parameters</li> <li>- Chemical contamination</li> <li>- Surface finish defects</li> </ul>

Table 3-1 SUMMARY OF DB SURVEY RESULTS

Table 3.2 DEFICIENCY CATALOGUE

	Single Bond			Multiple Bond			3 Axis		
	Quantity	Size of Deficiency	Rolling Direction	Quantity	Size of Deficiency	Rolling Direction	Quantity	Size of Deficiency	Rolling Direction
BONDING PARAMETERS		Deformation Long Dir.	↑		Deformation Long Dir.	↑		Deformation Short Trans Dir.	↑
	3	7% Def.	↑	3	7% Def.	↑	3	4% Def.	↑
	3	2 1/2% Def.	↑	3	2 1/2% Def.	↑	3	3% Def.	↑
	3	1 1/2% Def.	↑	3	1 1/2% Def.	↑	3	2% Def.	↑
CONTAMINATION									
	3	(.093" dia (.002" dpth .013" dia	↑	3	(.186" dia (.002" dpth .0065" dia	↑	3	.002" dpth Chamfer: .025" Side Chamfer: .025" Side	↑
	3	.013" dia	↑	3	.0065" dia	↑	3		↑
SURFACE DEFECTS									
	3	Cyl Voids L/D 1	↑	3	Cyl. Voids L/D 1	↑	3	Chamfer	↑
	3	.0065" dia	↑	3	.0065" dia	↑	3	0.008"	↑
	3	.010" dia	↑	3	.010" dia	↑	3	0.018"	↑
	3	.020" dia	↑	3	.020" dia	↑	3	0.030"	↑
GRAIN SIZE									
	3	ASTM 10	↑	3	ASTM 10	↑	3	ASTM 11	↑
	3	ASTM 9	↑	3	ASTM 9	↑	3	ASTM 8	↑
	3	ASTM 7.5	↑	3	ASTM 7.5	↑	3	ASTM 7	↑
*As Received or AR									



#### 4. INSTRUMENTATION DEVELOPMENT

The diffusion bonding cycle presents two main problems to nondestructive evaluation of bond quality in titanium. First, the thermal cycle (typically 1700°F for 5 hours) encourages grain growth. Simultaneously, the diffusional activity of titanium at high temperatures acts to reduce any unintentional voids to very small sizes. Thus, the problem exists of extracting low-level defect signals from background noise.

Secondly, a diffusion bonding cycle which utilizes high deformations can displace and distort the bond area from its original flat configuration. Consequently, an unintentional deficiency may not have its major plan area parallel to the surface from which inspection takes place. Given this set of circumstances, the defect signal must be optimized to produce depth and orientation information.

##### 4.1 Signal Processing System

###### 4.1.1 Grain Structure Noise

If a polycrystalline material contains large grains with inhomogeneous elastic properties, scattering and refraction of any incident acoustic energy will occur (Ref. 2). The receiving transducer of an ultrasonic system at any instant in time will be impressed with a multitude of interfering strains corresponding to the many possible paths and phase shifts within the materials. The electrical output of the transducer will be voltage pulses which result from integration of the unit strains over the crystal surface area. In diffusion bonded titanium, this grain structure noise can be of the same order of magnitude as signals resulting from bondline defects. For example, ultrasonically undetectable microvoids with grain size dimensions were shown to exist in a bond plane without affecting the static tensile properties of the diffusion bonded joint (Ref. 1). Thus, a means must be found to extract legitimate defect signals from grain structure noise. The problem is compounded by the fact that the grain structure noise is coherent, i.e., the received waveform does not change with time so long as the transducer remains stationary.

The technique used to reduce coherent noise/reflected signals from internal grain structure is based on making the

above noise/signals spatially incoherent. This is accomplished by perturbing the transducer-specimen geometry so as to alter the ray patterns and path lengths of waves scattered and refracted by the internal grain structure. At the same time, the path length to a defect must be only minimally affected. Thus, the reflected waveforms corresponding to each transducer position will shift and change height except for the pulse resulting from a defect which will not shift but only change in amplitude.

The task then is to obtain waveforms at n different spatial positions in the vicinity of a defect location and electronically extract the defect signal from the grain noise.

Several different techniques for obtaining these waveforms for subsequent manipulation or visual analysis have been described in the literature (Refs. 3, 4, 5). In one method (Ref. 3), the transducer is rotated so that its asymmetric pressure amplitude profile produces different waveforms as a function of azimuth angle. Discrimination of a flaw response from the shifting grain noise is accomplished visually by the operator.

In this program, the electronic signal processing consists of averaging the collection of n waveforms point by point to obtain an improvement in defect signal-to-grain noise ratio.

#### 4.1.2 Signal Averaging System

The basic components of the signal averaging system are given in Figure 4.1 and consist of:

- (a) Transducer manipulator
- (b) Pulser/receiver, UM721 Reflectoscope
- (c) Sampling oscilloscope
- (d) Modified Princeton Applied Research TDH-9 Waveform Educator
- (e) Dual trace display oscilloscope
- (f) X-Y recorder

The setup of these components is shown in Figure 4.2. The operation of the system is described below.

At any transducer position, ultrasonic signals are generated at a constant repetition rate. The ISI sampling unit constructs a lower frequency signal (but identical in form) for input into the TDH-9 Waveform Educator. The

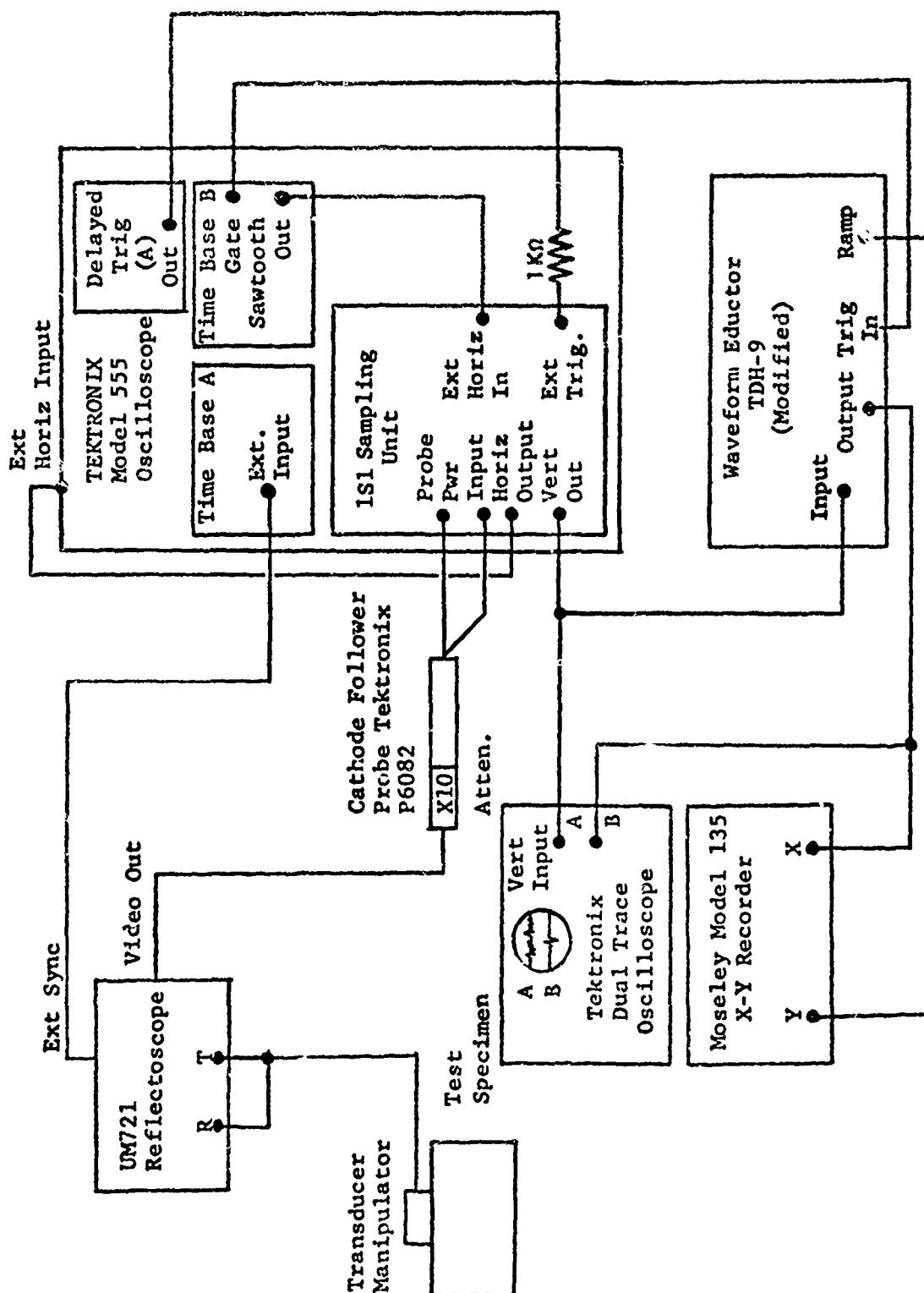


Figure 4.1 Signal Averaging System

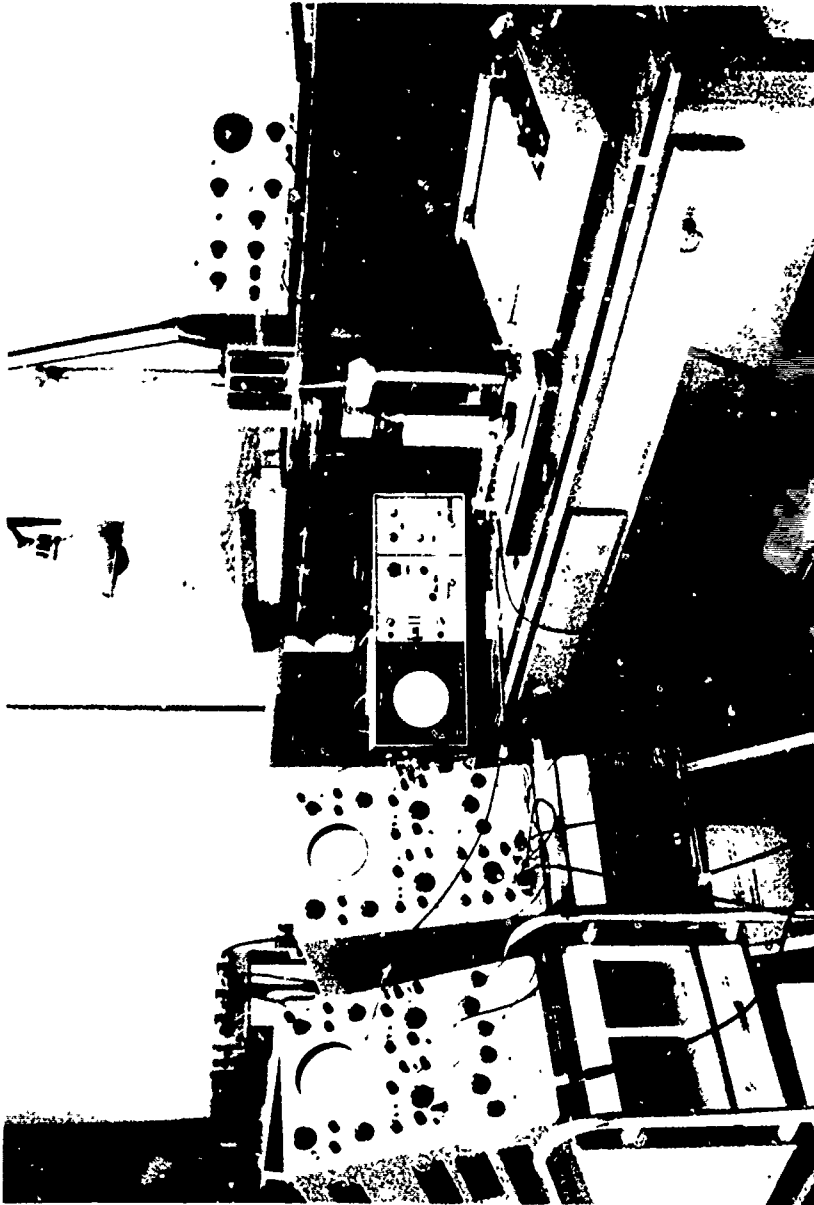


Figure 4.2 Laboratory Setup of Signal Averaging System

sampled waveform is divided into 100 equal segments (voltages) which are stored in a 100 capacitor memory network.

The cycle begins again with the transducer shifted to a new position over the test piece. This next sampled waveform is read into the capacitor memory network which reaches a state equivalent to the average of the input waveforms.

Any segment of the repetitively input waveforms which remains "in phase" (i.e., does not shift with respect to a fiducial trigger pulse) will approach a non-zero average value. Segments of the waveform which are affected by the transducer movement so as to shift in time are suppressed. That is, because of their quasi-random nature, they tend to average to zero.

The average of the waveforms is constantly displayed on one trace of a dual-trace scope, while the other trace displays the changing waveforms contribution to the average. A permanent record of the averaged waveform is obtained by switching the Waveform Eductor from the ANALYZE AND READOUT mode to the READOUT ONLY mode. The average waveform stored in the capacitor memory is read out at any desired rate into the X-Y recorder or other data recording device.

Other features of the Waveform Eductor are variable delay and sweep rates which allow any portion of the ultrasonic return to be analyzed in detail. Also, the characteristic time constant ( $T_c$ ) of the integrating circuitry can be varied for optimum signal buildup and noise suppression. The TDH-9 used in this system can vary  $T_c$  from 0.05 sec. to 5 sec. (Standard  $T_c$  is 5 sec. to 500 sec.)

#### 4.1.3 System Operation

##### Transducer Manipulation

The manner in which ultrasonic waveforms should be collected for efficient signal averaging required some foreknowledge of the variation of grain noise with transducer motion. A measure of this variation is the cross correlation factor of two waveforms obtained at different positions. Pertinent results of such cross-correlation studies of grain noise vs. transducer displacement are given in Appendix B of reference 6. These results indicated that a greater number

of waveforms can be obtained for averaging by rotating the transducer about its axial centerline than by translation along the surface of the test item. In this manner, the desired perturbation of the ultrasound-grain structure interactions is accomplished by the asymmetry of the pressure amplitude profile of real transducers.

At the same time, the defect remains illuminated by the transducer beam and contributes higher amplitude reflections to each waveform than if the transducer were to be translated over the defect.

#### Operational Procedure:

The process of applying the signal averaging system to diffusion bond inspection begins with establishing the geometry shown in Figure 4.3a. The transducer is held in contact with the top surface of the specimen by a metal bellows-degree wheel arrangement, (see Figure 4.3ab) which minimizes coupling variations and allows the transducer to be rotated incrementally about its longitudinal axis.

The specimen is interrogated at five different locations within the bond plane (locations 1, 1a, 2, 2a and 3). The ultrasonic return utilized for signal averaging is gated to correspond to a .6" band of material around the bond plane.

At each location a "single return" waveform is first recorded. This waveform is constructed by the sampling oscilloscope from 200 real time pulses generated by the UM 721 Reflectoscope operating at a repetition rate of 300 Hz. Five such wave forms as required for waveform build up within the Waveform Eductor (set at a characteristic time constant of .5 sec). This "single return" waveform is then recorded by the X-Y plotter and represents a conventional pulse-echo record. Next, signal averaging of 24 waveforms is accomplished by rotating the transducer through  $360^{\circ}$  in  $15^{\circ}$  increments. At each azimuthal increment, the waveform is built up as before from five "sampled" waveforms. At the end of each complete revolution, the averaged waveform is read out of the Waveform Eductor and recorded by the X-Y plotter. This process is repeated for each location, the result being "single return" and signal averaged waveforms for each defect location (1, 2, and 3) and defect-free location (1a and 2a).

To obtain background waveforms representative of grain

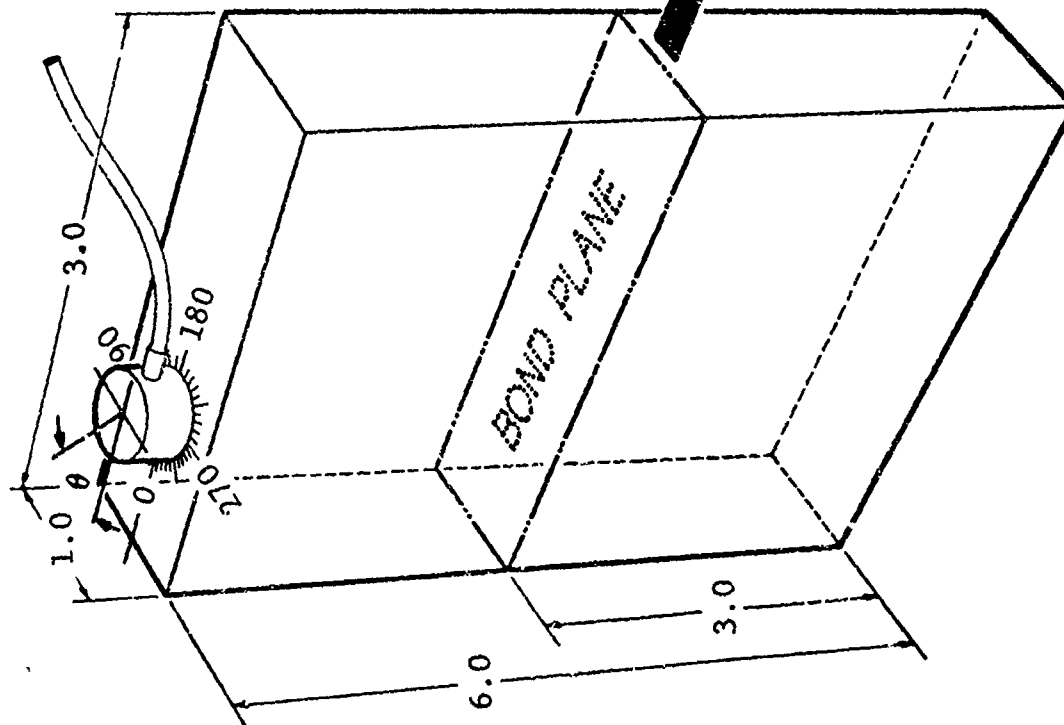


Figure 4.3a Location of Signal-Averaged Data Points on Diffusion Bonded Specimens

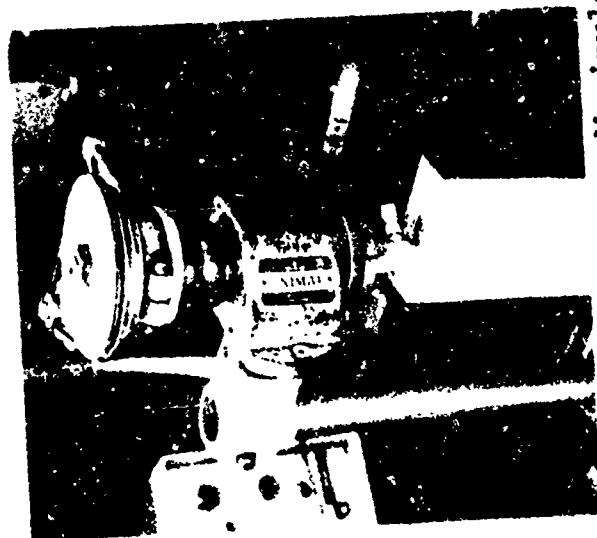


Figure 4.3b Transducer Manipulator

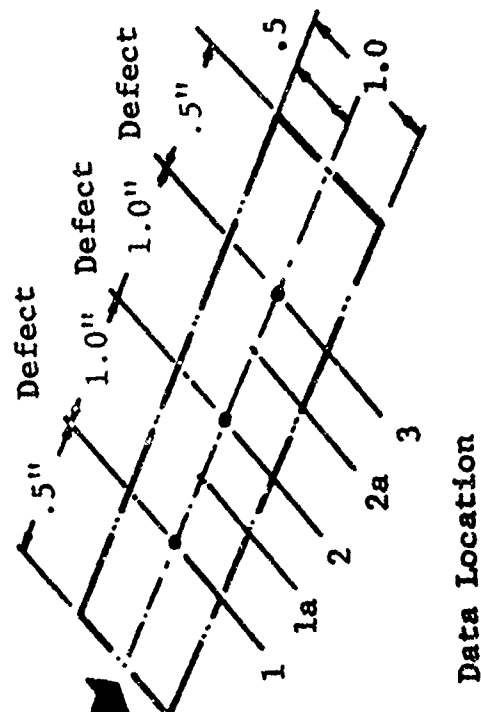


Figure 4.3a Location of Signal-Averaged Data Points on Diffusion Bonded Specimens

structure noise the waveform gate is moved to include .6" of material outside the bond plane at locations 1ab and 2ab.

Figure 4.4 shows (a) the real-time A-scan from the Reflectoscope with the response from a 3/64" flat-bottom hole (FBH) indicated; (b) the output of the sampling oscilloscope gated for the 3/64 FBH signal and (c) the output of the Waveform Eductor with a "single return" FBH.

## 4.2 Displacement and Angularization System

Discontinuities in angularized bond planes are not usually oriented parallel to the material top surface. In this case, the return signal in a pulse-echo system can be optimized by tilting the transmitting transducer with respect to the top surface such that the refracted pulse impinges on the maximum area of the discontinuity. A proposed system utilizing this refracted pulse-echo technique via a mechanically-oscillated transducer is described in Ref. 7.

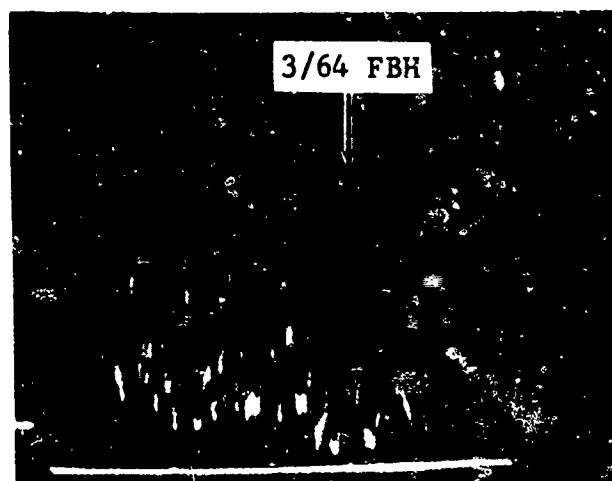
### 4.2.1 Multiple Transducer Array System

The "oscillation" of the transmitted wave can also be accomplished electronically using an array of multiple transducers. The system originally proposed for this program is schematically depicted in Figures 4.5 and 4.6. The cyclic output from a pulse-echo unit is distributed to each transducer in sequence by a gate and switching network. Only one transducer is pulsed at a time and the same transducer is used as a receiver during that cycle. Just prior to the next pulse from the pulse-echo unit, another transducer is switched into operation. This will continue until all the transducers have been pulsed and the data recorded. Then the cycle starts again and is repeated at a rate determined by the material thickness.

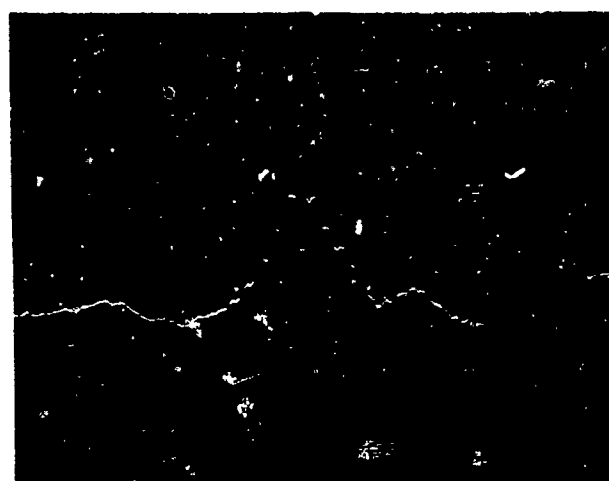
Upon detection of a flaw or defect, a signal from the event detector causes the pulse amplitude, depth of the defect signal, transducer output code, and X-Y coordinates to be printed out or input to a small computer. The transducer code indicates the angle of the transducer and thereby the orientation of the flaw.

After the above approach was proposed and shortly before contract go ahead, another AFML program was awarded to General Dynamics, Fort Worth Division, i.e. "Computer Automated Ultrasonic Inspection System for Aircraft Forgings," Contract

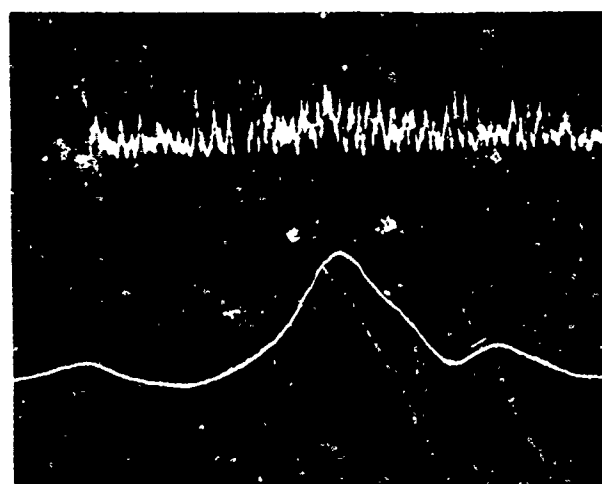




a) Reflectoscope



b) Sampling Oscilloscope



(timing trace)

c) Waveform Educator

Figure 4.4 Reflectoscope, Sampling Oscilloscope, and Waveform Educator Outputs

No. F33615-72-C-1328. As the two programs progressed, it became evident that the flexibility of the AFML Computer Automated Inspection System would allow it to perform the displaced and angularized diffusion bond plane inspection task more efficiently and with less technical risk than the multiple transducer system being developed.

The AFML Computer Automated Inspection System can generate a "synthetic transducer array", i.e. a single transducer oriented and interrogated at any desired number of angles with the local vertical as opposed to four separate transducers. This procedure eliminates the problems associated with variations in output amplitude and beam dispersion characteristics between separate transducers.

Other advantages are:

- Faster inspection due to the use of a PDP 11/45 computer as opposed to a HP 9820 Computing Calculator as originally proposed.
- More permanent record options (i.e., hardcopy maps, punched tape, disc storage as opposed to printed paper tape from the HP 9820).
- Better angular resolution in defect data, since variable tilt of a single transducer replaces the 4 discrete angles at which the separate transducers are aligned.

Consequently, the developmental effort was transferred from the multiple transducer system to application of the AFML Computer Automated Inspection System to inspection of displaced and angularized bond planes.

#### 4.2.2 Description of the AFML Computer-Automated Inspection System

The system was designed to inspect forgings of relatively complex geometries in the immersion reflection and Delta-Scan mode. The basic components are (a) a 6' x 4' x 3' immersion tank, (b) a five-axis scanner and transducer manipulator, (c) an ultrasonic test unit and (d) a computer for control and analysis.

### Computer and Ultrasonic Components

The system utilizes a PDP 11/45 general-purpose computer for real-time control, data acquisition, data processing, data recording, and flaw-data display of the ultrasonic inspection.

Figure 4.7 is a block diagram of the ultrasonic and computer components of the system. The ultrasonic unit consists of an Automation Industries Type UM 771 reflectoscope and special computer interface circuits in another chassis. This unit supplies electrical pulses at ultrasonic frequencies to the transmitting transducers and amplifies and processes the ultrasonic signals picked up by the receiving transducers. The signals are processed to separate the various reflections and convert them to signals which enter the computer via analog or digital inputs.

Any indication of anomalies above a predetermined threshold level of the incoming ultrasonic signals is detected by the computer and will be recorded as a flaw. The 5-axes coordinates of the scanner where the indication occurred will also be recorded along with other pertinent parameters.

In the standard reflection mode, the thickness of the test material and the depth of a flaw are determined by gates that are turned on by the front-surface-reflected signal and turned off by either a flaw or back surface signal.

The computer also controls the sensitivity setting on the ultrasonic equipment to compensate for transducer variations, equipment variations, and far-field effects. This operation provides equal sensitivity for detection of flaws located at different depths within the component and will minimize calibration and setup time. The computer also monitors the liquid coupling between the transducers and the component under inspection. Inspection does not commence until the computer verifies that sound energy is adequately coupled into the component.

After processing the information, the required outputs are displayed on the Tektronix Computer Terminal Display, Model 4010. The display can be hardcopied with the Tektronix Copier, Model 4601. These outputs typically included X, Y and Z coordinates, transducer rotate and tilt angles,

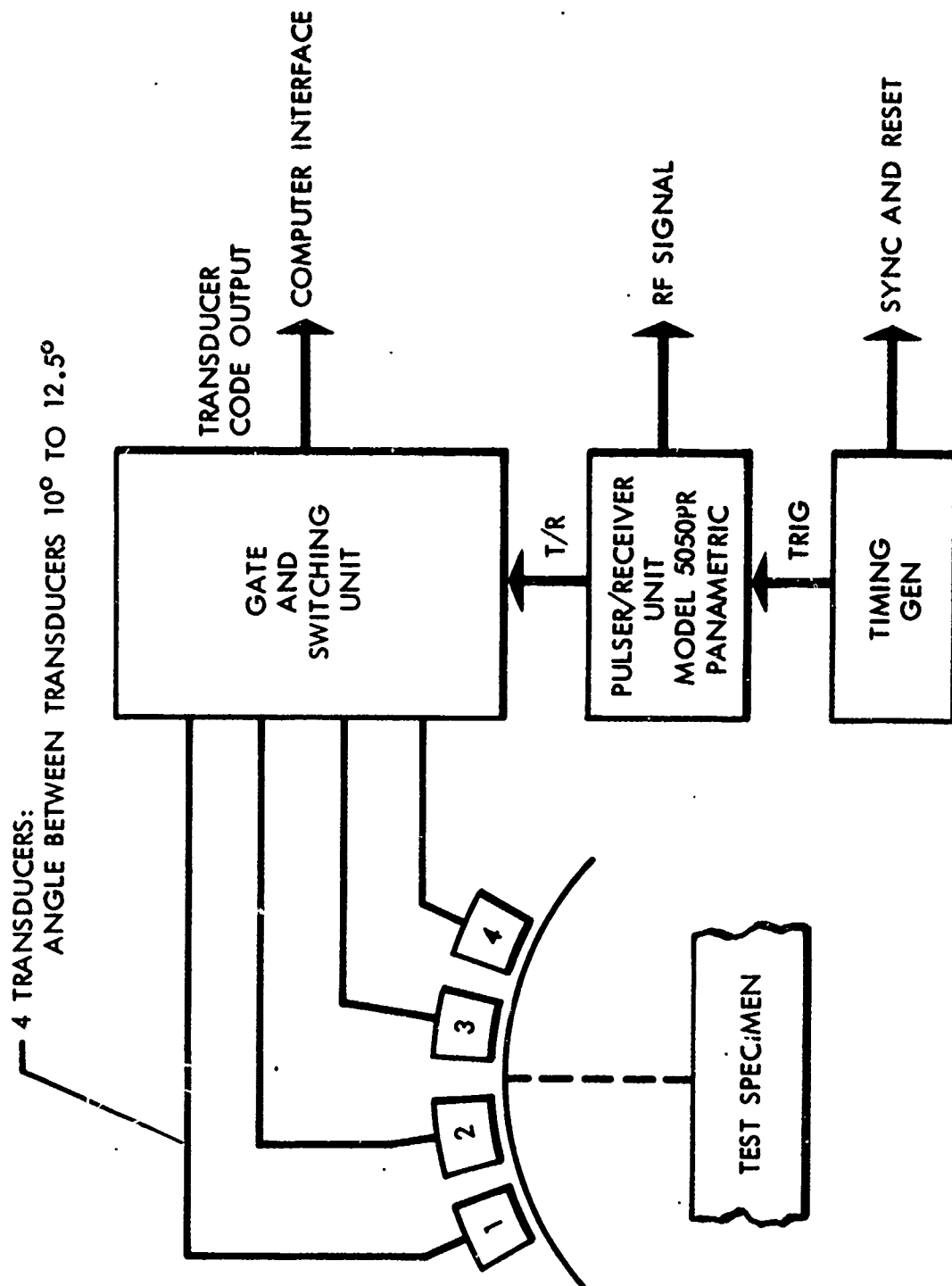
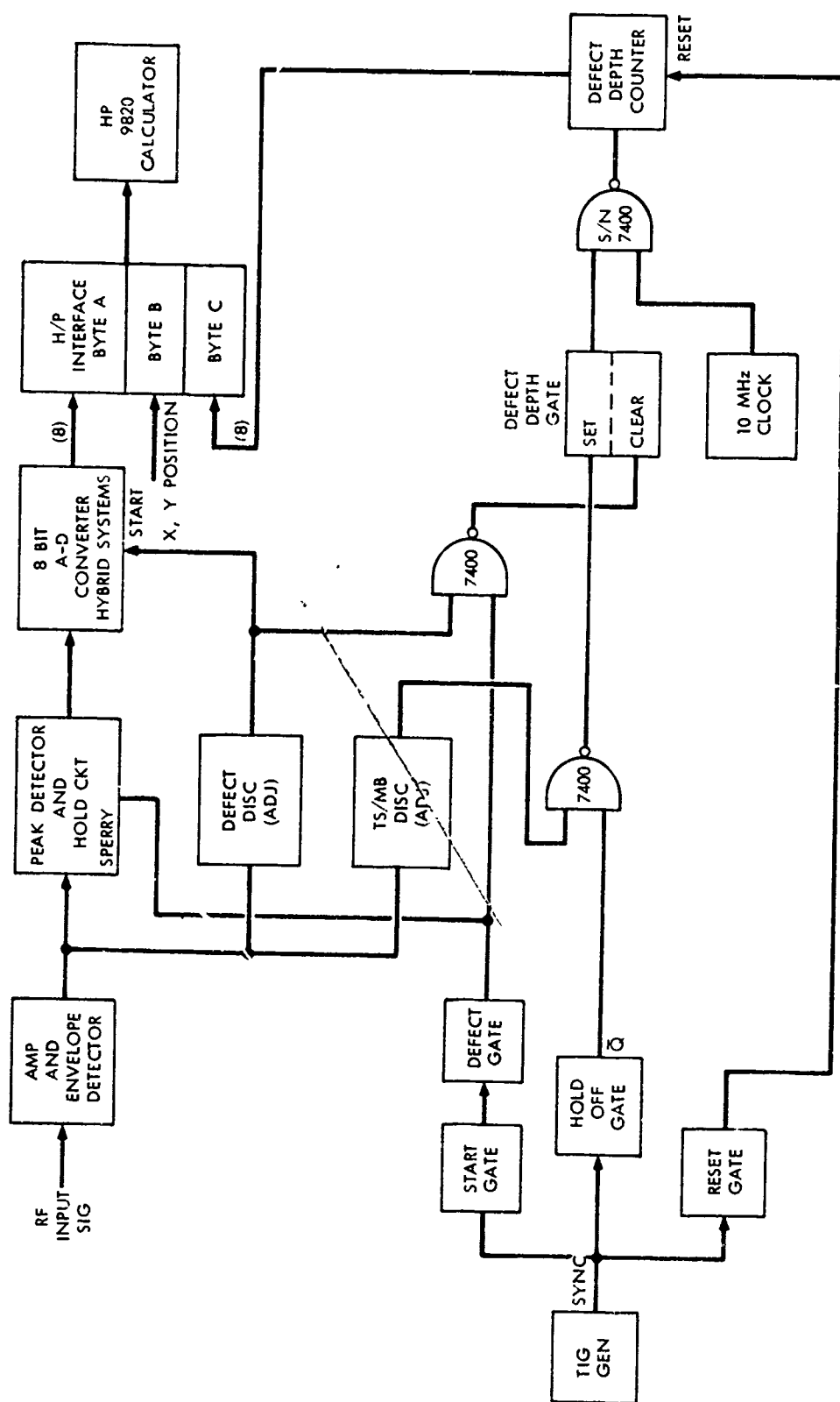
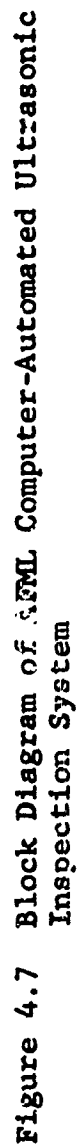


Figure 4.5 Proposed Displacement and Angularization System



**Figure 4.6 System Block Diagram**



flaw depth, flaw amplitude and part thickness.

#### X-Y Scanner and Transducer Manipulator System

The five-axes of motion are provided to align the transducer axis normal to an arbitrarily oriented surface. The motions are (a) translation in the X, Y and Z (vertical) directions, (b) rotation about the Z-axis and (c) tilt about an axis in the X-Y plane.

DC stepping motors drive all five axes and digital position encoders provide location data. The X and Y drive motors may be controlled in manual, automatic, or computer modes. The Z, Rotate and Tilt motions may be commanded manually or automatically by closed-loop feedback servo-systems. These systems control standoff distance and normality of the transducers with respect to the part surface.

Figure 4.8 is a schematic diagram of the X-Y scanner and transducer manipulator electronics showing the interaction between scanner and computer through the control console.

Figure 4.9 is a photograph of the AFML Computer-Automated Ultrasonic Inspection System. Figure 4.10 shows the transducer gimbal assembly which coordinates transducer tilt with an auxiliary translation of the transducer yoke. This translation insures that the longitudinal axis of the transducer intercepts the Z-axis at the part surface. Thus the X-Y coordinates of the Z-axis will be those of the point where ultrasound enters the specimen.

#### System Operation for Displaced and Angularized Bond Planes

Several combinations of scan, index and transducer tilt exist for performing the desired inspection. These include:

1. Increment in scan direction, tilt from  $-\theta$  to  $+\theta$ , increment in scan direction, tilt from  $+\theta$  to  $-\theta$ , etc. Index after scan is complete and reverse scan direction.
2. Scan one line with tilt angle fixed at  $-\theta$ , increment tilt angle, reverse scan over same line, increment tilt angle, etc. Index to next scan

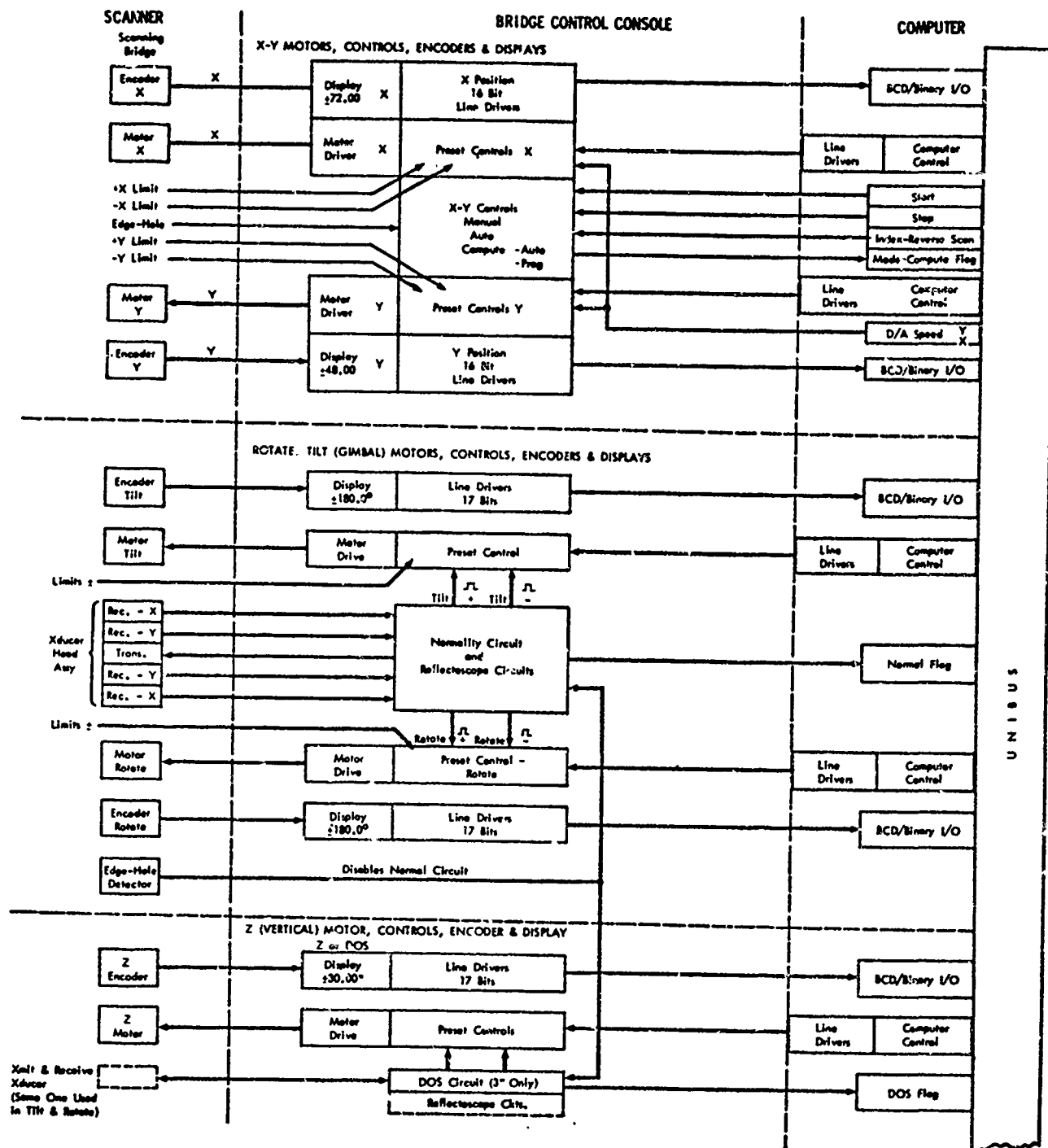


Figure 4.8 Block Diagram of Scanner System



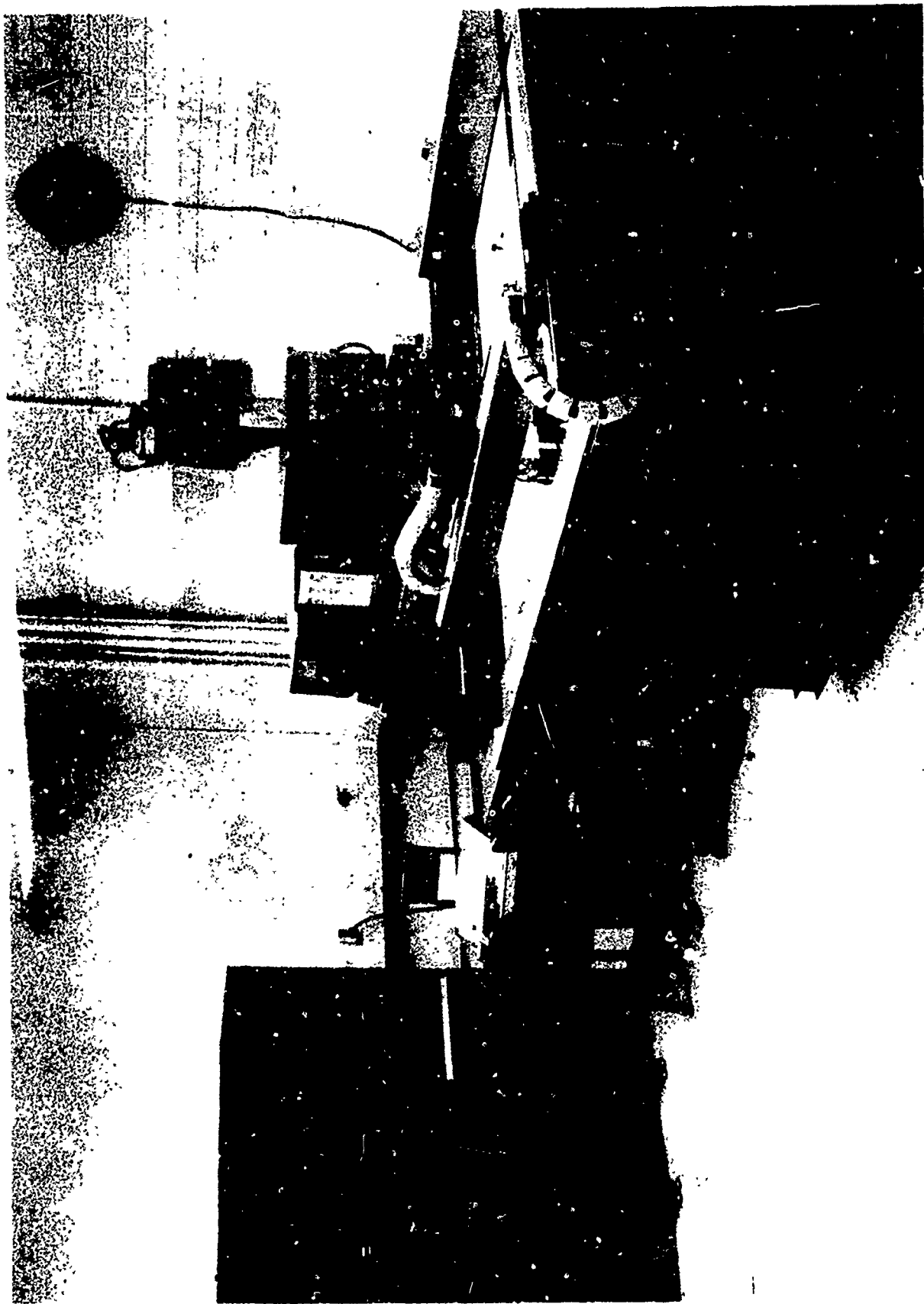


Figure 4.9 AFML Computer-Automated Ultrasonic Inspection System

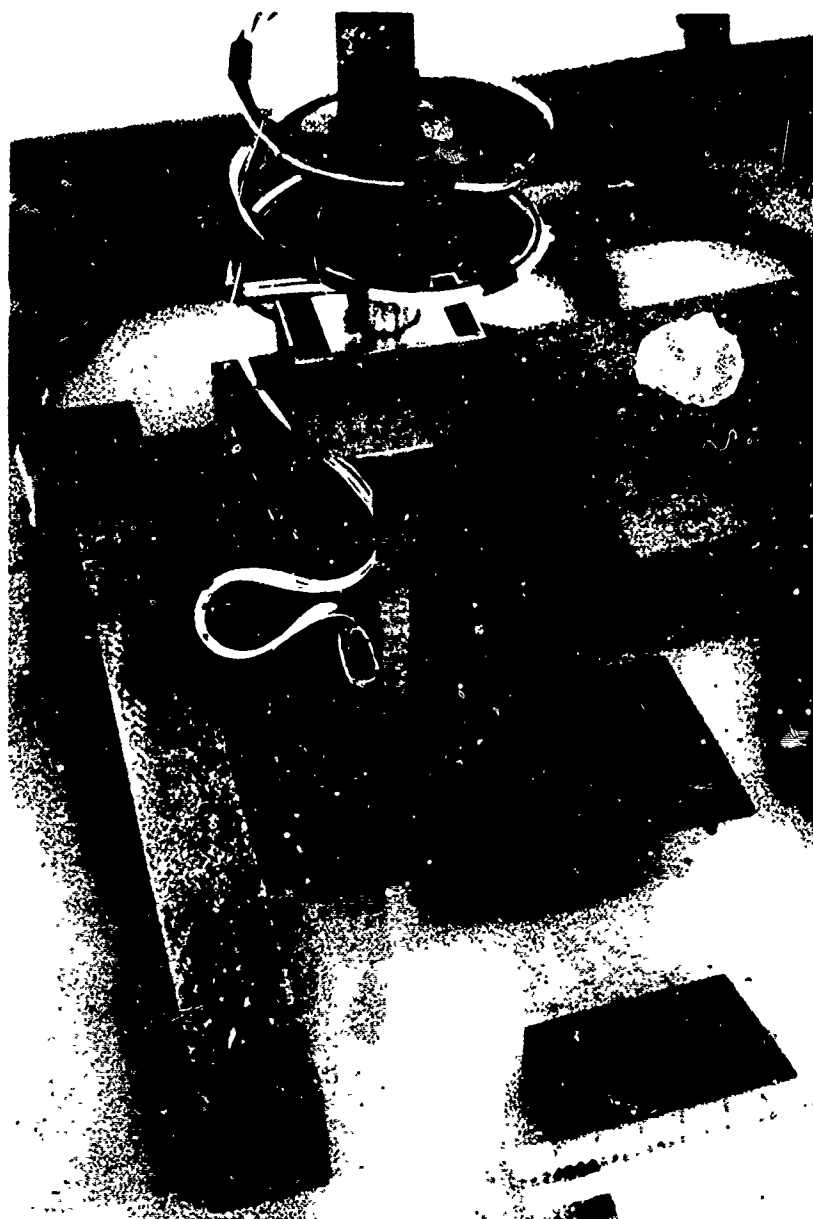


Figure 4.10 Transducer Gimbal Assembly

line after tilt angle reaches  $+\theta$ .

3. Scan and index over total area with tilt angle fixed at  $-\theta$ , increment tilt angle, repeat scan and index over total area, increment tilt angle, etc.

The last procedure has been termed the "variable-tilt/multiple scan" mode. A preliminary trial in this mode was accomplished at 5 MHz on an aluminum alloy reference block shown in Figure 4.11. The specimen contains 3/64 and 5/64 flat bottom holes (FBH) oriented at  $36^\circ$  from the vertical and a 5/64 FBH aligned with the vertical. Sensitivity of the UM 771 Reflectoscope was set by the computer-controlled attenuator to produce 80% screen saturation from a vertical 5/64 FBH 3 inches from the top surface with the transducer also vertical. Signal level was set at 20% screen saturation. Scans were made at transducer inclinations of  $0^\circ$ ,  $2^\circ$ ,  $4^\circ$ ,  $6^\circ$ , and  $8^\circ$ . The resulting records are shown in Figures 4.12 and 4.13.

As expected, response from the vertical hole decreases while that from the off-vertical holes increases as the transducer tilt angle increases. In Figure 4.12, response from the vertical hole disappears completely at an attenuation setting of 37 dB. The vertical hole response was regained at  $6^\circ$  and  $8^\circ$  by reducing the reflectoscope attenuation setting.

The ability of the AFML Computer Automated Inspection System to operate in the variable-tilt/multiple scan mode with minimum hardware and software modifications verified its suitability for the large diffusion bonded structure evaluation.

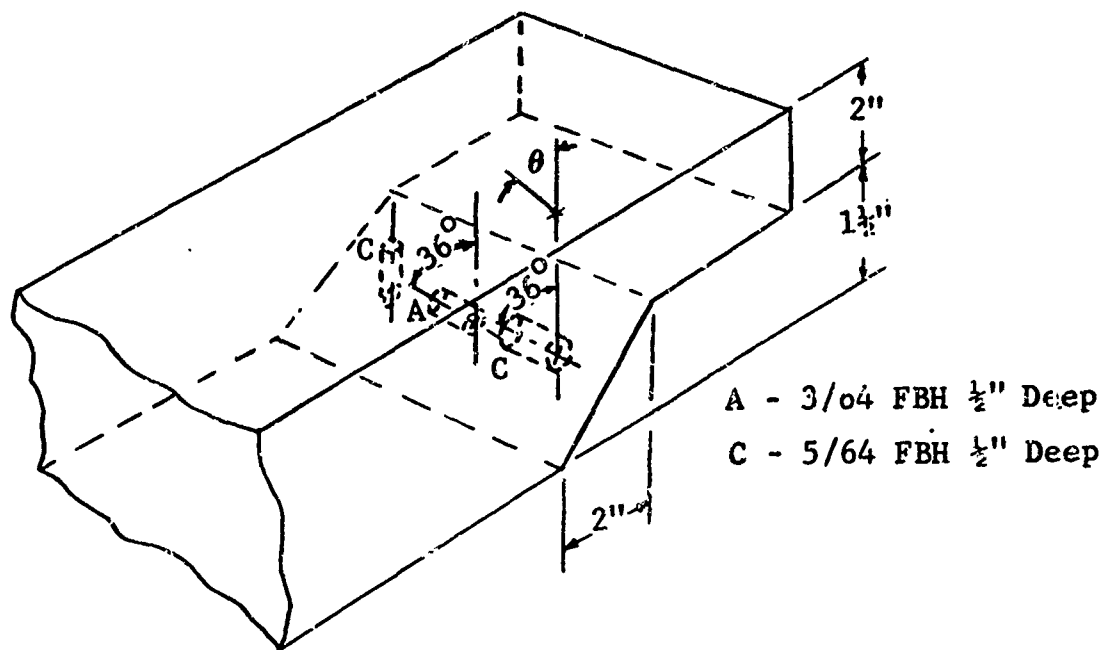


Figure 4.11 Geometry of Reference Block

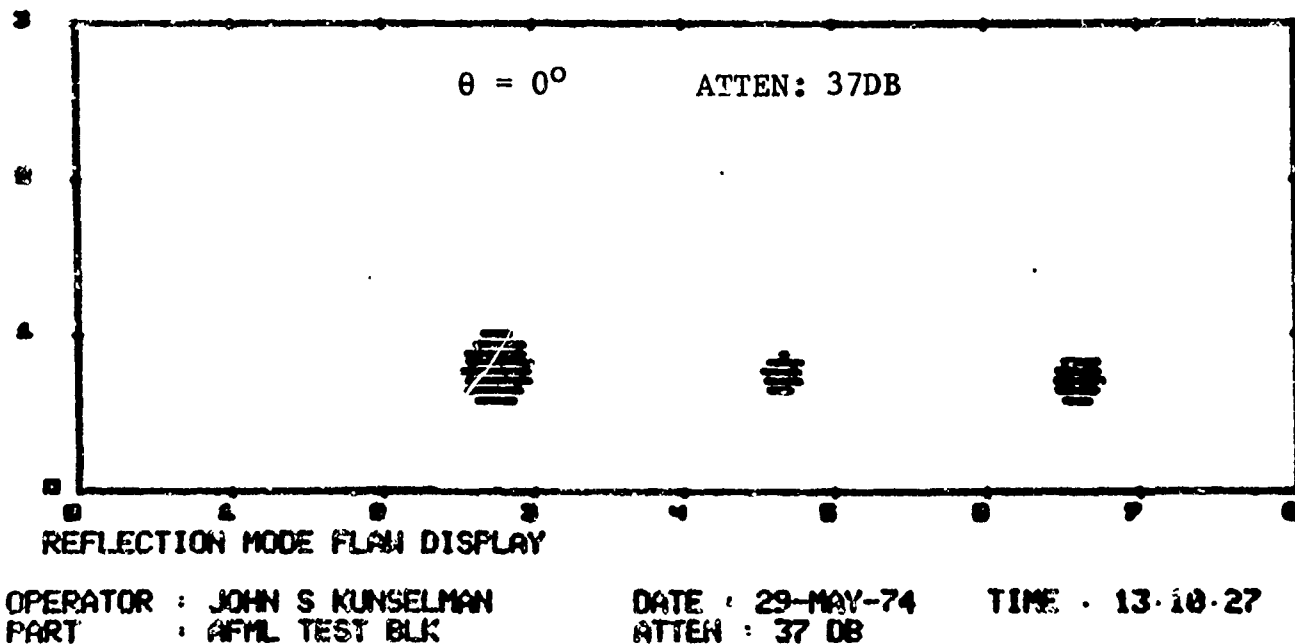
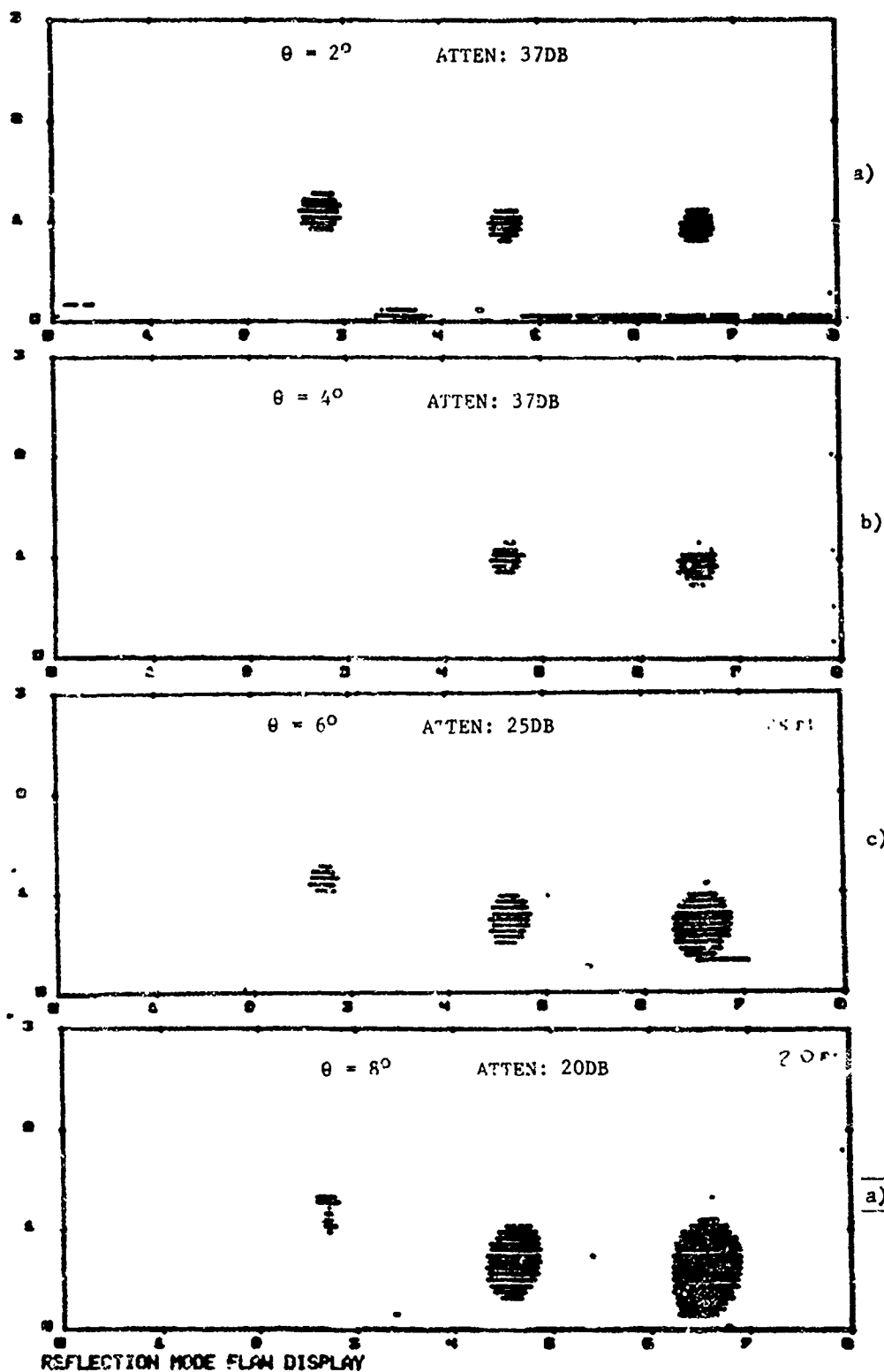


Figure 4.12 Pulse-Echo Record of Reference Block at  $0^\circ$  Transducer Inclination



OPERATOR : JOHN S KUNSELMAN  
 PART : APRIL TEST BLK  
 DATE : 29-MAY-74  
 TIME : 13:10 27  
 ATTEN : 08

Figure 4.13 Pulse-Echo Records of Reference Block at  $2^\circ$ ,  $4^\circ$ ,  $6^\circ$  and  $8^\circ$  Transducer Inclinations

## 5. FEASIBILITY STUDIES

### 5.1 Acoustic Emission Monitoring

The goal of this study was to determine whether the presence of a diffusion bond deficiency could be determined by detecting the acoustic energy emitted by the generation of a deficiency-initiated free surface in response to an applied external load. Ideally, the applied load will not result in plastic strains thereby allowing this evaluation technique to be considered non-destructive.

In this study, acoustic emission monitoring was performed on selected tensile specimens pulled to failure. Thus, in consonance with the above goal, feasibility will be determined by emphasis on the data within the elastic range.

#### 5.1.1 Experimental Setup and Procedures

Phase I - Experimental Setup - Figure 5.1 is a block diagram of the experimental setup. Some changes were made in the mounting method of the acoustic emission sensor during the second phase to obtain better noise rejection.

One receiver transducer, Gulton HST-41, lead-zirconate-titanate plates, 1.27 mm thick, polarized in the thickness direction, and cut to 5 x 5-mm square pieces, was attached to a steel standoff which was machined to an inside radius equal to the outside radius of the test specimen. Silicone high-vacuum grease was used as a couplant between the transducer and the standoff. The standoff was also coupled to the test specimen with the silicone grease. This sensor arrangement was clamped to the test specimen with a Teflon-insulated clamp. Two additional transducers were magnetically mounted on the specimen loading grips for rejection of noise generated in this area and signals originating from the loading machine.

Phase II - During this phase, the diffusion bonded specimens were monitored for acoustic emissions. Two modifications were made to the experimental setup to obtain better noise rejection. These modifications are illustrated in Figure 5.2.

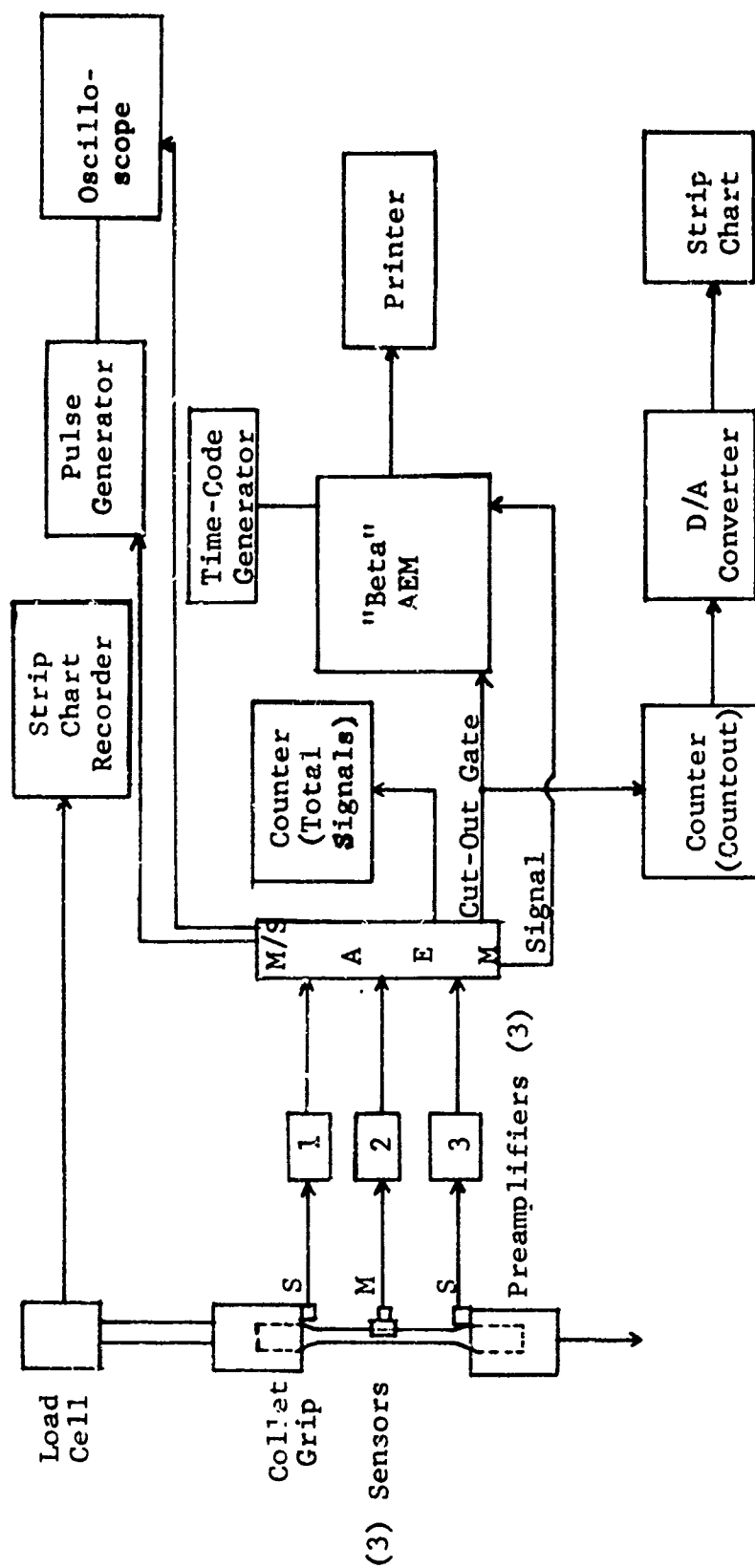
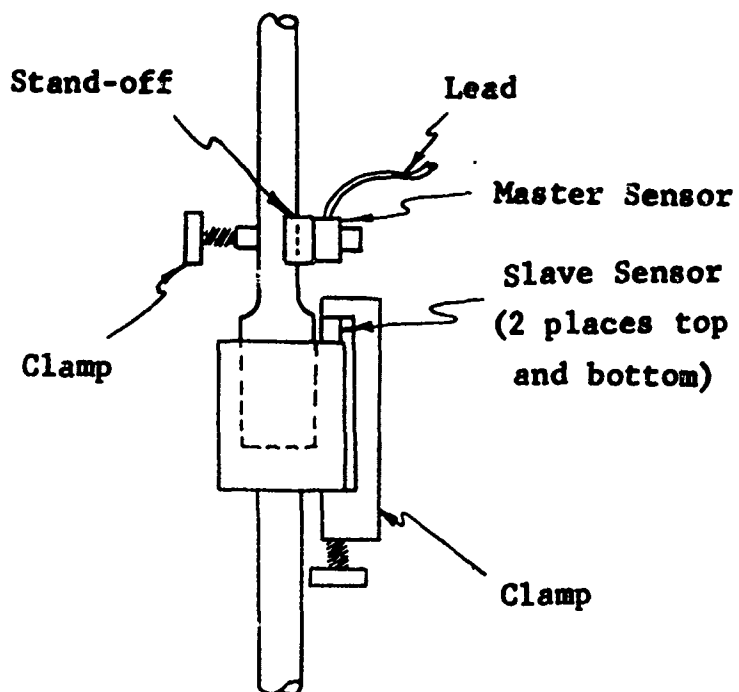


Figure 5.1 Block Diagram of Experiment Setup for Acoustic Emission Monitoring



**Figure 5.2 Sensor Mounting for Phase II Test**



Modification #1 - The magnetic mounted sensors (slave sensors) were removed from the specimen grips and replaced with sensors which were bonded at a thin aluminum plated standoff. The aluminum plates were machined on one end to encircle one-half the circumference of the specimen just below and above the grips. These sensor assemblies were clamped to the specimen grips with the standoff in contact with the specimen (see Figure 5.2).

Modification #2 - To eliminate the possibility of erroneous signals originating at the interface of the specimen and the master-sensor assembly during the elongation of the specimen, this sensor assembly was mounted below the vertical centerline of the specimen at the beginning of the tapered section (see Figure 5.2).

The signals from each transducer were amplified by a modified Arvee S-30 wide-band preamplifier. The preamplifier had a low frequency cutoff at 100 KHz.

The preamplified acoustic signals were fed into a Master-Slave acoustic signal processor. The Master-Slave (M/S) unit receives signals from multiple master and slave sensors and performs a logic processing such that a count output is produced only when a master sensor receives an acoustic signal prior to any of the slave sensors. A type of spatial filtration is performed to eliminate acoustic signals originating in the area of the slave sensor.

When the acoustic emission processor produced a countout signal, it was accumulated on a HP 5216A counter and converted from digital to analog by a HP 58A D/A converter for recording on a strip-chart recorder.

The signals from the Master sensor of the M/S unit are fed into the "Beta" AEM unit which is gated by the countout from the M/S signal processor to eliminate the contamination of the data by noise. The Beta-AEM unit measures the amplitude distribution of acoustic emission signals in real-time. It determines the peak amplitude of each acoustic event and prints out the accumulated results along with the time from the time-code generator. The "Beta" AEM unit was set to print each 5-sec period and/or when 50 counts have been accumulated.

The total signals were counted on a HP 5216 counter. The total signal count consists of the signals from all sensors and may be compared with the countout to determine the noise rejection level by the M/S AEM unit.

A homemade pulser and a 555 Tektronic oscilloscope were used to set the sensitivity of the M/S and Beta AE units and to check the overall operation of the system.

The threshold of the AEM units was set at 10 MV and the gain of the preamplifier was 140, giving a system sensitivity of 71.4 MV referred to the sensor.

Experimental Procedure - Testing of tensile specimens selected for this AEM study was performed in the Applied Research Laboratory. The tensile test machine employed for loading the specimens to fracture was a Model T1-C Instron calibrated to 10,000 lbs. Collet-type grips were used for gripping the tensile specimens during the loading sequence.

Standard ASTM procedures regarding strain-rate pacing, extensometer measurements, and selection of 0.2% offset yield points of tensile specimens could not be followed during the tensile testing due to the transducer locations in the gage length section of the test specimens. Placement of the three AEM transducers (2 slaves and 1 master) did not allow sufficient space for the attachment of an extensometer. Therefore, the specimens were tested to fracture under the following conditions:

- (1) A constant crosshead speed of 0.05 in./min was used throughout the loading sequence.
- (2) Elongation percentages were determined from gage marks (1.5 in. apart) placed on the test specimens.
- (3) The 0.2% offset yield points were determined by assignment of an effective gage-length value of 1.50 in. and the following relationship to chart travel, crosshead speed, etc.:

$$\text{Chart Travel} = \frac{0.002 \times \text{Chart Speed} \times \text{Effective Gage Length}}{\text{Crosshead Speed}}$$

where: Chart speed was 2 in./min,  
Crosshead speed was 0.05 in./min,  
Effective gage length was 1.50 in.

Thereby giving a value of 0.06 in. displacement in chart travel for constructing a line parallel to the slope of the Instron curve in the elastic region. The point of intersection of this line with load in the "knee" of the Instron curve was taken as the 0.2% offset yield point.

Bench measurement data used for calculating cross-sectional area and percent elongation were obtained with a Scherr-Tumico Model P-1500 optical comparator.

Calibration of the Instron machine was performed prior to testing of each tensile specimen. After the test setup was completed and the instruments were calibrated, the specimen was first cycled to the 100 pounds to set the specimen grips. Immediately following the 100-lb load level, the specimen was tensile loaded at constant crosshead speed of 0.05 in./min until complete failure occurred. The data were recorded continuously throughout this phase of the test.

The acoustic emission monitoring of these specimens was accomplished in real time. The data obtained were the summation of acoustic emission events, the amplitude distributions of these events, and the summation of these events plus acoustic noise sensed by all transducers.

#### 5.1.2 Results

Cumulative Acoustic Emissions - The cumulative numbers of acoustic emissions detected by the Master/Slave unit for each specimen are plotted against time. The load levels are also plotted with the same time scale.

Amplitude Distribution of Acoustic Emission Signals - The amplitude distribution of the acoustic emission signals from all specimens was obtained. These distributions are presented in log-cumulative form. The quantity plotted in these figures is the cumulative number, in a logarithmic scale of emission events of amplitudes greater than a given value. In the same logarithmic scale, data for three time-load intervals are plotted separately to show the shift of the distribution with time intervals. Those intervals are (a) below the 0.2% offset yield point, (b) the yield period, and (c) the final five seconds, including the event leading directly to the failure.

The parent material specimens tested during this study are listed in Table 5-1.

As-Received Material Specimens - Specimens D1-2, Y1A-3, and Z1-5 were from as-received material. The cumulative numbers of acoustic emissions processed by the Master/Slave unit from these specimens are plotted in Figures 5.3 through 5.5. The acoustic emissions from Specimen Y1A-3 which were observed during the first 1.75 minutes were from noise signals originating from slippage of the specimen's grip. This slippage is also indicated by the load curve in the first minute of the loading period. The cumulative number of events from Specimen Y1A-3 during the remaining loading to failure is very similar to those from Specimen D1-2 for the same period.

The cumulative number of acoustic emissions detected from Specimen Z1-5 is much greater than from Specimens Y1A-3 and D1-2. The greater number of these events occurred during the yielding of the specimen. Since this specimen has the same grain orientation as D1-2, there is only one reason for the large number of emissions. That reason is that the major portion of these emissions was generated by rubbing between the sensor steel standoff and the specimen during the elongation period of Specimen Z1-5.

The amplitude distribution of the acoustic emission signals from Specimen D1-2, Y1A-3, and Z1-5 is presented in Figures 5.6 through 5.8. These curves show that all of the acoustic emission signals which occurred prior to yield point on the load curve were of low amplitude (6-12 dB) which is in the amplitude range of acoustic signal from rubbing between metals. As shown in the acoustic emission cumulative curves, Specimen Y1A-3 test produced a larger number of these small amplitude signals.

Comparison of the amplitude distribution of the acoustic emission events occurring during the yielding of these specimens (Figures 5.6 through 5.8) shows that there is one medium amplitude signal during this period from all specimens. However, specimen Z1-5 produced a great number of signals in the small amplitude range (6 to 12 dB) indicating that most of these signals for specimen Z1-5 were generated by slippage between the sensor standoff and the specimen.

Table 5.1

TENSILE PROPERTIES OF ANNEALED Ti-6Al-4V PLATE,  
1" THICK

Condition	Grain Direction	Specimen Number	TYS KSI	UTS KSI	Elong. % in 1.5"	R.A. %
As-Received	L	Y1A-3	132.7	140.1	12.0	25.2
	T	Z1-5	130.2	136.4	11.5	24.3
Heat-Cycled 6 Hrs @ 1700°F	L	A2-3	126.6	134.5	12.5	27.5
		B2-3	125.4	135.3	13.1	27.5
	T	D1-2	129.8	140.3	14.0	25.7
		D2-1	122.6	134.3	13.3	28.7
Heat-Cycled 6 Hrs @ 1735°F	T	E1-2	125.6	137.6	12.7	27.4
Heat-Cycled 6 Hrs @ 1775°F	T	F1-1	120.4	133.7	13.6	25.6

Parent Material: As-Received, Perpendicular to RD

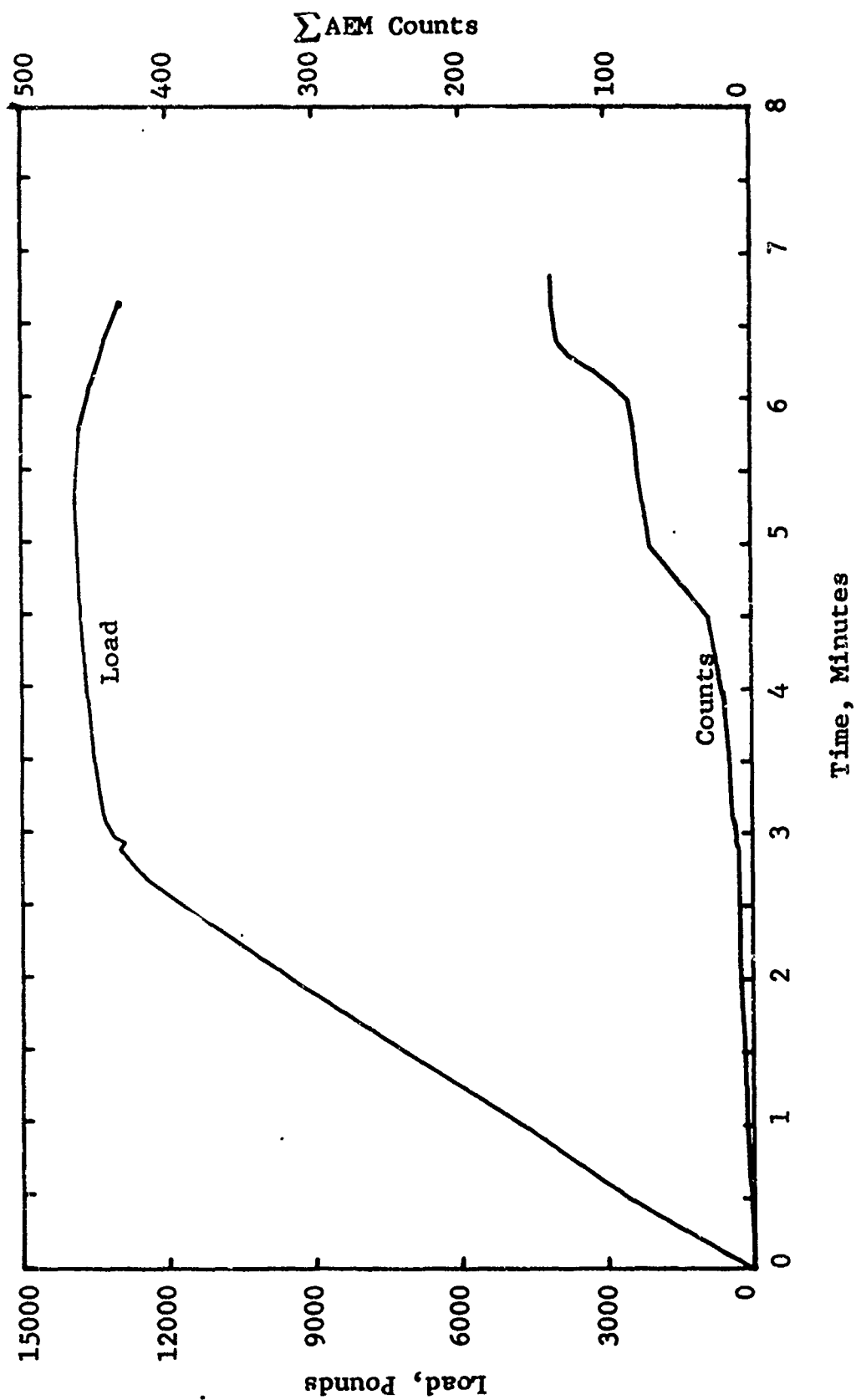


Figure 5.3 AEM Characteristics of Tensile Specimen D1-2

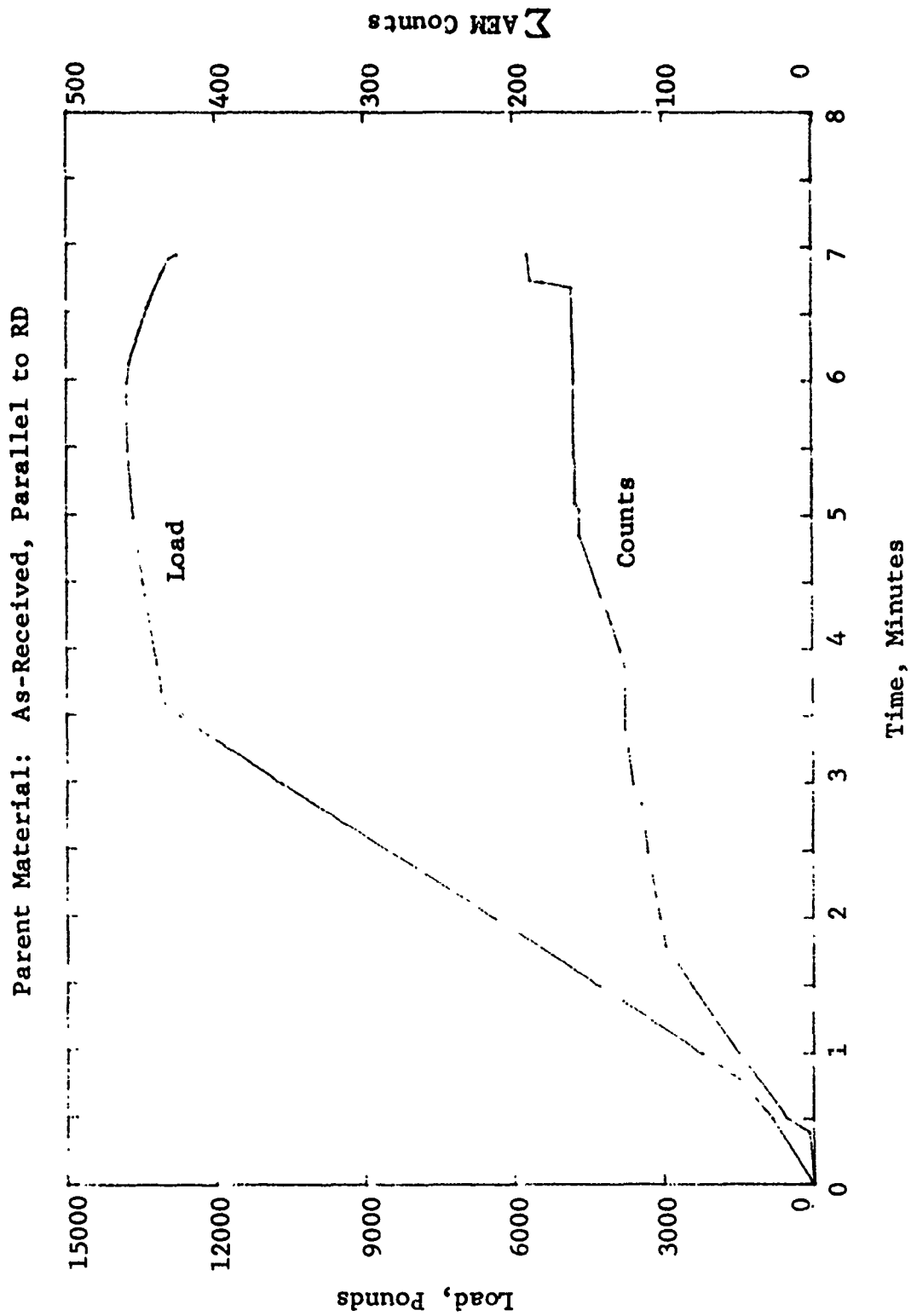


Figure 5.4 AEM Characteristics of Tensile Specimen YLA-3

Parent Material: As-Received, Perpendicular to RD

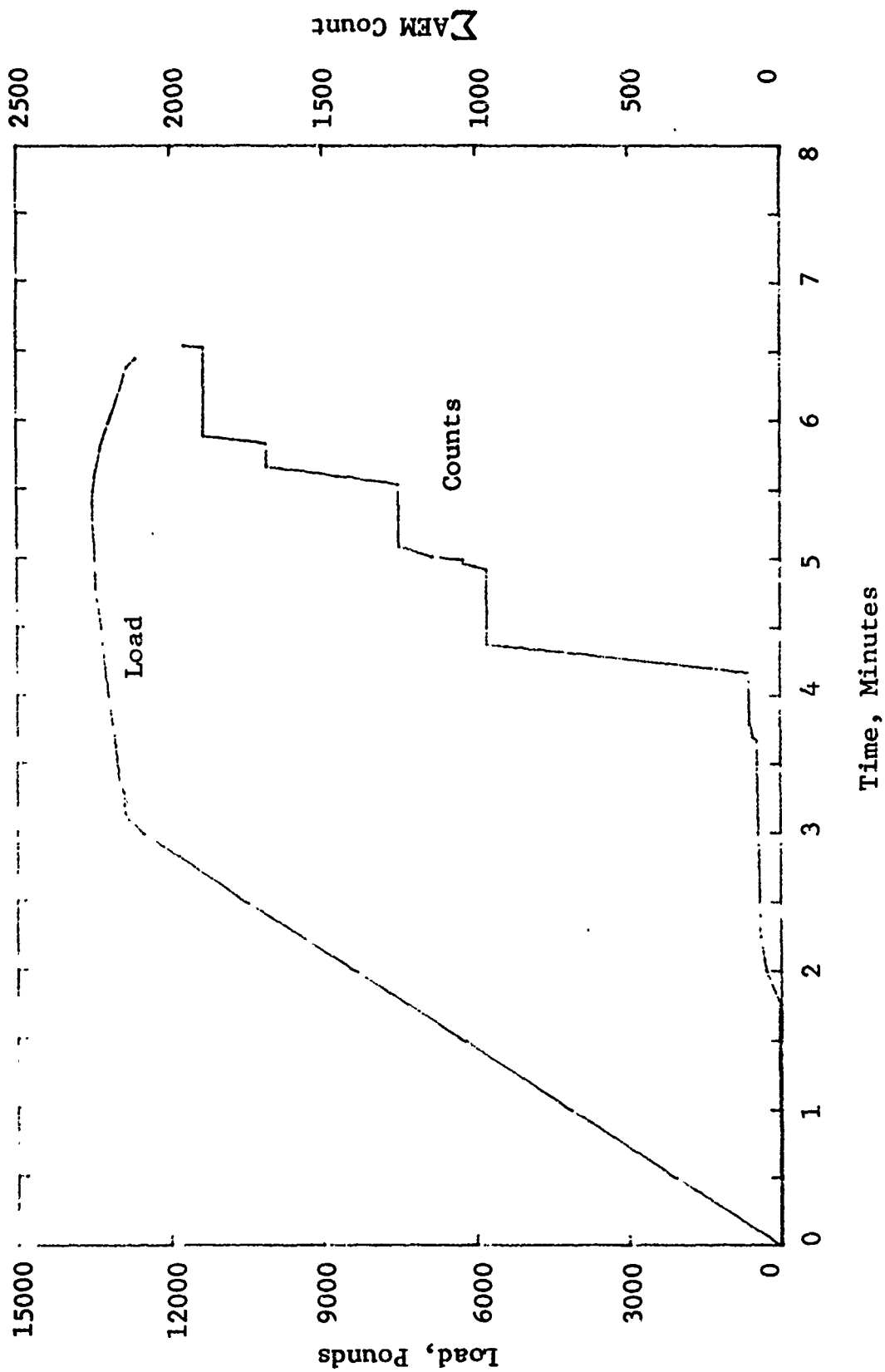


Figure 5.5 AEM Characteristics of Tensile Specimen Z1-5



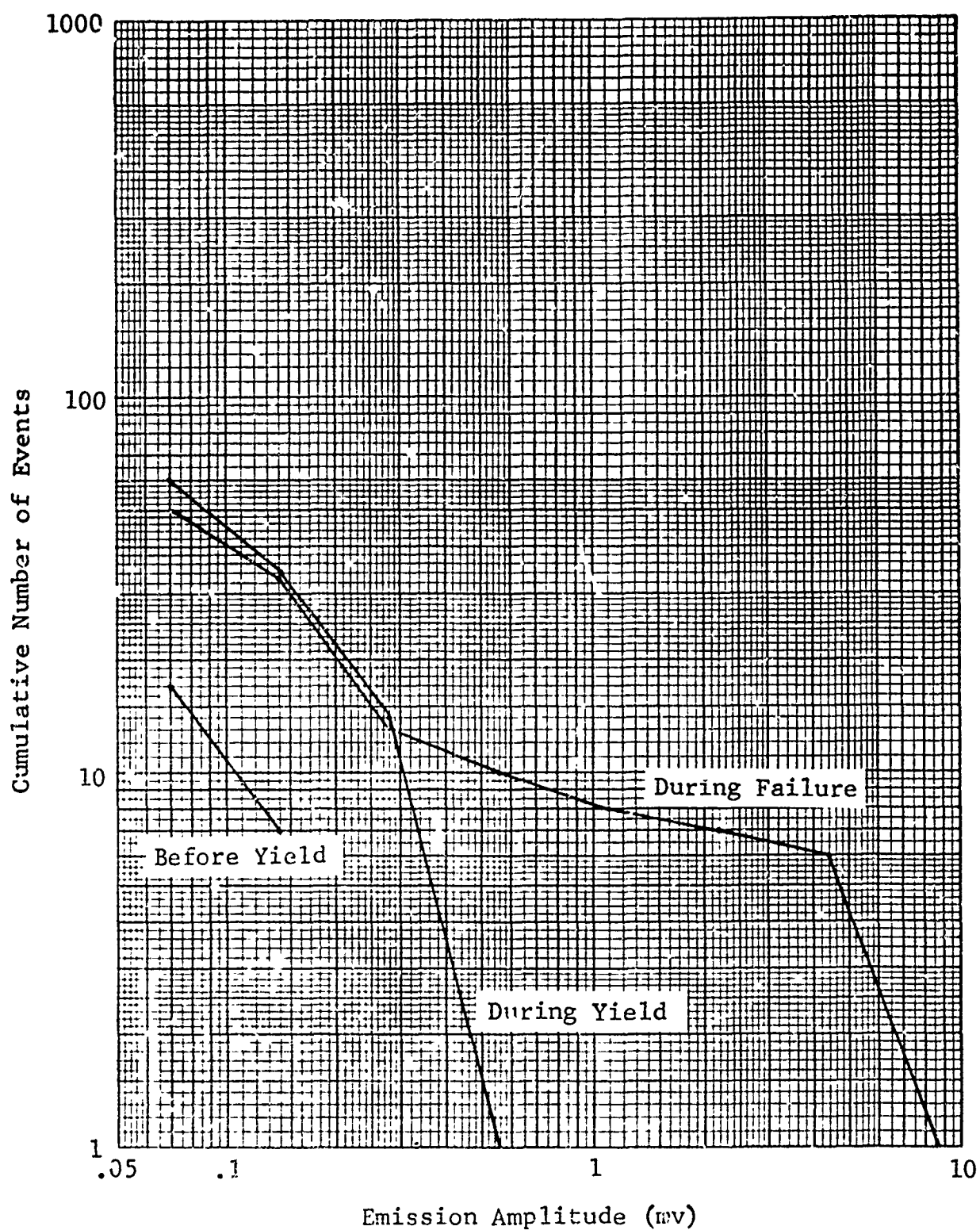


Figure 5.6 Amplitude Distribution of Emission Signals for Specimen D1-2

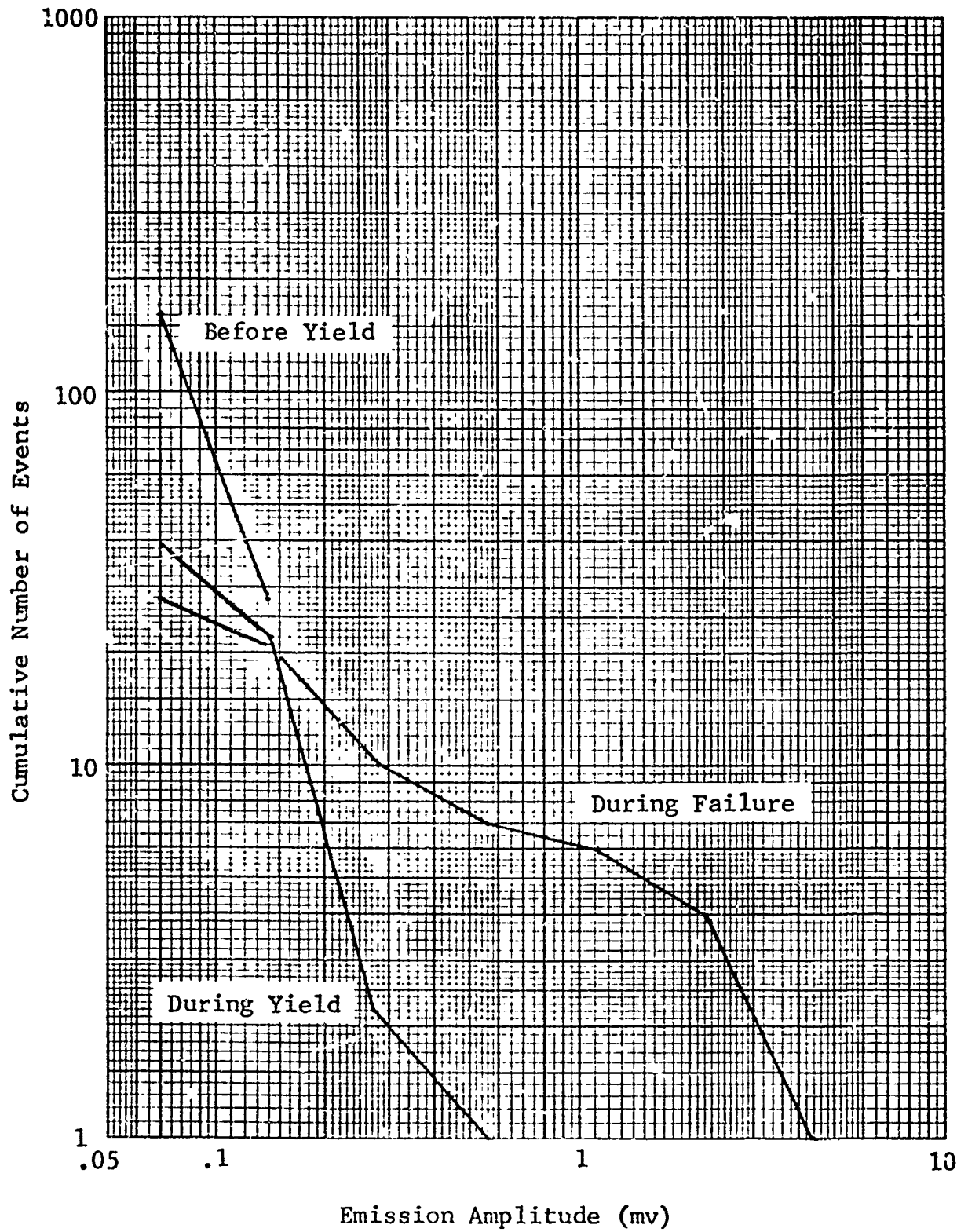


Figure 5.7 Amplitude Distribution of Emission Signals for Specimen Y1A-7

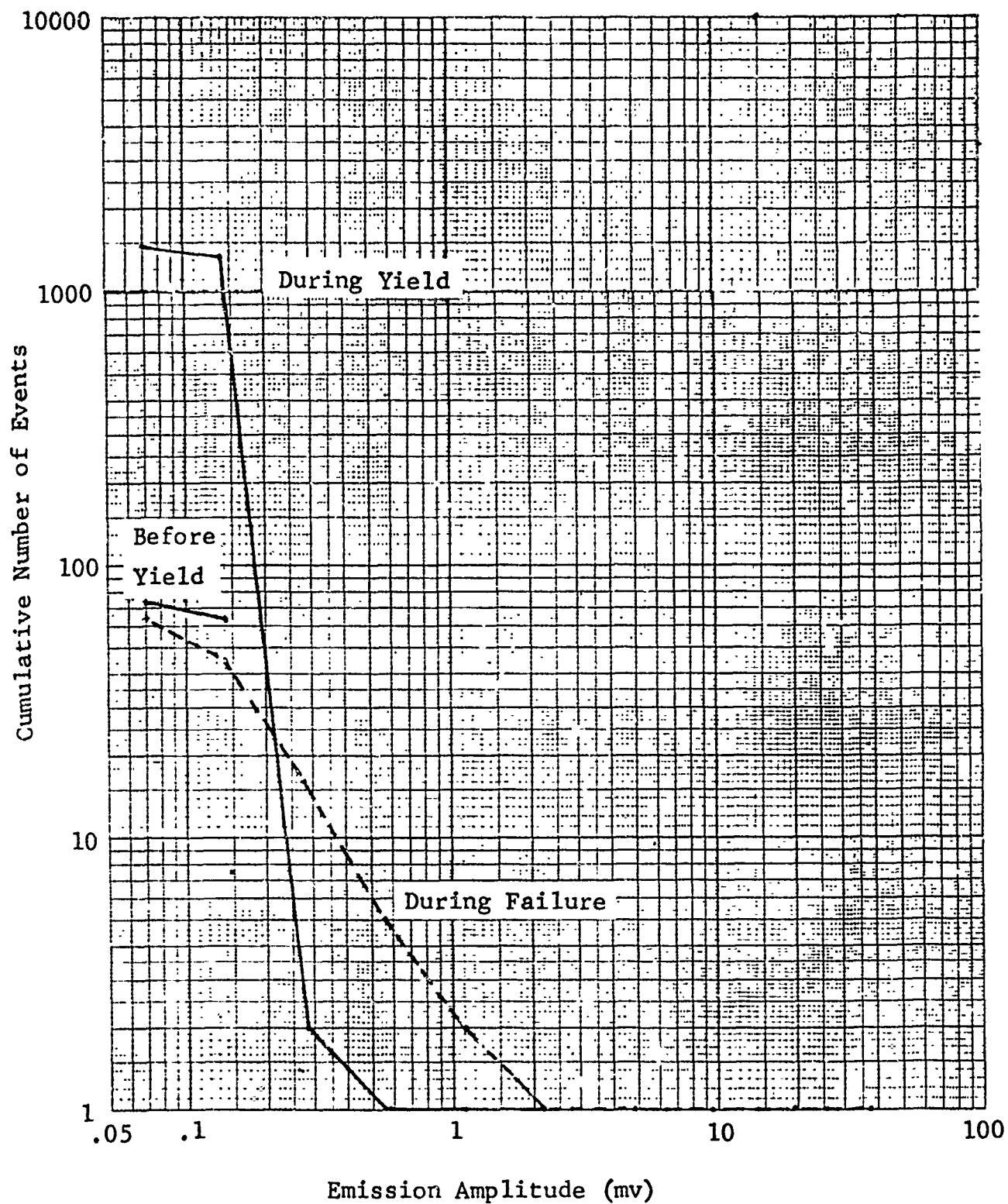


Figure 5.8 Amplitude Distribution of Emission Signals for Specimen Z1-5

All three of the specimens discussed above showed a decrease in the slope of the amplitude distribution curve during failure. Specimens D1-2 and Y1A-3 emitted a greater number of large amplitude signals, while Specimen Z1-5 emitted one very large amplitude signal during this period.

Heat-Cycled Material Specimens - 1700°F - Specimens A2-3, B2-3, and D2-1 were manufactured from material that had been heat treated for 6 hours at 1700°F. The cumulative acoustic emission signals from these specimens are presented in Figures 5.9 through 5.11. Specimen A2-3 emitted a very large number of emission signals during the yielding period again indicating that slippage between the sensor standoff and the specimen generated most of these signals.

Specimen D2-1 which had the grains running perpendicular to the long axis of the specimen emitted fewer acoustic signals during loading to failure (Fig. 5.11) than did Specimen B2-3 (Fig. 5.10) which had the grain direction parallel to the long axis of the specimen. However, Specimen B2-3 data showed a larger number of emissions before reaching the yield point. Again, these signals were generated by slippage between the specimen and grips and were not rejected by the slave sensors. This slippage is also indicated in the early stage of the load curves.

A comparison of the amplitude distribution of Specimen D2-1 (Fig. 5.12) and Specimen B2-3 (Fig. 5.13) shows that D2-1 emitted large amplitude signals during failure, compared to those emitted during the yielding segment of the load curve, while B2-3 emitted the same relative signal distribution during both segments. The amplitude distribution of acoustic emissions from Specimen A2-3 is presented in Figure 5.14. Due to the large number of small amplitude signals detected from the sensor standoff slippage during the yielding of the specimen, the slope of this curve is steeper than the amplitude distribution curve for Specimen B2-3 (Fig. 5.13) which is the same type of specimen. The amplitude distribution of the signals from these two specimens is similar during the failure period, except Specimen A2-3 emitted 5 large signals not observed from Specimen B2-3.

Heat-Cycled Material Specimen E1-2 1735°F - Specimen E1-2 had been heat-cycled to 1735°F for 6 hours. The cumulative acoustic emission signals from this specimen are plotted in

Parent Material: Heat Cycled at 1700°F for 6 Hours, 6% Deformation

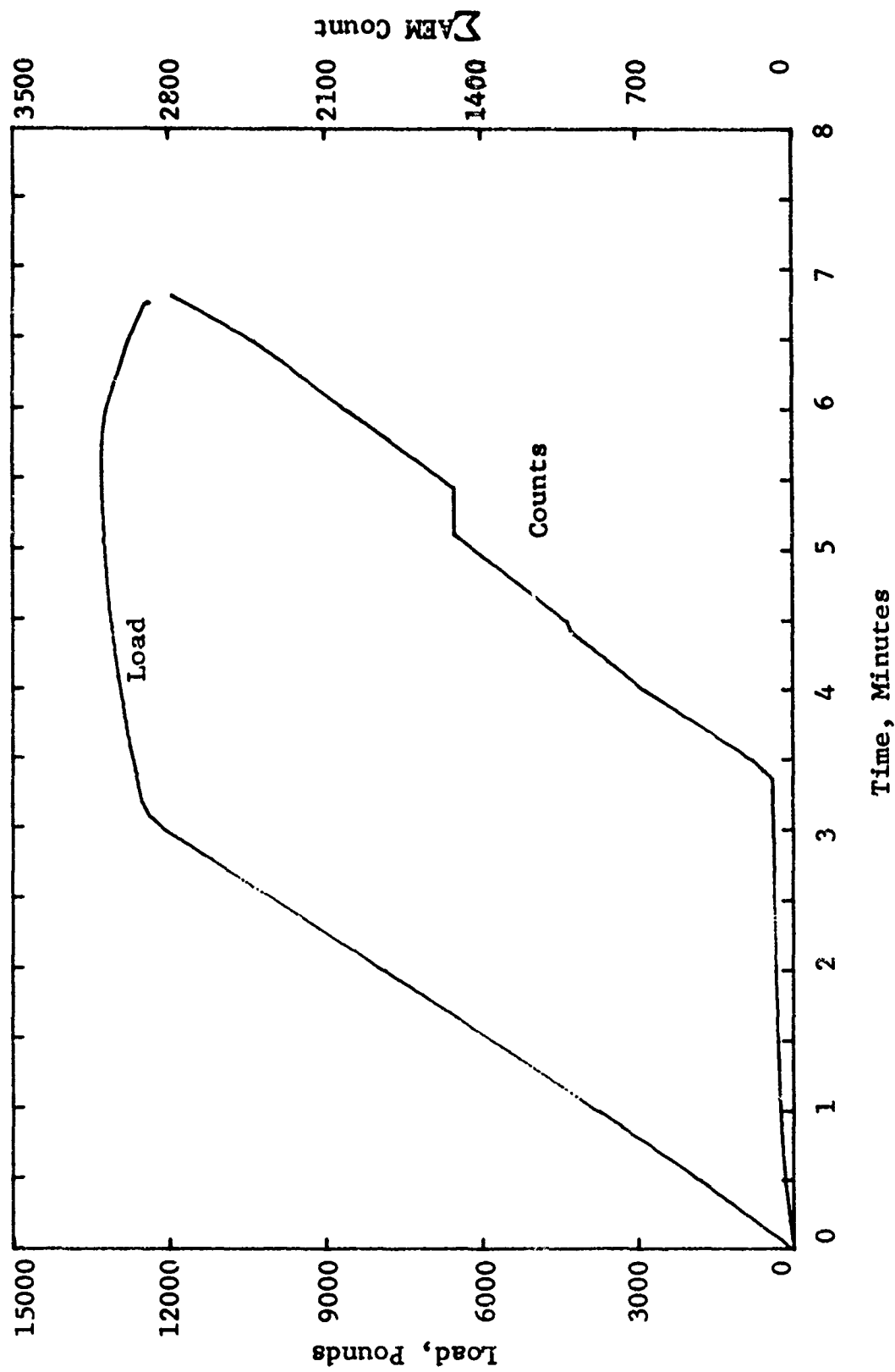


Figure 5.9 AEM Characteristics of Tensile Specimen A2-3

Parent Material: Heat Cycled at 1700°F for 6 Hours, 2.5% Deformation

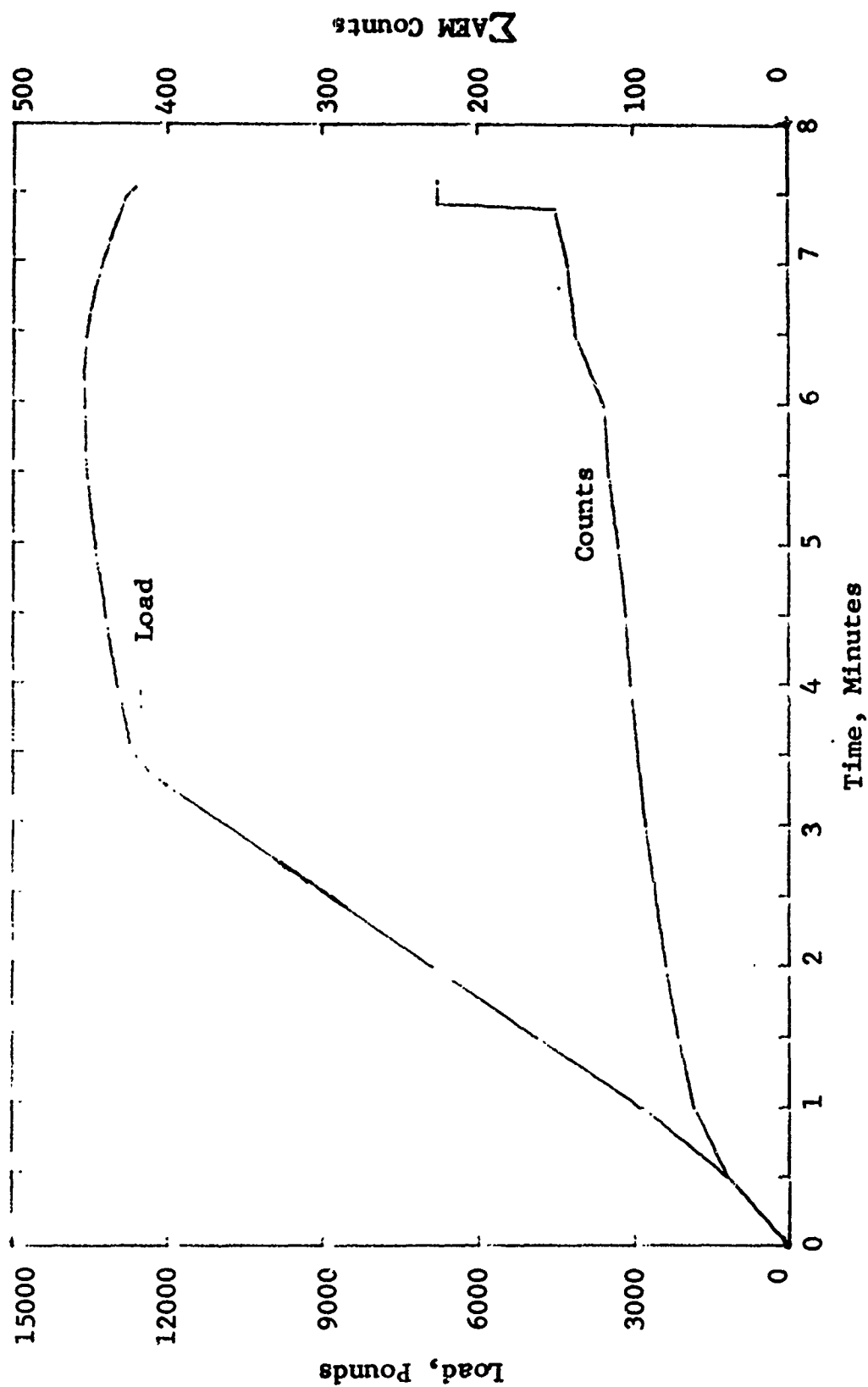


Figure 5.10 AEM Characteristics of Tensile Specimen B2-3

Parent Material: Heat Cycled at 1700°F for 6 Hours

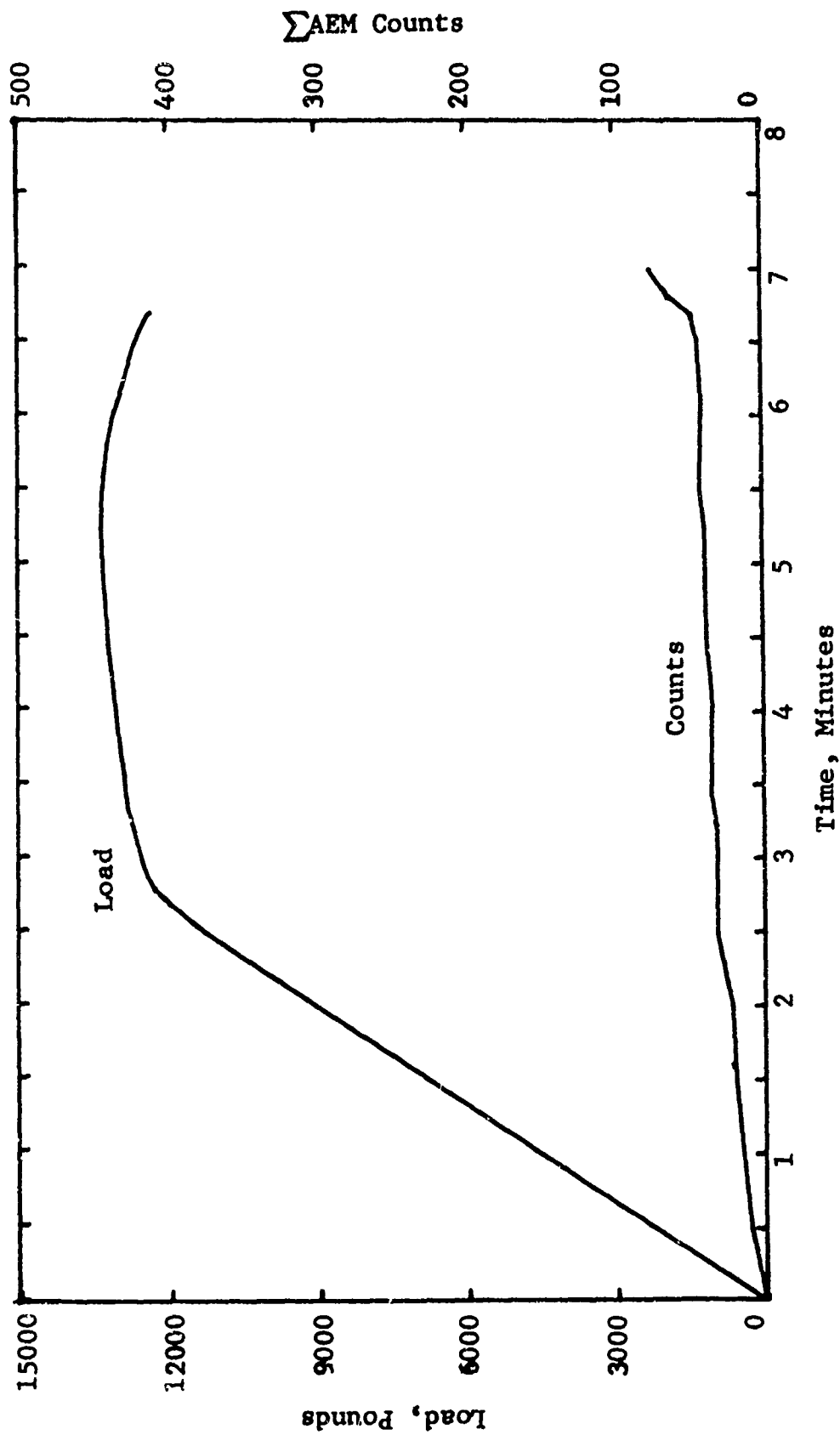


Figure 5.11 AEM Characteristics of Tensile Specimen D2-1

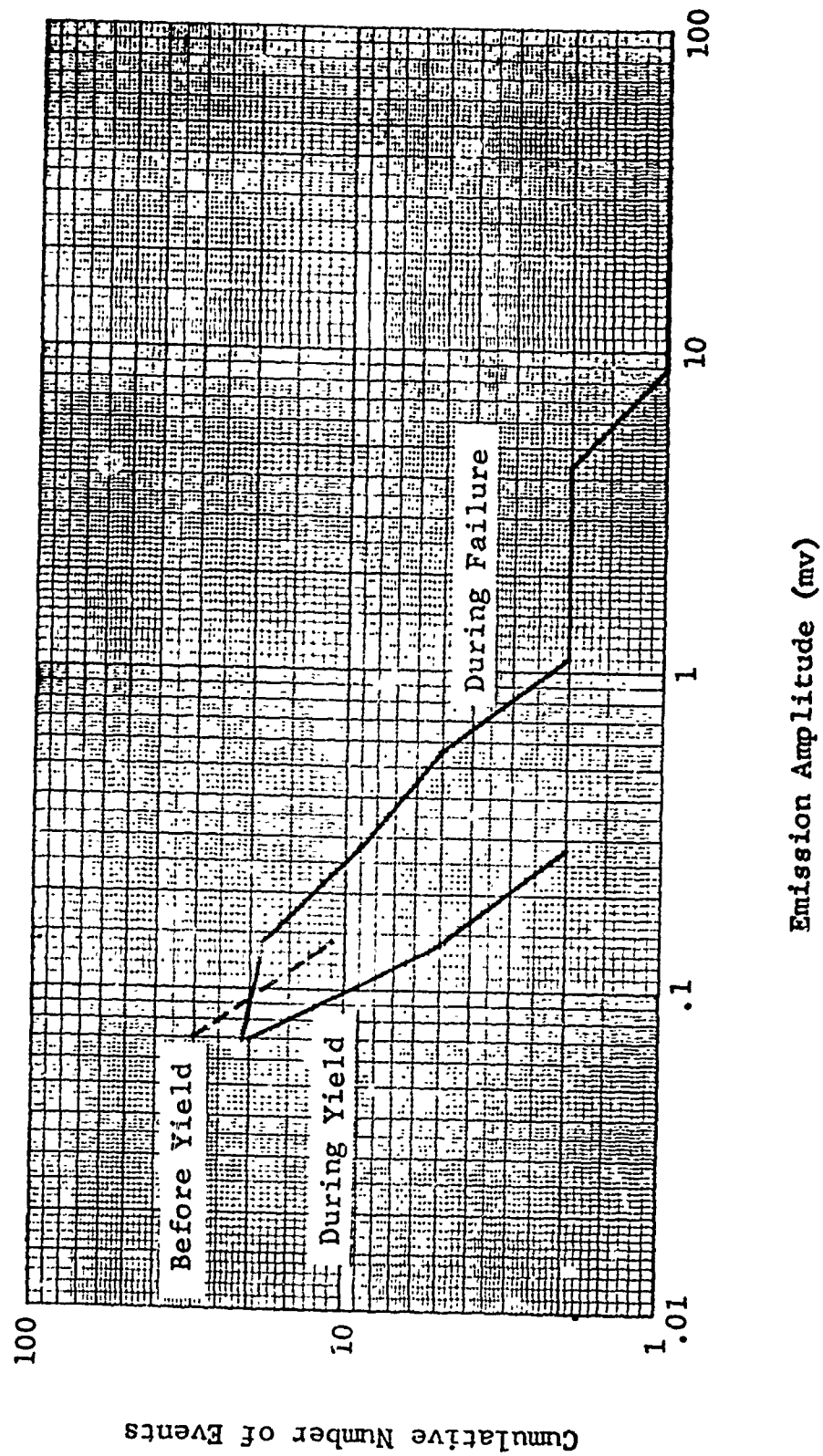


Figure 5.12 Amplitude Distribution of Emission Signals for Specimen D2-1



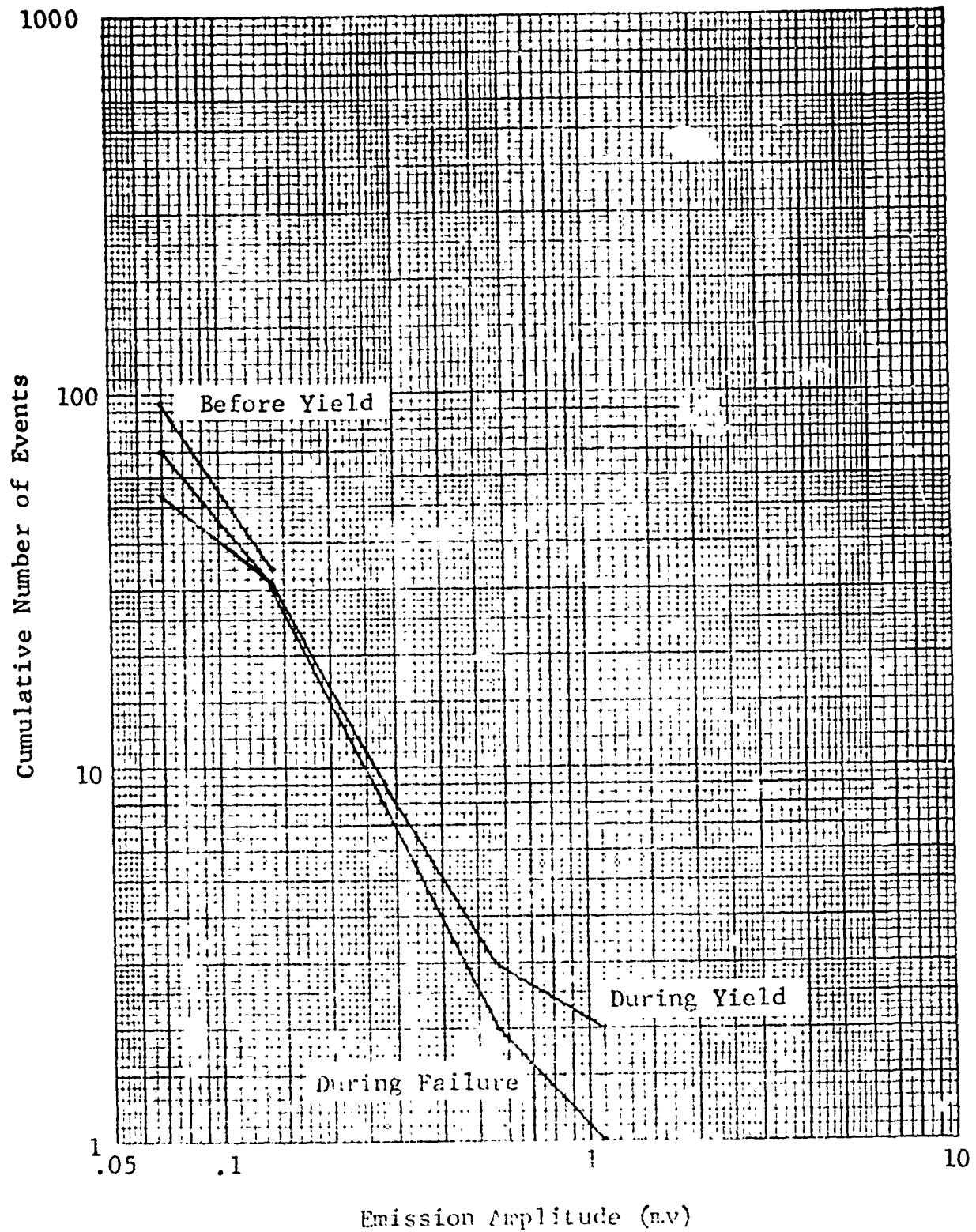


Figure 5.13 Amplitude Distribution of Emission Signals for Specimen B2-3

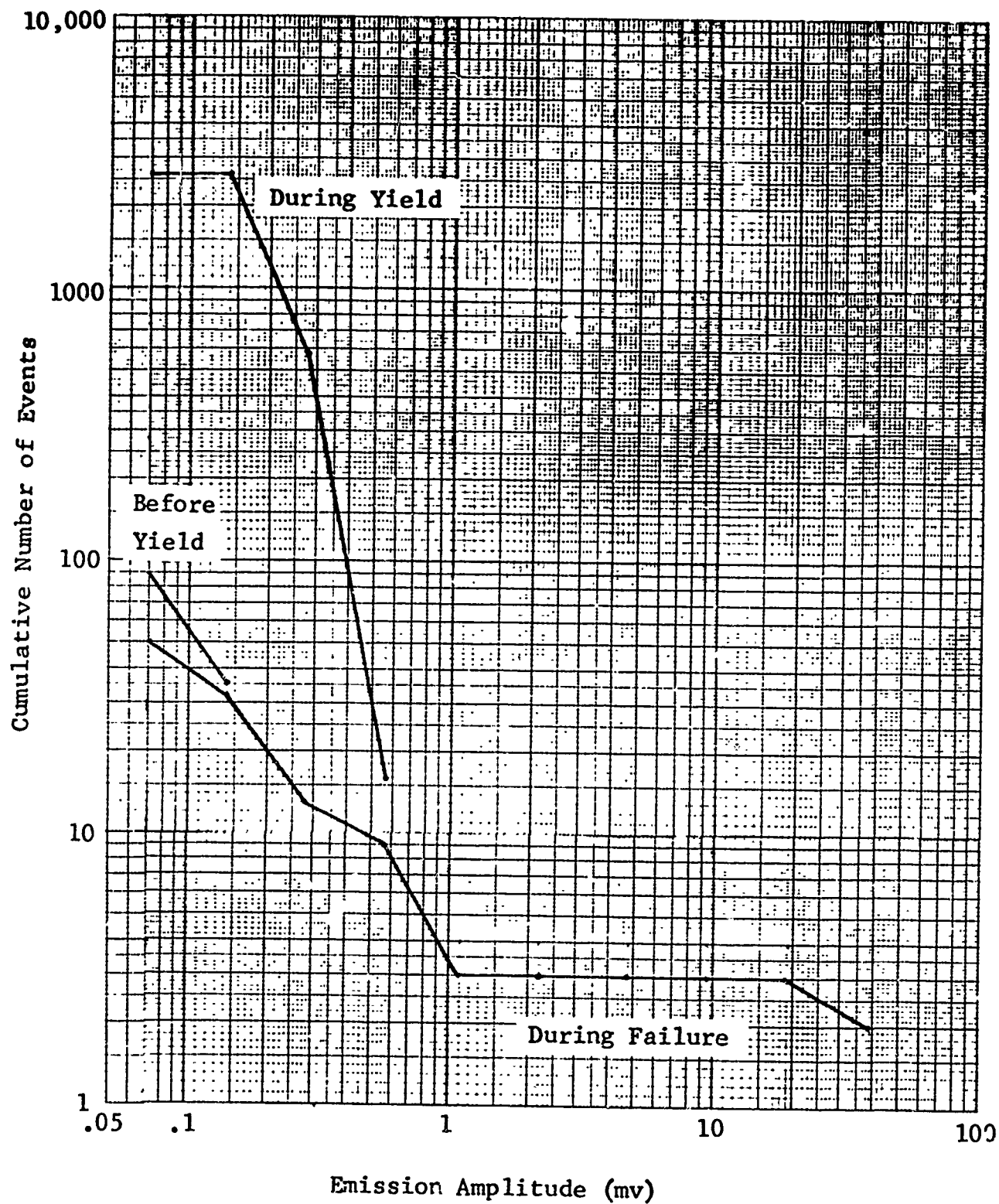


Figure 5.14 Amplitude Distribution of Emission Signals for Specimen A2-3

Figure 5.15. Signals were emitted at low load levels and continued at a constant rate until the specimens began to yield. These signals originated at the specimen grip interface and were not rejected by the slave sensors. The amplitude distributed of acoustic signals recorded from this specimen is presented in Figure 5.16. These curves show that most of the signals were of small amplitude until failure was reached.

Heat-Cycled Material Specimen F1-1 1775<sup>0</sup>F - Specimen F1-1 had been heat-cycled to 1775<sup>0</sup>F for 6 hours. The cumulative acoustic emission signals from this specimen are presented in Figure 5.17. Some emissions were observed during the early stage of the loading ramp. However, they were not so numerous as was observed from Specimen E1-2, indicating that the noise from the specimen grip was much less for this specimen than the Specimen E1-2 test. The amplitude distribution of the acoustic emission signals from this specimen is presented in Figure 5.18.

Intentional Defect Diffusion Bonded Specimens - The specimens used for this phase of the study contained internal deficiencies implanted in the diffusion bonded specimens as described in Section 6.

After making the modifications to the sensor mounting procedure as discussed in Section 5.1.1, the bonded specimens were tested.

Single-Bonded/Single-Axis Specimens - Specimen A3-2 had a good bond with 7.72% deformation of materials during bonding. Specimen B3-2 had a good bond with 2.71% optimum deformation. However, the ultrasonic inspection of these specimens showed that Specimen A3-2 had a better bond than B3-2. The cumulative acoustic emission events from Specimen A3-2 are plotted in Figure 5.19. These data show that only five acoustic emission events were emitted prior to the failure segment of the load. During failure, 100 events were recorded. The amplitude distribution curve (Fig. 5.20) presents the distribution of these events and shows that the five signals emitted during the yielding of the specimen were only 0 to 6 dB or less above the threshold of the instrumentation.

The cumulative acoustic emission events from Specimen B3-2 are present in graphic form in Figure 5.21. Several acoustic signals were emitted by this specimen as the specimen began to

Parent Material: Heat Cycled at 1735°F for 6 Hours

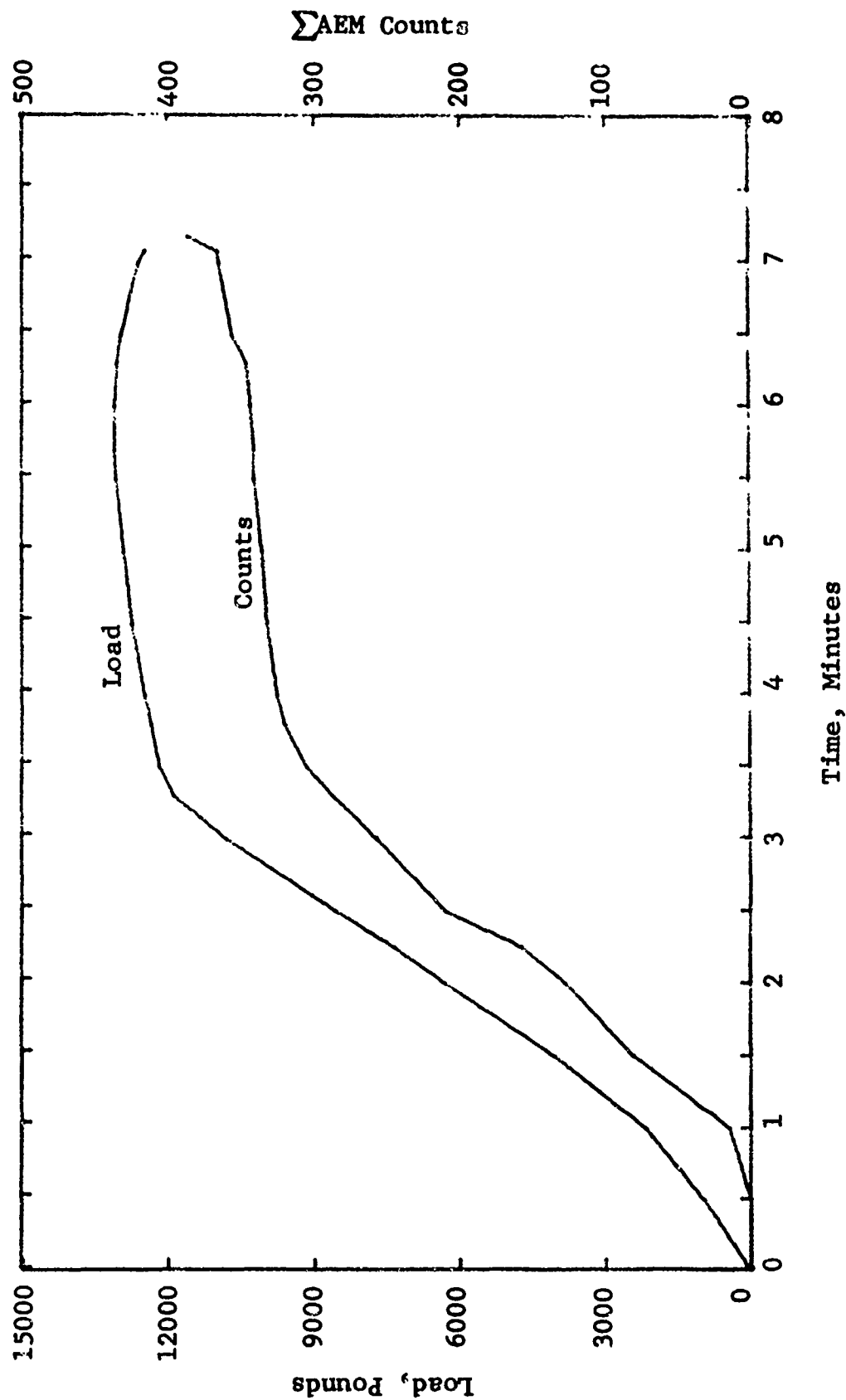


Figure 5.15 AEM Characteristics of Tensile Specimen E1-2

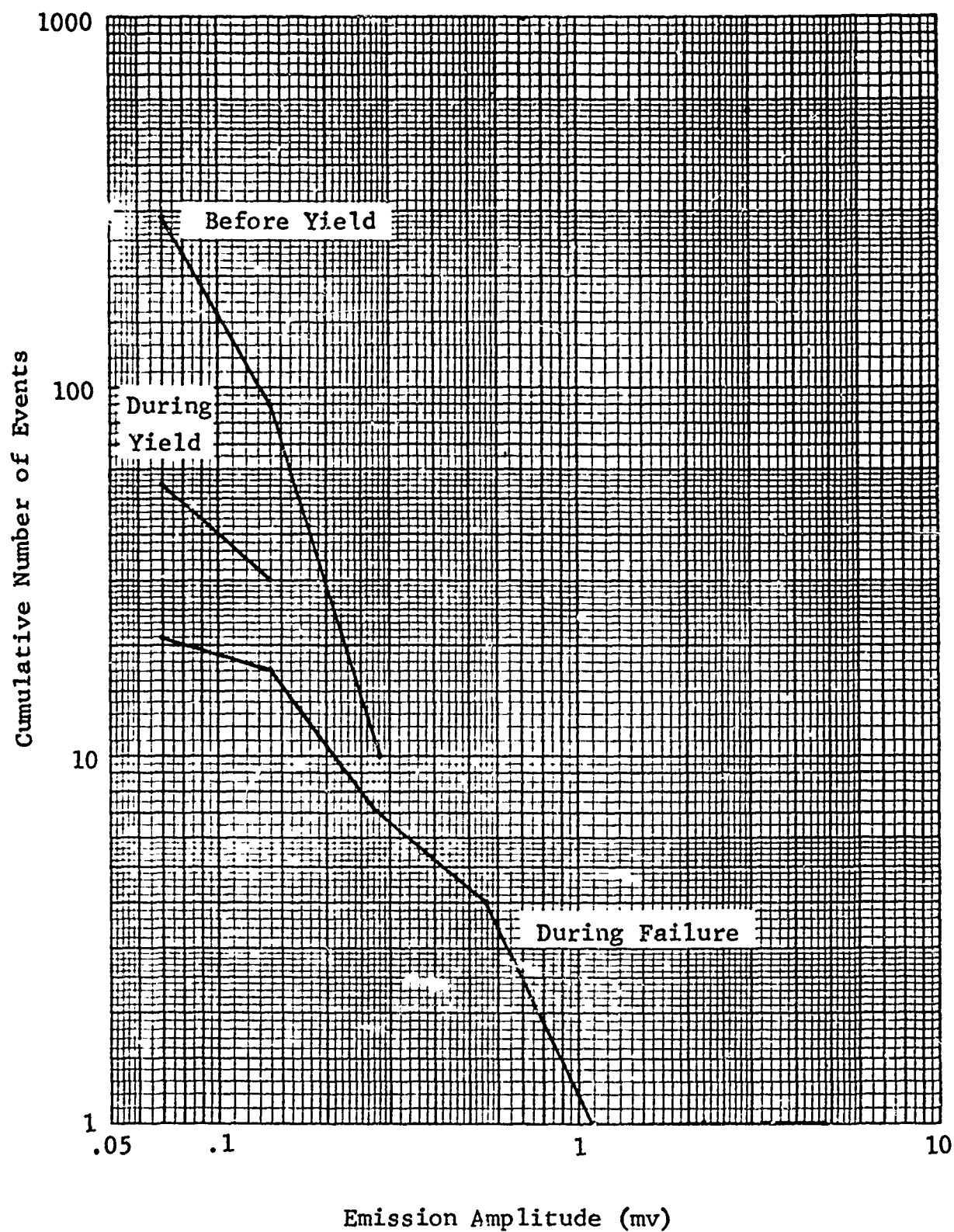


Figure 5.16 Amplitude Distribution of Emission Signals for Specimen E1-2

Parent Material: Heat Cycled at 1775 F for 6 Hours

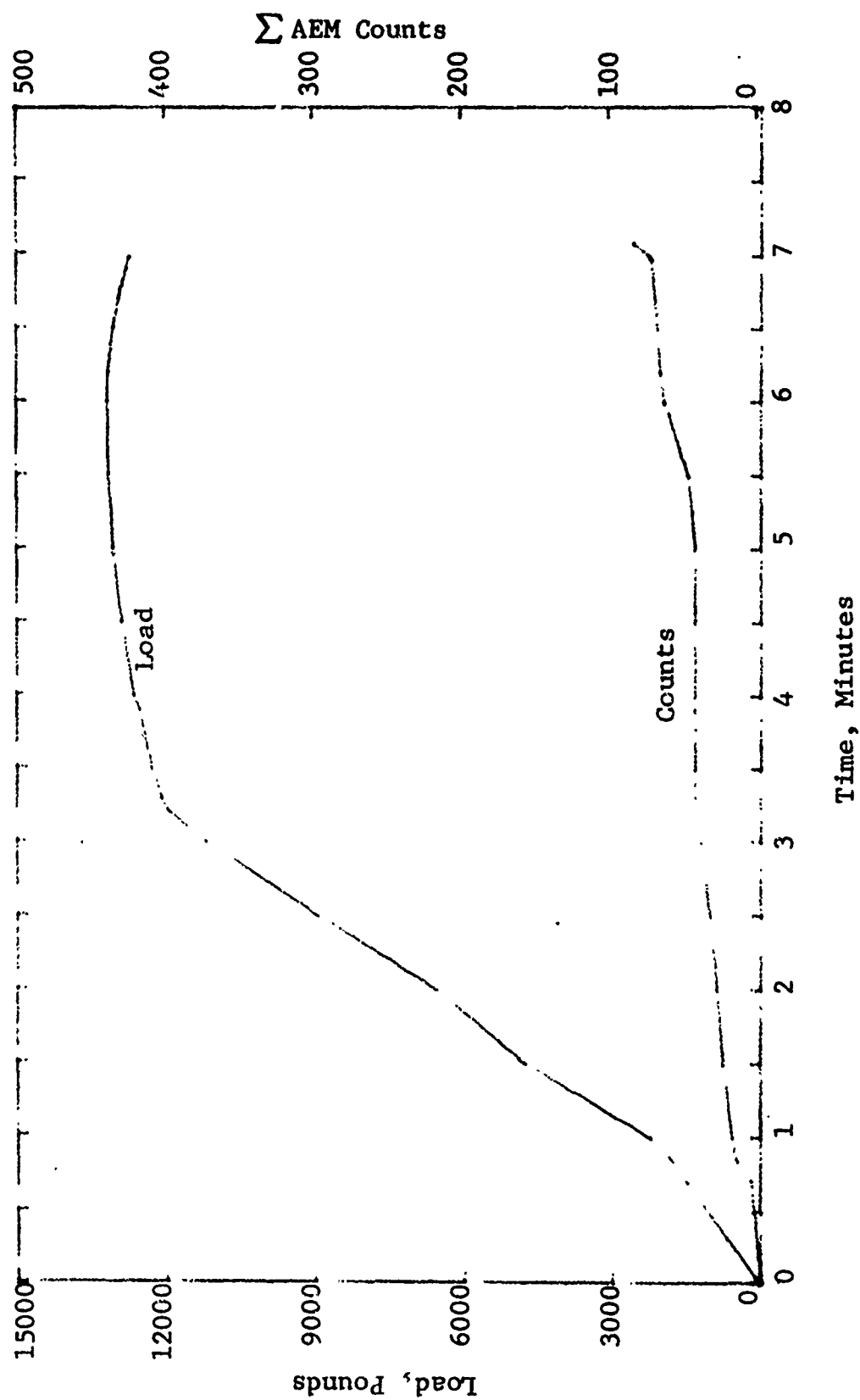


Figure 5.17 AEM Characteristics of Tensile Specimen F1-1

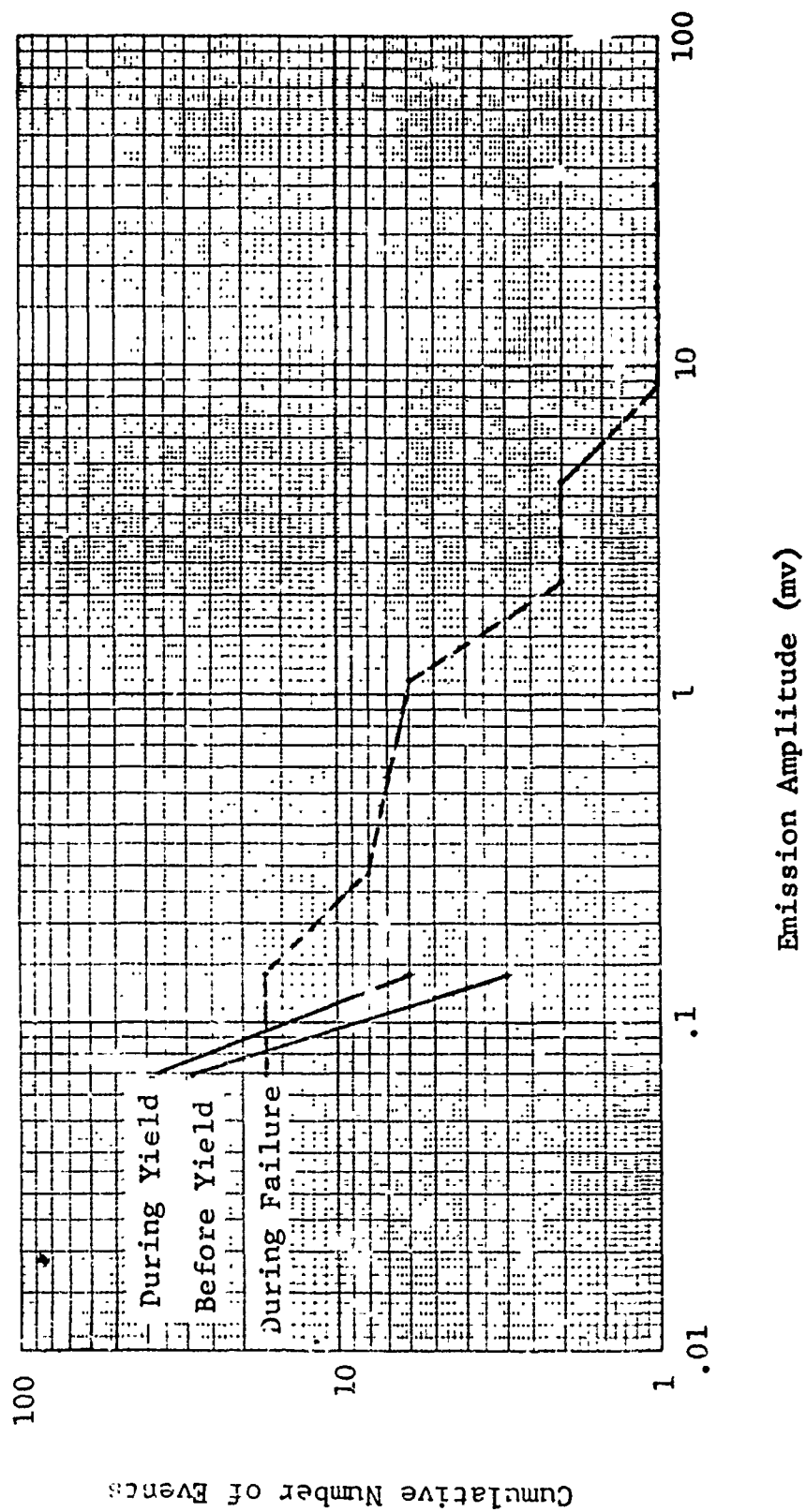


Figure 5.18 Amplitude Distribution of Emission Signal for Specimen FI-1

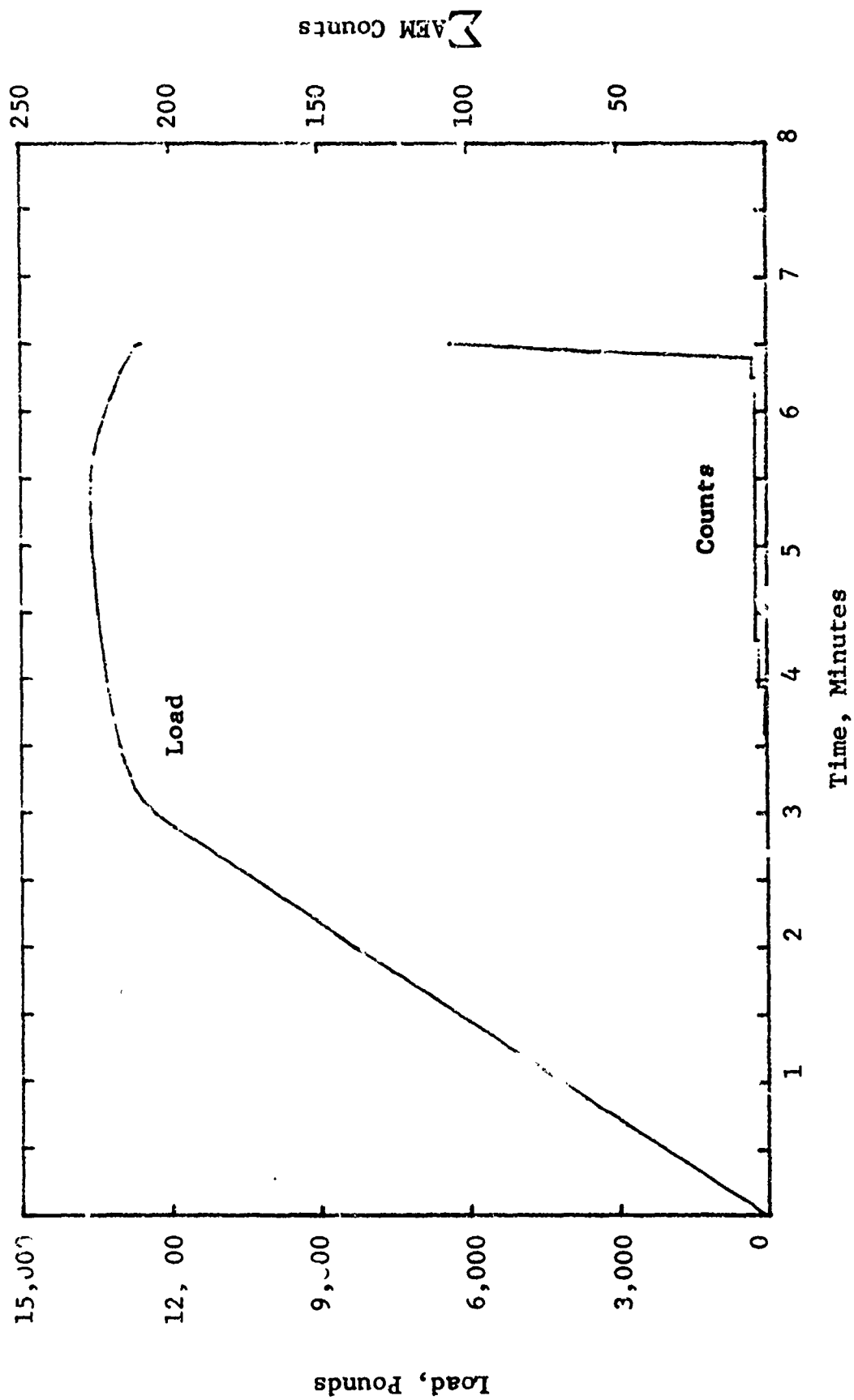


Figure 5.19 AEM Characteristics of Tensile Specimen A3-2



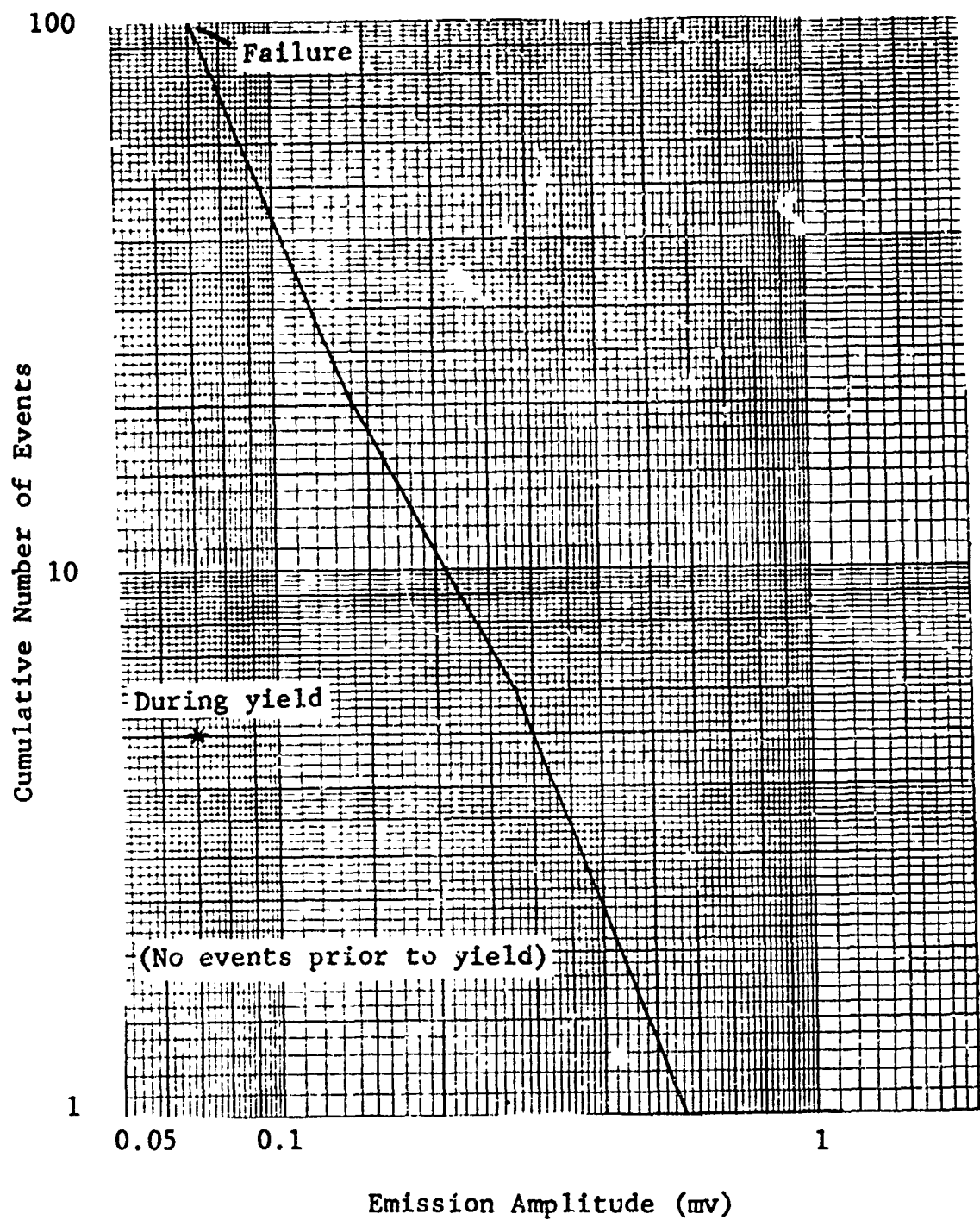


Figure 5.20 Amplitude Distribution of Emission Signals  
for Specimen A3-2

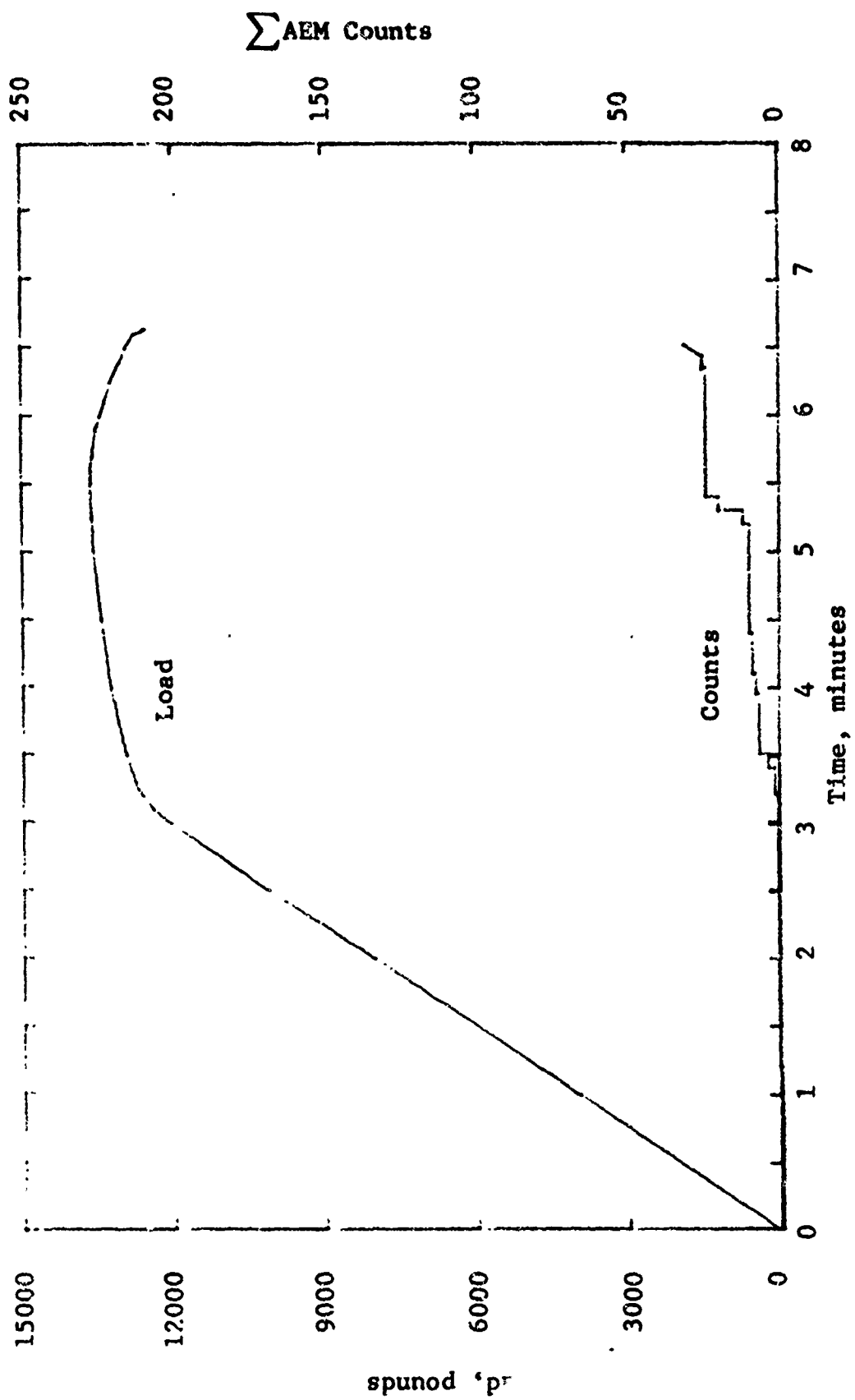


Figure 5.21 AEM Characteristics of Tensile Specimen B3-2

yield. A strong indication of imminent failure was observed at the peak load prior to actual failure. The amplitude distribution of the acoustic emission signals from this specimen (Fig. 5.22) shows that not only did this specimen emit a greater number of signals during yield than it did during failure, but the larger amplitude signals were emitted during the yielding period. The acoustic emission data from Specimen B3-2 show that debonding did occur, and flaw growth was present during yielding.

Internal Void Specimen - Specimen I3-3 contained a 20-mil diameter cylinder void in the bondline. The cumulative acoustic emission from this specimen is presented in Figure 5.23. Acoustic emissions from this specimen were first observed at 3500 lbs and continued at a slow rate until the yield point was reached. Corresponding to the yield point on the load curve, a rapid increase in emission rate occurred, showing rapid flaw growth during this period. The amplitude distribution curves for Specimen I3-3 are presented in Figure 5.24. The difference in these distribution curves for the three load periods is the ratio of small amplitude signal to large amplitude signal during failure as compared to the periods before and during yielding of the specimen. This verifies that flaw growth did occur during the yielding of the specimen.

Large Alpha Grain Specimens - Specimen E3-3 had large primary alpha grains prior to bonding and Specimen F3-1 had much larger primary alpha grains than Specimen E3-3. The cumulative acoustic emissions from Specimen E3-3 and F3-1 are presented in Figure 5.25 and 5.26, respectively. The acoustic events from Specimen E3-3 began at a low load level. The rate of acoustic events increased rapidly as the specimen began to yield and continued until the peak load was reached. Only a few emissions were observed during the last half of the yield period and the acoustic emission rate increased greatly during the failure period of this specimen. Specimen F3-1 did not emit any detectable acoustic emission signals until it was well into the yield period on the load curve. However, the rate of emissions in the last period of the load curve was very similar to the acoustic emission rate from Specimen E3-3 in the same period. The acoustic emission from Specimen E3-3 was a factor of two higher than from Specimen F3-1 during this segment of the loading period.

The amplitude distribution of the acoustic emission signals from Specimens E3-3 and F3-1 is plotted in Figures 5.27 and 5.28, respectively. The relative amplitude distribution of acoustic

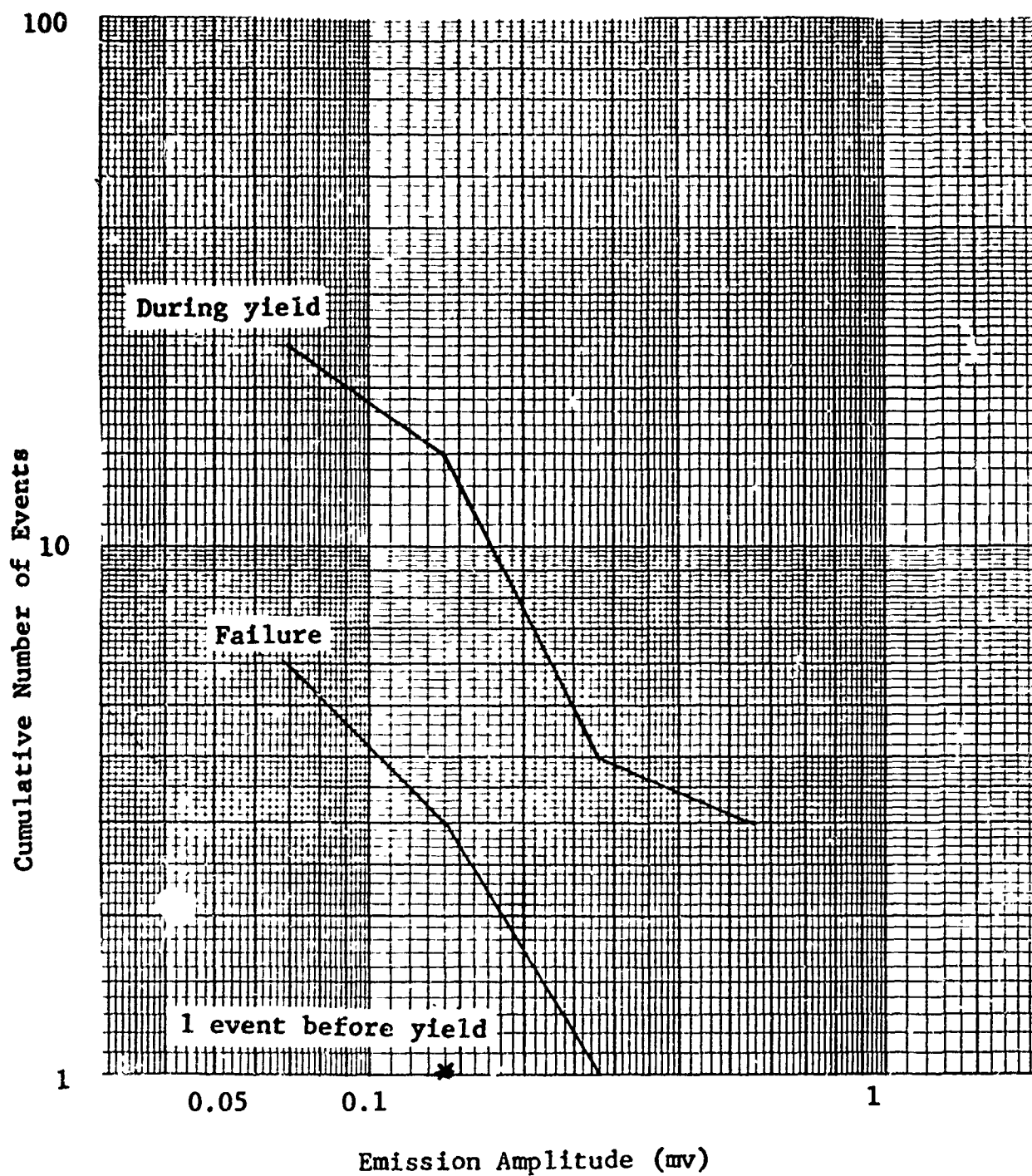


Figure 5.22 Amplitude Distribution of Emission Signals for Specimen B3-2

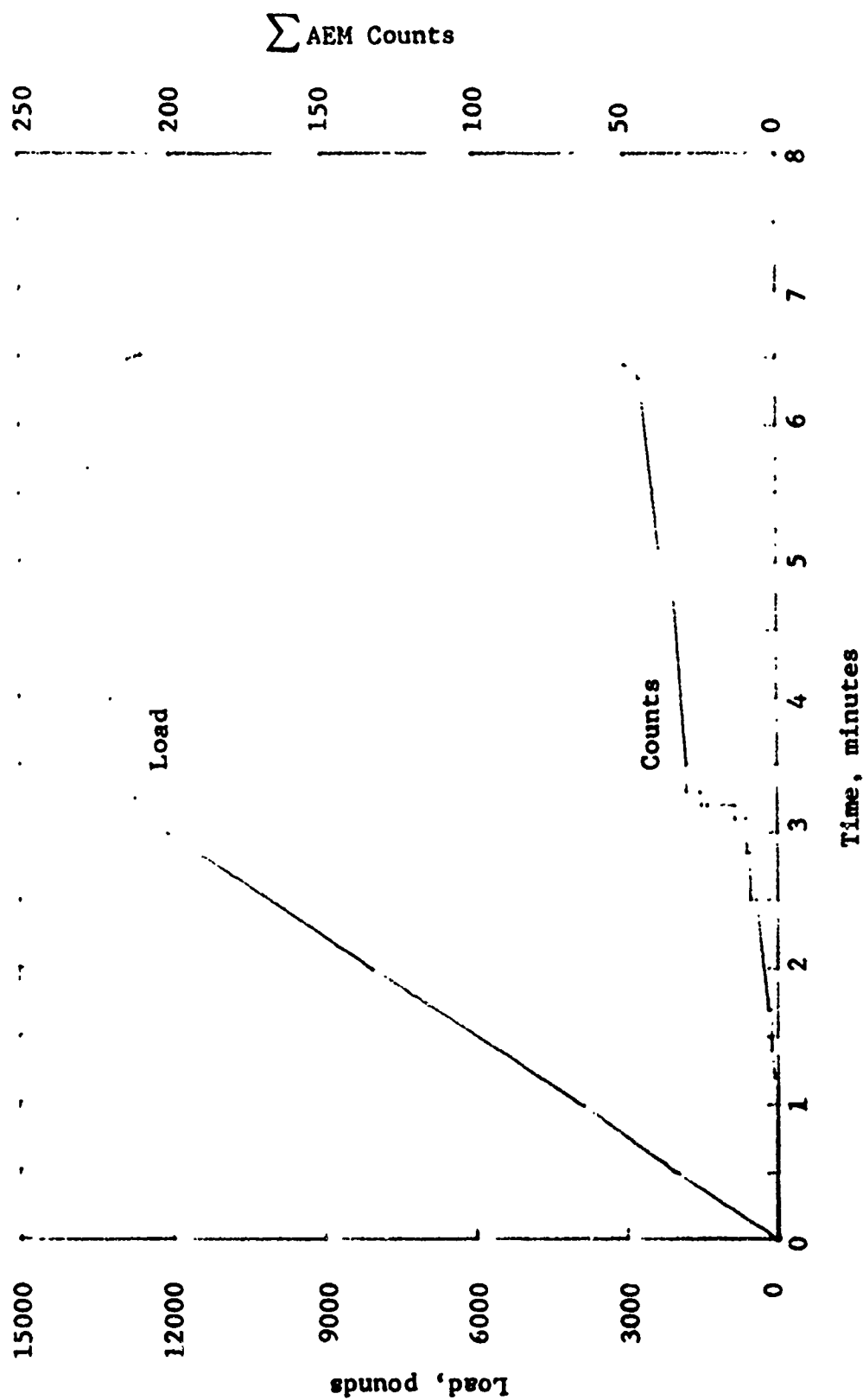


Figure 5.23 AEM Characteristics of Tensile Specimen I3-3

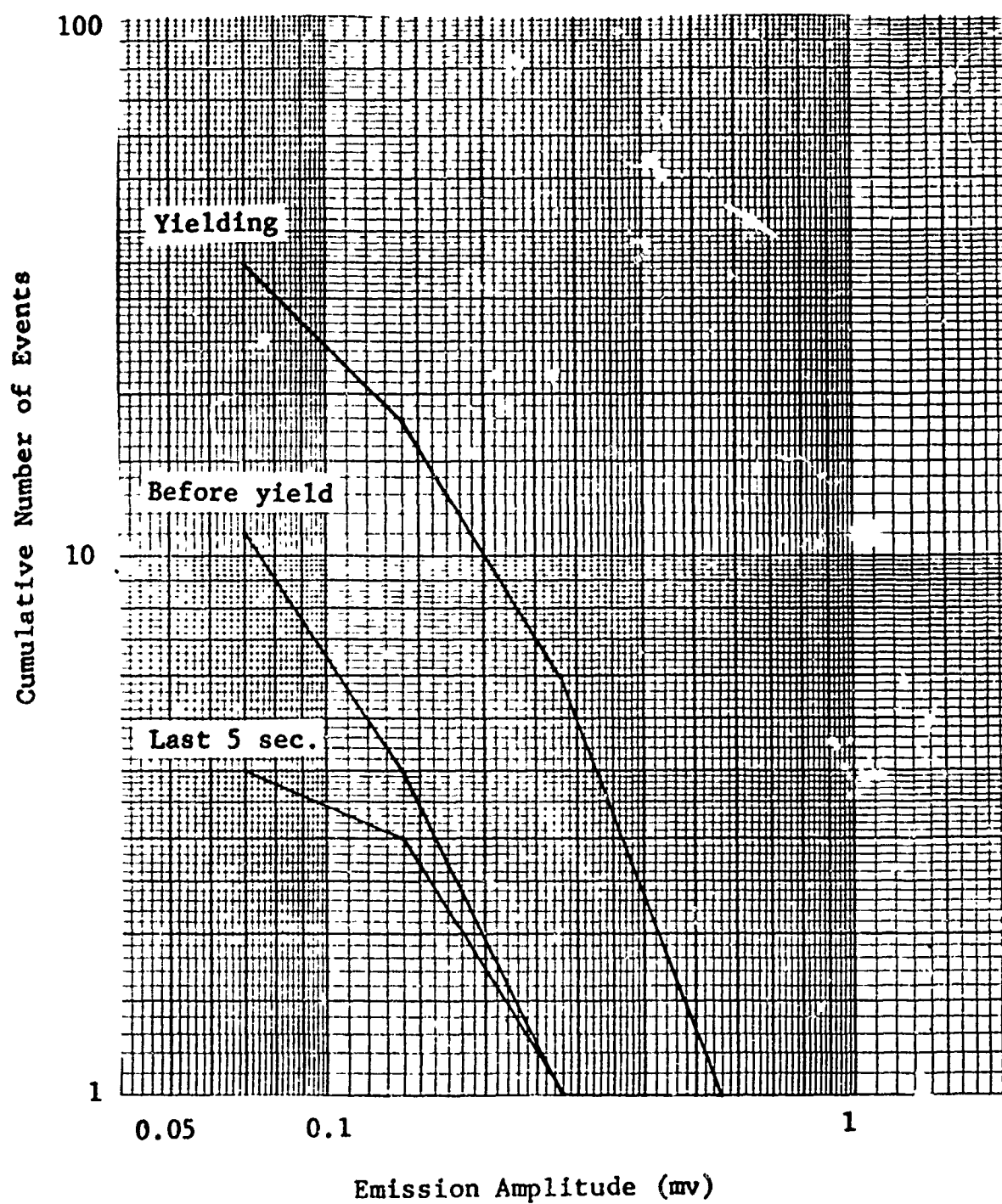


Figure 5.24 Amplitude Distribution of Emission Signals for Specimen: I3-3

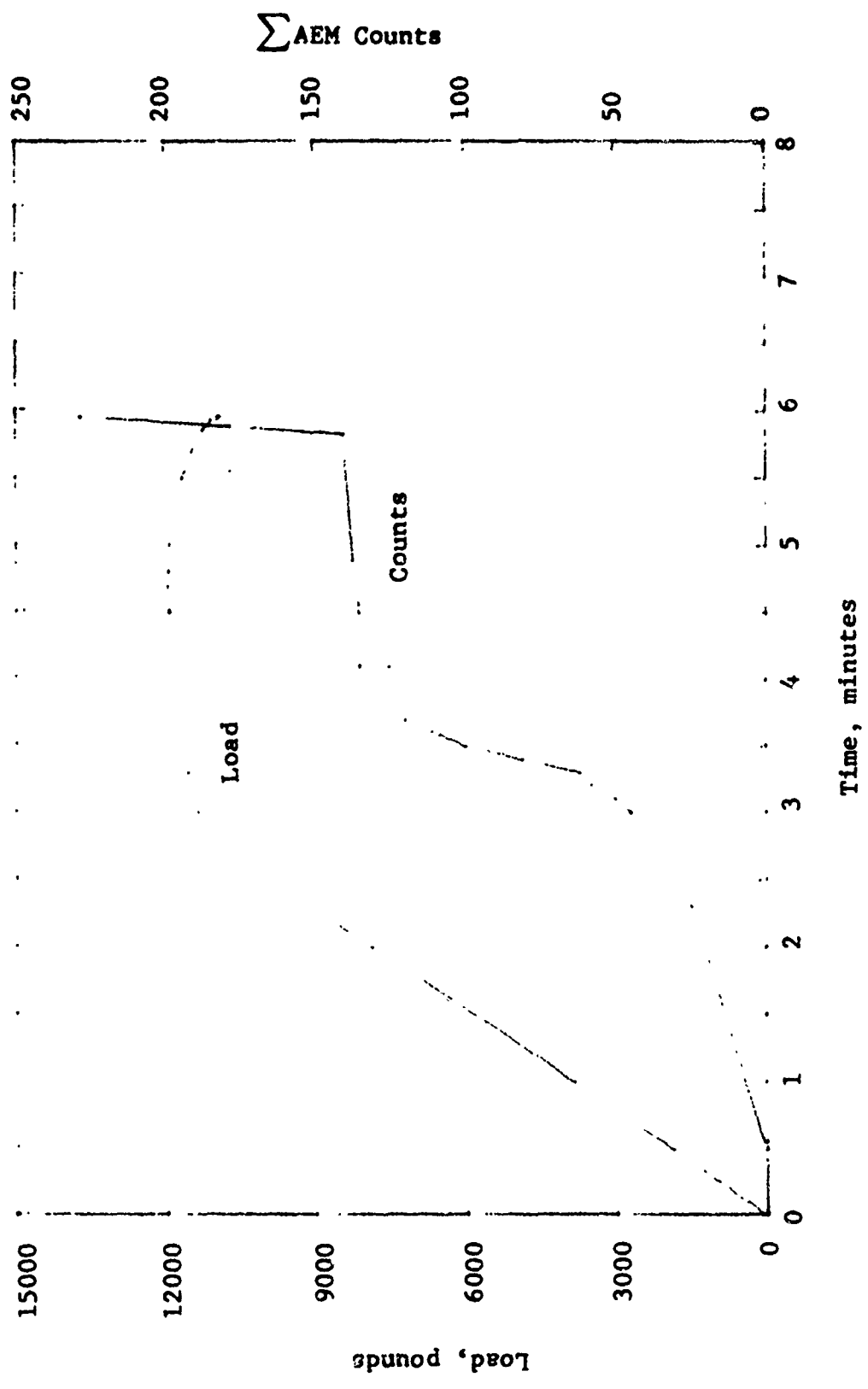


Figure 5.25 AEM Characteristics of Tensile Specimen E3-3

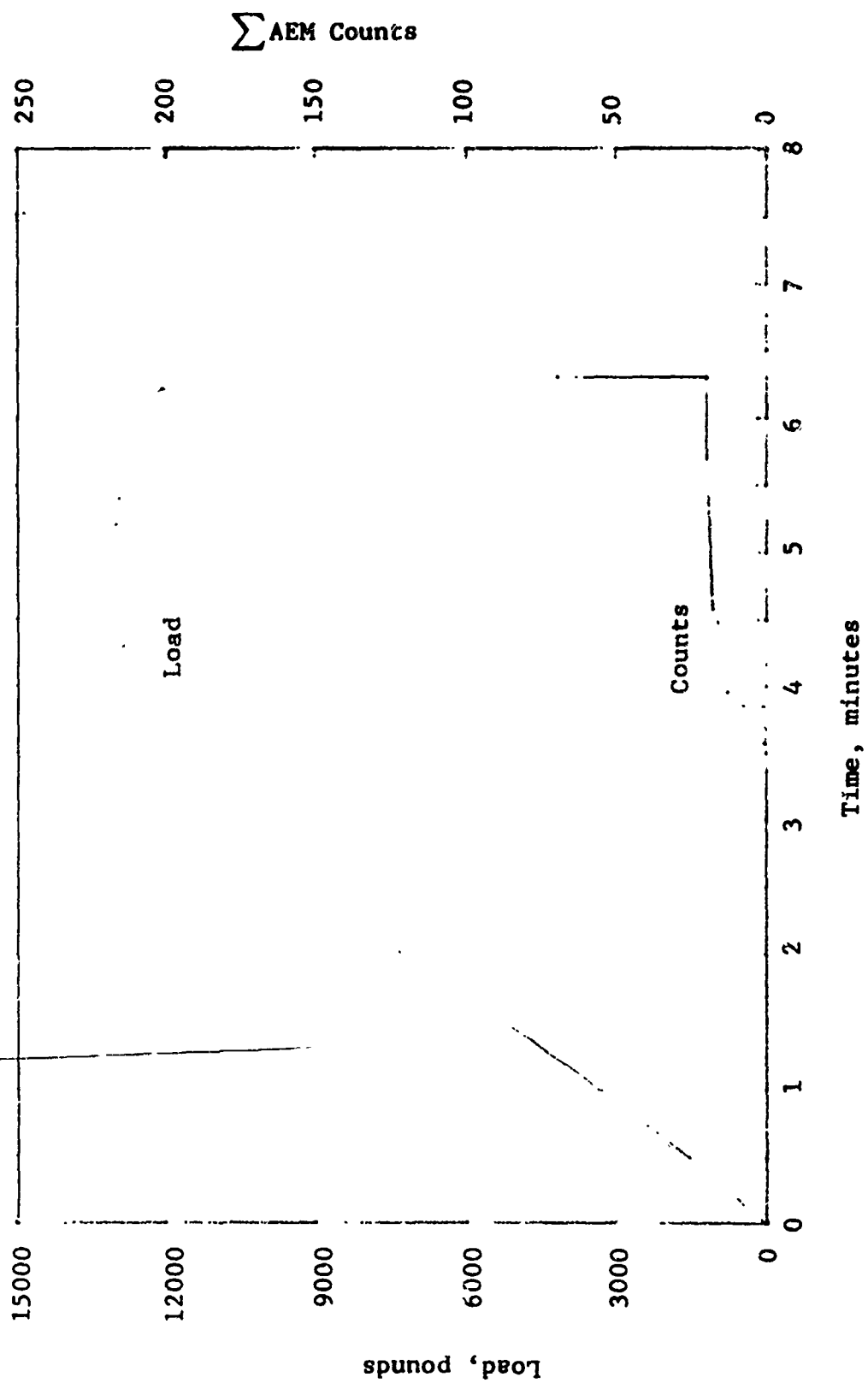


Figure 5.26 AEM Characteristics of Tensile Specimen F3-1



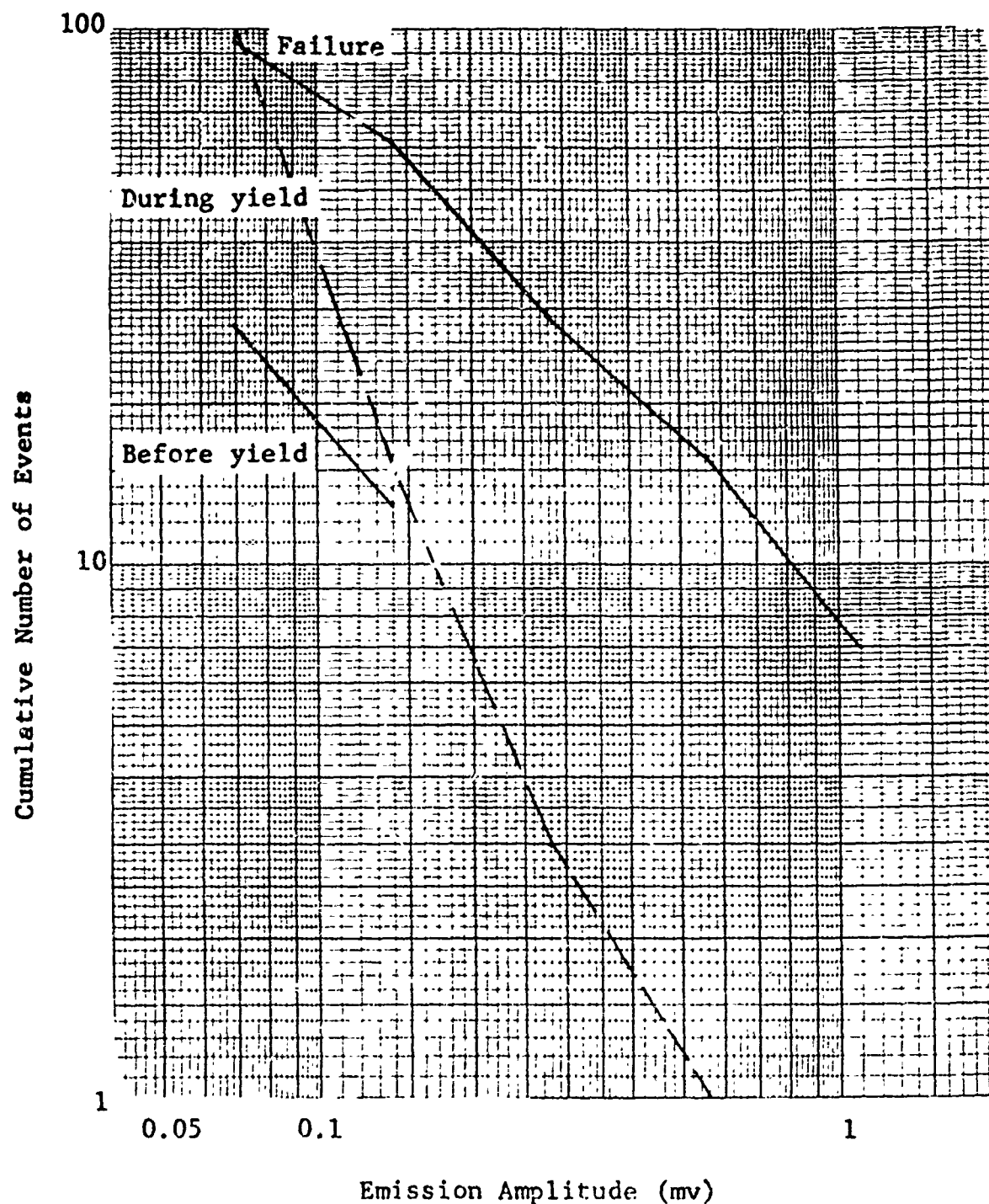


Figure 5.27 Amplitude Distribution of Emission Signals for Specimen E3-3

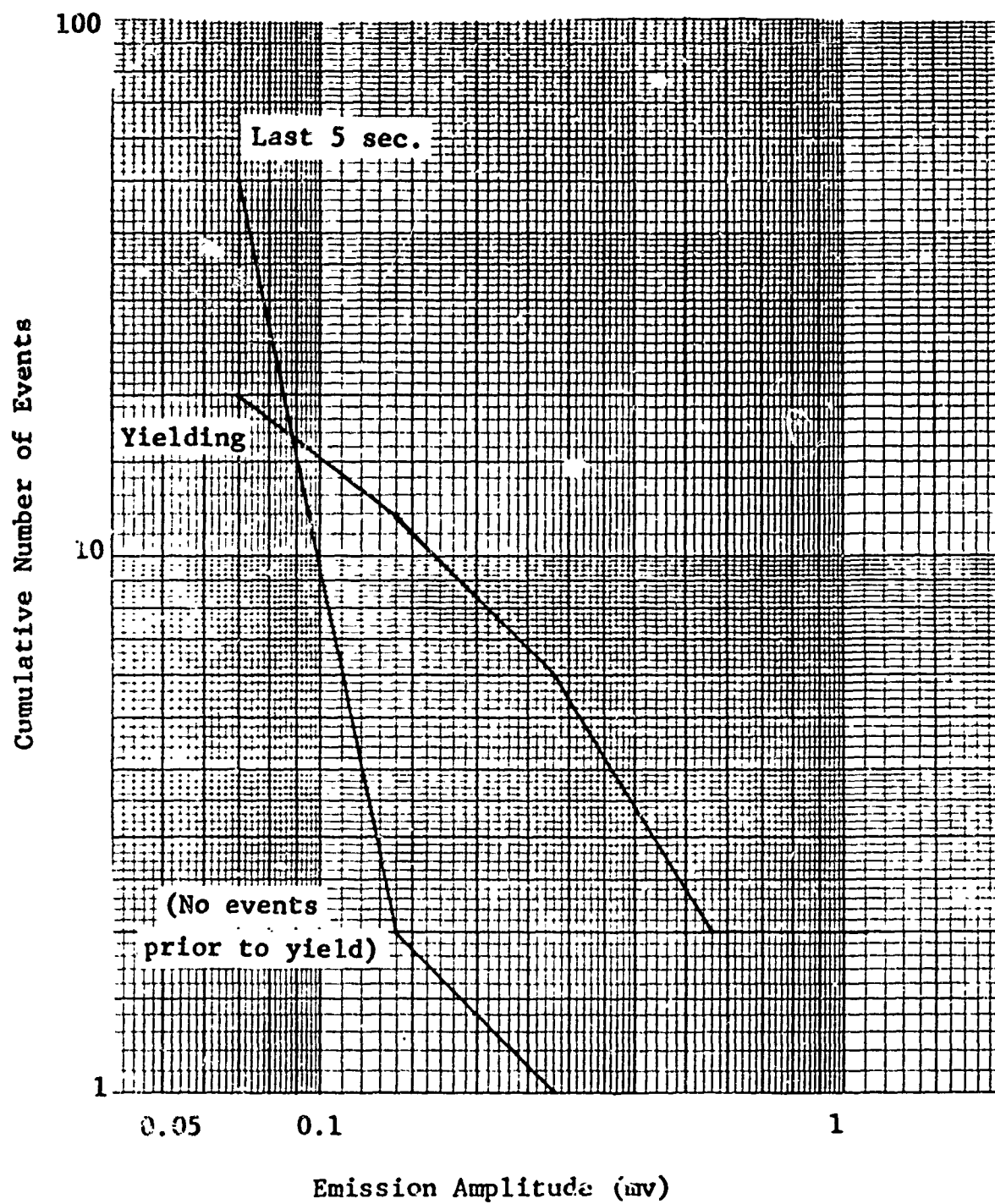


Figure 5.28 Amplitude Distribution of Emission Signals for Specimen F3-1

emission events from these two specimens is similar during the yield and failure segments of the load curves. The greater number of medium and large amplitude signals occurred during the yielding of the specimens.

Multiple-Bond/3-Axes Joint Specimens - Three multiple-bond specimens were monitored for acoustic emissions during this phase of the study: (1) Specimen A6-1 had a good bond; (2) Specimen H6-3 had a small defect ( $d = 0.018$ ) and a partial bond area; and (3) Specimen K-6 had a type 304 stainless steel inclusion ( $d = 0.025$ ).

The accumulative number of acoustic emission events recorded from Specimen A6-1 is presented in Figure 5.29. Specimen A6-1 emitted three events prior to the yield point on the load curve. There were two rapid changes in the acoustic emission rate during yield of the specimen. One rapid increase occurred 30 seconds in the yield period and another occurred as the peak load was reached. More than 50% of the acoustic emission events from this specimen occurred during the failure period. The amplitude of acoustic emission events from Specimen A6-1 is presented graphically in Figure 5.30. It should be noted that some medium amplitude signals were detected during yielding. However, all of the large amplitude signals were emitted during failure of this specimen.

The cumulative number of acoustic emission events from Specimen H6-3 is presented in Figure 5.31. Specimen H6-3 emitted 60% fewer signals than Specimen A6-1 before failing in a much shorter period after yield began than did Specimen A6-1. The greater number of emissions from Specimen H6-3 occurred during the short yield period; however, there was no strong indication of failure of this specimen before failure occurred, either from the acoustic emission monitoring or the load curve. The amplitude distribution of acoustic emission events from Specimen H6-3 is presented in Figure 5.32. These curves show that all acoustic emission signals from this specimen were in the 6 to 24 dB range. Although no large amplitude signals were observed, the slope of the yield period curve is less than the slope of the curve for signals recorded before the yield point on the load curve, giving some indication of flaw growth prior to failure.

The cumulative acoustic emission events from Specimen K6-3 are plotted in Figure 5.33. This data plot shows that the

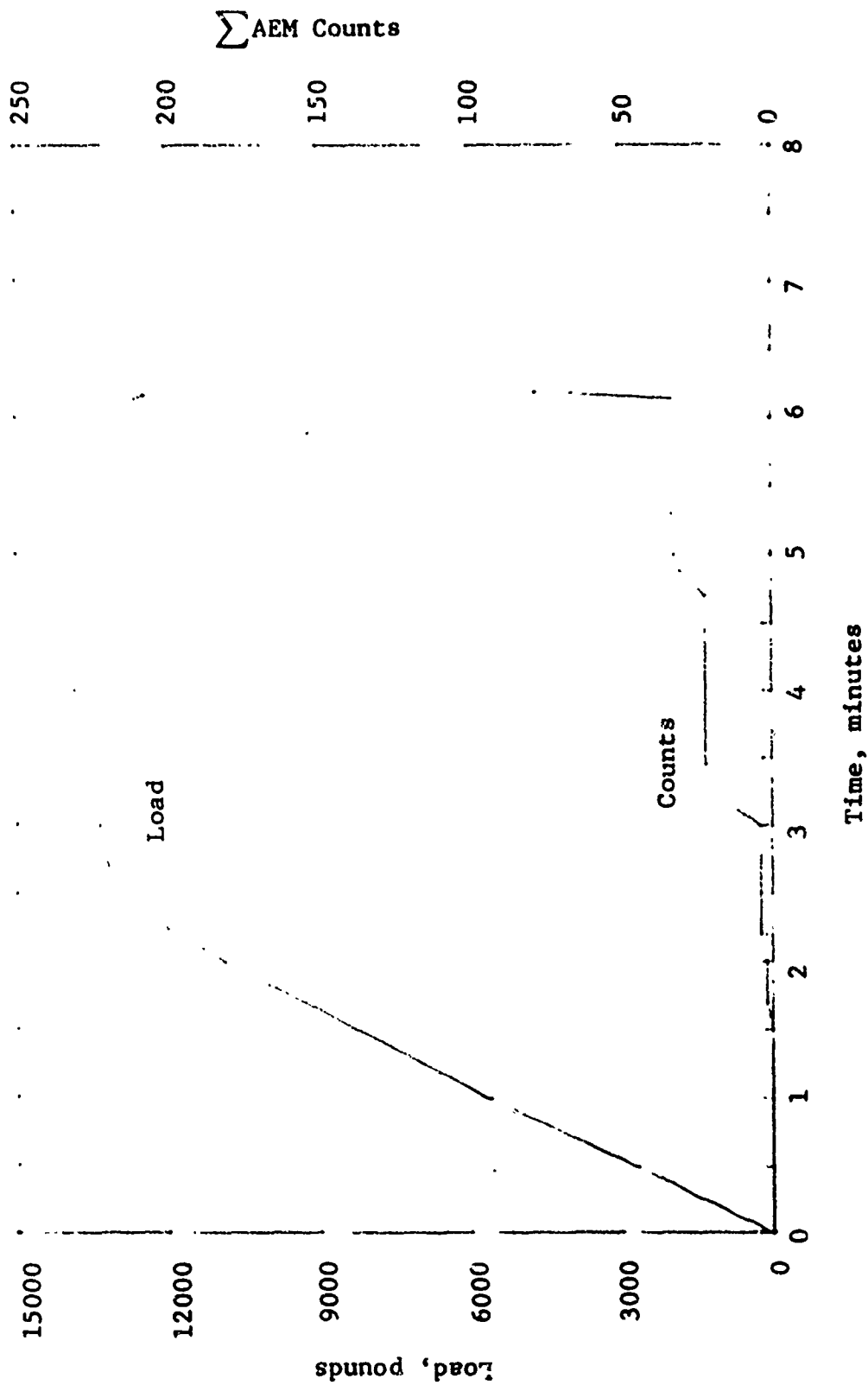


Figure 5.29 AEM Characteristics of Tensile Specimen A6-1

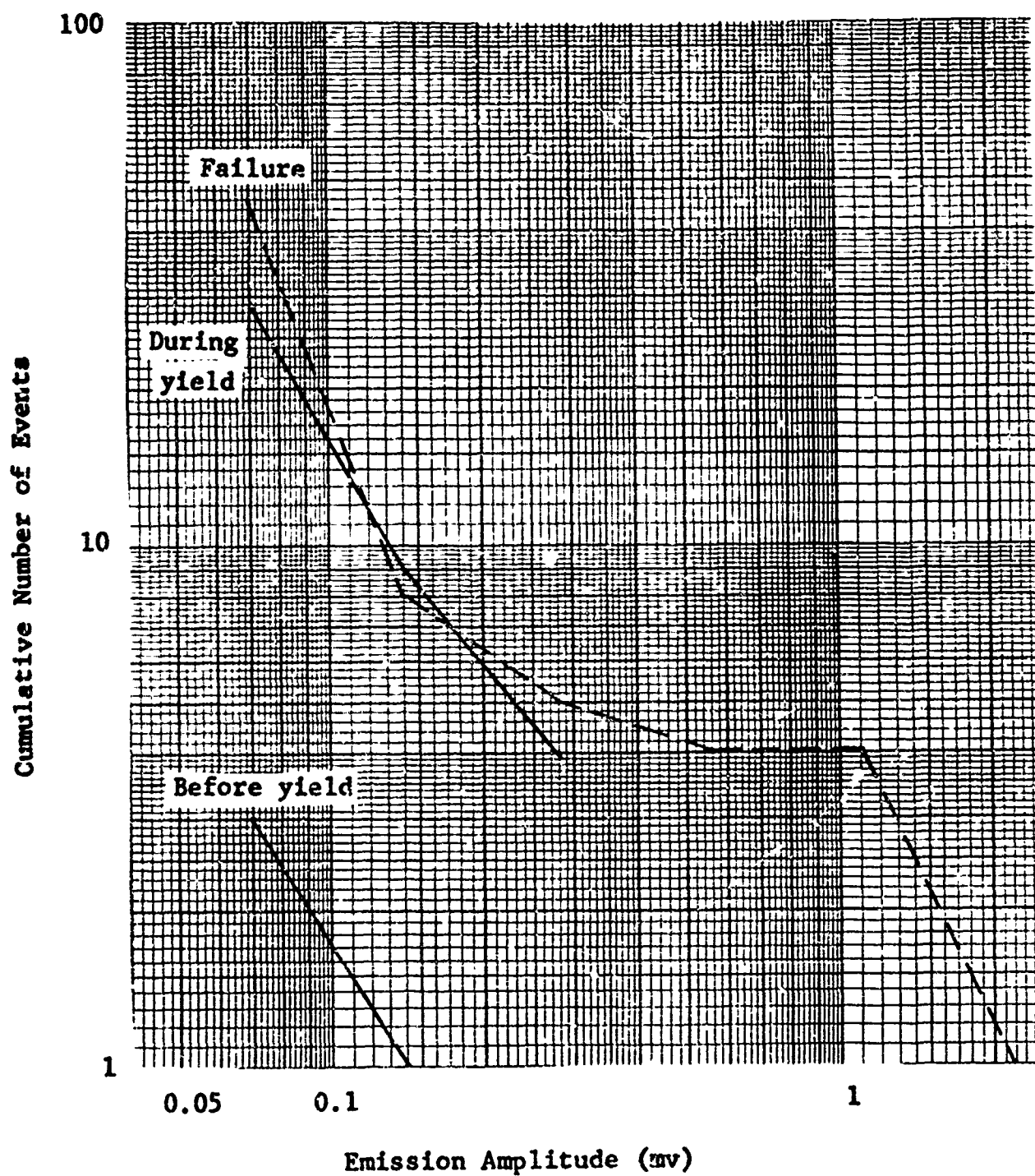


Figure 5.30 Amplitude Distribution of Emission Signals for Specimen A6-1

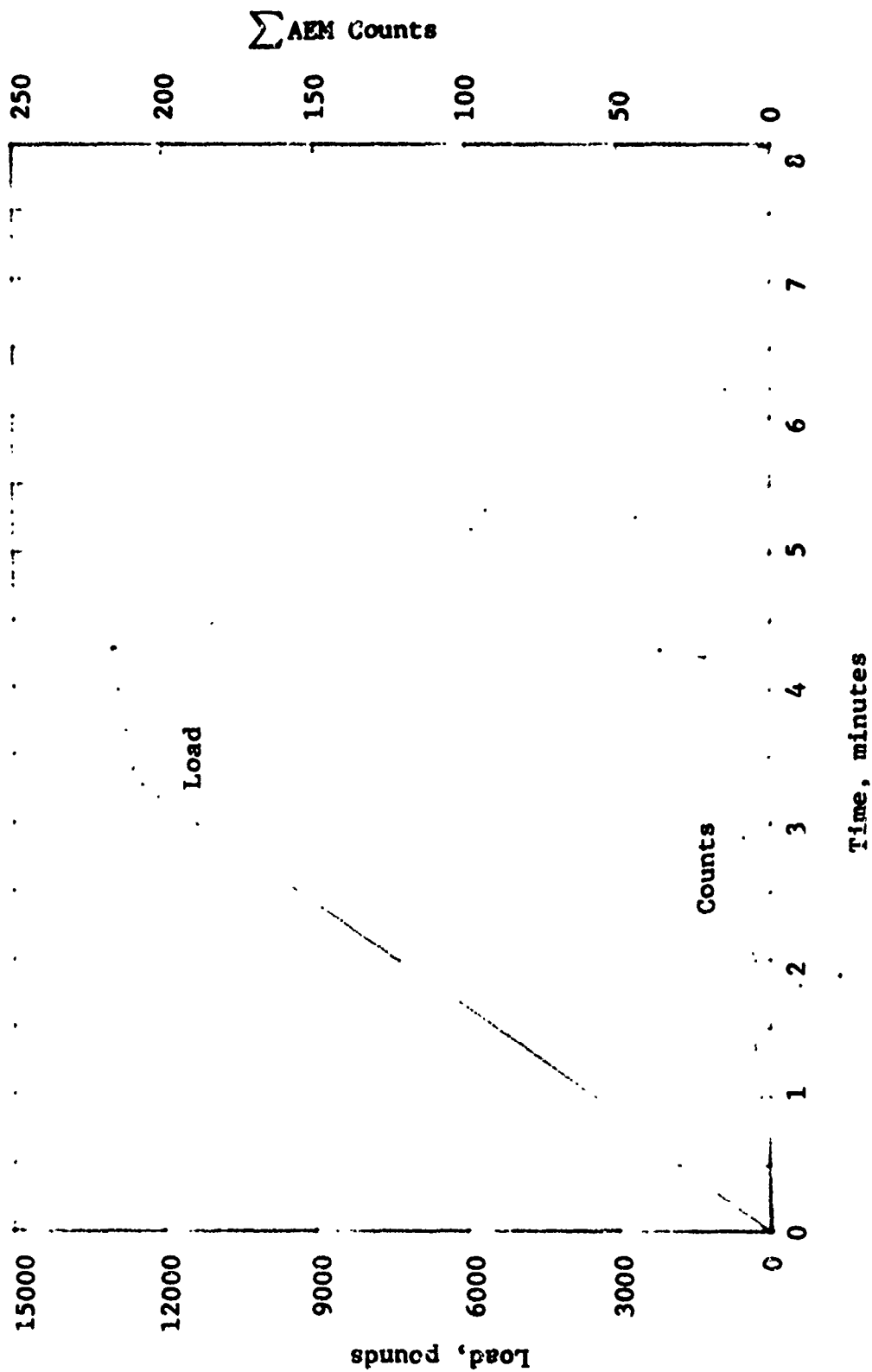


Figure 5.31 AEM Characteristics of Tensile Specimen H6-3

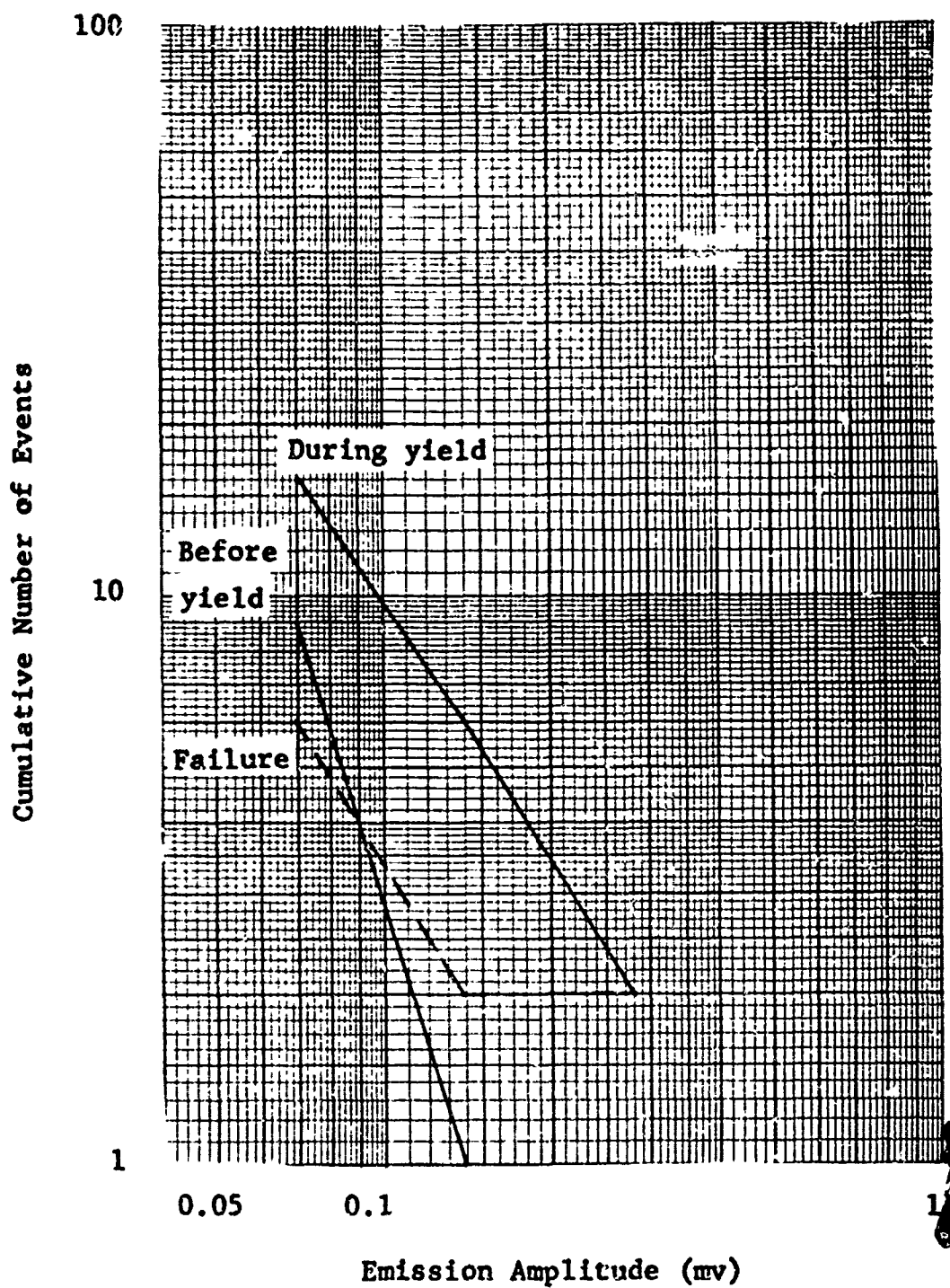


Figure 5.32 Amplitude Distribution of Emission Signals for Specimen H6-3

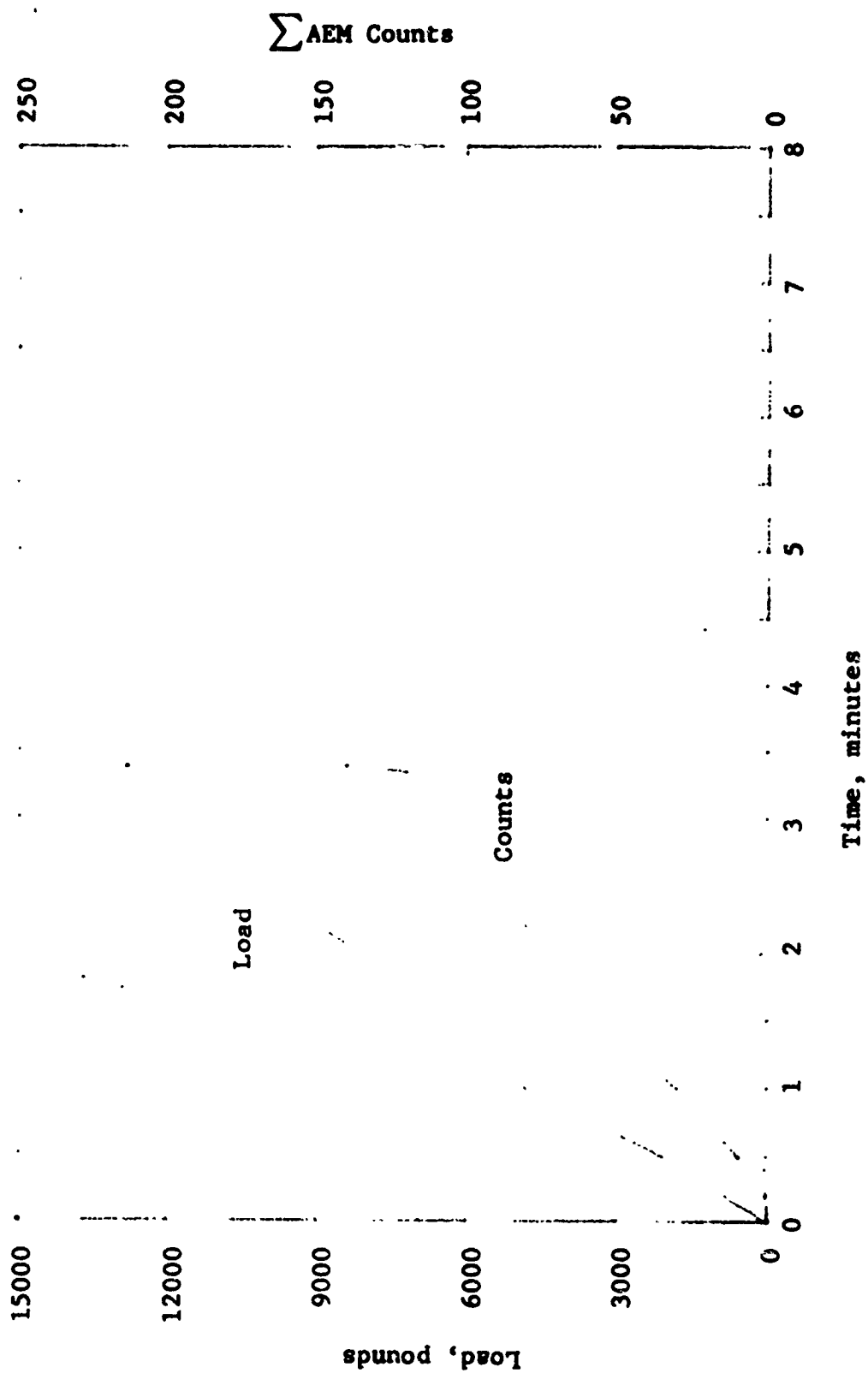


Figure 5.33 AEM Characteristics of Tensile Specimen K6-3



acoustic emission events were emitted at a very low load level and the acoustic emission rate is quite constant. These signals occurring at this load level from an unflawed specimen would give suspicion that noise signals were being recorded as events. The signals may have been from the stainless steel inclusion. Figure 5.34 is a graphic presentation of the amplitude distribution of the acoustic emission events from Specimen K6-3. These plots show that many large signals were emitted prior to reaching the yield stress of the specimen. The printout of the amplitude of these signals showed that the first emission was of an amplitude of 12 to 18 dB and that 10 seconds later a group of 4 signals was emitted with one signal in the 42-48 dB range. Therefore, an early detection of flaw growth in this type specimen was evident by acoustic emission monitoring.

Specimen D3-3 - Specimen D3-3 was cyclic loaded for the number of cycles over the load ranges tabulated in the following table.

<u>No. of Cycles</u>	<u>Load Range, Lbs</u>
2145	135 - 1095
204	135 - 1200
46	135 - 1245

The first 2100 cycles were at a rate of 2.5 cycles per minute. The additional cycles at the higher loads were at a slower rate of 1 cycle per 45 seconds.

During the first 2100 cycles, the loading machine generated large numbers of signals which were counted by the acoustic emission monitoring system. These acoustic emission signals were in the 6 to 12 dB range in amplitude. Most of the acoustic signals were generated in the mechanical and electrical system of the loading machine.

After grounding the loading machine and operating the machine in the cyclic mode, the specimen was cycled at the 135 to 1095 load level for 45 additional cycles. During these 45 cycles, 7 acoustic signals were recorded as events. These signals were all in the 0-6 dB range.

The specimen was then cycled an additional 204 cycles at a load range of 135 to 1200 lbs. During these 204 cycles, 121 acoustic emission events were recorded. These events occurred at random load levels. One of the most constant signal generators

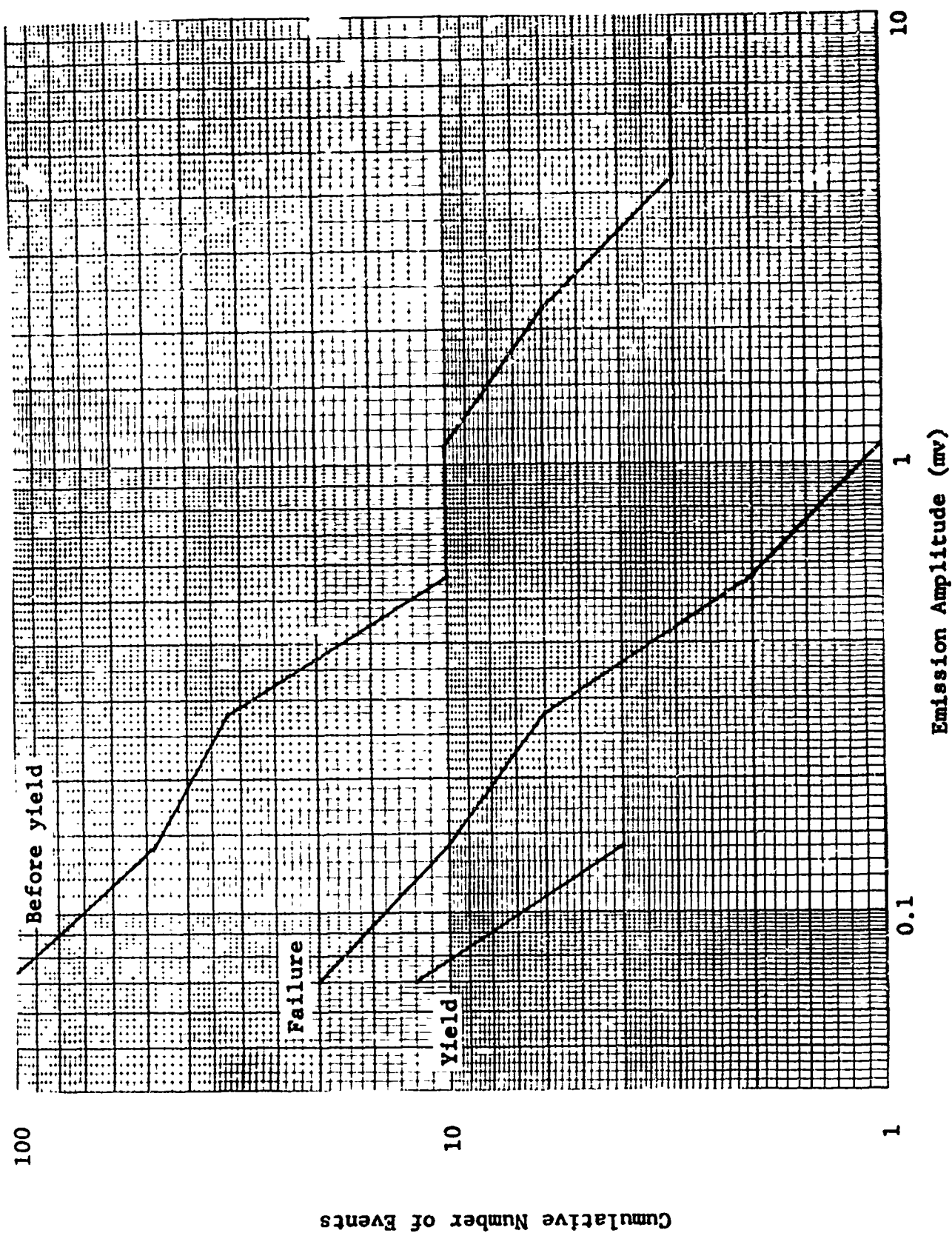


Figure 5.34 Amplitude Distribution of Emission Signals for Specimen K6-3

during this test was the relay switch which controlled the cycling. Fourteen signals were generated at the highest load level and 19 at the lowest load level. These signals were observed at the click of the relay switch.

The amplitude of these signals was distributed as follows: 3 signals, 12-18 dB; 9 signals, 6-12 dB; and 209 signals, 0-6 dB.

This specimen was cycled an additional 46 cycles at a load range of 135-1245 lbs. During these cycles, 83 acoustic signals were observed. These signals were at random positions on the loading and unloading cycles. The amplitude of these 83 signals was two in the 6-12 dB range and 81 in the 0-6 dB range above threshold of the instrumental.

After Specimen D3-3 had been cyclic loaded as discussed above, it was ramp loaded to failure. The cumulative acoustic emission events from this specimen are presented in Figure 5.35. Specimen D3-3 emitted fewer acoustic signals than the other specimens. Also, the load curve shows a sharp knee at the yield point indicating some fatigue. The amplitude distribution of the acoustic emissions from Specimen D3-3 is plotted in Figure 5.36. These data show that no signals were emitted prior to failure that had an amplitude above 6 dB.

In summary, it was determined that all the parent material specimens and the two optimum bond specimens (Specimens A3-2 and A6-1) emitted the large amplitude signals during failure or in the last five seconds. Those specimens having flaws or partial bonds emitted large amplitude signals during the yield period. The one exception to the above statements was Specimen K6-3. Specimen K6-3 emitted the largest amplitude signals during the period prior to the beginning of yield on the load curve. Thus, those specimens having some type of defect emitted acoustic emissions of an amplitude large enough to indicate critical defect prior to failure.

### 5.1.3 Conclusions

To obtain meaningful data from this type of specimen in real time, the experimenter must establish a low-noise-to-event ratio.

When collet-type specimen groups are used, some type of noise rejection is required to obtain useful data.

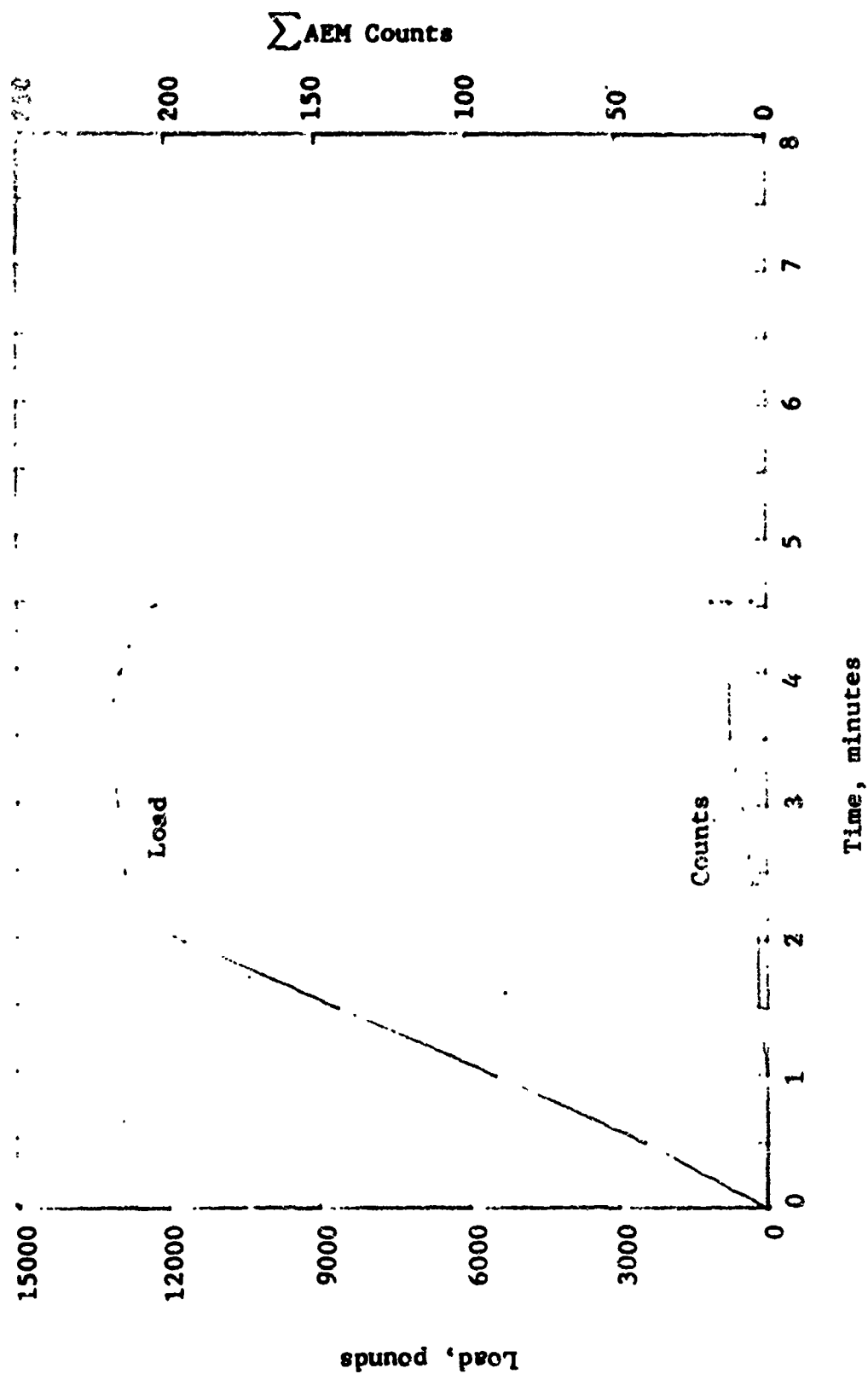


Figure 5.35 AEM Characteristics of Tensile Specimen D3-3

Cumulative Number of Events

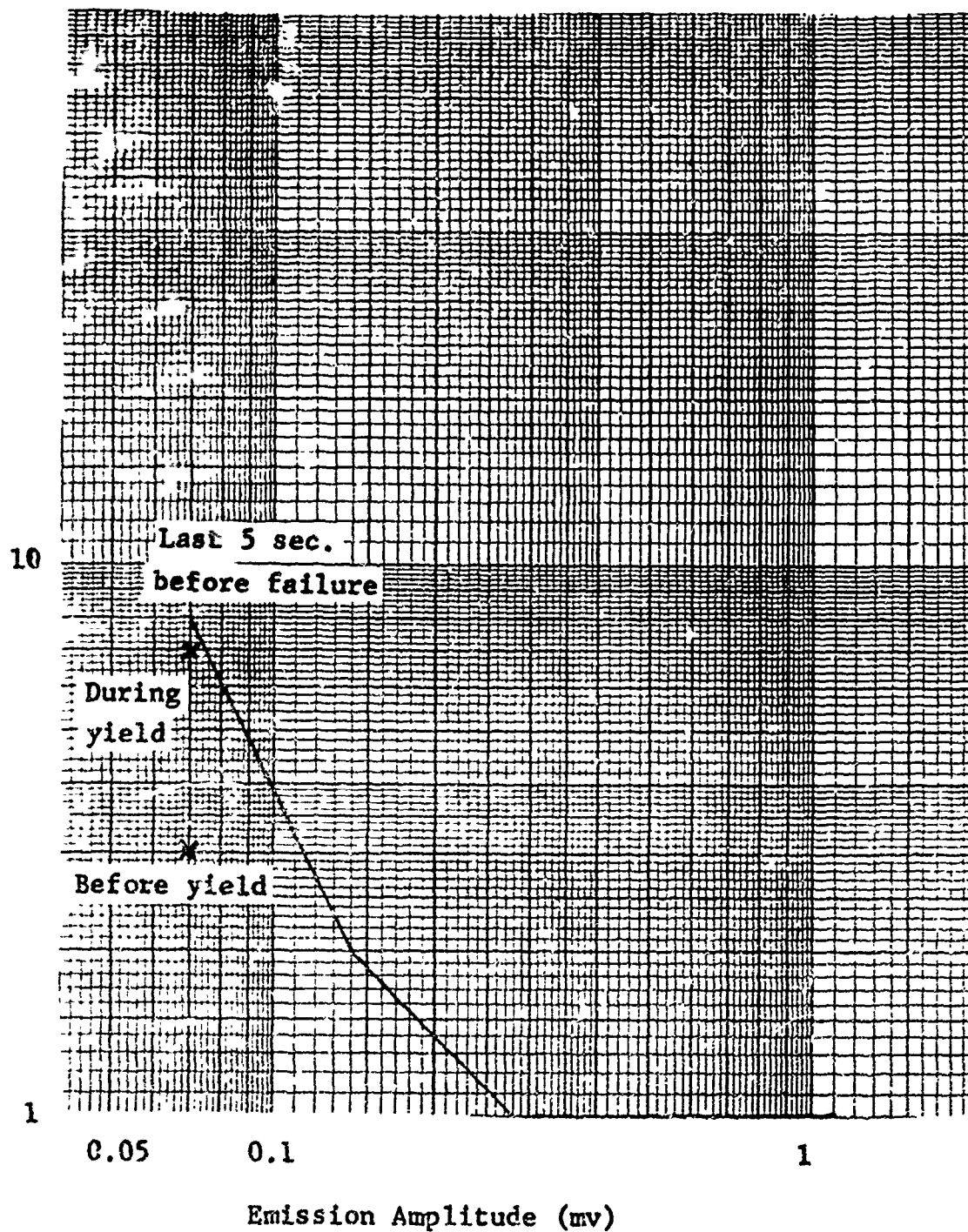


Figure 5.36 Amplitude Distribution of Emission Signals for Specimen D3-3

The amplitude distribution of the acoustic emissions from a specimen test can be useful in determining the criticality of defects in materials during structural test.

Flaws, debonding, and inclusions are detectable by acoustic emission monitoring in the type of material used in this study.

More specimens having the same type flaw should be monitored to establish reproducibility.

No discernible differences were observed in the characteristics of acoustic emission signals from the "as-received" material and the heat treated material.

## 5.2 Grain Size Variations vs Attenuation

### 5.2.1 Attenuation Theory

In view of the fact that the attenuation, particularly the scattering in a material, is one of the main difficulties encountered in ultrasonic testing, it is of practical importance to be able to estimate the influence of the crystal structure on the attenuation.

The attenuation in a material can be divided into two parts (Ref. 8 ),

$$\alpha = \alpha_A + \alpha_S \quad (1)$$

where  $\alpha_A$  is the attenuation due to absorption or the direct conversion of sound energy into heat. This attenuation can be written

$$\alpha_A = C_1 f \quad (2)$$

where  $C_1$  is a constant unaffected by grain size and anisotropy. The attenuation due to scattering results from material not being homogeneous. Metals contain boundaries on which the acoustic impedance changes abruptly because two materials of different density or sound velocity meet at these interfaces.

For frequency ranges where grain size 1/1000th to 1/100th wavelength, scattering is negligible. It increases very rapidly, however, approximately as the 3rd power of the grain

size, to make itself felt at sizes from 1/10th to the full value of the wavelength. For the grain size much less than the wavelength,

$$\alpha_S = C_2 F_A D_K^3 f^4 (D_K \ll \lambda) \quad (3)$$

where  $D_K$  is the grain size,  $F_A$  is an anisotropy factor,  $C_2$  is a constant and  $f$  is the frequency.

### 5.2.2 Attenuation Measurement Technique

The feasibility of using ultrasonic attenuation measurements to determine grain size variations in titanium alloys was examined. Effects of anisotropy in grain structure were also studied. The buffer rod method proposed by Papadakis (Ref. 9) was utilized.

This method requires the measurement of the first buffer-sample reflection amplitude (A), the first sample back reflection (B), and the second sample back reflection (C). Figure 5.37 is a diagram of the reflections giving rise to echoes of amplitude A, B, and C.

In this situation, the relative amplitudes A, B, and C are

$$A = R$$

$$B = (1 - R^2)e^{-2\alpha L}$$

$$C = R(1 - R^2)e^{-4\alpha L}$$

where

$R$  = reflection coefficient at the buffer-sample interface,

$\alpha$  = ultrasonic attenuation (neper/unit length)

and

$L$  = length of the sample.

From the above equations, one can derive

$$R = \frac{\tilde{A}\tilde{C}}{(1 + \tilde{A}\tilde{C})^{\frac{1}{2}}}$$

and

$$\alpha = (1/2L) \ln(R/\tilde{C})$$

where

$$\tilde{A} = A/B \text{ and } \tilde{C} = C/B.$$

The waveform analysis sytem described in Appendix B of Reference 6 was programmed to (a) extract the peak-to-peak pulse amplitudes A, B, and C from the digitized waveforms and (b) calculate the reflection coefficient R and attenuation  $\alpha$ .

### 5.2.3 Experimental Setup

The buffer rod system consisted of a plexiglas block housing transducers of different sizes. The transducer was coupled to the sample via a cylindrical cavity filled with light machine oil (see Figure 5.38). Three different types of transducers were used. These transducers are listed below.

1. 1.0 MHz/.500 SFZ 57A2439, Automation Industries.
2. 2.25 MHz/.375 SFZ 57A2275, Automation Industries.
3. 10.0 MHz/.250 SFZ 57A5623, Automation Industries.

A Panametrics Model 5050 PR Ultrasonic Pulser/Receiver was used in conjunction with these transducers. The power output using the Panametrics Model 5050 PR Pulser/Receiver with the three transducers was measured. The response of the 2.25 MHz transducer is shown in Figure 5.39.

### 5.2.4 Experimental Measurements

Ultrasonic attenuation measurements were made on specimens having different primary alpha grain sizes and different orientations with respect to the rolling direction of the original plate material, prior to bonding. The results of these attenuation measurements are shown in Table 5.2. In general, only a slight increase in attenuation was observed in the larger grain sized material. In Figure 5.40, the attenuation is plotted as a function of alpha grain size after bonding. As noted earlier, the attenuation due to scattering is strongly dependent on the ratio of grain size to wavelength.



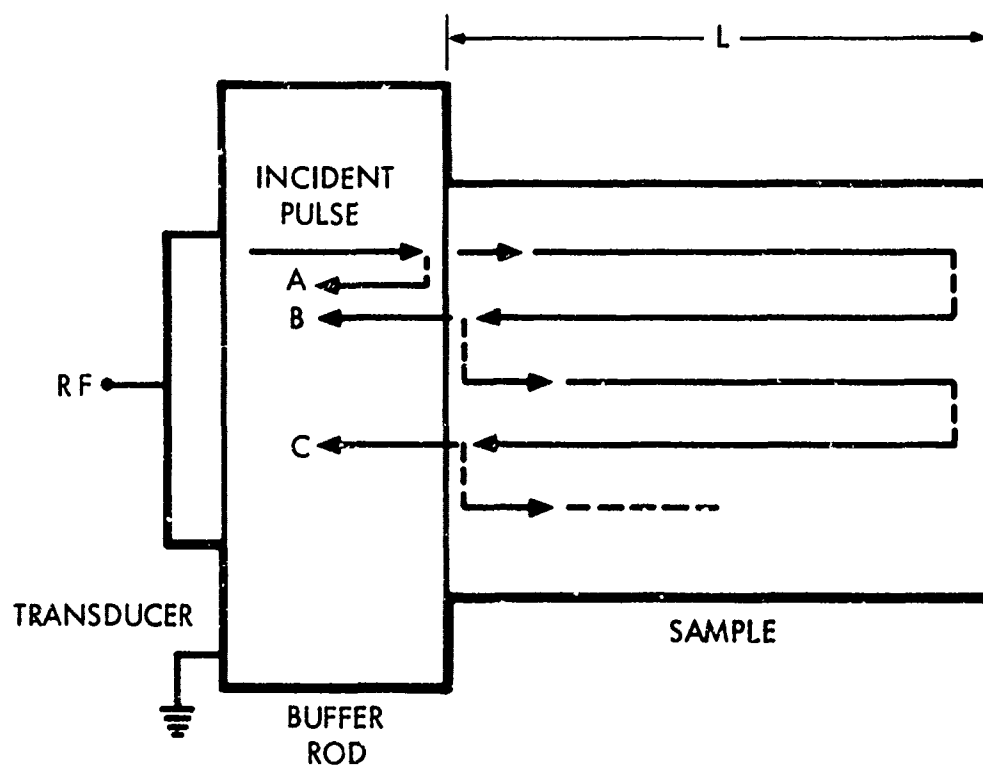


Figure 5.37 Reflection Diagram for Buffer Rod System

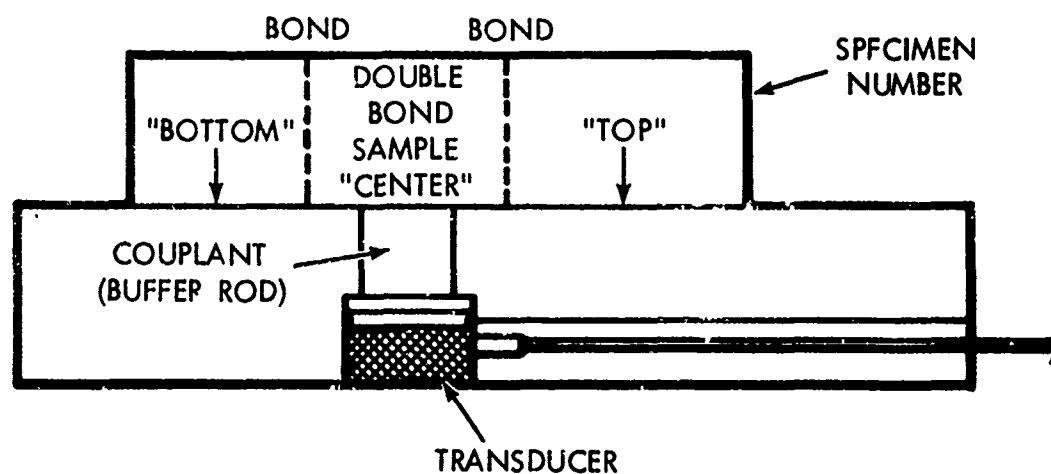


Figure 5.38 Experimental Set Up for Attenuation Measurements

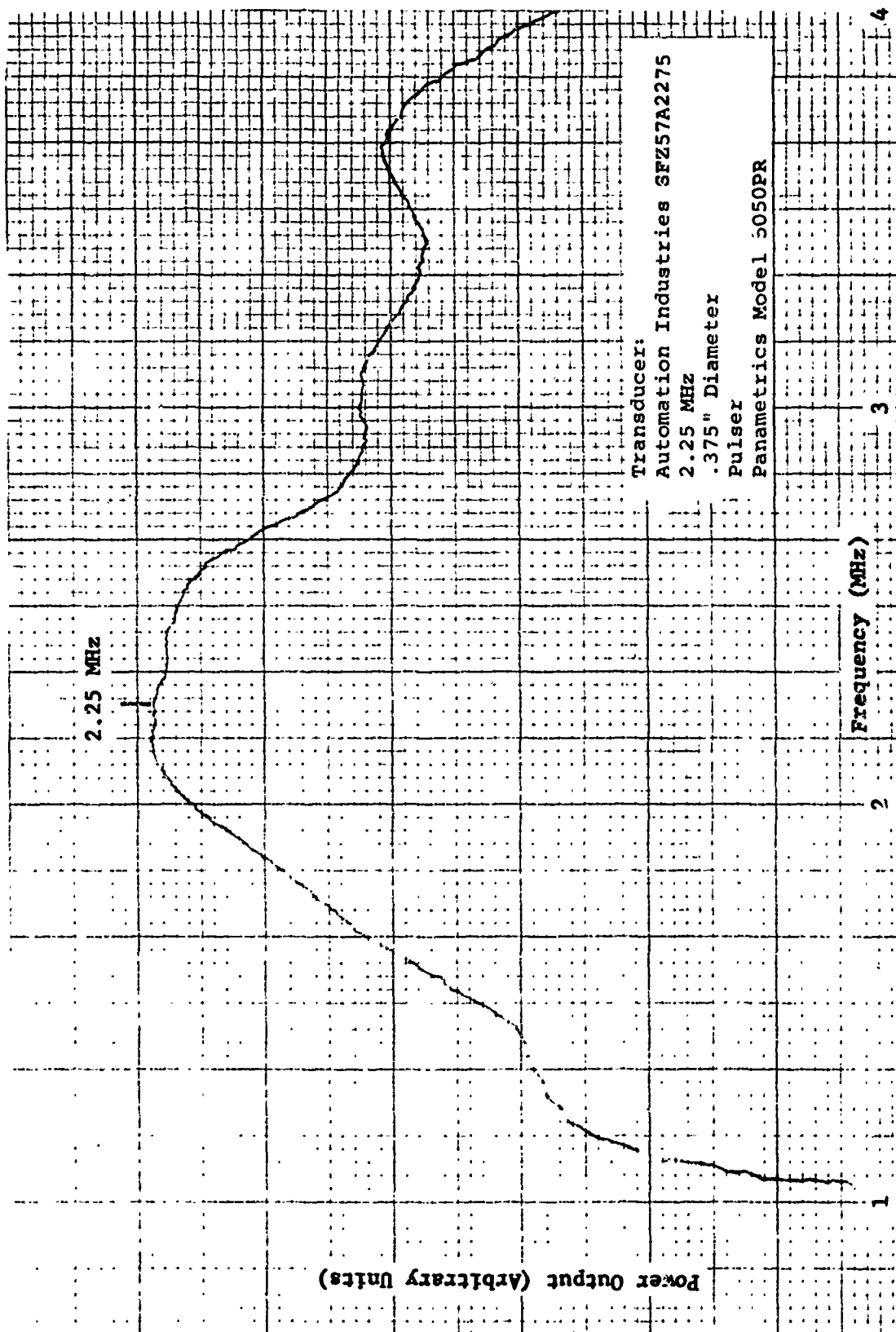
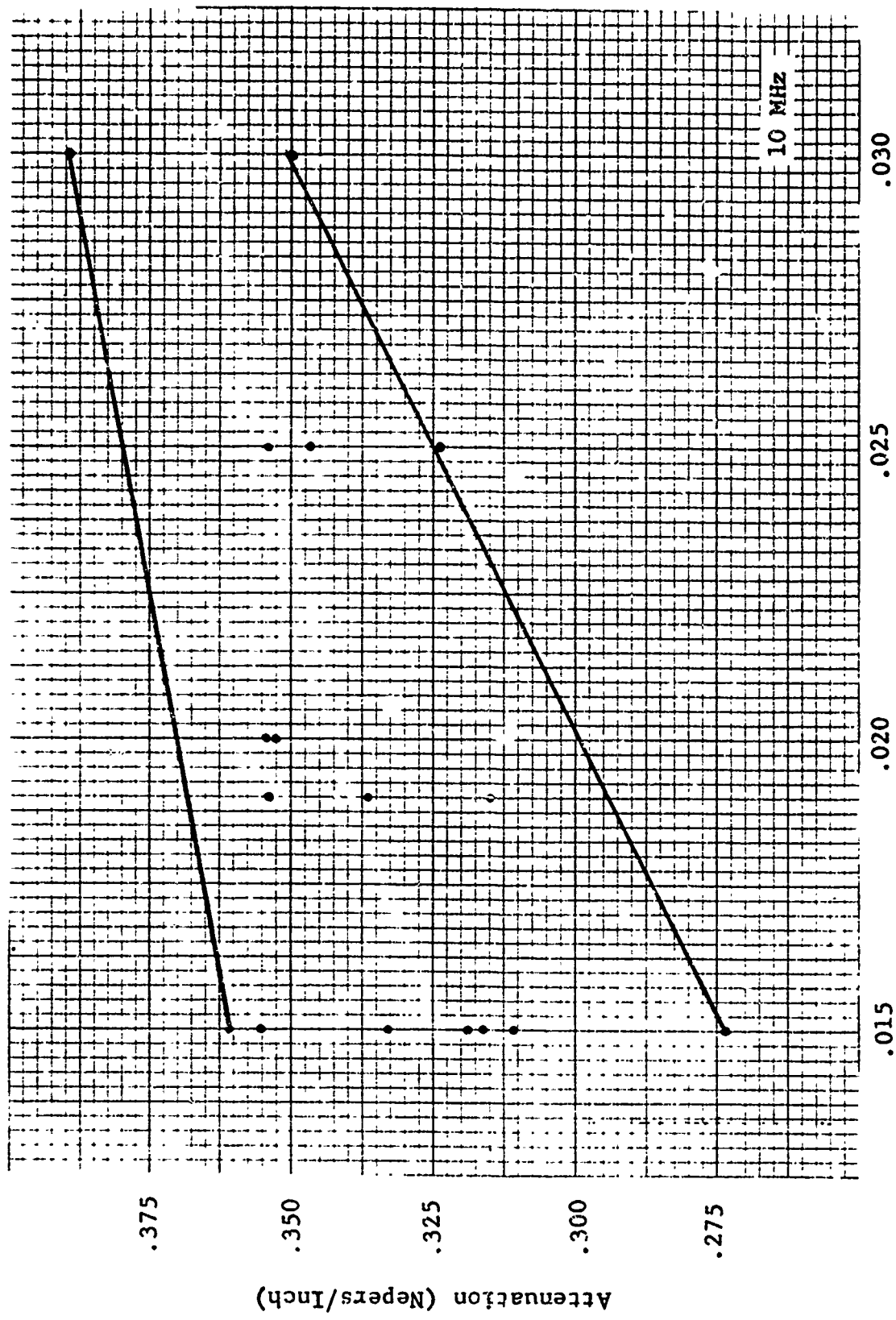


Figure 5.39 Power Output vs. Frequency for a 2.25 MHz/.375 Dia Transducer



Average Diameter of Primary Alpha Grain (mm)

Figure 5.40 Attenuation vs. Primary Alpha Grain Size

In the material used in these experiments, the ratio of average grain size to wavelength was  $\approx 1/50$ , thus attenuation due to scattering should not be too prominent.

No significant changes in attenuation were measured in specimens having different orientations with respect to the rolling direction. The effect of the bonding cycle on samples having grain orientation differences between mating parts prior to bonding was to make differences in texture practically impossible to observe due to equiaxed alpha grains being present after bonding. Thus, no significant changes would be expected.

#### 5.2.5 Other Titanium Alloys

Attenuation measurements were also made on two other 6Al-4V titanium alloy types. The first had properties conforming to Specification MIL-T-9046C, Class II, with mechanical properties and microstructure similar to the material corresponding to North American Rockwell Specification ST0170LB0032. The other 6Al-4V titanium alloy material came from a forging, which had been procured in the beta-forged condition. This material had substantially larger beta grains of the order of .6 mm average diameter.

Attenuation measurements were also made on a Beta III titanium specimen which had been aged at 1000°F for 8 hours. The average beta grain size in this material was approximately the same as that of the beta forged 6Al-4V titanium material.

Results of the attenuation measurements using different frequency transducers are shown in Figure 5.41. The effect of the large beta grains in the beta forged Ti-6Al-4V and Beta III titanium material can be observed in the attenuation at higher frequencies. However at 1 MHz, less spread is obtained between the different types of material.

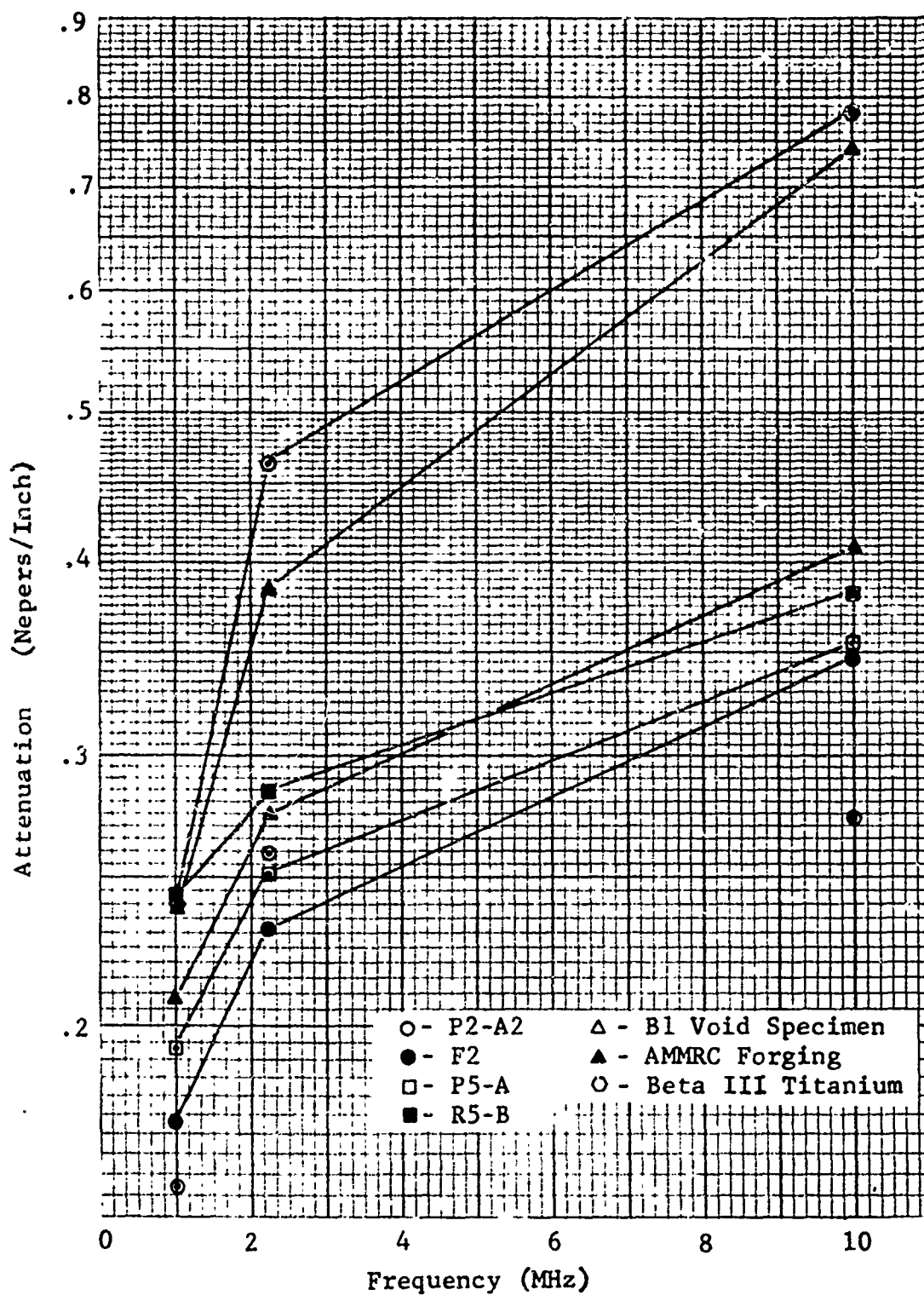


Figure 5.41 Ultrasonic Attenuation vs. Frequency in Several Titanium Alloys

**Table 5.2 ULTRASONIC ATTENUATION IN DIFFUSION BONDED AND PARENT HEAT CYCLED Ti-6Al-4V SPECIMENS WITH DIFFERENT ROLLING ORIENTATIONS AND PRIMARY ALPHA GRAIN SIZES**

Specimen Number	Condition & Rolling Direction	Attenuation (Nepers/Inch)			
		Top	Center	Bottom	Average
P2-A	Parent Heat Cycled	.267	.301	.251	.273
E2	Parent Heat Cycled	.370	.339	.353	.354
F2	Parent Heat Cycled	.324	.357	.359	.347
A3	Single Bond	.323	.311	.300	.311
P3-B	Single Bond	.317	.315	.316	.316
E3	Single Bond	.319	.337	.355	.337
A3-A	Single Bond	.344	.376	.343	.354
A4	Double Bond	.336	.286	.331	.318
D4	Double Bond	.343	.332	.325	.333
E4	Double Bond	.322	.303	.321	.315
F4	Double Bond	.334	.312	.319	.322
P5-A	Multiple Bond/Double Axes	.336	.357	.390	.361
Q5-B		.333	.379	.349	.354
R5-A		.384	.383	.385	.384
P6-A	Multiple Bond/Three Axes	.348	.360	.375	.361
Q6-A		.330	.392	.336	.353
F6		.334	.378	.335	.350

Data taken with a 10 MHz Transducer

## 6. BOND TESTING

### 6.1 Sample Preparation

Diffusion bonded specimen configurations and sectioning diagrams are given in Figures 6.1 and 6.2. Prior to any fabrication step, the laminate details were laid out on the plate material and coded alphanumerically to indicate:

1. Original location within the plate;
2. Rolling direction (which is maintained throughout the machining steps);
3. Type of test specimen (static tensile, fatigue, etc.).

The fabrication steps followed were:

#### Diffusion Bonded Specimens

1. Saw cut to rough dimensions.
2. Heat treat in vacuum furnace to obtain required grain size variation.
3. Mill to bonding dimensions.
4. Measure surface finish.
5. Etch.
6. Insert and catalogue intentional deficiencies (as determined from survey).
7. Bond at 1700<sup>0</sup>F, 6 hours, deformation as required.
8. Saw cut rough specimens.
9. Machine specimen blank.
10. Bond line metallography
11. Machine test specimen.

#### Heat Cycled Specimens

1. Saw cut test specimen blanks
2. Heat cycle at DB time and temperature.
3. Machine final test specimen

#### Parent Material Specimens

1. Saw cut test specimen blanks.
2. Machine final test specimen.

### 6.1.1 Diffusion Bonding Procedures

The different diffusion bonded specimen configurations from which tensile and fatigue samples were subsequently machined are shown in Figure 6.1 and 6.2.

Bonding temperature and time were held constant as bond quality was varied by changing the total amount of deformation received or by insertion of artificial deficiencies. Based on previous studies of the optimum bonding parameters for Ti 6Al-4V (Ref. 1 ), samples were bonded at 1700°F for 6 hours. For the single-bond/single-axis and double-bond/single-axis joints, total deformations greater than 3% were obtained under optimum bonding conditions. In two axes and three axes joints, bond quality in terms of deformation is less clearly defined. In making the multiple-bond/2-axes specimens, wedge tooling was designed such that the required deformation was first obtained along the longitudinal direction followed by deformation through the thickness.

In the multiple-bond/3-axes specimens, very little change in dimension was obtained in the longitudinal and long transverse directions. The tooling was designed such that the sides of the 3-axes specimens are constrained during pressure application. Approximately 5% deformation was obtained through the thickness of the material under optimum conditions. The amount of pressure applied was a function of deformation rate and deformation desired during the bond cycle. Ninety percent of the desired deformation was applied to all of the specimens during the first hour of pressure application. A residual pressure was then maintained on the specimen for the rest of the cycle which was determined by the creep rate desired. Vacuums in the  $10^{-4}$  torr range were maintained in the vacuum furnace throughout the bonding cycle.

The surface finish was measured on all bonding surfaces prior to bonding. A Bendix Profilometer was used to measure all surface finishes while selected surfaces were also checked with a Bendix Proficorder. Surface finishes better than 65 RMS were required on all surfaces to be bonded. Milled surfaces having greater than 62 RMS surface were sanded lightly with 320 grit sandpaper to improve the surface finish. All surface finishes measured between 10 RMS and 60 RMS after this procedure.



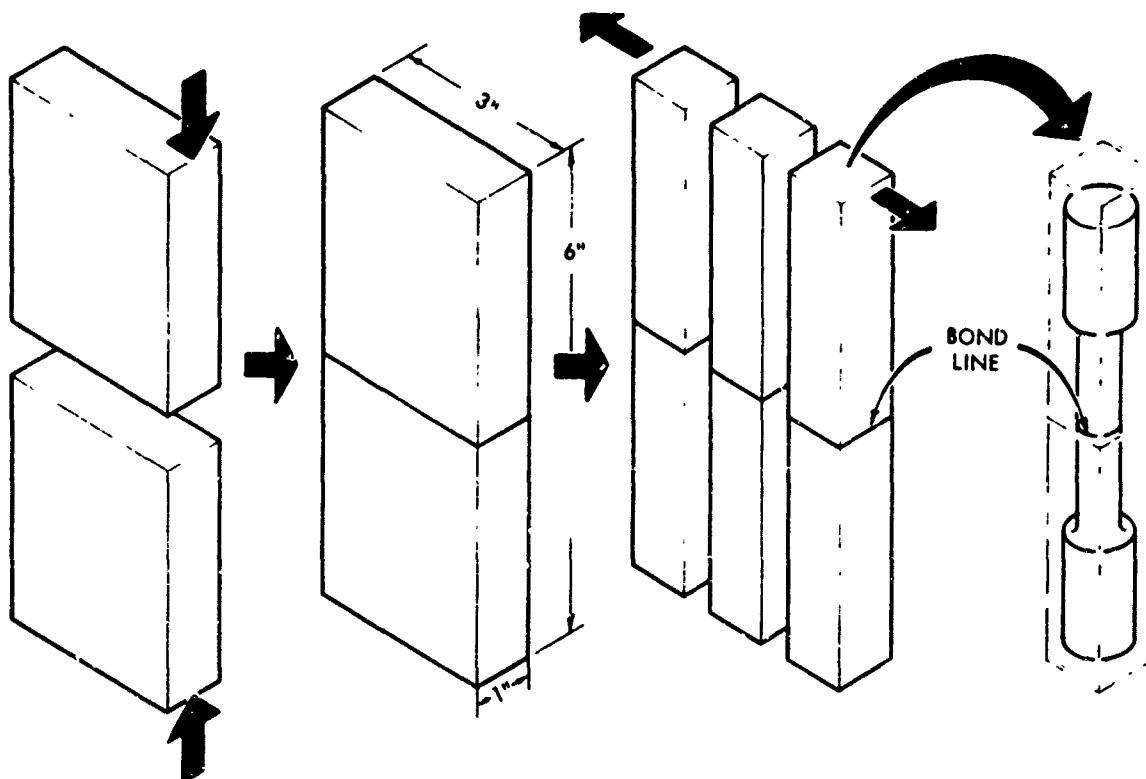


Figure 6.1a Preparation of Single Bond Tensile and Fatigue Specimens

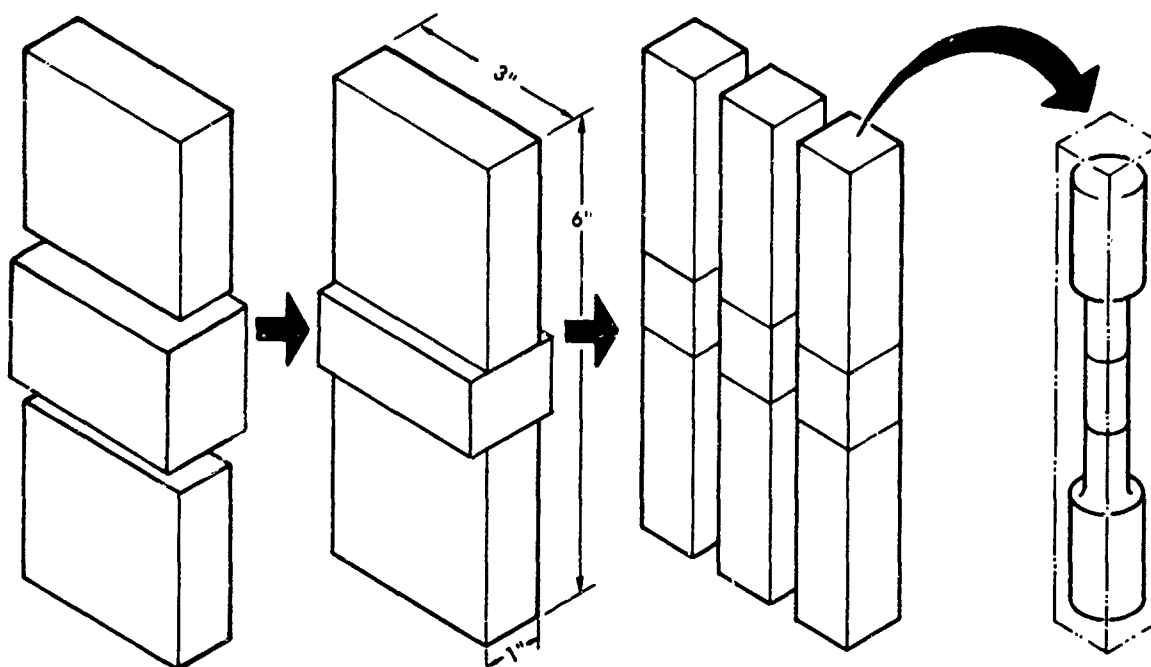


Figure 6.1b Preparation of Single Axis Multiple Bond Tensile and Fatigue Specimens

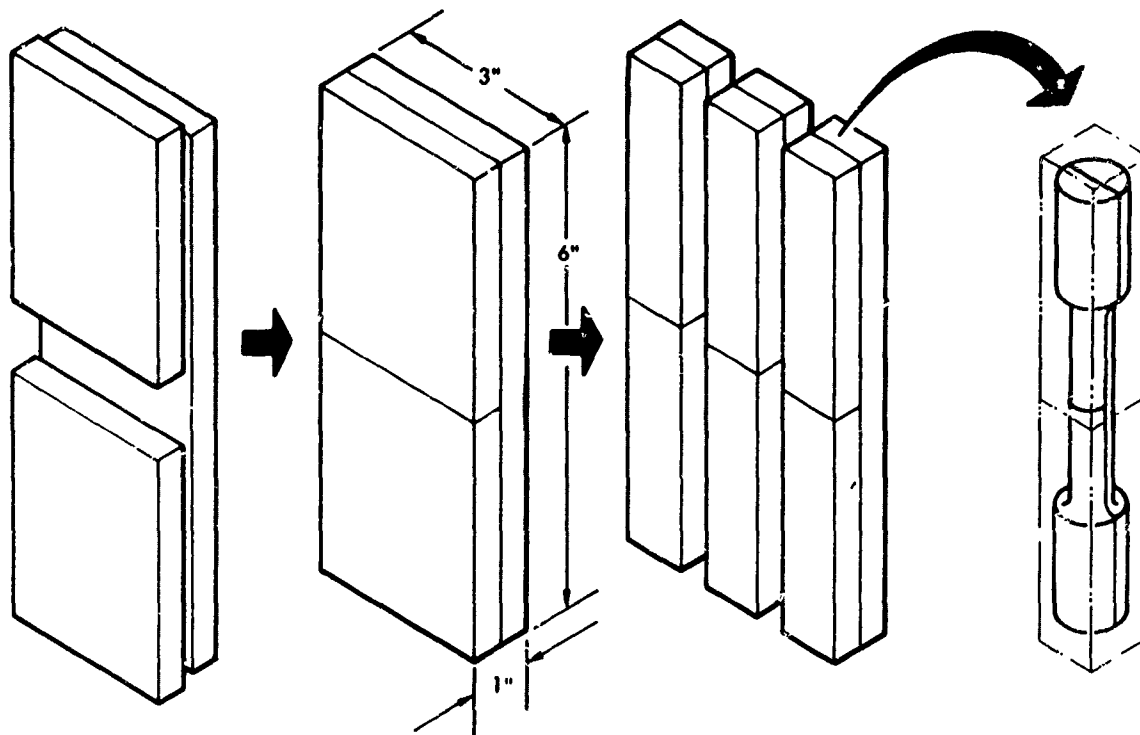


Figure 6.2a Preparation of 2-Axis Multiple Bond Tensile and Fatigue Specimens

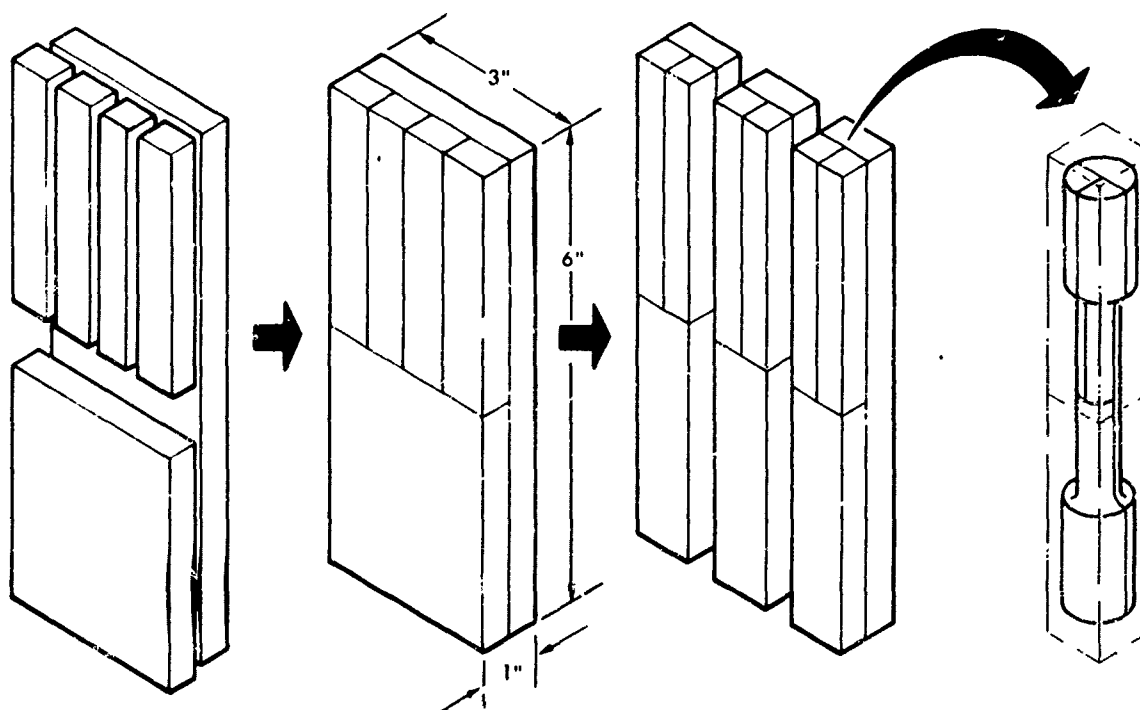


Figure 6.2b Preparation of 3-Axis Multiple Bond Tensile and Fatigue Specimens

The Ti 6Al-4V cleaning procedure used has been described previously (Ref. 1 ).

### Assembly Procedure and Tooling

The assembly procedure for bonding the single-bond/single-axis and double-bond/single-axis consisted of loading six sets of specimens in the vacuum furnace along with two parent material specimens to be cycled. No tooling was required in bonding these specimens. A thermocouple was embedded in one of the 1-inch thick Ti 6Al-4V pieces to be bonded. In bonding the multiple-bond/2-axes joints, two sets of wedge tooling shown in Figure 6.3 were loaded into the vacuum furnace. The thermocouple was embedded in the wedge tooling near the middle of the titanium specimen to be bonded. In bonding the multiple-bond/3-axes joints, one set of wedge tooling shown in Figure 6.4 was loaded in the furnace. Again, the thermocouple was embedded in the wedge tooling near the middle of the titanium specimen to be bonded.

#### 6.1.2 Production of Intentional Deficiencies

A specimen parameter matrix (Table 6-1) was established which included four different types of deficiencies: (a) bonding parameter variations, (b) grain size variations and orientation effects, (c) void defects, and (d) contamination. The program can thus be separated into four phases. In each phase of the program, one particular deficiency was varied while holding all other deficiency parameters constant.

The various types of deficiencies are based on the diffusion bonding survey described in Section 3.

#### Phase I - Bonding Parameter Variations

In this phase of the program, defects were introduced in the form of less than optimum bonding conditions. These conditions were produced by giving the deficient specimens insufficient deformation. Total deformations received by these samples are shown in Tables 6.2, 3 & 4. All samples were oriented such that the long axis of the tensile and notched fatigue specimens were parallel to the rolling direction of the material.

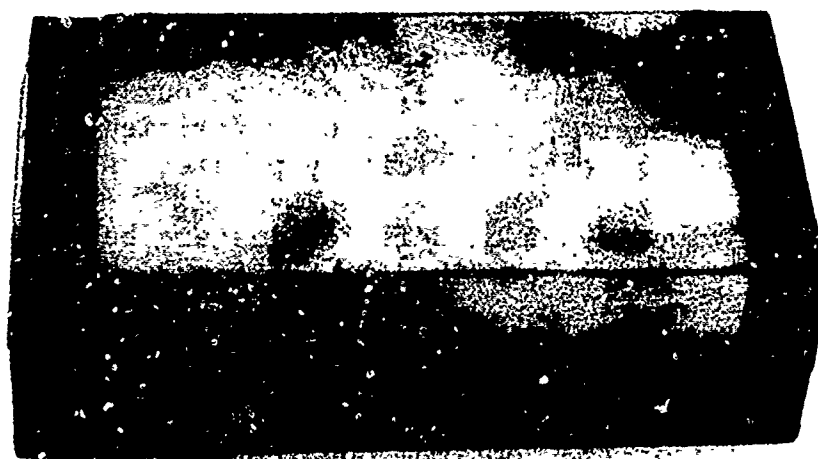


Figure 6.3 Wedge Tooling for 2-Axes Diffusion Bonded Specimens

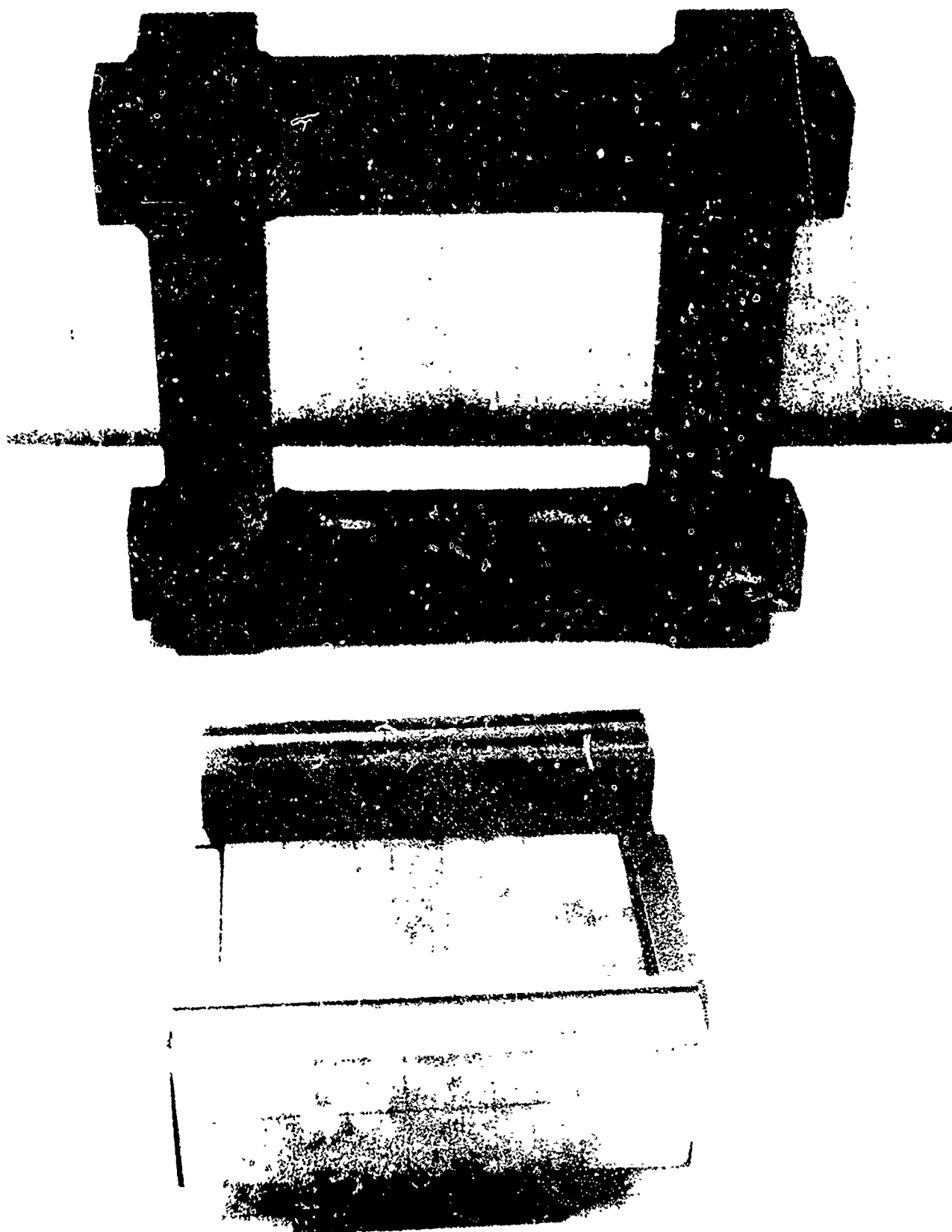


Figure 6.4 Wedge Tooling for 3-Axes Diffusion Bonded Specimens

Table 3.1 TEST SPECIMEN PARAMETER MATRIX & QUANTITIES

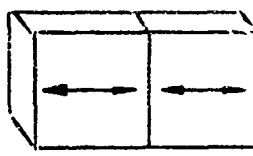
	Specimen Type	Parent	Parent	Single	Multiple Bond		
		AR*	T/C**	Bond	1 Axis	2 Axes	3 Axes
		1	2	3	4	5	6
TENSILE	Bonding Parameters						
	1700°F, 6 hrs, 7% def.	A	3	3	3	3	3
	1700°F, 6 hrs, 2½% def.	B	3	3	3	3	3
	1700°F, 6 hrs, 1½% def.	C	3	3	3	3	3
	Grain Size						
	AR (ASTM Size 10)	D	3	3	3	3	3
	2 x AR (ASTM Size 9)	E	3	3	3	3	3
	4 x AR (ASTM Size 7.5)	F	3	3	3	3	3
	Surface Finish						
	0.0065"d x 0.006" deep	G	1	3	3	3	3
	0.010"d x 0.010" deep	H	1	3	3	3	3
	0.020"d x 0.020" deep	I	1	3	3	3	3
FATIGUE	Surface Contamination						
	α Case Layer	J	1	3	3	3	3
	St. Steel Enclusion	K	1	3	3	3	3
	SiO <sub>2</sub> Enclusion	L	1	3	3	3	3
	Bonding Parameters						
	1700°F, 6 hrs, 7% def.	M	25	6	6	6	6
	1700°F, 6 hrs, 2½% def.	N	6	6	6	6	6
	1700°F, 6 hrs, 1½% def.	O	6	6	6	6	6
	Grain Size						
	AR (ASTM Size 10)	P	6	6	6	6	6
	2 x AR (ASTM Size 9)	Q	6	6	6	6	6
	4 x AR (ASTM Size 7.5)	R	6	6	6	6	6
FATIGUE TENSILE	Surface Finish						
	0.0065"d x 0.006" deep	S	6	6	6	6	6
	0.010"d x 0.010" deep	T	6	6	6	6	6
	0.020"d x 0.020" deep	U	6	6	6	6	6
	Surface Contamination						
	α Case Layer	V	6	6	6	6	6
	St. Steel Enclusion	W	6	6	6	6	6
	SiO <sub>2</sub> Enclusion	X	6	6	6	6	6
	As-Received						
	RD	Y	6				
	⊥ RD	Z	6				
	As-Received						
	RD	AA	6				
	⊥ RD	AB	6				

\* AR = As-Received

\*\* T/C = DB Thermal Cycle

Table 6.2

BONDING PARAMETER VARIATIONS IN SINGLE-BOND/SINGLE-AXIS  
AND DOUBLE BOND-SINGLE AXIS JOINT'S

Specimen Number	Type of Bond	Deficiency	Total Deformation (%)	Rolling Direction
A3 M3-A* M3-B*	Single Bond/Single Axis	None	7.72 7.28 7.12	
B3 N3-A N3-B	Single Bond/Single Axis	<Optimum Deformation	2.71 2.66 2.76	
C3 O3-A O3-B	Single Bond/Single Axis	<<Optimum Deformation	1.38 1.48 1.44	
A4* M4-A* M4-B*	Double Bond/Single Axis	None	7.05 8.28 6.87	
B4 N4-A N4-B	Double Bond/Single Axis	<Optimum Deformation	2.67 2.62 2.85	
C4 O4-A O4-B	Double Bond/Single Axis	<<Optimum Deformation	1.54 1.65 1.59	

\* Bonding time = 4 hours.

Table 6.3  
BONDING PARAMETER VARIATIONS IN MULTIPLE-BOND/2-AXES JOINTS

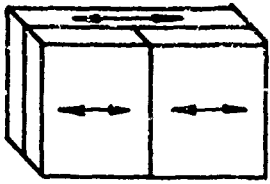
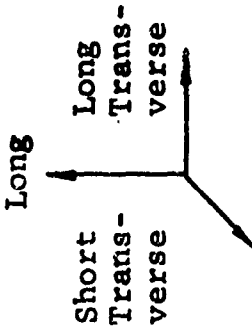
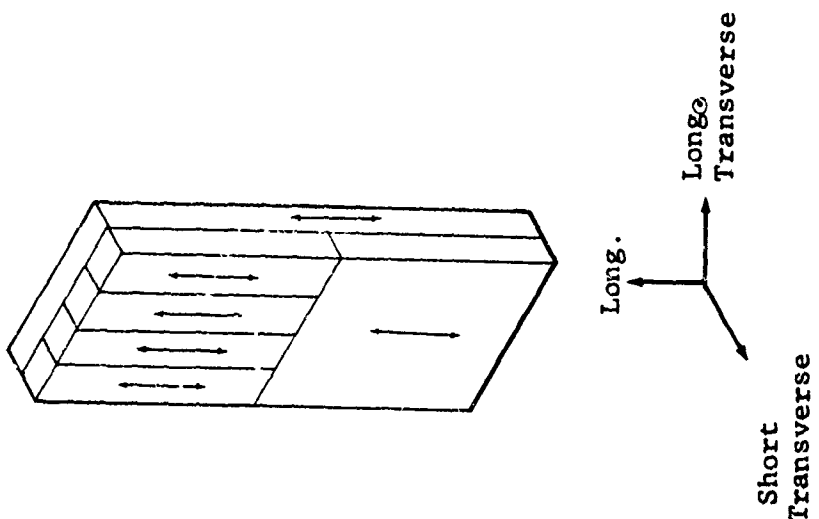
Specimen Number	Deficiency	Total Deformation Longitudinal Direction (%)	Total Deformation Short Transverse Direction (%)	Rolling Direction
A5	None	6.09	3.8	
M5-A	"	5.96	3.5	
M5-B	"	4.75	8.3	
B5	< Optimum Deformation	2.38	10.0	
N5-A	"	2.44	5.0	
N5-B	"	2.22	1.0	
C5	<< Optimum Deformation	0.74	2.2	Deformation Directions Related to Specimen Geometry
O5-A	"	0.74	2.0	
O5-B	"	0.60	3.0	



Table 6.4

## BONDING PARAMETER VARIATIONS IN MULTIPLE-BOND/3-AXES JOINTS

SPECIMEN NUMBER	DEFICIENCY	TOTAL DEFORMATION SHORT TRANSVERSE DIRECTION (%)	ROLLING DIRECTION
A6	None	4.1	
M6-A	None	3.8	
M6-B	None	4.0	
B6	<Optimum Deformation	3.1	
N6-A	<Optimum Deformation	4.3	
N6-B	<Optimum Deformation	2.0	
C6	<<Optimum Deformation	1.7	
O6-A	<<Optimum Deformation	2.5	
O6-B	<<Optimum Deformation	2.0	

Deformation Directions Related  
For Specimen Geometry

## Phase II - Grain Size Variations and Orientation Effects

In a series of experiments, samples having different sized primary alpha grains were bonded under optimum bonding conditions ( $1700^{\circ}\text{F}$  for 6 hours,  $\approx 5\%$  total deformation). Problems concerning grain orientation differences between mating parts (e.g., perpendicular orientation of rolling directions) were also studied in Phase II. As shown in Table 6.5, specimens having rolling directions perpendicular to each other were bonded together.

In making the single-bond/single-axis and double-bond/single-axis specimens, 1" Ti 6Al-4V plate was used. Before bonding, the microstructure of specimens D3, D4, P3-A, P3-B, P4-A, and P4-B consisted of elongated alpha grains in a matrix of transformed beta. The typical microstructure is shown in Figure 6.5. The average number of grains per cubic millimeter is  $1 \times 10^6$ , as determined by the intercept procedure (Ref. 10). This corresponds to ASTM Micro-Grain size Number 10.

Prior to bonding, specimens E3, E4, Q3-A, Q3-B, Q4-A, and Q4-B were heated at  $1735^{\circ}\text{F}$  for 6 hours in a vacuum furnace, followed by furnace cooling. The material heated at  $1735^{\circ}\text{F}$  for 6 hours has a microstructure closely resembling that of the material in the recrystallized-annealed (RA) condition. The microstructure is shown in Figure 6.6. The structure consists of nearly equiaxed primary alpha grains with intergranular beta. The average number of grains per cubic millimeter is  $0.25 \times 10^6$ . This corresponds to ASTM size number 9.

Specimens F3, F4, R3-A, R3-B, R4-A, and R4-B were heated at  $1775^{\circ}\text{F}$  for 6 hours prior to bonding. The microstructure of this material is shown in Figure 6.7. This material shows grains of primary alpha in a matrix of transformed beta containing acicular alpha. The average diameter of the primary alpha grains was 0.25 mm. (64,000 grains per cubic millimeter) corresponding to ASTM size number 7.5.

In making the multiple-bond/2-axes specimens and multiple-bond/3-axis specimens,  $\frac{1}{2}$ " Ti 6Al-4V plate was used. The typical microstructure of this material is shown in Figure 6.8. This microstructure consists of elongated alpha grains in a matrix of transformed beta. The average grain size of the as-received material is 6 or 0.006 mm average diameter. This corresponds to ASTM Micro-Grain Size Number 11. The grains are very elongated, however, making accurate readings very difficult.

Table 6.5

GRAIN SIZE AND ORIENTATION VARIATIONS: SINGLE-BOND/SINGLE-AXIS  
AND DOUBLE BOND SINGLE AXIS JOINTS

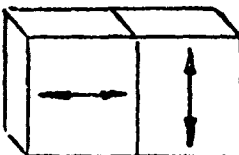
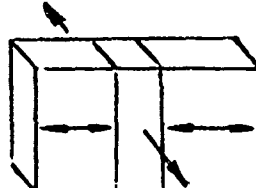
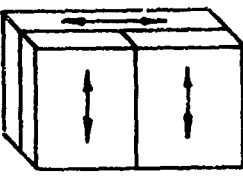
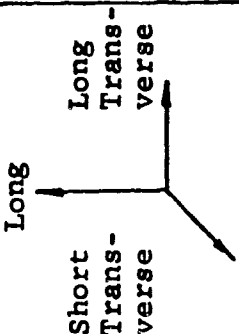
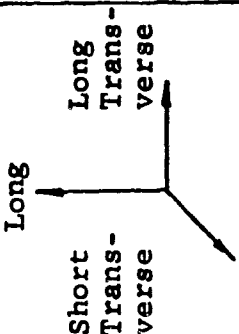
Specimen Number	Type of Bond	Deficiency	ASTM Micro-Grain Size Number	Rolling Direction
DC P3-A P3-B	Single Bond/Single Axis	None	10	
E3 Q3-A Q3-B	Single Bond/Single Axis	Larger Primary Alpha Grains Prior to Bonding	9	
F3 R3-A R3-B	Single Bond/Single Axis	Much Larger Primary Alpha Grains Prior to Bonding	7.5	
D4 P4-A P4-B	Double Bond/Single Axis	None	10	
E4 Q4-A Q4-B	Double Bond/Single Axis	Larger Primary Alpha Grains Prior to Bonding	9	
F4 R4-A R4-B	Double Bond/Single Axis	Much Larger Primary Alpha Grains Prior to Bonding	7.5	

Table 6.5 (cont'd)

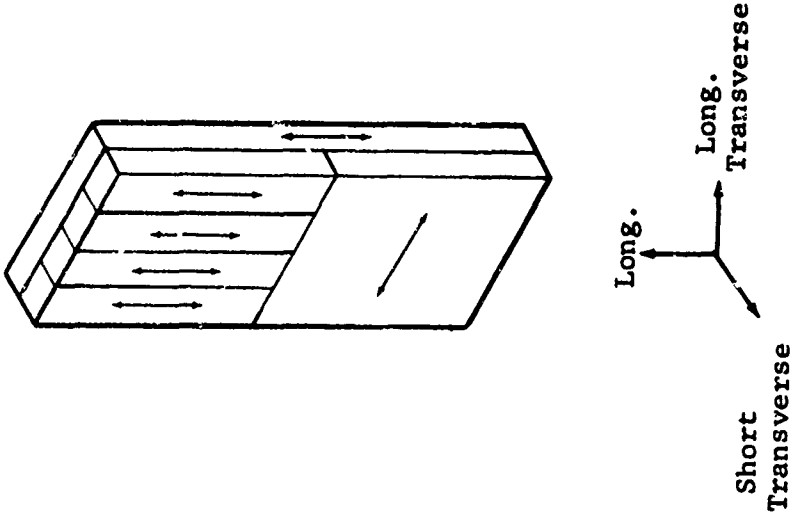
## GRAIN SIZE AND ORIENTATION VARIATIONS: MULTIPLE-BOND/2-AXES JOINTS

Specimen Number	Deficiency	ASTM Micro-Grain Size Number	Total Deformation Longitudinal Direction (%)	Total Deformation Short Transverse Direction (%)	Rolling Direction
D5	None	11	5.91	2.20	
P5-A			6.02	3.50	
P5-B			5.90	5.80	
E5	Larger Primary Alpha Grains Prior to Bonding	8	5.93	0*	
			5.37	6.06	
			5.80	2.02	
F5	Much Larger Primary Alpha Grains Prior to Bonding	7	5.675	5.52	
			5.42	2.20	
			6.00	2.00	

\* Insufficient deformation obtained during the bonding cycle.

Table 6.5 (cont'd)

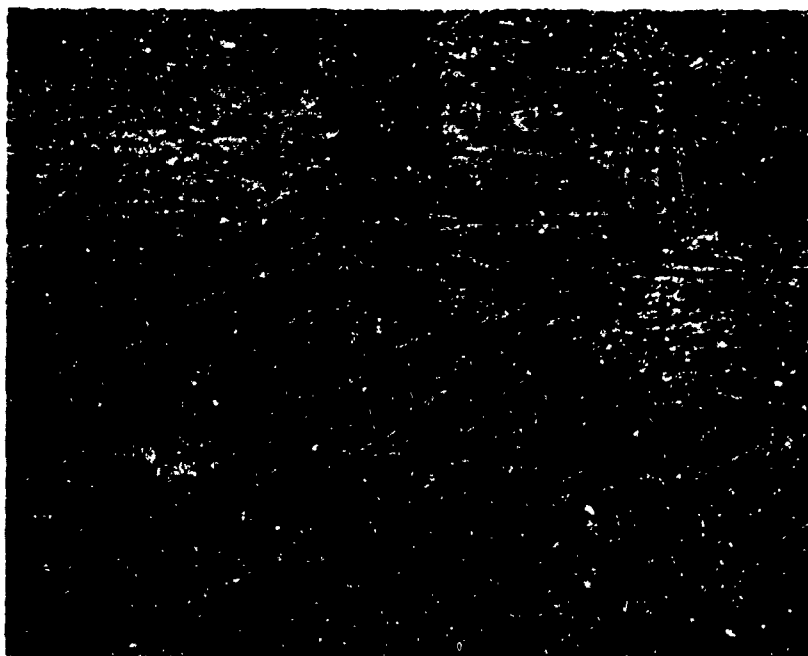
GRAIN SIZE AND ORIENTATION VARIATIONS: MULTIPLE BOND/3-AXES JOINTS

SPECIMEN NUMBER	DEFICIENCY	ASTM MICRO-GRAIN SIZE NO.	TOTAL DEFORMATION SHORT TRANSVERSE DIRECTION (%)	ROLLING DIRECTION
D6 P6-A P6-B	None None None	11	4.5 4.2 4.0	
E6 Q6-A	Larger Primary Alpha Grain Prior to Bond- ing	8	4.8 4.5 4.8	
F6 R6-A R6-B	Much Larger Primary Alpha Grains Prior to Bonding	7	3.7 3.5 3.5	

Deformation Directions Related to  
Specimen Geometry



RMI MATERIAL  
H.T. 890204-02-1A  
CENTER OF MATERIAL  
AS-RECEIVED  
100X MAG



RMI MATERIAL  
H.T. 890204-02-1A  
CENTER OF MATERIAL  
AS-RECEIVED  
500X MAG

Figure 6.5 Photomicrographs of Center of 1-inch Ti 6Al-4V Plate,  
Annealed, Longitudinal Direction



400X

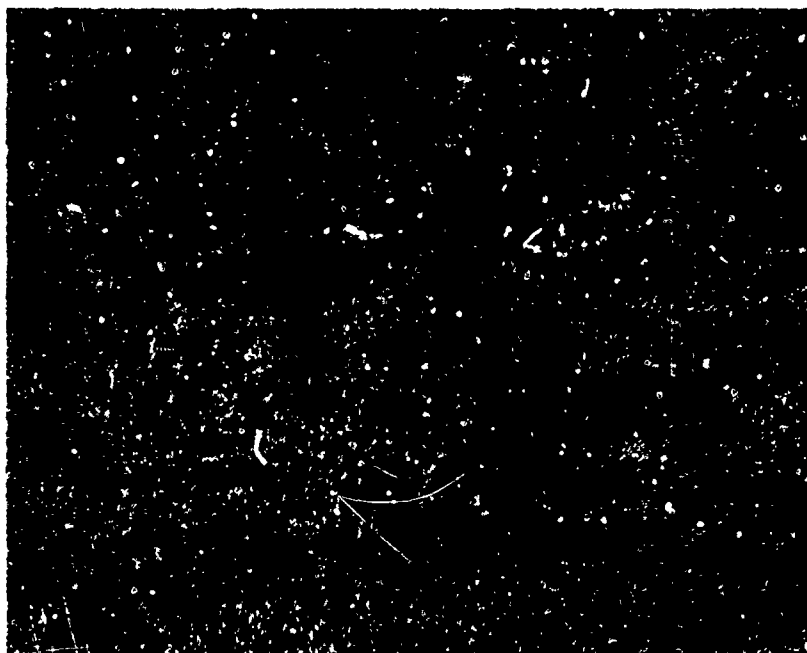
Figure 6.6 Photomicrograph of 1-inch Ti-6Al-4V Plate,  
Heated at 1735°F for 6 Hours



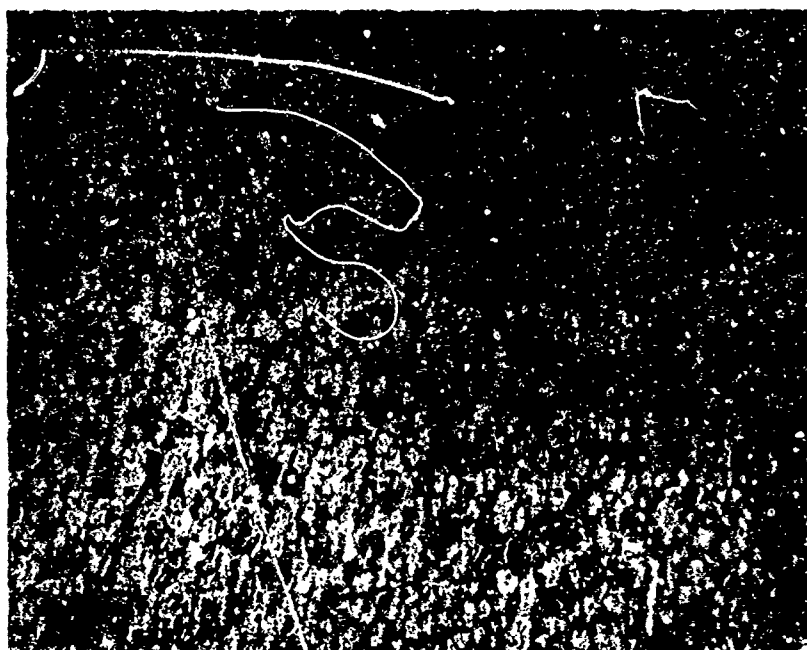
400X

**Figure 6.7** Photomicrograph of 1-inch Ti-6Al-4V Plate,  
Heated at 1775°F for 6 Hours



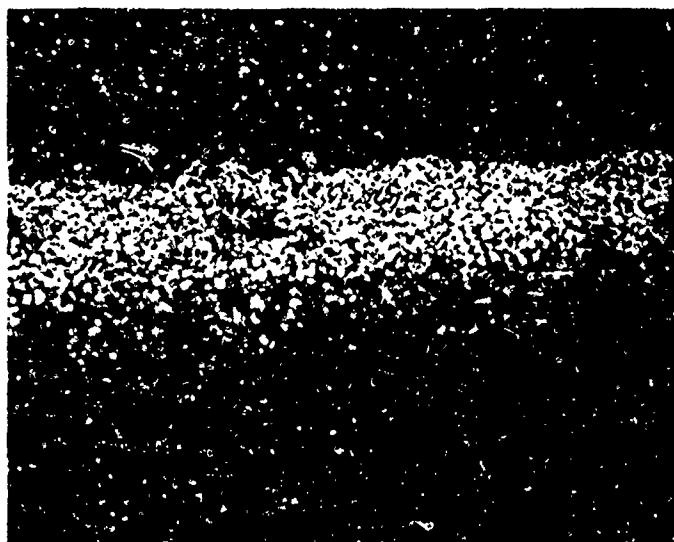


RMI MATERIAL  
H.T. 890204-02-1A  
CENTER OF MATERIAL  
AS-RECEIVED  
100X MAG

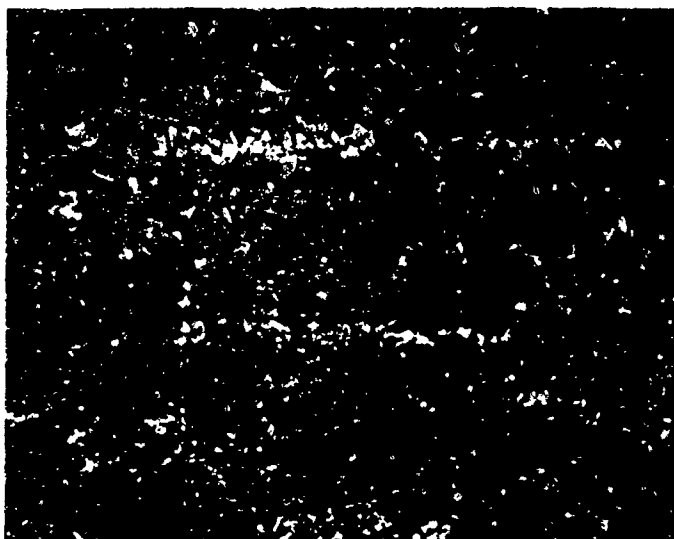


RMI MATERIAL  
H.T. 890204-02-1A  
CENTER OF MATERIAL  
AS-RECEIVED  
500X MAG

Figure 6.8 Photomicrographs of Central Interior of  $\frac{1}{8}$ -inch Ti 6Al-4V Plate, Annealed



RMI MATERIAL  
H.T. 890225-03-1A  
SURFACE OF MATERIAL  
LAB R.A.  
100X MAG



RMI MATERIAL  
H.T. 890225-03-1A  
CENTER OF MATERIAL  
LAB R.A.  
100X MAG

Figure 6.9 Photomicrographs of  $\frac{1}{2}$ -inch Ti 6Al-4V Plate, Condition  
Lab RA per NAR Spec STO-170-LB0-032, Rev. E

Prior to bonding, specimens E5, Q5-A, Q5-B, E6, Q6-A, and Q6-B were heated at 1750°F for 6 hours in a vacuum furnace, followed by furnace cooling. This material has a microstructure closely resembling that of the material in the recrystallized-annealed (RA) condition. Its microstructure is shown in Figure 6.9. The structure consists of nearly equiaxed primary alpha grains with intergranular beta. The average grain diameter is 0.020 mm corresponding to ASTM Micro-Grain Size Number 8.

Specimens F5, R5-A, R5-B, F6, R6-A, and R6-B were heated at 1790°F for 6 hours prior to bonding. This material shows grains of primary alpha in a matrix of transformed beta containing acicular alpha. The average grain size of this material corresponds to ASTM Micro-Grain Size Number 7.

### Phase III - Surface Defects (Voids)

In this phase of the program, defects in the form of voids at the bond plane were introduced. In the single-bond/single-axis and double-bond/single-axis joints, cylindrical voids with a length/diameter ratio  $\approx 1$  were intentionally placed in the bond plane. As shown in Figure 6.10, these voids were uniformly placed on the bonding surfaces of -B specimens. In the single-bond/single-axis joints, a total of 3 voids was intentionally placed, while in the double-bond/single-axis joints, a total of 12 voids was made. In the double-bond/single-axis specimens, four voids were spaced along a circle of diameter 3/16 in. at each of the positions shown in Figure 6.11.

Void diameters used were 0.0065, 0.010, and 0.020 in., respectively. Void depths are shown in Table 6.6. In making the 0.0065- and 0.010-in. diameter voids, tantalum and tungsten wires of 0.005- and 0.010-in. diameter, respectively, were used. These wires were attached to a Servomet Spark Machine, Type SMD (Metals Research Ltd., Cambridge, England). Strain-free drilling of small holes is obtained by this procedure. A small drill was used in making the 0.020-in. diameter voids.

In the multiple-bond/2-axes specimens, voids were introduced in the form of chamfers. The back of the top bonding surfaces of the ( )5-B mating parts were leveled as shown in Figure 6.12. The dimensions of the removed material are shown in Table 6.7. The chamfering was done by filing under a microscope at 100X magnification.

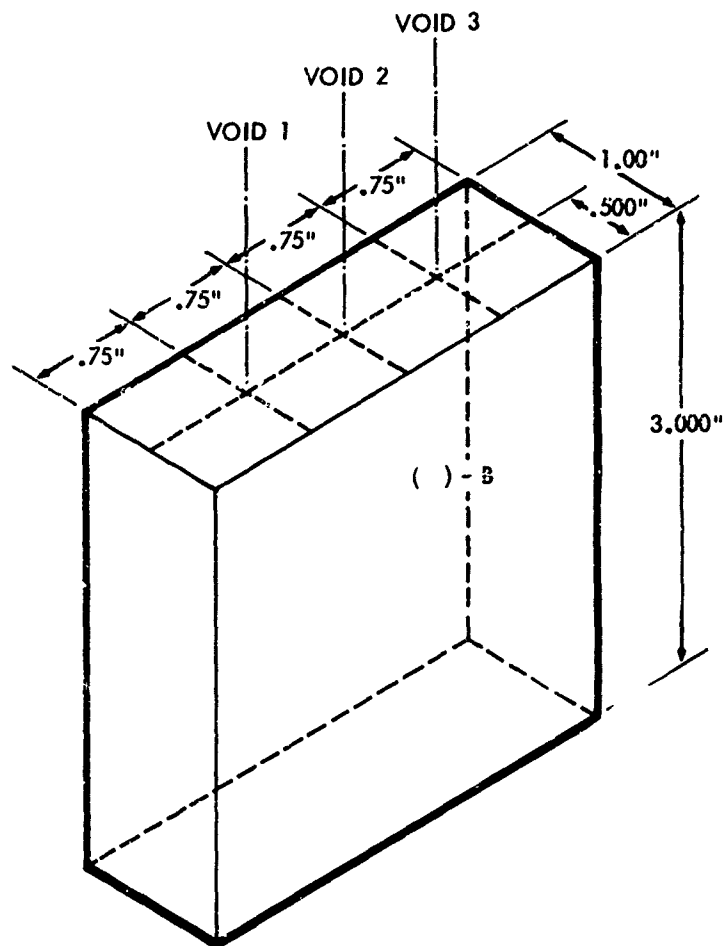


Figure 6.10 Location of Voids in Single Bond - Single Axis Joints

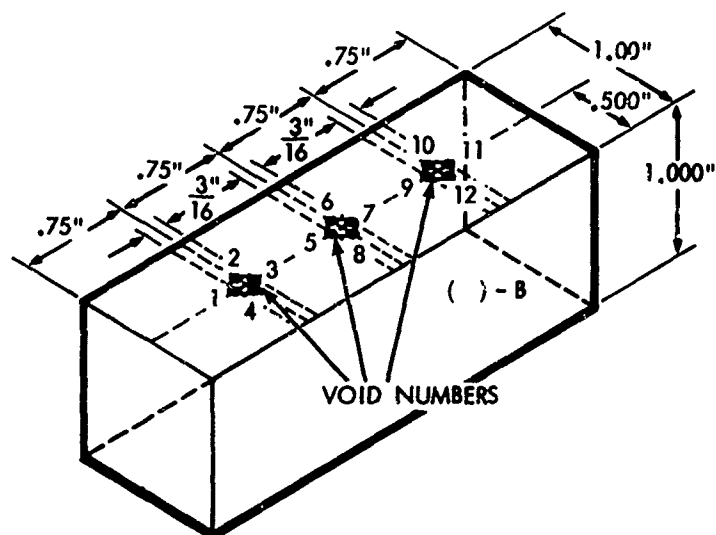


Figure 6.11 Location of Voids in Double Bond - Single Axis Joints

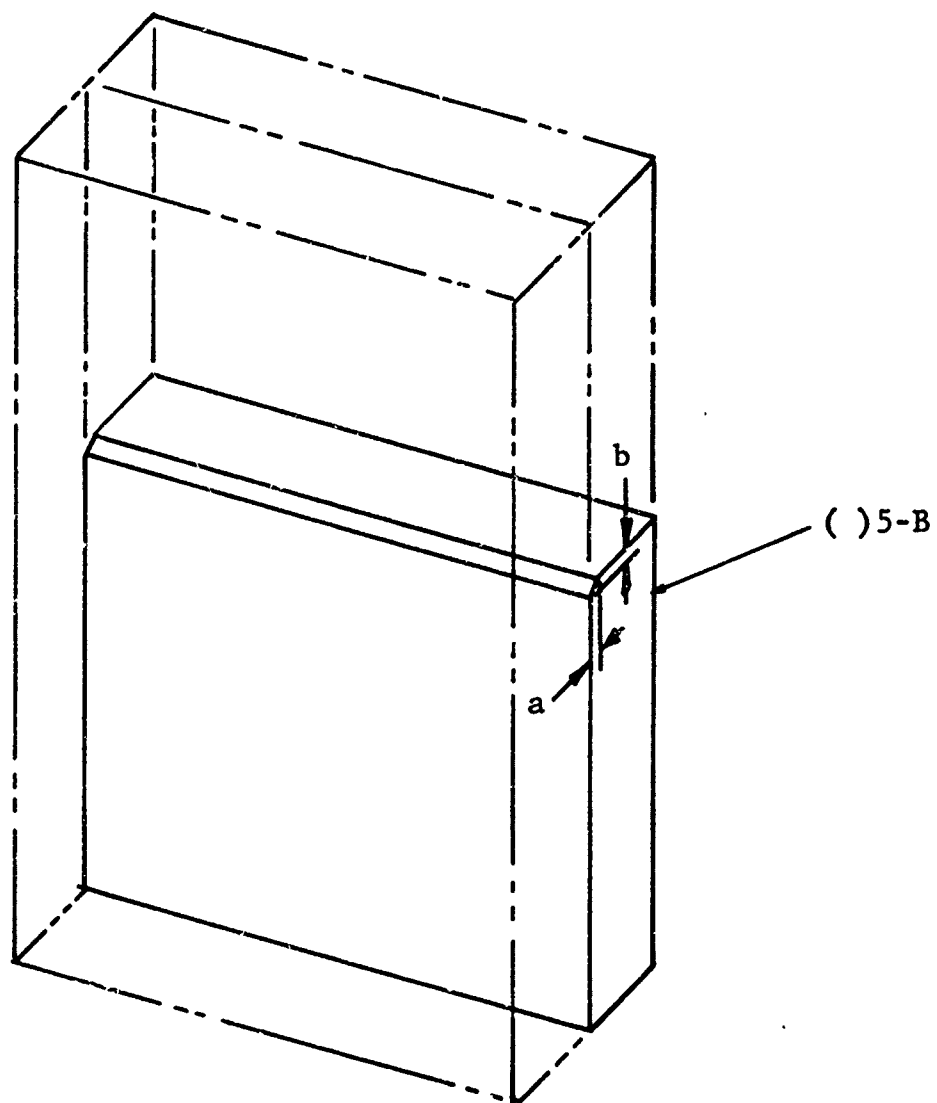


Figure 6.12 Location of Voids in Multiple-Bond/2-Axes Joints

Table 6. 6

SIZE OF VOIDS IN SINGLE-BOND /SINGLE-AXIS AND  
DOUBLE-BOND /SINGLE-AXIS JOINTS

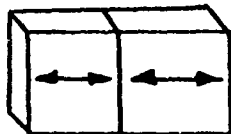
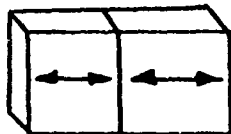
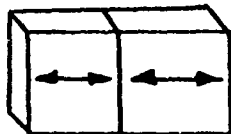
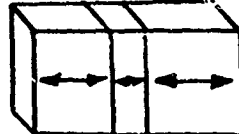
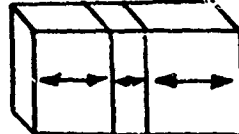
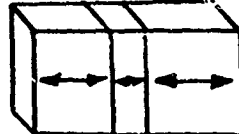
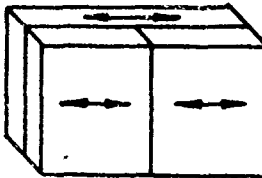
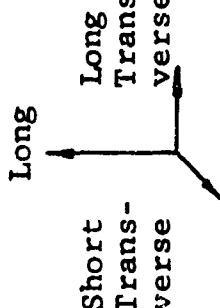
Specimen Number	Type of Bond	Deficiency	Dia. (Mils)	Size of Void												Rolling Direction
				Depth of Void (Mils)												
				1	2	3	4	5	6	7	8	9	10	11	12	
G3 S3-A S3-B	Single Bond/ Single Axis	Cyl. Voids L/D = 1	6.5	-	-	-	-	-	-	-	-	-	-	-	-	
				5	5	6	-	-	-	-	-	-	-	-	-	
				6	3	6	-	-	-	-	-	-	-	-	-	
H3 T3-A T3-B	Single Bond/ Single Axis	Cyl. Voids L/D = 1	10	9	10	11	-	-	-	-	-	-	-	-	-	
				10	11	10	-	-	-	-	-	-	-	-	-	
				9	9	9	-	-	-	-	-	-	-	-	-	
I3 U3-A U3-B	Single Bond/ Single Axis	Cyl. Voids L/D = 1	20	20	19	19	-	-	-	-	-	-	-	-	-	
				18	18	18	-	-	-	-	-	-	-	-	-	
				19	20	19	-	-	-	-	-	-	-	-	-	
G4 S4-A S4-B	Double Bond/ Single Axis	Cyl. Voids L/D = 1	6.5	5	6	6	6	5	6	7	6	5	7	5	5	
				6	5	6	7	5	5	5	4	6	5	5	5	
				6	5	5	6	5	6	5	5	4	5	5	6	
H4 T4-A T4-B	Double Bond/ Single Axis	Cyl. Voids L/D = 1	10	10	10	9	10	11	10	11	10	9	8	10	10	
				10	11	10	10	11	10	10	9	10	9	9	10	
				10	11	10	10	11	10	10	9	10	9	9	10	
I4 U4-A U4-B	Double Bond/ Single Axis	Cyl. Voids L/D = 1	20	18	20	18	17	17	17	20	19	18	17	16	16	
				21	19	20	19	20	17	21	20	20	20	19	18	
				19	20	21	18	19	20	18	19	18	18	18	18	

Table 6.7  
SIZE OF VOIDS IN MULTIPLE-BOND/2-AXES JOINTS

Specimen Number	Deficiency	Total Deformation Longitudinal Direction (%)	Total Deformation Short Transverse Direction (%)	Rolling Direction
	<u>Void in The Form of a Chamfered Edge*</u>			
G5	$a = b = 0.005''$	5.57	6.36	
S5-A	$a = b = 0.005''$	5.41	5.55	
S5-B	$a = b = 0.005''$	5.40	6.76	
H5	$a = b = 0.010''$	5.23	7.00	<p>Deformation Directions Related to Specimen Geometry</p> 
T5-A	$a = b = 0.010''$	5.63	6.50	
T5-B	$a = b = 0.010''$	5.20	6.50	
U5	$a = b = 0.020''$	5.05	6.56	
U5-A	$a = b = 0.020''$	5.80	6.50	
U5-B	$a = b = 0.020''$	4.68	8.00	

\* See Figure 6.12 for definitions of a and b.

In making inclusions in the multiple-bond/three-axes specimens, voids were introduced in the form of chamfered edges. The placement of these voids is shown in Figure 6.13. The dimensions of these voids are shown in Table 6.8.

#### Phase IV - Contamination

In this phase of the program, defects in the form of contamination at the bond plane were used. The types of contamination used were: (a) alpha case layer, (b) inclusions in the form of stainless steel and  $\text{SiO}_2$  powders.

(a) Alpha Case: At elevated temperatures, titanium alloys have a strong affinity for the elements, oxygen and nitrogen. These elements will dissolve in high percentages in alpha titanium, causing an embrittled surface layer (alpha case) which can thus cause cracking. Oxygen contamination occurs when parts are heated in air at temperatures above approximately  $1000^\circ\text{F}$ . The depth of the alpha-case is dependent on both temperature and time at temperature. This layer can also be formed when parts are heated in a relatively poor vacuum.

Defects consisting of an alpha case layer were formed by heating specimens at  $1450^\circ\text{F}$  for 6 hours in an air furnace. The outer scale composed mainly of  $\text{TiO}_2$  was then removed leaving a layer of alpha case. X-ray diffraction and microhardness measurements indicate an alpha case depth of  $\approx 0.002$  in. The microhardness as a function of depth below the exposed surface is shown in Figure 6.14.

In making the alpha case defects in the single-bond/single-axis and double-bond/single-axis specimens, three different areas spaced an equal distance apart were masked off such that chemical milling would not remove these areas. The remainder of the bonding surface was then chemically milled in a 5% HF - 35%  $\text{HNO}_3$  titanium etching solution. This procedure left a much larger alpha case layer at the three masked areas. The dimensions of these areas are shown in Table 6.9. A similar procedure was used in making alpha case defects in the multiple-bond/two-axes specimens. The placement of these defects are shown in Figure 6.15. In the multiple-bond/three-axes specimens, no masking was done. The -A, -B, -C, -D (See Figure 6.13), were heated at  $1450^\circ\text{F}$  for 5 hours. After heating, the  $\text{TiO}_2$  layer was removed by grit blasting. Samples were then sanded to give the required surface finish.



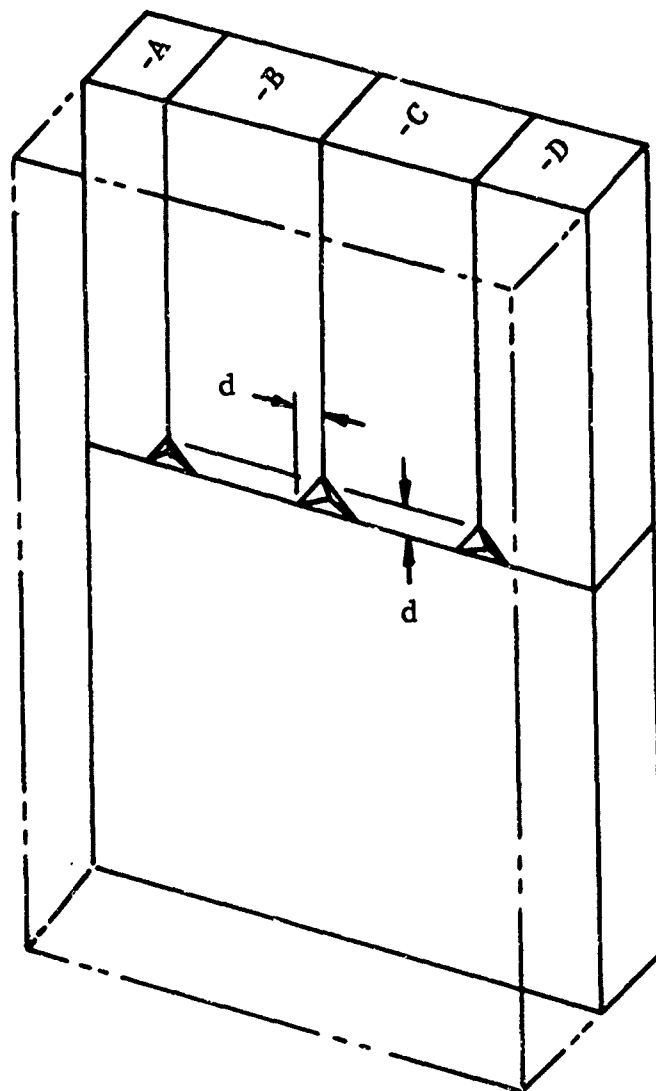


Figure 6.13 Location of Chamfered Corner Voids in Multiple Bond/Three Axes Joints

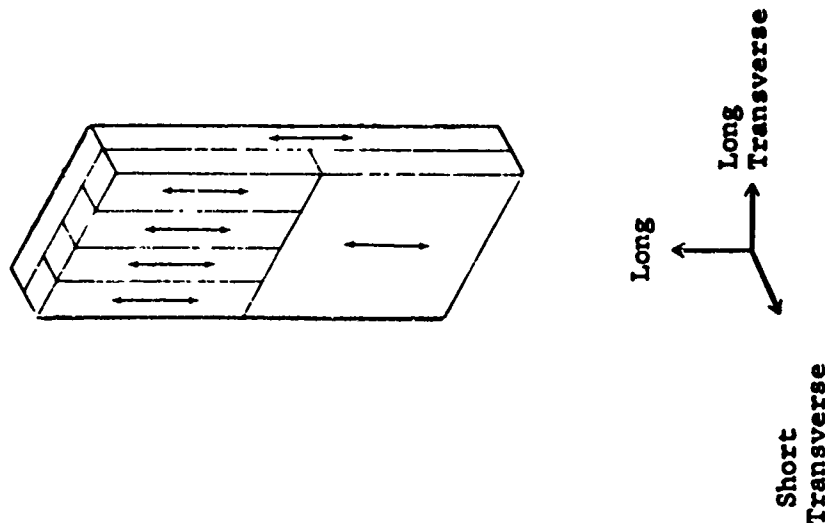
Table 6.8

SIZE OF VOIDS IN MULTIPLE-BOND/3-AXES JOINTS

SPECIMEN NUMBER	DEFICIENCY	SIZE OF DEFECT (in)	TOTAL DEFORMATION SHORT TRANSVERSE DIRECTION (%)	ROLLING DIRECTION
-----------------	------------	---------------------	--	-------------------

Void in the form of a chamfered corner\*

G6		d=.008"±.003"	4.0	
S6-A		d=.008"±.003"	4.2	
S6-B		d=.008"±.003"	5.0	
H6		d=.018"±.004"	4.5	
T6-A		d=.018"±.004"	3.5	
T6-B		d=.018"±.004"	4.2	
I6		d=.030"±.005"	4.8	
U6-A		d=.030"±.005"	5.0	
U6-B		d=.030"±.005"	4.3	



Deformation Directions Related to Specimen Geometry

\*See Figure 6.13 for definition of d

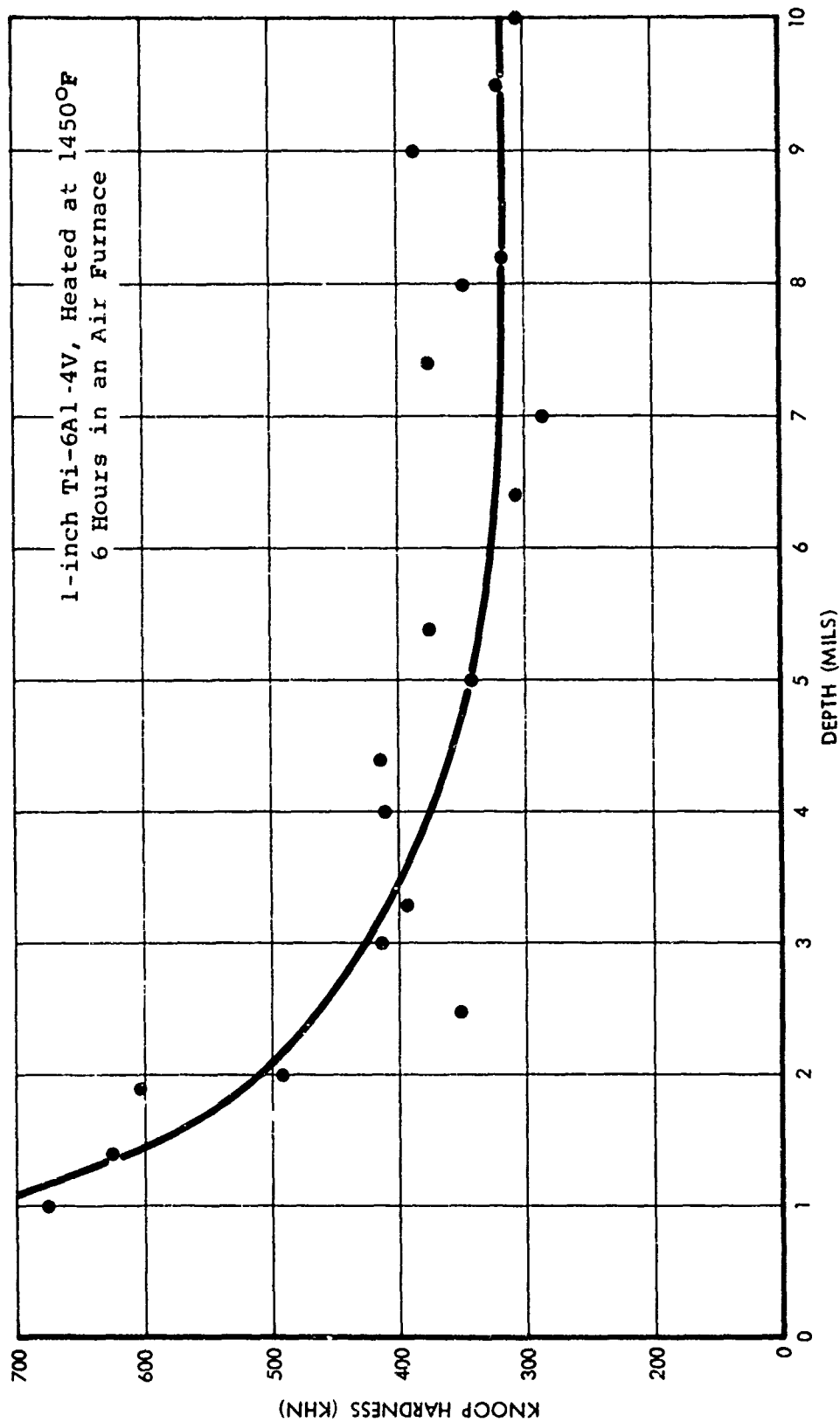


Figure 6.14 Microhardness vs. Depth Below an Exposed Surface

(b) Inclusions: Type 304/Stainless Steel was selected as a contaminant since ferrous inclusions from the tooling material could possibly get into the areas to be bonded either during assembly of the parts or during the bonding cycle itself.

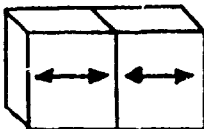
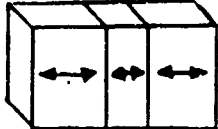
$\text{SiO}_2$  was chosen because it is typical of a ceramic inclusion and is a form of particulate contamination (e.g., alumina, silica, airborne particles, parting agents, etc.). Like contamination due to ferrous inclusions, parting agents, etc. could inadvertently get into bonding areas.

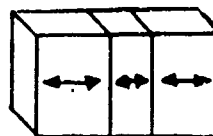
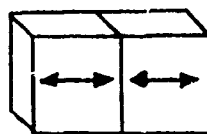
For single-bond/single-axis and double-bond/single-axis specimens containing contamination in the form of Type 304 Stainless Steel and  $\text{SiO}_2$  powders, voids were first made in the same procedure as used for single bond-single axis joints in Phase III. These voids were then filled with stainless steel and  $\text{SiO}_2$  powders. The diameter and depth of the defects are given in Table 6.9.

In the multiple-bond/two-axes specimens, voids were first placed in the ( )5-B parts at the positions shown in Figure 6.16. The holes were then packed with powder. The dimensions of the holes are shown in Table 6.10. The holes were placed as near the back of the ( )5-B parts as possible.

In the multiple-bond/three-axes specimens, voids were made in the form of chamfered edges as shown in Figure 6.13. These voids were then packed with powder. The dimensions of the defects are shown in Table 6.10.

Table 6.9  
FORMS AND SIZE OF CONTAMINATION IN SINGLE-BOND/SINGLE-AXIS  
AND DOUBLE-BOND/SINGLE-AXIS JOINTS

Specimen Number	Type of Bond	Deficiency	Size of Defect			Rolling Direction	
			Diameter (in.)	Depth (in.)			
				1	2		3
J3 V3-A V3-B	Single Bond/Single Axis	Alpha Case Layer	0.093	0.002			
K3 W3-A W3-B	Single Bond/Single Axis	Type 304 Stainless Steel Powder Inclusions	0.013	0.011 0.005 0.010	0.009 0.012 0.011	0.011 0.012 0.010	
L3 X3-A X3-B	Single Bond/Single Axis	SiO <sub>2</sub> Powder Inclusions	0.013	0.005 0.010 0.010	0.004 0.008 0.011	0.003 0.010 0.010	
J4 V4-A V4-B	Double Bond/Single Axis	Alpha Case Layer	0.186	0.002			
K4 W4-A W4-B	Double Bond/Single Axis	Type 304 Stainless Steel Powder Inclusions	0.0065	0.008 0.010 0.005	0.007 0.008 0.006	0.008 0.009 0.007	
L4 X4-A X4-B	Double Bond/Single Axis	SiO <sub>2</sub> Powder Inclusions	0.0065	0.007 0.007 0.007	0.007 0.008 0.007	0.007 0.007 0.006	



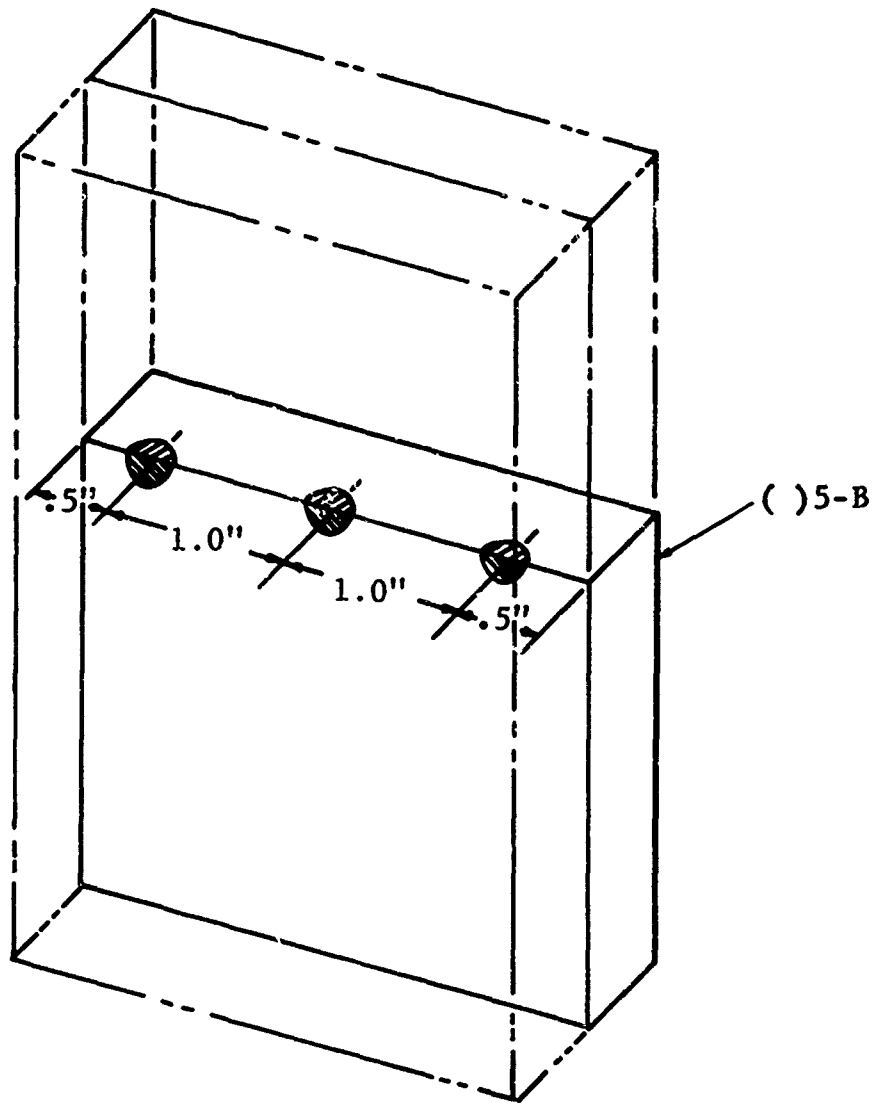
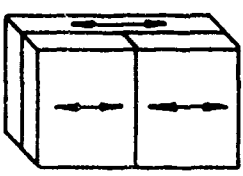
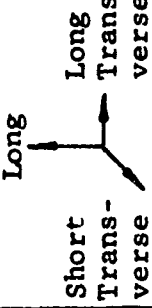


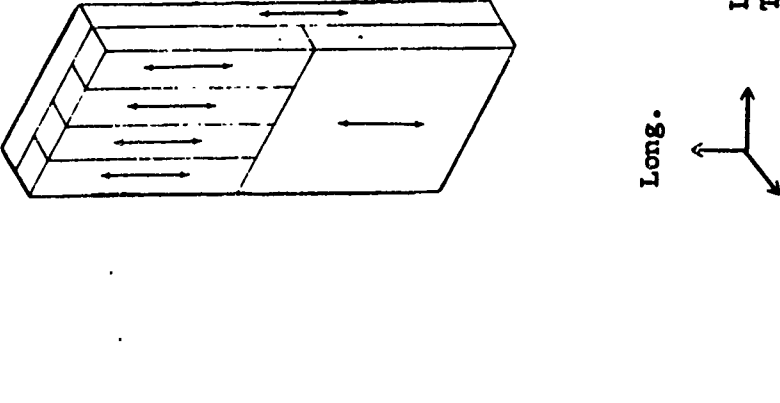
Figure 6.15 Location of Alpha Case Layer in Multiple-Bond/2-Axes Joints

Table 6.10  
FORMS AND SIZE OF CONTAMINATION IN MULTIPLE-BOND/2-AXES JOINTS

Spec. No.	Deficiency	Size of Defect			Total Deformation Longitudinal Direction (%)	Total Deformation Short Transverse Direction (%)	Rolling Direction
		Dia. (in.)	1	2	3		
J5	Alpha Case Layer	0.375	0.002	0.002	0.002	6.60	
V5-A		0.375	0.002	0.002	0.002	7.10	
V5-B		0.375	0.002	0.002	0.002	6.60	
K5	Type 304 Stainless Steel Powder Inclusions	0.022	0.032	0.032	0.025	9.10	
W5-A		0.022	0.018	0.023	0.022	7.50	
W5-B		0.022	0.023	0.018	0.017	9.30	
L5	SiO <sub>2</sub> Powder Inclusions	0.048	0.030	0.040	0.035	7.10	
X5-A		0.048	0.045	0.046	0.065	7.50	
X5-B		0.052	0.038	0.042	0.040	8.60	

(cont'd)

Table 6.10(cont'd)

SPECIMEN NUMBER	DEFICIENCY	SIZE OF DEFECT (In.)	TOTAL DEFORMATION SHORT TRANSVERSE DIRECTION (%)	ROLLING DIRECTION
J6	Alpha Case Layer	.002" Depth	4.0	
V6-A	Alpha Case Layer	.002" Depth	5.0	
V6-B	Alpha Case Layer	.002" Depth	4.0	
K6	Type 304	d* = .025" ± .005"	4.3	
W6-A	Stainless	d* = .025" ± .005"	4.0	
W6-B	Steel Inclusions	d* = .025" ± .005"	4.5	
L6	SiO <sub>2</sub> Powder	d* = .025" ± .005"	4.5	
X6-A	Inclusions	d* = .025" ± .005"	4.5	
X6-B		d* = .025" ± .005"	4.0	

\*See Figure 6.13 for definition of d

Short  
TransverseDeformation Directions Related to  
Specimen Geometry



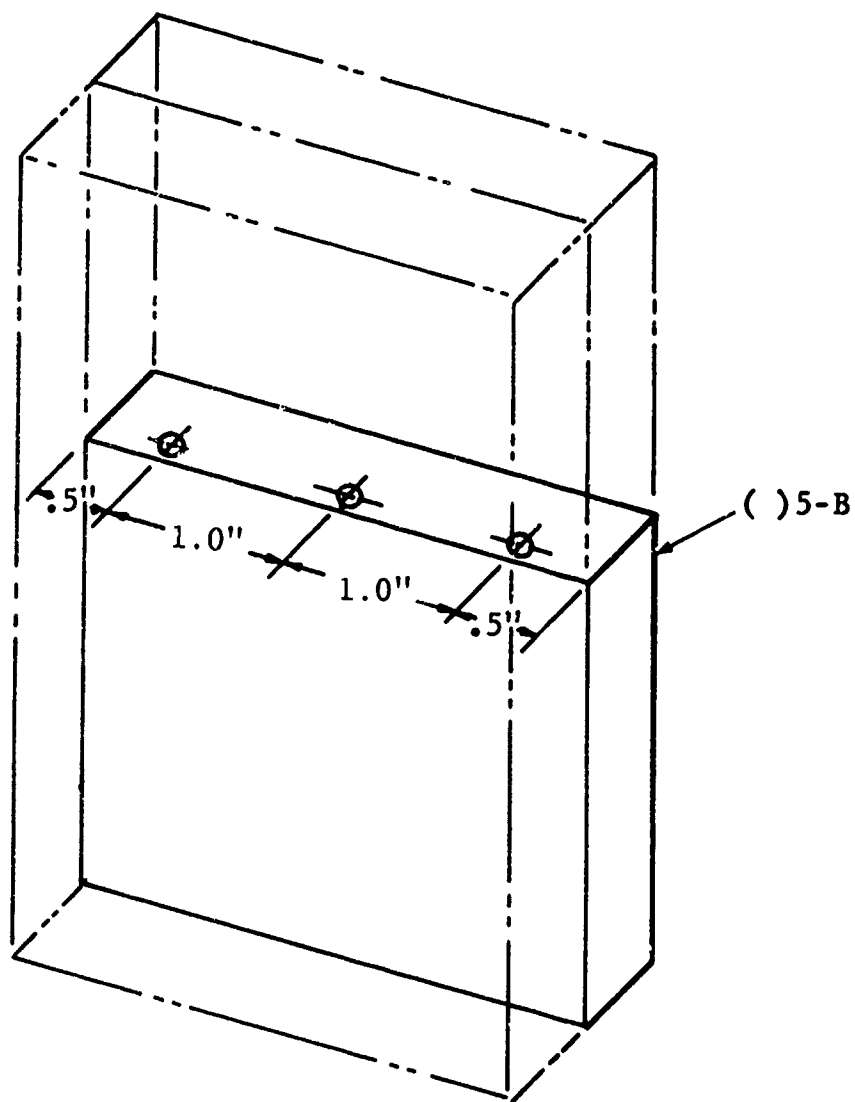


Figure 6.16 Location of Inclusions in Multiple-Bond/2-Axes Joints

### 6.1.3 Verification of Defects

Diffusion bonded single-bond/single-axis and double-bond/single-axis joints containing defects in the form of voids and different types of contamination were sectioned to determine the effect of bonding on the size and shape of these defects.

The specimens were:

- M-4B - Optimum Bonding Parameters
- B-3 - 2½% Deformation
- C-3 - 1½% Deformation
- H-4 - 0.010" Dia. x 0.010" Deep Voids
- J-4 - Alpha Case Layer
- K-3 - St. Steel Inclusion
- L-3 - Silica Inclusion
- P-4B - Grain Size ASTM 10
- Q-4B - Grain Size ASTM 9
- R-4B - Grain Size ASTM 7.5

### Procedure

The diffusion bonded specimens were sectioned longitudinally (perpendicular to the bond plane) and milled to within 0.015" of the recorded defect location. The defect area was isolated by relieving the surfaces on either side. The specimens were then sanded carefully until the defects became visible. Final polishing and etching were done after maximum defect definition was obtained.

Some metal smearing over the defects due to sanding and polishing was observed. Therefore, defect dimensions after bonding are given as minimums due to this limitation.

The figures which follow the discussions below include the original defect dimension, those after bonding, and comments on other effects of the bonding cycle on the defect characteristics.

### Bonding Parameter Variations

Specimen C3, which was bonded under much less than optimum bonding conditions (1½% deformation), showed large areas of non-bonding after the bonding cycle. Specimen B3, which had 2½% deformation, contains only one small area where bonding did not occur. No voids were found around the bonding area in specimens

M4B, P4B, Q4B, and R4B, which were bonded under optimum bonding conditions. See Figures 6.17, 6.18 and 6.19.

#### Grain Size Variations

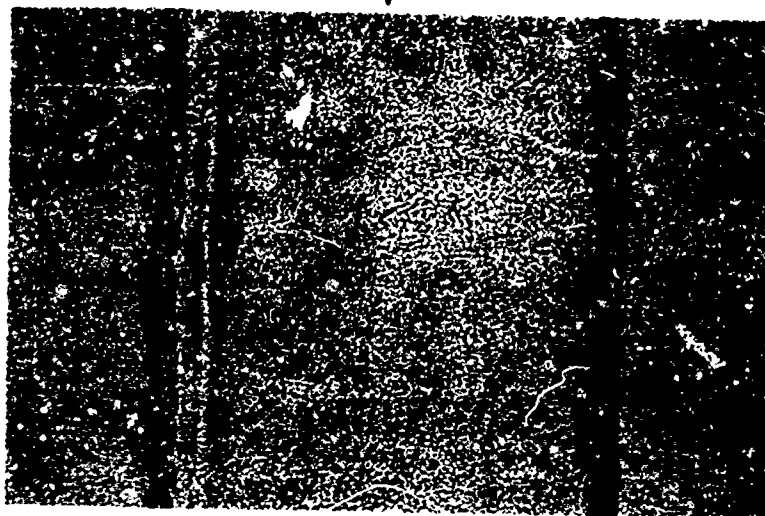
In specimens P4B, Q4B, and R4B, which had different-sized primary alpha grains prior to bonding, a smaller variation was found in their grain sizes after the bonding cycle. The effect of the bonding cycle was to increase the grain size of the previous smaller grain-sized samples more. Specimens P4B, Q4B, and R4B also had grain orientation differences between mating parts prior to bonding. After the bonding cycle, the presence of equiaxed alpha grains made the differences practically impossible to observe. See Figures 6.20, 6.21 and 6.22.

#### Void and Inclusion-Type Defects

A void of 0.010" diameter and 0.010" depth was placed in specimen H4 prior to bonding. After bonding, this void is still detectable. Minimum dimensions for this void were 0.007" diameter with 0.007" depth. In specimen J4, an alpha case layer of 0.187" diameter, 0.002" depth was placed in the bond plane prior to bonding. After the bonding cycle, the thickness of the alpha case layer appears to be much less due to the diffusion of oxygen and nitrogen into the interior of the sample. In specimen K3, Type 304 stainless steel was packed into a void, 0.013" diameter and 0.009" depth, prior to bonding. After bonding, the defect region is still observed having minimum dimensions of 0.002" x 0.007" with practically no depth. The presence of stainless steel powder in the defect region after the bonding cycle was inconclusive, although the void containing no depth was indicative that powder was still contained within that void. In specimen L3, SiO<sub>2</sub> powder was packed into a void with the dimensions 0.013" diameter and 0.005" depth prior to bonding. After bonding, the defect area is still observable with a minimum dimension of 0.001" x 0.002" with no depth. Particles are observable in the void area after the bonding cycle. See Figures 6.23, 6.24, 6.25, and 6.26.

SPECIMEN M-4B (Double Bond/Single Axis)

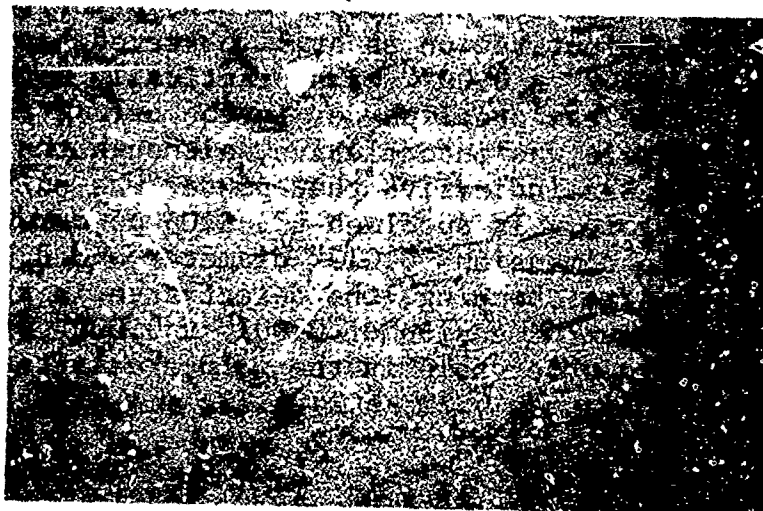
Bonding Parameters: 1700°F, 6 Hrs, 7% Deformation  
Defect Type: None



A

75X

Bond Plane



A

600X

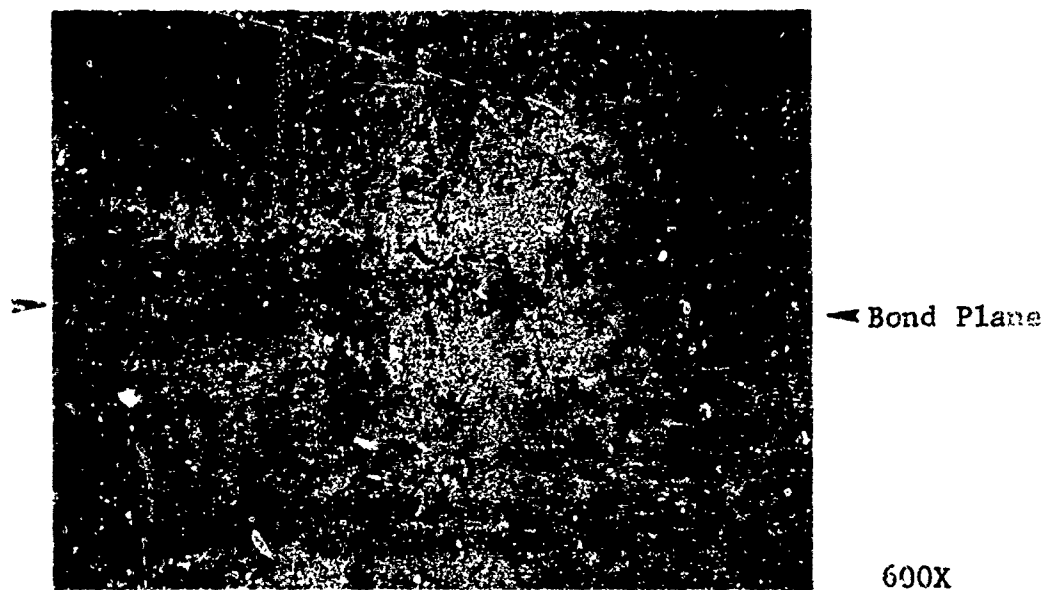
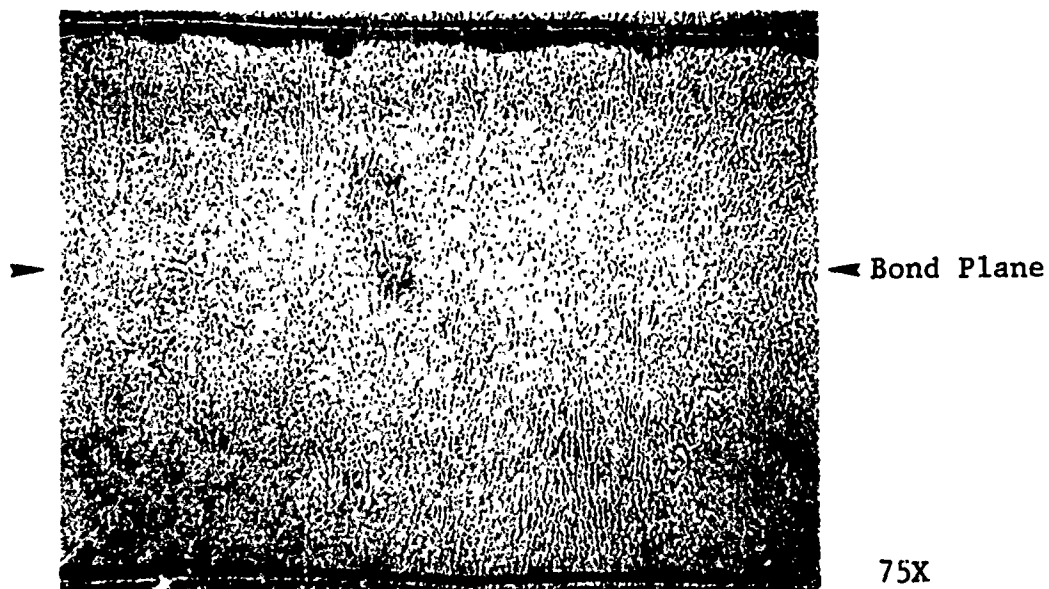
Comments: Bond plane indistinguishable except for extremely localized grain size variations across the bond plane

Figure 6.17 Photomicrographs at Bond Plane of DB Specimen M-4B

SPECIMEN B-3 (Single Bond)

Bonding Parameters: 1700°F, 6 Hrs, 2½% Deformation

Defect Type: Non-optimum bonding parameters (2½% deformation)



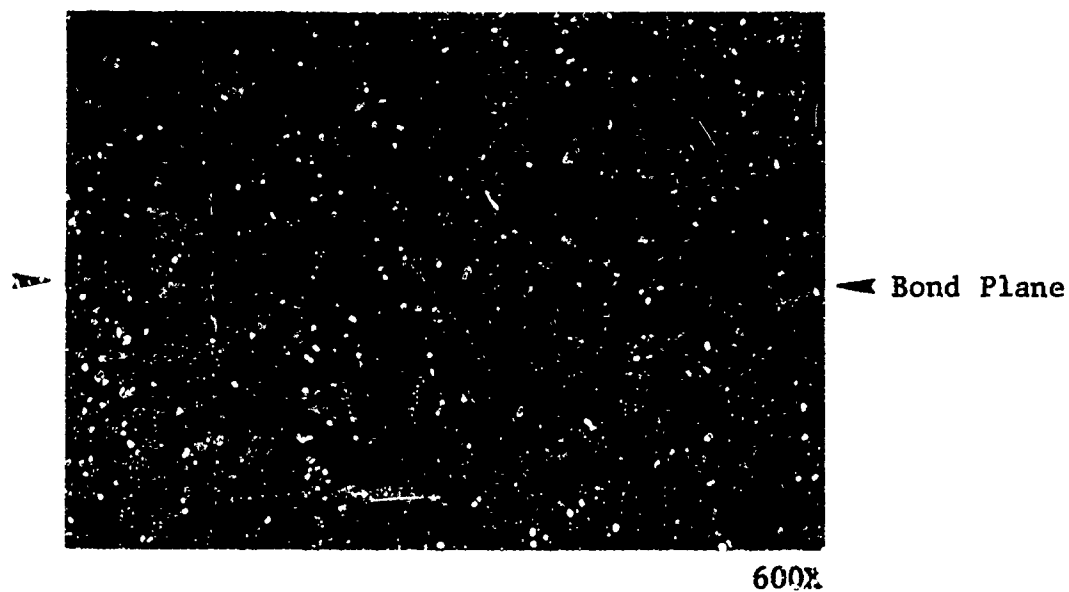
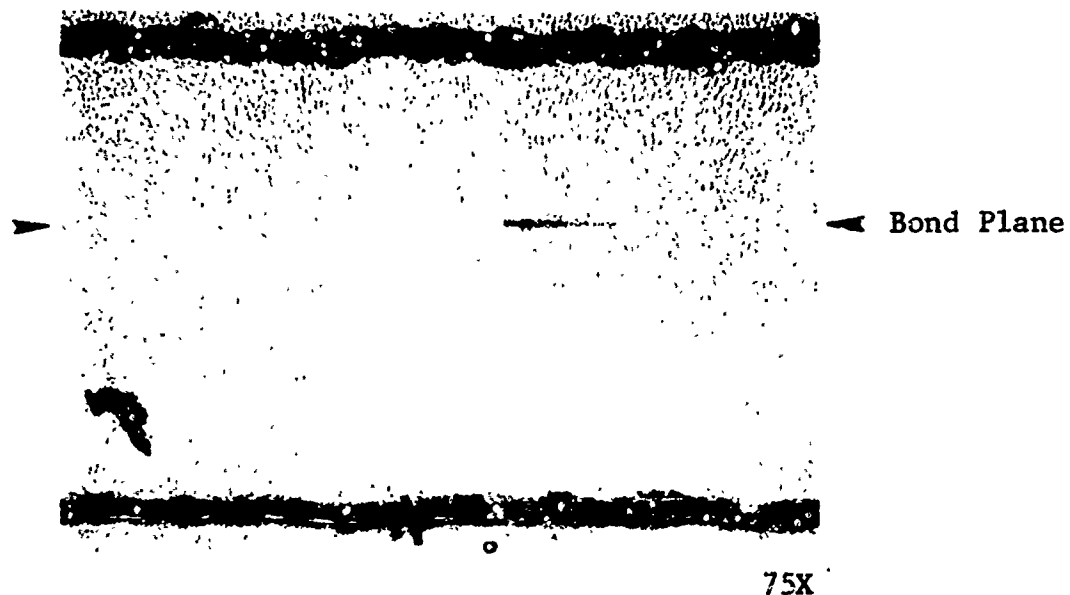
Comments: Bond area includes grain boundaries aligned with bond plane in localized areas. Unintentional void or inclusion visible.

Figure 6.18 Photomicrographs at Bond Plane of DB Specimen B-3

SPECIMEN C-3 (Single Bond)

Bonding Parameters: 1700°F, 6 Hrs, 1½% Deformation

Defect Type: Non-optimum bonding parameters (1½% deformation)



Comments: Little grain growth across the bond plane. Unbonded area indicating localized lack of contact between faying surfaces.

Figure 6.19 Photomicrographs at Bond Plane of DB Specimen C-3

SPECIMEN P-4B (Double Bond/Single Axis)

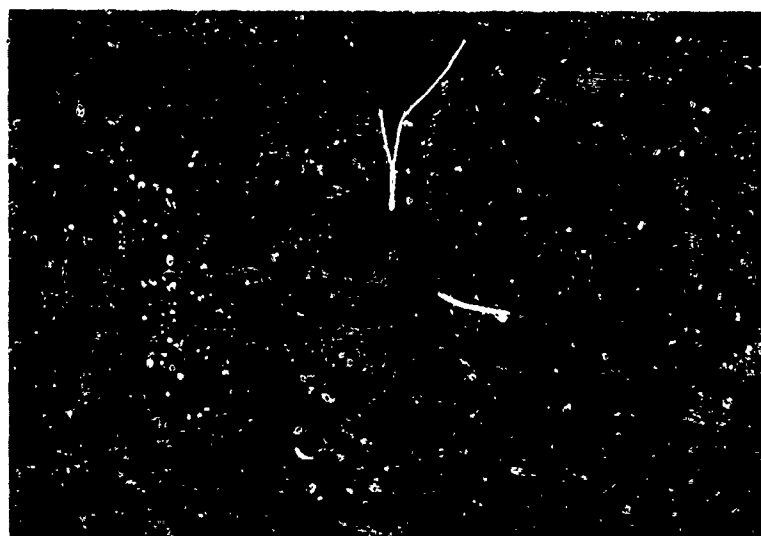
Bonding Parameters: 1700°F, 6 Hrs, 7% Deformation

Defect Type: Grain size ASTM 10 and opposed rolling directions



75X

Bond Plane



600X

Comments:

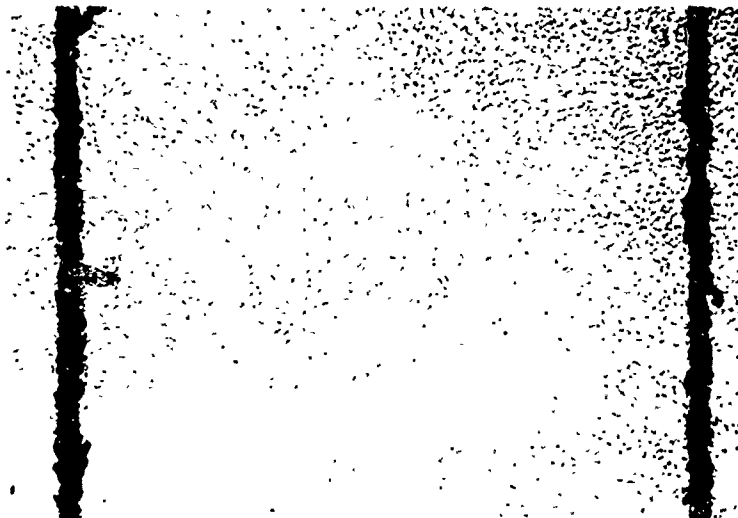
Variations in preferred grain orientations not visible across bond plane. Equiaxed alpha grain structure after bonding cycle. Size of primary alpha grains has increased after being held at 1700°F for 6 hours.

Figure 6.20 Photomicrographs at Bond Plane of DB Specimen P-4B

SPECIMEN Q-4B (Double Bond/Single Axis)

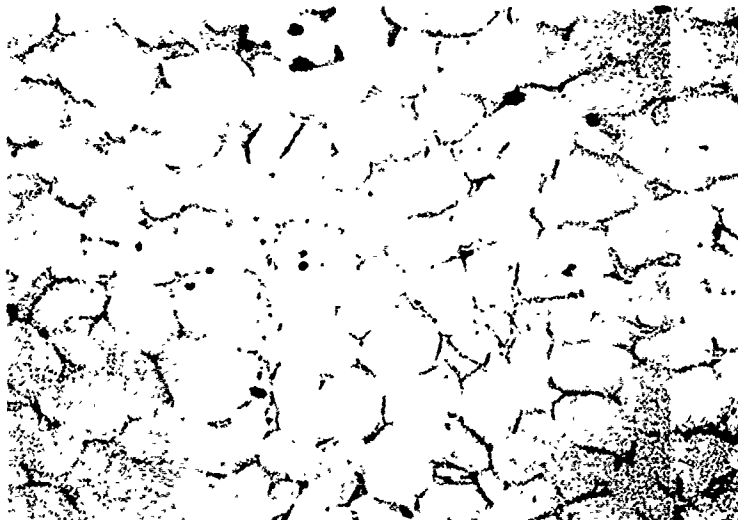
Bonding Parameters: 1700°F, 6 Hrs, 7% Deformation

Defect Type: Grain size ASTM 9 and opposed rolling directions



75X

Bond Plane



600X

Comments: Bondline largely indistinguishable. Preferred orientations appear to have disappeared. Very little change in primary alpha grain size due to bonding cycle.

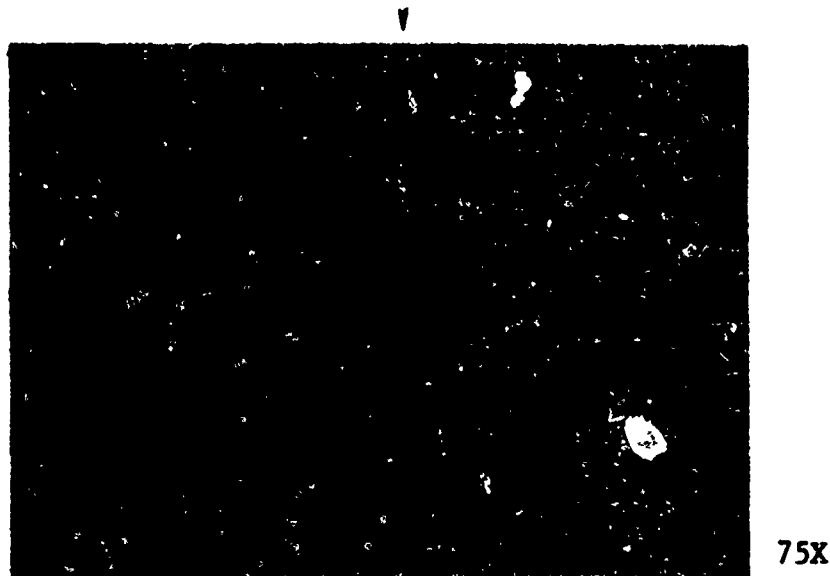
Figure 6.21 Photomicrographs at Bond Plane of DB Specimen Q-4B



SPECIMEN R-4B (Double Bond/Single Axis)

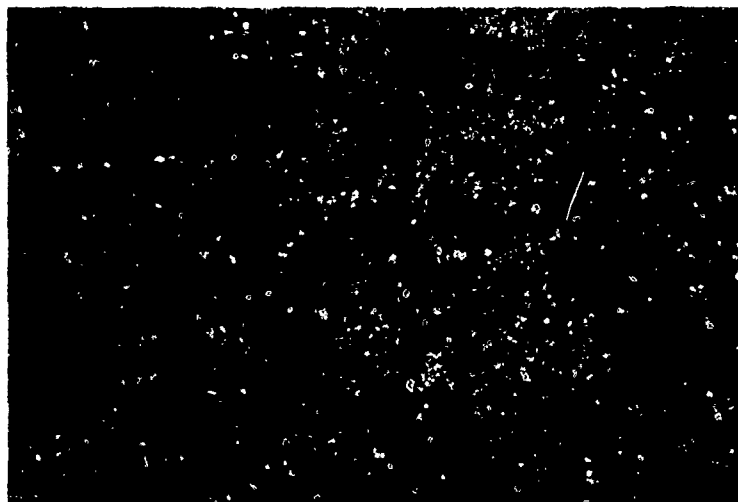
Bonding Parameters: 1700°F, 6 Hrs, 7% Deformation

Defect Type: ASTM size 7.5 and opposed rolling directions



75X

Bond Plane



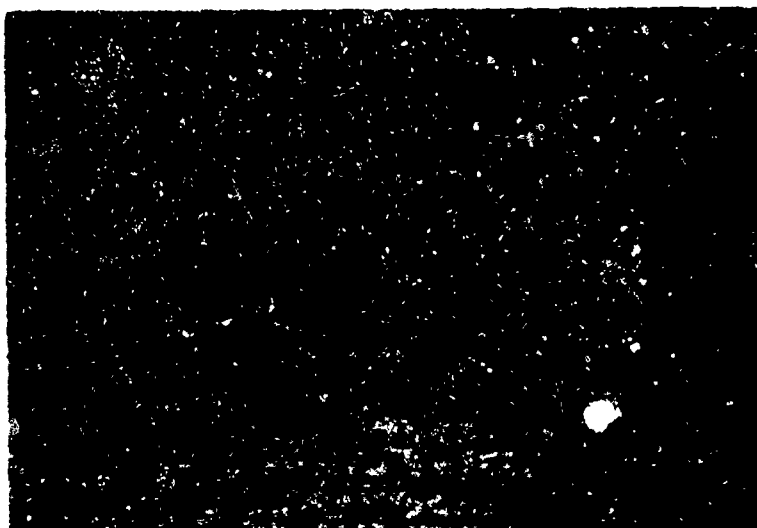
600X

Comments: Bond plane distinguishable only by microstructural variations on either side. Very little change in microstructure due to bonding cycle.

Figure 6.22 Photomicrographs at Bond Plane of DB Specimen R-4B

SPECIMEN H-4 (Double Bond/Single Axis)

Bonding Parameters: 1700°F, 6 Hrs, 7% Deformation  
Defect Type: Cylindrical Void  
Dimensions: Before bonding - 0.010" dia. x 0.010" deep  
After bonding - 0.007" dia. x 0.007" deep (minimum)



150X  
(Unetched)

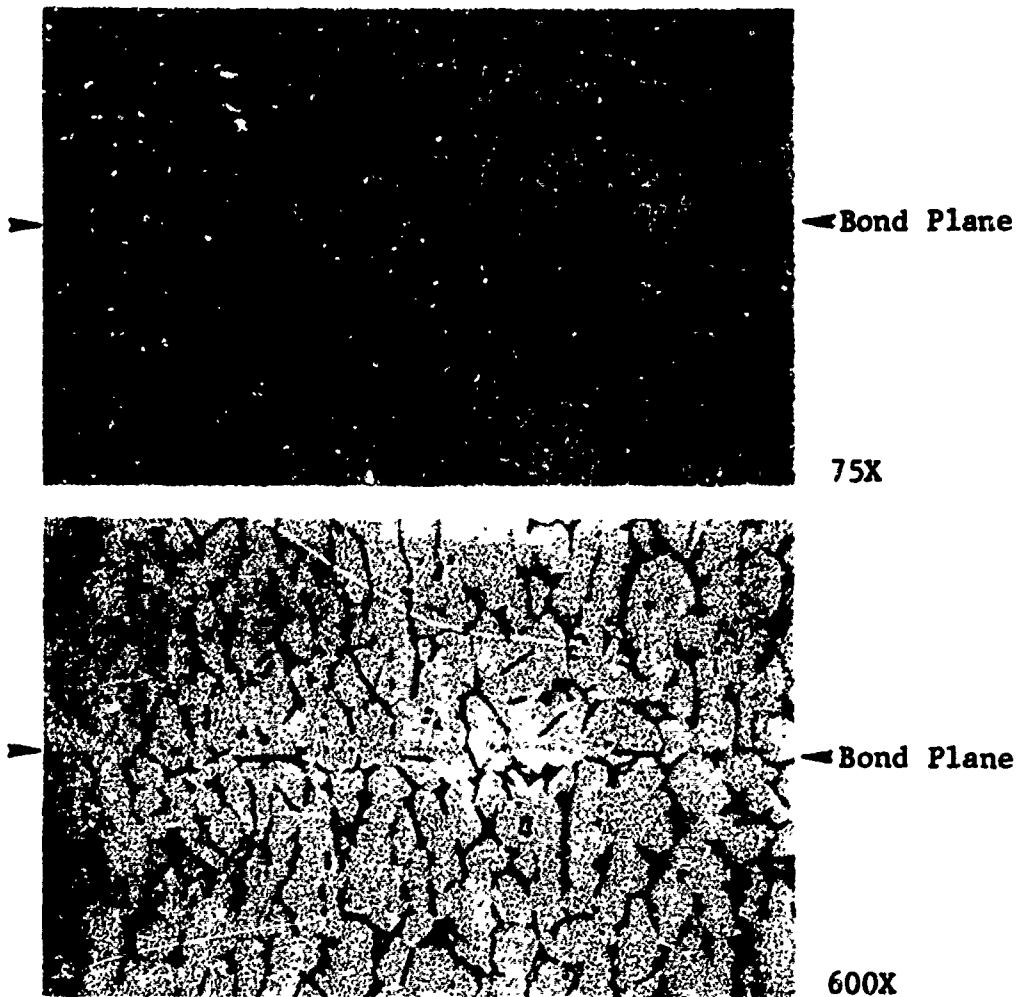
Bond Plane

Comments: Void easily detectable after bonding cycle. Metal smearing over the void due to sanding and polishing makes void dimensions after bonding difficult to determine. Bonding appears to have decreased the size of the void only slightly.

Figure 6.23 Photomicrographs at Bond Plane of DB Specimen H-4

**SPECIMEN J-4 (Double Bond/Single Axis)**

**Bonding Parameters:** 1700°F, 6 Hrs, 7% Deformation  
**Defect Type:** Alpha case layer  
**Dimensions:** Before bonding - 0.187" dia. x 0.002" thick  
After bonding - (see comments)

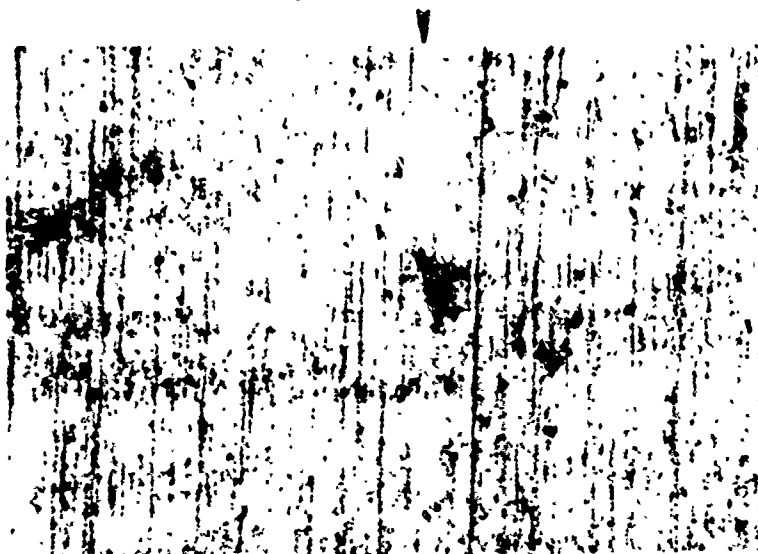


**Comments:** Diffusion of the oxygen & nitrogen away from the bond plane resulted in a partial loss of identity of the original alpha case layer. Subgrain size features remain including microvoids and minute unbonded areas aligned with the original bond plane. Effects on the adjacent microstructure are visible. Microhardness measurements transverse to the bondline after bonding indicate a hardness maxima at the bondline of 486 KHN. The hardness decreases slowly as a function of depth below the bondline. A distance of 0.035" is required before the microhardness reaches a value typical of heat-treated parent material (350 KHN).

**Figure 6.24 Photomicrographs at Bond Plane of DB Specimen J-4**

SPECIMEN K-3 (Single Bond)

Bonding Parameters: 1700°F, 6 Hrs, 7% Deformation  
Defect Type: 304 Stainless steel inclusion  
Dimensions: Before bonding - 0.013" dia. x 0.009" deep  
After bonding - 0.007" x 0.002" (minimum) (see comments)



80X  
(Unetched)

Bond Plane



160X  
(Unetched)

Comments: Defect appears after the bonding cycle, although with reduced size. The original defect cavity remained filled after bonding. The chemistry of the inclusion (304 stainless steel) remains to be verified.

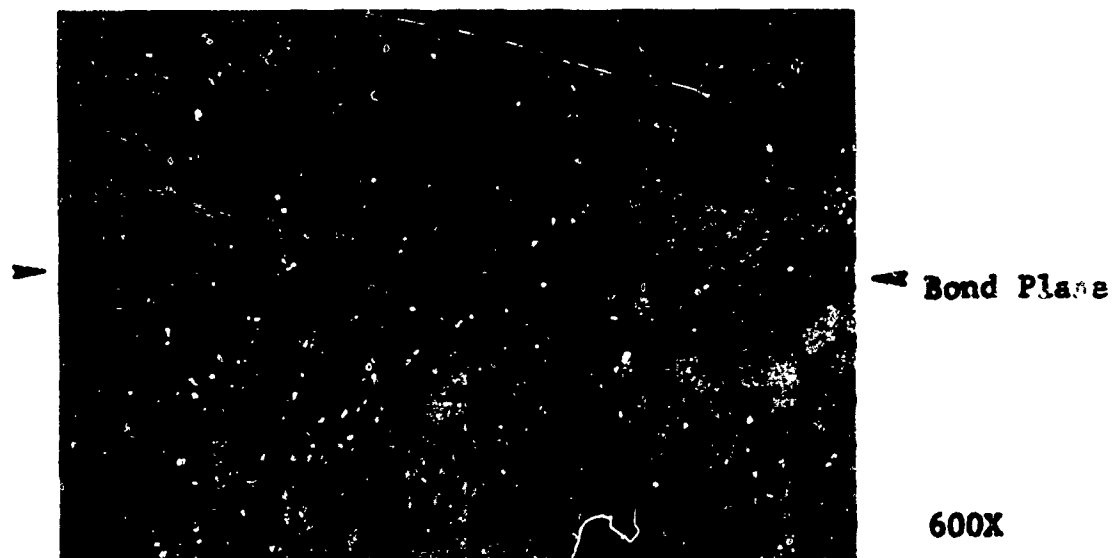
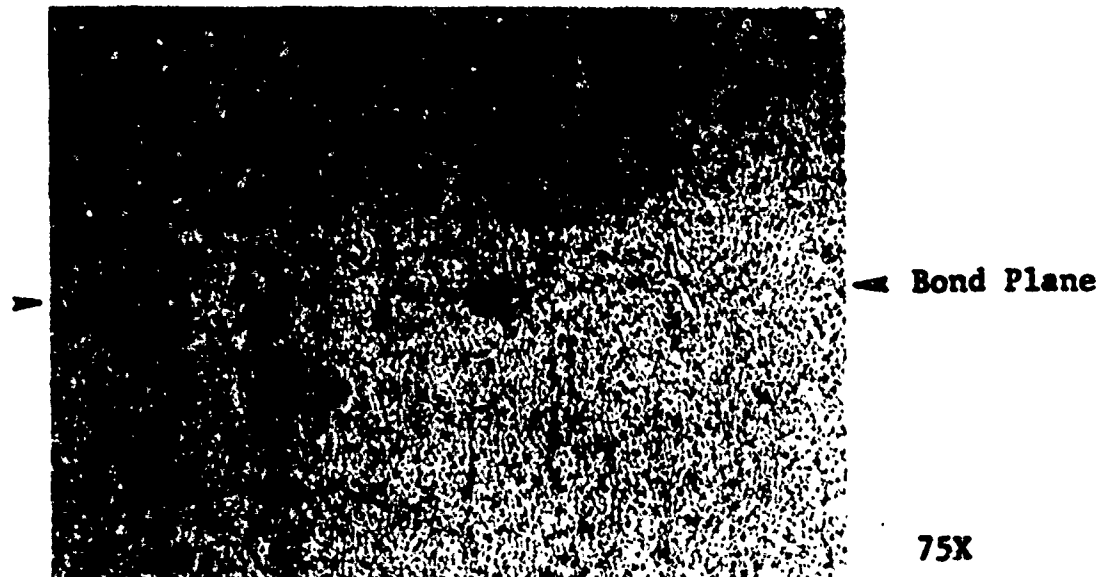
Figure 6.25 Photomicrographs at Bond Plane of DB Specimen K-3

**SPECIMEN L-3 (Single Bond)**

**Bonding Parameter:** 1700°F, 6 Hrs, 7% Deformation

**Defect Type:** Silica inclusion

**Dimensions:** Before bonding - 0.013" dia. x 0.005" deep  
After bonding - 0.005" x 0.003" (see comments)



**Comments:** Bondline outside defect area is indistinguishable. Little or no interaction of the silica at the silica-ti-interface. Particles are still observable in the defect after the bonding cycle.

**Figure 6.26 Photomicrographs at Bond Plane of DB Specimen L-3**

## 6.2 Nondestructive Evaluation

### 6.2.1 Blue Etch-Anodize Process

The blue etch-anodize (BEA) process was used as a nondestructive inspection technique on selected diffusion bonded specimens. This technique has previously been used in detecting alloy segregation and areas of high interstitial content in titanium alloys (Ref.11). The process involves immersing a thoroughly clean titanium part in an anodizing solution (trisodium phosphate) and subsequent immersion in an aqueous nitric-hydrofluoric acid solution. Details of the blue etch-anodize method are shown in Appendix B. Using this technique, aluminum and interstitial element-stabilized alpha appear deep blue in a lighter blue or gray background, while vanadium-stabilized beta appears gray or white.

This process was used after the selected bonded specimens had been blank machined. Specimens were milled to  $\approx 40$  RMS surface finish. If samples were not milled prior to anodizing, the process did not work well as surface contamination interfered with blueing.

The results of the blue etch-anodize (BEA) examination on selected diffusion bonded specimens are shown in Tables 6.11 and 6.12. In the single-bond/single-axis and double-bond/single axis specimens, no color discontinuities were observed at the bond line, except in specimen J4. This indicates the absence of alloy segregation and interstitial elements around the bonding area after the bond cycle.

In the multiple-bond/two-axes and multiple-bond/three-axes specimens, the most pronounced color discontinuities at the bond line were in specimens containing an alpha case layer. As shown in specimen V5-A (Figure 6.27), the alpha case layer shows as a dark blue color in a light blue background. The microhardness as a function of distance away from the bond line was measured on this same sample after bonding. These results are shown in Figure 6.28. A region of high hardness is observed for approximately .015" on each side of the bond line. However, the maximum hardness obtained,  $\approx 480$  KHN, is quite smaller than that obtained at the surface containing the alpha case layer before bonding,  $\approx 700$  KHN. Apparently, the 6-hour bonding time is sufficient to allow some diffusion of interstitials away from the bond line.

In the multiple-bond/two-axes specimens, color changes

Table 6.11 BLUE ETCH-ANODIZE (BEA) RESULTS ON SELECTED SINGLE-BOND/SINGLE-AXIS  
AND DOUBLE-BOND/SINGLE-AXIS DIFFUSION BONDED JOINTS

Specimen Number	Deficiency	Color Discontinuity Observed at Bondline	Comments (Destructive Test Results)
M3-B	None	No	Good Fatigue Properties
N3-B	< Opt. Deformation	No	Good Fatigue Properties
O3-A	< < Opt. Deformation	No	Bad Fatigue Properties
Q3-B	Larger Primary Alpha Grains Prior to Bonding	No	Good Fatigue Properties
D4	None	No	Good Tensile Properties
F4	Much Larger Primary Alpha Grains Prior to Bonding	No	Good Tensile Properties
S4-B	Multiple Surface Voids, .0065" diameter	No	Good Fatigue Properties
T4-A	Multiple Surface Voids, .010" diameter	No	Bad Fatigue Properties
U4-B	Multiple Surface Voids, .020" diameter	No	Bad Fatigue Properties
J4	Alpha Case Layer	Yes	Reduction of Area Poorer Than That of Parent Material
V4-B	Alpha Case Layer	No	Bad Fatigue Properties
X4-A	SiO <sub>2</sub> Powder Inclusions	No	Bad Fatigue Properties

Table 6.12 BLUE ETCH ANODIZE (BEA) RESULTS ON VARIOUS MULTIPLE BOND - 2-AXES SPECIMENS

SPECIMEN NUMBER	DEFICIENCY	TOTAL DEFORMATION (Z) (LONG. DIRECTION)	BOND LINE INDICATION (LONG. DIRECTION)	TOTAL DEFORMATION (%) (SHORT TRANS. DIRECTION)	BOND LINE INDICATION (SHORT TRANS. DIRECTION)	COMMENTS
MS-A	None	5.96	No	3.5	Slight	Fatigue failures due to incomplete bond in short transverse direction
B5	<Opt. Deformation	2.38	No	10.0	No	Tensile failures due to incomplete bond in long. direction
MS-B	<Opt. Deformation	2.22	Yes (1)	1.0	Yes	(1) Shows more prominently on NSB1 specimen fatigue failures due to incomplete bond in short transverse direction
OS-A	<<Opt. Deformation	0.74	Yes (2)	2.0	Yes	(2) Shows more prominently on OSB1 specimen fatigue failures due to incomplete bond in short transverse direction
PS-A	None	6.02	No	3.5	Yes (3)	(3) Only shows on PSA3 specimen. PSA1 and PSA3 had fatigue failures due to incomplete bond in short transverse direction
QS-B	Larger primary alpha grains prior to bonding	5.80	No	2.0	Yes (4)	(4) Only shows on QSA1 specimen. Good fatigue properties
RS-B	Much larger primary alpha grains prior to bonding	6.00	No	2.0	No	RSB1 and RSB2 had poor fatigue properties
SS-A	Voids in the form of chamfered edges	5.41	No	5.5	Very slight	Fatigue failures due to defects
H5	Voids in the form of chamfered edges	5.23	No	7.0	Very slight	Good tensile properties
US-A	Voids in the form of chamfered edges	5.80	No	6.5	No	Fatigue failures due to defects
J5	Alpha Case Layer	4.60	Yes (5)	6.6	Yes (5)	(5) Prominent on all [(J,V)5-B] surfaces
VS-A	Alpha Case Layer	5.30	Yes (5)	7.1	Yes (5)	(5) Prominent on all [(J,V)5-B] surfaces. Fatigue failures due to defects
WS-A	Type 304 Stainless Steel Powder Inclusions	4.58	No	7.5	No	Fatigue failures due to defects
LS	SiO <sub>2</sub> Powder Inclusions	4.83	No	7.1	No	Tensile failures due to defects



Table 6.13 BLUE ETC.-ANODIZE (BEA) RESULTS ON SELECTED MULTIPLE-BOND/3-AXES SPECIMENS

Specimen Number	Bond Plane Indication (Long Dir)	Bond Plane Indication (Long Trans Dir)	Bond Plane Indication (Short Trans Dir)	Comments
M6-B	No	No	No	Poor Fatigue Properties
N6-A	Yes (1)	No	No	(1) Only observed on N6A1 and N6A3 specimens (N6A1 and N6A3 had poor fatigue properties)
U6-A	Yes (2)	No	No	(2) Only observed on U6A2 specimen (only U6A3 had poor fatigue properties)
V6-A	Yes	Yes	No	Poor Fatigue Properties

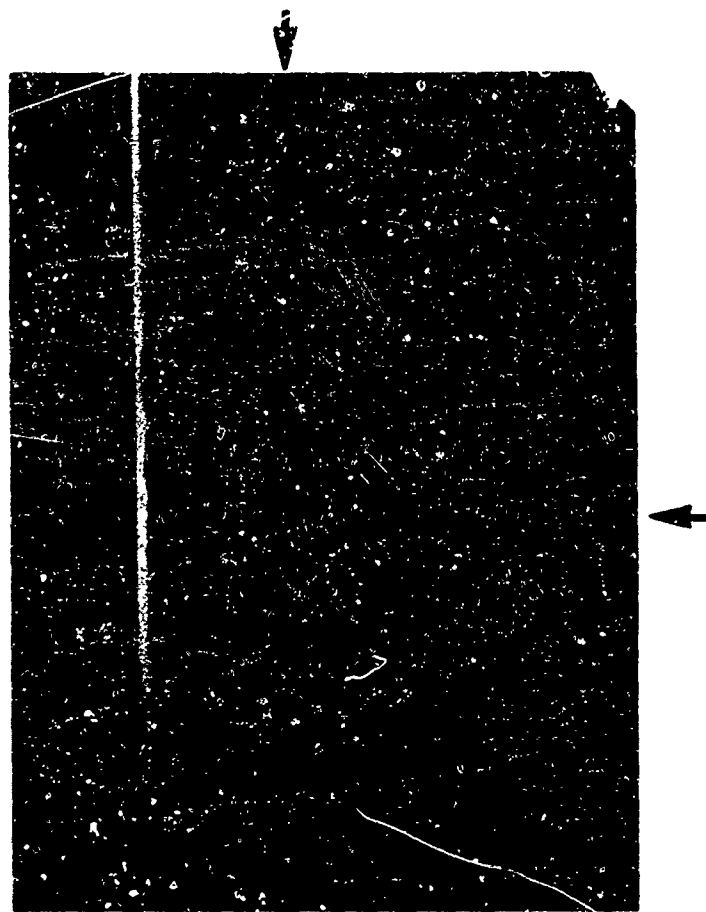


Figure 6.27 Photograph Showing Alpha Case Layer at Bondline  
in Specimen V5-A

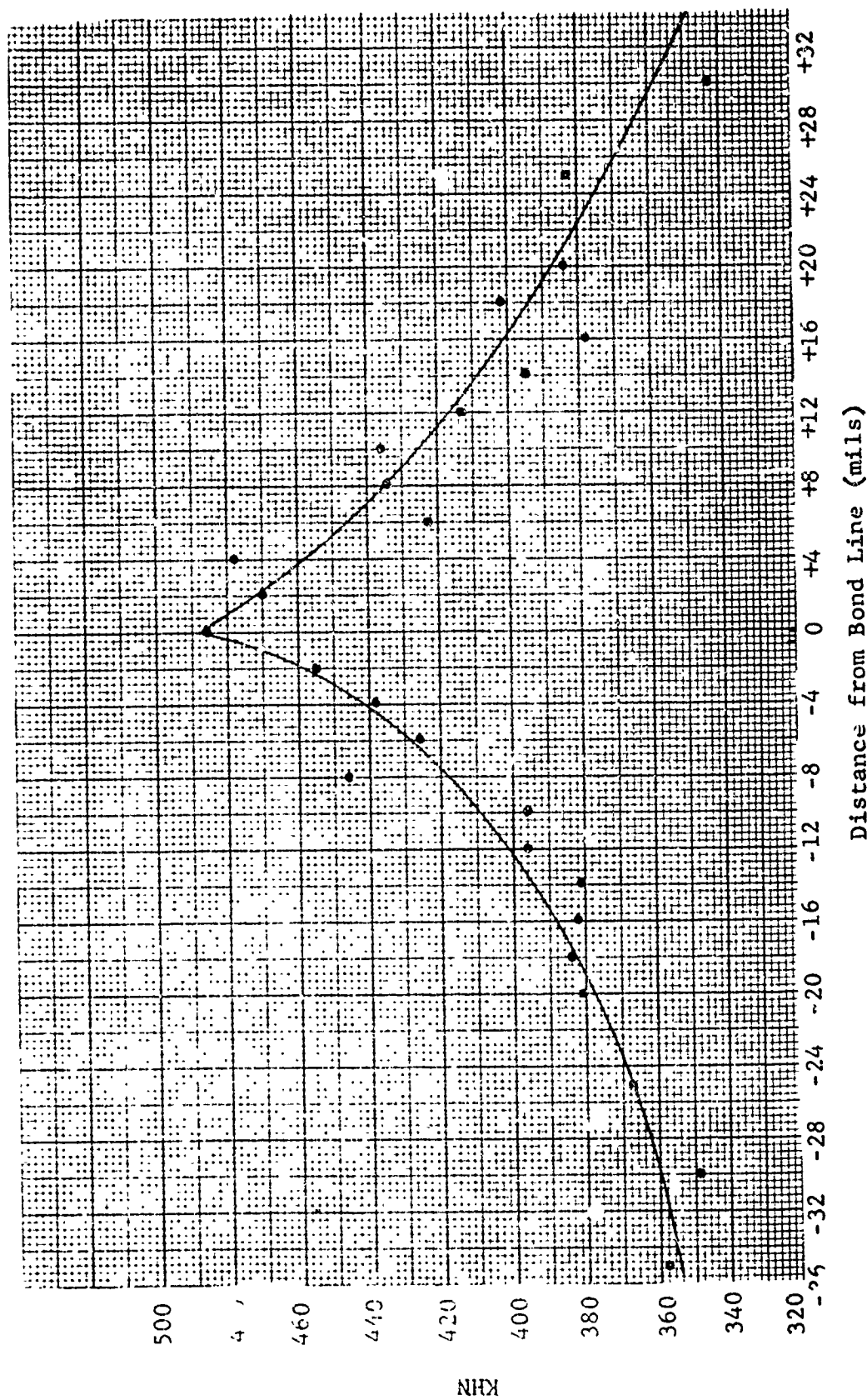


Figure 6.28 Microhardness vs. Distance from Bond Line

were observed at some of the bond planes, particularly ones where smaller deformations had occurred, although not as pronounced as in specimens containing an alpha case layer. Photographs of some of these areas are shown in Figures 6.29 thru 6.33. Bond planes most pronounced were those formed through the thickness of the material (short transverse direction). Most of the origins of failure in axial fatigue specimens formed from these samples occurred due to incomplete bonding in the short transverse direction. As shown in Table 6.12 except for the specimens containing alpha case layers, whether the bond lines were observed after the blue etch-anodize inspection depended strongly on deformations received.

In the multiple bond/three axes specimens, color discontinuities were again most prevalent in the alpha case specimen V6-A. The discontinuities observed for the bond plane lying in the long transverse direction are shown in Figure 6.33b. In some specimens, bond lines were only observed in small areas. The location of these areas are described in the tables.

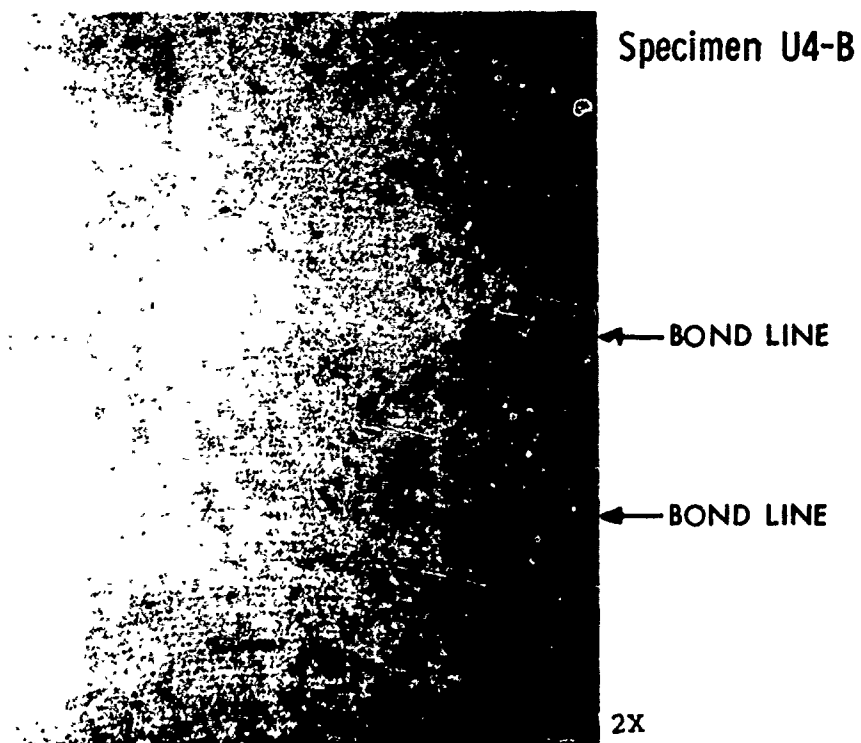
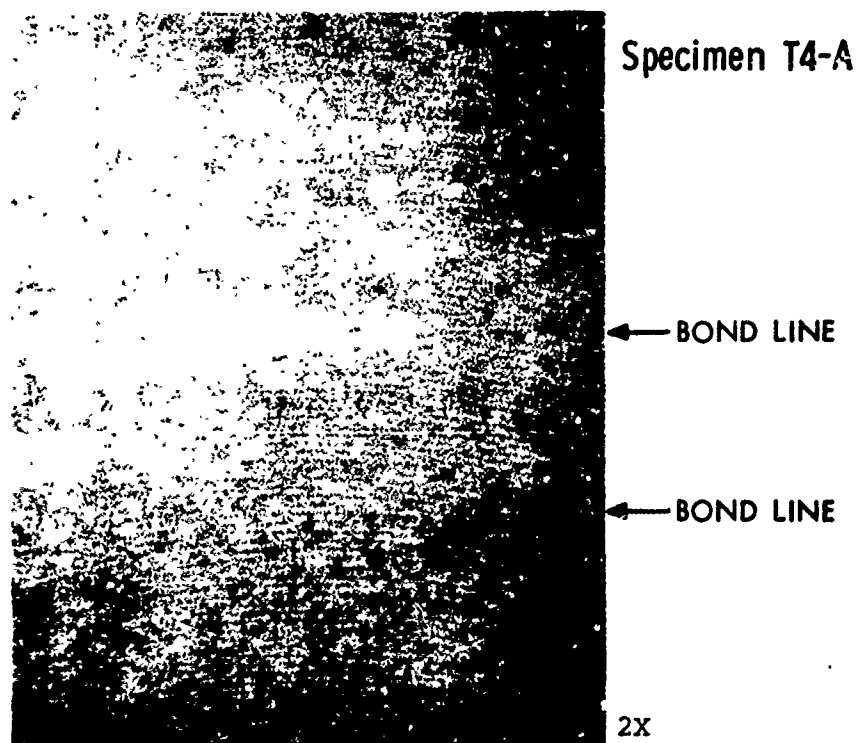
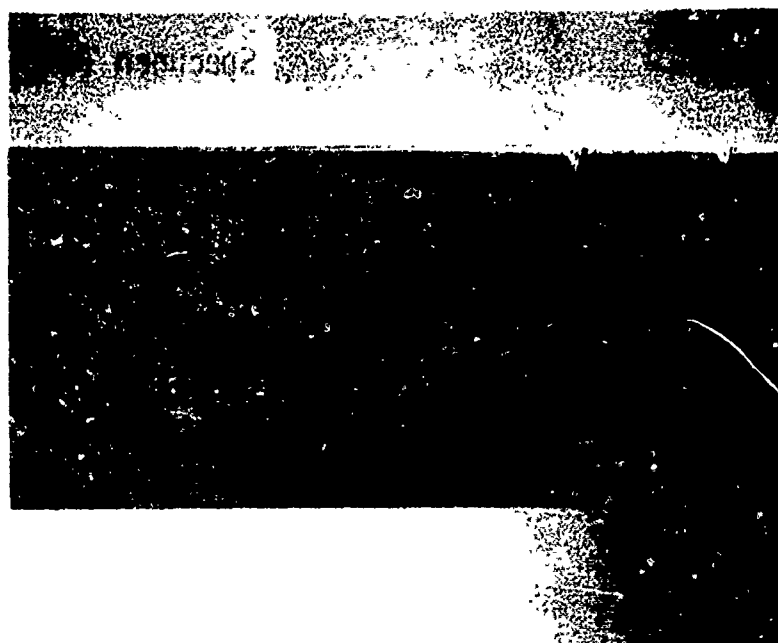


Figure 6.29 Photographs of Specimens T4-A and U4-B After Blue Etch-Anodize (BEA) Processing.



← Bond Plane

2X

N5-B (Short Transverse Direction)

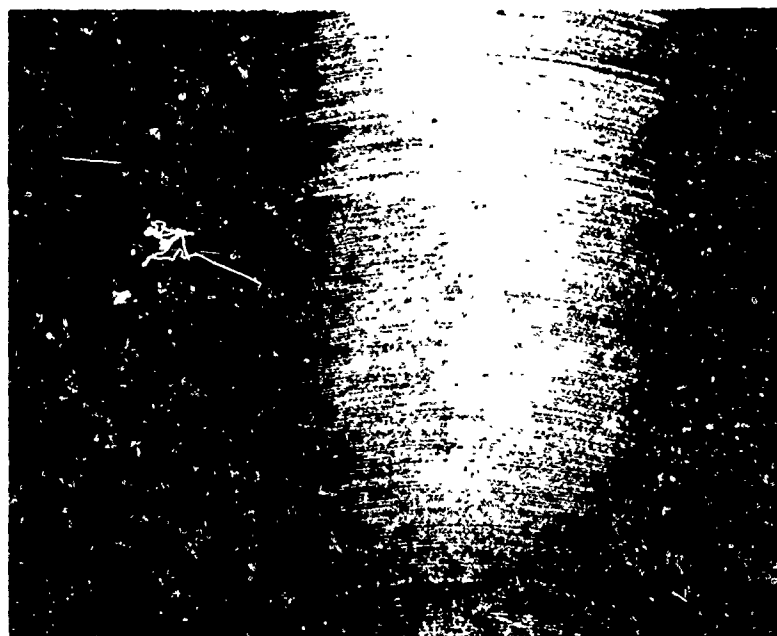


← Bond Plane

2X

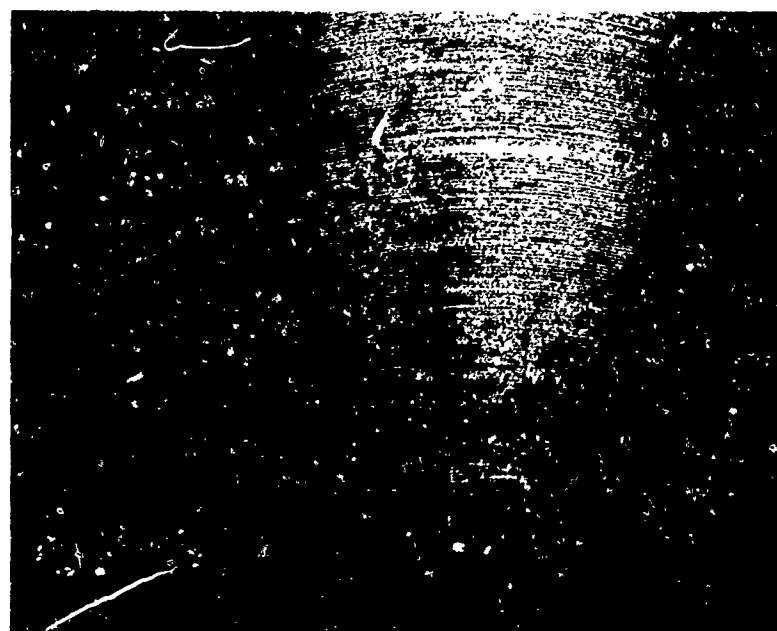
05-A (Short Transverse Direction)

Figure 6.30 Blue Etch-Anodize Records of Specimens N5-B and 05-A



2X

L5 (Long. Direction)



2X

P5-A (Long. Direction)

Figure 6.31 Blue Etch-Anodize Records of Specimens L5 and P5-A

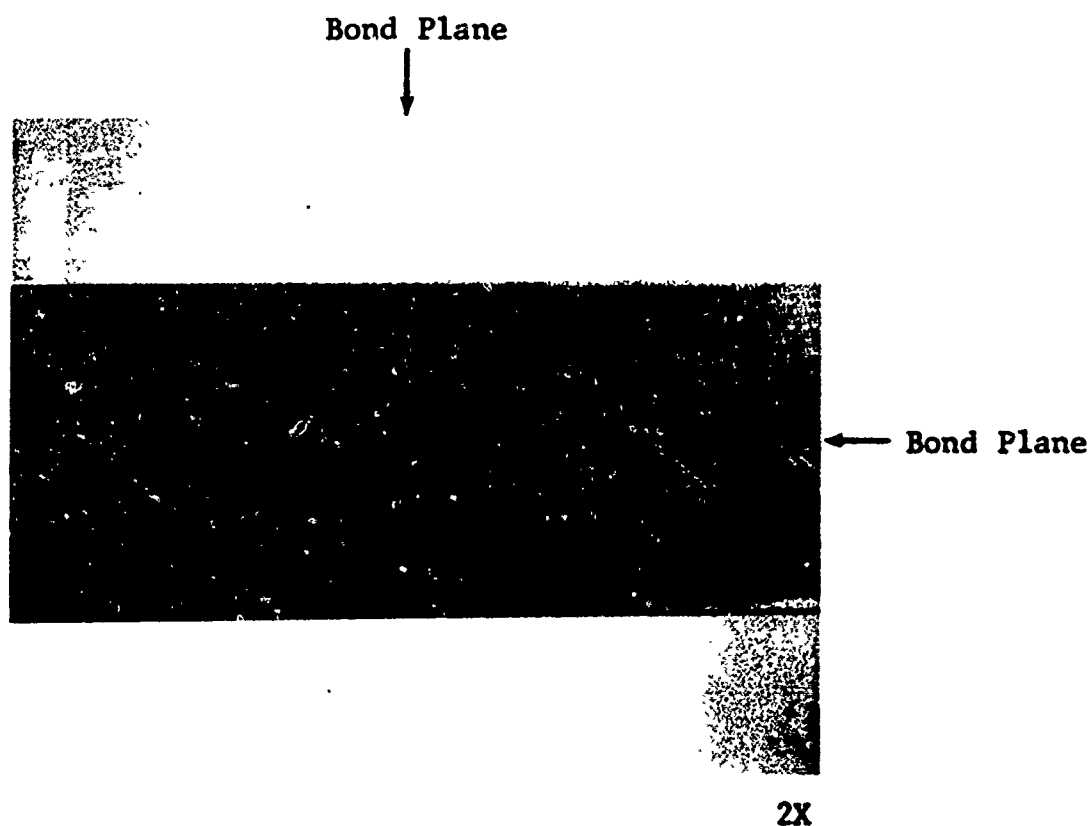
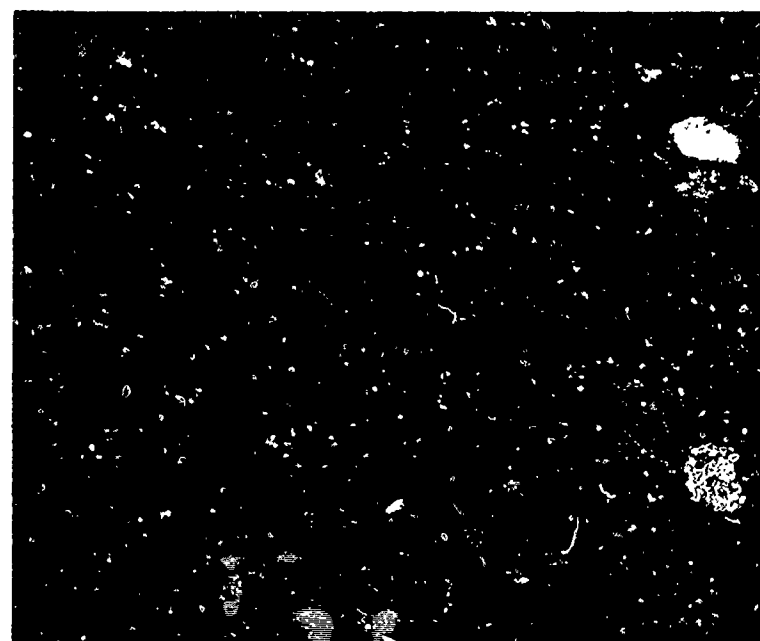


Figure 6.32 Blue Etch-Anodize Record of Specimen J5  
(Alpha Case Layer in Bond Planes)

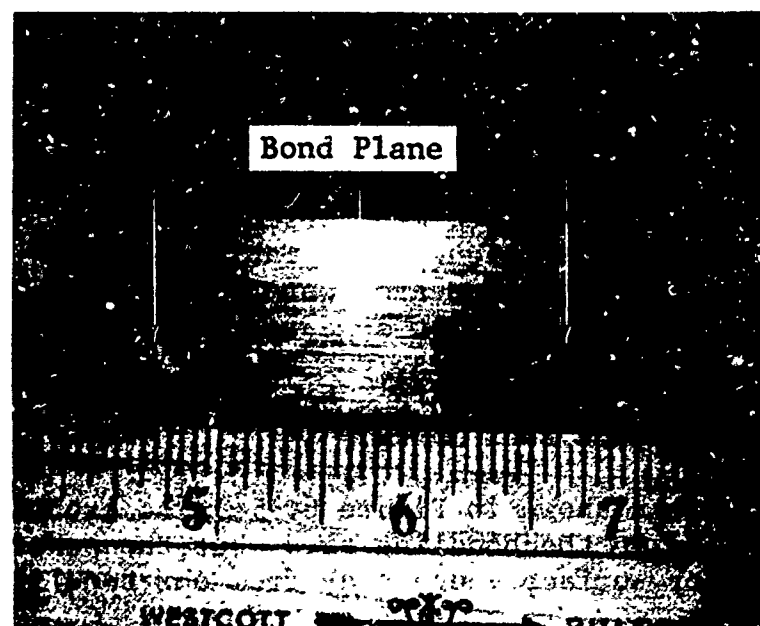




← Bond Plane

2X

J5 (Long. Direction)



Bond Plane

2X

V6-A (Short Transverse Direction)

Figure 6.33 Blue Etch-Anodize Records of Specimens J5 and V6-A

### 6.2.2 Fluorescent Penetrant Inspection

Diffusion bonded 6Al-4V titanium specimens containing intentional defects were fluorescent-penetrant evaluated for the detection of surface connected discontinuities, especially along the bond line.

Procedure: The technique used to most effectively detect a wide variety of cracks, porosity, and possible debond areas was a MIL-I-25135, Group V, post-emulsifiable penetrant, with a dry powder developer. Penetrant dwell time was at least 20 minutes, penetrant bleed-out time of at least 5 minutes, and an emulsification time of less than 3 minutes. The manufacturer's designation of penetrant material was ZL-2A penetrant, ZE-3 emulsifier, and ZP-4 dry powder developer. This technique was based on data from the March 1973 McDonnell-Douglas technical report on "Evaluation of the Reliability and Sensitivity of NDT Methods for Titanium Alloys." A production-line facility was used for this evaluation.

Specimens were first milled to a 40 RMS surface finish, prior to evaluation. Two and three-axes specimens were then chemically etched to remove approximately .001" from the surface. This procedure has been found to eliminate metal smearing over the surface due to the milling operation (Ref. 12) and can improve resolution in the detection of surface cracks. Three of the double-bond/single-axis specimens were evaluated both before and after chemically etching.

Results: Fifty-eight single-bond/single-axis and double-bond/single axis specimens were evaluated using the post-emulsifiable penetrant technique (6 specimens were evaluated using the water-washable penetrant technique) (see Table 6.14). No discontinuities in the bond-plane area were noted on any of the specimens. It was noted that some specimens contained surface tool marks, nicks, and gouges, due to machining and handling. Figure 6.34 shows a specimen and bond-line without discontinuities or surface tool marks.

The specimen shown in Figure 6.35 also exhibits no discontinuities in the bondline area, but the penetrant did pick up a minor surface gouge away from the bondline.

Specimens 03-A, 03-B, N4-A, N4-B, 04-A, and 04-B, which were diffusion bonded with low percent deformations (e.g., 1½%), should have been most susceptible to penetrant inspection.

Table 6. 14 FLUORESCENT PENETRANT INSPECTION RESULTS

Specimen No.	Bondline Indications	Other Indications	Specimen No.	Bondline Indications	Other Indications
A3 *	No Defect ↑	None	P3-A	No Defect ↓	1
A4		None	P3-B		None
B3		None	P4-A		None
B4		None	P4-B		None
C3		None	Q3-A		None
C4 *		None	Q4-A		None
D3		None	Q4-B		None
F3		None	R3-A		None
G3		None	R3-B		None
G4		1	R4-A		1
H3		None	R4-B		None
H4		None	S3-A		1
I3		None	S3-B		None
I4		1	S4-A		None
J3		None	T3-A		None
J4 *		1	T3-B		None
K3		None	T4-A		None
K4		None	U3-A		None
L3		None	U3-B		None
L4		None	U4-A		None
M3-A		None	V3-A		None
M4-A		None	V3-B		None
M4-B		None	V4-A		2
N3-A		None	W3-A		None
N4-A		None	W3-B		None
N4-B		None	W4-B		None
O3-B		1	X3-A		None
O4-A		None	X3-B		None
O4-B	No Defect ↓	None	X4-B	No Defect	None

\* Inspections were made both before and after chemical etching.

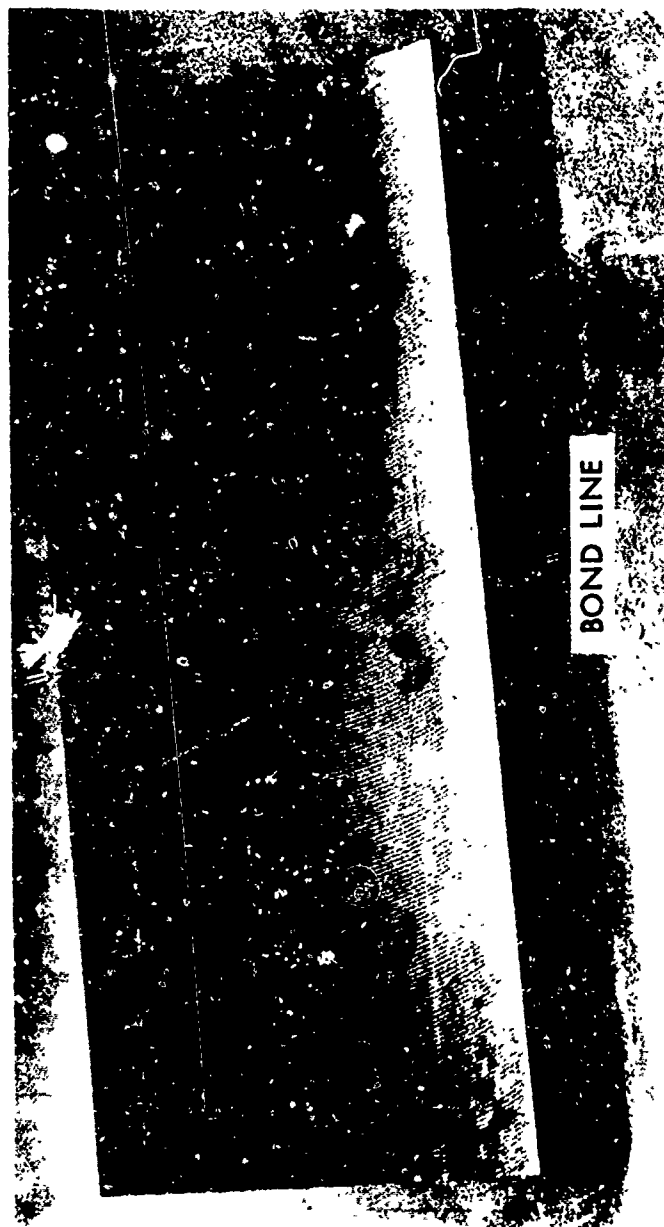


Figure 6.34 Fluorescent Penetrant Record of Diffusion Bonded Titanium Specimen with No Defects

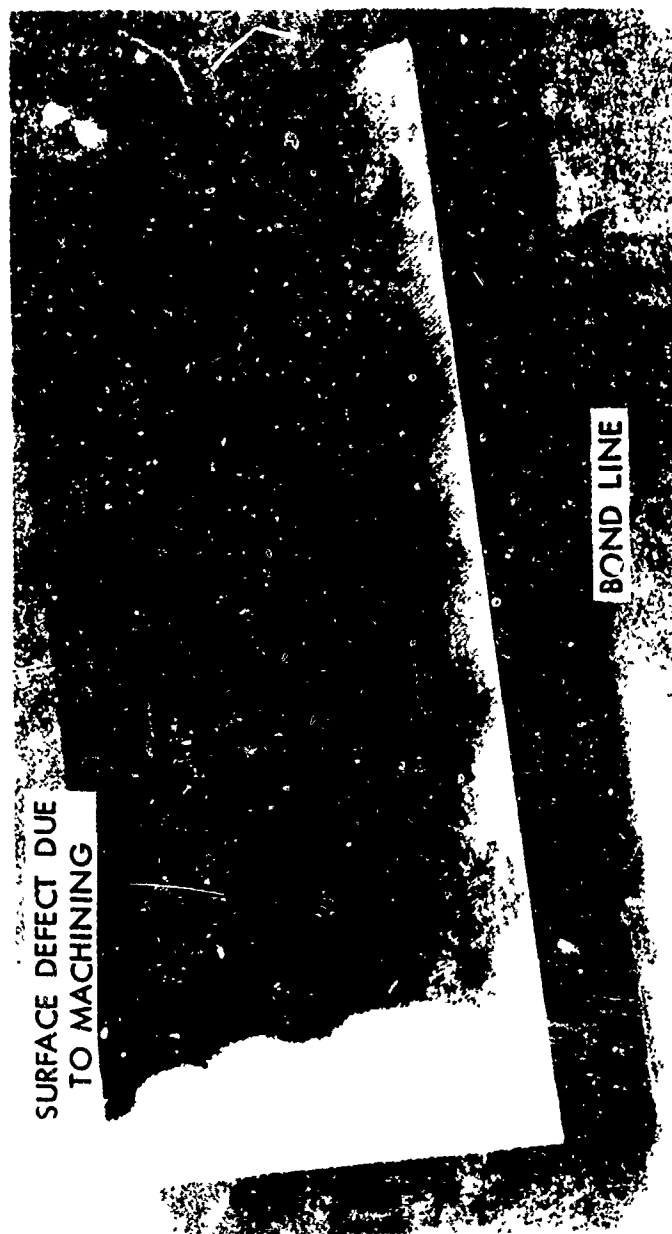


Figure 6.35 Fluorescent Penetrant Record of Diffusion Bonded Titanium Specimen with Surface Gouge

tion. As noted above, no indications were found.

Specimens A4, C4, and J4 were also inspected after chemically etching. No bondline indications were observed after the etching procedure.

Twenty-five multiple-bond/2-axes and multiple-bond/3-axes specimens were also evaluated by fluorescent penetrant inspection techniques. As mentioned earlier, these specimens were chemically etched after milling to improve resolution capabilities. Results of these inspections are given in Tables 6.15 and 6.16. Some bond lines were detected in the multiple-bond/2-axes specimens. Bond line intersections were also observed in several instances as denoted in Table 6.16.

Table 6.15 FLUORESCENT PENETRANT RESULTS ON SELECTED MULTIPLE-BOND/2-AXES SPECIMENS

Specimen Number	Bond Plane		Comments
	Indication (Long Dir)	Indication (Short Trans Dir)	
M5-A	No	No (1)	(1) 5-A, 5-B, and 5-C Interface, Left side of sample observed
B5	No	No	
N5-B	Yes	Yes (2)	(2) Observed only on left side
O5-A	No	Yes (3)	(3) Observed only at 5-A, 5-C Interface
P5-A	No	No	
Q5-B	No	Yes	
R5-B	No	No	
S5-A	No	No (4)	(4) 5-A, 5-B, 5-C Interface observed on both sides.
H5	No	No	
U5-A	No	No	
J5	No	No	
W5-A	No	No	
L5	No	No (5)	(5) Small hole observed at 5-A, 5-B and 5-C Interface, right side

Table 6.16 FLUORESCENT PENETRANT RESULTS ON SELECTED MULTIPLE-BOND/3-AXES SPECIMENS

Specimen Number	Bond Plane Indication (Long Dir)		Bond Plane Indication (Short Trans Dir)		Comments
	Indication		Indication		
M6-A	No	No	No	No	
B6	No	No	No	No	
N6-A	No	No	No	No (1)	(1) Intersection of bond planes in long. dir. and short trans. dir. observed
P6-B	No	No	No	No	
Q6-B	No	No	No	No	
R6-A	No	No	No	No (2)	(2) Bond line at top corners observed
S6-A	No	No	No	No	
T6-A	No	No	No	No	
U6-A	No	No	No	No (3)	(3) Flaws detected but not related to bond lines
V6-A	No	No	No	No (4)	(4) Intersection of bond planes in long. dir. and short trans. dir. observed
W6-A	No	No	No	No	
X6-B	No	No	No	No	



### 6.2.3 Ultrasonic Inspection

#### 6.2.3.1 Delta-Scan Technique

Principle of Operation - The Delta-Scan mode of nondestructive inspection utilizes a pulsed ultrasound in the megahertz range. A typical configuration is shown in Figure 6.36. A tilted transducer, T, transmits longitudinal waves through a liquid couplant onto the surface of a test specimen. The refracted shear waves in the specimen are reflected at the bottom surface and incident on the flaw surface. The ultrasonic waves, re-directed by the flaw, are received by the transducer, R, positioned above the flaw, indicating the existence of the flaw.

The geometrical parameters in the Delta configuration affect the detection sensitivity of the technique. Among these parameters are the angle of incidence of the transmitting beam, the lateral distance of separation (DOS) between transducers, T and R, DOS between the transducers and the specimen surface, and the type of transducer used.

Equipment - A Sperry-Rand UM 721 reflectoscope with a 10N pulser-receiver unit and a fast transigate was used in the Delta-Scan technique. The focused transmitting transducer was of the lead zirconate type with a focal length of 2-7 in. in water and a resonating frequency of 5.0 MHz. The focused receiving transducer was of the lithium sulphate type with the same focal length and resonating frequency as the transmitting transducer.

The specimens were immersed in an Automation Industries research tank, style 57A5432, and the Delta-Scan head was attached to an X-Y scanner with variable scanning and indexing speeds. A photograph of the tank, scanner, and the reflectoscope is presented in Figure 6.37.

An Alden No. 311DA recorder was synchronized with the X-Y scanner in the tank and provided ultrasonic facsimiles or C-scan recordings of the inspection result. The voltage pulse activating the recording pen originated from the gated signal due to scattering from a flaw. A darkened area on the C-scan recording represents a flaw with the flaw size proportional to the area.

Reference Standards - Quantitative determinations of flaw sizes as indicated on C-scan recordings were made by using Ti-6Al-4V diffusion bonded specimens with implanted flaws at the bondline as reference standards. Dimensions of the standard used in detecting flaws of single-bond/single-axis and multiple-bond/single-axis specimens and the locations of these reference flaws are shown in Figure 6.38. The choice of this specimen as

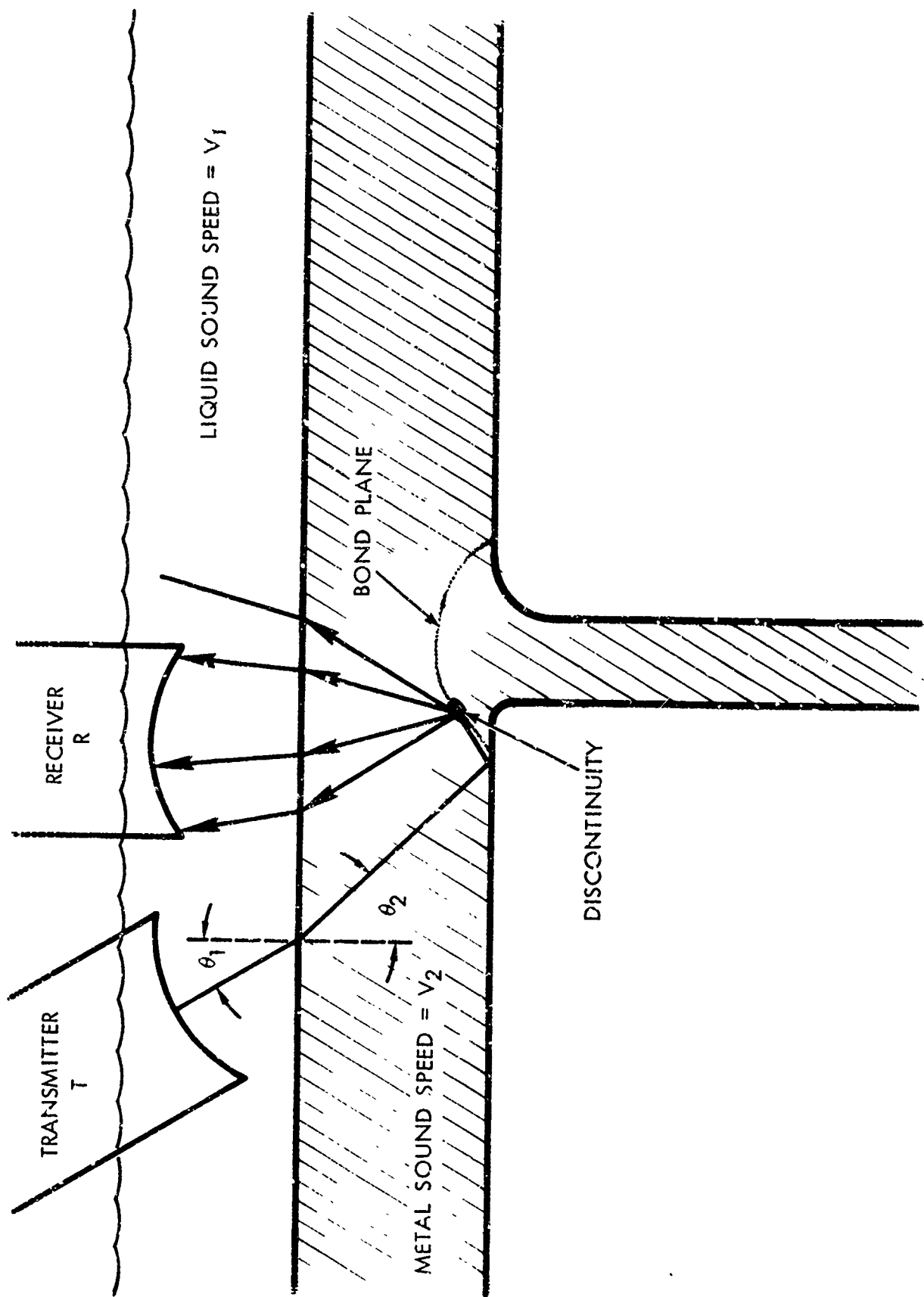


Figure 6.36 Delta-Scan Applied to Distorted Bond Plane

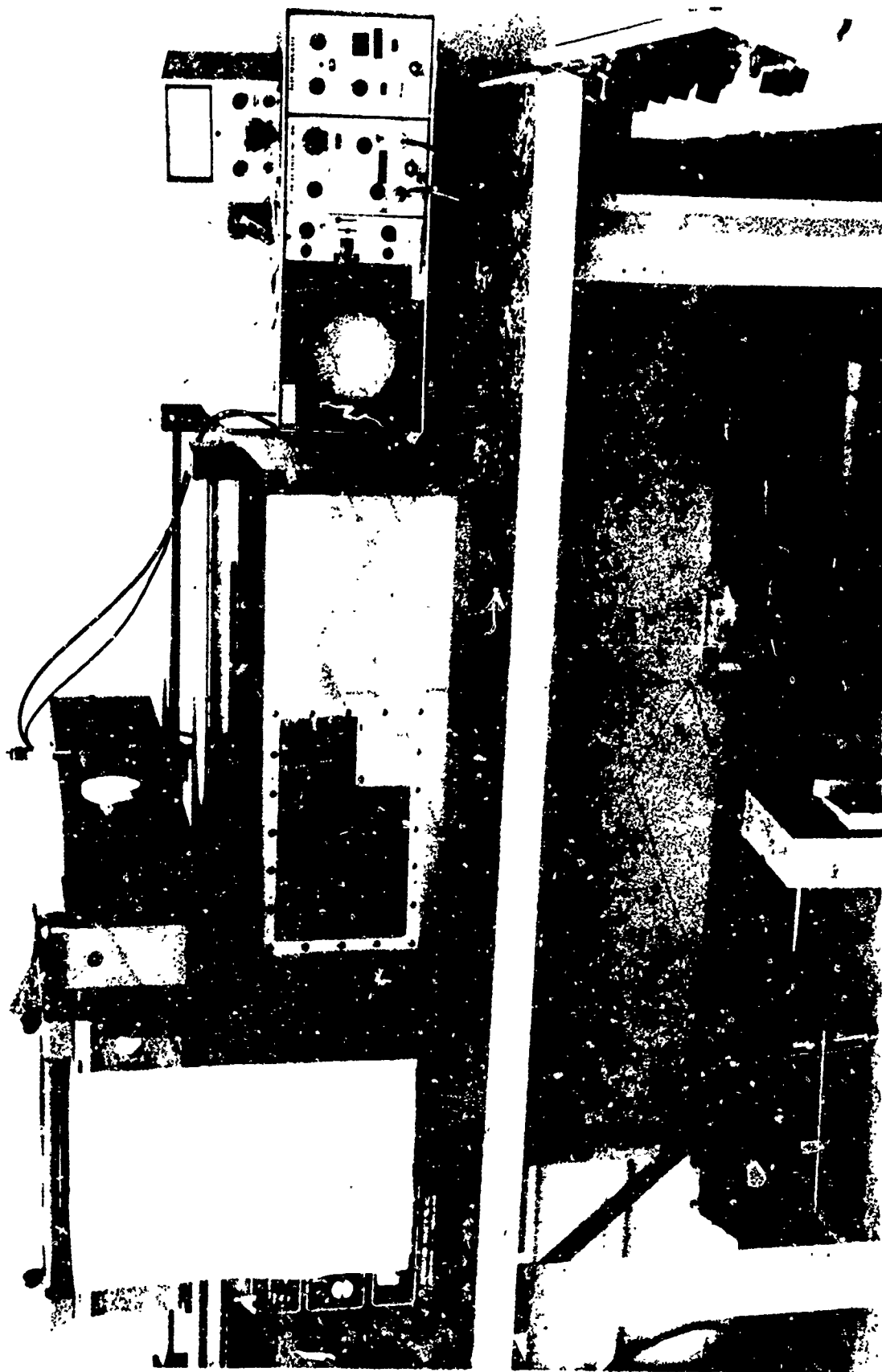


Figure 6.37 Laboratory Set-Up of Delta/C-Scan System

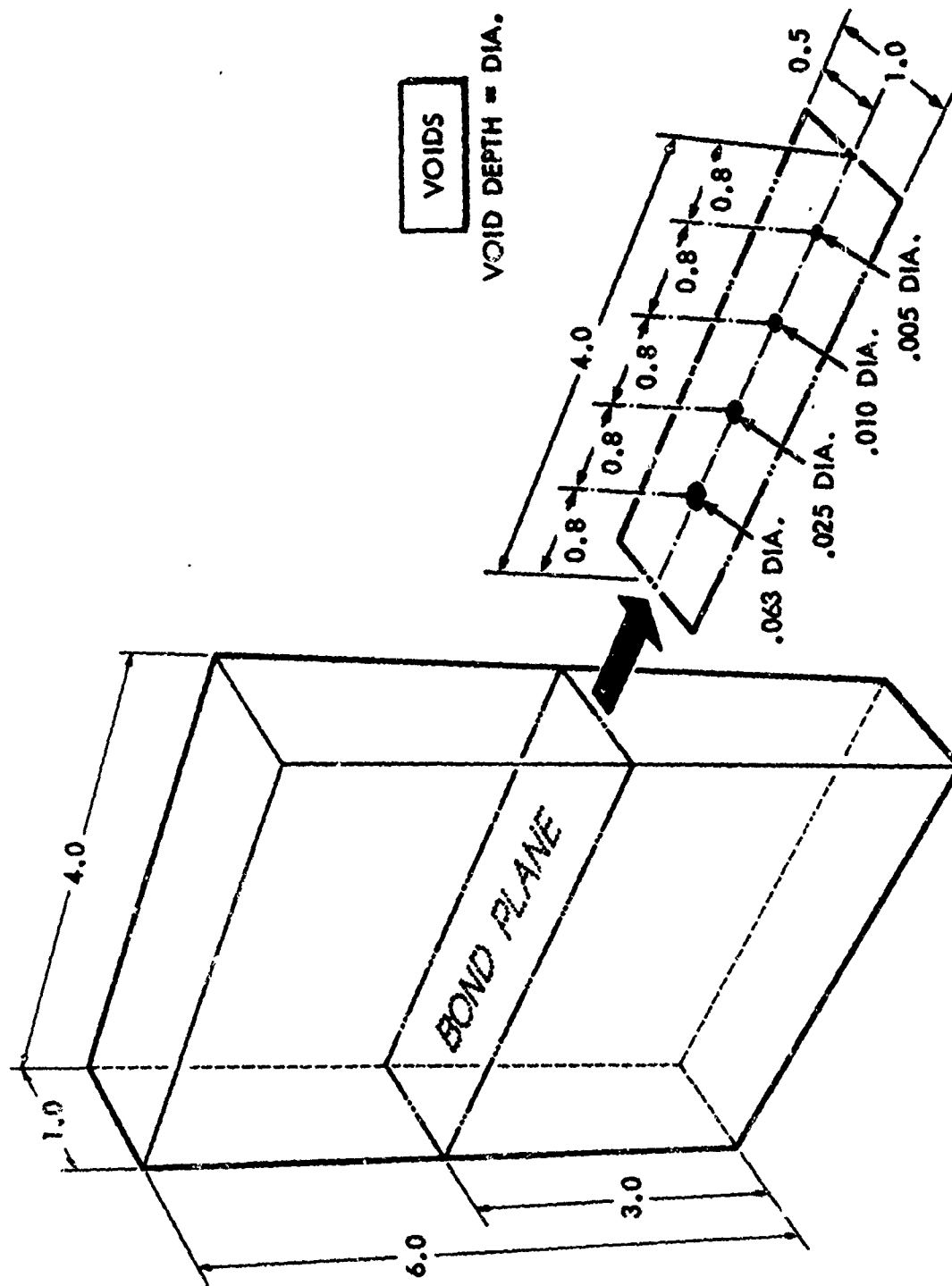


Figure 6.38 Diffusion Bonded Ultrasonic Reference Standard

a reference standard was based on the fact that its geometrical shape and bondline locations are quite similar to the single axis test specimens inspected.

The reference standard for the multiple-bond/2-axes and multiple-bond/3-axes specimens was designed to closely represent the size and location of defects to be found in these specimens. This was accomplished by drilling two 3/64-inch diameter flat bottom holes in the excess material area for multiple-bond/2-axes specimen number U5-A. The holes were drilled into the bondline to a depth corresponding to one-half of the specimen thickness.

Delta Configuration Optimization - The optimization of the Delta configuration was directed at detecting flaws located on bondlines in diffusion-bonded titanium specimens. Using the reference specimen as a standard, the tilt angles and DOS of the transducers of the Delta-head were determined. The physical parameters of the optimized configuration are presented in Figure 6.39. The tilt angle for the transmitting transducer was  $20^{\circ}$  so that only refracting shear waves would be propagating in the specimens, while the detection sensitivity for flaws in the mid-plane of the specimens would be maximum. The receiving transducer was also tilted at a  $4^{\circ}$  angle in the forward direction to maximize the signal amplitude for test specimens of 1-in. thickness.

It will be noted in Figure 6.39 that the research Delta-head used in this series of inspections had separate transducer holders connected by two 0.125-in. diameter metal rods. The lateral distance separating the two transducers may be varied by sliding one of the blocks along the metal rails. A separating distance of 1.7 in. between the centers of the two transducers was found to produce the best result.

While the off-the-shelf Delta-Scan heads have fixed lift-off distance, the research head was designed so that the transducers could be moved in the holes provided in the holding blocks. The optimum DOS's recorded in Figure 6.39 were obtained by fixing the transmitting transducer as close to the block as possible without protruding through the base and varying the position of the receiving transducer in the holder, as well as the lift-off distance of the whole assembly from the specimen surface. C-scan recordings of the reference flaws in the calibration specimens are presented in Figures

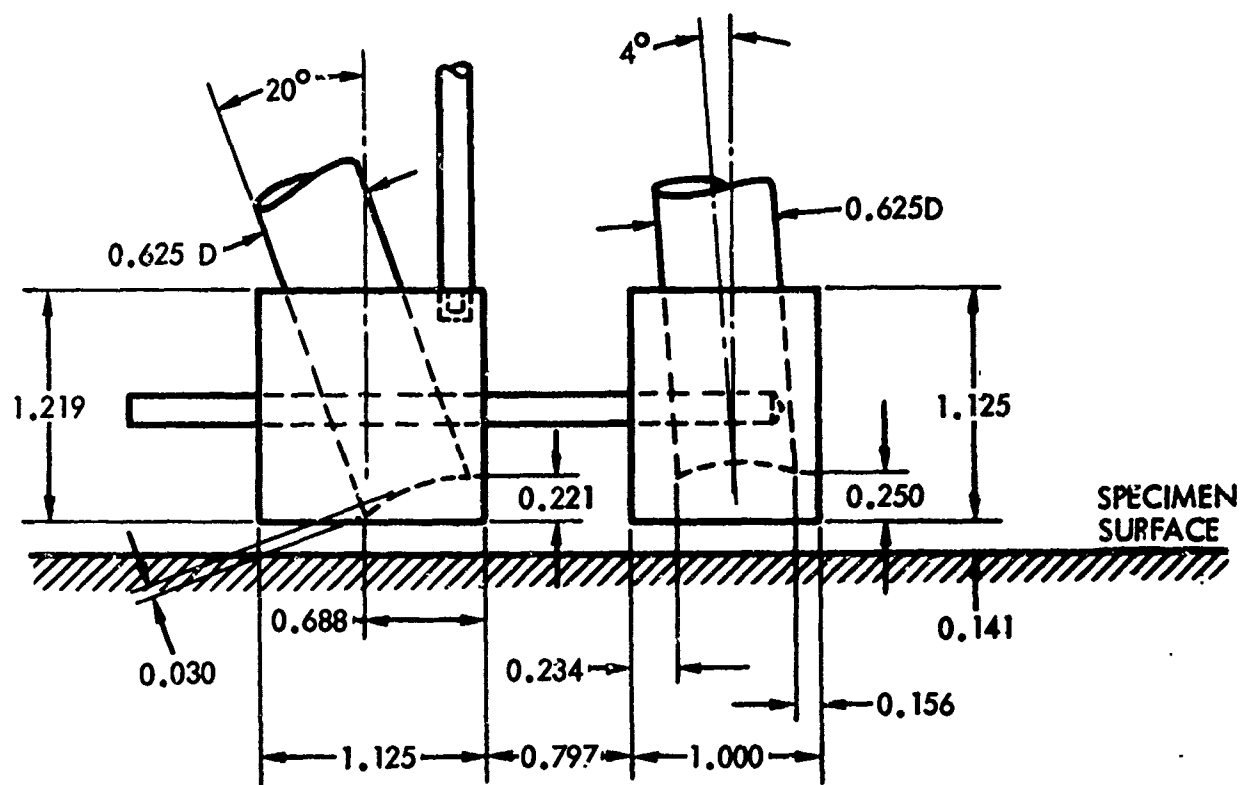
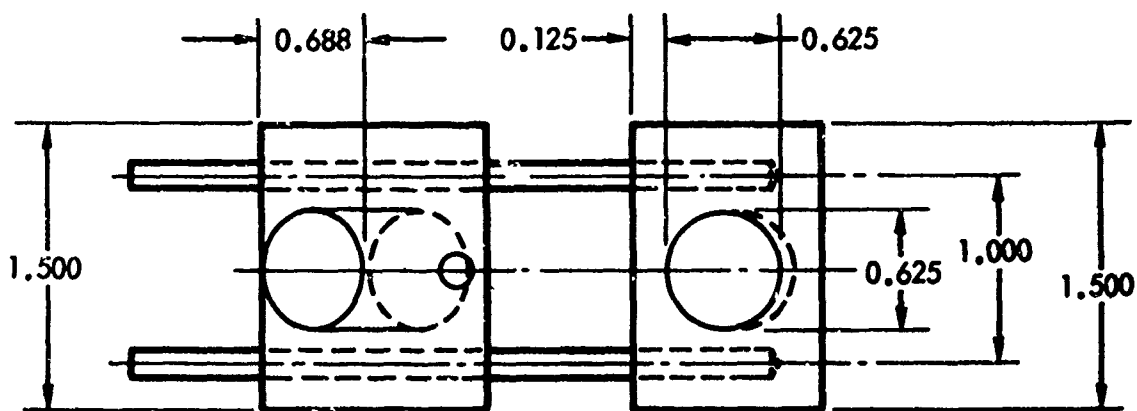


Figure 6.39 Optimized Delta-Scan Configuration

6.40 and 6.41. The flaw indications in these recordings were used for flaw size correlation and resolution determination.

Inspection Results - Delta Scan inspections were made on most of the single-axis specimens and all of the two- and three-axes specimens. The reference standard was also used as a calibration standard for setting the location of the gate, triggering level of the recording pen, and the optimization of the parameters in the Delta configuration. Equipment calibration and resolution check were repeated before inspections started each day. The test specimens were inspected by scanning the Delta-Scan head along the long dimension of the specimens.

Results of inspections of single-axis joints are tabulated in Table 6.17. C-scan recordings of three specimens with indications of 0.0065, 0.010, and 0.020 in. are presented in Figures 6.42, 6.43, and 6.44, respectively.

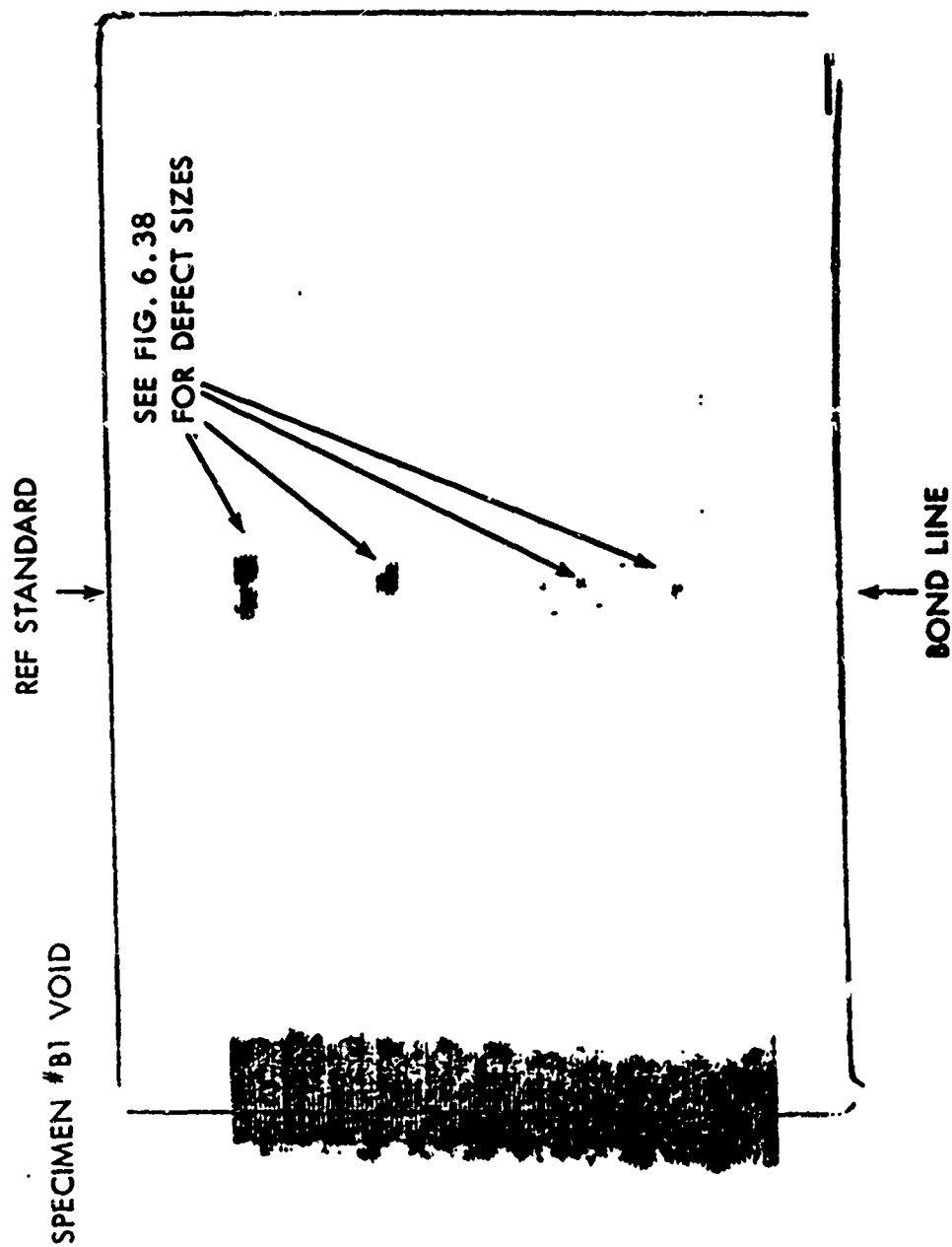
Results of inspections of multiple-bond/2-axes and multiple-bond/3-axes specimens are shown in Tables 6.18 and 6.19. C-scan recordings of specimens M6-A, N6-B, O5-B, C6, H5, O5-A, S6-B, H6, V6-A, K5, X5-A, and X6-B showing different types of defects are shown in Figures 6.45 through 6.51.

#### 6.2.3.2 Signal-Averaged Pulse-Echo Measurements

Data Collection - The signal-averaging pulse-echo system described in Section 4.1 was used in the contact mode (machine oil couplant) to obtain waveforms at (a) defect locations in the bond plane, (b) defect-free locations in the bond plane, and (c) parent material locations outside the bond plane per Figure 4.3.

Measurements were made using a UM 721 Reflectoscope with 10N Pulser/Receiver to energize an Automation Industries Transducer, 10.0 MHz/0.250 SFZ 57A5623. Standard reference blocks were fabricated with 3/64 flat bottom holes located at depths corresponding to diffusion bond locations. The reference blocks were utilized on a daily basis to check operation of the signal averaging system and offer a potential base-line for normalization of defect-amplitude data.

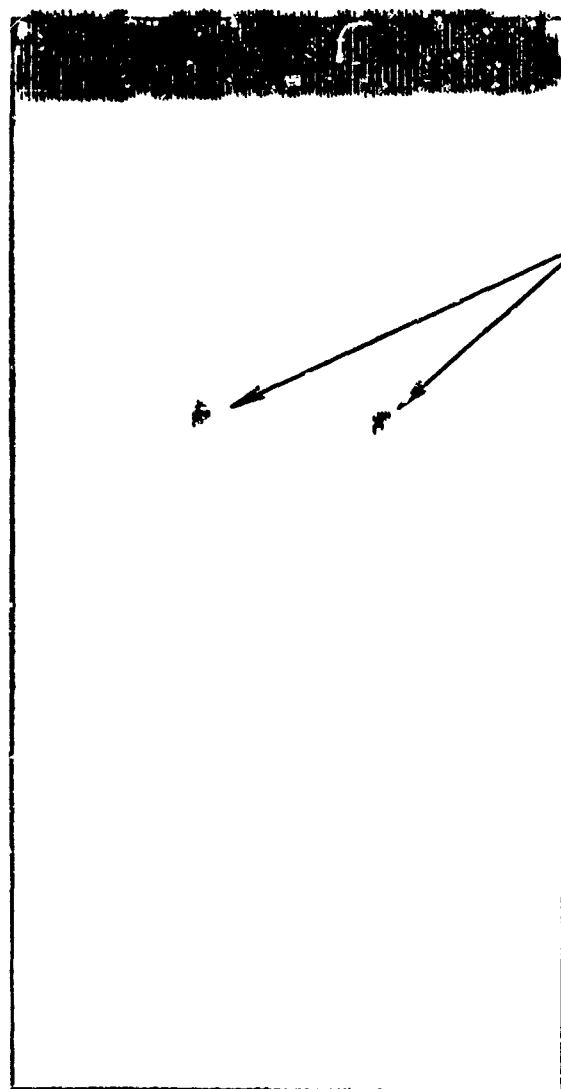
Reflectoscope sensitivity was varied as required to prevent screen saturation. Reference standard measurements were made at all sensitivity levels used during data collection.



DELTA SCAN TECHNIQUE  
 5 MHz FREQ 10 NP/R  
 SEN. LEVEL 5.4 x 1  
 TRIG. LEVEL 1.2/2.6

Figure 6.40 Ultrasonic Delta Scan Record of Reference Standard





Two .045-Inch Diameter  
Flat Bottom Holes  
Reaching to the Bond Plane

Figure 6.41 Delta-Scan Reference Standard for Multiple Bond Specimens

Table 6.17 ULTRASONIC DELTA-SCAN FLAW INDICATION RESULTS FOR SINGLE BOND/SINGLE AXIS AND MULTIPLE BOND/SINGLE AXIS SPECIMENS

Specimen Number	Deficiencies	Number of Flaw Indication (At Bondline)	Specimen Number	Deficiencies	Number of Flaw Indication (At Bondline)
A3	None	None	A4	None	None
M3-A	None	None	M4-A	None	None
M3-B	None	None	M4-B	None	None
B3	<Optimum Deformation	None	B4	<Optimum Deformation	1
N3-A	<Optimum Deformation	None	N4-A	<Optimum Deformation	1
N3-B	<Optimum Deformation	Not Evaluated	N4-B	<Optimum Deformation	None
C3	<<Optimum Deformation	3	C4	<<Optimum Deformation	None
O3-A	<<Optimum Deformation	Not Evaluated	O4-A	<<Optimum Deformation	1
O3-B	<<Optimum Deformation	Not Evaluated	O4-B	<<Optimum Deformation	None
D3	None	None	D4	None	Not Evaluated
P3-A	None	None	P4-A	None	2
P3-B	None	None	P4-B	None	None
E3	Larger Primary Alpha Grain (Prior to Bonding)	None	E4	Larger Primary Alpha Grain (Prior to Bonding)	Not Evaluated
Q3-A	None	None	Q4-A	None	2
Q3-B	None	Not Evaluated	Q4-B	None	1
F3	Much Larger Primary Alpha Grain (Prior to Bonding)	None	F4	Much Larger Primary Alpha Grain (Prior to Bonding)	Not Evaluated
R3-A	None	Not Evaluated	R4-A	None	1
K3-B	None	1	R4-F	None	Not Evaluated
G3	Cylindrical Voids (3 each = 6.5 Mils Dia.)	1	G4	Cylindrical Voids (3 group; 4 voids/ gp. = 6.5 Mils Dia.)	Not Evaluated
S3-A	None	Not Evaluated	S4-A	None	Not Evaluated
S3-B	None	1	S4-B	None	Not Evaluated
H3	Cylindrical Voids (3 each ~ 10 Mils Dia.)	None	H4	Cylindrical Voids (3 group; 4 voids/ gp. = 10 Mils Dia.)	2 Group
T3-A	None	1	T4-A	None	Not Evaluated
T3-B	None	None	T4-B	None	2 Group
I3	Cylindrical Voids (3 each = 20 Mils Dia.)	3	I4	Cylindrical Voids (3 group; 4 voids/ gp. = 20 Mils Dia.)	3 Group
U3-A	None	1	U4-A	None	3 Group
U3-B	None	2	U4-B	None	Not Evaluated

(Continued)

Table 6.17(Continued)

Specimen Number	Deficiencies	Number of Flaw Indication (At Bondline)	Specimen Number	Deficiencies	Number of Flaw Indication (At Bondline)
J3	Alpha Case Layer	1	J4	Alpha Case Layer	4
V3-A	Alpha Case Layer	1	V4-A	Alpha Case Layer	1
V3-B	Alpha Case Layer	None	V4-B	Alpha Case Layer	1
K3	Type 304 Stainless	3	K4	Type 304 Stainless	None
W3-A	Steel Powder In-	1	W4-A	Steel Powder In-	3
W3-B	clusions	None	W4-B	clusions	1
L3	Silica (SiO <sub>2</sub> )	1	L4	Silica (SiO <sub>2</sub> )	1
X3-A	Powder Inclu-	1	X4-A	Powder Inclu-	Not Evaluated
X3-B	sions	None	X4-B	sions	3

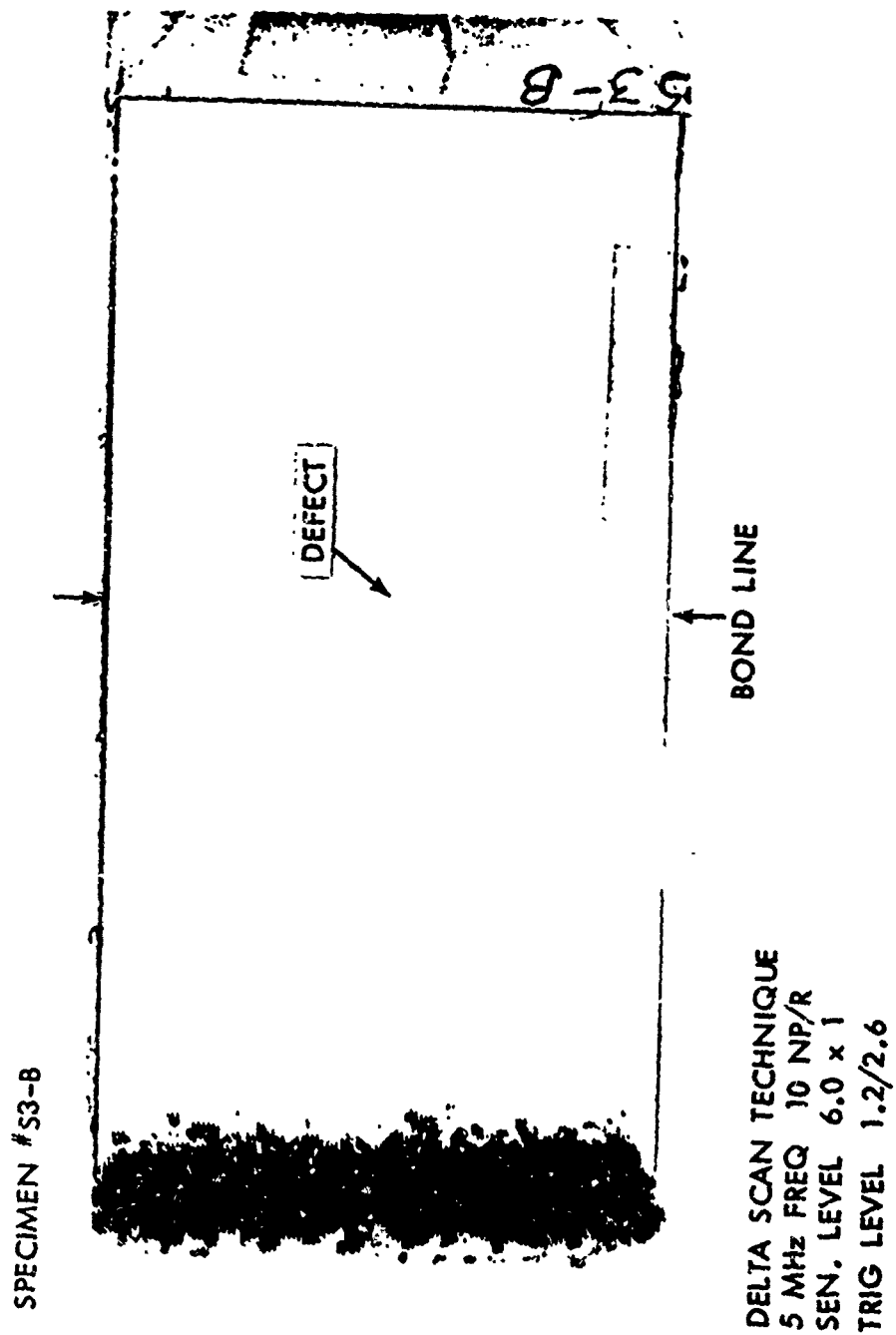


Figure 6.42 Delta/C-Scan Recording of Specimen S3-B

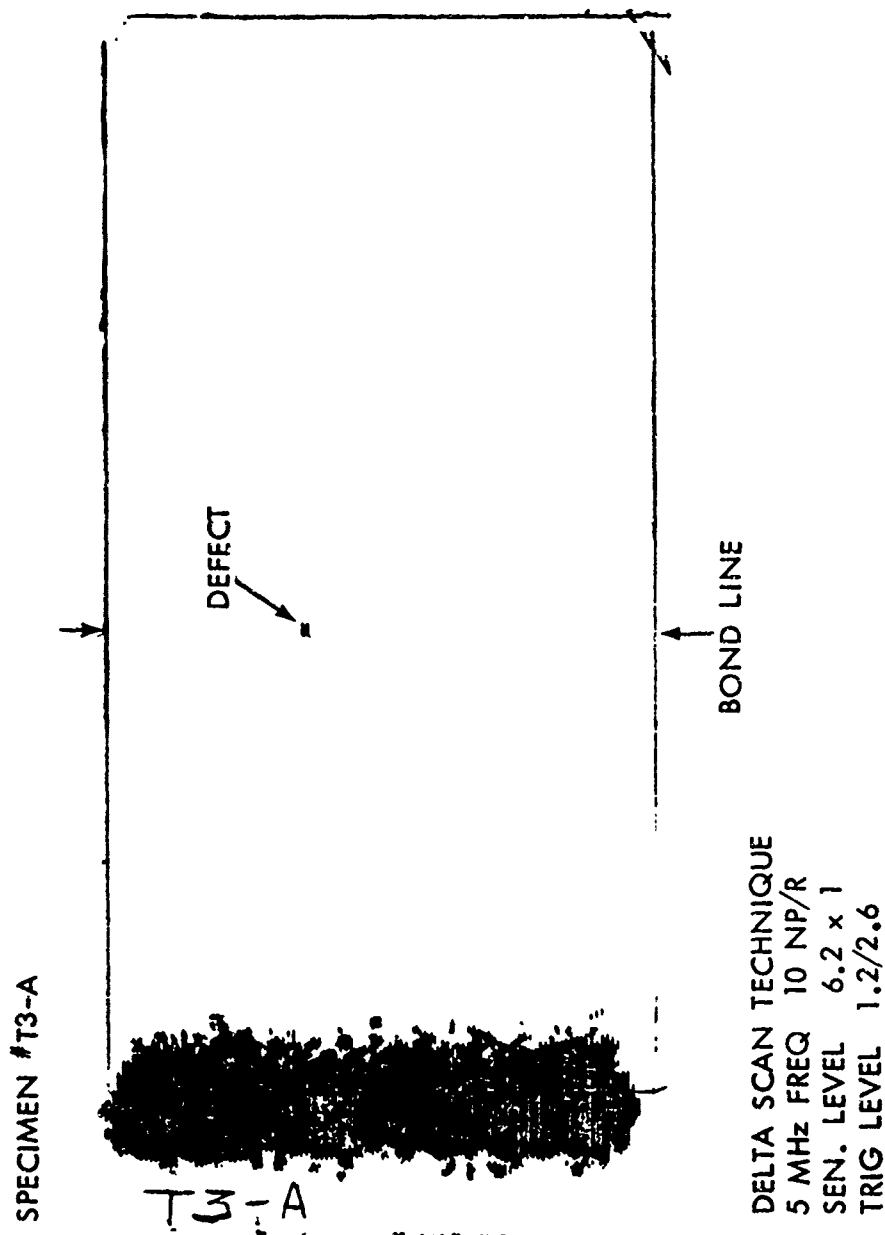


Figure 6.43 Delta/C-Scan Recording of Specimen T3-A

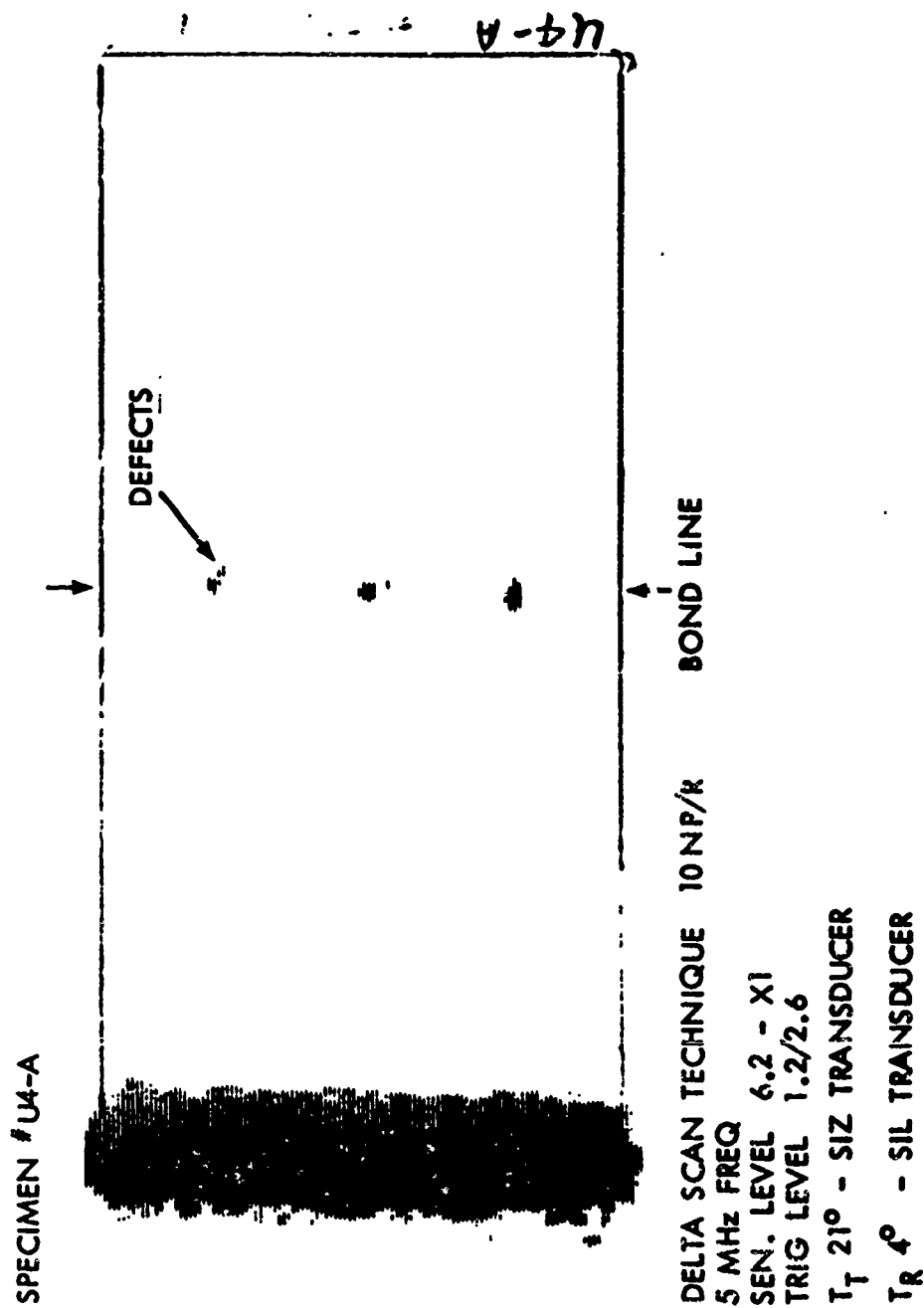


Figure 6.44 Delta/C-Scan Recording of Specimen U4-A

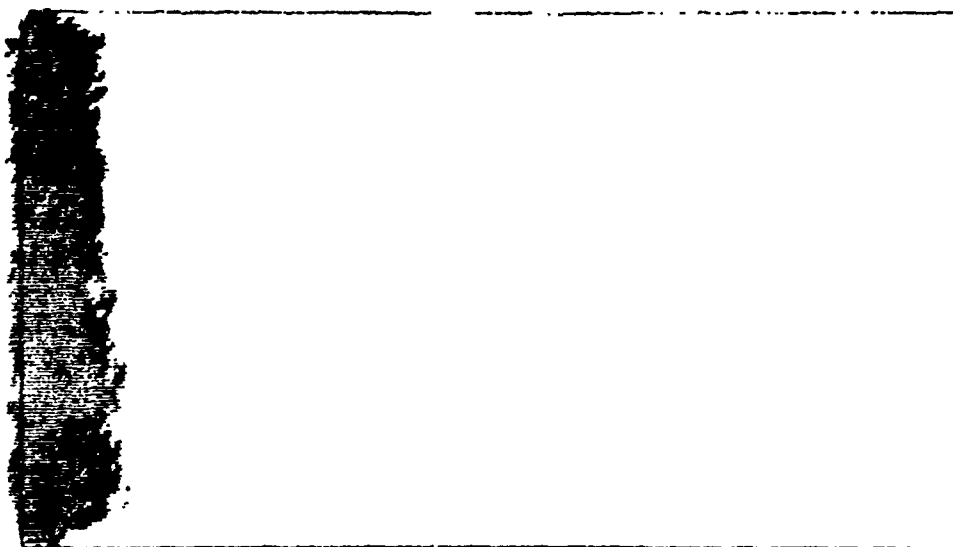
Table 6.18 ULTRASONIC DELTA-SCAN INDICATION RESULTS FOR  
MULTIPLE-BOND/TWO-AXES SPECIMENS

Specimen Number	Deficiency	Defect Indication at Bondline	Location of Defect
A5	None	Yes	More pronounced on right side (A5-2 and A5-3)
M5-A		Yes	Sides M5A1 and M5A3
M5-B		No	-
B5	< Opt. Deformation	No	-
N5-A		No	-
N5-B		Yes	More pronounced on left side (N5B1 and N5B2)
C5	<< Opt. Deformation	Yes	Middle and right side (C5-2 and C5-3)
O5-A		Yes	Left Side (D5A1)
O5-B		Yes	Along entire width of specimen (O5B1, O5B2, and O5B3)
D5	None	Yes	Middle and left side (D5-1 and D5-2)
P5-A		Yes	Right side (P5A3)
P5-B		No	-
E5	Larger primary alpha grains prior to bonding	Yes	Along entire width of specimen (E5-1, E5-2, and E5-3)
Q5-A		No	-
Q5-B		No	-
F5	Much larger primary alpha grains prior to bonding	Yes	More pronounced on right side (F5-3)
R5-A		No	-
R5-B		Yes	Left side (R5B1)
G5	Voids in the form of chamfers	Yes	Very slight indication, middle (G5-2)
S5-A		Yes	Left and right sides (S5A1 and S5A3)
S5-B		No	-
H5	Voids in the form of chamfers	Yes	Very slight indication (H5-1 and H5-3)
T5-A		No	-
T5-B		No	-
I5	Voids in the form of chamfers	Yes	Very slight indication (I5-1 and I5-3)
U5-A		Yes	More pronounced on left side (U5A1 and U5A2)
U5-B		Yes	Extreme right side (U5B3)
J5	Alpha case layer	Yes	Very slight indication, a (J5-1, J5-2, J5-3)
V5-A		No	-
V5-B		No	-
K5	Type 304 stainless steel powder inclusions	Yes	All 3 intentional defects located
W5-A		Yes	2 intentional defects located (W5A2 and W5A3)
W5-B		Yes	2 intentional defects located (W5B2 and W5B3)
L5	SiO <sub>2</sub> powder inclusions	Yes	All 3 intentional defects located
X5-A		Yes	All 3 intentional defects located
X5-B		Yes	All 3 intentional defects located

Table 6.19 ULTRASONIC DELTA-SCAN DEFECT INDICATION RESULTS  
FOR MULTIPLE-BOND/THREE-AXES SPECIMENS

Specimen Number	Deficiency	Defect Indication at Bondline	Location of Defect
A6 M6-A M6-B	None	No No No	- - -
B6 N6-A N6-B	< Opt. Deformation	No No Yes	- - More pronounced on left side (N6B1)
C6 O6-A O6-B	<< Opt. Deformation	Yes No Yes	Along entire width (C6-1, C6-2, and C6-3) - (O6B1, O6B2, and O6B3)
D6 P6-A P6-B	None	No Yes No	- (P6A1 and P6A2) -
E6 Q6-A Q6-B	Larger primary alpha grains prior to bonding	No No No	- - -
F6 R6-A R6-B	Much larger primary alpha grains prior to bonding	No No No	- - -
G6 S6-A S6-B	Voids in the form of chamfered edges	No No Yes	- - Intentional defect in center (S6B2)
H6 T6-A T6-B	Voids in the form of chamfered edges	Yes Yes Yes	All 3 intentional defects located Intentional defect in center (T6A2) Occurs along most of the width (T6B1, T6B2, and T6B3)
I6 U6-A U6-B	Voids in the form of chamfered edges	No No Yes	- - Extreme edges (U6B1 and U6B3)
J6 V6-A V6-B	Alpha Case layer	No Yes No	- (V6A1, V6A2, and V6A3) -
K6 W6-A W6-B	Type 304 stainless Steel Powder Inclusions	Yes Yes Yes	Extreme left side (K6-1) 2 intentional defects located (W6A2 and W6A3) 2 intentional defects located (W6B1 and W6B3)
L6 X6-A	SiO <sub>2</sub> Powder Inclusions	Yes Yes	2 intentional defects located (L6-1 and L6-2) All 3 intentional defects located (X6A1, X6A2, X6A3)



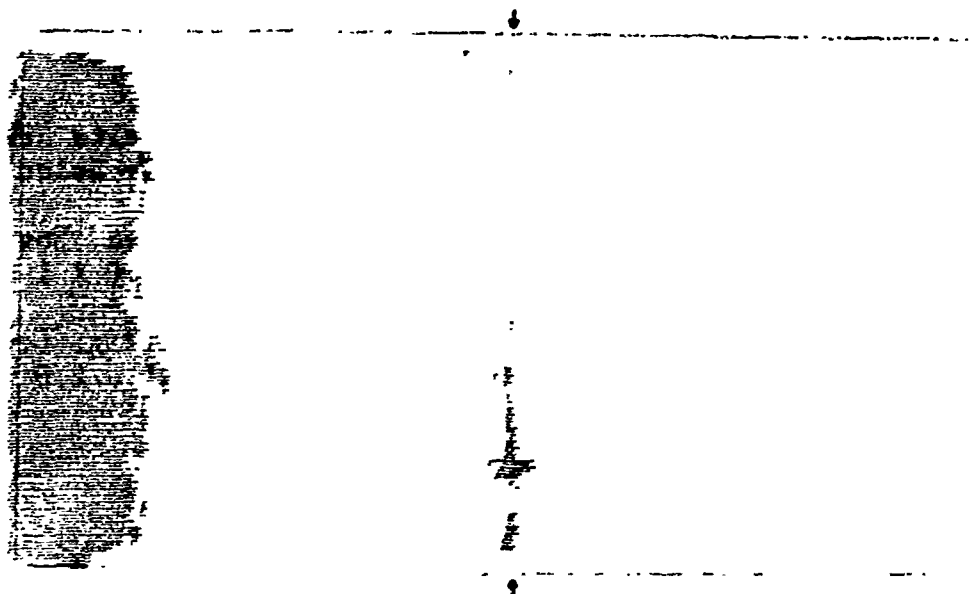


Delta Scan  
Technique

Sen. Level  
1.0 X 1

Trig. Level  
1.0/2.0

Specimen M6-A (Good Bond)



Delta Scan  
Technique

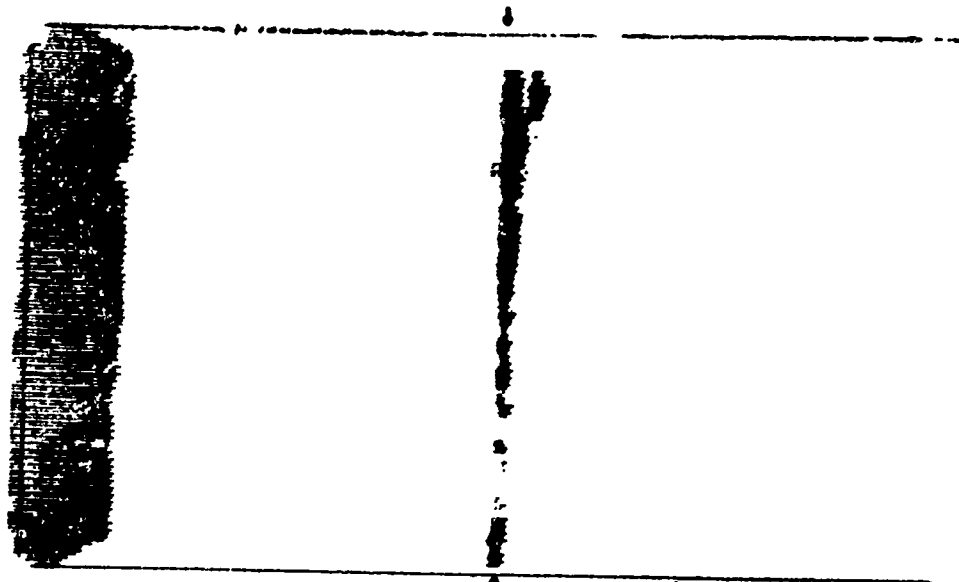
Sen. Level  
1.0 X 1

Trig. Level  
1.0/2.0

Bond Line

Specimen N6-B (Partially Bad Bond)

Figure 6.45 Delta/C-Scan Records of Specimens  
N6-B and M6-A



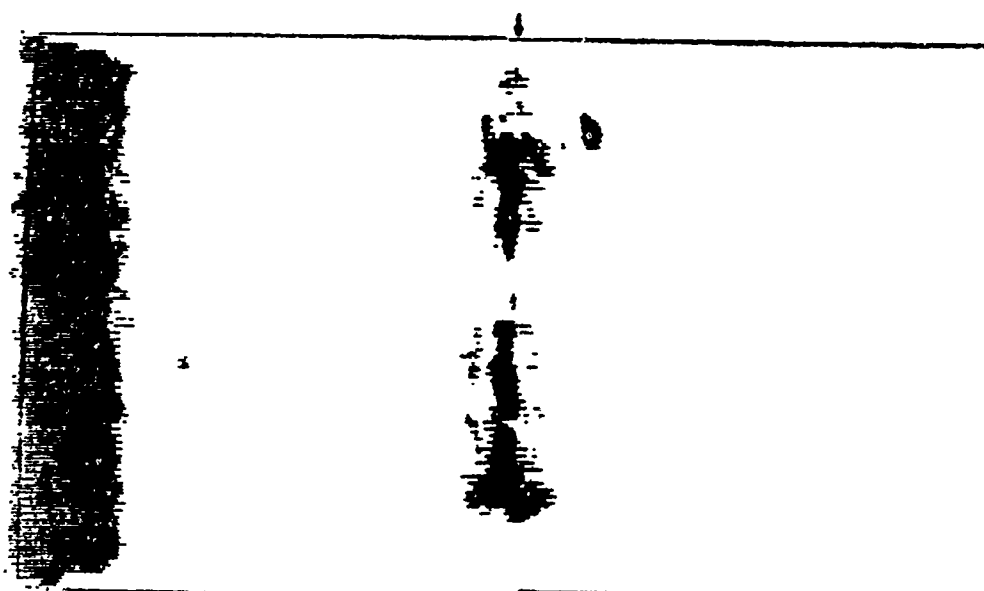
Delta Scan  
Technique

Sen. Level  
1.0 X 1

Trig. Level  
1.0/2.0

Bond Line

Specimen 05-B (Bad Bond)



Delta Scan  
Technique

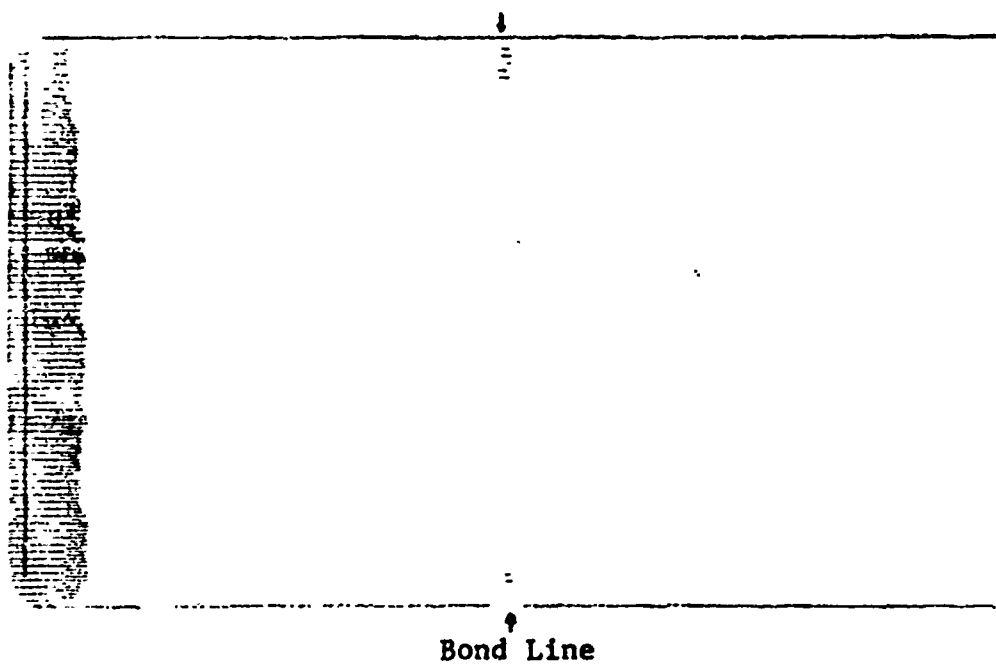
Sen. Level  
1.0 X 1

Trig. Level  
1.0/2.0

Bond Line

Specimen C-6 (Bad Bond)

Figure 6.46 Delta/C-Scan Records of Specimens C6 and 05-B

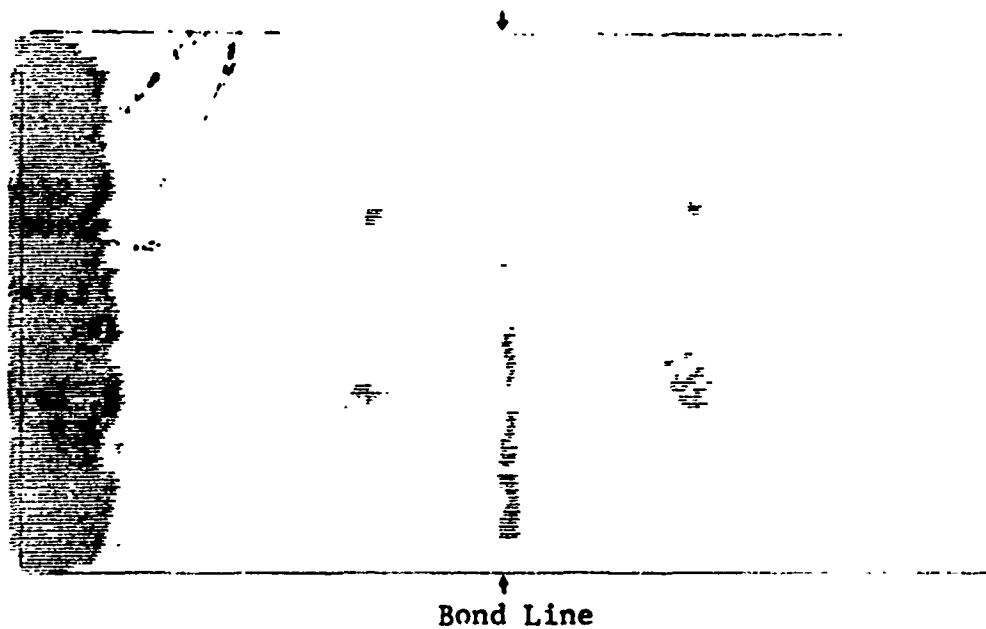


Delta Scan  
Technique

Sen. Level  
12 db

Trig. Level  
0.6/2.0

Specimen H5 (Chamfered Edge Void at the Bond Line)



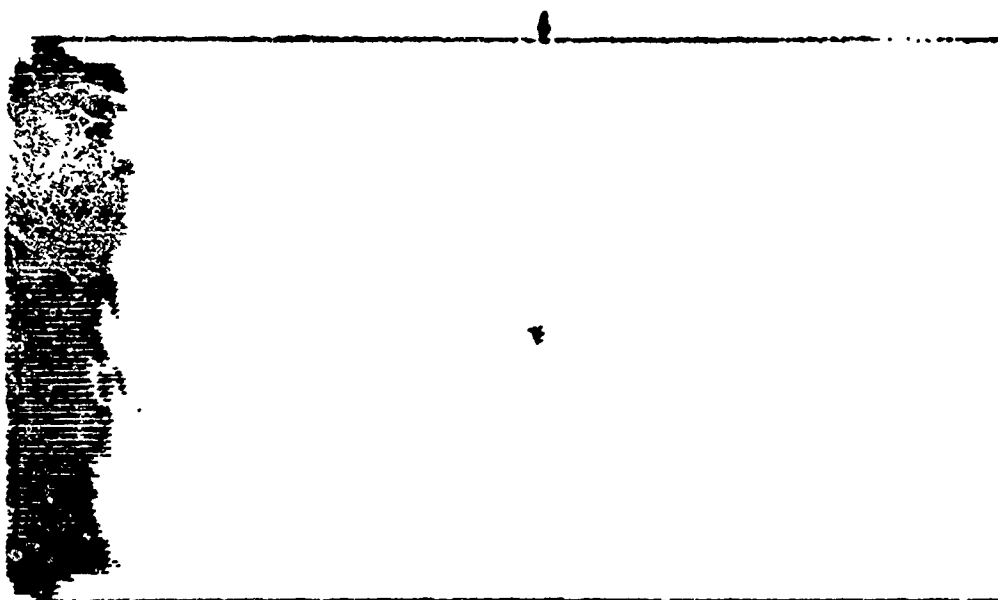
Delta Scan  
Technique

Sen. Level  
1.0 X 1

Trig. Level  
1.0/2.0

Specimen U5-A (Chamfered Edge Void at the Bond Line)

Figure 6.47 Delta/C-Scan Records of Specimens H5 and U5-A



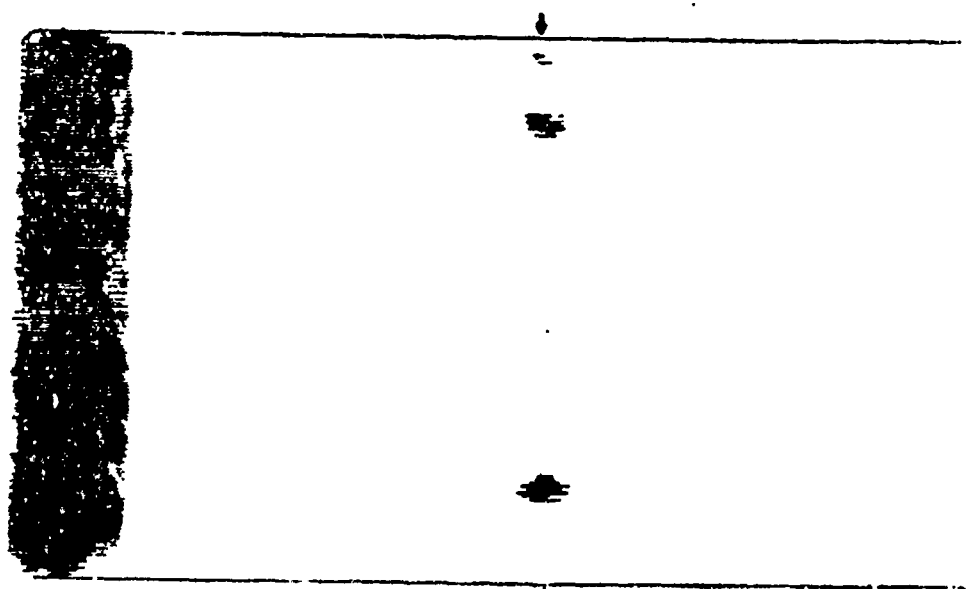
**Delta Scan  
Technique**

**Sen. Level  
1.0 X 1**

**Trig. Level  
1.0/2.0**

**Bond Line**

**Specimen S6-B (Chamfered Corner Void)**



**Delta Scan  
Technique**

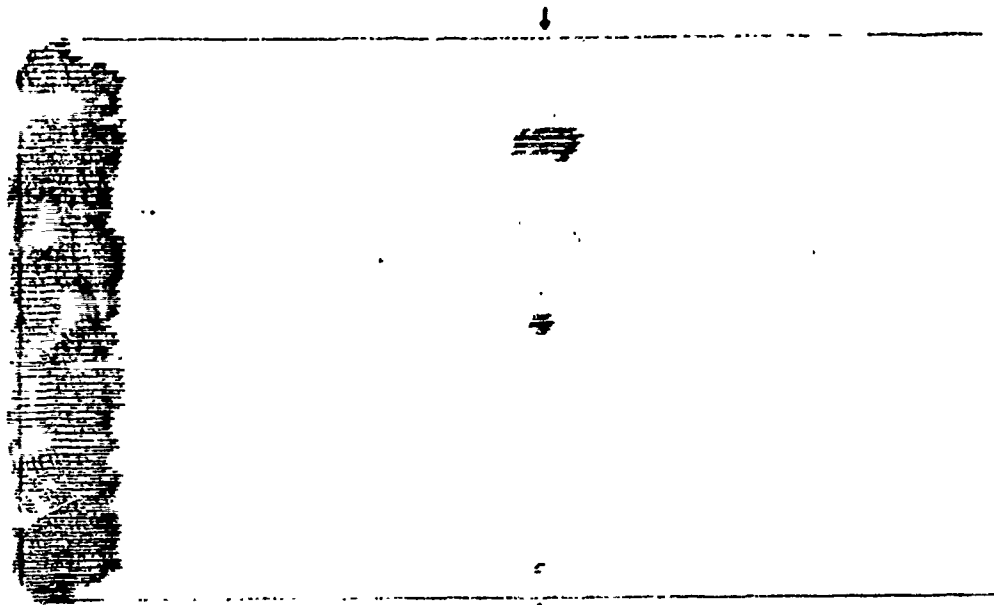
**Sen. Level  
12 db**

**Trig. Level  
0.6/2.0**

**Bond Line**

**Specimen H6 (Two Chamfered Corner Voids)**

**Figure 6.48 Delta/C-Scan Records of Specimens  
H6 and S6-B**



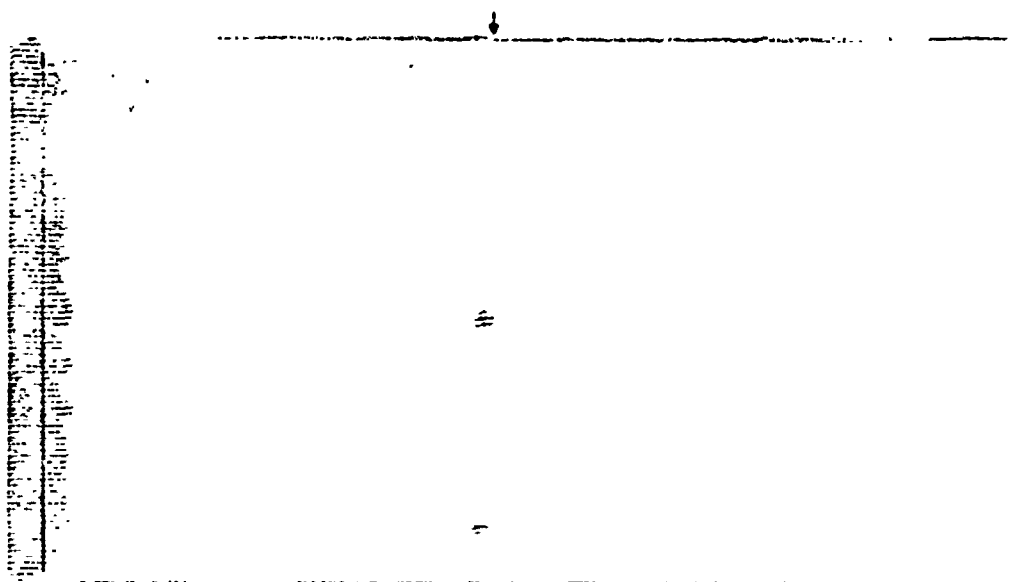
Delta Scan  
Technique

Sen. Level  
1.0 X 1

Trig. Level  
1.0/2.0

↑  
Bond Line

Specimen V6-A (Defects Due to Alpha Case)



Delta Scan  
Technique

Sen. Level  
28 db

Trig. Level  
0.6/2.6

↑  
Bond Line

Specimen K5 (304 Stainless Steel Inclusions .022 in. Diameter)

Figure 6.49 Delta/C-Scan Records of Specimens V6-A and K5

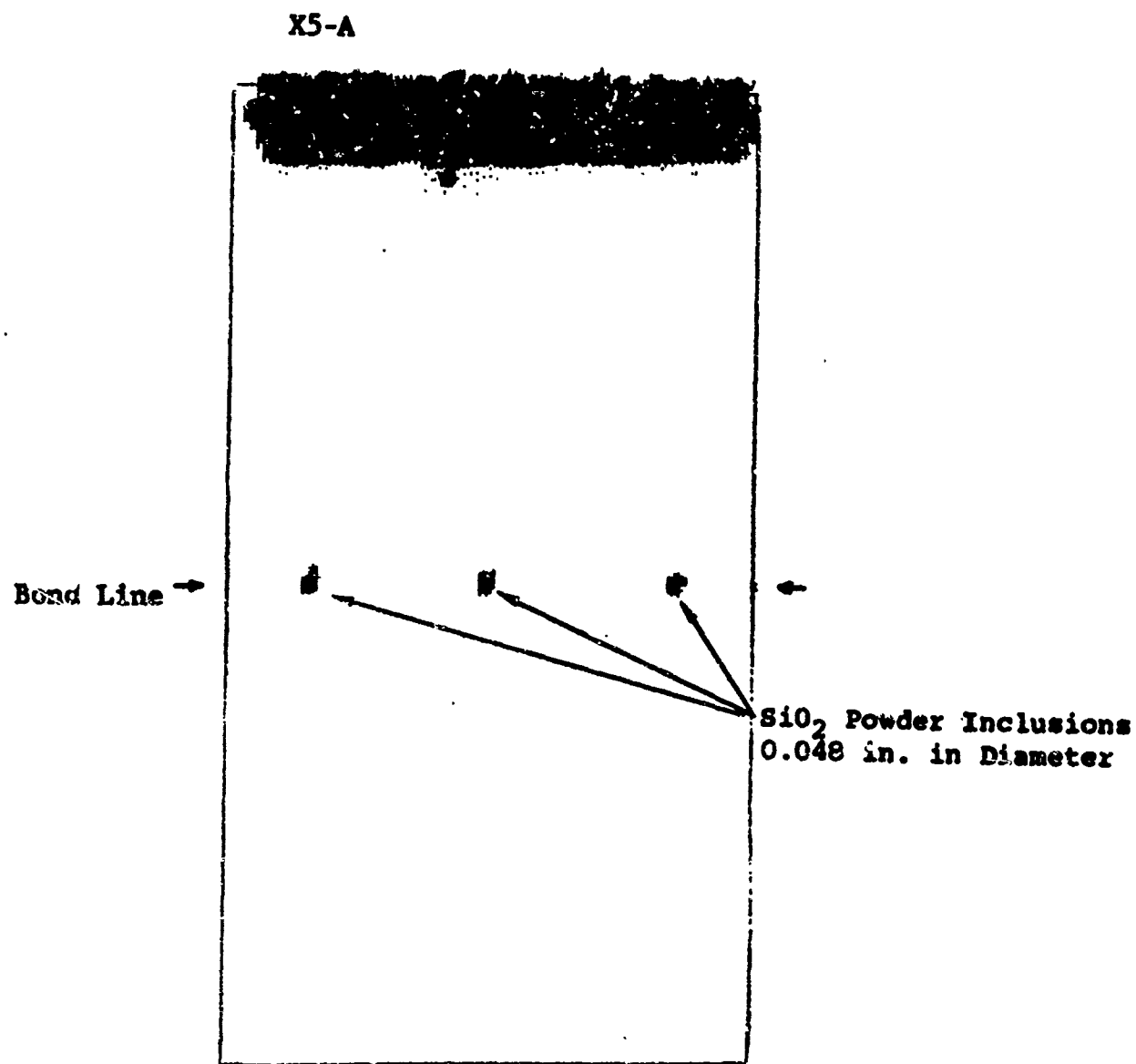


Figure 6.50 Delta/C-Scan of Specimen X5-A

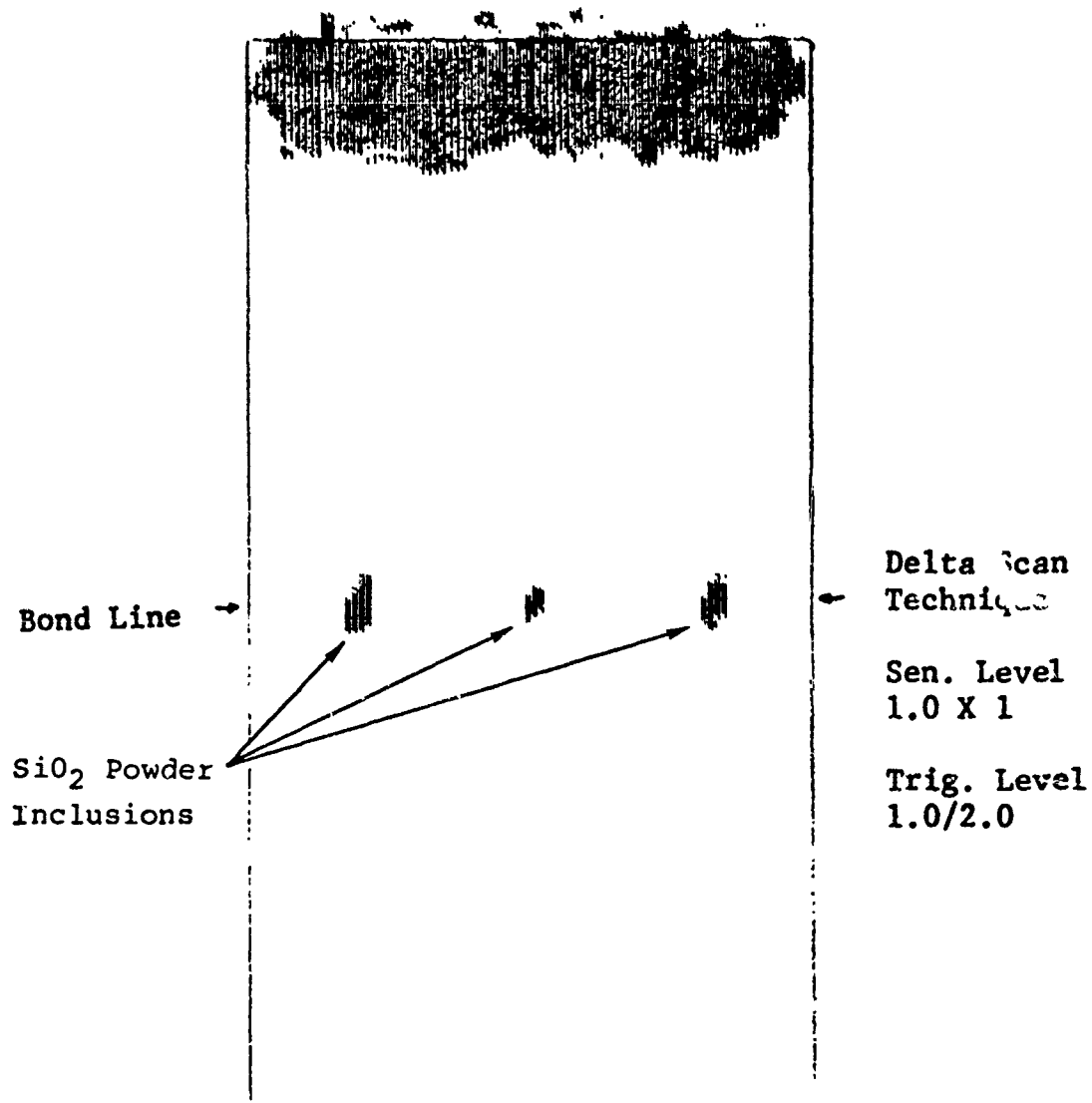


Figure 6.51 Delta/C-Scan Recording of Specimen X6-B

Figure 6.52 shows a typical inspection record of specimen No. Q6-A which was thermally treated before bonding to produce large alpha grains (ASTM Micro-grain Size No. 8).

Figure 6.53 is a corresponding record of the 3/64 FBH reference block at the same sensitivity.

Data Reduction - Quantifying each waveform to generate a function indicative of bond quality was accomplished by measuring (a) the centerline average (CLA), (b) the arithmetic average (AA), and (c) a peak amplitude above the centerline average.

A HP 9820 computing calculator with an X-Y digitizer was programmed to perform the above measurements. Figure 6.54 shows a typical readout versus the corresponding waveforms.

In this manner, the grain noise at a particular sensitivity may be represented by a single number, i.e., the arithmetic average. Perturbations above this level are represented by comparing the peak amplitude measurement with the arithmetic average.

In performing the actual measurements, the HP 9820 was programmed to accommodate two cases:

1. Defect signal-to-noise ratio  $\leq 1$ ;
2. Defect signal-to-noise ratio  $> 1$ .

In the first case, the cut-off length (baseline for digitizing) was set to include the entire recorded waveform. In the second case, the cut-off length was set to exclude the defect signal. This minimizes the effect of the defect signal on the centerline average from which all amplitudes were measured.

With these data, the grain noise arithmetic average may be used to normalize the defect amplitude as opposed to normalization by a reference standard amplitude.

The former is preferred since all measurements are made under identical circumstances of sensitivity, coupling, material, material processing history, and condition of instrumentation.

Accordingly, the signal-averaged pulse-echo data was reduced to include (a) AA and defect signal amplitude for each location of inspection on the diffusion bonded specimen (where applicable) and (b) the defect signal amplitude normalized by the arithmetic average at the defect locations.



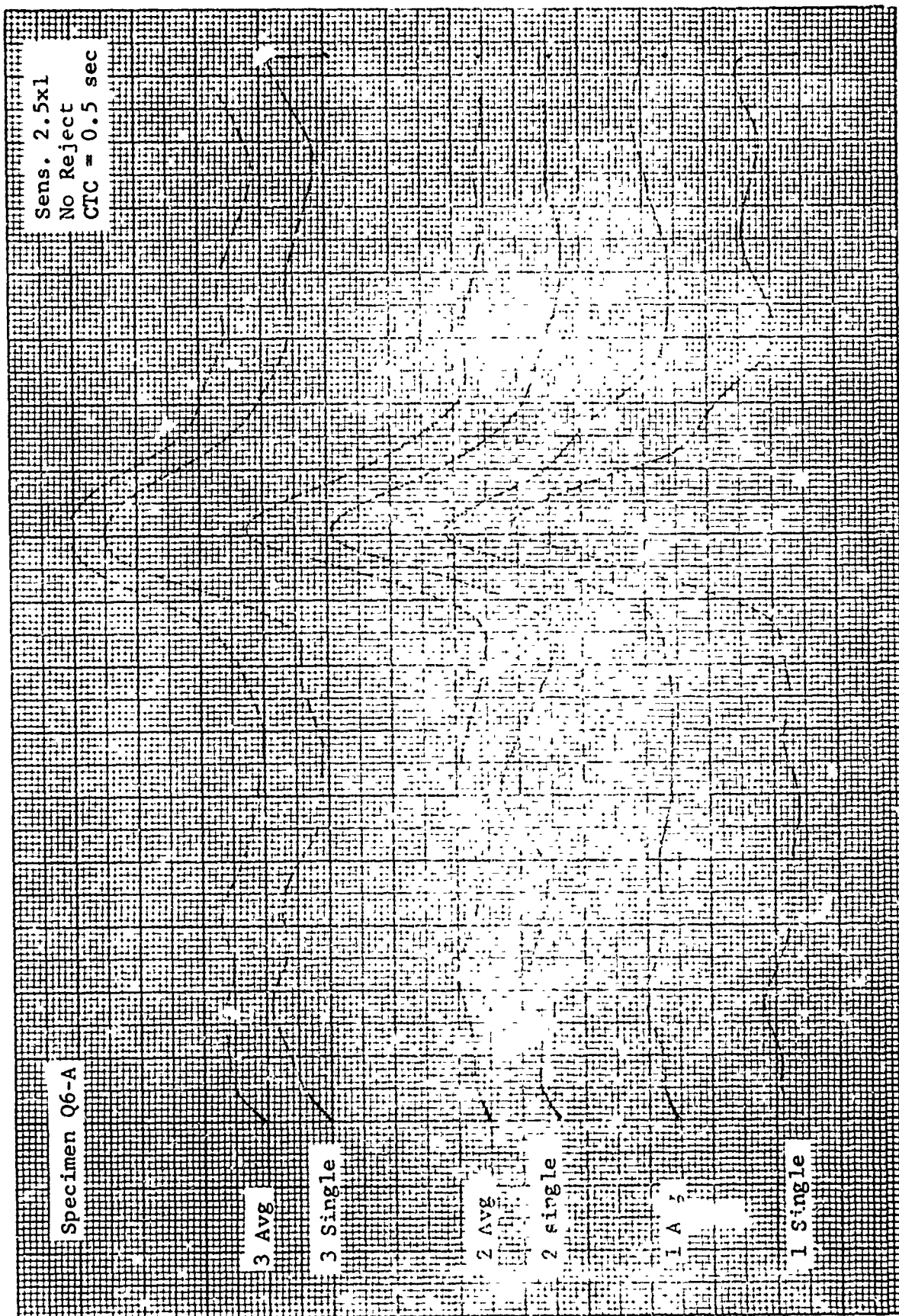


Figure 6.52 Single and Averaged Waveforms from Bond Plane of Specimen Q6-A (ASTM Grain Size No. 8)

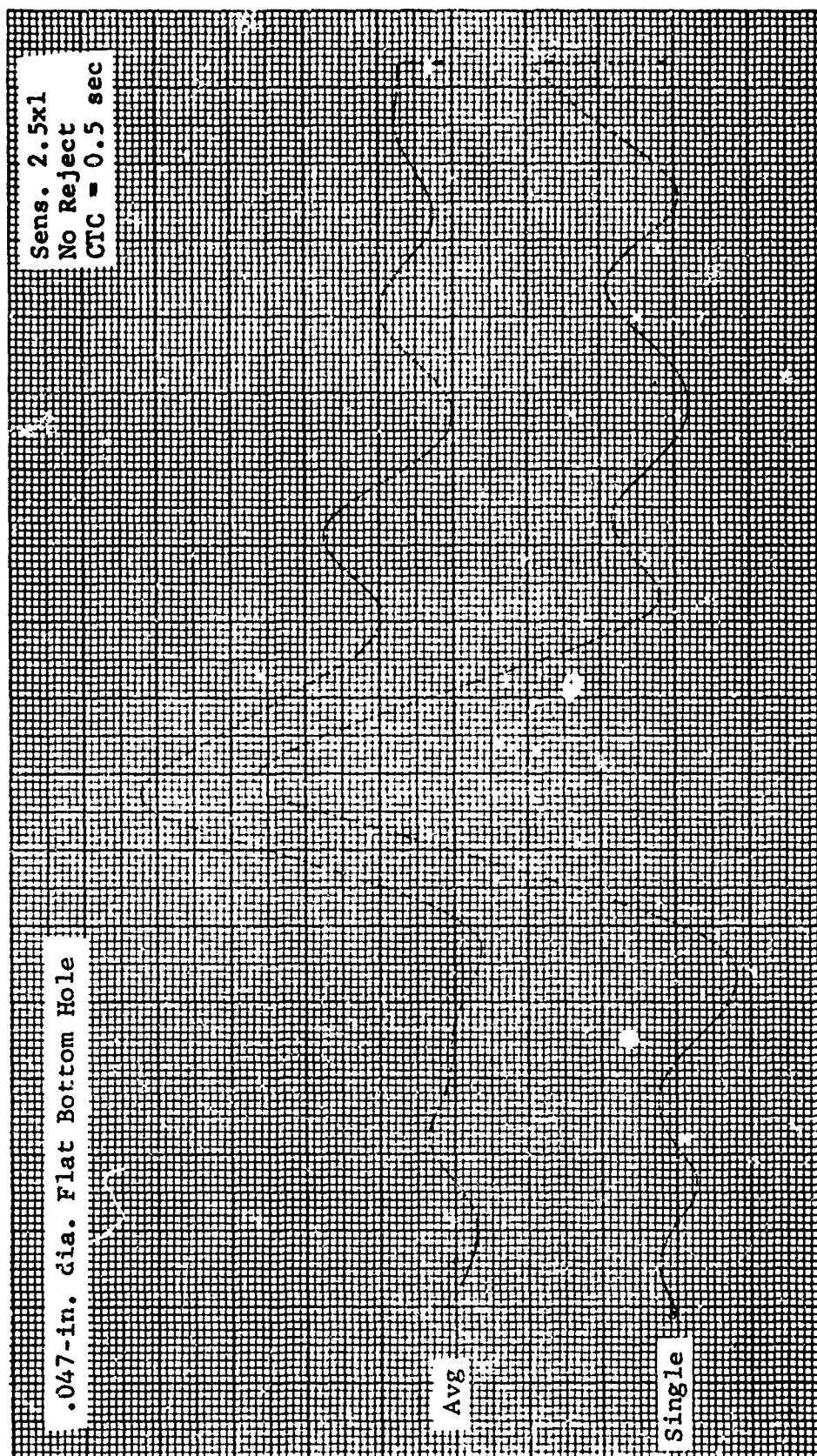


Figure 6.53 Single and Averaged Waveforms from 3/64-in. Flat Bottom Hole Reference Standard



Correlation between the latter item and mechanical properties is accomplished in Section 3.

## 7. MECHANICAL PROPERTY TESTING

### 7.1 Specimen Configuration, Equipment, and Procedure

#### 7.1.1 Test Specimen Configurations

Test specimens employed for mechanical properties testing in this program were of two basic types: round tensile and round fatigue. Configuration of the tensile specimens is shown in Figure 7.1. The 0.357-inch diameter was maintained for all tensile specimens.

The basic configuration of the smooth fatigue specimens for parent, heat-cycled, and diffusion bonded specimens with single bonds is shown in Figure 7.2. The -1 configuration was employed with parent and heat-cycled specimens and the -2 configuration was utilized with single-bonded specimens to ensure adequate spacings of specimen blanks during sectioning of the diffusion bonded blocks. In view of the fact that the -2 configuration specimens had a 0.25-inch minimum diameter, the same diameter was employed on all other diffusion bonded fatigue specimens (i.e., double-bond/single-axis, multiple-bond/2-axes, and multiple-bond/3-axes). Specimen design was modified to ensure that all bonded joints fell within the 0.25-inch diameter section between the radii of the specimen shoulders (see Figure 7.3). The theoretical stress concentration factor was maintained at  $K_t = 1$  for all specimens.

Figures 7.4 and 7.5 show configurations of the fracture toughness and stress corrosion specimens employed in the diffusion bonding studies.

#### 7.1.2 Test Equipment and Procedures

Tensile Tests - Tensile tests, with the exception of specimens monitored for acoustic emission, were performed in accordance with ASTM Method E8-68 and Federal Test Method Standard 151a, Method 211.1. Test machines for pulling the specimens to fracture were a Model TT-C Instron Tester (used in acoustic emission monitoring tests only) and a 120,000-lb capacity BLH Hydraulic Universal Test Machine. The 0.2% offset yield strength was determined using a PS-2M extensometer. The specimens were strain paced at 0.005-in./in./min.

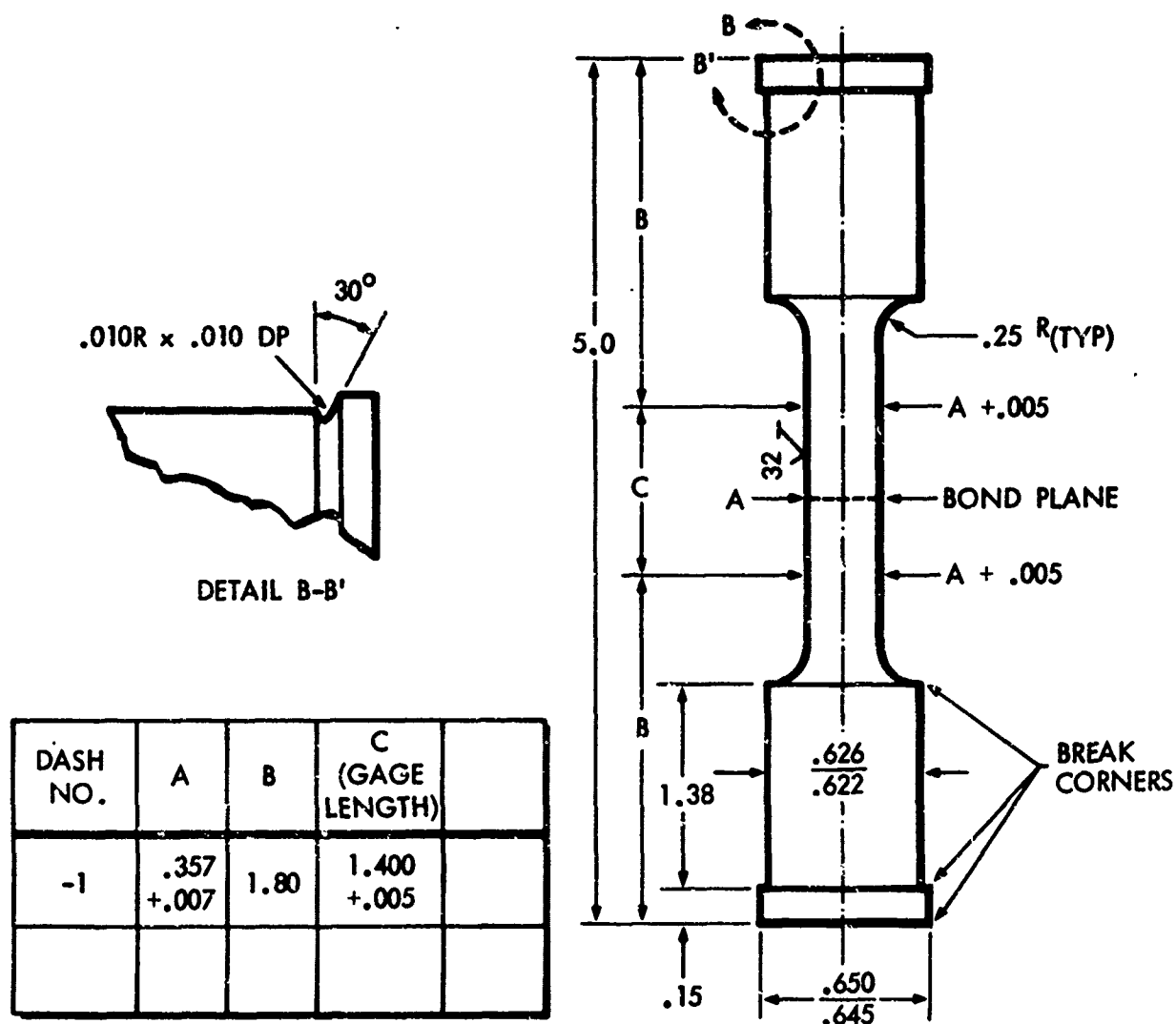
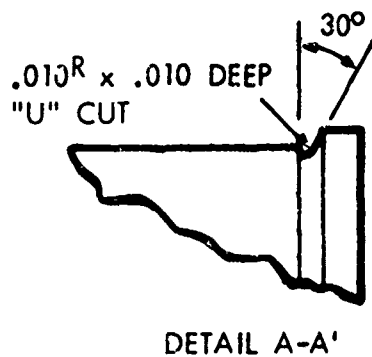
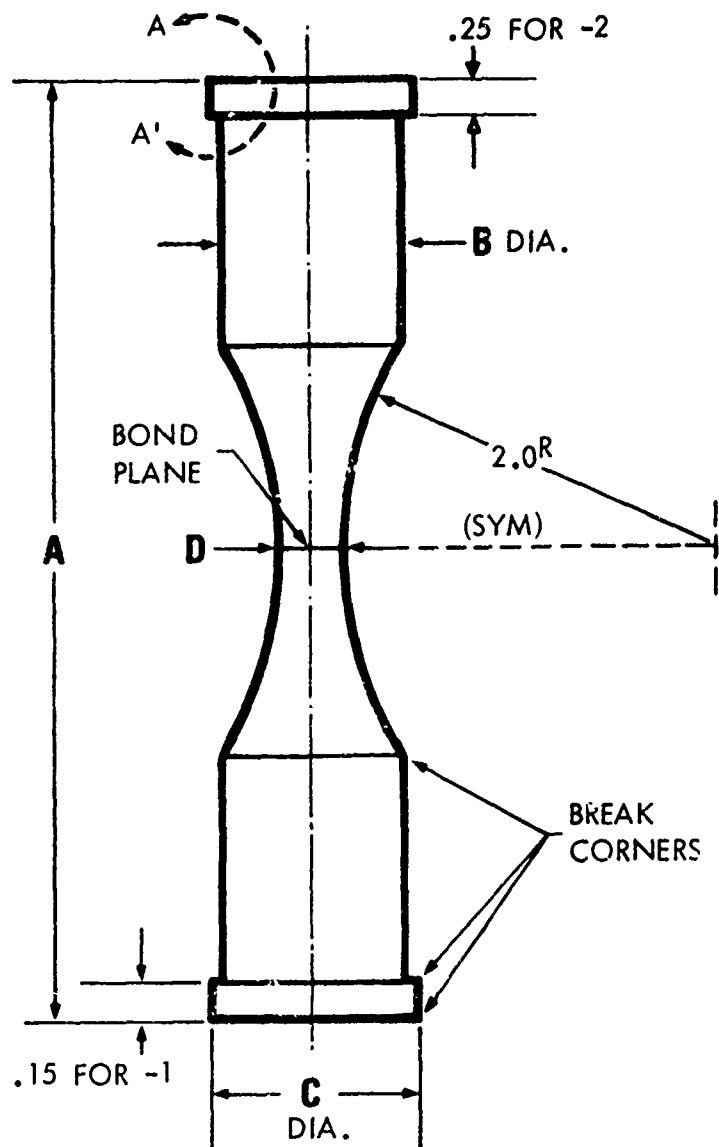


Figure 7.1 Configuration of Tensile Test Specimen - Collet Grip



DASH NO.	A	B	C	D ± .005
-1	5.0	$\frac{.876}{.872}$	$\frac{.900}{.895}$	.357
-2	4.75	$\frac{.625}{.620}$	$\frac{.650}{.645}$	.250



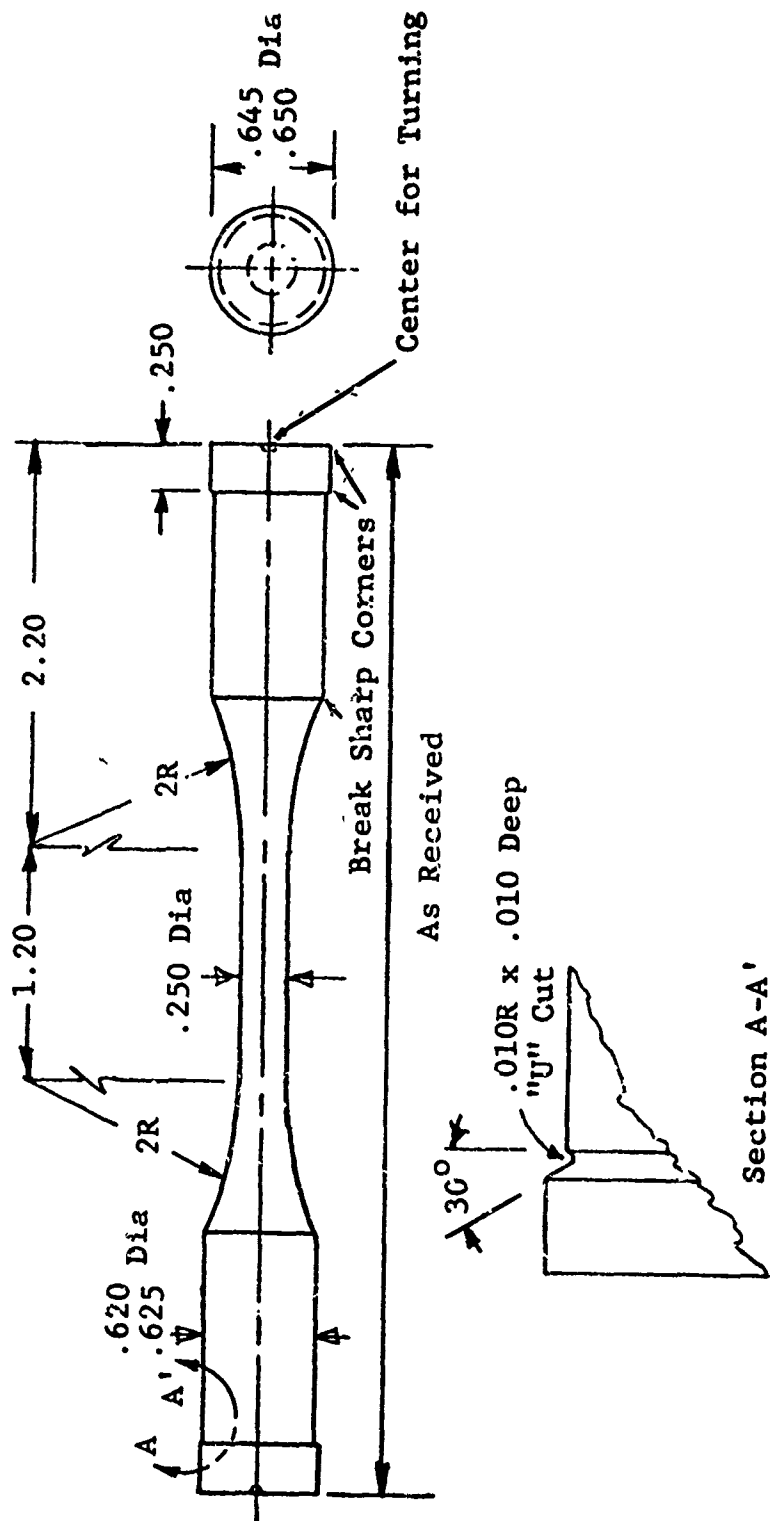
NOTES:

1. Diffusion Bond Plane to be Located at Minimum Diameter "D"
2. Turning Centers to be Machined Off in Obtaining 5.0 Dimension. Ends to be Flat & Parallel within .005 T.I.R.

3.	TOL	0.0 ± .10	0.00 ± .030	0.000 ± .010	Ang. ± 0°30'
----	-----	-----------	-------------	--------------	--------------

4. All Dimensions Concentric within .002 T.I.R.
5. Polish Test Section to 000 Emery in Longitudinal Direction

Figure 7.2 Configuration of Fatigue Test Specimen,  $K_t = 1$ , Collet Grip



Notes:

1. Turn on Centers
2. All Diameters Concentric within .002 TIR
3. Polish Test Section with 400 Emery Paper

Figure 7.3 Fatigue Specimen - Double Diffusion Bond,  
 $K_t = 1$ , Collet Grip



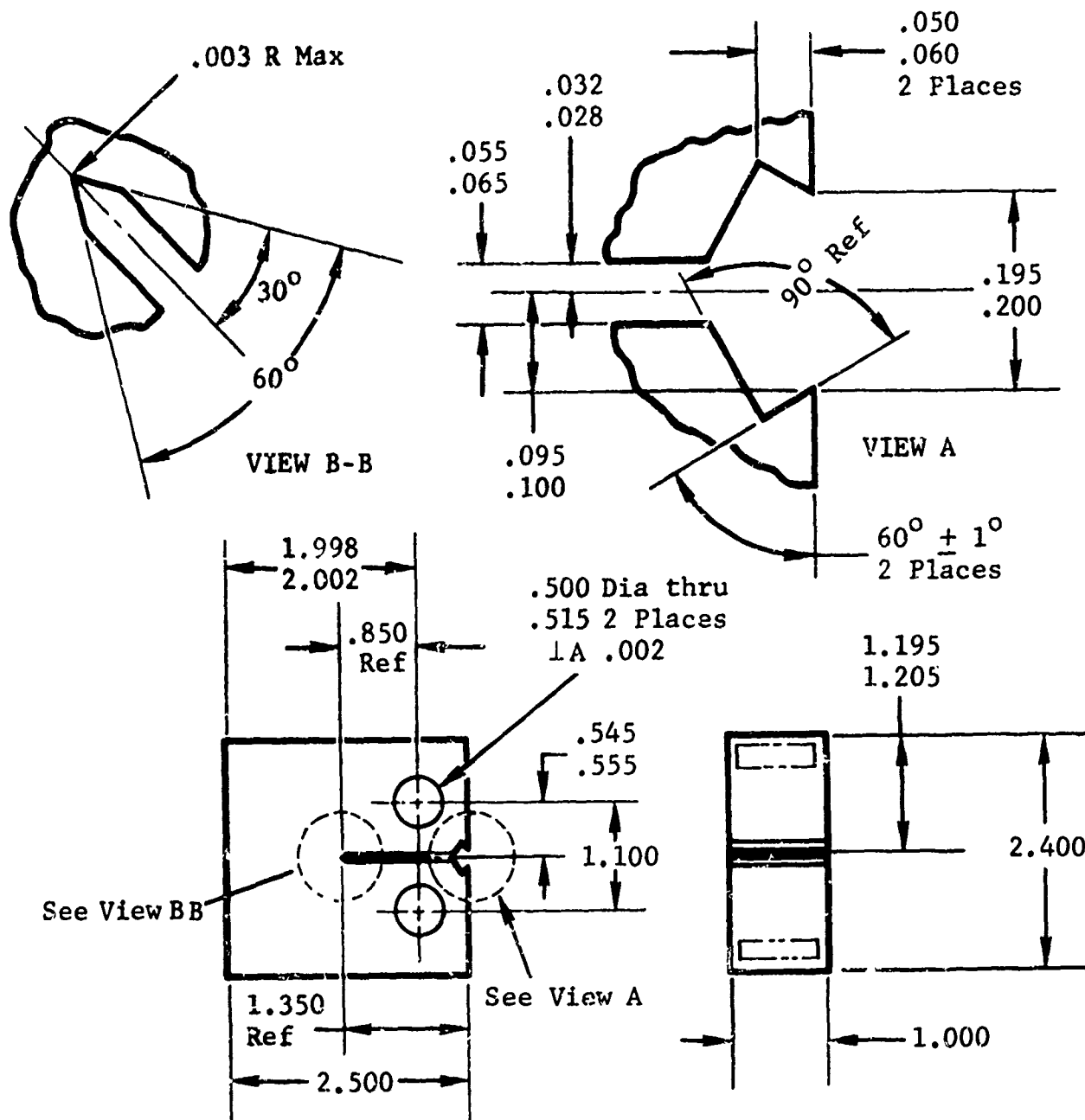


Figure 7.4 Configuration of Compact Tension Fracture Toughness Specimen

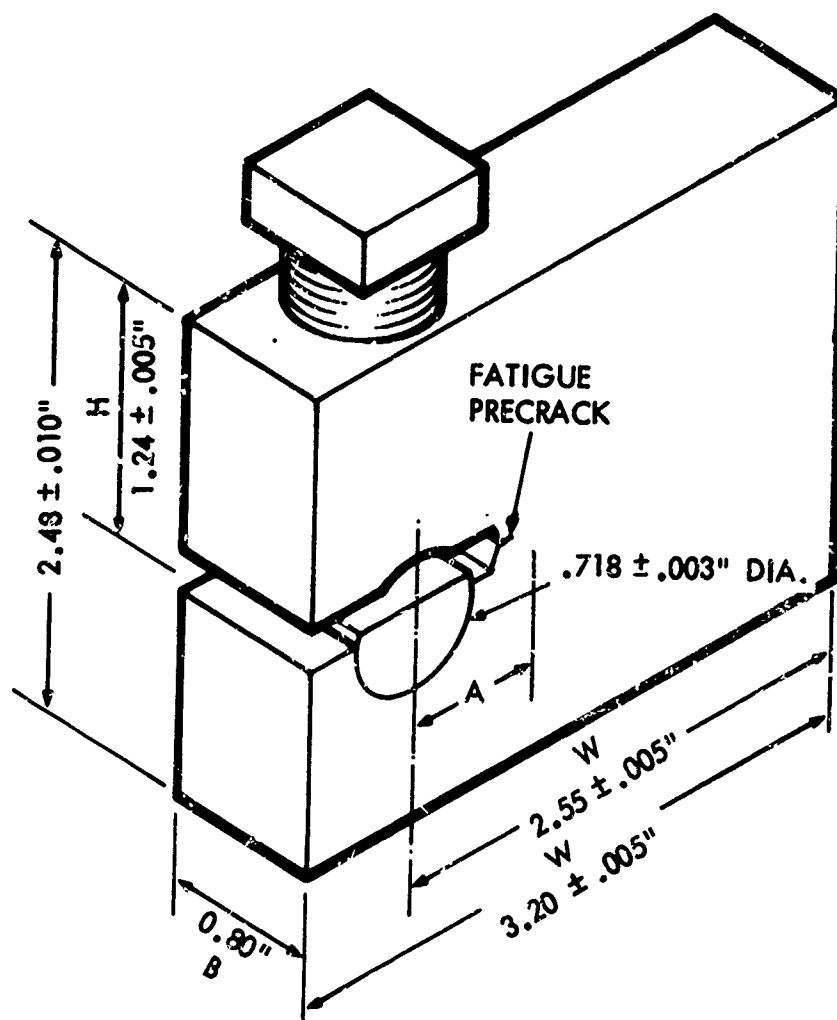


Figure 7.5 Configuration of Constant Deflection Specimen

Cyclic Fatigue Tests - Constant amplitude, axial fatigue testing of the  $K_t = 1$  smooth fatigue specimens was conducted in two test machines, a Sonntag Model SF-10-U and a 50,000-lb MTS. All testing was performed at a stress ratio of  $R = 0.1$  and at frequencies from 6 to 30 Hz. Two stress levels, 110 ksi and 80 ksi, were selected to provide high stress-low cycle and low stress-high cycle failures for comparison of the effects of defects in the diffusion bond joint. Other stress levels investigated were 130, 120, 105, and 90 ksi.

Fracture Toughness Tests - Fracture toughness testing was conducted in accordance with ASTM Method E399-72. The test machine for pulling the specimens to fracture was a Model TT-L Instron.

Precracking of the fracture toughness specimens was accomplished on a Sonntag Model SF-1-U fatigue machine.

Stress-Corrosion Tests - The constant displacement type WOL specimens employed to determine the stress corrosion cracking susceptibilities were of the design developed by Novak and Rolfe (Ref.13). Precracks were grown in these specimens using a Sonntag Model SF-1-U fatigue machine. Loading was accomplished by torquing the bolts while observing the crack opening displacement (COD) with a calibrated clip gage. When the COD corresponding to the desired stress intensity level was reached, torquing was ceased and the steel bolt and tap were coated with a maskant to prevent corrosion. Crack lengths were then measured using an optical comparator and the initial stress intensities calculated. The specimens were then placed in a 3-1/2 weight percent solution of NaCl in distilled water. Weekly, the specimens were removed from the salt water to measure the crack lengths and immediately returned to the corrodant before drying had occurred. The initial stress intensities used in these tests ranged from about one-half of the fracture toughness value in air to just slightly less than that value. A minimum 2000 hours immersion time is normally used in tests of this type to insure that all crack growth has ended. The minimum threshold stress intensity as determined in these tests that will just support stress corrosion cracking is designated  $K_{Isc}$  provided that the requirements of plane strain testing are met.

## 7.2 Mechanical Properties Data

Because of the large number of tensile and fatigue specimens tested, along with the numerous bonding parameters associated therewith, mechanical properties data for a particular type or group of specimens are compiled in separate

sections. In this manner, data for a given type joint may be found without undue difficulty.

Tensile and fatigue data for parent and heat-cycled Ti-6Al-4V are presented in Section 7.2.1, while tensile and fatigue data for single-bond/single-axis, double-bond/single-axis, multiple-bond/two-axes, and multiple-bond/three-axes specimens are presented in Sections 7.2.2, 7.2.3, 7.2.4, and 7.2.5, respectively. Each section contains a bar graph showing fatigue properties of the specimen group and the effects of intentional bonding anomalies, a statistical analysis of the fatigue data, test results for each fatigue specimen, and tabulated tensile test results.

Results of fracture toughness and stress-corrosion studies of diffusion bonded Ti-6Al-4V are presented in Section 7.2.6.

Section 7.2.1

Parent and Heat-Cycled Ti-6Al-4V  
Fatigue and Tensile Data

Table 7.1 TENSILE PROPERTIES OF ANNEALED TI-6AL-4V PLATE, 1" THICK

Condition	Grain Direction	Spec. No.	TYS KSI	UTS KSI	Elong. % in 1.4"	R.A. %
As Rec'd ↓	L ↓	Y1A-1	131.2	138.5	10.7	26.5
		Y1A-2	129.9	138.3	10.7	25.6
		Y1B-1	131.0	137.3	11.4	25.4
		Y1B-2	132.2	140.1	11.4	25.6
		Y1B-3	131.7	139.1	11.4	24.6
		Y1A-3	132.7	140.1	12.0	25.2
		AVG.	131.5	138.9	11.3	25.5
	T ↓	Z1-1	132.1	137.2	11.4	26.1
		Z1-2	132.2	137.3	11.4	26.5
		Z1-3	132.3	137.0	12.1	28.9
		Z1-4	131.9	138.0	12.1	29.1
		Z1-6	132.1	138.1	11.4	26.5
		Z1-5	130.2	136.4	11.5	24.3
		D1-1	134.1	139.1	11.4	26.5
D1-2	129.8	140.3	14.0	25.7		
AVG.	131.8	137.9	11.9	26.7		
Heat Cycled 6 Hrs @ 1700F ↓	L ↓	A2-1	127.3	134.5	12.1	29.6
		A2-2	126.0	133.6	11.4	29.3
		A2-3	126.6	134.5	12.5	27.5
		B2-1	124.1	132.9	12.1	27.2
		B2-2	127.0	135.1	12.1	26.6
		B2-3	125.4	135.3	13.1	27.5
		C2-1	125.1	134.1	11.4	26.9
	C2-2	125.7	133.5	11.4	26.2	
	C2-3	125.8	135.5	12.3	25.3	
	AVG.	125.9	134.3	12.0	27.3	
	T ↓	D2-1	122.6	134.3	13.5	28.7
		D2-2	124.9	133.3	12.1	27.3
		D2-3				
		AVG.				
Heat Cycled 6 Hrs. @ 1735F ↓	T ↓	E1-1	129.1	137.7	11.4	24.1
		E1-2	125.6	137.6	12.7	27.4
		E1-3	124.9	135.3	11.4	22.9
		AVG.	126.5	136.8	11.8	24.8
Heat Cycled 6 Hrs. @ 1775F ↓	T ↓	F1-1	120.4	133.7	13.6	25.6
		F1-2	121.5	133.9	11.4	25.3
		F1-3	122.2	134.9	11.4	26.8
		AVG.	121.4	134.2	12.1	25.9

1. Plate size, 1 x 40 x 90 inch.
2. RMI Heat 896284, NAR Spec. ST0170LB0032, Rev. E, Cond. A
3. Nominal test specimen dia. = 0.357 inch.
4. Strain rate .005 inch/inch/min. to yield point.

Table 7.2

## AXIAL FATIGUE PROPERTIES OF 1" THICK

Ti-6Al-4V,  $K_t = 1.0$ ,  $R = 0.1$ 

Condition	Grain Direction	Spec. No.	Max. Fatigue Stress, ksi	Cycles to Fail X 1000
As Rec'd	L ↓	AA-B-1	130	17.8
		AA-B-3	110	62.7
		AA-1-A2	110	238.2
		AA-1-A3	80	2202
		AA-B-2	80	2409
	T ↓	AB-1-1	110	246
		AB-1-3	↓	311
		AB-1-5	↓	281
		AB-1-2	80	2525
		AB-1-4	↓	2724
		AB-1-6	↓	2542
Heat Cycled 6 Hrs. @ 1700F	L ↓	M2-B-1	130	12.6
		M2-B-2	↓	17.8
		M2-D-2	↓	23.5
		M2-H-1	↓	19.6
		M2-E-2	120	34.7
		M2-E-3	↓	43.2
		M2-D-3	↓	75.9
		M2-C-2	110	488.2
		M2-C-3	↓	340
		M2-C-1	↓	356.8
		M2-A-3	↓	212.4
		M2-B-3	105	62.1
		M2-A-2	105	280.9
		M2-H-2	100	316.2
		M2-H-3	90	689.3
		M2-F-3	90	860.5
		M2-G-2	80	1962
		M2-D-1	↓	1761
		M2-G-1	↓	4049
		M2-F-1	↓	3117
		M2-G-3	70	3235
		M2-E-1	↓	5518
		M2-F-2	60	10245 NF
				145.5 ksi Ult

Table 7.2 (cont'd)

## AXIAL FATIGUE PROPERTIES OF 1" THICK

Ti-6Al-4V,  $K_t = 1.0$ ,  $R = 0.1$ 

Condition	Grain Direction	Spec. No.	Max. Fatigue Stress, ksi	Cycles to Fail X 1000
Heat Cycled 6 Hrs. @1775F	T ↓	R2B-1	130	16.7
		R2B-2	110	56.0
		R2A-1	110	106.6
		R2A-2	80	1347
		R2A-3	80	1544
		R2B-3	80	1420
Heat Cycled 6 Hrs. @1735F	T ↓	Q2A-3	130	15.5
		Q2A-1	110	42.6
		Q2A-2	110	199.4
		Q2B-1	80	1304
		Q2B-2	↓	1449
		Q2B-3	↓	957



Section 7.2.2

Single-Bond/Single-Axis Ti-6Al-4V  
Fatigue and Tensile Data

Figure 7.6 Axial Fatigue Properties of Single-Bond/  
Single-Axis Diffusion Bonded Specimens  
as Affected by Bonding Anomalies

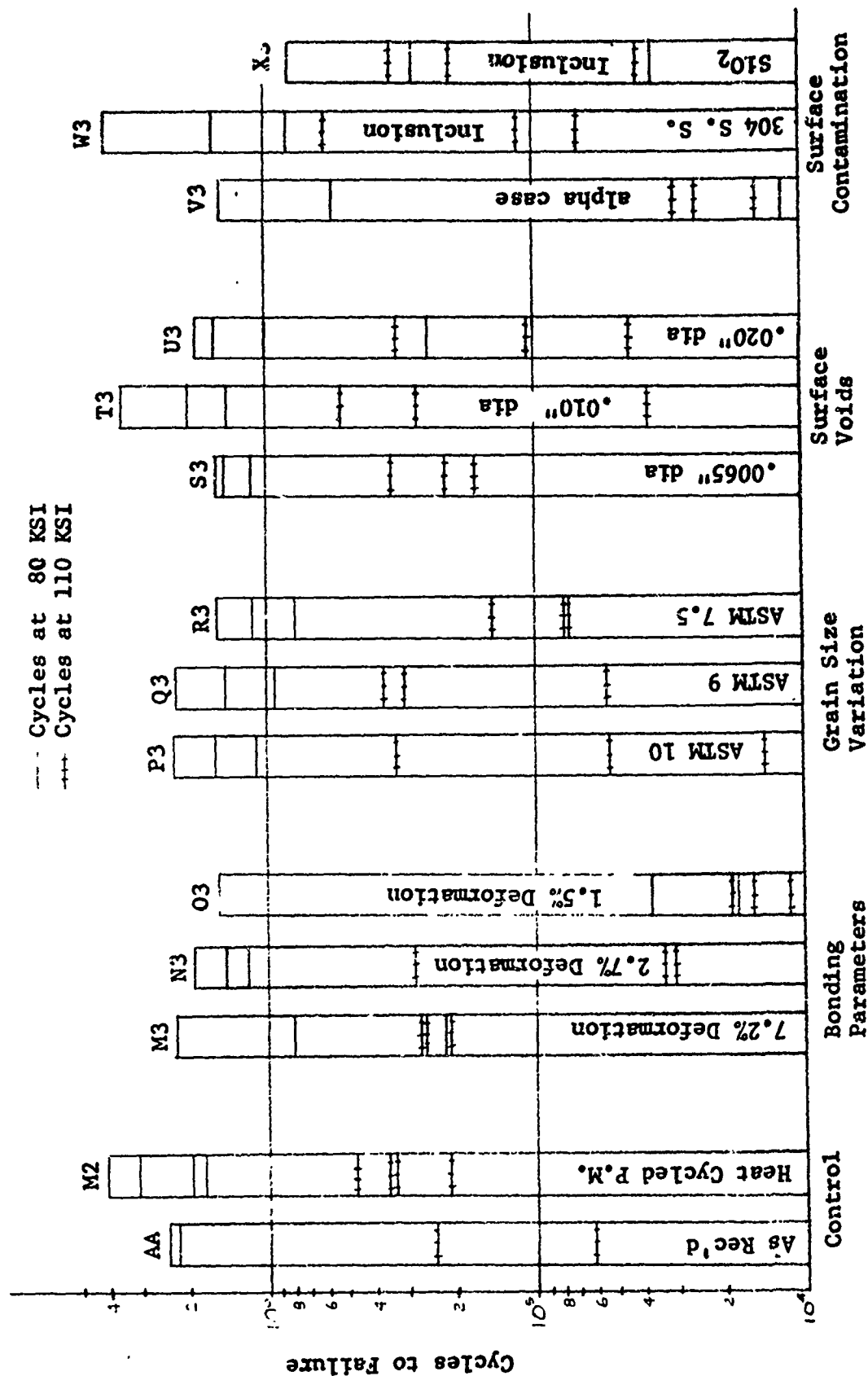


Table 7.3

Table 7.3 STATISTICAL ANALYSIS OF AXIAL FATIGUE DATA, SINGLE-BOND/SINGLE-AXIS,  
 $K_t = 1$ ,  $R = 0.1$ 

	AVG. FATIGUE LIFE, CYCLES X1000 Max = 110 KSI		AVG. FATIGUE LIFE, CYCLES X1000 Max = 80 KSI	
	AVG.	Standard Deviation	AVG.	Standard Deviation
<u>PARENT METAL LONGITUDINAL</u>				
As Rec'd (AA)	150	88	2306	104
Heat Cycled 6Hr @ 1700F (M2)	349	98	2722	924
<u>DIFFUSION BONDED, SINGLE JOINT</u>				
1. Bonding Parameter Variation				
Optimum, 7.2% deformation (M3)	249	27	1095	854
Optimum, 2.7% deformation (N3)	117	119	1525	285
Optimum, 1.5% deformation (O3)	15.3	3.1	548	736
2. Grain Size Variations				
ASTM Grain Size 10 (F3)	132	141	1643	472
ASTM Grain Size 9 (Q3)	243	135	1527	523
ASTM Grain Size 7.5 (R3)	99	31	1150	306
3. Surface Voids				
.0065" dia. surface void (S3)	239	73	1369	170
.010" dia. surface void (T3)	271	192	2269	878
.020" dia. surface void (U3)	156	118	1206	686
4. Surface Contamination				
.093" dia. alpha case inclusion (V3)	23.4	6	683	604
.013" dia. 304 powder inclusion (W3)	257	236	2117	1333
.013" dia. SiO <sub>2</sub> powder inclusion (X3)	193	121	375	322

Table 7.4 EFFECT OF BONDING PARAMETER VARIATIONS ON AXIAL FATIGUE PROPERTIES, SINGLE-BOND/SINGLE-AXIS,  $K_t = 1$ ,  $R = 0.1$

Condition	Spec. No.	Max. Fatigue Stress, KSI	Cycles to Fail X1000	Location of Origin
7.2% deformation (optimum) 1700F for 4 hrs ↓	M3B1	110	261.7	S
	M3B2	↓	212.2	S
	M3B3B	↓	273.5	S
	M3A1	80	2254	S
	M3A2	↓	221	S-DBI
	M3B3A	↓	808.9	S
2.71% deformation 1700F for 6 hrs ↓	N3A2	110	34.4	S-DBI
	N3B1	↓	284.4	S
	N3B2	↓	31.4	S-DBI
	N3A1	80	1208	S
	N3A3	↓	1898	S
	N3B3	↓	1468	S
1.46% deformation 1700F for 6 hrs ↓	O3B1	110	18.9	S-DBI
	O3A1	↓	15.7	DBI
	O3A2	↓	11.4	DBI
	O3B2	80	38.2	S-DBI
	O3B3	↓	18.0	DBI
	O3A3	↓	1589	S

1. Longitudinal grain direction
2. Specimen dia. = .250"

S - Surface

DBI - Diffusion Bond Interface

Table 7.5 EFFECT OF GRAIN SIZE VARIATIONS ON AXIAL FATIGUE PROPERTIES,  
SINGLE-BOND/SINGLE-AXIS,  $R = 0.1$ ,  $K_t = 1$

ASTM Grain Size	Spec. No.	Max. Fatigue Stress, KSI	Cycles to Fail X1000	Location of Origin
10 ↓	P3A3	110	330	S
	P3B1		14	IB
	P3B2	↓	53	2S-IB
	P3A1	80	1572	S
	P3A2	↓	2253	S
	P3B3	↓	1104	S
9 ↓	Q3B2	110	55	S
	Q3A1		306	S
	Q3A2	↓	368	S
	Q3B1	80	936	S
	Q3B3		2208	S
	Q3A3	↓	1437	S
7.5 ↓	R3A1	110	78	S
	R3A3		76	S
	R3B2	↓	143	S
	R3A2	80	791	S
	R3B1	↓	1538	S
	R3B3	↓	1122	S

1. All specimens bonded at 1700F for 6 hours with 5% total deformation.
2. Longitudinal grain direction
3. S - Surface, IB - incomplete bond

Table 7.6 EFFECT OF VOIDS ON AXIAL FATIGUE PROPERTIES,  
SINGLE-BOND/SINGLE-AXIS,  $K_t = 1$ ,  $R = 0.1$

Void Size, Diameter	Inch Depth	Spec. No.	Max. Fatigue Stress, KSI	Cycle to Fail X1000	Location of Origin
.0065	.005	S3A2	110	165.4	S-ND
	.006	S3B1	↓	338.5	I-D
	.006	S3B3	↓	212.5	S-ND
	.005	S3A1	80	1540	S-ND
	.006	S3A3	↓	1137	S
	.003	S3B2	↓	1429	I-D
.010	.010	T3A1	110	37.4	S-D
	.009	T3B1	↓	264.4	S-D
	.009	T3B2	↓	509.9	I-D
	.011	T3A2	80	1404	S
	.010	T3A3	↓	3473	S
	.009	T3B3	↓	1931	I
.020	.018	U3A2	110	43.6	S-ND
	.018	U3A3	↓	318.7	S-ND
	.019	U3B3	↓	106	I
	.018	U3A1	80	1572	I-D
	.019	U3B1	↓	245	I-D
	.020	U3B1A	↓	1800	I-D

1. All specimens bonded at 1700F for 6 hours with  $\approx 5\%$  total deformation.
2. Longitudinal grain direction
3. Specimen dia = .250"
4. All voids cylindrical in shape with length/diameter  $\approx 1$ .
5. S - surface, ND - no defect, D - defect, I - internal

Table 7.7 EFFECT OF CONTAMINATION ON AXIAL FATIGUE PROPERTIES,  
SINGLE-BOND/SINGLE-AXIS,  $K_t = 1$ ,  $R = 0.1$

Contamination, Inch			Spec. No.	Max. Fatigue Stress, KSI	Cycle to Fail X1000	Location of Origin
Type	Dia.	Depth				
Alpha case layer	.093 ↓	.002 ↓	V3B2	110	30	I-D
			V3A1	↓	25.2	I-D
			V3A2	↓	15	I-D
			V3A3	80	12	S-D
			V3B1	↓	562	S-D
			V3B3	↓	1476	S-D
304 S.S. powder inclusion	.013 ↓	.012	W3A3	110	590	I
		.010	W3B1	↓	113.8	I-D
		.011	W3B2	↓	68	I-D
		.005	W3A1	80	3952	S
		.012	W3A2	↓	826	I
		.010	W3B3	↓	1573	I-D
SiO <sub>2</sub> powder inclusion	.013 ↓	.010	X3A1	110	40.9	I-D
		.008	X3A2	↓	201.5	I-D
		.010	X3A3	↓	336	S
		.010	X3B1	80	281	S
		.011	X3B2	↓	36	I-D
		.010	X3B3	↓	809	S

1. All specimens bonded at 1700F for 6 hours with  $\approx 5\%$  total deformation.
2. Longitudinal grain direction
3. Specimen dia = .250"
4. I - internal, S - surface, D - defect

Table 7.8 TENSILE PROPERTIES OF SINGLE-BOND/SINGLE-AXIS SPECIMENS

Condition	Spec. No.	YS ksi	UTS ksi	Elongation % in 1.4"	R.A. %		
1. Bonding Parameter Variation							
7.7% Deformation	A3-1	125.3	134.4	10.0	27.1		
	-2	126.1	134.7	10.5	28.7		
	-3	ES	136.1	10.7	27.4		
	AVG.	125.7	135.1	10.4	27.7		
2.7% Deformation	B3-1	127.4	137.5	10.7	27.2		
	-2	127.4	136.6	10.4	27.8		
	-3	125.9	135.1	10.7	25.6		
	AVG.	126.9	136.4	10.6	26.9		
1.4% Deformation	C3-1	126.1	134.8	7.1	14.2*		
	-2	125.1	137.5	7.1	14.0*		
	-3	127.5	136.7	7.1	13.7*		
	AVG.	126.2	136.3	7.1	14.2		
2. Grain Size Variations							
ASTM No. 10	D3-1	125.2	133.3	10.7	26.5		
	-2	125.6	132.6	9.3	24.3		
	-3Δ	129.2	132.3	7.4	19.8		
	AVG.	126.5	132.7	9.1	20.8		
ASTM No. 9	E3-1	119.4	128.7	10.0	29.3		
	-2	124.1	136.8□	10.7	24.1		
	-3	119.4	126.4	10.0	28.6		
	AVG.	121.0	130.6	10.2	27.3		
ASTM No. 7.5	F3-1	122.1	136.8	9.2	26.1		
	-2	119.8	131.5	10.0	27.4		
	-3	118.7	129.5	9.3	25.9		
	AVG.	120.2	130.6	9.5	26.5		
3. Surface Voids							
Dia.	Depth, Inch						
.0065 ↓	• •	G3-1	124.7	133.7	10.7	25.5	
		-2	125.1	140.8□	9.6	23.5	
		-3	125.9	135.4	10.7	25.7 +	
		AVG.	125.2	136.6	10.3	24.9	
.010 ↓	.009 .010 .011	H3-1	123.5	134.5	10.7	24.1	
		-2	123.1	132.9	10.7	24.8 +	
		-3	123.6	132.1	10.7	24.8 +	
		AVG.	123.3	133.2	10.7	24.6	
.020 ↓	.020 .019 .019	I3-1	127.9	137.9	10.0	22.8	
		-2	128.5	137.4	9.3	20.7 +	
		-3	127.8	137.2	9.4	24.4 +	
		AVG.	128.1	137.5	9.6	22.6	
4. Surface Contamination							
Type	Dia.	Depth, Inch					
Alpha Case	.093 ↓	.002 ↓	J3-1	126.1	134.3	6.4	15.2 +
			-2	127.4	133.9	5.7	12.0 +
			-3	126.2	132.7	4.3	11.1 +
			AVG.	126.6	133.6	5.5	12.8
304 S.S. Inclusion	.017 ↓	.011 .009	K3-1	126.1	137.0	9.3	18.2 +
			-2	126.5	137.5	9.3	23.6 +
			AVG.	126.3	137.2	9.3	20.6
SiC <sub>3</sub> Inclusion	.013 ↓	.005 .004	L3-1	125.9	136.6	7.9	14.2 +
			-2	125.0	137.4	8.6	18.7 +
			AVG.	125.9	137.0	8.2	16.4

.317" dia. test section  
 Longitudinal grain direction  
 RMI Heat #690284  
 $\square$  Retested after grip failed beyond yield

\* Incomplete bond  
 $\diamond$  Failed thru: intentional defect  
 ES extensometer slipped  
 $\Delta$  Fatigue cycled



Section 7.2.3

Double-Bond/Single-Axis Ti-6Al-4V  
Fatigue and Tensile Data

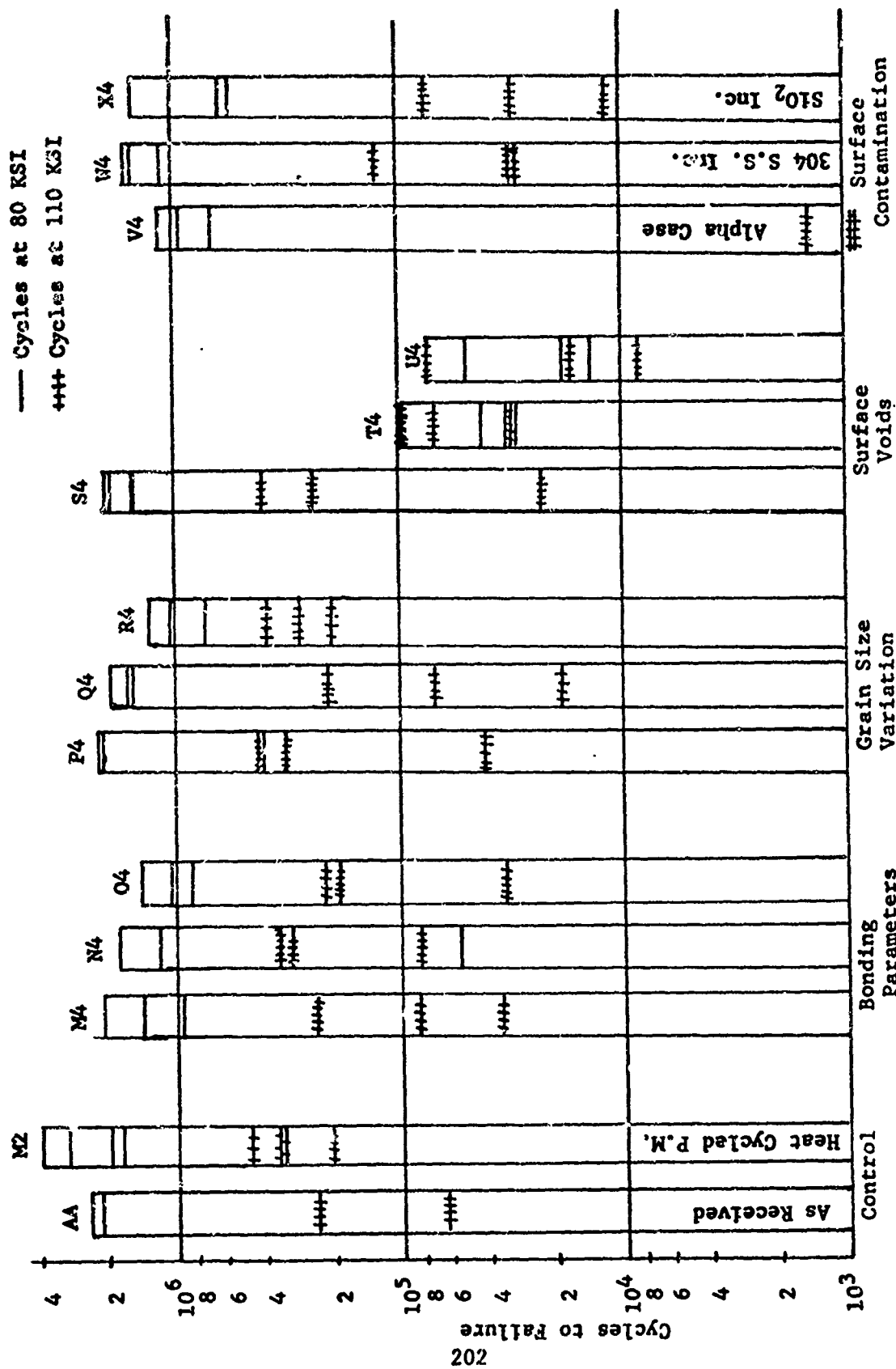


Figure 7.7 Axial Fatigue Properties of Double-Bond/Single-Axis Specimens as Affected by Bonding Anomalies

Table 7.9 STATISTICAL ANALYSIS OF AXIAL FATIGUE DATA,  
DOUBLE-BOND/SINGLE-AXIS,  $K_t = 1$ ,  $R = 0.1$

Condition	AVG. FATIGUE LIFE, CYCLES X1000			
	$\sigma_{Max} = 110$ KSI		$\sigma_{Max} = 80$ KSI	
	Avg.	Standard Deviation $1\sigma$	Avg.	Standard Deviation $1\sigma$
1. Bonding Parameter Variation				
7.6% Deformation (optimum) (M4)	122.4	89.8	1471	464
2.7% Deformation (N4/B4)	246.8	118.2	1020	729
1.6% Deformation (O4)	150.3	83.1	1113	215
2. Grain Size Variations				
ASTM Grain Size No. 10 (P4)	264.0	161.5	1538	799
ASTM Grain Size No. 9 (Q4)	102.1	84.1	1736	171
ASTM Grain Size No. 7.5 (R4)	292.5	77.8	1037	247
3. Multiple Surface Voids				
.0065" dia. x .006" deep (S4)	225.1	158.1	1858	227
.010" dia. x .011" deep (T4)	63.0	24.1	35	5
.020" dia. x .020" deep (U4)	33.8	30.0	27	16
4. Surface Contamination				
.186" dia. alpha case (V4)	0.87	0.42	918	205
.0065" dia. 304 S.S. inclusion (W4)	62.1	44.9	1455	200
.0065" dia. SiO <sub>2</sub> inclusion (X4)	35.2	21.6	902	423

Table 7.10 EFFECT OF BONDING PARAMETER VARIATIONS ON AXIAL  
FATIGUE PROPERTIES, DOUBLE-BOND/SINGLE-AXIS,  
 $K_t = 1$ ,  $R = 0.1$

Condition	Spec. No.	Max. Fatigue Stress, KSI	Cycles to Fail X1000	Location of Origin
7.6% deformation (optimum) 1700F for 4 hrs	M4A1	110	85.5	I-IB
	M4A3	↓	35.6	S
	M4B2	↓	246.1	S
	M4A2	80	941	NBL-S
	M4B1	↓	1401	S
	M4B3	↓	2072	S
2.7 % deformation 1700F for 6 hrs	N4A2	110	343.4	S
	N4A3	↓	80.4	I-IB
	B4-3	↓	315.7	S
	N4A1	80	1190	S-NBL
	B4-1	↓	1815	S-NBL
	B4-2	↓	55	S-IB
1.6 % deformation 1700F for 6 hrs	O4A1	110	34.5	S
	O4A3	↓	225.5	S-NBL
	O4B1	↓	191	S
	O4A2	80	1401	S-NBL
	O4B2	↓	1053	S-NBL
	O4B3	↓	886	S-IB

I - internal  
IB - incomplete bond  
S - surface  
NBL - not in bond line  
1" thick plate, RMI #890284

Table 7.11 EFFECT OF GRAIN SIZE VARIATIONS ON AXIAL FATIGUE  
PROPERTIES, DOUBLE-BOND/SINGLE-AXIS,  $K_t = 1$ ,  $R = 0.1$

ASTM Grain Size	Spec. No.	Max. Fatigue Stress, KSI	Cycles to Fail X1000	Location of Origin
10	P4B1	110	424	I
	P4B2	↓	325.1	S
	P4B3	↓	42.9	I-IB
	P4A1	80	412	I
	P4A2	↓	2183	I-NBL
	P4A3	↓	2019	I-NBL
9	Q4B1	110	217.4	2I-IB
	Q4B2	↓	19	S-2I (IB)
	Q4B3	↓	70	I-IB
	Q4A1	80	1683	S-NBL
	Q4A2	↓	1967	S
	Q4A3	↓	1559	S
7.5	R4B1	110	390.8	I
	R4B2	↓	286	S
	R4B3	↓	200.6	S-NBL
	R4A1	80	1051	S-NBL
	R4A2	↓	1332	S-NBL
	R4A3	↓	727	2I-IB

I - internal

S - surface

IB - incomplete bond

NBL - not in bond line

1" thick plate, RMI #890284

Table 7.12 EFFECT OF VOIDS ON AXIAL FATIGUE PROPERTIES,  
DOUBLE-BOND/SINGLE-AXIS,  $K_t = 1$ ,  $R = 0.1$

Void Size, Inch		Spec. No.	Max. Fatigue Stress, KSI	Cycles to Fail X1000	Location of Origin
Diameter	Max. Depth				
.0065	.006	S4B1	110	22.8	SD-ID
	.006	S4B2	↓	408.6	S-NBL
	.006	S4B3	↓	244	3ID
	.007	S4A1	80	1538	S-ID
	.005	S4A2	↓	2004	S-NBL
	.006	S4A3	↓	2032	S
.010	.011	T4B1	110	31.3	SD-2ID
	.011	T4B2	↓	89.8	2I-IB
	.010	T4B3	↓	68	2ID
	.011	T4A1	80	31	SD-3ID
	.011	T4A2	↓	32	SD-3ID
	.010	T4A3	↓	42	SD-3ID
.020	.021	U4B1	110	17.0	2ID
	.020	U4B2	↓	76.0	3ID
	.018	U4B3	↓	8.5	7ID
	.021	U4A1	80	50	S-ID
	.021	U4A2	↓	14	2ID
	.020	U4A3	↓	18	3SD-2ID

Each specimen contained 4 voids located 90° apart on 3/16" diagonal centers.

SD - surface defect

ID - internal defect

S - surface

NBL- not in bond line

IB - incomplete bond

I - internal

1" thick plate, RMI #890284

Table 7.13 EFFECT OF CONTAMINATION ON AXIAL FATIGUE PROPERTIES,  
DOUBLE-BOND/SINGLE-AXIS,  $K_t = 1$ ,  $R = 0.1$

Contamination, Inch Type	Inch		Spec. No.	Max. Fatigue Stress, KSI	Cycles to Fail X1000	Location of Origin
	Dia.	Depth				
Alpha Case Layer	.186 ↓	.002 ↓	V4B1	110	1.46	ID
			V4B2		0.58	ID
			V4B3	√	0.56	ID
			V4A1	80	675	S-ID
			V4A2		1177	SD
			V4A3	√	903	ID
304 S.S. powder inclusion	.0065 ↓	.008	W4A2	110	125.5	SD
		.006	W4B2		31.8	2ID
		.007	W4B3	√	28.9	2ID
		.010	W4A1	80	1642	S-NBL
		.009	W4A3		1545	S-NBL
		.005	W4B1	√	1177	S-NBL
SiO <sub>2</sub> powder inclusion	.0065 ↓	.007	X4A1	110	63.7	3ID-IB
		.008	X4A2		30.5	7ID-SD
		.007	X4A3	√	11.3	9ID
		.007	X4B1	80	578	ID
		.007	X4B2		629	7ID
		.006	X4B3	√	1499	ID

I - internal

SD - surface defect

ID - internal defect

IB - incomplete bond

1" thick plate, RMI #890284

Table 7.14 TENSILE PROPERTIES OF DOUBLE-BOND/SINGLE-AXIS SPECIMENS

Condition			Spec. No.	TYS KSI	UTS KSI	Elong. % in 1.4"	R.A. %
1. Bonding Parameter Variation 7.1% Deformation			A4-1	123.5	133.1	12.8	22.7
			-2	121.8	133.3	12.8	25.4
			-3	125.7	134.5	14.3	21.2
			AVG.	123.7	133.6	13.3	23.1
2.9% Deformation			N4B1	120.4	135.6□	11.4	20.0
			N4B2	124.5	135.1	12.1	26.1
			N4B3	126.3	136.9	14.3	25.1
			AVG.	123.7	135.9	12.6	23.7
1.5% Deformation			C4-1	125.1	135.9	12.1	21.2
			-2	122.3	136.4	10.7	22.0
			-3	123.3	134.8	15.0	23.0
			AVG.	123.6	135.7	12.6	22.1
2. Grain Size Variations							
ASTM No. 10			D4-1	122.5	133.0	14.3	25.8
			-2	123.9	133.4	14.3	22.5
			-3	123.6	133.5	14.3	26.6
			AVG.	123.3	133.3	14.3	25.0
ASTM No. 9			E4-1	123.6	133.6	14.3	28.2
			-2	123.7	133.4	14.3	28.3
			-3	123.2	133.3	12.8	23.5
			AVG.	123.5	133.5	13.8	26.7
ASTM No. 7.5			F4-1	121.3	135.4	12.8	29.0
			-2	122.7	135.5	12.8	23.9
			-3	121.6	135.5	14.3	25.1
			AVG.	121.9	135.5	13.3	26.0
3. Multiple Surface Voids							
No.	Dia.	Avg. Depth					
4	.0065"	.006" .006" .0055"	G4-1	122.0	133.8□	12.9	27.2
			-2	120.2	138.0□	12.1	22.1
			-3	124.1	136.2	9.3	24.4
			AVG.	122.1	136.0	11.4	24.6
4	.010"	.010" .105"	H4-1	124.0	133.8	13.6	25.0
			-2	123.5	132.9	13.6	25.7
			AVG.	123.7	133.4	13.6	25.3
4	.020"	.0180" .0180" .017"	I4-1	127.3	136.7	8.6	13.8*
			-2	126.8	133.3	3.6	10.4*
			-3	126.6	134.1	5.7	13.0*
			AVG.	126.9	134.7	6.0	12.4*
4. Surface Contamination							
Type	Dia.	Avg. Depth					
Alpha Case	.196"	.002" ↓	J4-2	123.1	134.4	14.3	20.2
			J4-3	124.4	134.4	14.3	22.2
			AVG.	123.7	134.4	14.3	21.2
304 S.S. inclusion	.0065"	.008" .007" .008"	K4-1	125.6	132.3	14.3	25.3
			-2	123.9	132.7	14.3	25.9
			-3	123.6	132.4	14.3	28.8
			AVG.	124.4	132.5	14.3	26.7
SiO <sub>2</sub> inclusion	.0065"	.007" ↓	L4-1	123.0	136.9	15.0	26.5
			-2	124.5	133.3	14.3	26.5
			-3	120.3	129.9	12.1	25.8
			AVG.	122.6	133.4	13.8	26.3

.357" Dia. test section  
Longitudinal grain direction  
RMI #890284

\*Failed thru defects in diffusion bond interface

□ Retested after grip failed beyond yield



Section 7.2.4

Multiple-Bond/Two-Axes Ti-6Al-4V  
Fatigue and Tensile Data

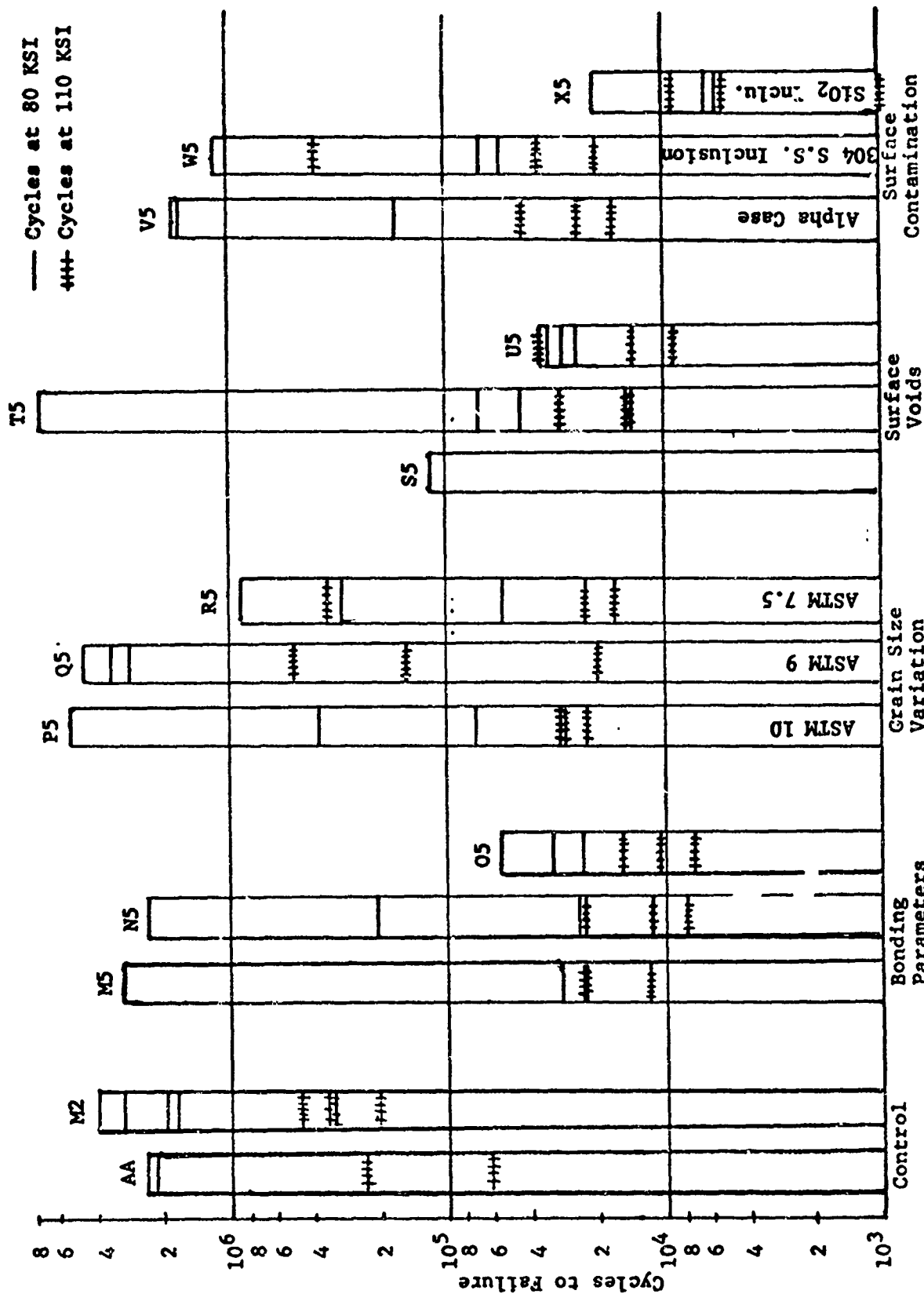


Figure 7.8 Axial Fatigue Properties of Multiple-Bond/Two Axes Specimens as Affected by Bonding Anomalies

Table 7.15 STATISTICAL ANALYSIS OF AXIAL FATIGUE DATA,  
DOUBLE-BOND/TWO-AXES,  $K_t = 1$ ,  $R = 0.1$

Condition	Avg. Fatigue Life, Cycles x1000			
	Max = 110 KSI		Max = 80 KSI	
	Average	Standard Deviation	Average	Standard Deviation
1. Bonding Parameter Variation				
4.8 to 6% L. & 3.5 to 8.3% S.T. deformation (M5)	19.7	5.4	1059	1459
2.2 to 2.4% L. & 1 to 5% S.T. deformation (N5)	14.2	6.4	829	1003
0.6 to 0.7% L. & 2 to 3% S.T. deformation (O5)	11.2	3.5	37.7	14.0
2. Grain Size Variations				
ASTM No. 10 (P5)	27.7	3.4	1808	2233
ASTM No. 8 (Q5)	229	206	3505	508
ASTM No. 7 (R5)	131	157	400	328
3. Surface Voids				
.005" edge chamfer (S5)	39.3	20.0	60.0	41.5
.010" edge chamfer (T5)	19.7	7.3	2460	3396
.020" edge chamfer (U5)	19.9	12.1	34.3	2.1
4. Surface Contamination				
.375" dia. alpha case (V5)	28.9	11.6	1191	723
.022" dia. 304 S.S. inclusion (W5)	151	175	418	502
.05" dia. SiO <sub>2</sub> inclusion (X5)	5.0	3.3	10.8	6.8

Table 7.16 EFFECT OF BONDING PARAMETER VARIATIONS ON AXIAL  
FATIGUE PROPERTIES, DOUBLE-BOND/TWO-AXES,  
 $K_t = 1$ ,  $R = 0.1$

Condition		Spec. No.	Max. Fatigue Stress, KSI	Cycles to Fail X1000	Location of Origin
Deformation, %					
Long.	Short Trans.				
6.0	3.5	M5A2	110	24	IBST
4.8	8.3	M5B1	↓	23	IBST
4.8	8.3	M5B3	↓	12	IBST
6.0	3.5	M5A1	80	24	IBST
6.0	3.5	M5A3	↓	30	IBST
4.8	8.3	M5B2	↓	3122	S
2.4	5.0	N5A3	110	23	I/S-BP
2.2	1.0	N5B1	↓	8	IBST
2.2	1.0	N5B2	↓	11.5	IBST
2.4	5.0	N5A1	80	219	S-NBP
2.4	5.0	N5A2	↓	2244	I-IB
2.2	1.0	N5B3	↓	25	IBST
0.7	2.0	O5A2	110	15.8	IBST
0.6	3.0	O5B1	↓	10.3	IBST
0.6	3.0	O5B3	↓	7.4	IBST
0.7	2.0	O5A1	80	24	IBST
0.7	2.0	O5A3	↓	57	IBST
0.6	3.0	O5B2	↓	32	IBST

0.250" dia. test section

IBST - incomplete bond in short transverse direction

S - Surface

NBP - not in bond plane

I - internal

BP - at bond plane

IB - incomplete bond

Table 7.17 EFFECT OF GRAIN SIZE VARIATIONS ON AXIAL FATIGUE PROPERTIES, DOUBLE BOND/TWO-AXES,  $K_t = 1$ ,  $R = 0.1$

Condition		Spec. No.	Max. Fatigue Stress, KSI	Cycles To Fail X1000	Location of Origin
Deformation, %					
Long.	Short Trans.				
ASTM Grain Size No. 10					
6.0	3.5	P5A3	110	29	IBST
5.9	5.8	P5B2	↓	31	I-IB
5.9	5.8	P5B3	↓	23	IBST
6.0	3.5	P5A1	80	73	IBST
6.0	3.5	P5A2	↓	4961	S-NP
5.9	5.8	P5B1	↓	389	I-IB
ASTM Grain Size No. 8					
5.4	6.0	Q5A2	110	510	S-NP
5.4	6.0	Q5A3	↓	21	IBST
5.8	2.0	Q5B3	↓	156	I-IB
5.4	6.0	Q5A1	80	3489	S-NP
5.8	2.0	Q5B1	↓	4135	S-NP
5.8	2.0	Q5B2	↓	2891	S-NP
ASTM Grain Size No. 7					
5.4	2.2	R5A2	110	354	S-NP
6.0	2.0	R5B1	↓	17	IBST
6.0	2.0	R5B3	↓	23	S-NP
5.4	2.2	R5A1	80	56	IBST
5.4	2.2	R5A3	↓	304	S-BP
6.0	2.0	R5B2	↓	841	S-NP

IBST - incomplete bond in short transverse direction

I - internal

IB - incomplete bond

S - surface

NP - not in bond plane

BP - in bond plane

Table 7.18 EFFECT OF CHAMFERED EDGE VOIDS ON AXIAL FATIGUE  
PROPERTIES, DOUBLE-BOND/TWO-AXES,  $K_t = 1$ ,  $R = 0.1$

Chamfer Size	Deformation, %		Spec. No.	Max. Fatigue Stress, KSI	Cycles to Fail X1000	Location of origin
	Long.	Short Trans.				
.005"	5.4	5.5	S5A2	110	18	I/SD
	↓	6.8	S5B2	↓	66	I-NP
		6.8	S5B3	↓	34	IBTP
		5.5	S5A1	80	39	I/SD
	↓	5.5	S5A3	↓	23	I/SD
		6.8	S5B1	↓	118	I/SD-I-IB
.010"	5.6	6.5	T5A1	110	14	I/SD
	5.6	↓	T5A2	↓	30	I/SD
	5.2		T5B3	↓	15	I/SD
	5.6		T5A3	80	70	I/SD
	5.2		T5B1	↓	46	I/SD
	5.2	↓	T5B2	↓	7263	S-NP
.020"	5.8	6.5	U5A2	110	36.7	I/SD-IB
	4.7	8.0	U5B2	↓	14	I/SD
	4.7	8.0	U5B3	↓	9	IBTP
	5.8	6.5	U5A1	80	29	I/SD
	5.8	6.5	U5A3	↓	34	I/SD-IB
	4.7	8.0	U5B1	↓	31	I/SD

I/SD - internal/surface defect

IBTP - incomplete bond in transverse plane

I - internal

NP - not in bond plane

IB - incomplete bond

S - surface

Table 7.19 EFFECT OF CONTAMINATION ON AXIAL FATIGUE PROPERTIES,  
DOUBLE-BOND/TWO-AXES,  $K_t = 1$ ,  $R = 0.1$

Contami- nation	Deformation, %		Spec. No.	Max. Fatigue Stress, KSI	Cycles to Fail X1000	Location of Failure
	Long.	Short Trans.				
Alpha	5.3	7.1	V5A1	110	25	I/SD
Case		7.1	V5A2		44.6	I/SD
.375"		6.6	V5B3		17	IBST
dia.		7.1	V5A3	80	1677	I/SD
x .002"		6.6	V5B1		168	S-IB
deep		6.6	V5B2		1727	I-IB
304 S.S.	4.6	7.5	W5A2	110	35	ID
inclu-	5.3	9.3	W5B2		21	ID
sion	5.3	9.3	W5B3		398	I-NP
.022"	4.6	7.5	W5A1	80	69	ID, IB
dia.	4.6	7.5	W5A3		56	ID
x .02"	5.3	9.3	W5B1		1128	S
deep						
SiO <sub>2</sub>	4.6	7.5	X5A2	110	5.1	ID
inclu-	5.2	8.6	X5B1		0.9	SD
sion	5.2	8.6	X5B3		9.0	S-IB
.05" dia	4.6	7.5	X5A1	80	5.6	SD
x .04"	4.6	7.5	X5A3		20.4	SD
deep	5.2	8.6	X5B2		6.4	ID

I/SD ~ internal/surface defect

IBST ~ incomplete bond in short transverse direction

S ~ surface

IB ~ incomplete bond

ID ~ internal defect

I-NP ~ internal, not in bond plane

SD ~ surface defect

Table 7.20 TENSILE PROPERTIES OF DOUBLE-BOND/TWO-AXIS SPECIMENS

Condition			Spec. No.	YTS ksi	UTS ksi	Elong. % in 1.4"	E.A. %
1. Bonding Parameter Variation							
Deformation, %							
Long.	Short Trans.						
6.09	3.8		AS-1	129.2	132.9	5.6	10.8 *
			-2	129.4	137.1	5.6	13.5 *
			-3	128.8	135.5	5.7	14.3 *
			AVG.	129.1	135.2	6.0	12.9
2.38	10.0		BS-1	128.4	137.4	10.7	19.4 *
			-2	129.3	138.1	5.7	12.7 *
			-3	130.0	137.7	10.7	19.7 *
			AVG.	129.3	137.7	9.0	17.3
0.74	2.2		CS-1	128.7	137.0	12.1	27.8
			-2	127.5	136.9	12.1	31.6
			-3	128.5	136.9	9.3	20.3 **
			AVG.	128.2	136.9	11.2	26.4
2. Grain Size Variations							
Deformation, %							
ASTM No.	Long.	Short Trans.					
11	5.91	2.20	DS-1	128.8	135.9	9.3	20.7 **
			-2	129.4	136.5	10.0	22.4 **
			-3	129.4	136.7	10.7	23.0 **
			AVG.	129.2	136.4	10.6	22.0
8	5.91	0	ES-1	123.2	134.7	9.3	19.8 **
			-2	123.0	134.4	10.0	22.7 **
			-3	123.7	134.4	10.0	21.6 **
			AVG.	123.3	134.5	9.8	21.4
7	5.68	5.52	FS-1	118.7	130.4	10.7	22.3 *
			-2	118.4	130.3	11.4	22.6 *
			-3	117.5	129.9	11.4	25.4
			AVG.	118.2	130.2	11.2	23.4
3. Chamfered Edge Void							
Deformation, %							
Size	Long	Short Trans.					
.005"	5.57	6.36	GS-1	129.5	137.9	12.1	31.2
			-2	129.5	138.3	12.9	34.1
			-3	129.9	138.5	12.1	26.9 *
			AVG.	129.6	138.2	12.4	30.7
.010"	5.23	7.00	HS-1	130.0	138.5	12.1	30.1
			-2	130.5	138.4	12.1	28.1
			-3	128.9	138.3	12.9	31.8
			AVG.	129.8	138.4	12.4	30.0
.020"	5.05	6.56	IS-1	130.2	138.9	9.3	19.0 *
			-2	130.4	138.4	9.3	17.7 *
			-3	130.4	138.5	10.7	22.5 *
			AVG.	130.3	138.5	9.8	19.7
4. Surface Contamination							
Type	Dis.	Avg. Depth					
Alpha Case	.375"	.002"	JS-1	132.0	139.3	12.1	32.9
			-2	131.9	139.0	10.7	19.5 **
			-3	131.8	138.7	10.7	22.5 **
			AVG.	131.9	139.0	11.2	25.0
304 S.S. inclusion	.022"	.032" .032" .025"	ES-1	129.7	138.2	8.6	17.3 *
			-2	131.1	139.1	9.3	18.0 *
			-3	131.2	139.2	9.3	18.1 *
			AVG.	130.7	138.8	9.1	17.8
SiO <sub>2</sub> inclusion	.048"	.030" .040" .035"	LS-1	130.9	132.5	2.6	11.5 *
			-2	129.8	131.6	3.6	14.2 *
			-3	130.6	137.5	12.1	35.8
			AVG.	130.3	134.0	6.2	20.5

.357" dia. test section  
Longitudinal grain direction  
NMI Heat # 890225

- \* Incomplete bond in transverse plane
- \*\* Failed at multibond interface due to incomplete short transverse bond
- \* Failed thru intentional defect



### Section 7.2.5

#### Multiple-Bond/3-Axes Ti-6Al-4V Fatigue and Tensile Data

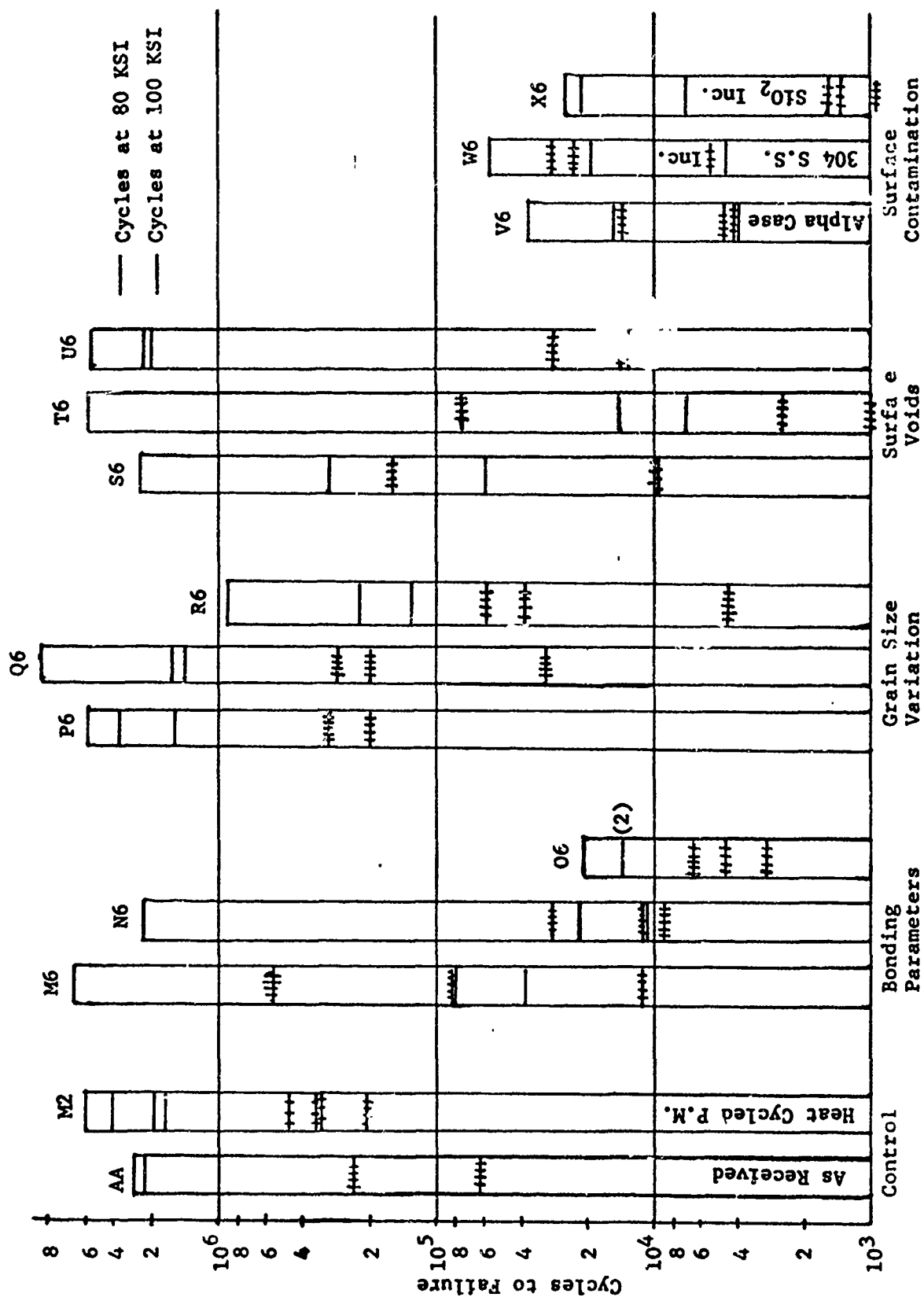


Figure 7.9 Axial Fatigue Properties of Multiple-Bond/Three-Axes Specimens as Affected by Bonding Anomalies

Table 7.21 STATISTICAL ANALYSIS OF AXIAL FATIGUE DATA,  
MULTIPLE-BOND/3-AXES,  $K_t = 1$ ,  $R = 0.1$

Condition	Avg. Fatigue Life, Cycles X100C			
	Max = 110 KSI		Max = 80 KSI	
	Average	Standard Deviation	Average	Standard Deviation
1. Bonding Parameter Variation		10 <sup>-3</sup>		10 <sup>-3</sup>
3.8 to 4.0% S.T. deformation (M6)	217.7	244.4	1600	2179
2.0 to 4.3% S.T. deformation (N6)	16.7	9.3	742	1026
2.0 to 2.5% S.T. deformation (O6)	4.7	1.4	16.3	3.3
2. Grain Size Variations				
ASTM No. 11 (P6)	263.4	57.7	2842	221
ASTM No. 8 (Q6)	173.7	106.6	3132	2250
ASTM No. 7 (R6)	34.4	22.8	424	348
3. Surface Voids				
.005" corner tetragonal (S6)	39.3	20.0	60.0	41.5
.010" corner tetragonal (T6)	19.7	7.3	2460	3396
.020" corner tetragonal (U6)	19.9	12.1	31.3	2.1
4. Surface Contamination				
Alpha Case (V6)	7.5	4.4	18.7	13.7
304 S.S. powder (W6)	19.1	10.0	26.3	21.3
SiO <sub>2</sub> powder (X6)	1.2	0.4	17.7	7.7

Table 7.22 EFFECT OF BONDING PARAMETER VARIATIONS ON AXIAL FATIGUE PROPERTIES, MULTIPLE-BOND/3-AXES,  $K_t = 1$ ,  $R = 0.1$

Short Transverse Deformation, %	Spec. No.	Max. Fatigue Stress, KSI	Cycles to Fail X1000	Location of Origin
3.8	M6A1	110	81	I-IB
3.8	M6A2	↓	561	S
4.0	M6B3	↓	11.2	IB
3.8	M6A3	80	4681	S-NBP
4.0	M6B1	↓	80	IB
4.0	M6B2	↓	39	IB
4.3	N6A1	110	29.7	IB
4.3	N6A3	↓	11.3	IB
2.0	N6B3	↓	9	IB
4.3	N6A2	80	2194	S
2.0	N6B1	↓	11	IB
2.0	N6B2	↓	22	IB
2.5	O6A1	110	4.6	IB
2.5	O6A2	↓	6.5	IB
2.0	O6B3	↓	3.0	IB
2.5	O6A3	80	21	IB
2.0	O6B1	↓	14	IB
2.0	O6B2	↓	14	IB

.25" dia. test section.

Longitudinal and transverse directions restrained but not deformed.  
Bonded 6 hours at 1700°F.

I - internal, IB - incomplete bond, S - Surface, NBP - Not in bond plane.

Table 7.23 EFFECT OF GRAIN SIZE VARIATIONS ON AXIAL FATIGUE PROPERTIES, MULTIPLE-BOND/3-AXES,  $K_t = 1$ ,  $R = 0.1$

ASTM Grain Size No.	Short Transverse Deformation, %	Spec. No.	Max. Fatigue Stress, KSI	Cycles to Fail X1000	Location of Origin
11	4.2	P6A1	110	205.7	S-NBP
	4.2	P6A2		321.1	I-NBP
	4.0	P6B3		Static	NBP
	4.2	P6A3	80	2943	S-NBP
	4.0	P6E1		3977	S
	4.0	P6B2		1605	S-NBP
8	4.5	Q6A1	110	287.8	S-NBP
	4.5	Q6A3		31.3	S-IB
	4.8	Q6B3		201.9	S-NBP
	4.5	Q6A2	80	1432	I
	4.8	Q6B1		1653	S-NBP
	4.8	Q6B2		6311	S-NBP
7	3.5	R6A1	110	38.9	IB
		R6A2		59.5	S-NBP
		R6B2		4.5	IB
		R6A3	80	132	IB
		R6B1		913	S
		R6B3		228	I-IB

S - Surface, NBP - not in bond plane,  
I - internal, IB - incomplete bond

Table 7.24 EFFECT OF CHAMFERED CORNER VOIDS ON AXIAL FATIGUE  
PROPERTIES, MULTIPLE-BOND/3-AXES,  $K_t = 1$ ,  $R = 0.1$

Chamfered Corner Void Size, Inch	Short Transverse Deformation %	Spec. No.	Max. Fatigue Stress, KSI	Cycles to Fail X1000	Location of Origin
.008	4.2	S6A3	110	160.3	I-IB
	5.0	S6B1	↓	10.0	IB
	5.0	S6B2	↓	9.8	IB
	4.2	S6A1	80	312	I-IB
	4.2	S6A2	↓	2274	I-NBP
	5.0	S6B3	↓	16	ID-IB
.018	3.5	T6A3	110	70.3	I-IB
	4.2	T6B1	↓	2.5	IB
	4.2	T6B3	↓	0.97	IB
	3.5	T6A1	80	3869	S
	3.5	T6A2	↓	14	IB
	4.2	T6B2	↓	7	IB
.030	5.0	U6A3	110	13.6	ID-IB
	4.3	U6B1	↓	13.0	ID-IB
	4.3	U6B3	↓	27.9	BP-IB
	5.0	U6A1	80	1997	S-NBP
	5.0	U6A2	↓	3663	SD-S/BP
	4.3	U6B2	↓	2211	S -NBP

I - internal, IB - incomplete bond, NBP - not in bond plane,  
ID - internal defect, BP - bonding plane, S - surface

Table 7.25 EFFECT OF CONTAMINATION ON AXIAL FATIGUE PROPERTIES,  
MULTIPLE-BOND/3-AXES,  $K_t = 1$ ,  $R = 0.1$

Type Contamination	Size Inch	Short Transverse Deformation, %	Spec. No.	Max. Fatigue Stress, KSI	Cycles to Fail X1000	Location of Origin
Alpha Case Layer	.002 deep	5.0	V6A1	110	4.2	IB
		5.0	V6A2	↓	4.6	IB
		4.0	V6B3	↓	13.8	BP
		5.0	V6A3	80	4	IB
		4.0	V6B1	↓	37	SD
		4.0	V6B2	↓	15	I/SD
304 S.S. powder	.025 tetragonal corner	4.0	W6A1	110	28.8	I/SD-ID
		4.0	W6A3	↓	23.1	I/SD
		4.5	W6B3	↓	5.4	I/SD-ID
		4.0	W6A2	80	4.5	ID-I/SD
		4.5	W6B1	↓	55.1	I/SD
		4.5	W6B2	↓	19.2	ID-SD
SiO <sub>2</sub> powder	.025 tetragonal corner	4.5	X6A2	110	1.57	I/SD
		4.5	X6A3	↓	0.59	I/SD-ID
		4.0	X6B3	↓	1.36	I/SD
		4.5	X6A1	80	7.02	I/SD
		4.0	X6B1	↓	21.5	I/SD
		4.0	X6B2	↓	24.7	I/SD

IB - incomplete bond, BP - bonding plane, I/SD - internal/surface defect,  
ID - internal defect, SD - surface defect

Table 7.26 TENSILE PROPERTIES OF MULTIPLE-BOND/3-AXIS SPECIMENS

Condition			Spec. No.	TYS KSI	TUS KSI	Elong. % 1 to 1.4"	R.A. %
1. Bonding Parameter Variation							
Deformation, %							
Long.		Short Trans.					
None	4.1		A6-1	130.3	140.8	13.0	30.6
			-2	129.1	138.7	12.9	34.1
			-3	130.3	138.4	12.9	32.7
			AVG.	129.9	139.3	12.9	32.5
None	3.1		B6-1	131.5	138.0	13.6	36.6
			-2	131.9	138.5	11.4	34.6
			-3	131.3	138.2	13.9	35.9
			AVG.	131.6	138.2	13.0	32.4
None	1.7		C6-1	129.7	135.0	7.0	13.2 *
			-2	130.5	136.5	10.4	15.0 *
			-3	129.1	131.8	5.4	8.9 *
			AVG.	129.8	134.4	7.9	12.4
2. Grain Size Variations							
Information, %							
ASTM No.	Long.	Short Trans.					
11	None	4.5	D6-1	127.7	136.9	8.6	26.3
			-2	129.4	137.6	9.3	26.3
			-3	129.2	137.3	10.0	26.9
			AVG.	128.8	137.3	9.3	25.8
8	None	4.8	E6-1	123.3	134.1	10.4	27.8
			-2	123.0	133.7	10.4	23.9
			-3	122.8	133.8	10.0	21.9
			AVG.	123.0	133.9	10.3	24.5
7	None	3.7	F6-1	118.7	133.1	11.4	23.3
			-2	119.2	132.0	11.4	22.2
			-3	117.5	131.3	8.6	18.2 *
			AVG.	118.5	132.1	10.5	21.2
3. Chamfered Corners Void							
Deformation, %							
Size	Long.	Short Trans.					
.008	None	4.0	G6-1	127.0	136.9	12.1	25.9 *
			-2	128.9	137.2	10.7	22.0 *
			-3	130.0	137.3	10.4	19.0 *
			AVG.	128.6	137.1	11.1	22.3
.018	None	4.5	H6-1	130.9	138.0	7.9	11.4 *
			-2	130.8	138.5	9.3	18.1 *
			-3	127.8	137.1	3.1	7.2 *
			AVG.	129.8	136.2	6.8	12.2
.036	None	4.4	I6-1	131.3	137.8	12.9	35.0
			-2	130.6	137.6	12.9	33.5
			-3	130.7	136.4	11.4	25.1 *
			AVG.	130.9	137.9	12.4	31.2
4. Surface Contamination							
Type	Size	Short Trans. Deformation, %					
Alpha Case	.002" deep	4.0	J6-1	130.0	139.1	11.8	26.8
			-2	130.8	139.6	12.1	27.4 *
			-3	130.7	139.2	11.9	23.2
			AVG.	130.5	139.3	11.9	25.1
304 S.S. powder	.025" tetragonal corner	4.3	K6-1	132.3	135.0	7.1	16.8 *
			-2	130.9	131.0	2.1	14.0 *
			-3	132.4	132.5	0.4	8.2 *
			AVG.	131.9	134.2	3.2	13.0
SiO <sub>2</sub> powder	.025" tetragonal corner	4.5	L6-1	129.6	134.5	7.1	18.5 *
			-2	130.8	133.4	7.1	11.6 *
			-3	130.8	135.6	5.0	12.7 *
			AVG.	130.5	134.5	6.4	11.6

\* Incomplete bond at multibond interface  
 \* Failed thru intentional defect



## Section 7.2.6

### Fracture Toughness and Stress Corrosion Data for Diffusion Bonded Ti-6Al-4V

Table 7.27 COMPACT TENSION FRACTURE TOUGHNESS OF DIFFUSION BONDED  
Ti-6Al-4V PLATE L-T DIRECTION, 1" THICK

Condition	Spec. No.	$K_{Ic}$ , KSI- $\sqrt{\text{in}}$	$2.5(K_{Ic}/\sigma_{ys})^2$	$P_{max}/P_Q$
As Received	1P	52.7	.40	1.00
	2P	52.9		1.00
	AVG.	52.8		
Diff. Bonded Plane Parallel to Notch	1CT	75.9*	.93	1.15
	2CT	78.0*		1.14
	AVG.	76.9*		
Diff. Bonded Plane Perpen- dicular to Notch	3CT	80.4*	.96	1.12
	4CT	77.3*		1.16
	AVG.	77.9*		

\*  $K_Q$  (did not pass para. 9.1.2 of ASTM E399-72 Requiring  $P_{max}/P_Q \leq 1.1$ )

### Stress Corrosion Cracking

The results of the stress corrosion cracking tests are summarized in Table 7.28. This material, in both the annealed and heat-cycled conditions, has shown virtually no susceptibility to cracking in salt water despite the fact that several of the specimens are stressed to within 90 to 100% of the fracture toughness values in air. The presence of a bond plane within the specimen, either coplanar with the fatigue precrack or perpendicular to it near the tip, does not appear to deteriorate this apparent immunity to stress corrosion cracking.

Table 7.28

RESULTS OF STRESS CORROSION CRACKING TESTS ON BONDED AND UNBONDED Ti-6Al-4V  
CORRODANT - 3½% NaCl SOLUTION

Specimen	Material Condition	Bond Plane Orientation	Fracture Toughness [Ksi(in.) <sup>½</sup> ]	Initial K <sub>I</sub> [Ksi(in.) <sup>½</sup> ]	Present K <sub>I</sub> [Ksi(in.) <sup>½</sup> ]	Days in Test
1P	Annealed	No Bond	~53	54.9	54.8	136
2P	Annealed	No Bond	~53	49.5	49.4	136
1H-CD	Heat Cycled*	No Bond	76-81	49.4	49.3	136
2N-CD	Heat Cycled	No Bond	76-81	54.6	54.6	136
1-CD	Heat Cycled	Co-planar with precrack	76-81	40.0	40.0	136
2-CD	Heat Cycled	Co-planar with precrack	76-81	49.0	49.0	136
3-CD	Heat Cycled	Co-planar with precrack	76-81	70.5	70.4	112
4-CD	Heat Cycled	Perpendicular to precrack	76-81	48.8	48.8	136
5-CD	Heat Cycled	Perpendicular to precrack	76-81	53.1	52.9	136
6-CD	Heat Cycled	Perpendicular to precrack	76-81	70.6	70.2	112

\*The heat cycle consisted of holding at 1700°F for 6 hours and then furnace cooling.

## 8. CORRELATION OF NDE DATA, MECHANICAL PROPERTIES, AND FRACTOGRAPHY

### 8.1 Tensile Properties

Yield strength and ultimate tensile strength are not sensitive indicators of bond quality in titanium diffusion bonded joints as joints which would be considered unacceptable by metallographic examination often have strengths equivalent to the base metal (Ref. 14). The ductility exhibited at fracture and the type of fracture have been found to give a better indication of bond quality. The reduced ductility in poor diffusion bonded joints is most strongly reflected in the reduction of area and less so in elongation. Therefore, nondestructive evaluation data was mainly compared to reduction of area in order to correlate tensile properties with NDT data. Fracture surfaces of many of the tensile specimens were examined after failure in an attempt to determine the origin of these failures. The effect of the different types of intentional defects on tensile properties was also examined. These effects were observed in Tables 7.8, 7.14, 7.20, and 7.26.

#### 8.1.1 Effects of Intentional Defects on Tensile Properties

##### (1) Bonding Parameter Variations

Total deformation can be used as a measure of bond strength in single-axis joints providing all other bonding parameters such as temperature, time at temperature, vacuum, surface finish of bonded parts, etc. are held constant. The effect of insufficient deformation of C3 is projected in lower reductions of area obtained as compared to A3. In specimen C4, section C4-B, had considerably better surface finish ( $\approx 12$  RMS) than bonding surfaces on C3 (30-60 RMS), this is apparently the reason for the better bond in C4 as compared to C3. For bonding surfaces having better surface finishes, lower deformations are required to obtain a good bond.

In multiple-axes joints, relating deformation with bond strength is much more complex. Deformations obtained on complex parts cannot always be related to localized pressure at the bonding surface. In bonding the multi-axes specimens, proper restraint by the tooling along the sides of the specimens appeared to be as important as obtaining large deformations. In A6, B6, and C6 specimens, with the sides

restricted by tooling, the bond quality as reflected by the reduction of area was dependent on the deformation received along the direction of applied pressure application (short transverse direction).

## (2) Grain Size Variations

No significant effects on ductility after bonding were observed in specimens having different primary alpha grain sizes (D-, E-, F- ). Yield strengths of the grain growth specimens were somewhat less, however. This is apparently due to increased annealing caused by heating the E- and F-specimens to higher temperatures.

## (3) Surface Voids

In the case of voids shaped in the form of cylinders ( $L/D \approx 1$ ), the only specimens whose tensile properties were significantly affected were the I4 specimens. These voids consisted of a cluster of four cylinders of  $\approx .020$ " dia. and  $\approx .020$ " depth. Voids having small diameters had no significant effect on reduction of area. For voids in the form of chamfered edges and corners, results are less conclusive. It appears that the side of the chamfer must have a dimension of  $\approx .018$ " before an appreciable effect on tensile properties is made.

## (4) Surface Contamination

(a) Alpha Case Layer - Slightly reduced ductility was observed in most of the tensile specimens containing an alpha case layer. Tensile properties appeared to be independent of diameter of the layer.

(b) Type 304 stainless steel and  $\text{SiO}_2$  Powder Inclusions - Powders packed into cylinders  $.0065$ " dia. had no effect on tensile properties. However, powder inclusions of  $.013$ " dia. effected ductility. Powders packed into chamfered edges and corners had quite a large effect on ductility where the side of the chamfer had a dimension ranging from  $.022$ " to  $.048$ ".

## 8.1.2 Correlation of NDE Data with Tensile Properties

Very little correlation can be made between fluorescent penetrant inspection results and tensile properties since no bond line indications were obtained from the penetrant inspec-

tions on any of the tensile specimens. Apparently poorer bonds than those obtained on the diffusion bonded test specimens are required for detectability by this technique.

Blue etch-anodize (BEA) inspection is much more sensitive to alpha case than to other types of intentional defects. For specimens not containing an alpha case layer, detection appeared to be dependent on deformation received. For specimens containing internal defects, neither blue etch-anodize (BEA) nor fluorescent penetrant inspection would be expected to find these flaws.

Ultrasonic delta scan inspection was particularly effective in finding internal defects of the form of stainless steel and  $\text{SiO}_2$  powder inclusions and incomplete bond areas. Most of the defects in the form of cylindrical voids and cylindrical surface contamination having diameters of .010" and greater were detected by this technique. Voids and inclusions in the form of chamfers were more difficult to detect.

Ultrasonic signal averaging data was related to tensile properties by plotting the ratio of defect signal amplitude to arithmetic average (defect amplitude/AA) as a function of reduction in area. These results are shown in Figure 8.1. In general, larger defect amplitude/AA ratios are associated with lower reductions in area. For instance, no reductions in area above 23.3% were found for specimens with defect amplitude/AA ratios greater than 10. The mean values of reduction in area over block increments of defect amplitude/AA along with their standard deviation are presented in Figure 8.2.

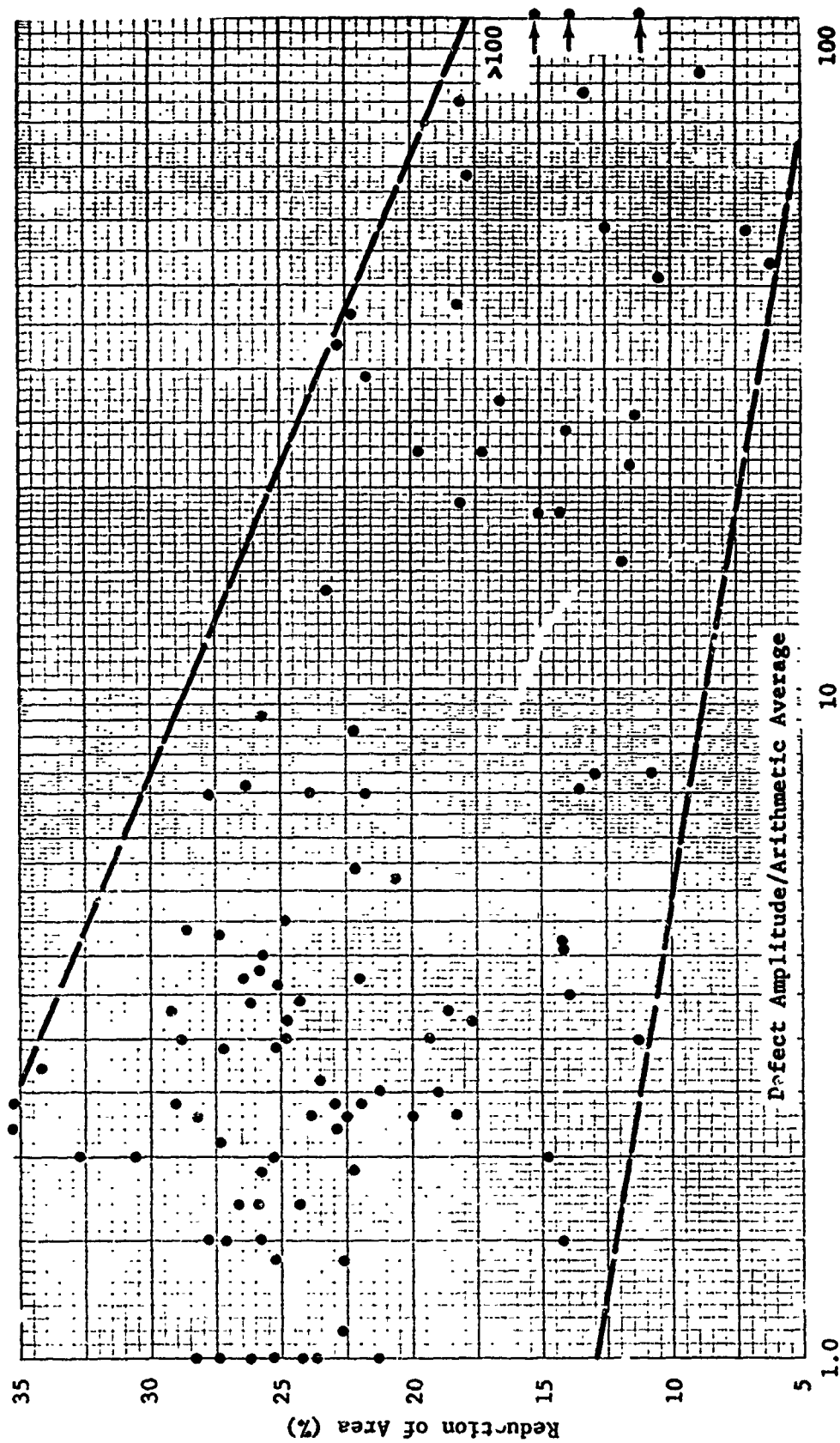


Figure 8.1 Reduction of Area vs. Defect Amplitude/Arithmetic Average  
for Diffusion Bonded Tensile Specimens



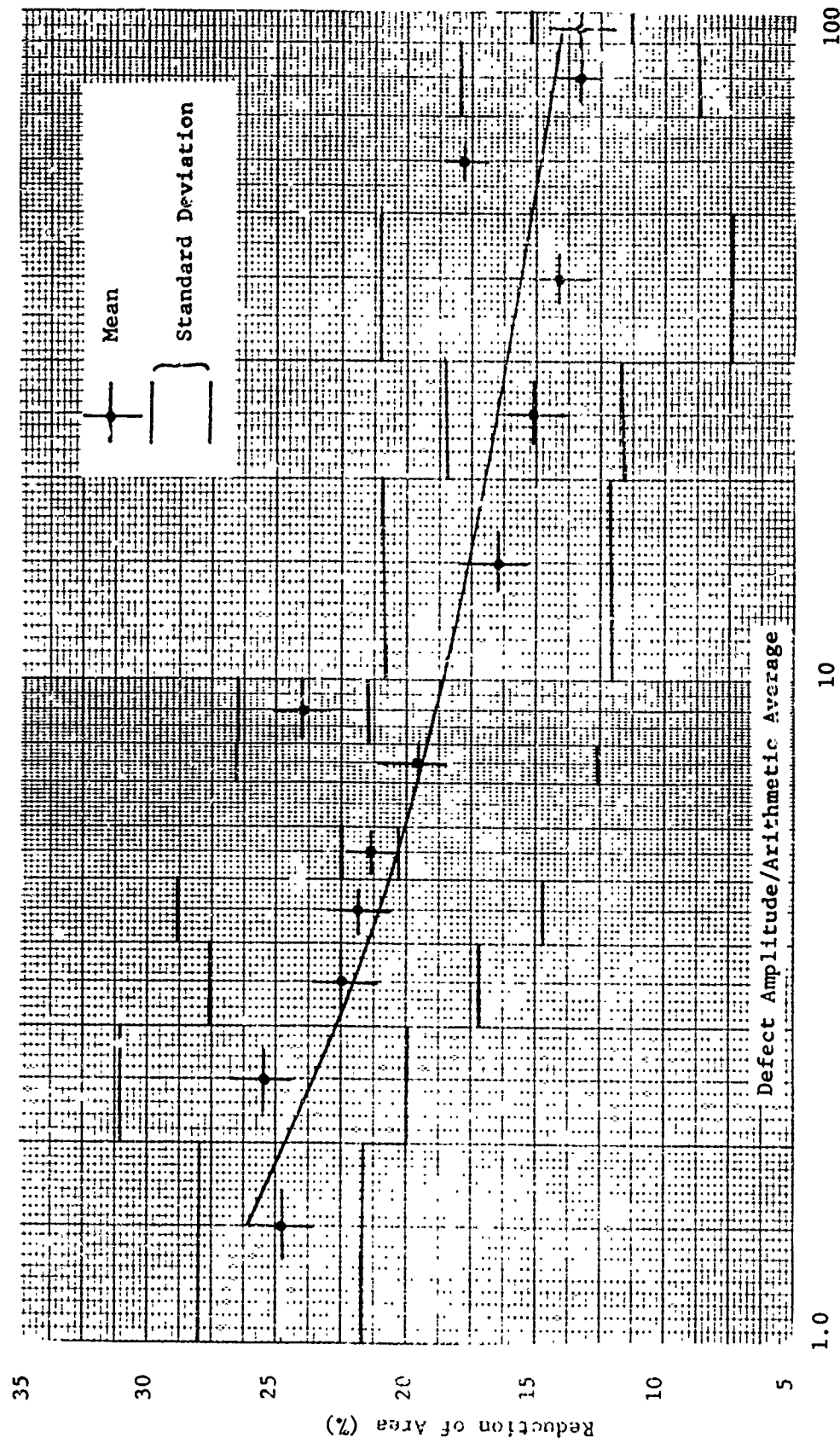


Figure 8.2 Statistical Analysis of Reduction of Area vs. Defect Amplitude/  
Arithmetic Average for Diffusion Bonded Specimens

## 8.2 Axial Fatigue Properties

Fatigue properties are expected to be sensitive indicators of bond quality in titanium diffusion bonded joints. Again, the mode of fracture can determine the origin of failure and thus effects of certain defects on fatigue properties.

### 8.2.1 Effects of Intentional Defects on Fatigue Properties

#### 1. Bonding Parameter Variations

Fatigue lives were considerably shorter for specimens having small deformations (0- ). In specimen 04, section 04-B like C4-B had a much better surface finish than 03, thus giving an improved fatigue life.

#### 2. Grain Size Variations

No definite trends were established between fatigue life and primary alpha grain size except that the larger grained specimens (R- ) had slightly lower fatigue life at 80 KSI maximum stress level.

The larger alpha grain size material having a lower fatigue life at the lower maximum stress of 80 KSI concurs with findings (Ref. 15) that a relationship exists between fatigue life and the inverse of the primary alpha grain size for low stress-high cycle ( $\sim 10^8$ ) fatigue.

#### 3. Surface Voids

No effect on fatigue life was found for single cylindrical voids of size .0065", .010", and .020" respectively. However, if you have two or more defects this size, in close proximity, there will be an effect (Ref. 16).

The effect of voids in the form of chamfered corners and edges was less predictable. Although most of these type voids lowered the fatigue life, the limit on size of the chamfer which would affect fatigue data was difficult to establish.

#### 4. Surface Contamination

(a) Alpha Case Layer - Fatigue life reduced considerably

on specimens having a maximum fatigue stress of 110 KSI. Much smaller effect observed on samples having a maximum fatigue stress of 80 KSI.

(b) Type 304 Stainless Steel and  $\text{SiO}_2$  Powder Inclusions - The effect of  $\text{SiO}_2$  powder on lowering fatigue life was greater than that of the stainless steel powder. Cylindrical  $\text{SiO}_2$  powder inclusions, .0065 dia. and greater lowered fatigue life. The lowering was greatest, however for the cylindrical inclusion .050" in diameter. Chamfered corners with sides .025" packed with both types of powder had a considerable effect.

#### 8.2.2 Correlation of NDE Data with Fatigue Properties

Fatigue lives were compared with the defect amplitude/AA ratio as determined from ultrasonic signal averaging measurements (see Section 6.2.3). Comparisons were made at both 110 KSI and 80 KSI stress levels. Fatigue failures were separated into two groups; (a) failures originating at the surface and (b) failures originating away from the surface. Fatigue life was plotted as a function of defect amplitude/AA for both types of failures. These results are given in Figures 8.3 through 8.6.

In general, specimens having failures originating at the surface had good fatigue properties and low defect amplitude/AA ratios. Fatigue specimens with failures originating away from the surface exhibited fatigue lives inversely proportional to the defect amplitude/AA ratio. In Figures 8.7 and 8.8, the mean values of fatigue life over increments in defect amplitude/AA are shown as a function of defect amplitude/AA. For defect amplitude/AA ratios greater than 30, fatigue properties are poor. For defect amplitude/AA ratios less than 30, one is less able to predict fatigue lifetimes. This is brought out by the large standard deviation of fatigue lifetime values for low ratios of defect amplitude/AA.

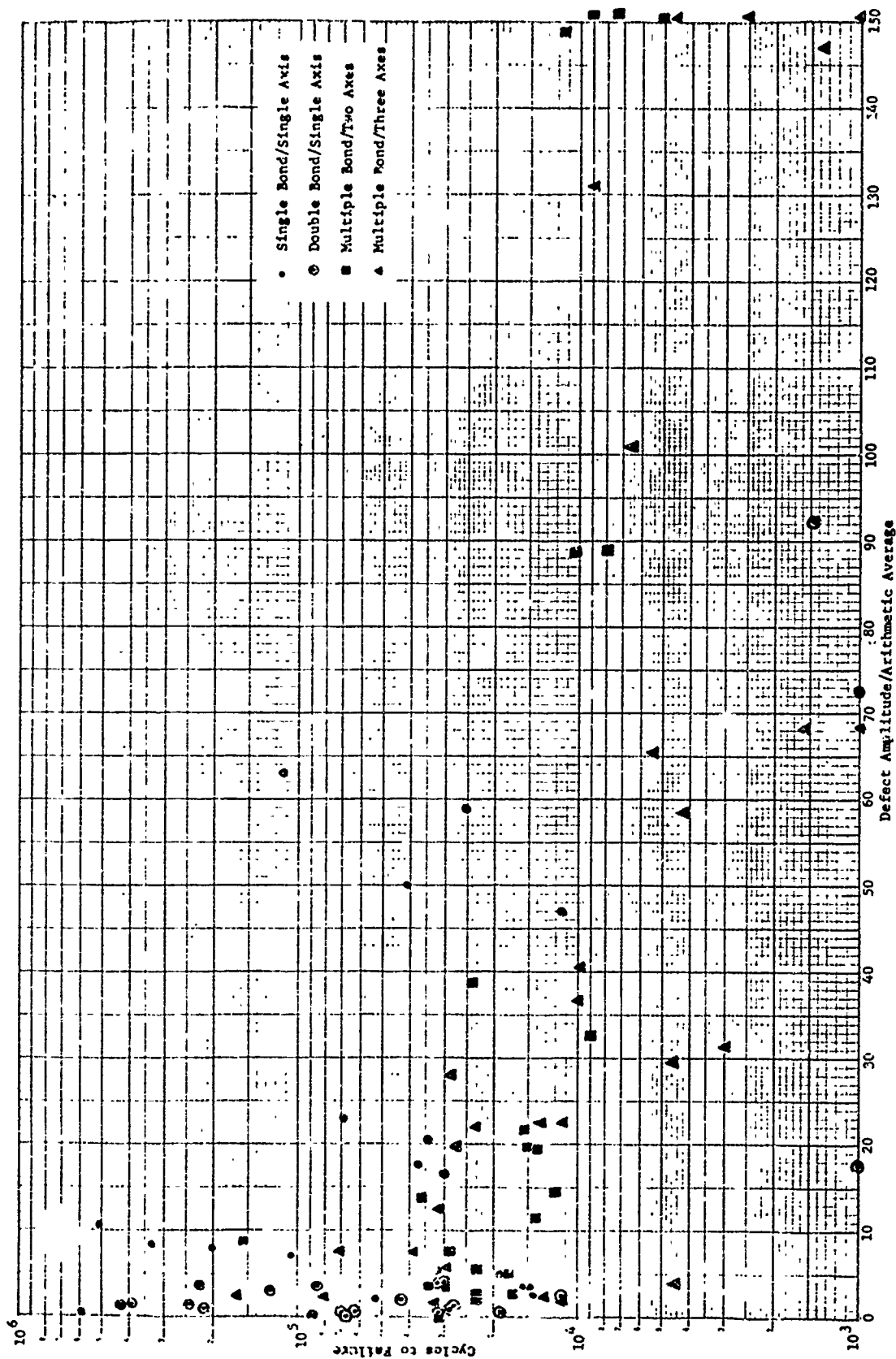


Figure 3.3 Fatigue Life vs Defect Amplitude/AA for Diffusion Bonded Specimens with Internally-Initiated Failures (Stress Level = 110 ksi)

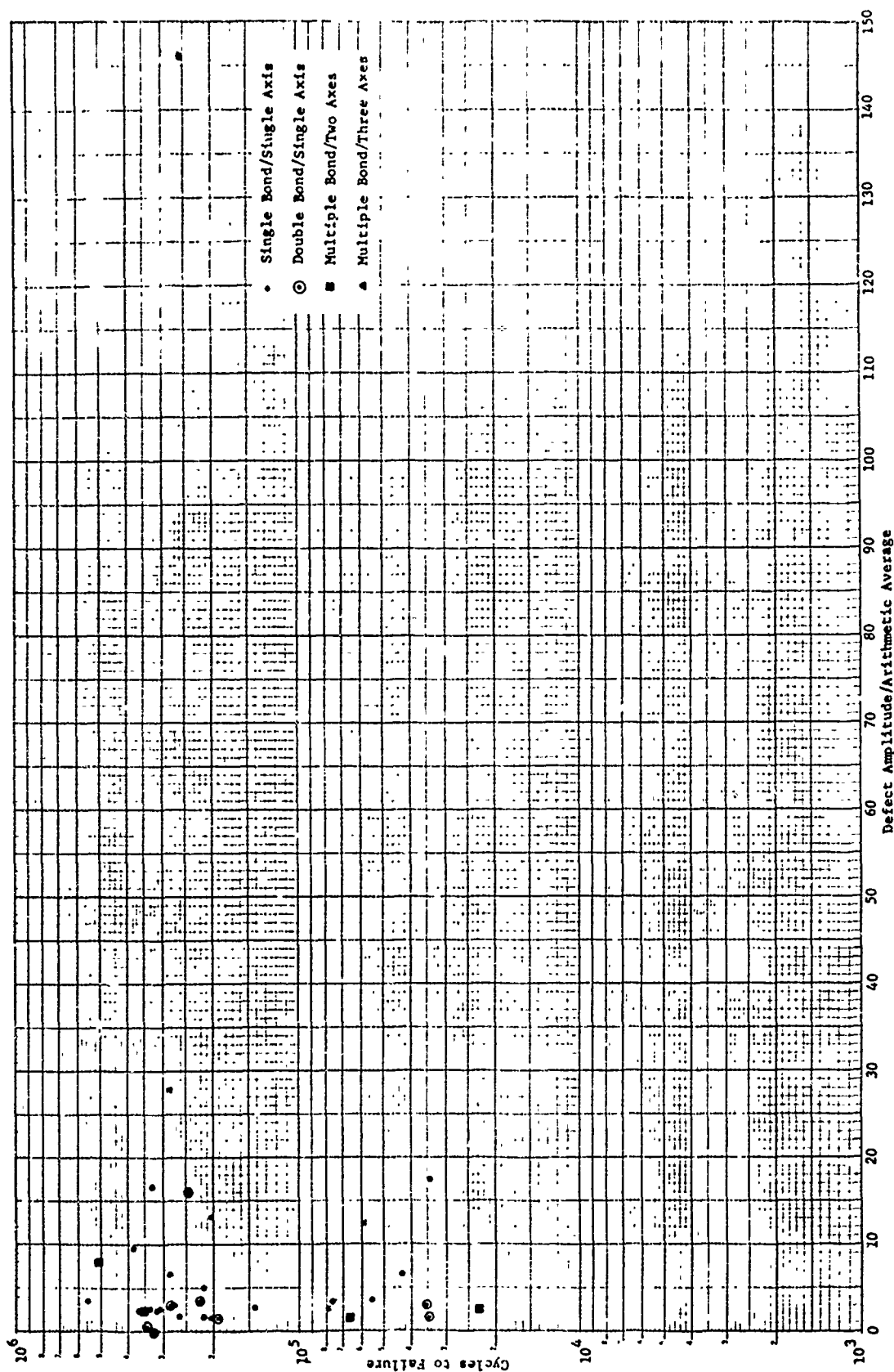


Figure 8.4 Fatigue Life vs Defect Amplitude/AA for Diffusion Bonded Specimens; with Surface-Initiated Failures (Stress Level = 110 ksi)

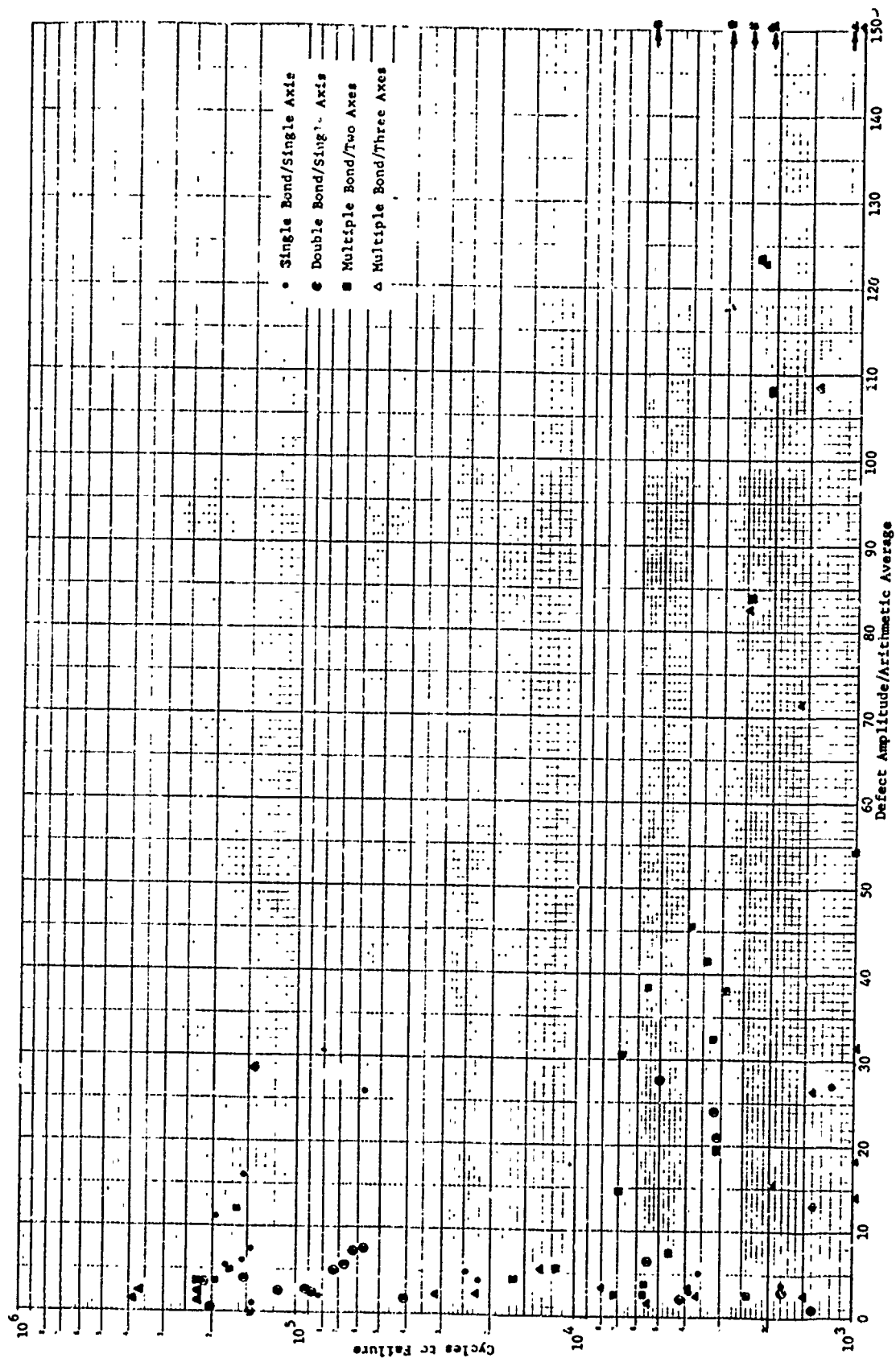


Figure 8.5 Fatigue Life vs Defect Amplitude/AA for Diffusion Bonded Specimens with Internally-Initiated Failures (Stress Level = 60 ksi)

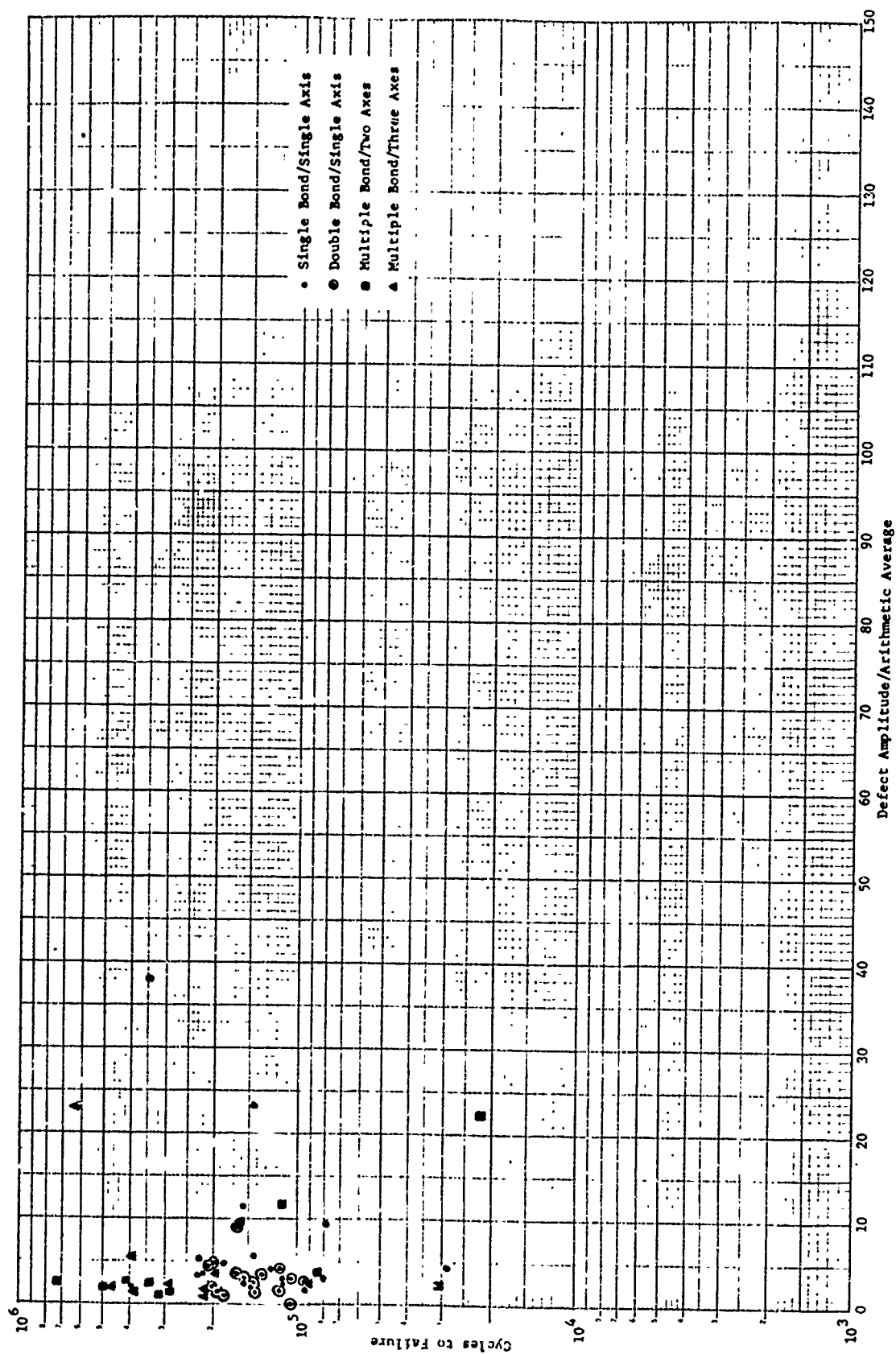


Figure 3.6 Fatigue Life vs Defect Amplitude/AA for Diffusion Bonded Specimens with Surface-Initiated Failures (Stress Level = 80 ksi)

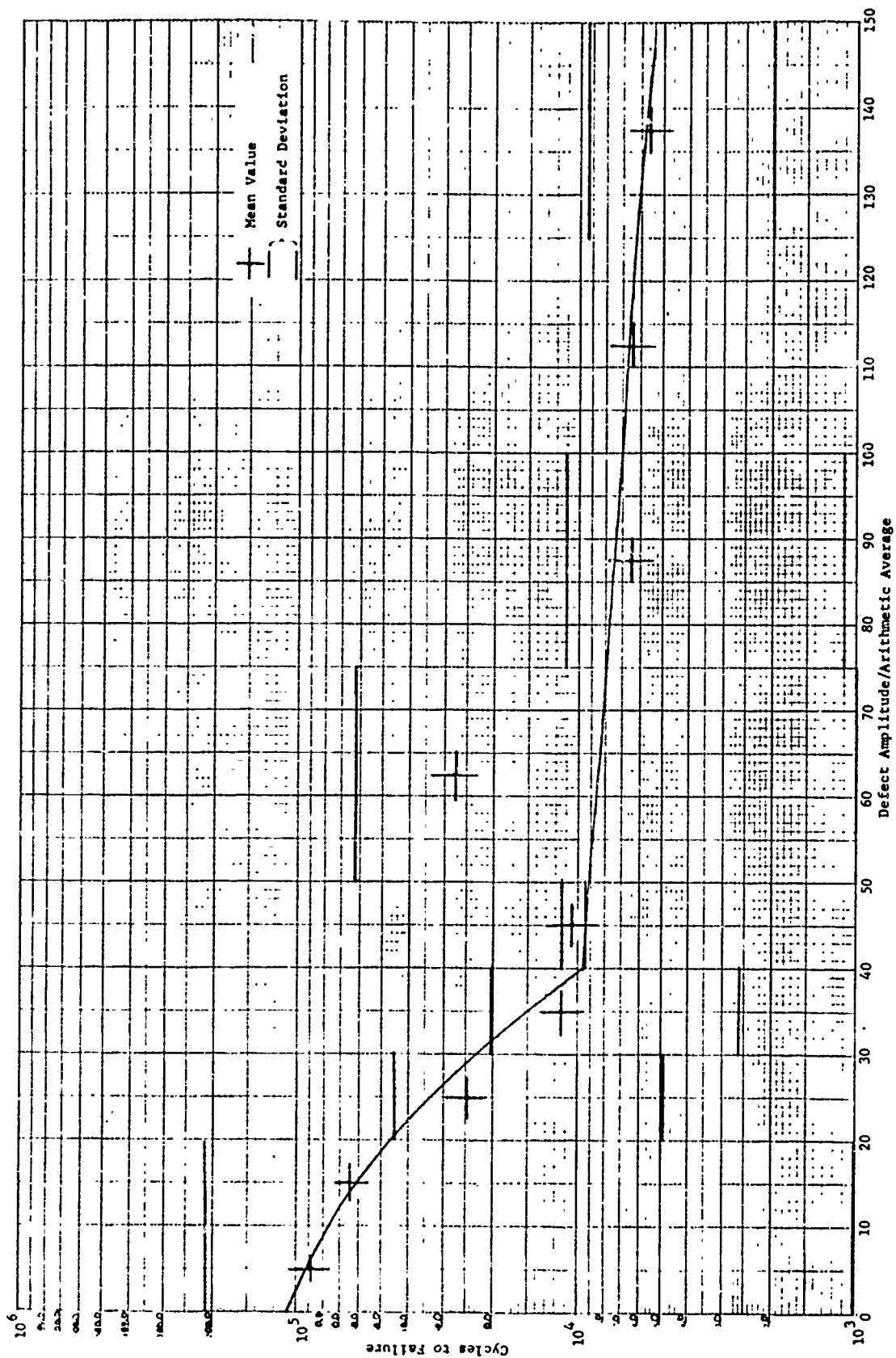


Figure 8.7 Statistical Analysis of Fatigue Life vs Defect Amplitude/AA  
(Stress Level = 110 ksi)



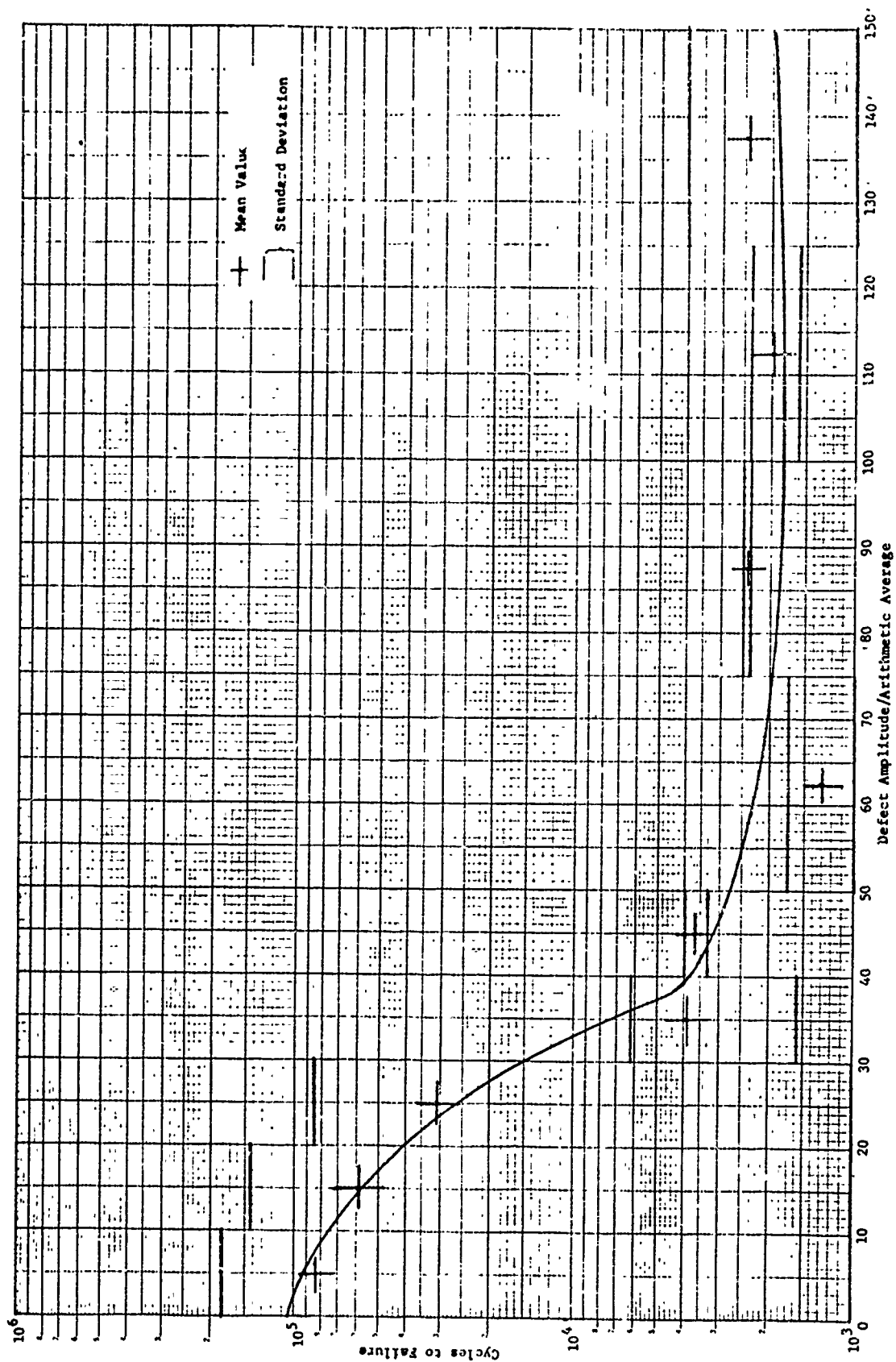


Figure 8.8 Statistical Analysis of Fatigue Life vs Defect Amplitude/AA  
(Stress Level = 80 ksi)

### 8.3 Fracture Analysis

#### 8.3.1 Scanning Electron Microscope Fractography

Figures 8.9 and 8.10 show low-magnification scanning electron micrographs of four fracture surfaces of 6-4 titanium representing four different thermal histories. Figure 8.9(a) depicts material from the 1" plate in the as-received condition. Figures 8.9(b), 8.10(a), and 8.10(b) show the fracture topography for material which had held for 6 hours at temperatures of 1700, 1735, and 1775°F, respectively. Although the as-received material shows a somewhat more irregular surface than the heat-soaked specimen, the basic texture is evident in all the specimens. The higher magnification (1000X) photomicrographs of Figures 8.11(a) and 8.11(b) show the mode of fracture to be primarily void coalescence for both the unheated material and the material which had been subjected to the highest temperature. The texture of the fracture network is coarser in the latter material than in the former. The two intermediate heat-soaking temperatures produced fracture networks which were intermediate to these two extremes in coarseness.

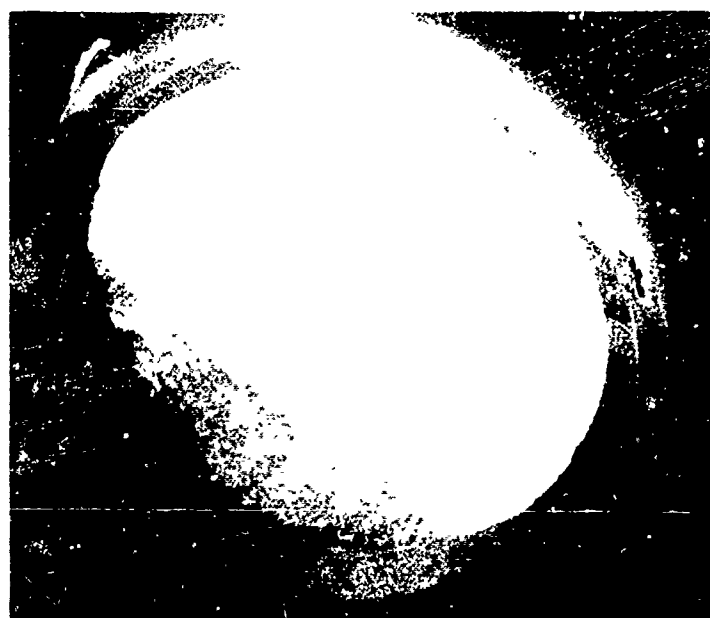
Figures 8.11 and 8.12 show the fracture topography for diffusion bonded specimens containing good bonds. The effect due to different primary alpha grain sizes between specimens, P4A1 and R4A3 on the texture of the fracture network can be observed in Figure 8.12. The texture is coarser in the larger grained material.

Both low-magnification and high-magnification scanning electron micrographs of a fracture surface where insufficient deformation was obtained during the bonding cycle is shown in Figure 8.14. Machining marks on the bonding surface are still visible in the low-magnification micrograph.

Micrographs showing the effects of cylindrical voids on fracture topography are shown in Figures 8.15, 8.16 and 8.17. Both low-magnification and high-magnification micrographs are shown. Thermal etching inside the holes can be observed in the high magnification photographs. Voids lying at the surface acted as crack initiators. The effect of a cylindrical void lying at the surface on the fracture topography can be seen in Figure 8.17. The effect of voids in the form of chamfered corners can be seen in Figures 8.18 and 8.19.

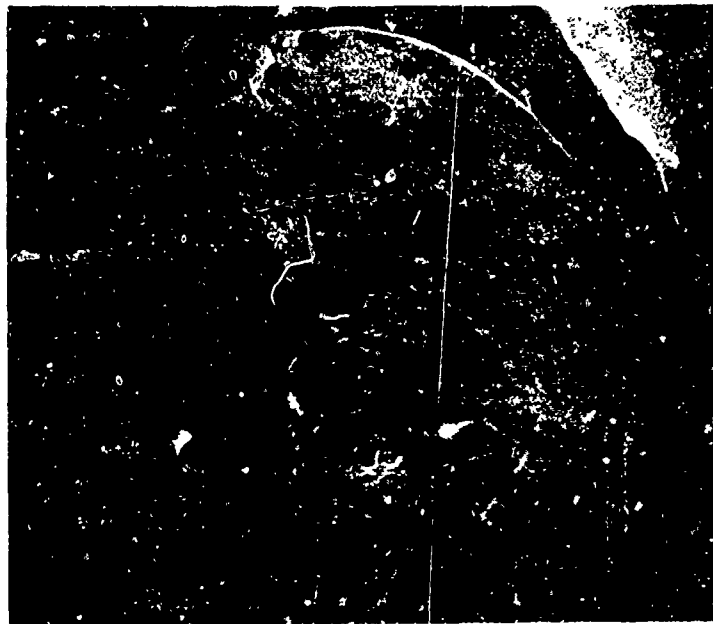


(a) D1-2, 1" Plate, As-Received Condition



(b) D2-1, 1" Plate, Heated at 1700°F for 6 Hours,  
Furnace Cooled

Figure 8.9 Scanning Electron Micrographs of Two Ti-6Al-4V Fracture Surfaces with Different Thermal Histories (10X)

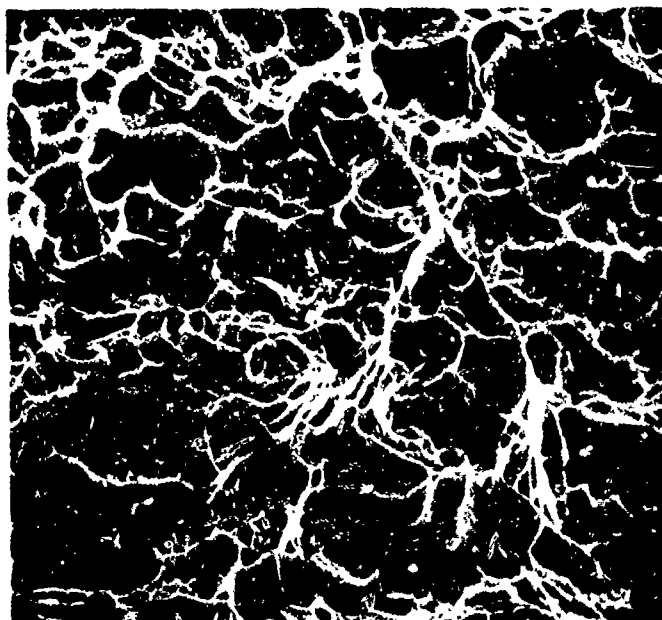


(a) E1-2, 1" Plate, Heated at 1735°F for 6 Hours, Furnace Cooled

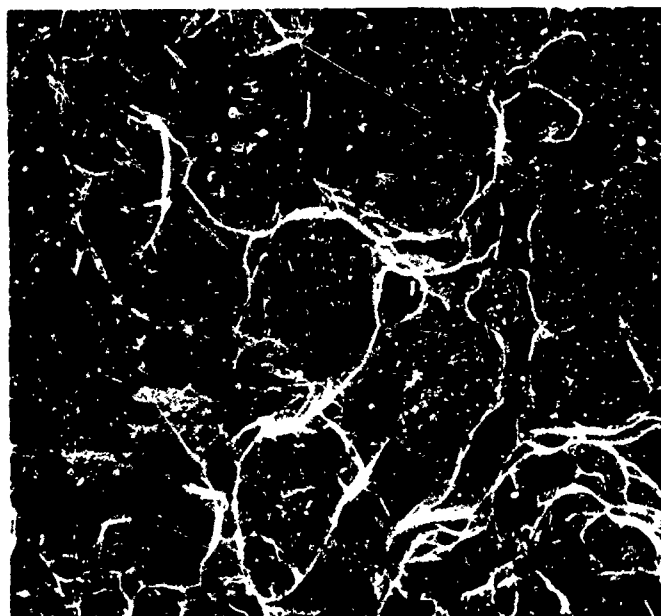


(b) F1-1, 1" Plate, Heated at 1775°F for 6 Hours, Furnace Cooled

Figure 8.10 Scanning Electron Micrographs of Two Ti-6Al-4V Fracture Surfaces with Different Thermal Histories (10X)

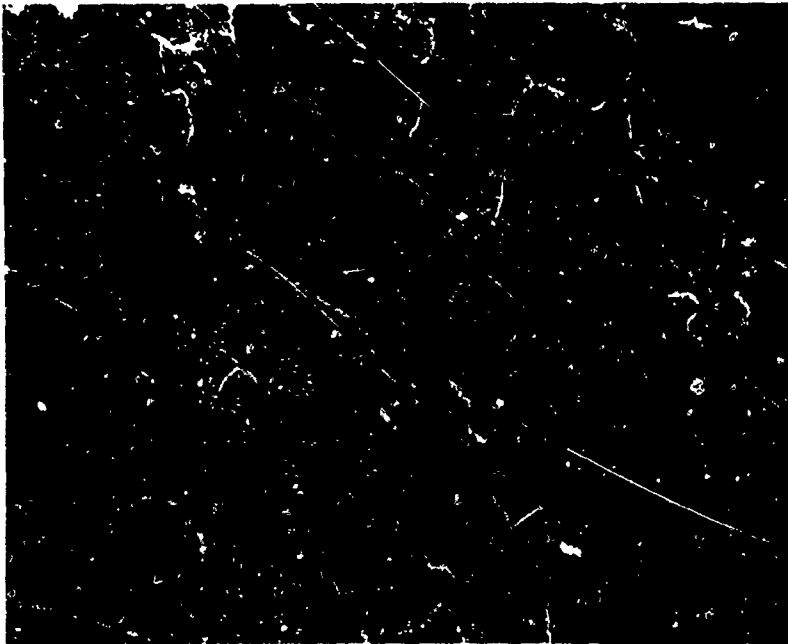


(a) D1-2, 1" Plate, As-Received Condition



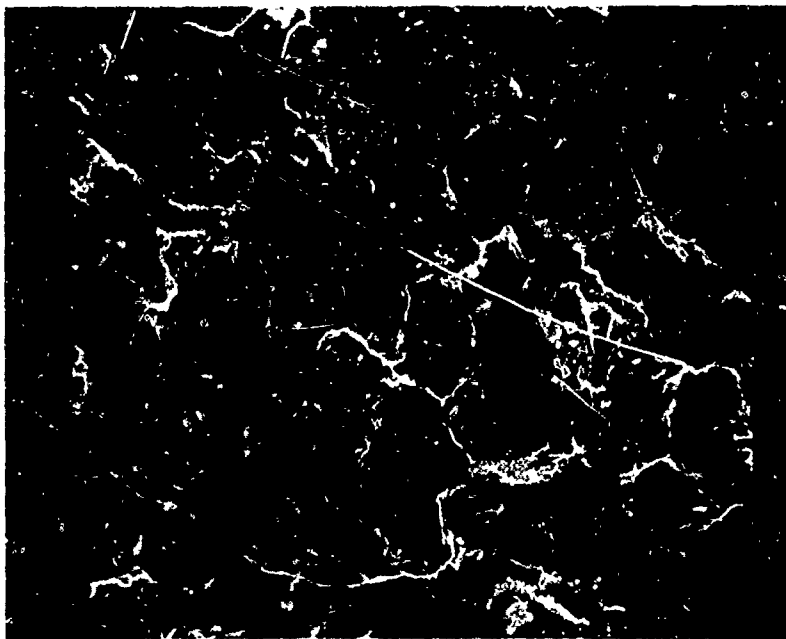
(b) F1-1, 1" Plate, Heated at 1775°F for 6 Hours,  
Furnace Cooled

Figure 8.11 Scanning Electron Micrographs of Two Ti-6Al-4V Fracture Surfaces (1000X)



1000X

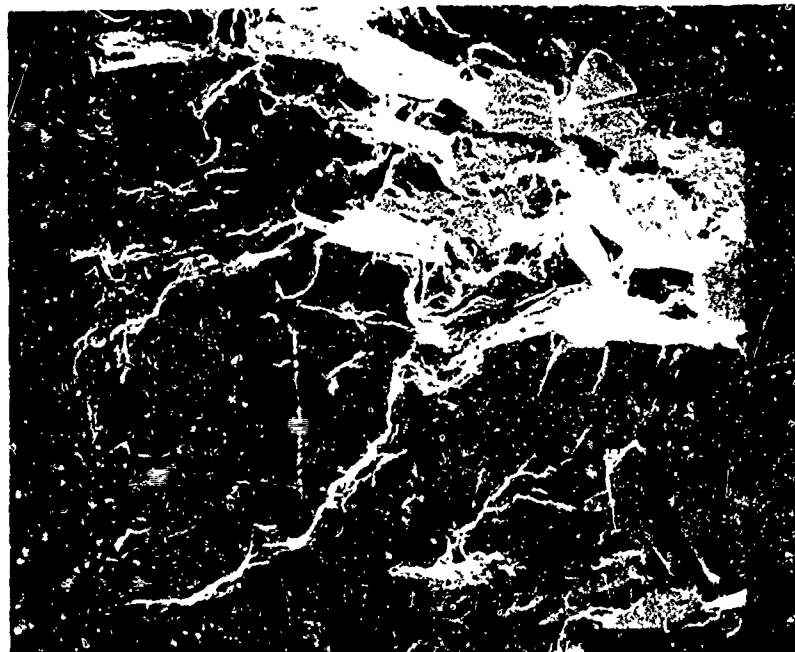
(a) M4A1



1000X

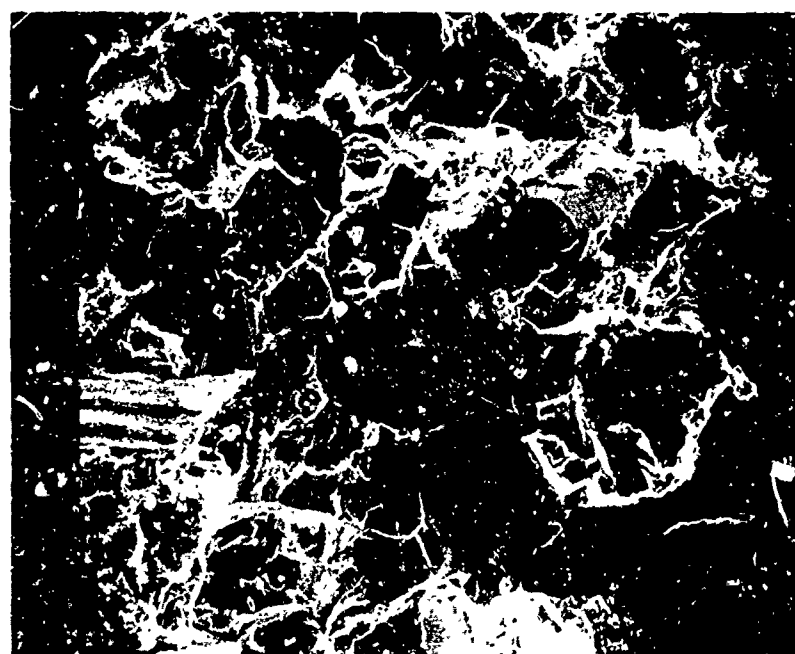
(b) P4B3

Figure 8.12 Scanning Electron Micrographs Showing Fracture Surfaces of Two Ti-6Al-4V Diffusion Bonded Specimens Containing Good Bonds



1000X

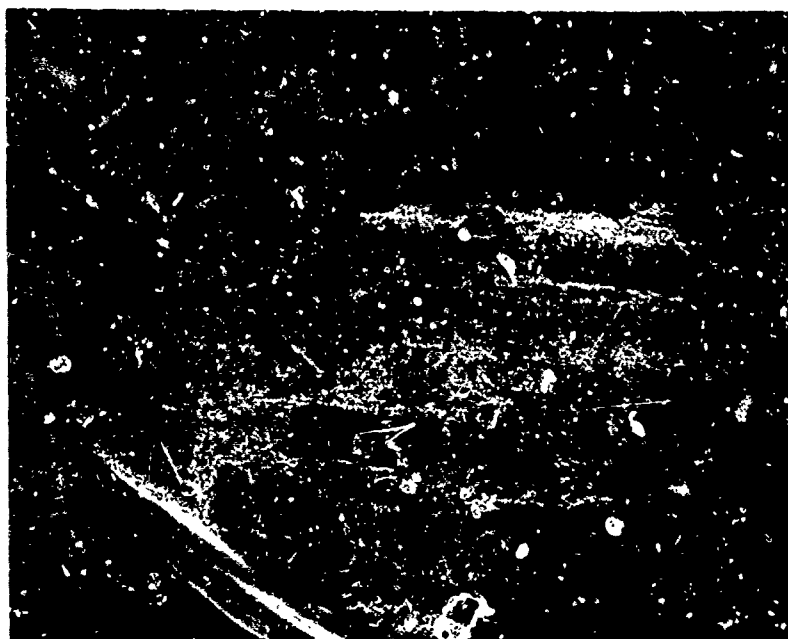
(a) P4A1



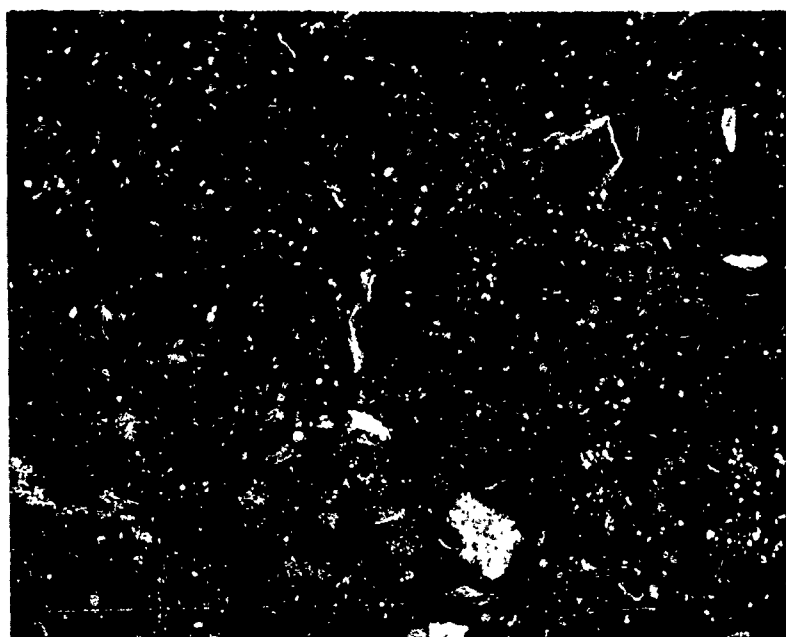
1000X

(b) R4A3

Figure 8.13 Scanning Electron Micrographs Showing Fracture Surfaces of Two Ti-6Al-4V Diffusion Bonded Specimens with Different Primary Alpha Grain Sizes



12X

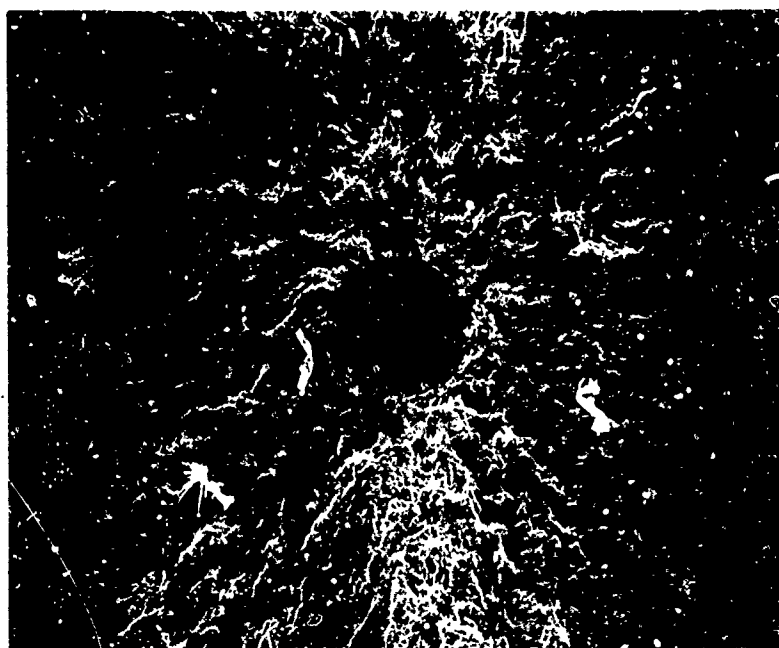


1000X

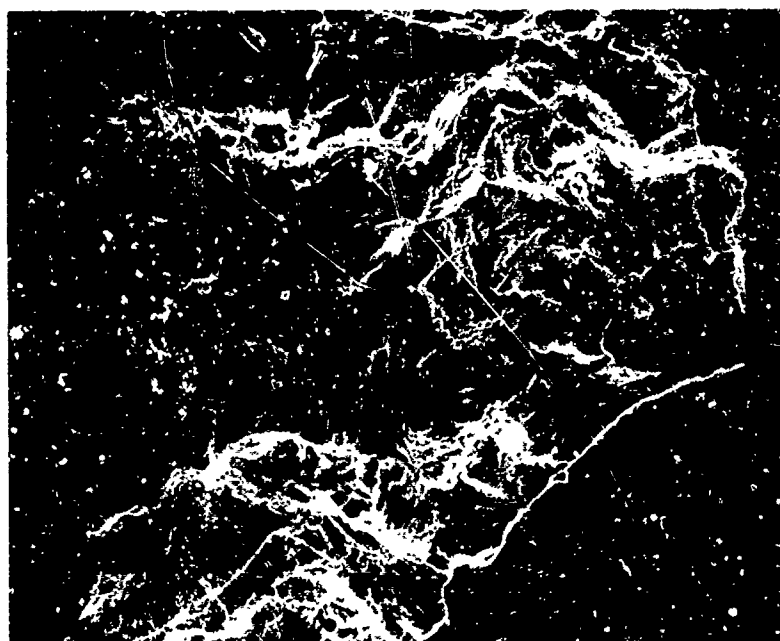
(03B1)

Figure .14 Scanning Electron Micrographs Showing the Fracture Surface of a Diffusion Bonded Specimen having a Bad Bond



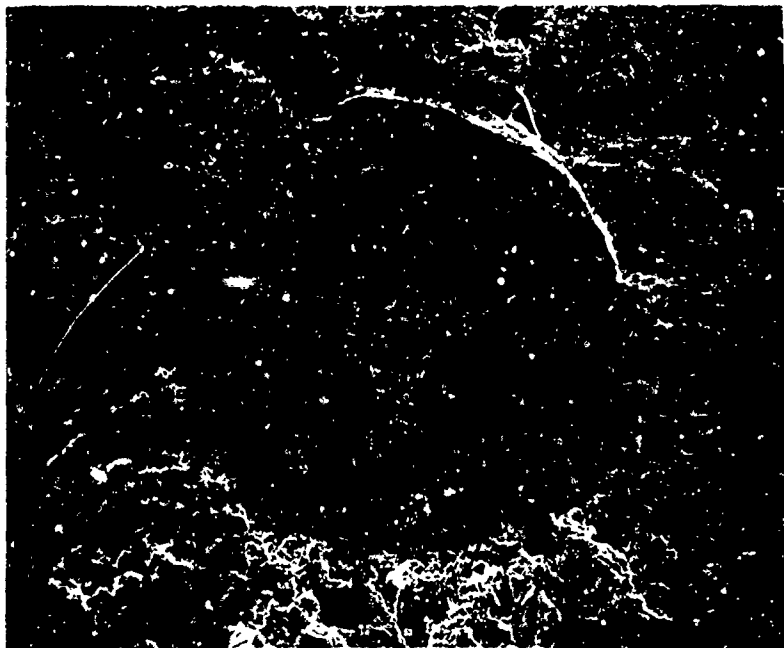


100X

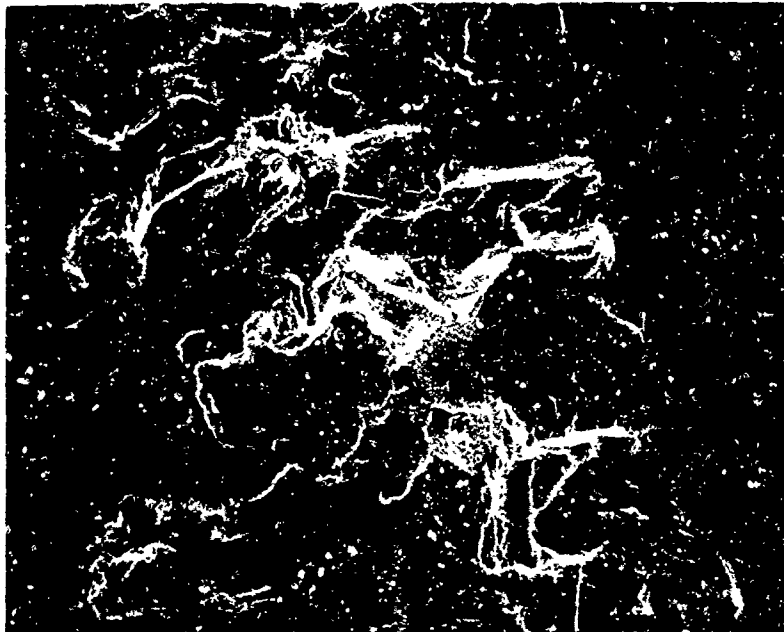


1000X

Figure 8.15 SEM Fractographs of Diffusion Bonded Specimen S4E3  
Containing a Cylindrical Void of .0065" Diameter

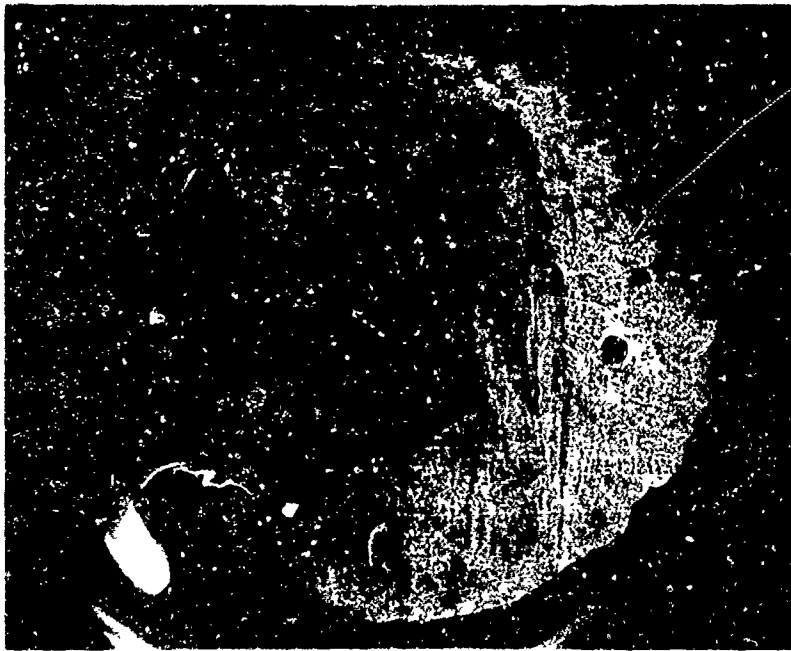


100X

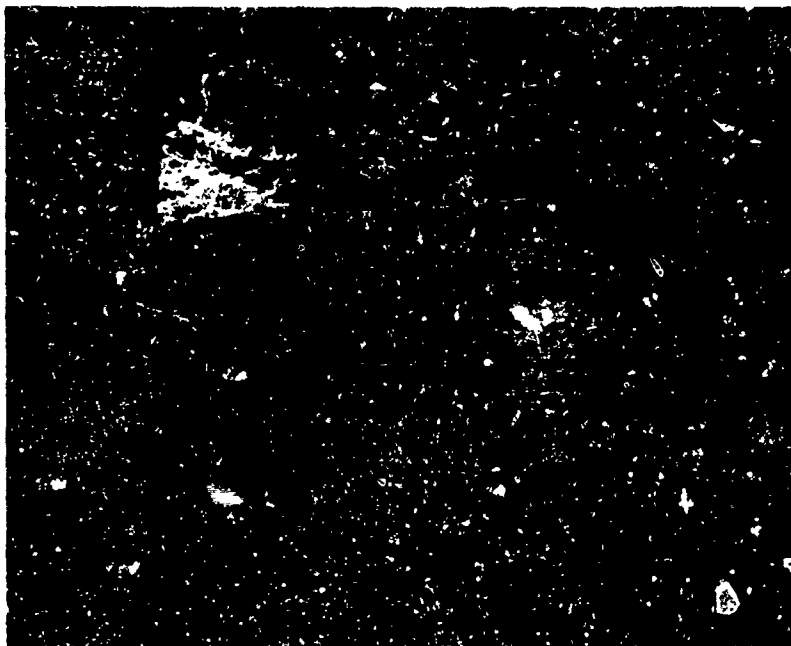


1000X

Figure 8.16 SEM Fractographs of Diffusion Bonded Specimen  
U5B1 Containing a Cylindrical Void of .020"  
Diameter

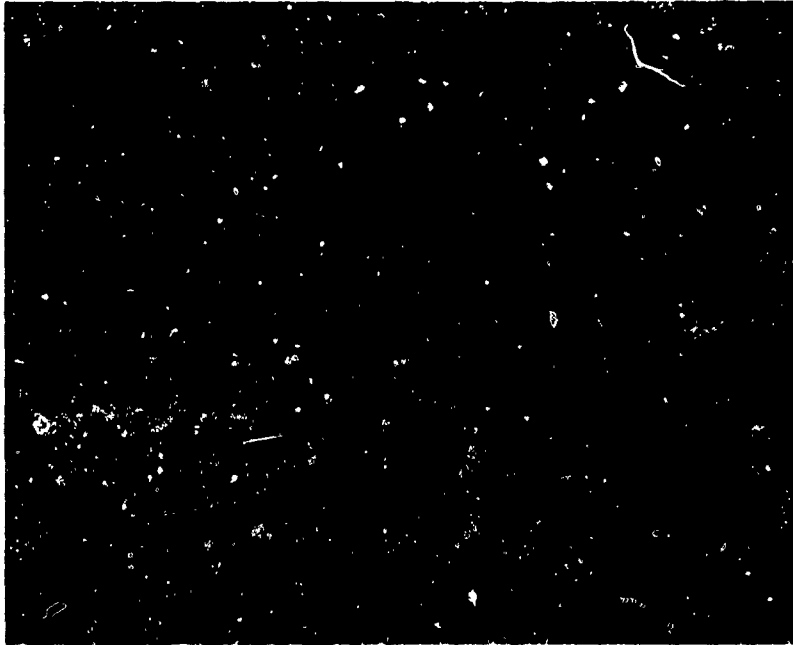


10X

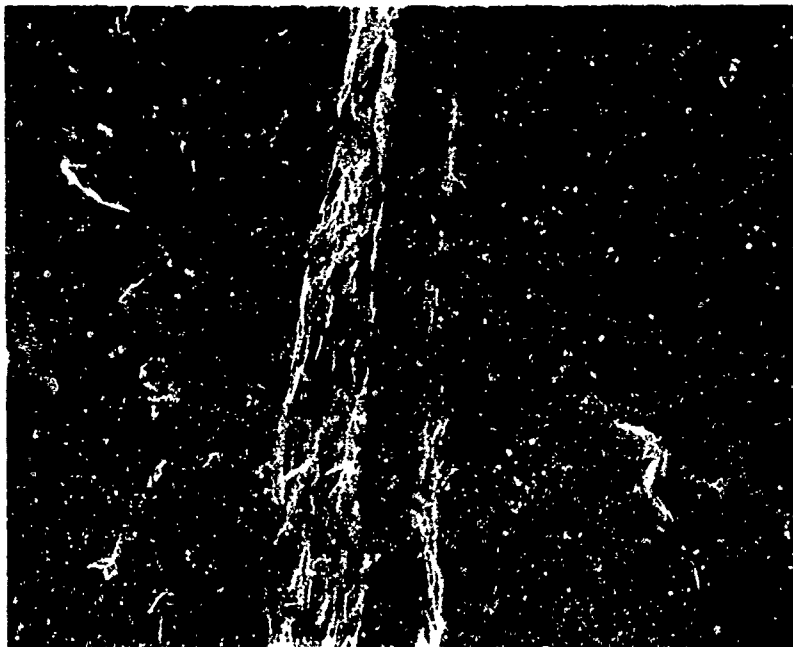


100X

Figure 8.17 SEM Fractographs of Diffusion Bonded Specimen  
T4Al Containing Four Cylindrical Voids of .010"  
Diameter

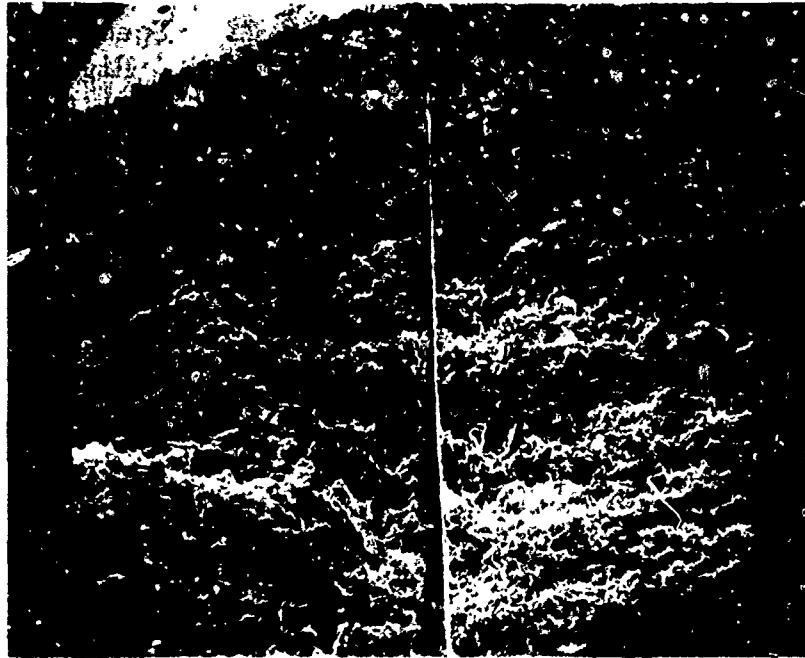


100X

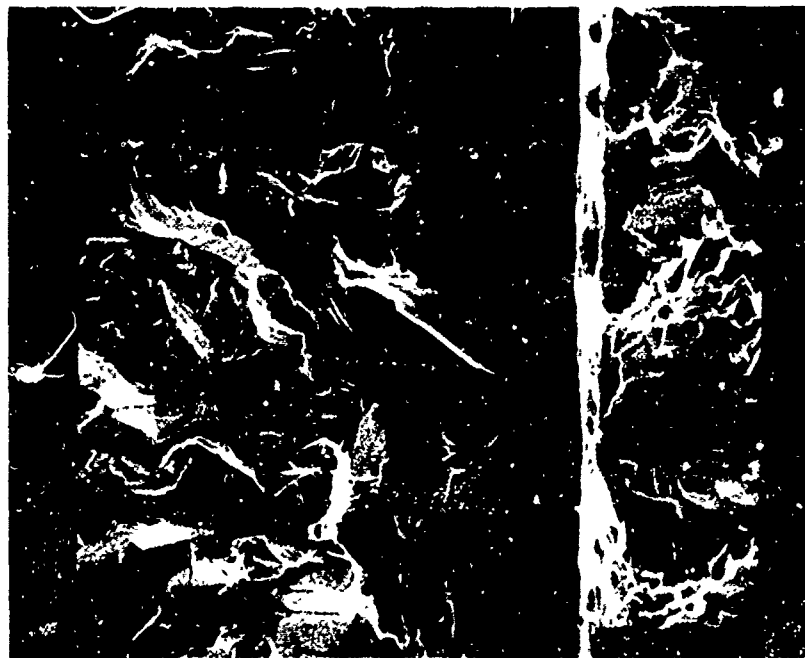


1000X

Figure 8.18 SEM Fractographs of Diffusion Bonded Specimen  
S5A1 Containing a Void in the  $\frac{1}{2}$  in of a Chamfer



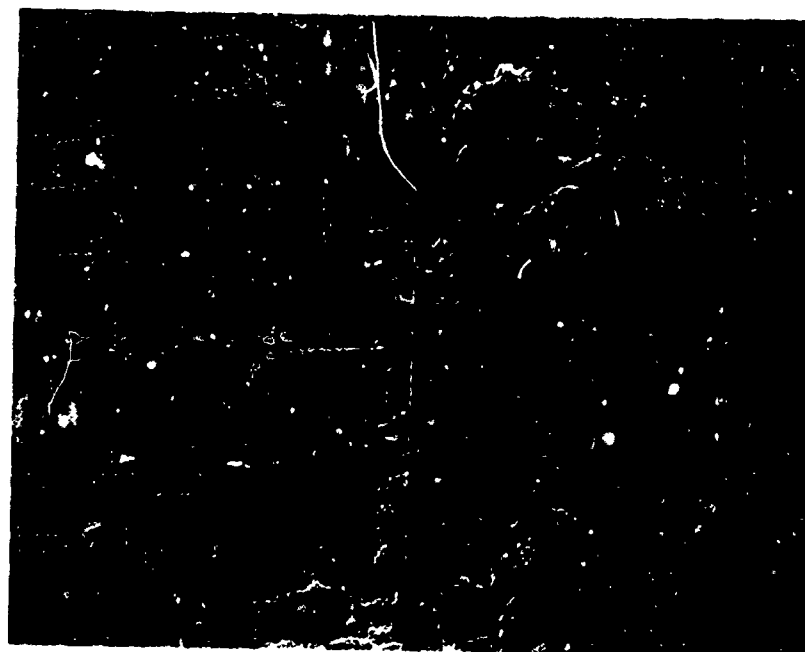
100X



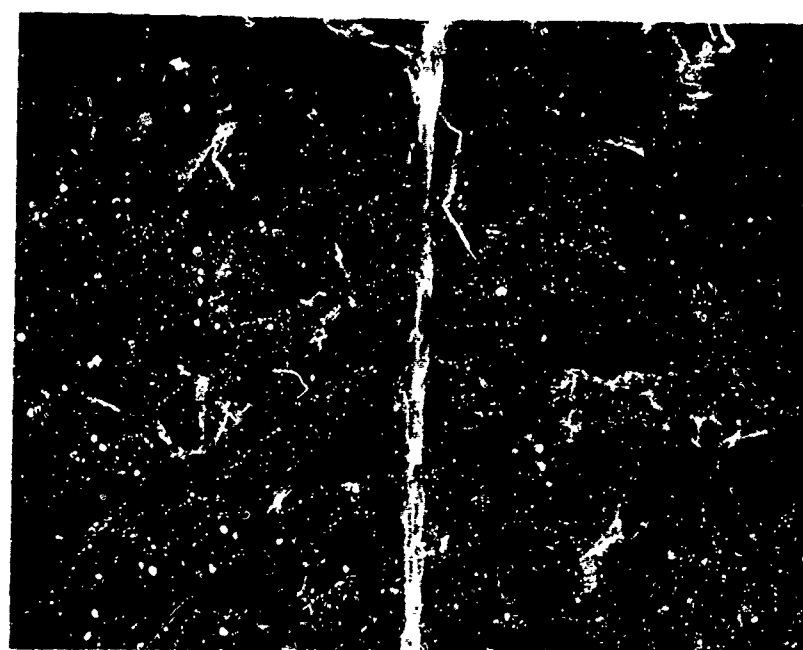
1000X

Figure 8.19 SEM Fractographs of Diffusion Bonded Specimen  
T5B1 Containing a Void in the Form of a Chamfer

The effects of different types of surface contamination are shown in Figures 8.20, 8.21, and 8.22. Specimen V5A1 contained an alpha case layer at the bond line. High-magnification micrographs show a crack running almost parallel to the bond line indicating the brittle nature of the alpha case layer. In Figure 8.21, stainless steel powder inclusions can still be observed in the fractured material. Some of the stainless steel powder reacts with the Ti-6Al-4V material as will be shown in Section 8.33. The low-magnification micrograph shows the origin of fracture at the hole. In Figure 8.22,  $\text{SiO}_2$  powder inclusions can be observed in the fractured material. The  $\text{SiO}_2$  powder reacted very little with the surrounding Ti-6Al-4V.



100X

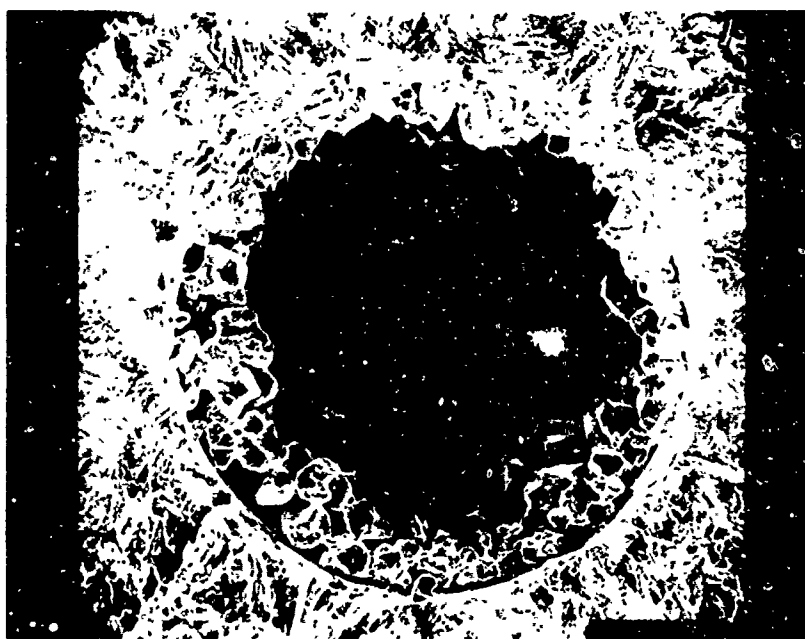


1000X

Figure 8.20 SEM Fractographs of Diffusion Bonded Specimen V5A1 Containing an Alpha Case Layer



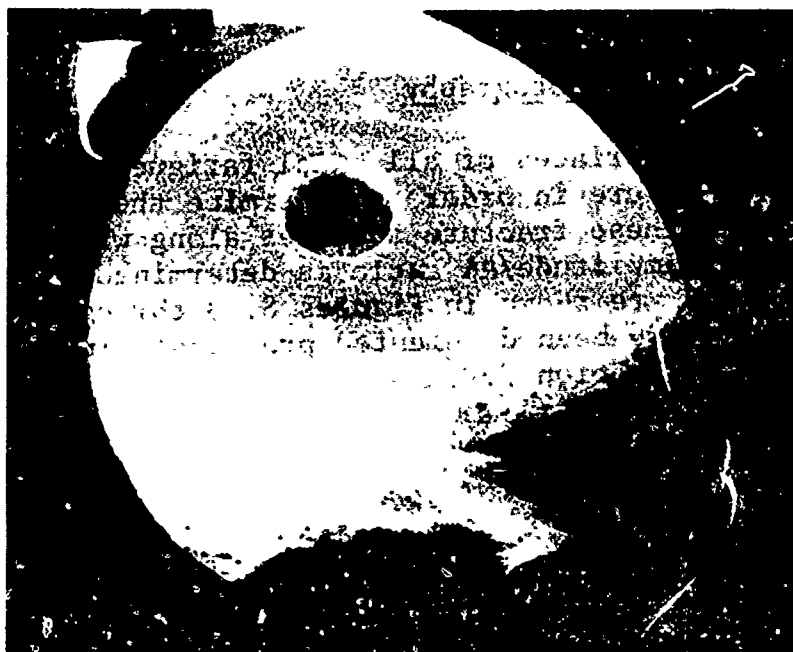
b) 13X



a) 200X

Figure 8.21 SEM Fractographs of Diffusion Bonded Specimen W3-A2  
Containing Stainless Steel Powder Inclusions





13X

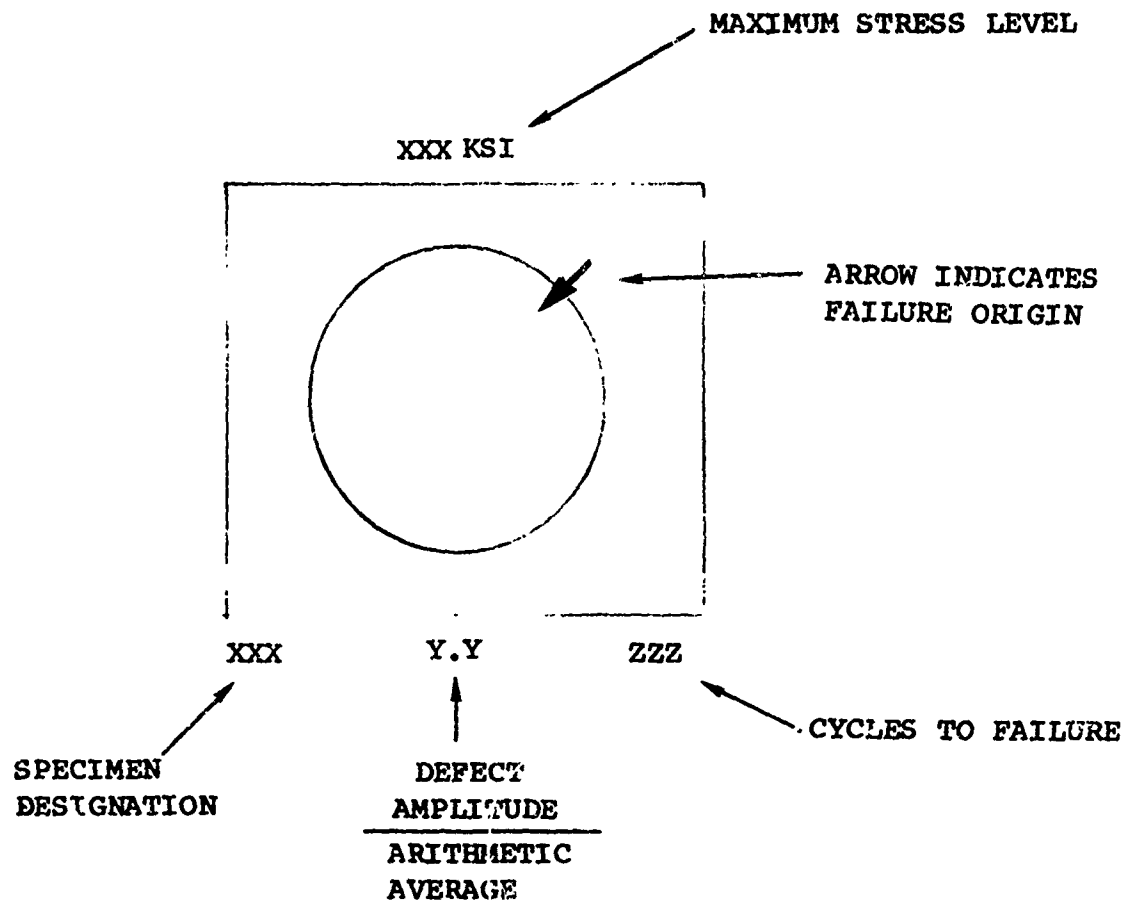


50X

Figure 8.22 SEM Fractographs of Diffusion Bonded Specimen X5A2 Containing  $\text{SiO}_2$  Powder Inclusions

### 8.3.2 Optical Fractography

The fracture surfaces of all axial fatigue specimens were examined after failure in order to determine the origin of these failures. These fracture surfaces along with fatigue lives and defect amplitude/AA ratio as determined from signal averaging results are shown in Figures 8.23 through 8.70. Failure origins have been documented previously in the tabulated data of Section 7.



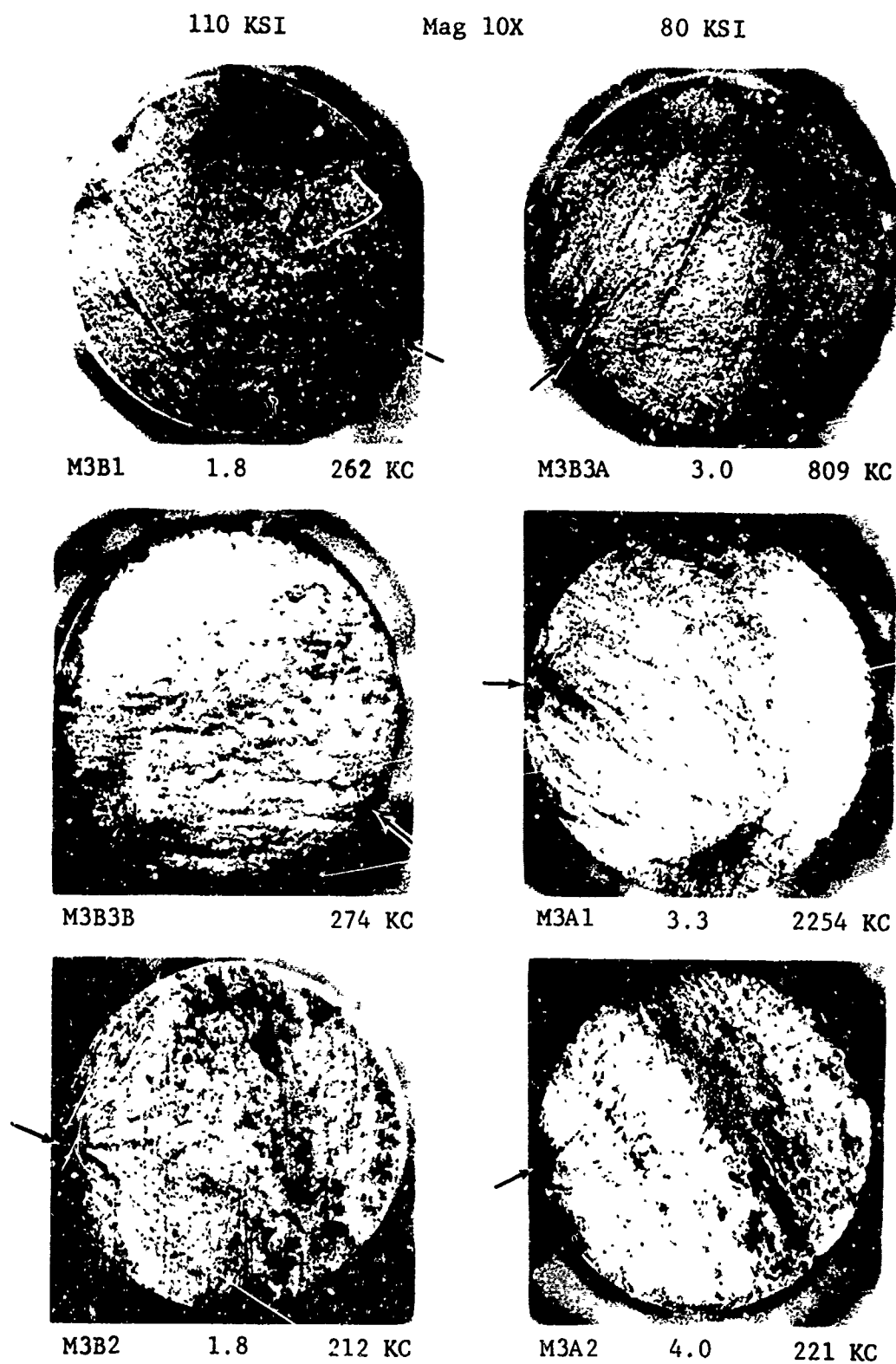


Figure 8.23 Fracture Surfaces of Failed Fatigue Specimens Series M3-Single Joint Optimum Diffusion Bonded with No Intentional Defects

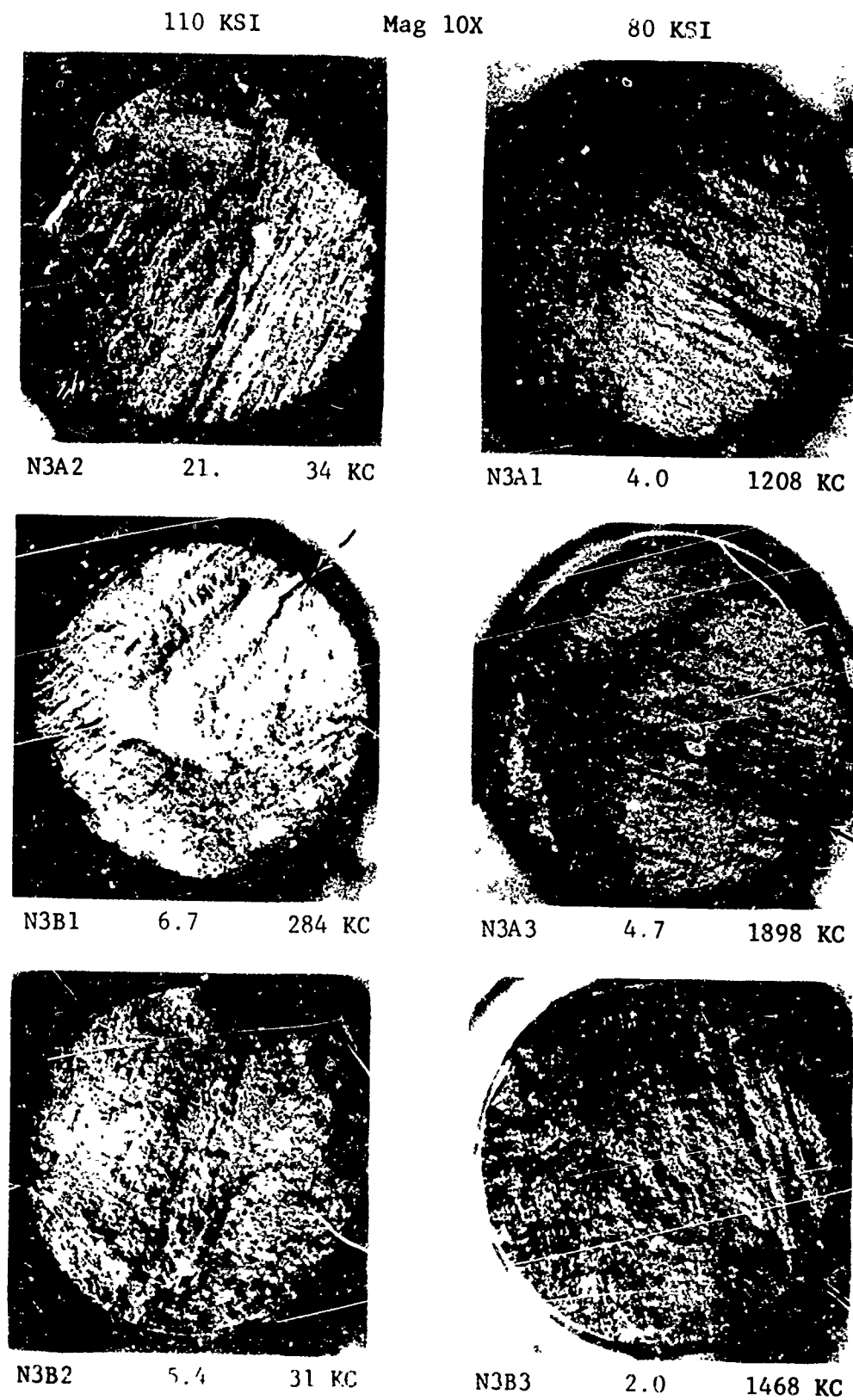


Figure 8.24 Fracture Surfaces of Failed Fatigue Specimens Series N3-  
Single Joint Diffusion Bonded with 2.7% Deformation

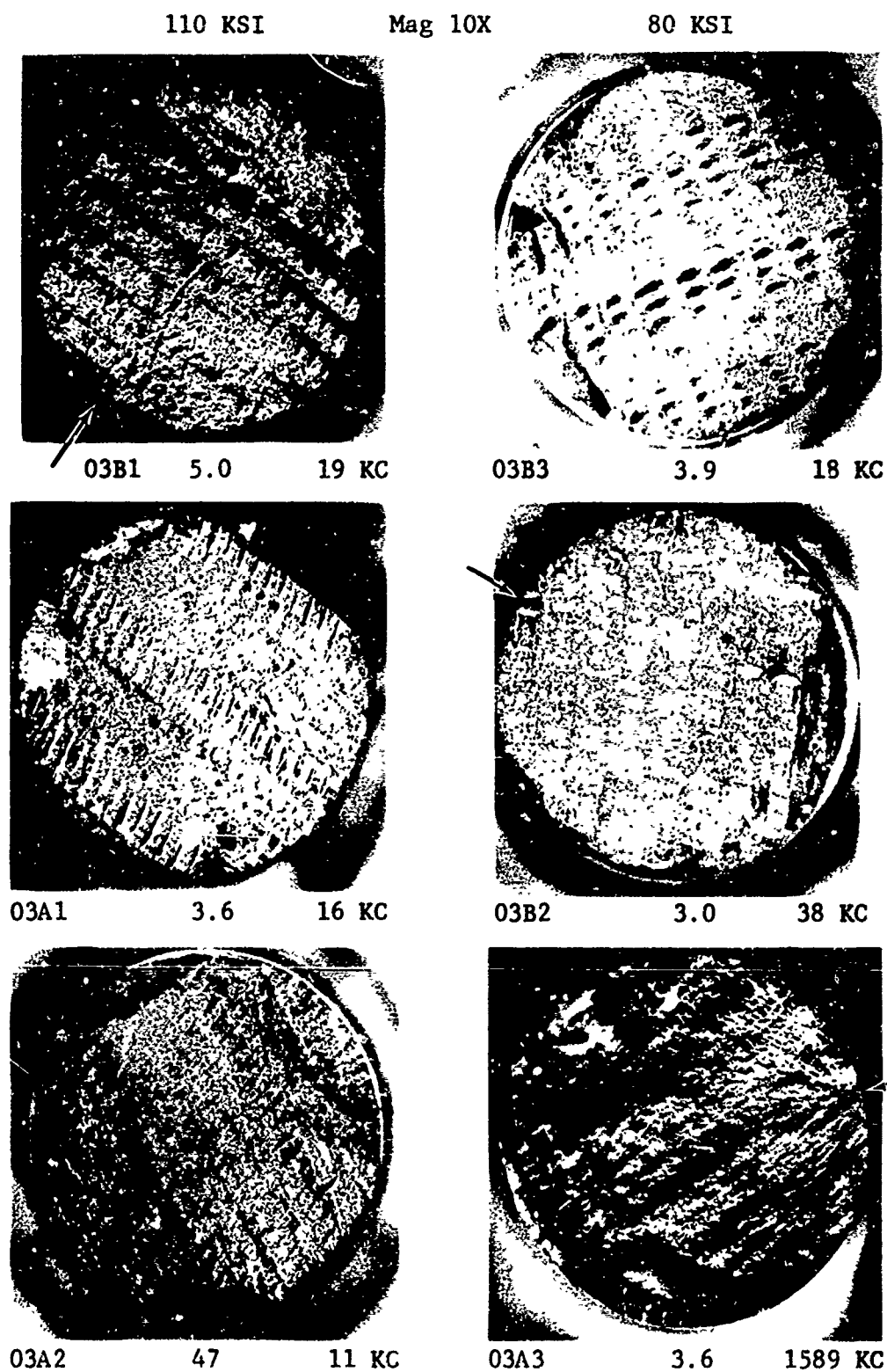


Figure 8.25 Fracture Surfaces of Failed Fatigue Specimens Series 03-  
Single Joint Diffusion Bonded with 1.5% Deformation

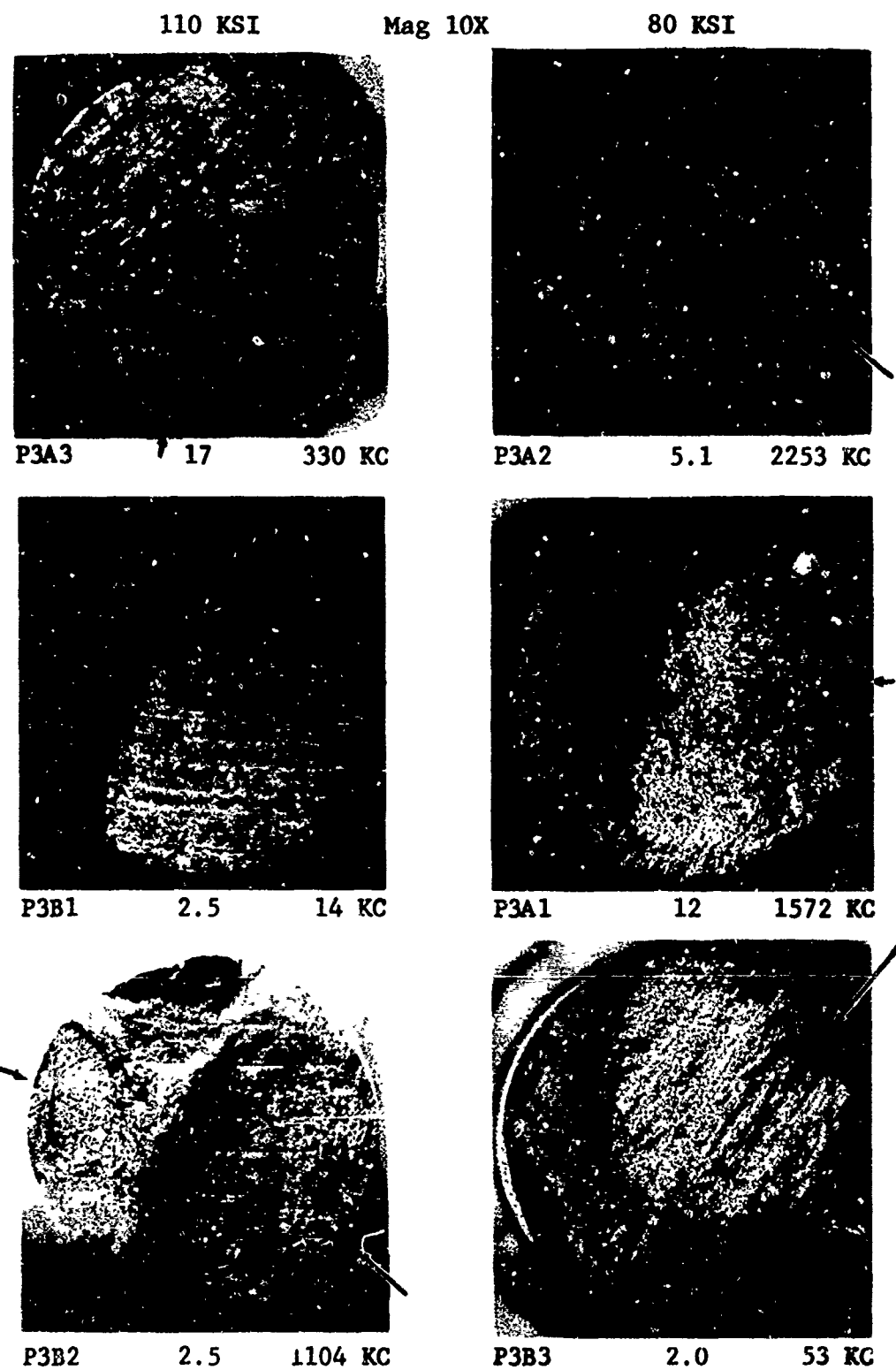


Figure 8.26 Fracture Surfaces of Failed Fatigue Specimens Series P3-  
Single Joint Diffusion Bonded - ASTM Grain Size No. 10

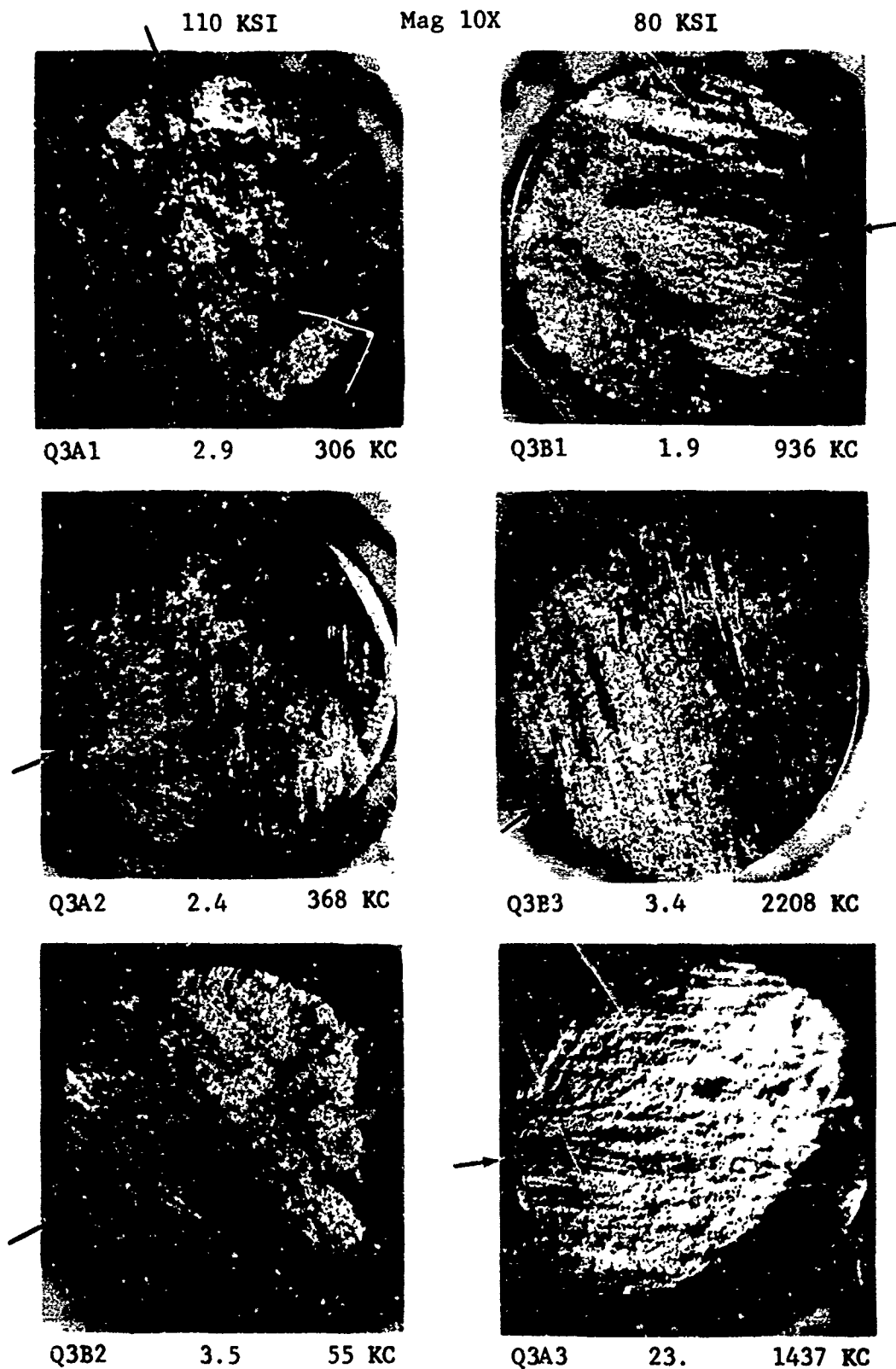


Figure 8.27 Fracture Surfaces of Failed Fatigue Specimens Series Q3-  
Single Joint Diffusion Bonded - ASTM Grain Size No. 9

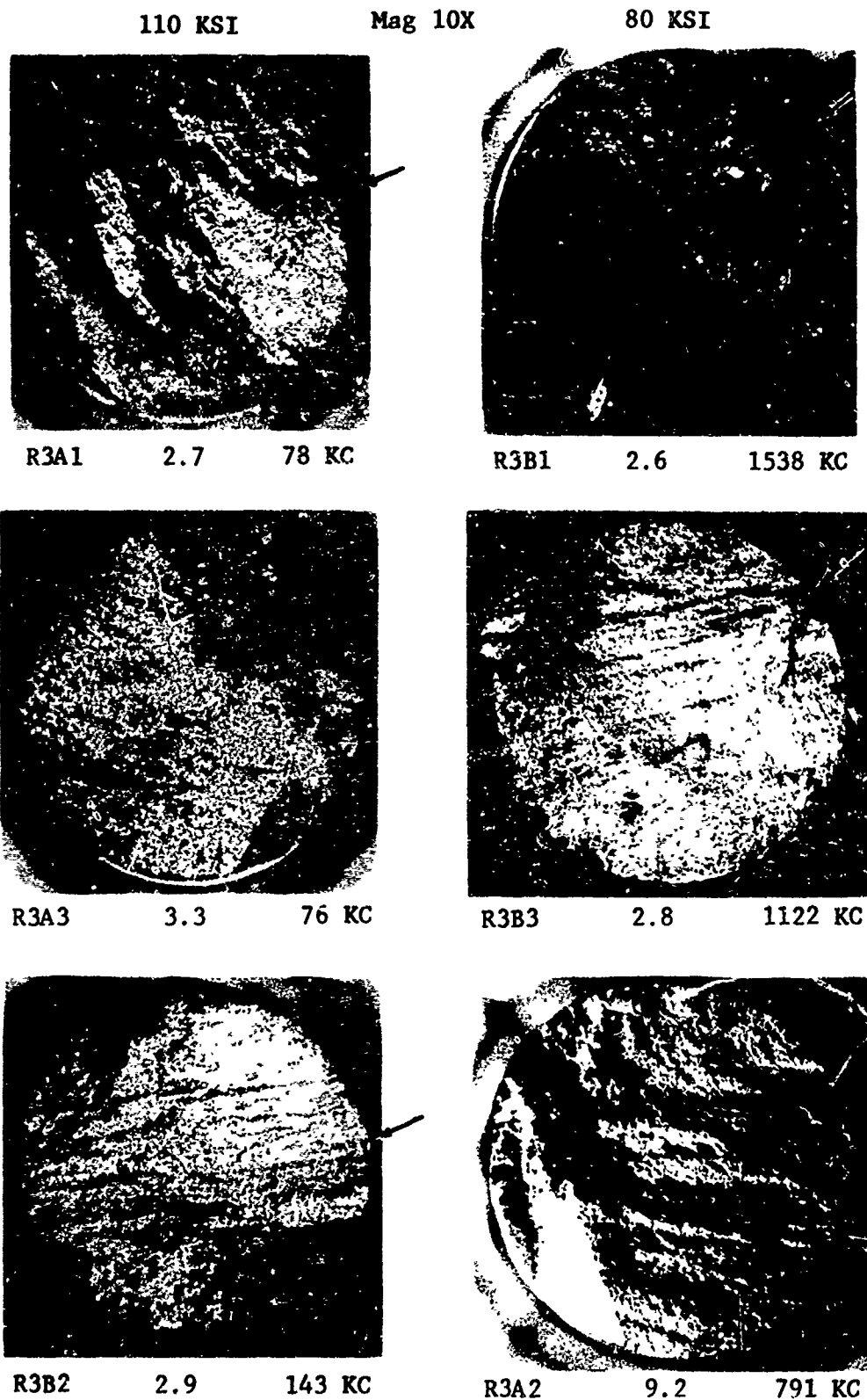


Figure 8.28 Fracture Surfaces of Failed Fatigue Specimens Series R3-  
Single Joint Diffusion Bonded - ASTM Grain Size No. 7.5



110 KSI

Mag 10X

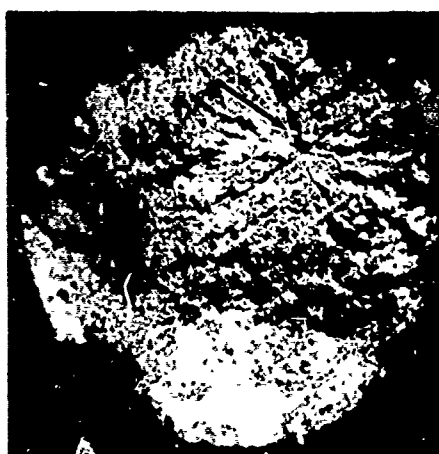
80 KSI



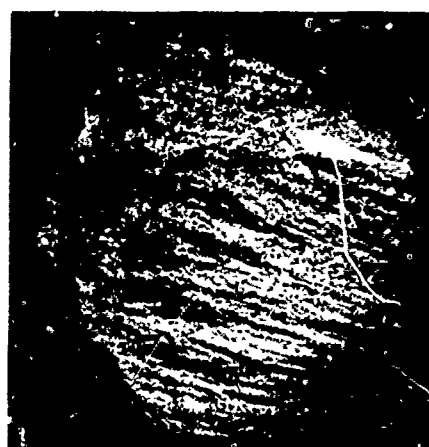
S3A2 - 165 KC



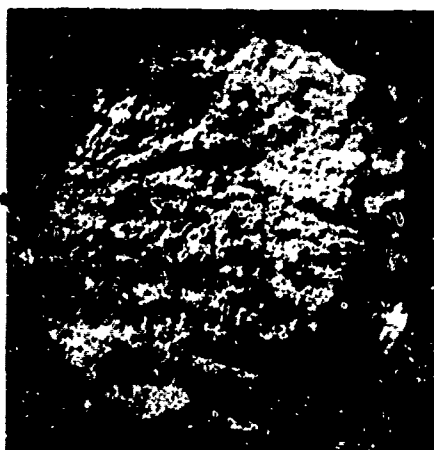
S3A1 - 1540 KC



S3B1 8.4 339 KC



S3A3 - 1137 KC



S3B3 5.0 213 KC



S3B2 1.0 1429 KC

Figure 8.29 Fracture Surfaces of Failed Fatigue Specimens Series S3-  
Single Joint Diffusion Bonded with .0065" Dia. Surface Void

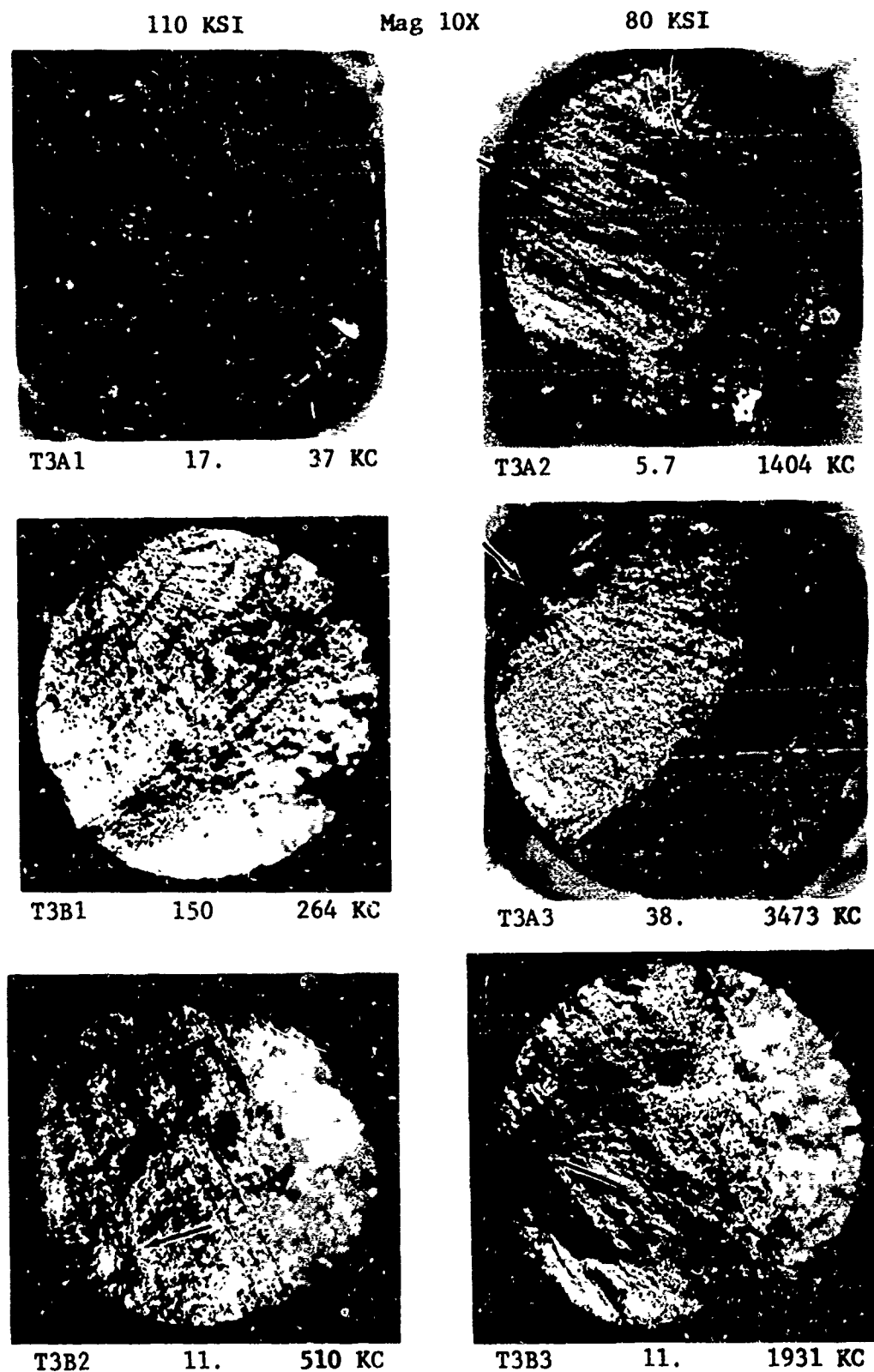


Figure 8.30 Fracture Surfaces of Failed Fatigue Specimens Series T3-  
Single Joint Diffusion Bonded with .01" Dia. Surface Void

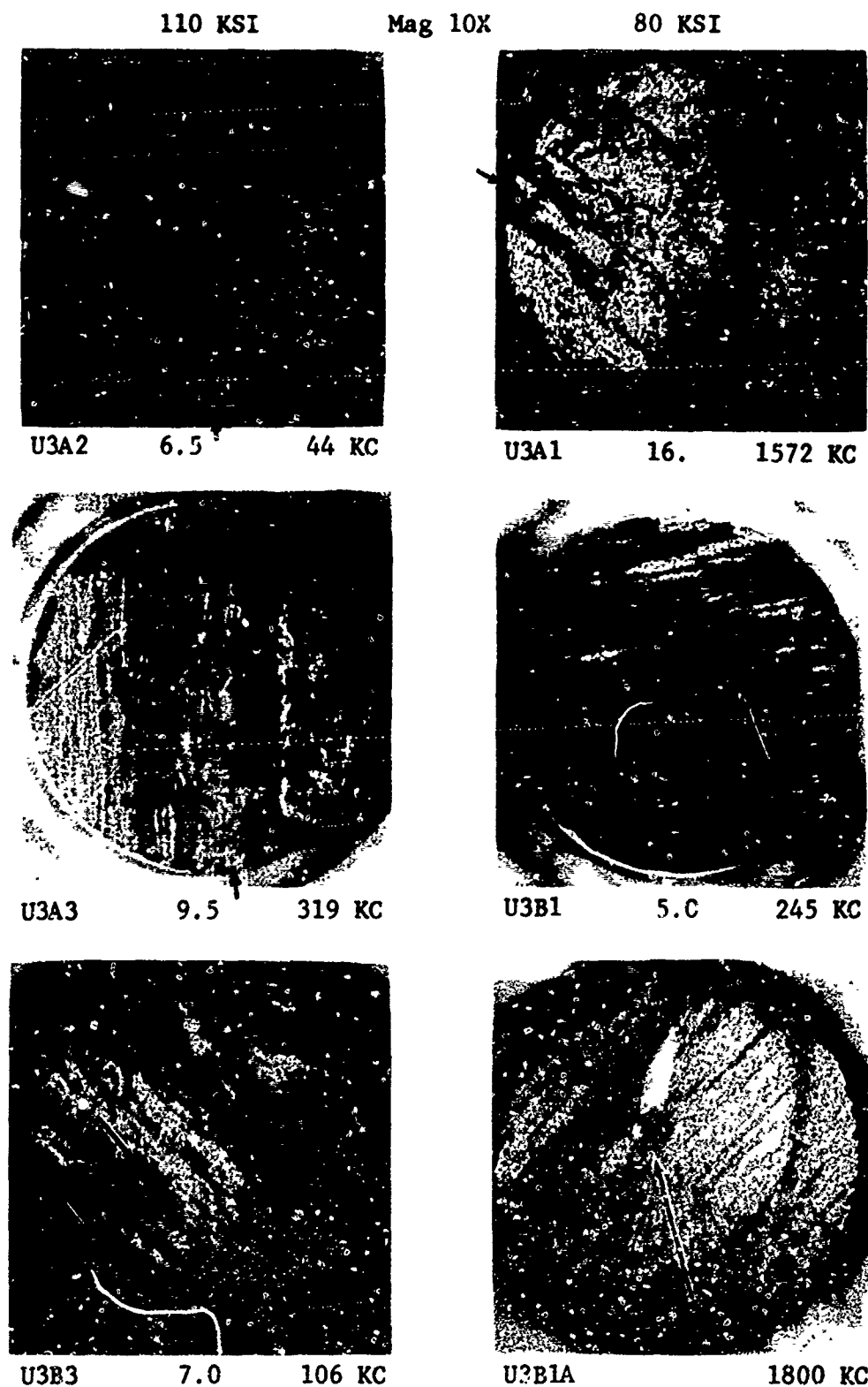


Figure 8.31 Fracture Surfaces of Failed Fatigue Specimens Series U3-  
Single Joint Diffusion Bonded with .02" Dia. Surface Void

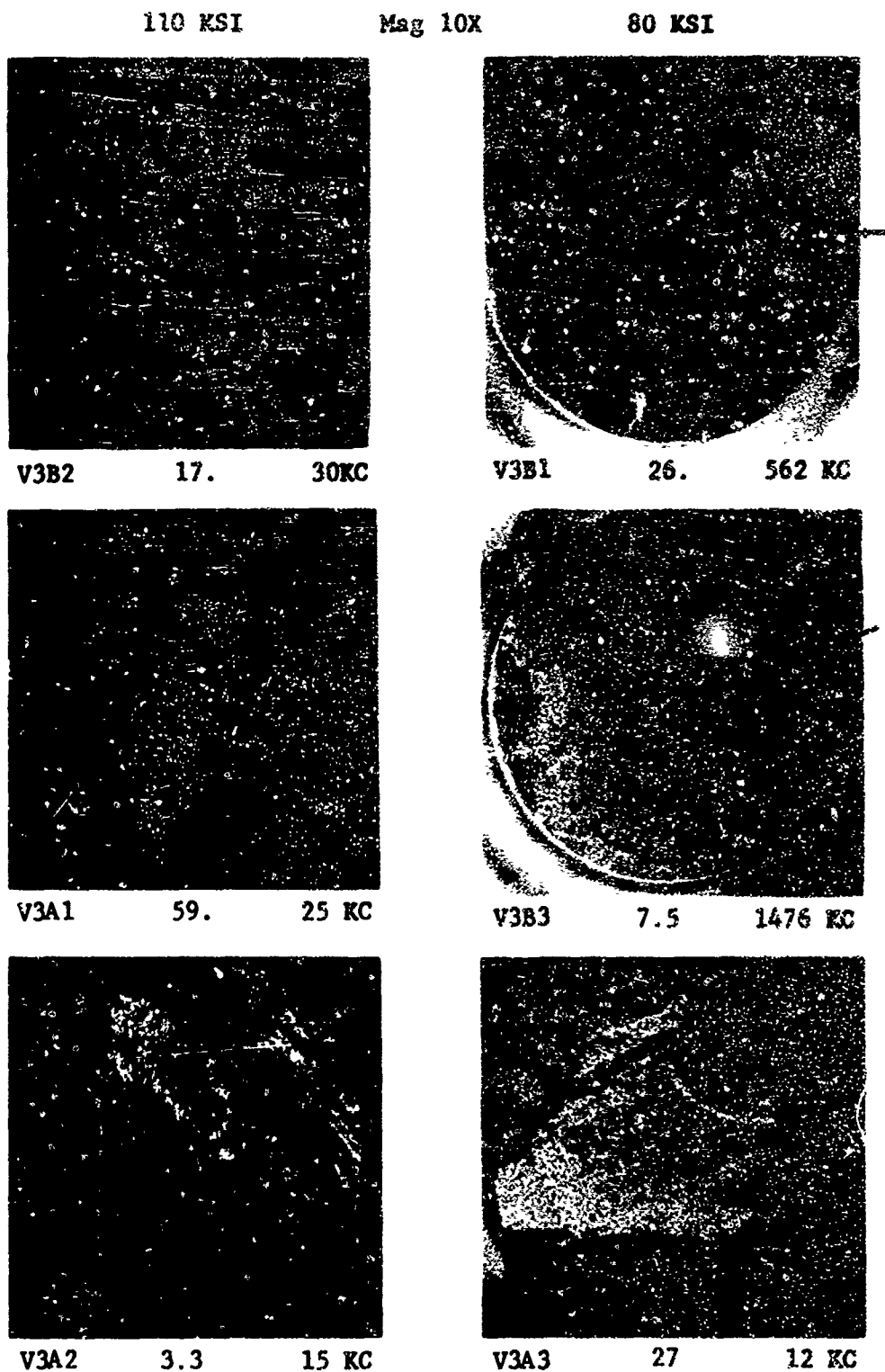


Figure 8.32 Fracture Surfaces of Failed Fatigue Specimens Series V3-  
Single Joint Diffusion Bonded with Alpha Case Defect

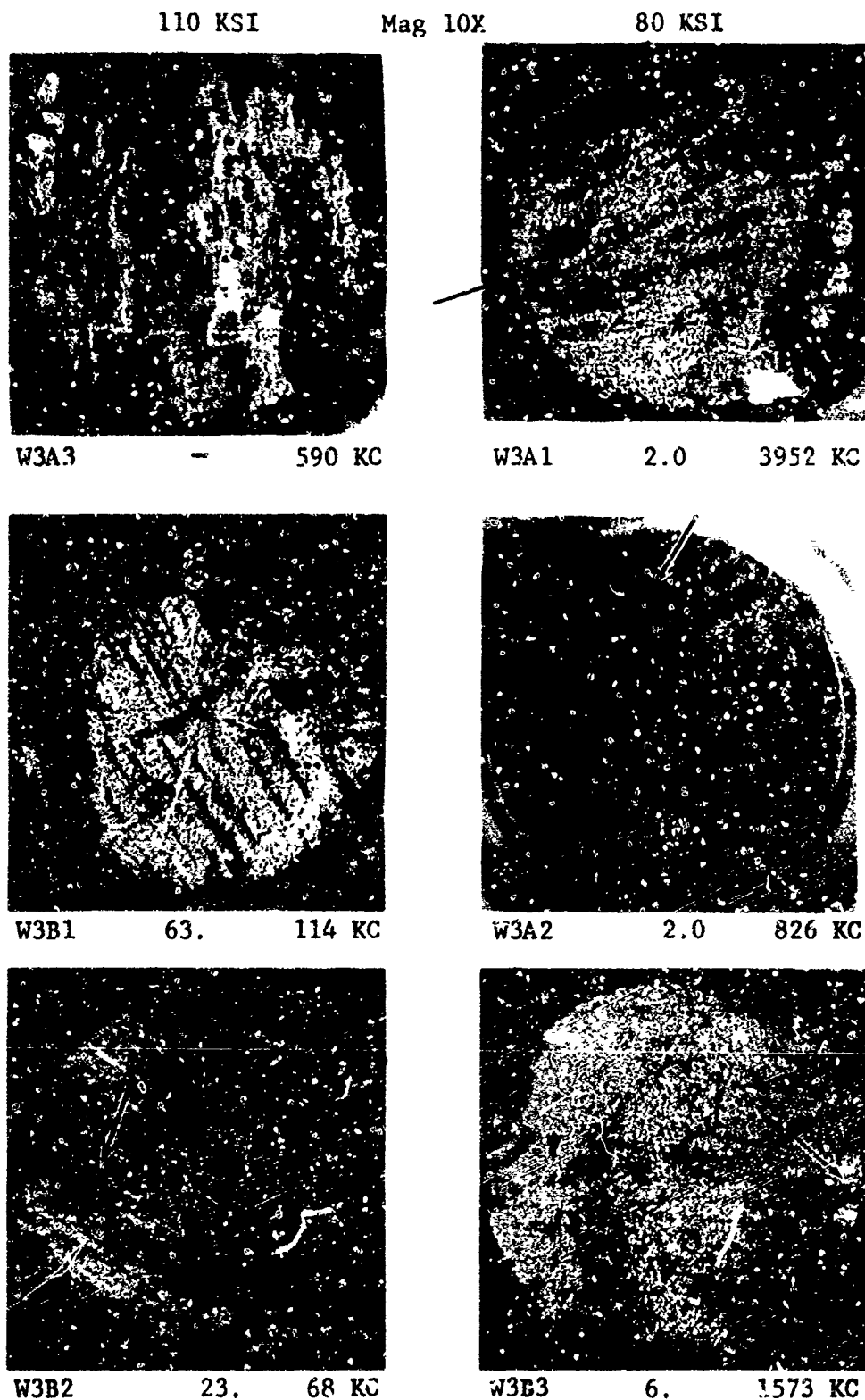


Figure 8.33 Fracture Surfaces of Failed Fatigue Specimens Series W3-  
Single Joint Diffusion Bonded with .013" Dia. Stainless  
Steel Powder Inclusion

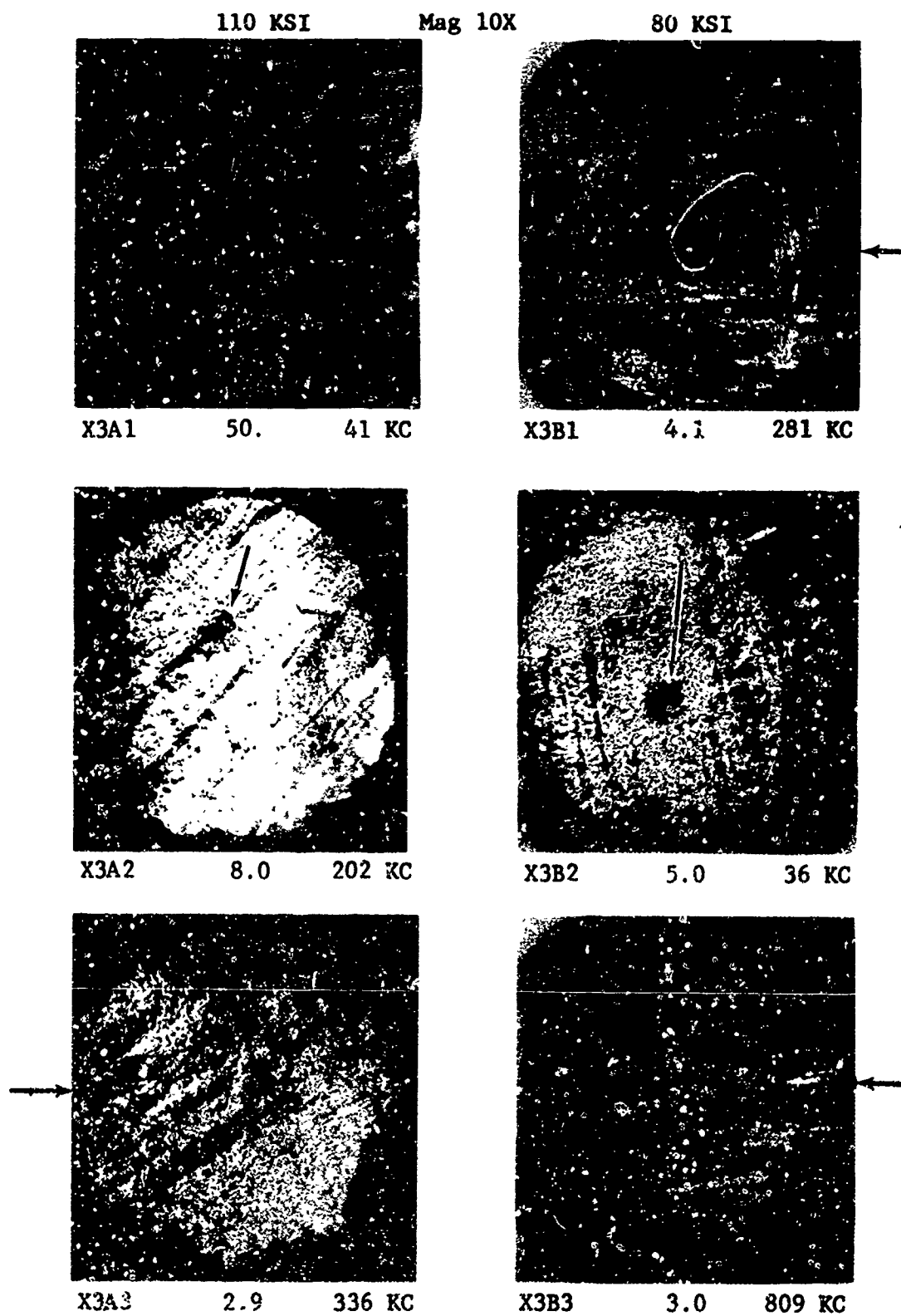


Figure 8.34 Fracture Surfaces of Failed Fatigue Specimens Series X3-  
Single Joint Diffusion Bonded with .013" Dia.  $\text{SiO}_2$   
Powder Inclusion

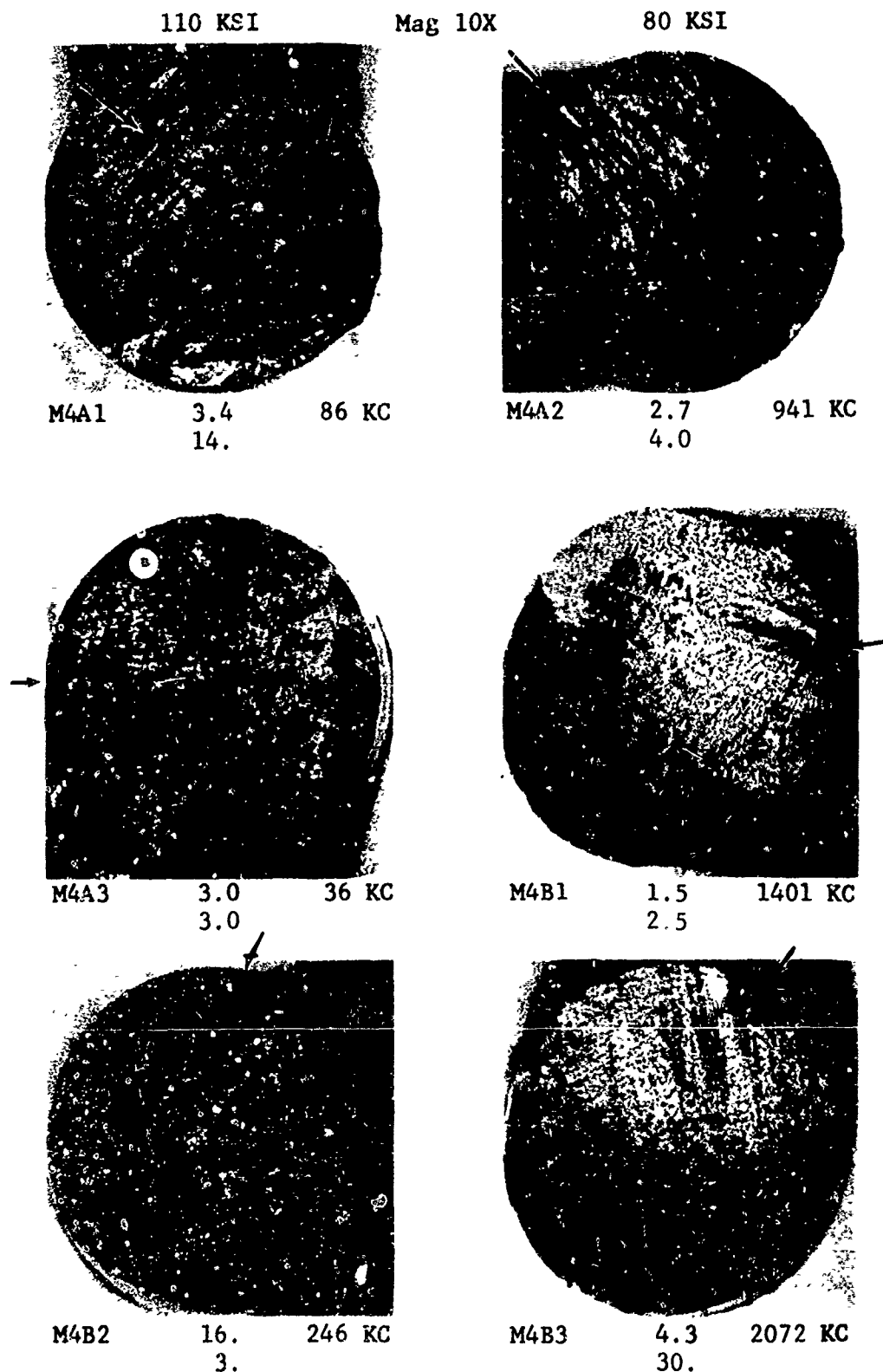


Figure 8.35 Fracture Surfaces of Failed Fatigue Specimens Series M4-Double-Bond/Single-Axis Diffusion Bonded with 7.5% Deformation

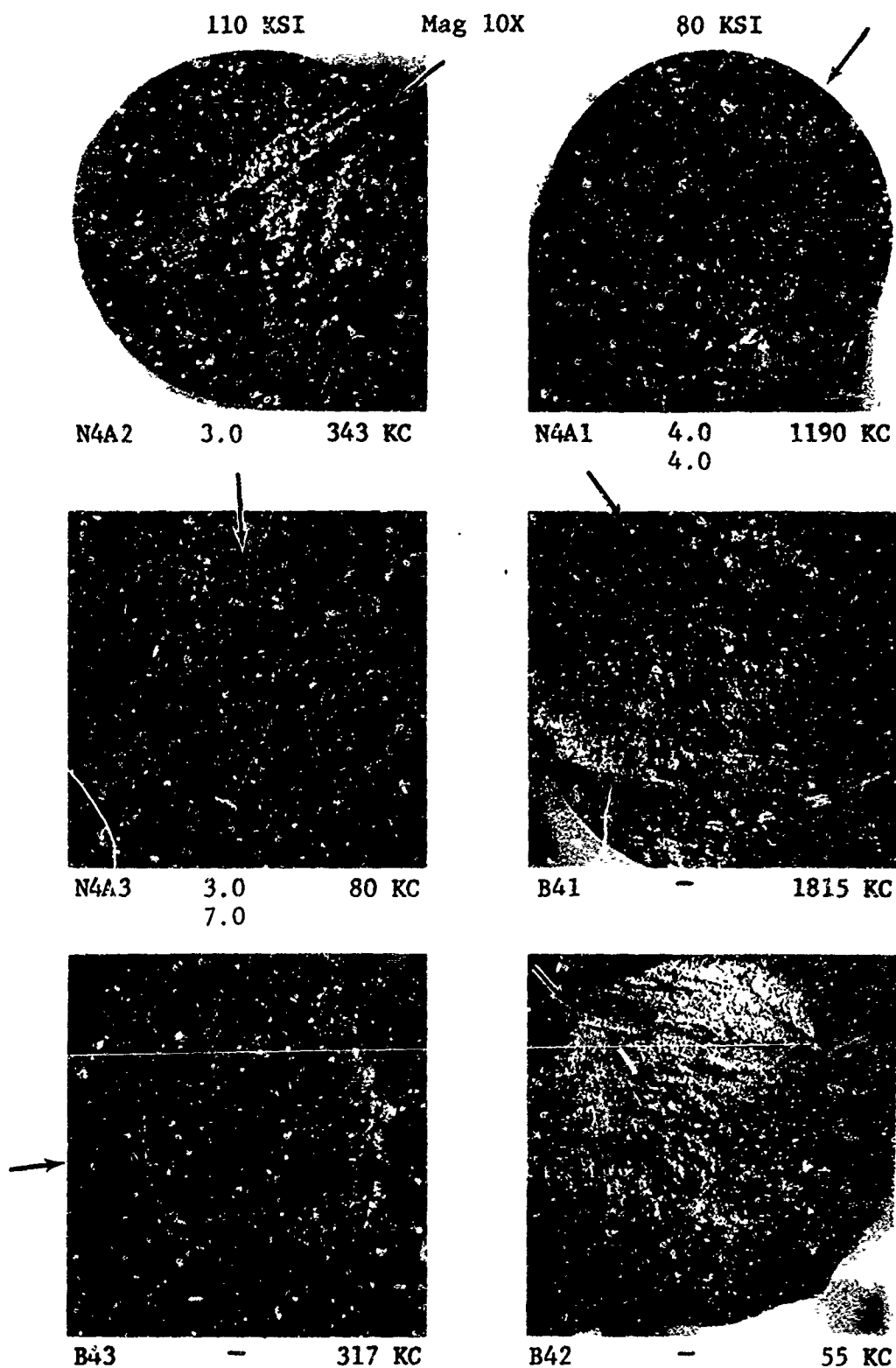


Figure 8.36 Fracture Surfaces of Failed Fatigue Specimens Series N4-  
Double-Bond/Single-Axis Diffusion Bonded with 2.7%  
Deformation



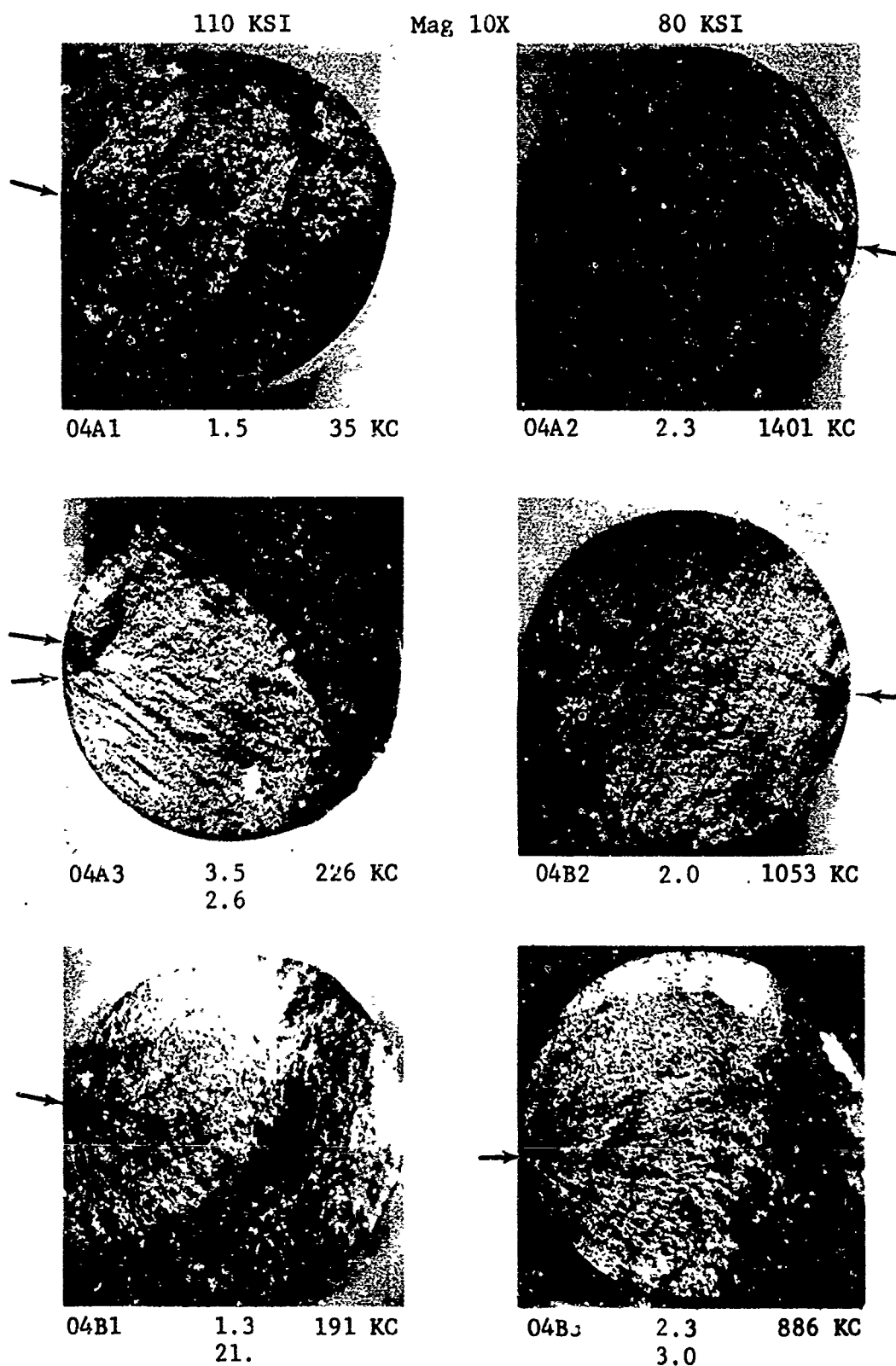


Figure 8.37 Fracture Surfaces of Failed Fatigue Specimens Series 04-Double-Bond/Single-Axis Diffusion Bonded with 1.5% Deformation

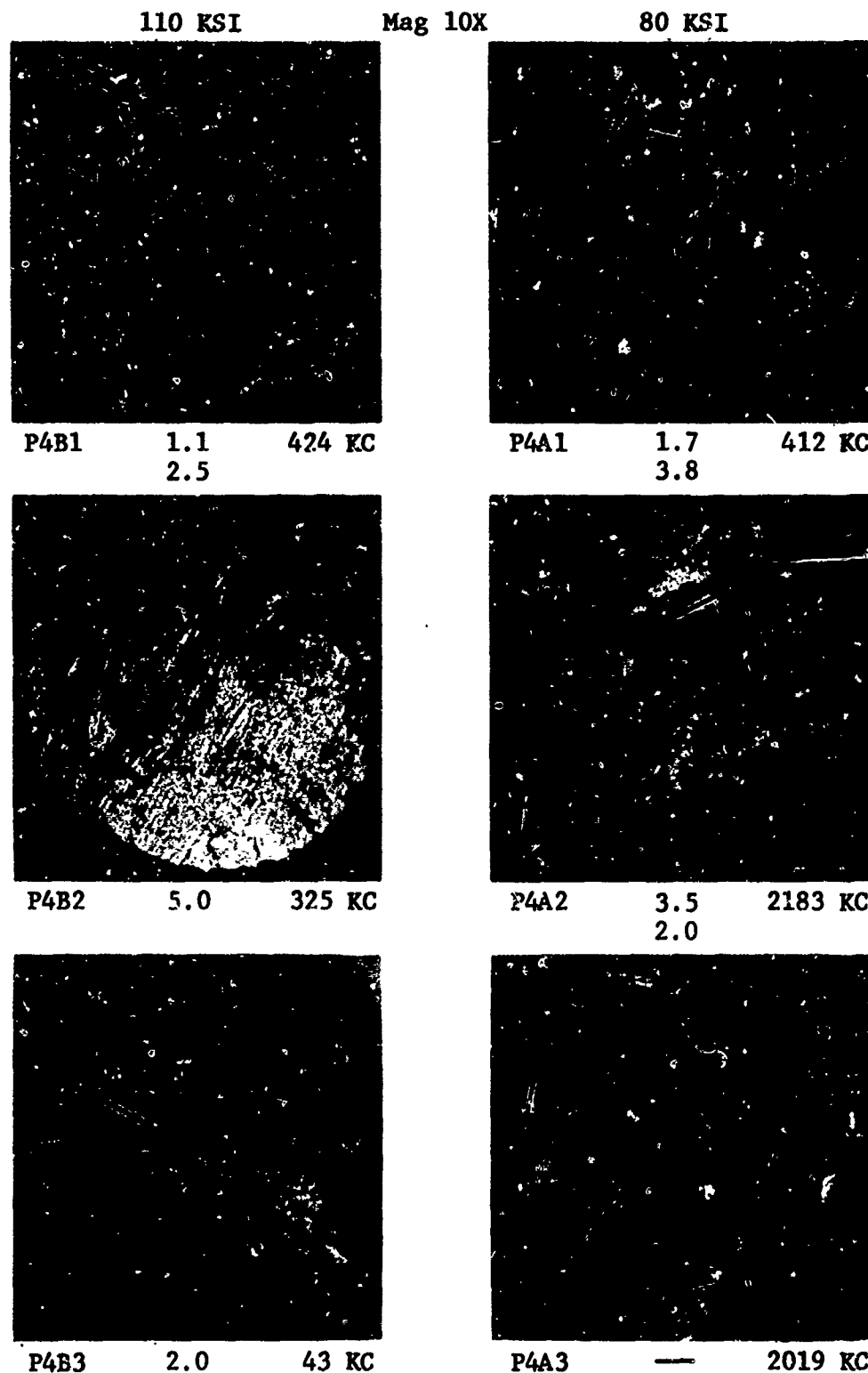


Figure 8.38 Fracture Surfaces of Failed Fatigue Specimens Series P4-Double-Bond/Single-Axis Diffusion Bonded - ASTM Grain Size No. 10

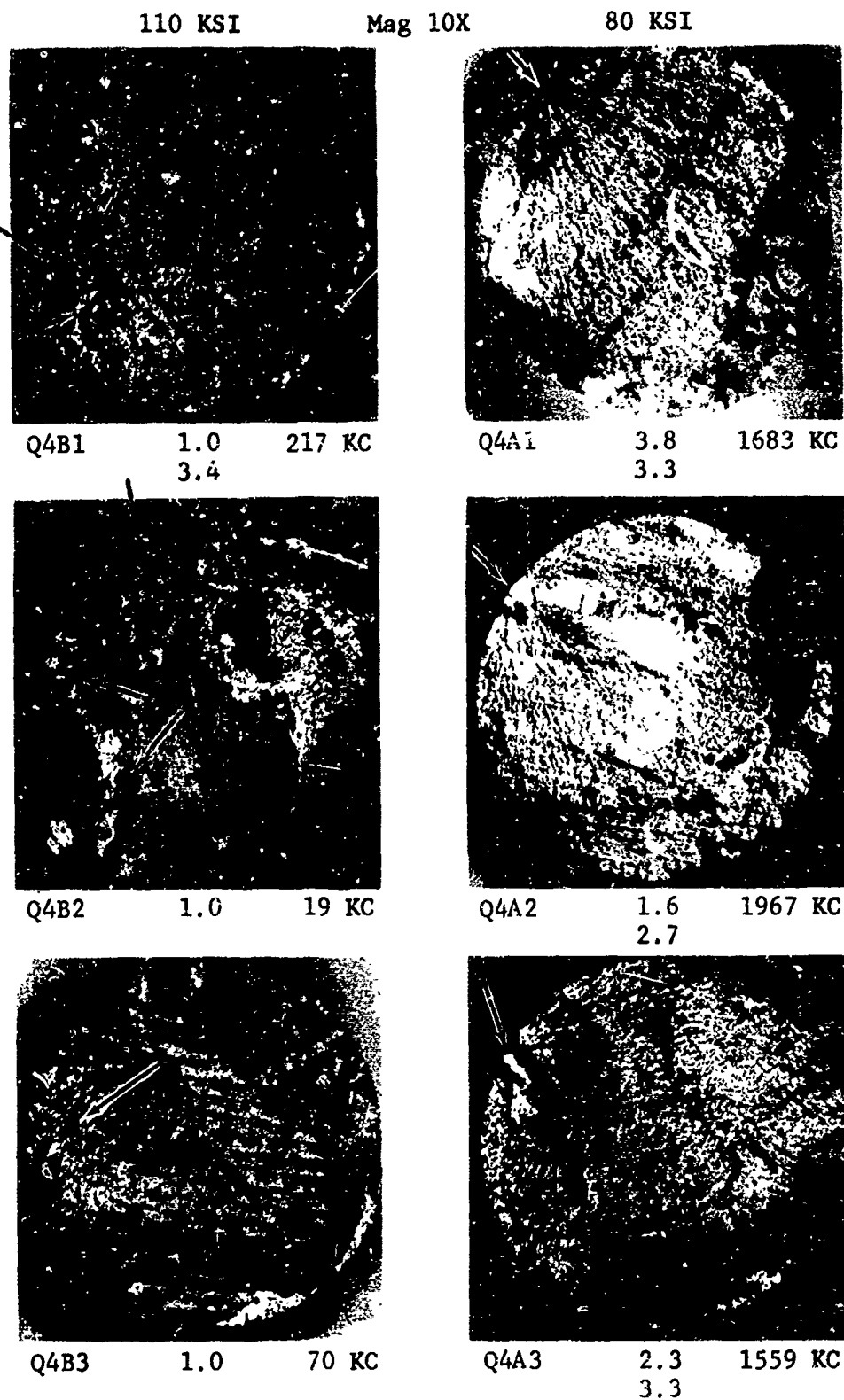


Figure 8.39 Fracture Surfaces of Failed Fatigue Specimens Series Q4-  
Double-Bond/Single-Axis Diffusion Bonded - ASTM Grain  
Size No. 9

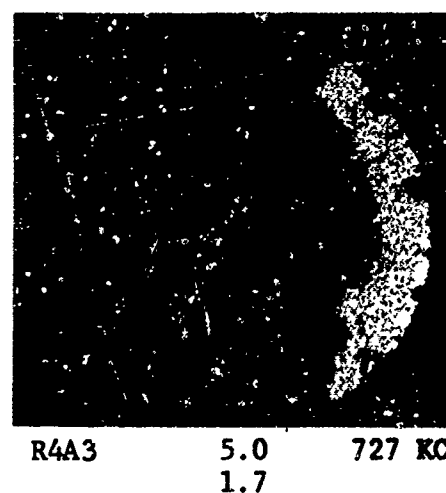
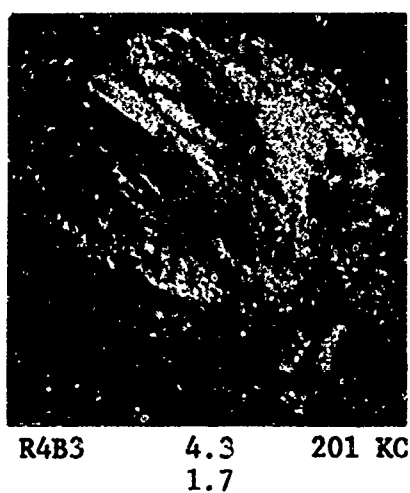
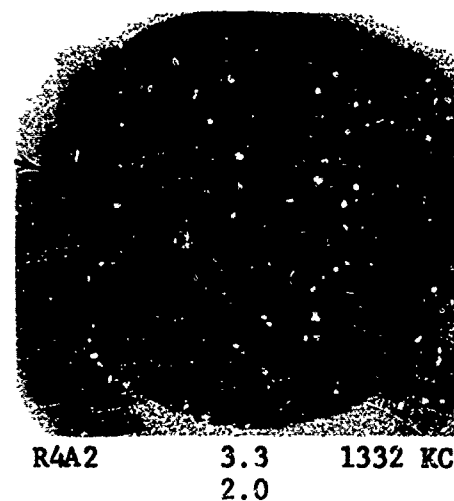
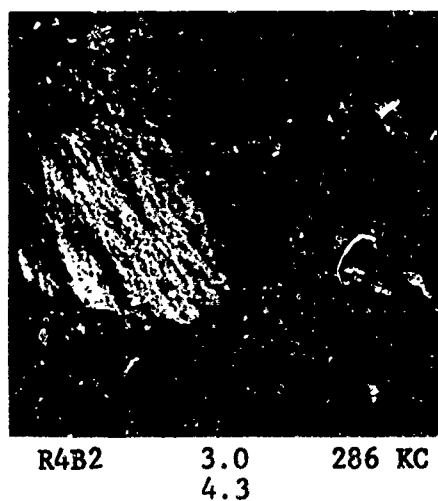
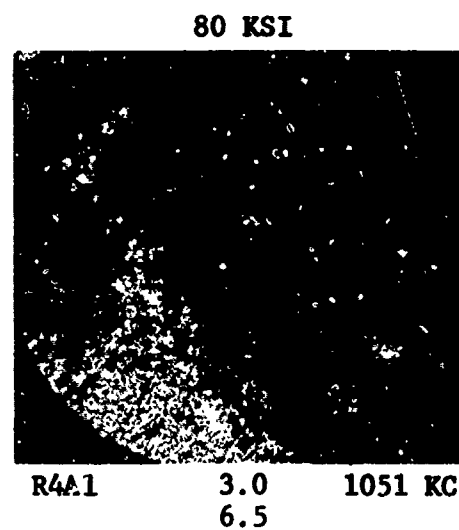
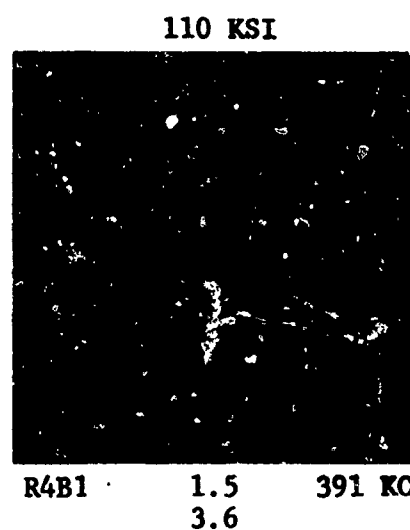
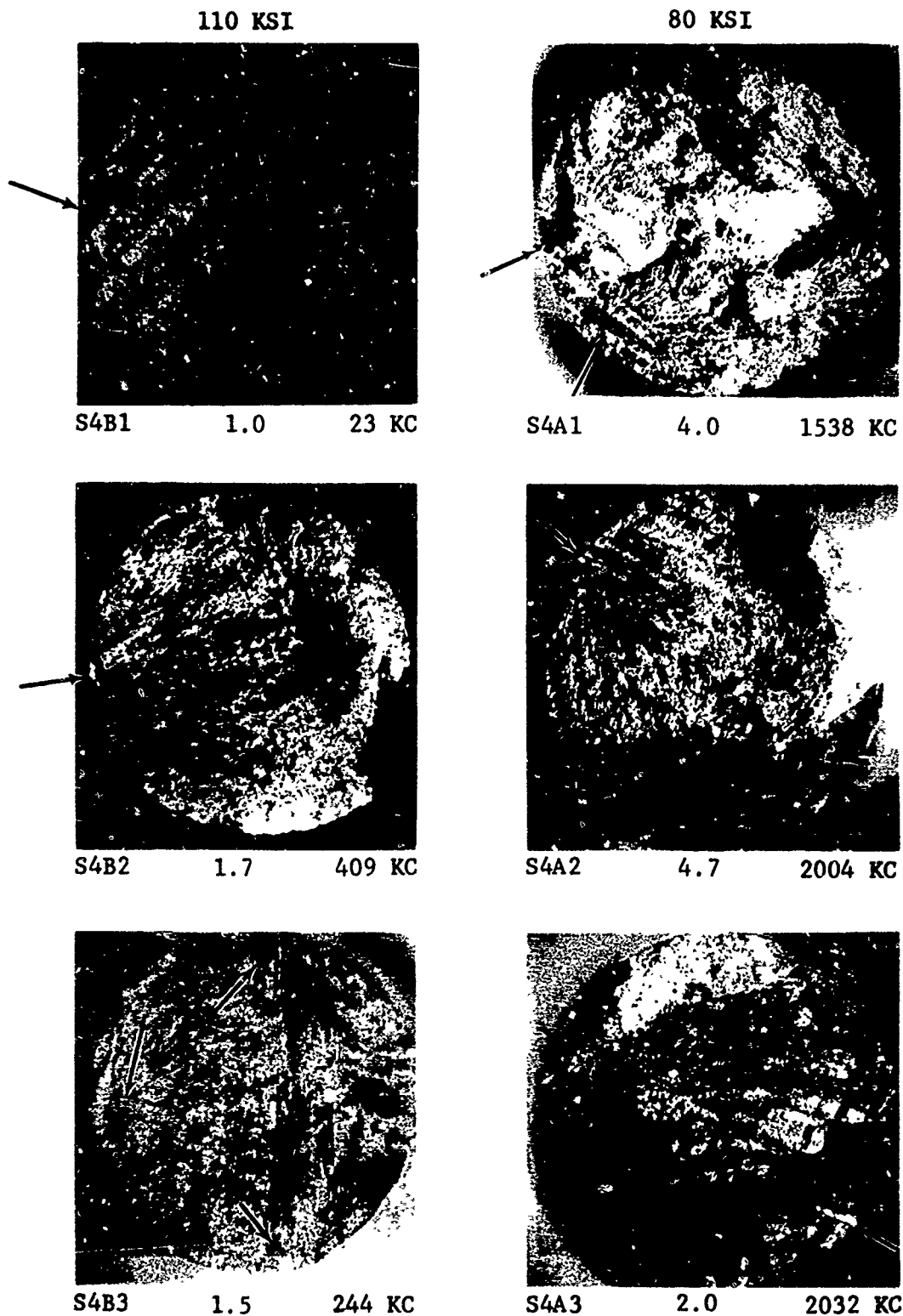
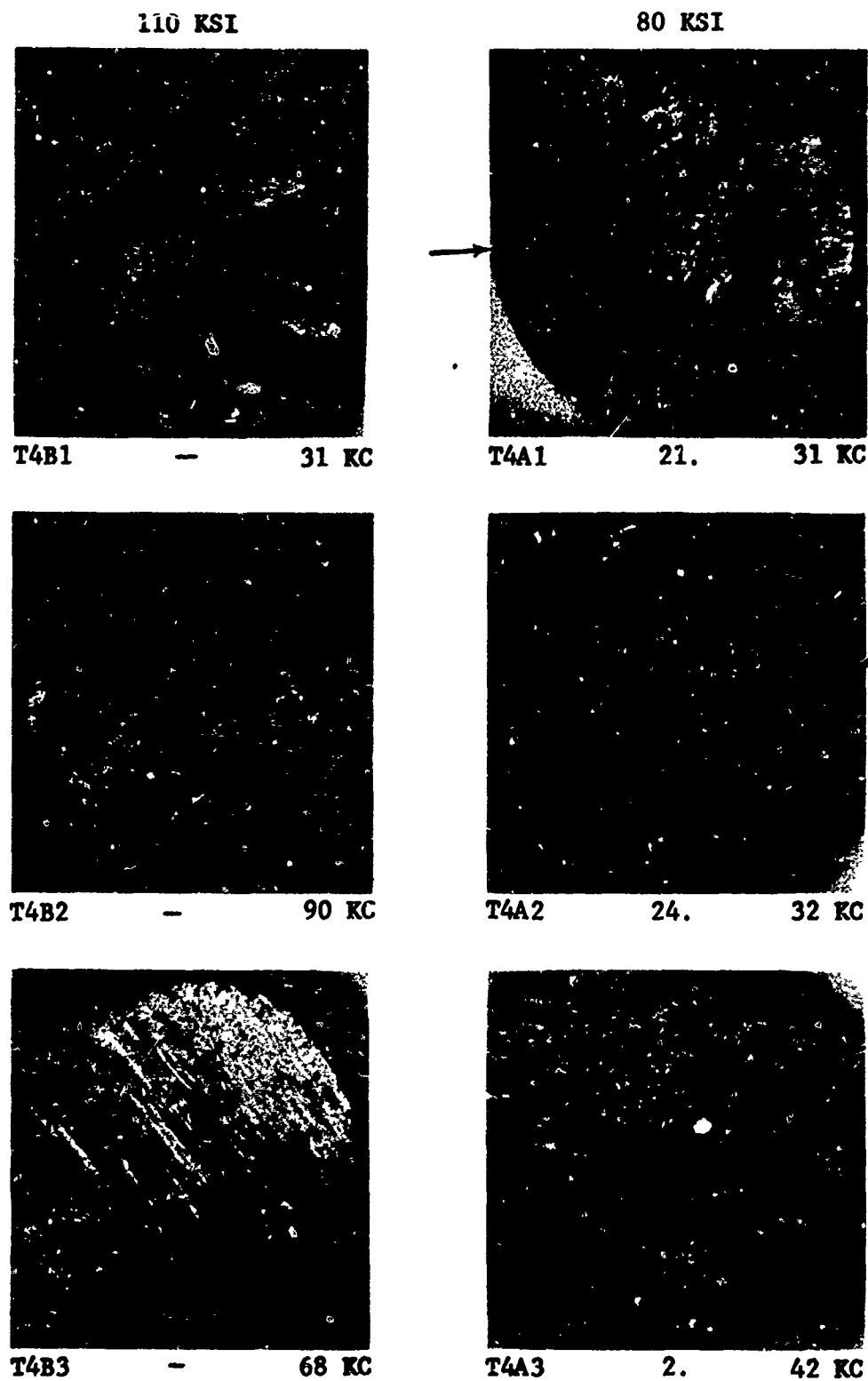


Figure 8.40 Fracture Surfaces of Failed Fatigue Specimens Series R4-  
Double-Bond/Single-Axis Diffusion Bonded - ASTM Grain  
Size No. 7.5



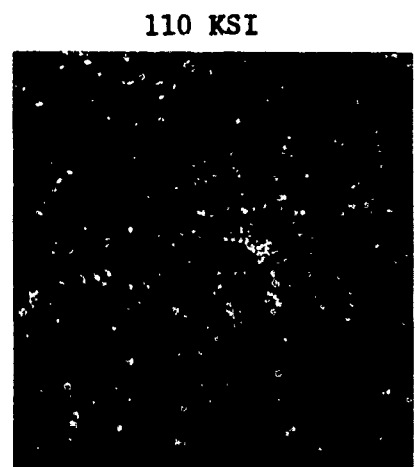
Mag 10X

Figure 8.41 Fracture Surfaces of Failed Fatigue Specimens Series S4-Double-Bond/Single-Axis Diffusion Bonded with Multiple 0.0065" Dia. Surface Voids

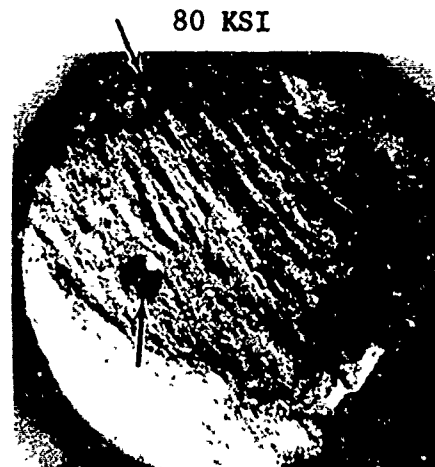


Mag 10X

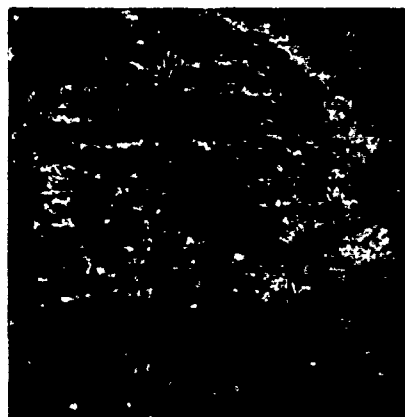
Figure 8.42 Fracture Surfaces of Failed Fatigue Specimens Series T4-Double-Bond/Single-Axis Diffusion Bonded with Multiple 0.010" Dia. Surface Voids



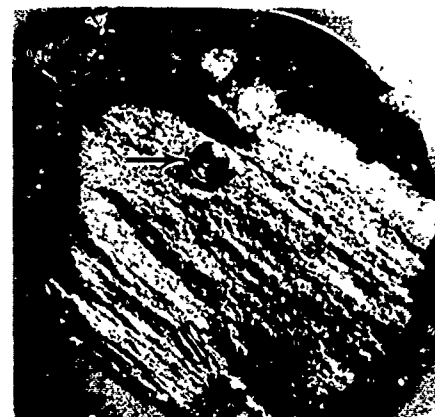
U4B1 - 17 KC



U4A1 28. 50 KC



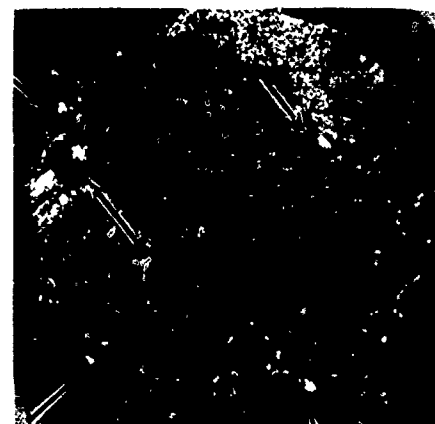
U4B2 - 76 KC



U4A2 1.0 14 KC



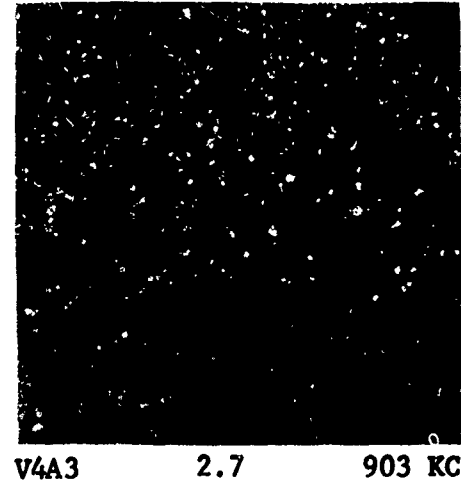
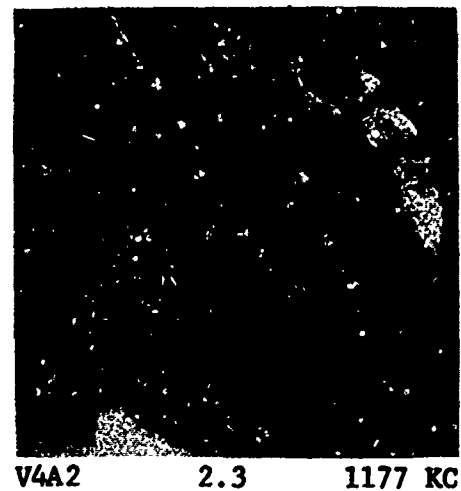
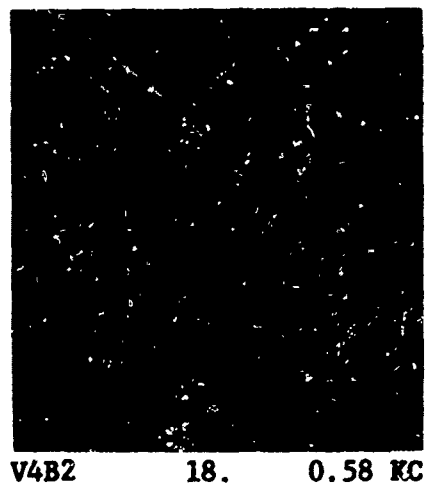
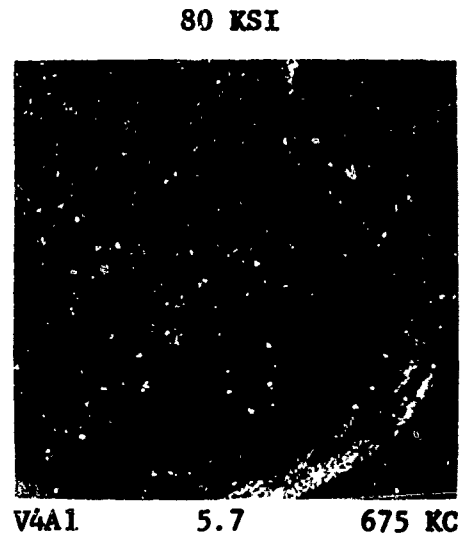
U4B3 - 8.5 KC



U4A3 3.0 18 KC

Mag 10X

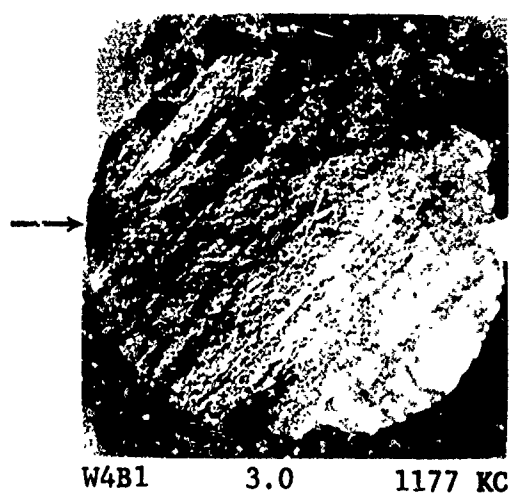
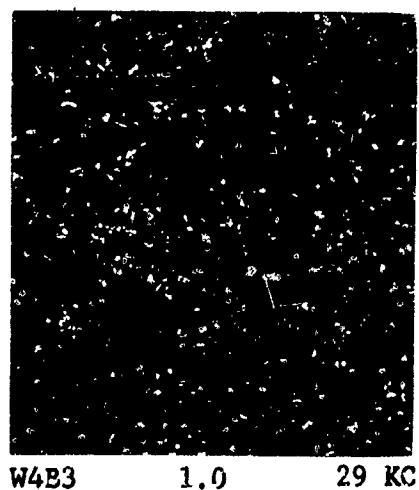
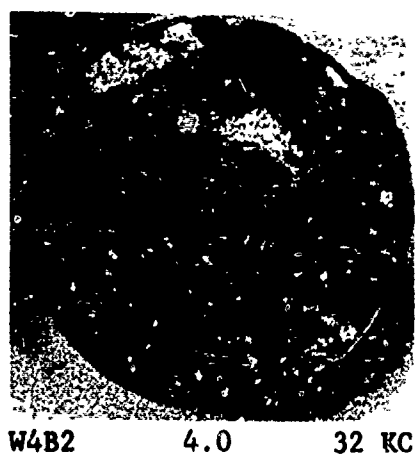
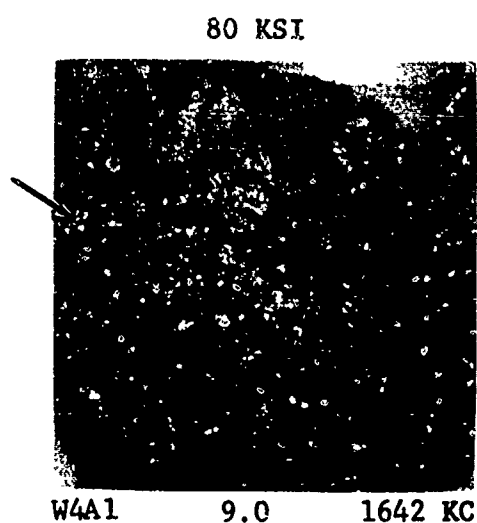
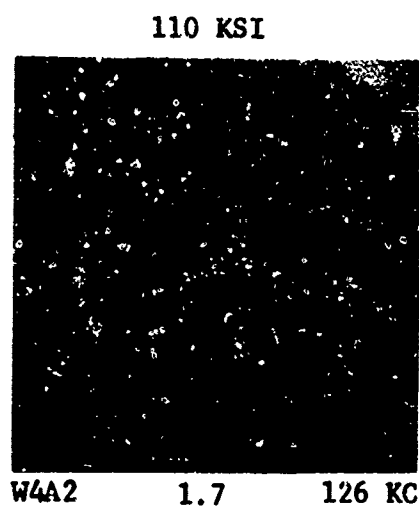
Figure 8.43 Fracture Surfaces of Failed Fatigue Specimens Series U4-Double-Bond/Single-Axis Diffusion Bonded with Multiple 0.020" Dia. Surface Voids



Mag 10X

Figure 8.44 Fracture Surfaces of Failed Fatigue Specimens Series V4 - Double-Bond/Single-Axis Diffusion Bonded with 0.186" Dia. Alpha Case Defect





Mag 10X

Figure 8.45 Fracture Surfaces of Failed Fatigue Specimens Series W4 - Double-Bond/Single-Axis Diffusion Bonded with 0.065" Dia. 304 S.S. Powder Inclusion

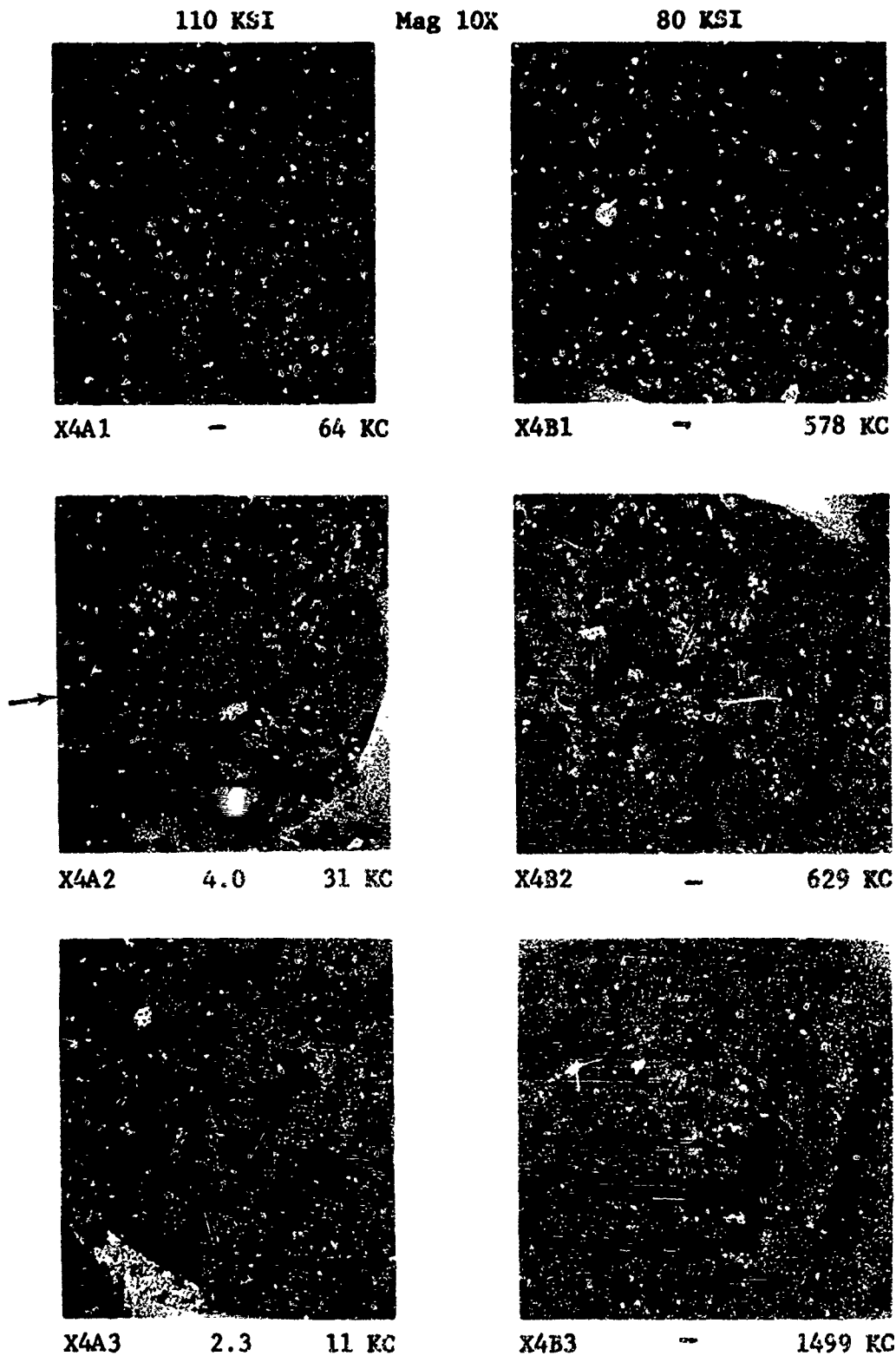


Figure 8.46 Fracture Surfaces of Failed Fatigue Specimens Series X4-  
Double-Bond/Single-Axis Diffusion Bonded with 0.065" Dia.  
SiO<sub>2</sub> Powder Inclusion

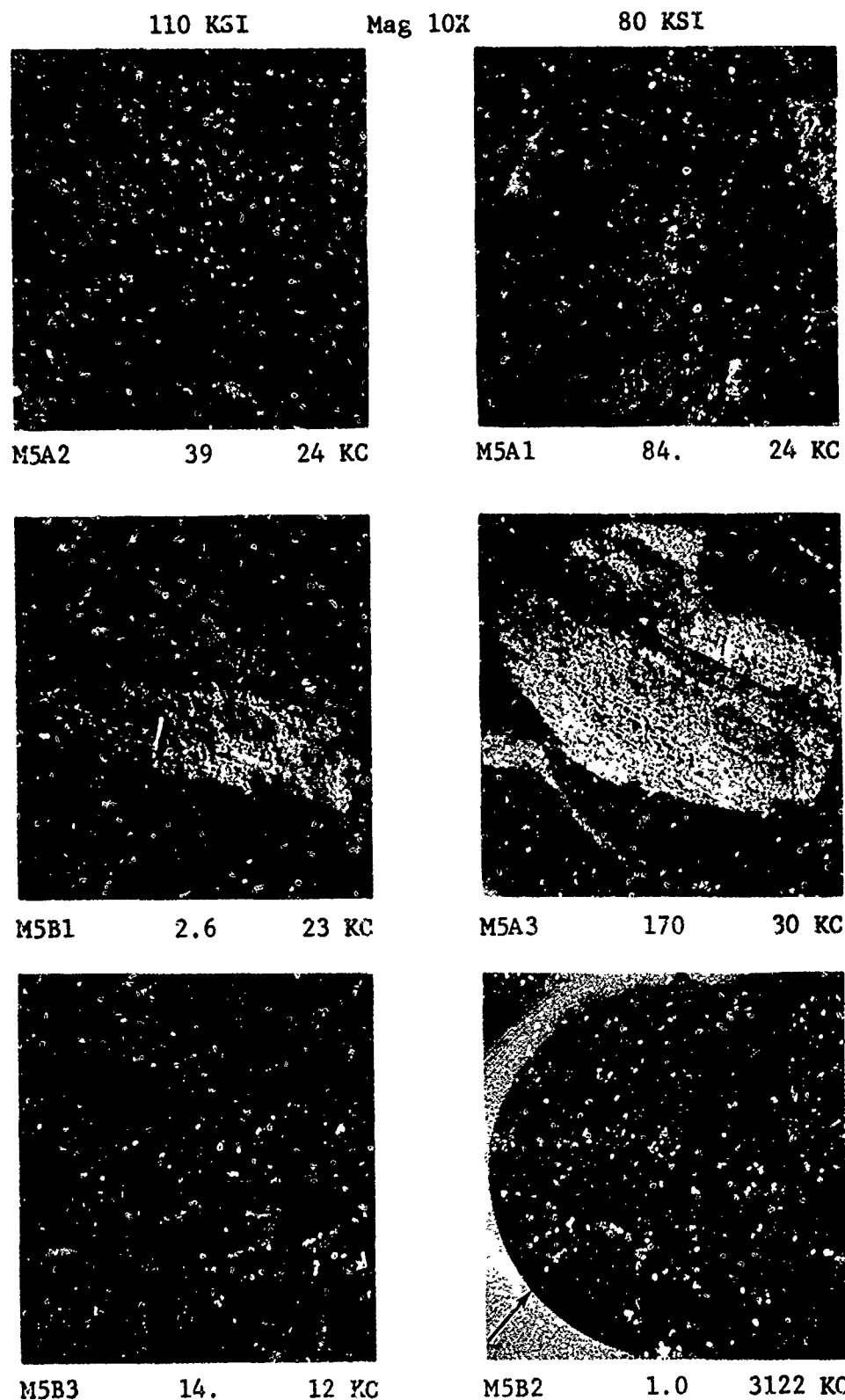


Figure 8.48 Fracture Surfaces of Failed Fatigue Specimens Series M5-Double-Bond/Two-Axis Diffusion Bonded with "Optimum" Deformation

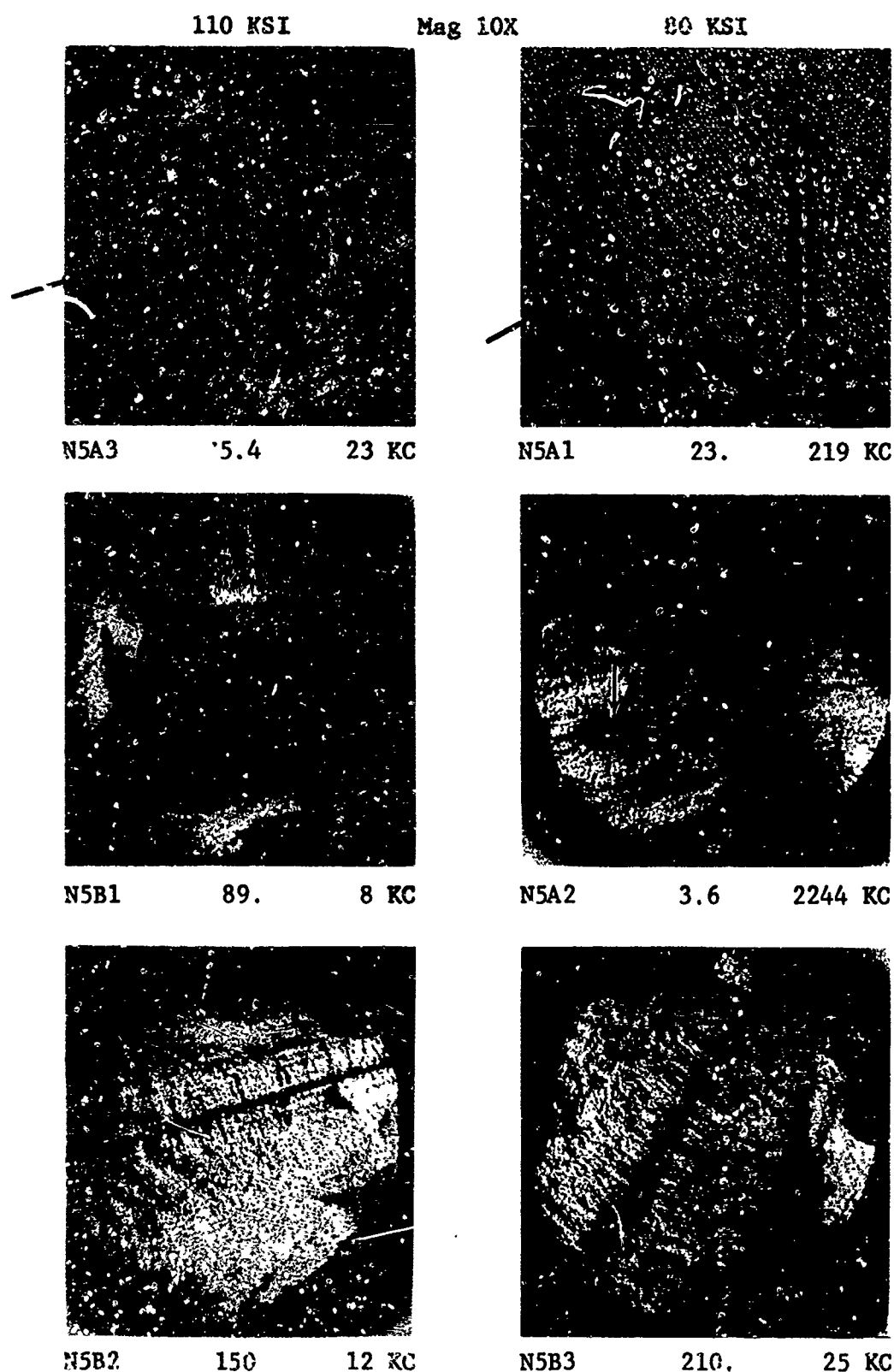


Figure 8.49 Fracture Surfaces of Failed Fatigue Specimen Series N5-Double-Bond/Two-Axis Diffusion Bonded with "Less than Optimum" Deformation

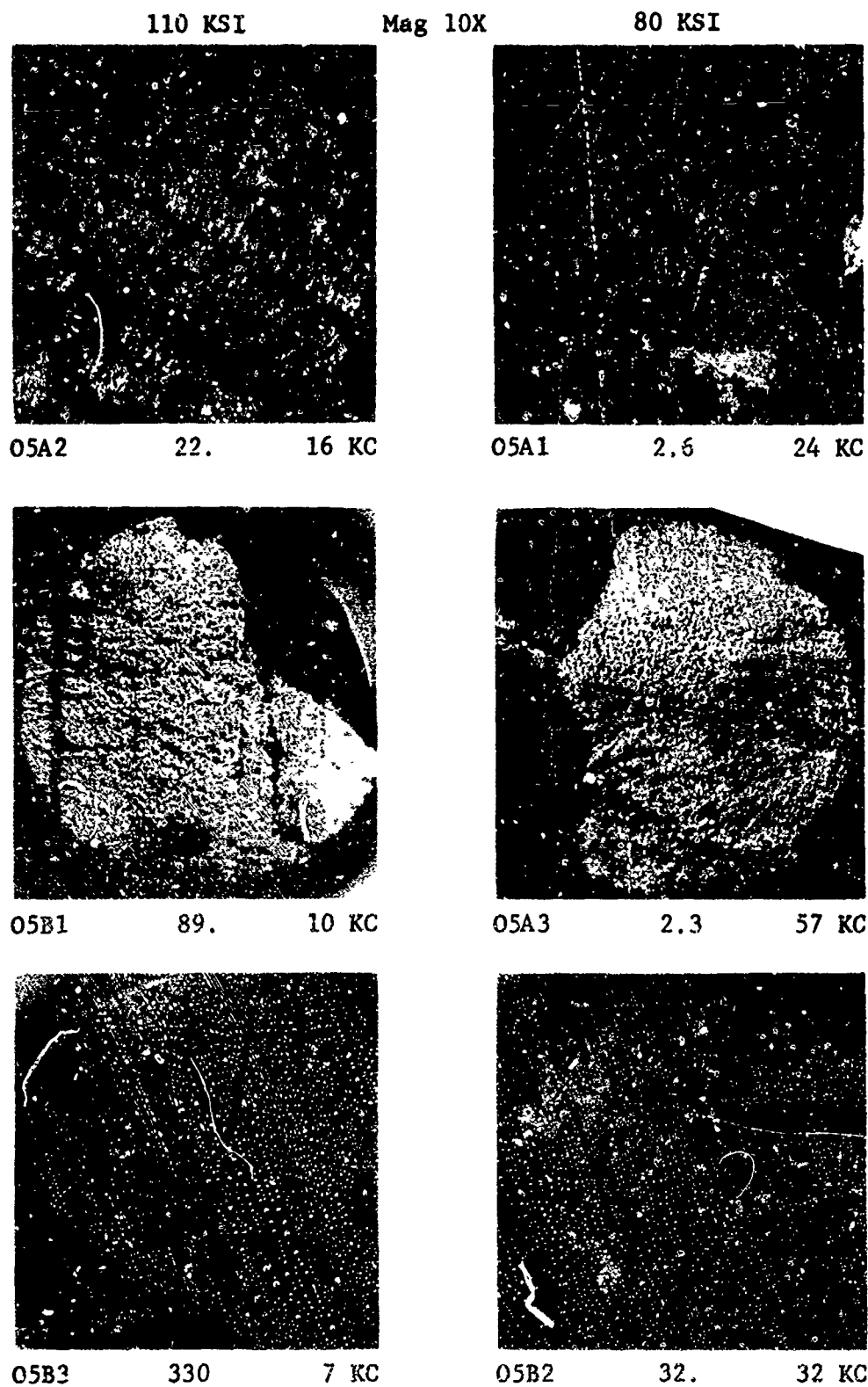


Figure 8.50 Fracture Surfaces of Failed Fatigue Specimens Series 05-Double-Bond/Two-Axis Diffusion Bonded with "Much Less than Optimum" Deformation

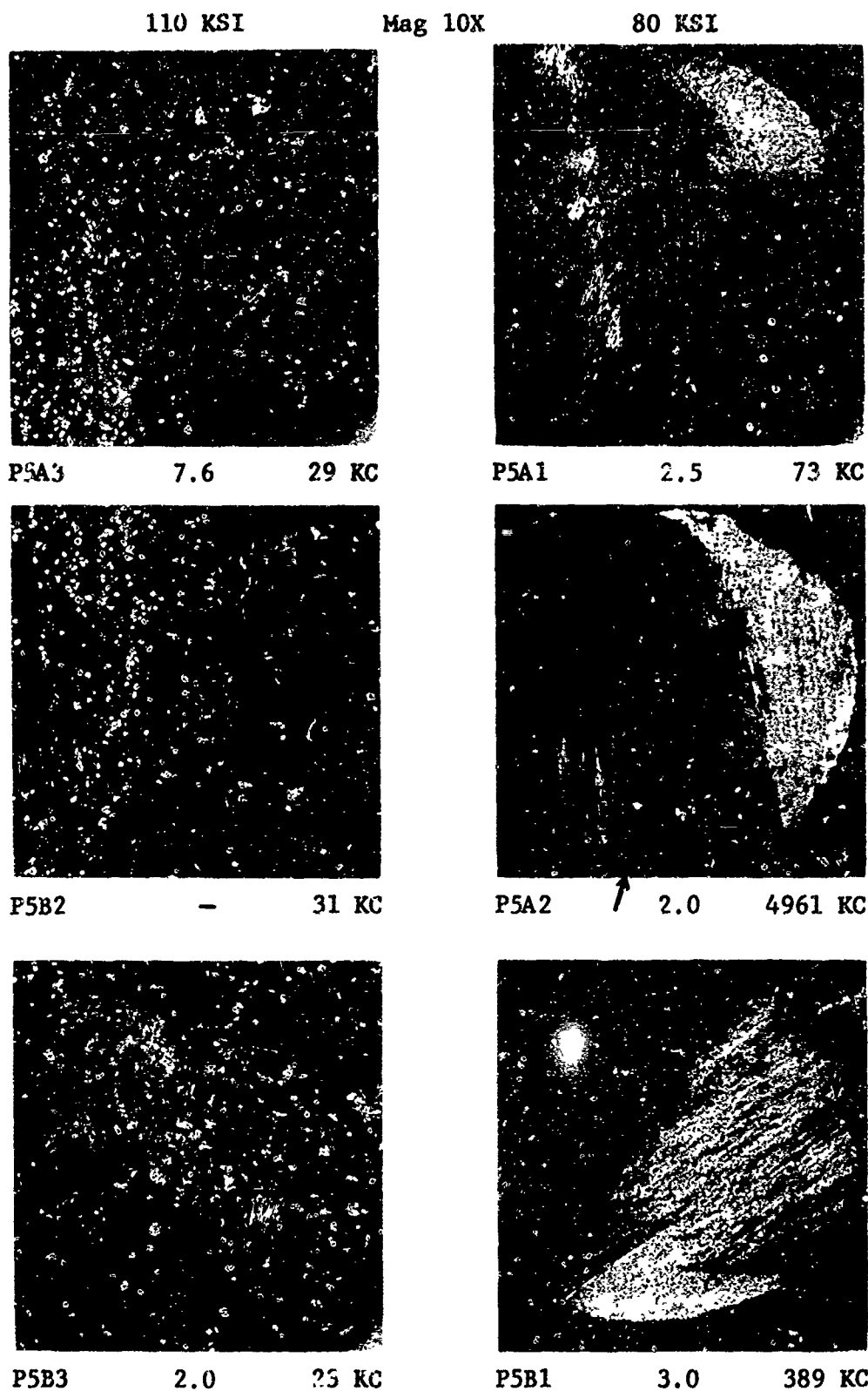


Figure 8.51 Fracture Surfaces of Failed Fatigue Specimens Series P5-Double-Bond/Two-Axis Diffusion Bonded with ASTM Grain Size No. 10

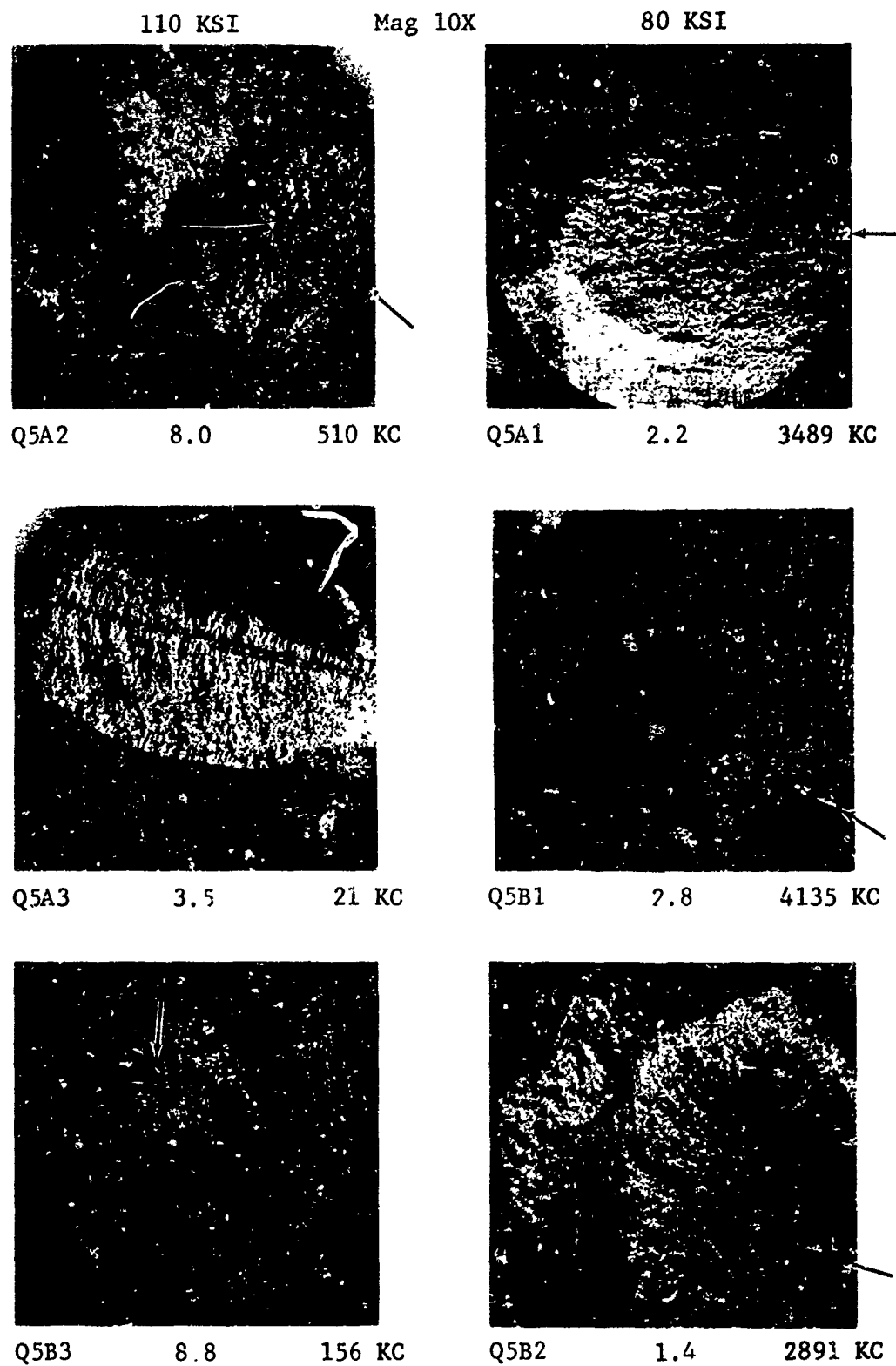


Figure 8.52 Fracture Surfaces of Failed Fatigue Specimens Series Q5-Double-Bond/Two-Axis Diffusion Bonded with ASTM Grain Size No. 8





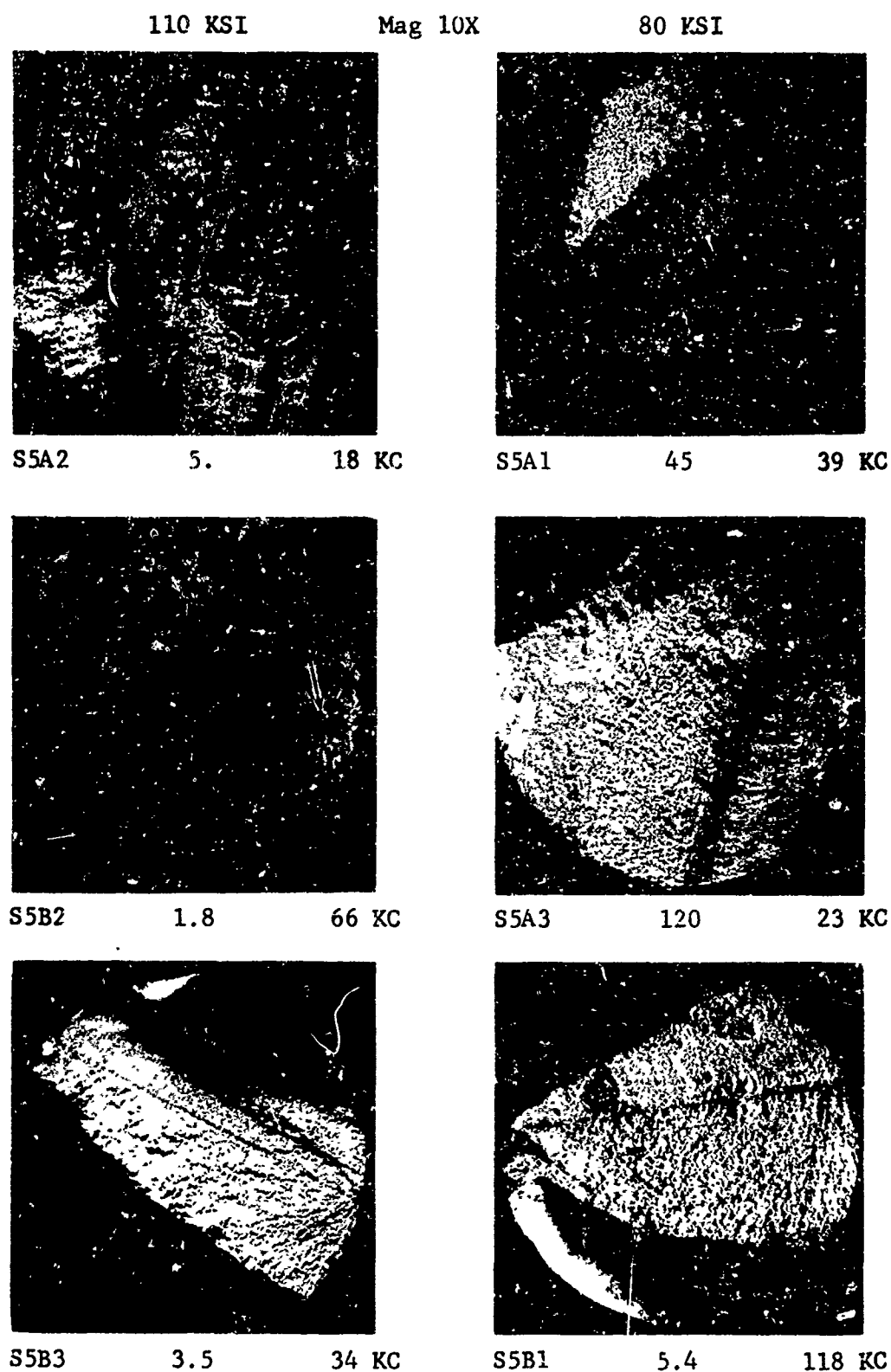


Figure 8.54 Fracture Surfaces of Failed Fatigue Specimens Series S5-  
Double-Bond/Two-Axis Diffusion Bonded with .005" Chamfered  
Edge Void

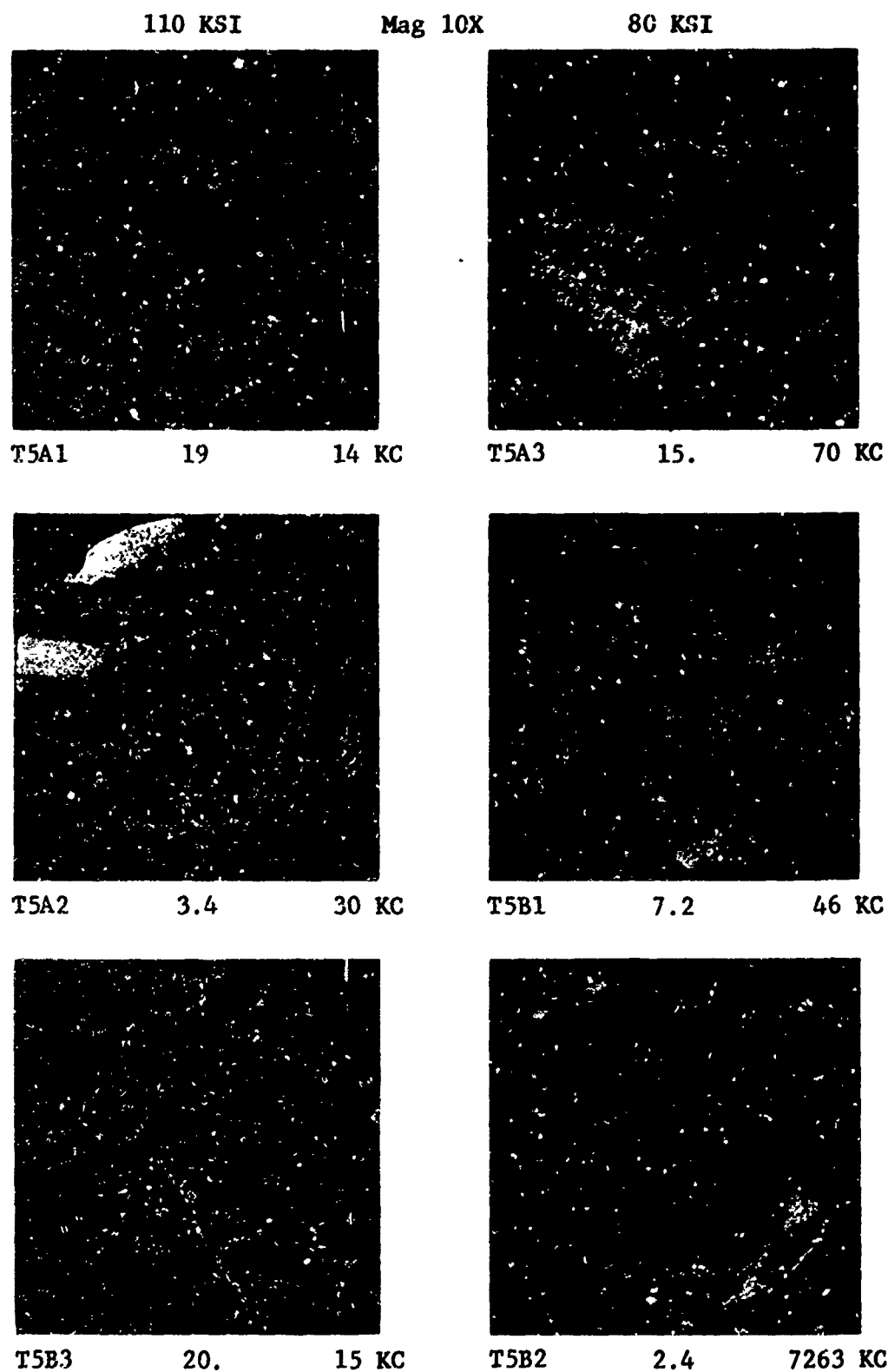


Figure 8.55 Fracture Surfaces of Failed Fatigue Specimens Series T5-  
Double-Bond/Two-Axis Diffusion Bonded with .010" Chamfered  
Edge Void

110 KSI

Mag 10X

80 KSI



U5A2

14.

37 KC



U5A1

38.

29 KC



U5B2

11.

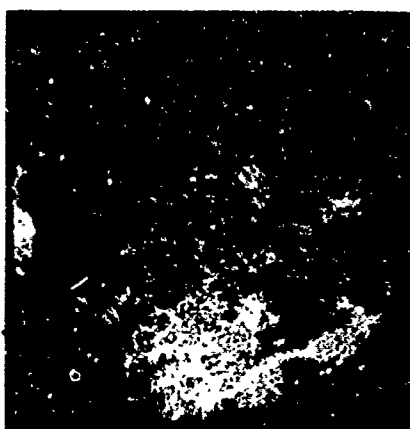
14 KC



U5A3

41.

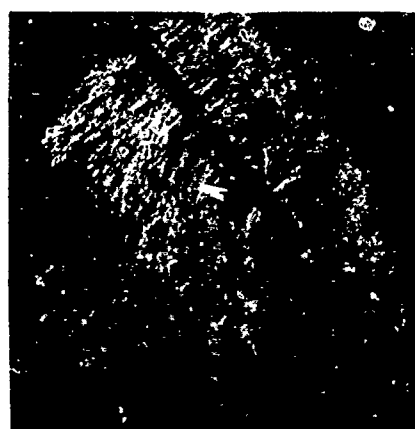
34 KC



U5B3

33.

9 KC



U5B1

19.

31 KC

Figure 8.47 Fracture Surfaces of Failed Fatigue Specimens Series U5-  
Double-Bond/Two-Axis Diffusion Bonded with .020" Chamfered  
Edge Void

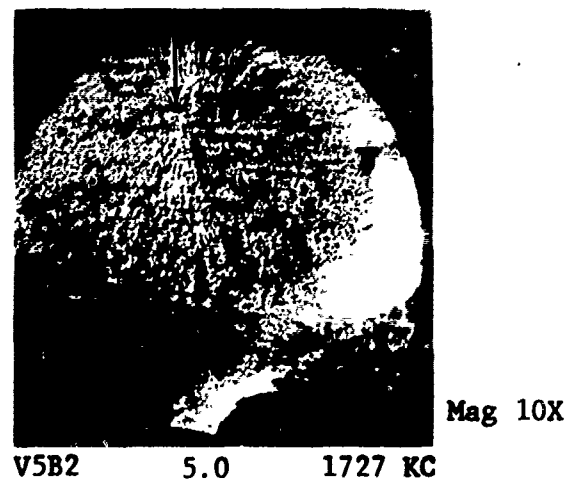
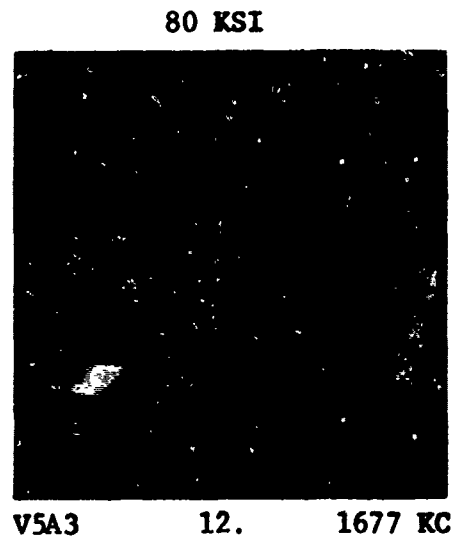


Figure 8.56 Fracture Surfaces of Failed Fatigue Specimens Series V5-Double-Bond/Two-Axis Diffusion Bonded with Alpha Case Contamination

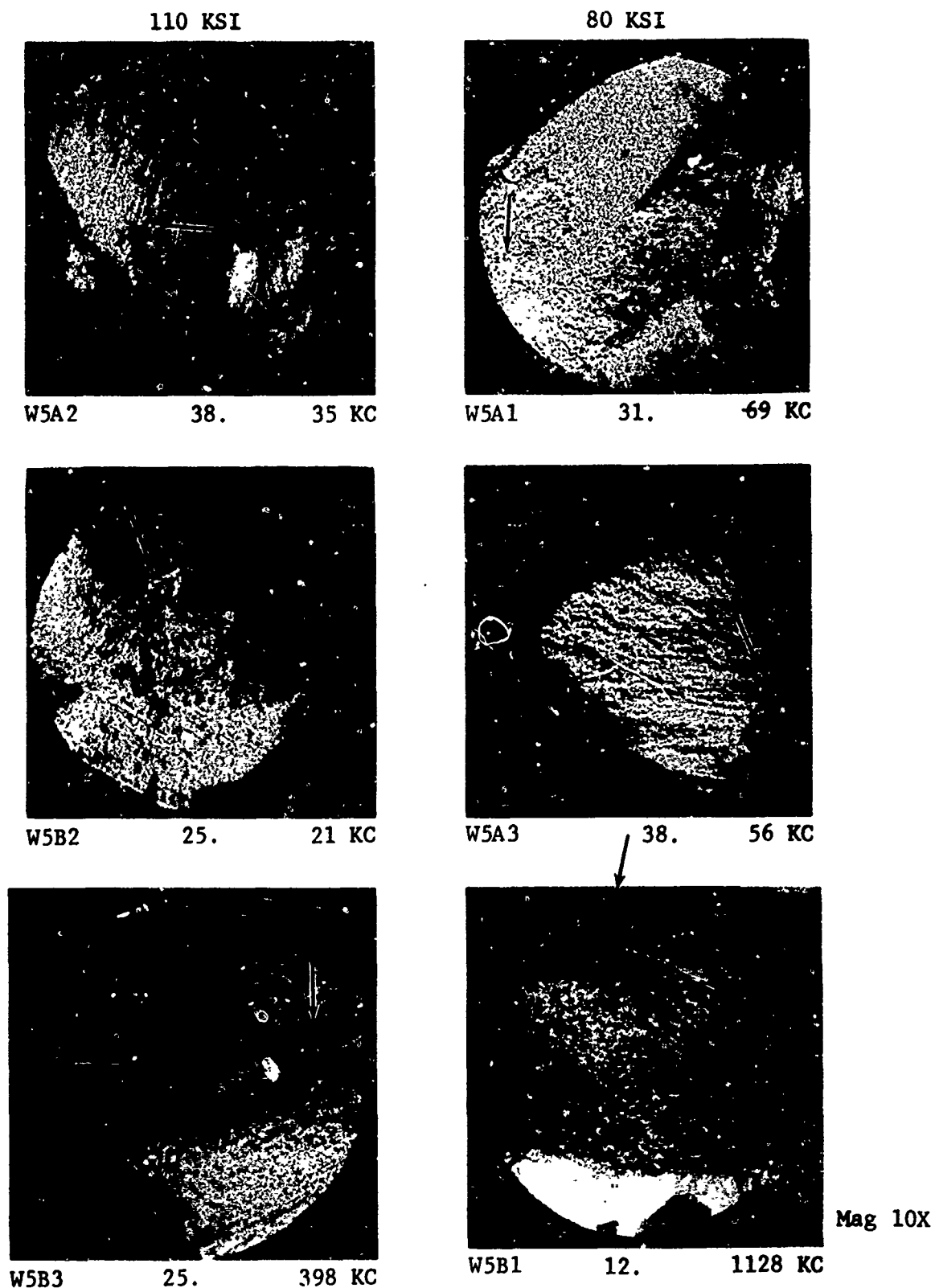


Figure 8.57 Fracture Surfaces of Failed Fatigue Specimens Series W5-Double-Bond/Two-Axis Diffusion Bonded with 304 S.S. Inclusion

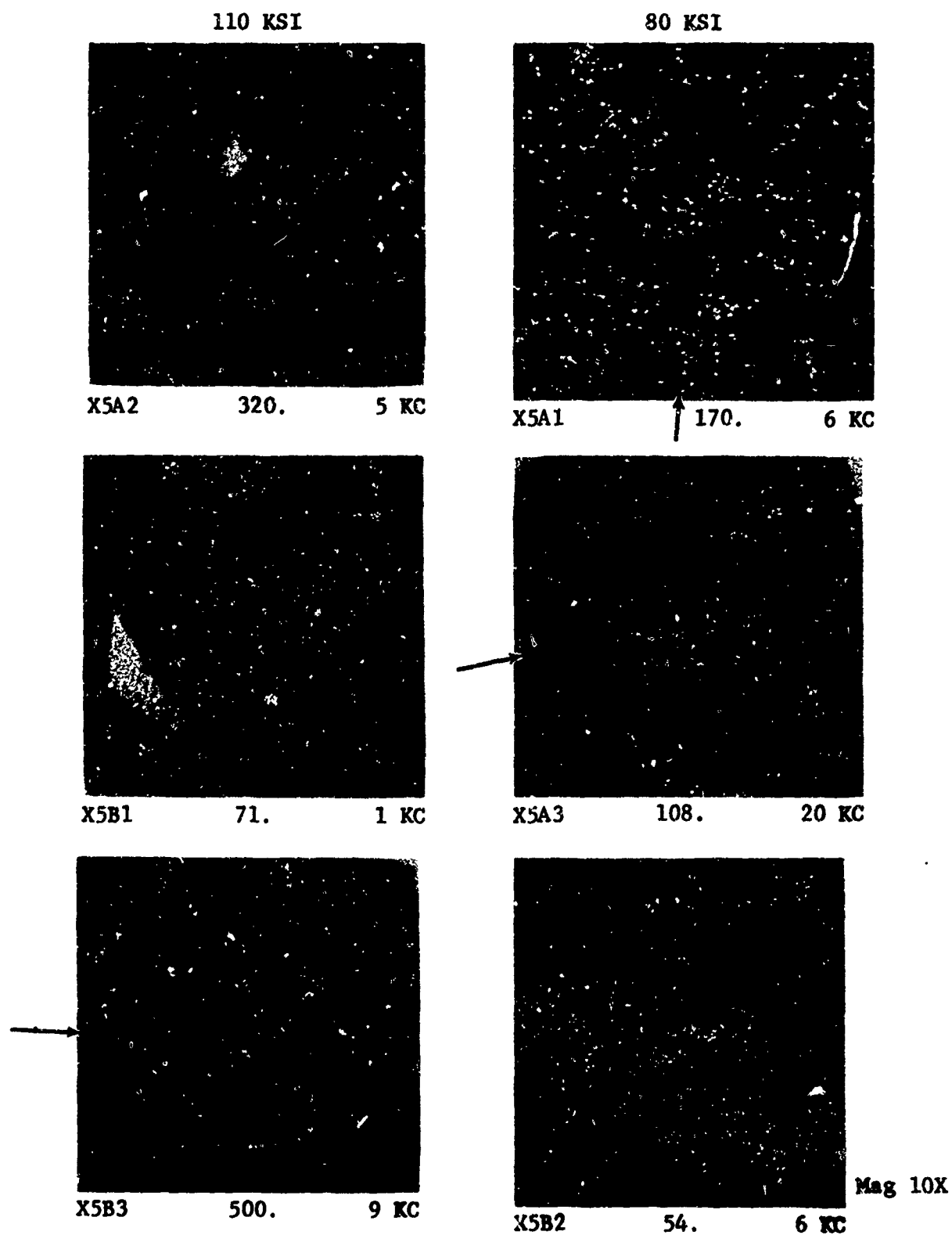
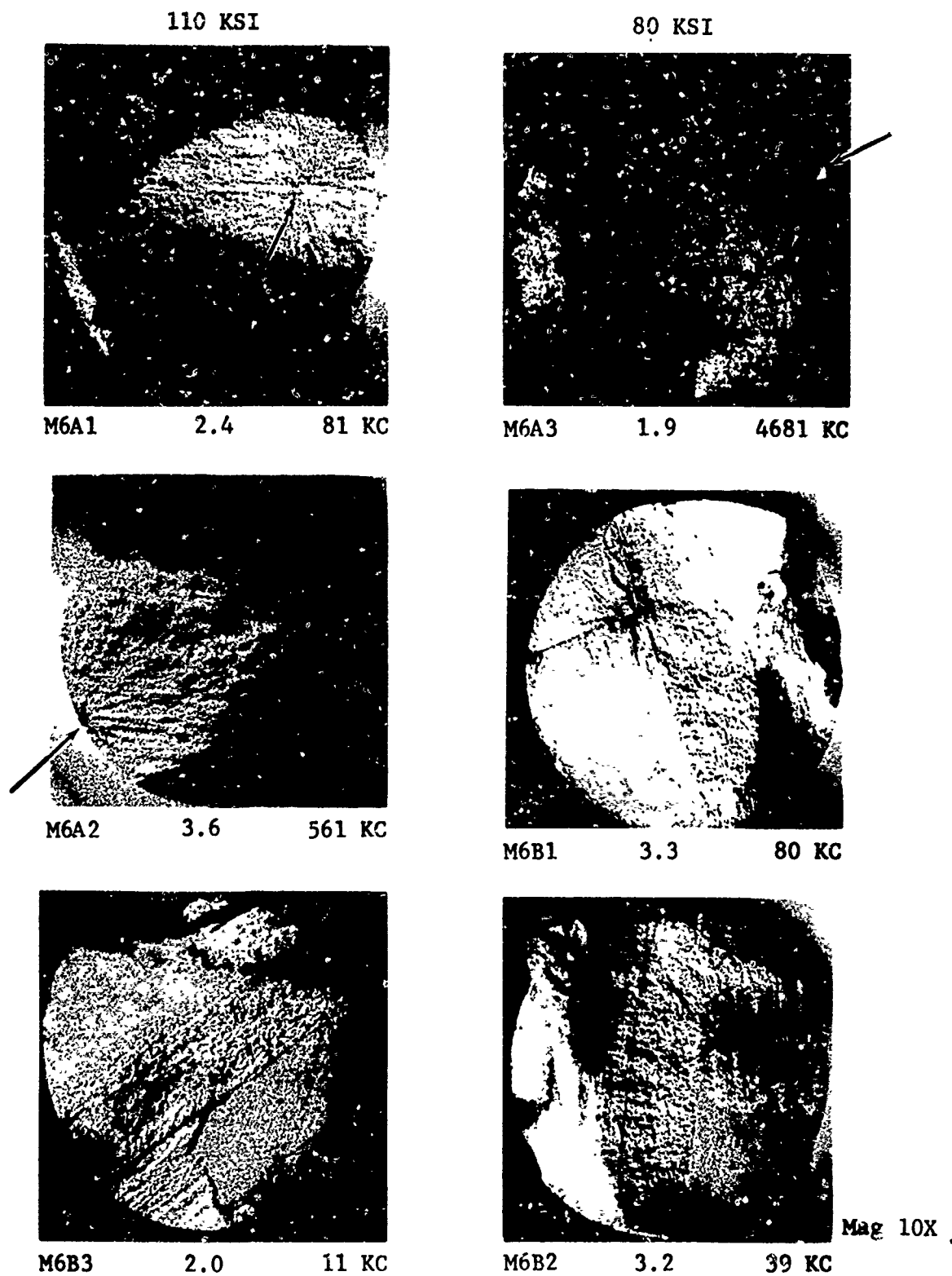


Figure 8.58 Fracture Surfaces of Failed Fatigue Specimens Series X5-  
Double-Bond/Two-Axis Diffusion Bonded with  $\text{SiO}_2$  Inclusion



**Figure 8.59** Fracture Surfaces of Failed Fatigue Specimens Series M6-Multiple-Bond/3-Axis Diffusion Bonded with 3.9% Average Short Transverse Deformation

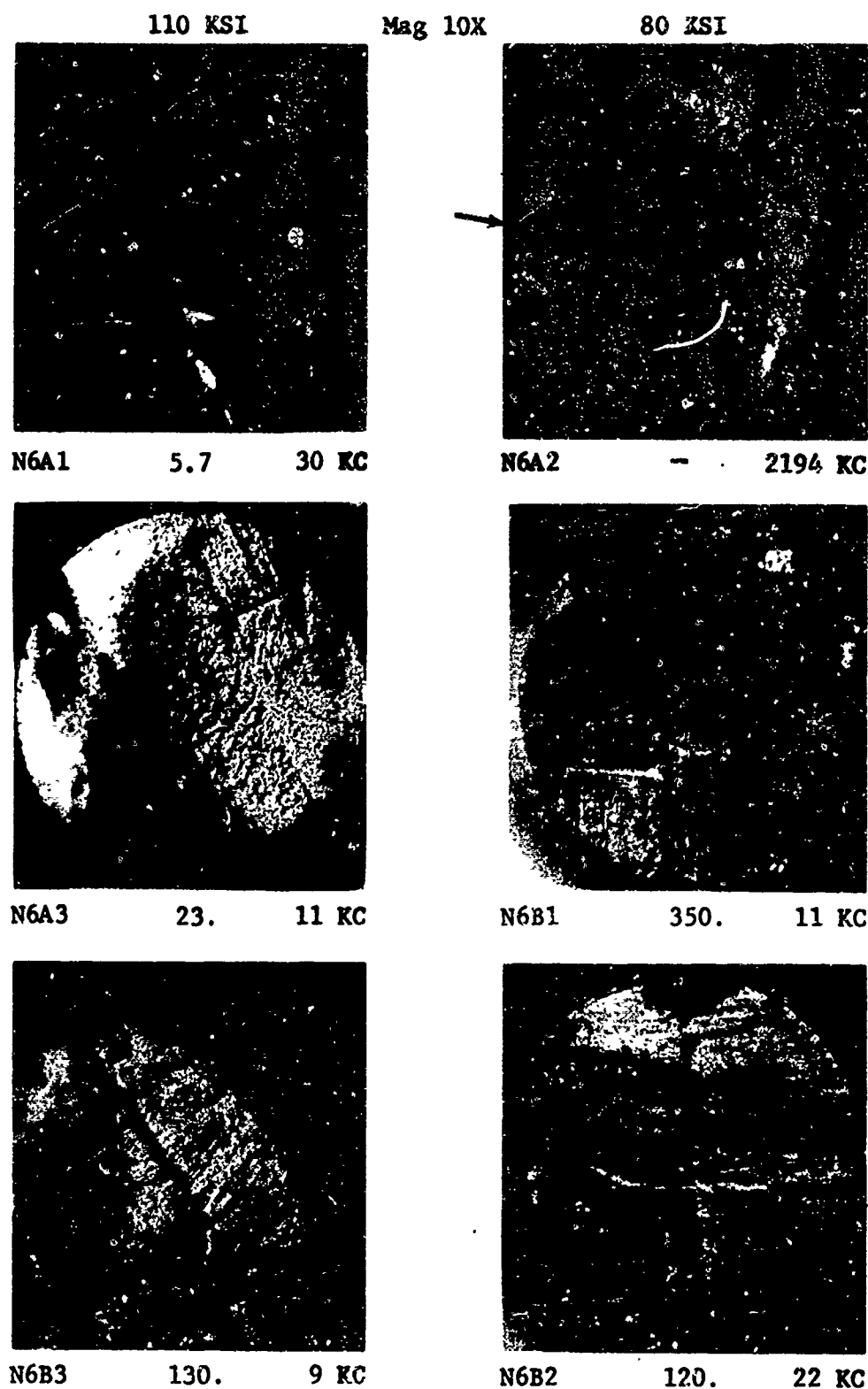


Figure 8.60 Fracture Surfaces of Failed Fatigue Specimens Series N6-Multiple-Bond/3-Axis Diffusion Bonded with 3.1% Average Short Transverse Deformation



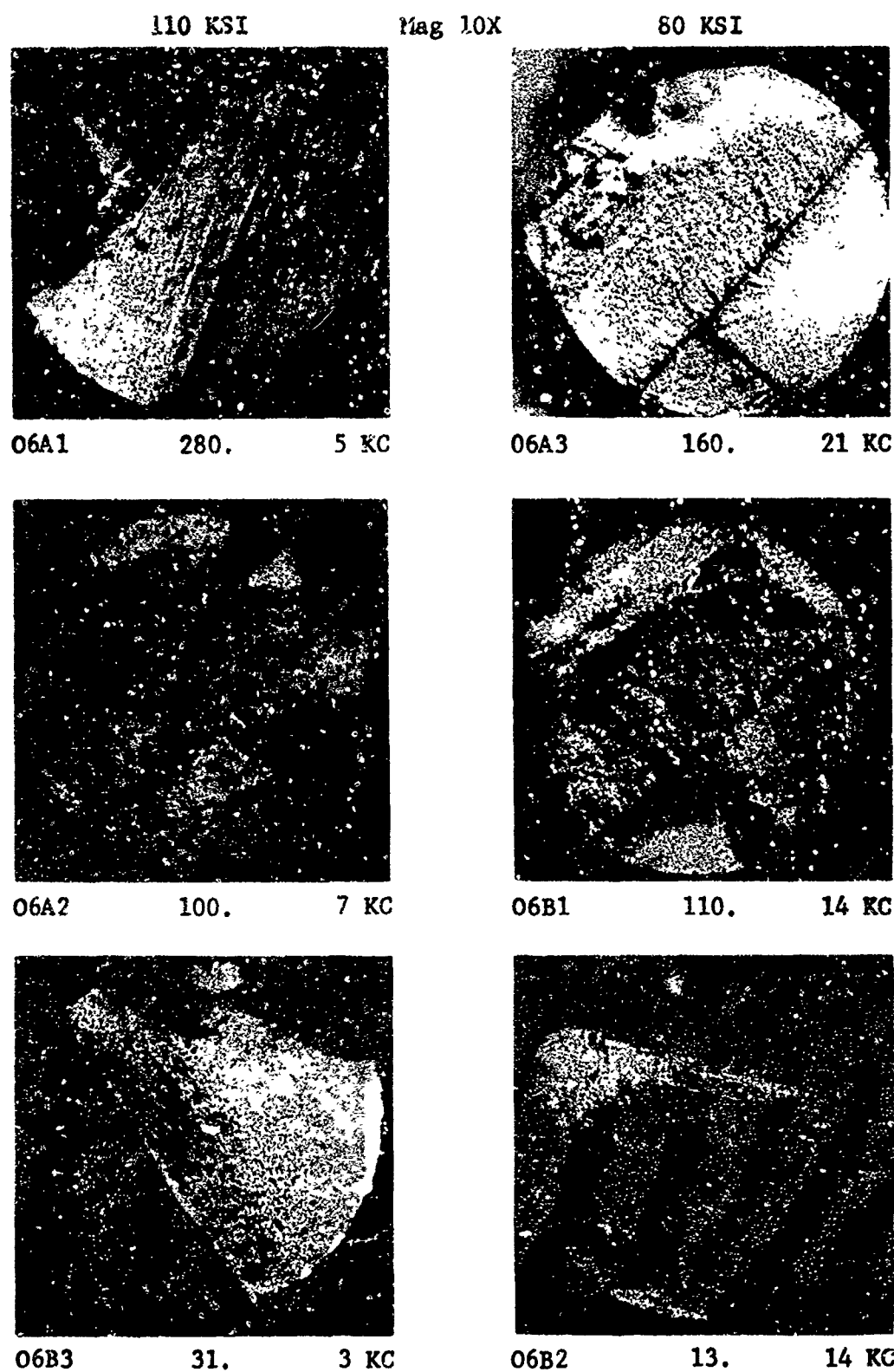


Figure 8.61 Fracture Surfaces of Failed Fatigue Specimens Series 06-  
Multiple-Bond/3-Axis Diffusion Bonded with 2.2% Average  
Short Transverse Deformation

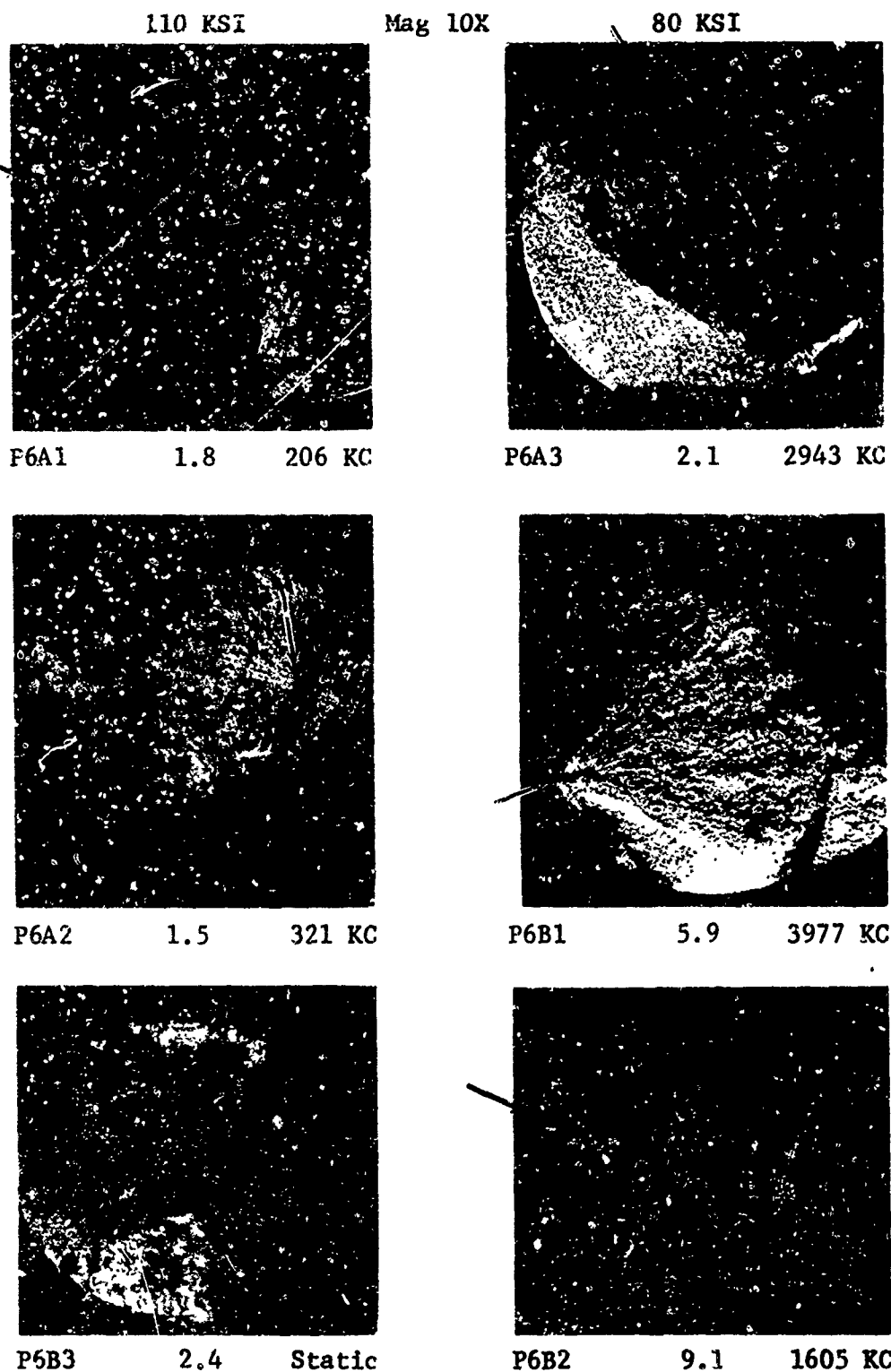


Figure 8.62 Fracture Surfaces of Failed Fatigue Specimens Series P6-Multiple-Bond/3-Axis Diffusion Bonded with ASTM Grain Size No. 11

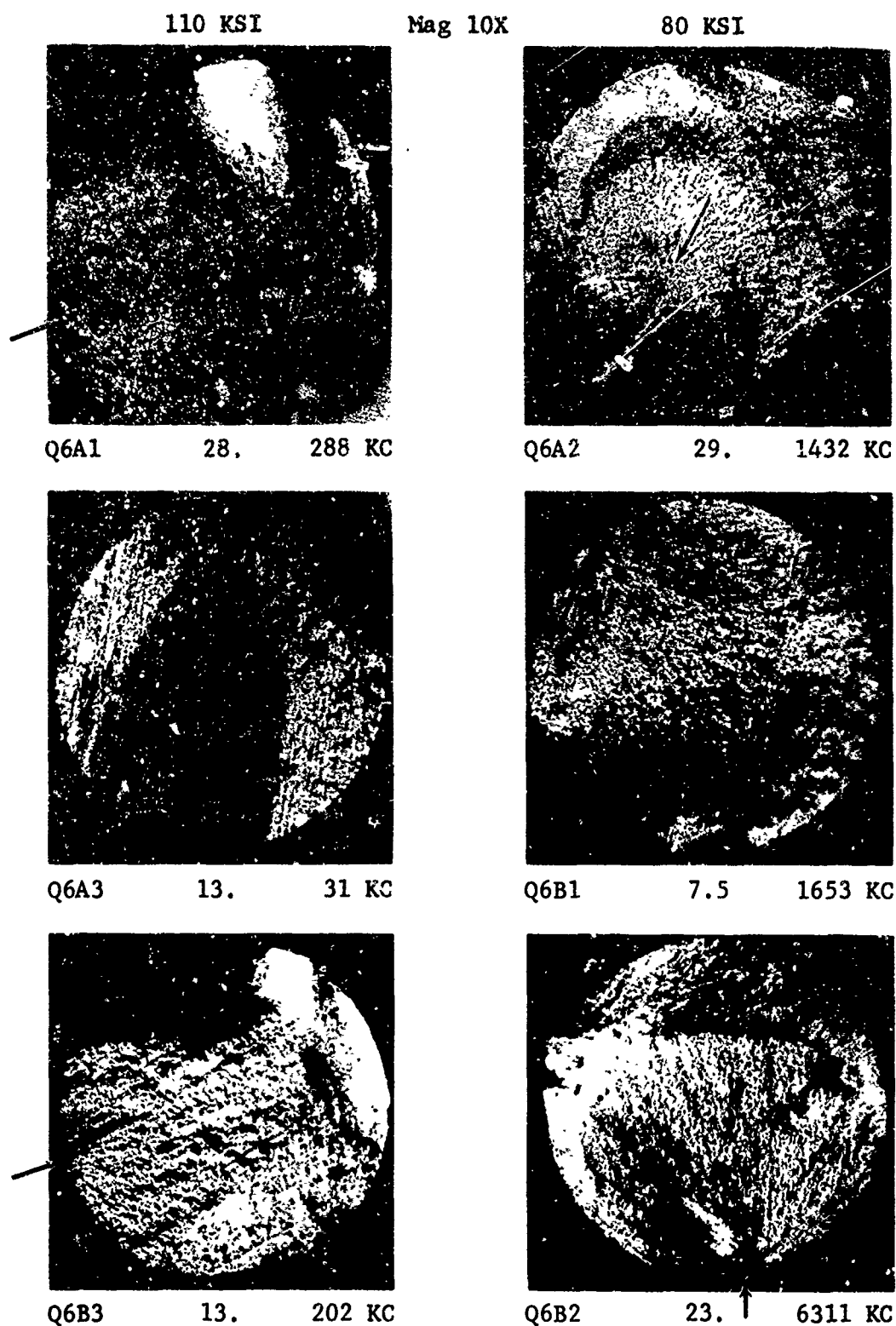


Figure 8.63 Fracture Surfaces of Failed Fatigue Specimens Series Q6-Multiple-Bond/3-Axis Diffusion Bonded with ASTM Grain Size No. 8

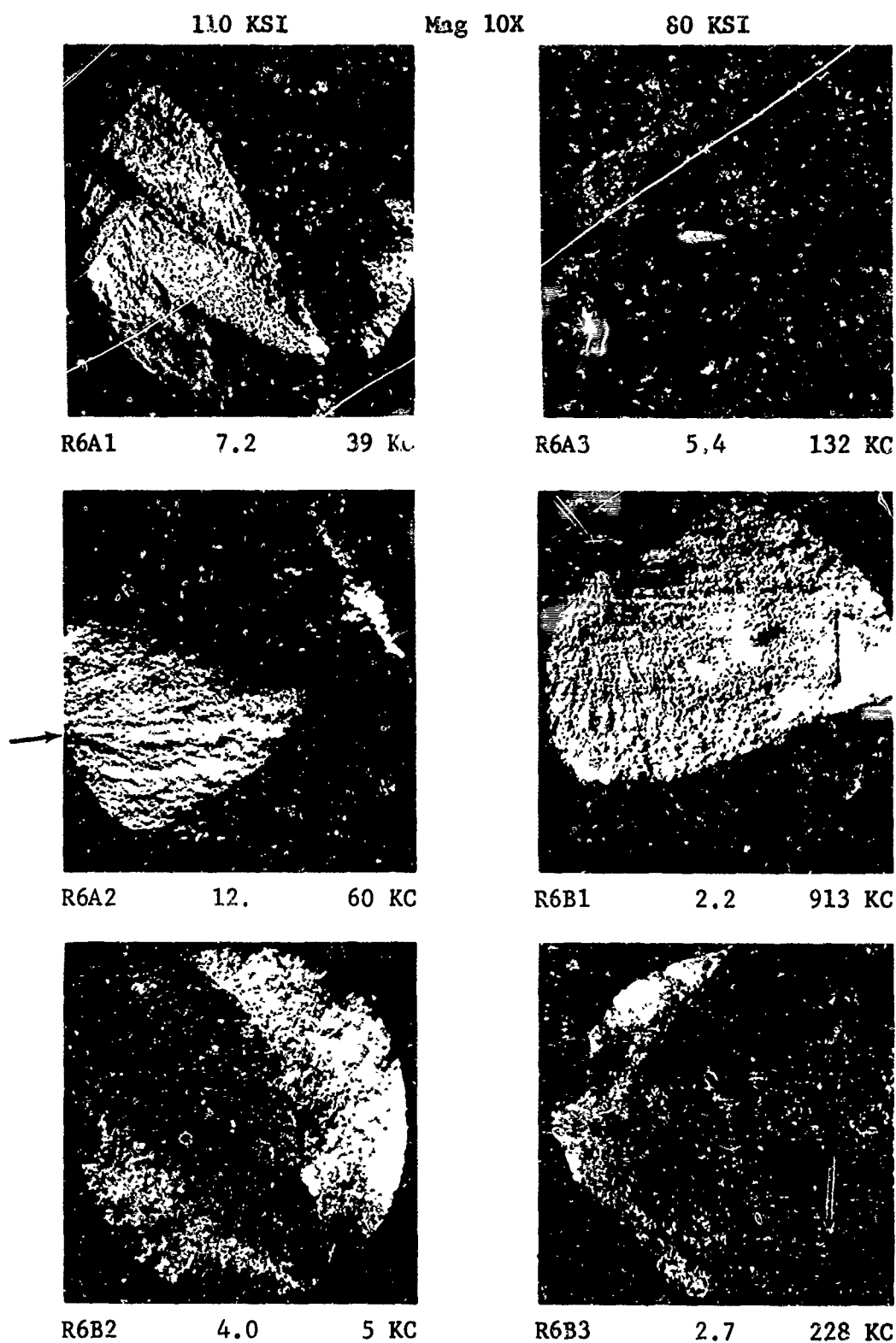


Figure 8.64 Fracture Surfaces of Failed Fatigue Specimens Series R6-  
Multiple-Bond/3-Axis Diffusion Bonded with ASTM Grain  
Size No. 7

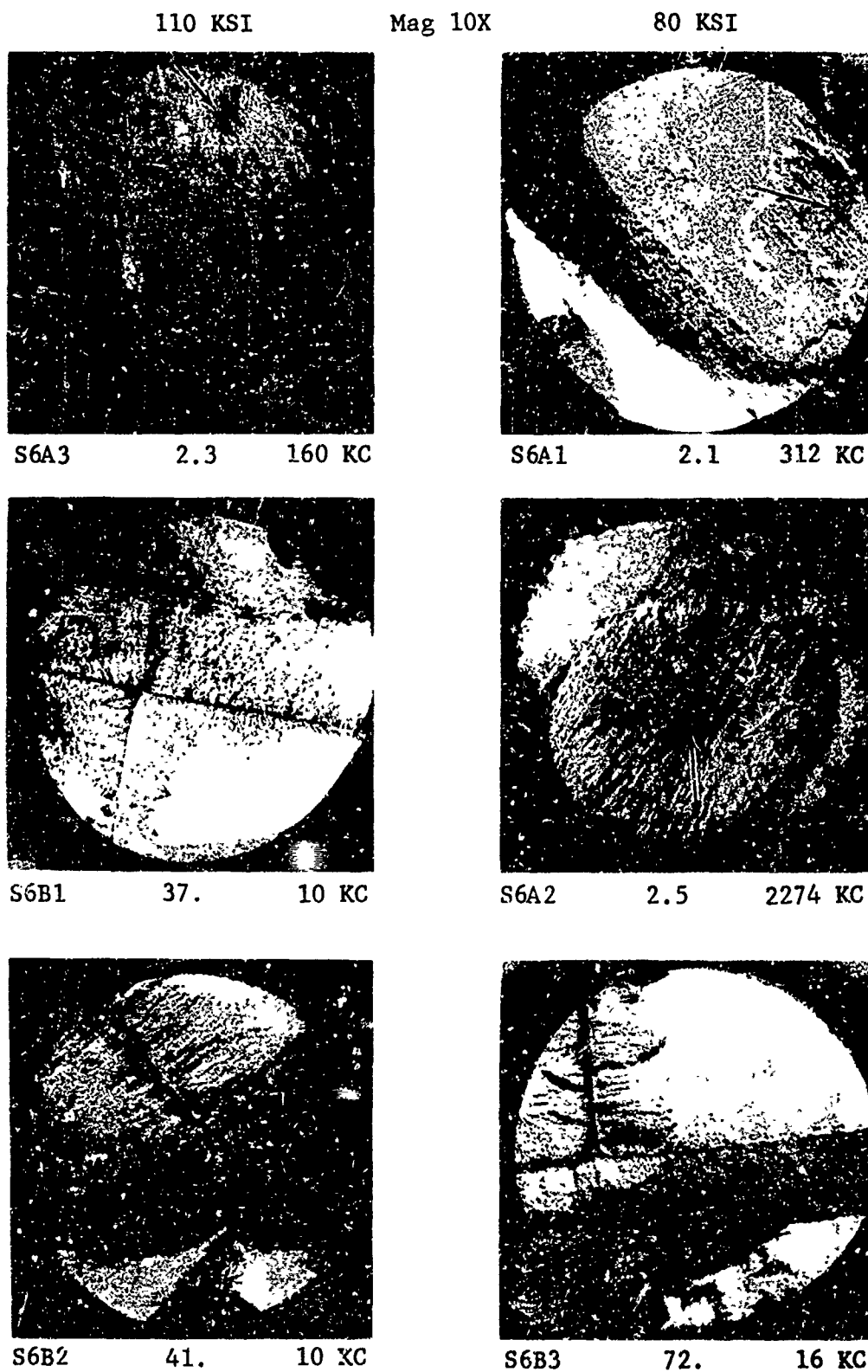


Figure 8.65 Fracture Surfaces of Failed Fatigue Specimens Series S6-  
Multiple Bond/3 Axis Diffusion Bonded with .008" Tetragonal  
Corner Void

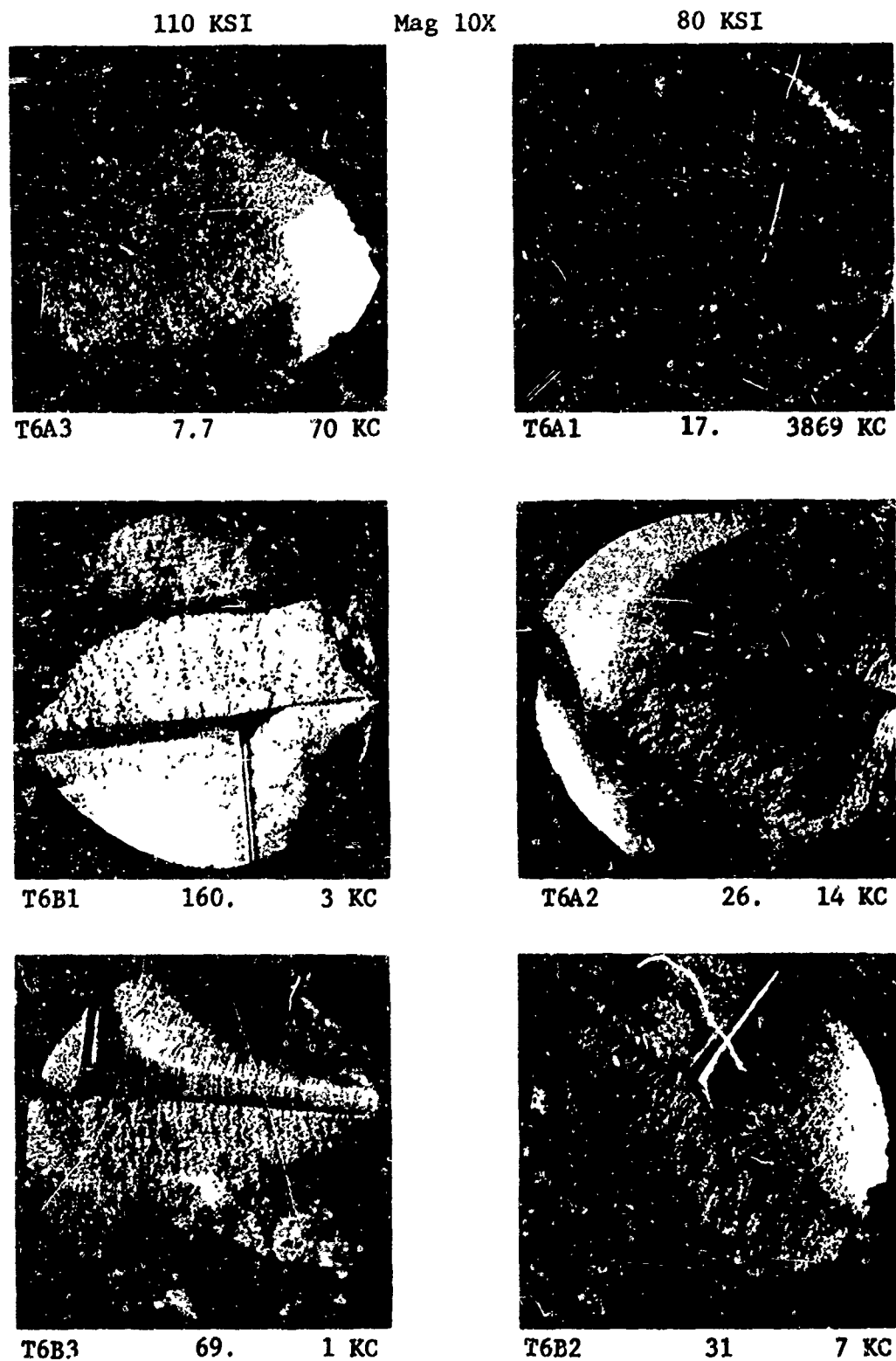


Figure 8.66 Fracture Surfaces of Failed Fatigue Specimens Series T6-Multiple-Bond/3-Axis Diffusion Bonded with .018" Tetragonal Corner Void

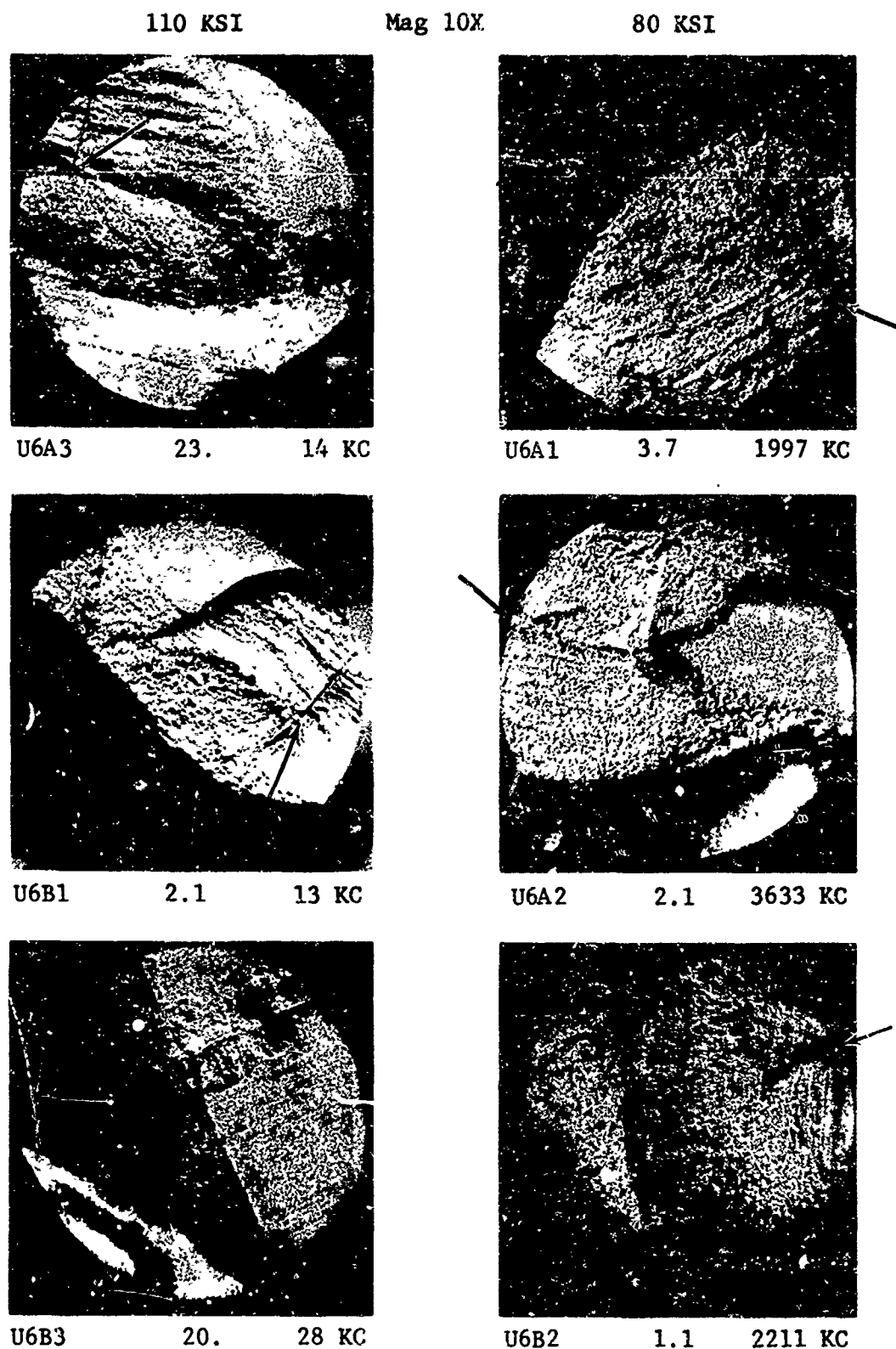


Figure 8.67 Fracture Surfaces of Failed Fatigue Specimens Series U6-Multiple-Bond/3-Axis Diffusion Bonded with .030" Tetragonal Corner Void

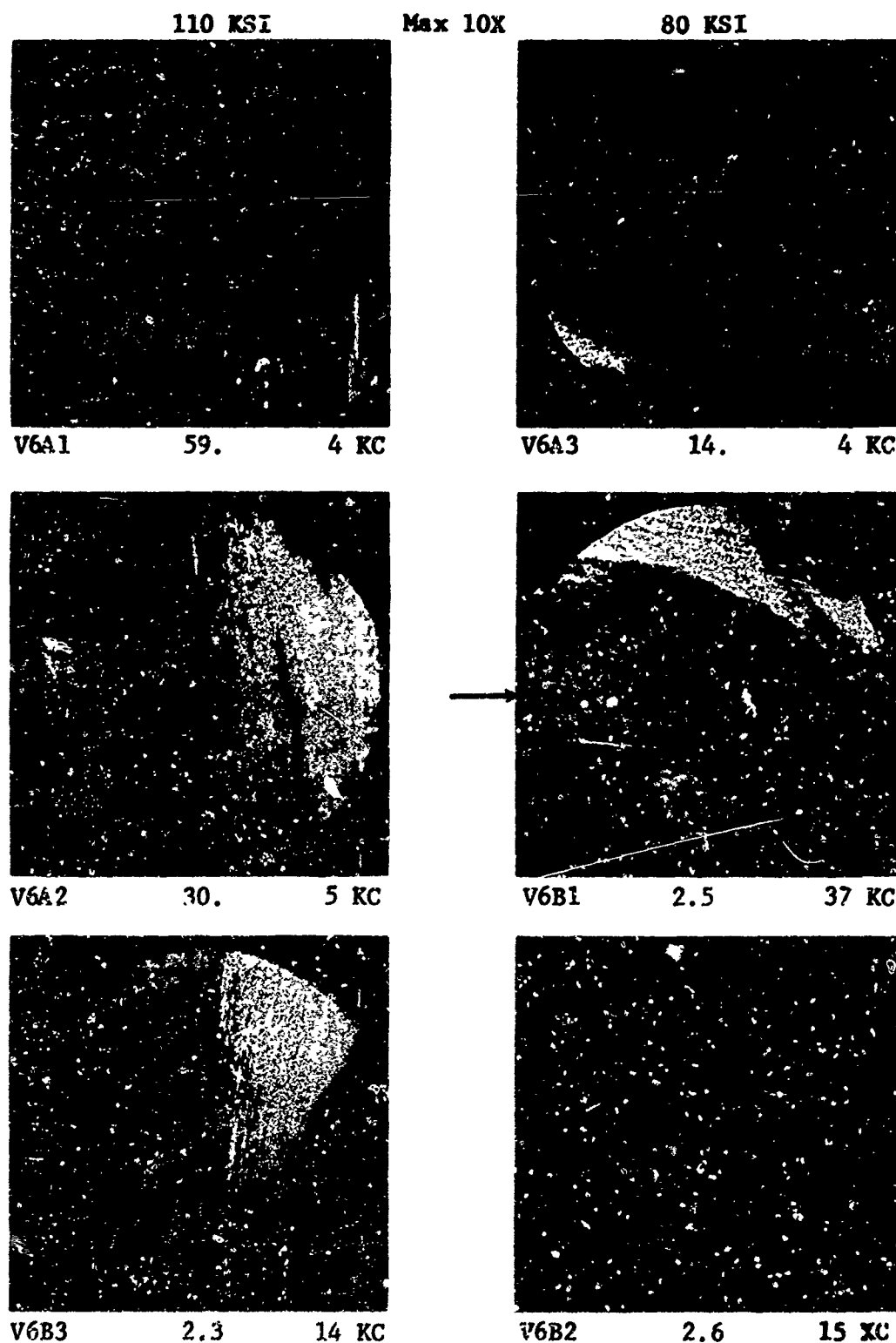


Figure 8.68 Fracture Surfaces of Failed Fatigue Specimens Series V6-Multiple-Bond/3-Axis Diffusion Bonded with Alpha Case Contamination



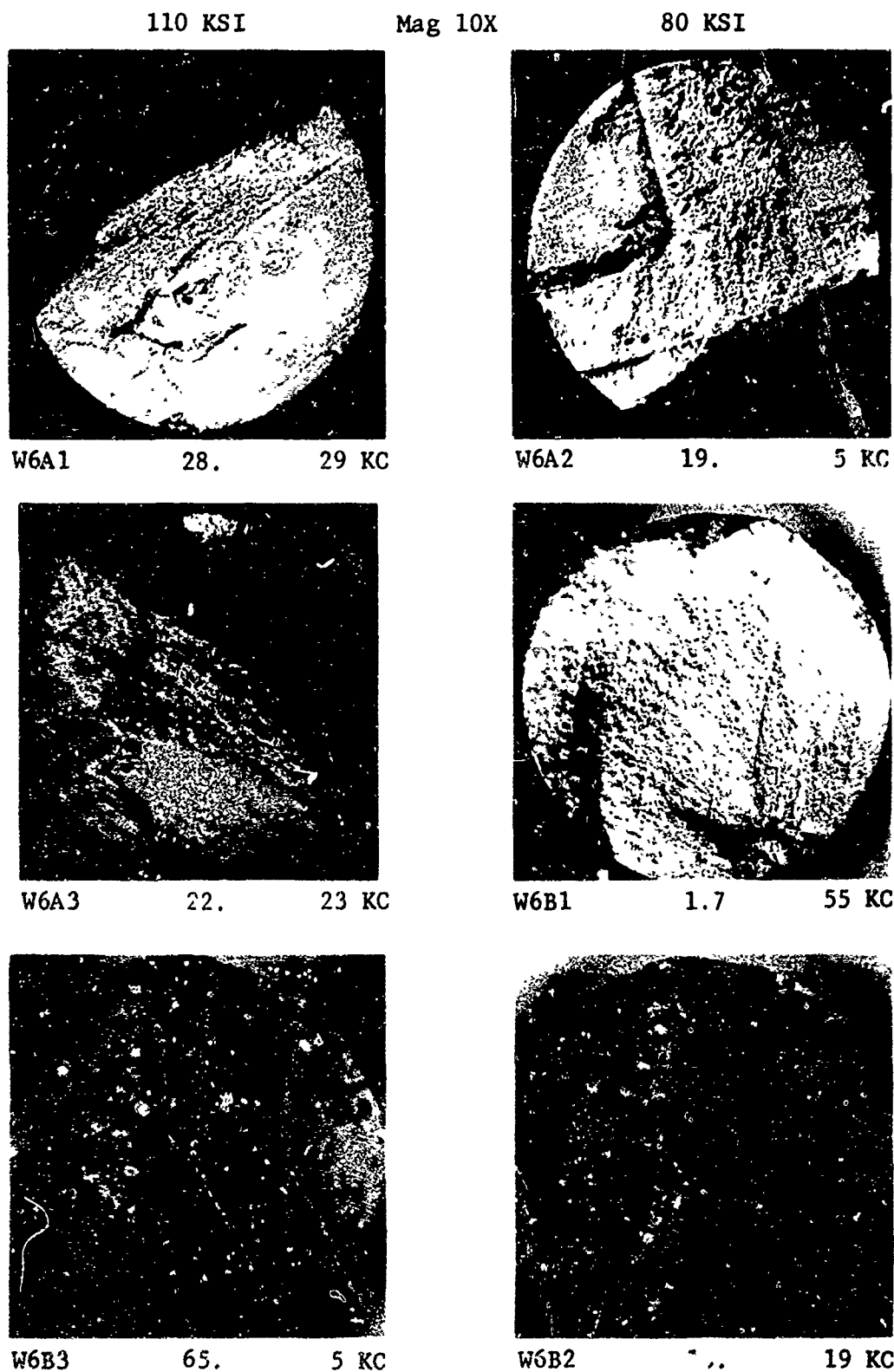
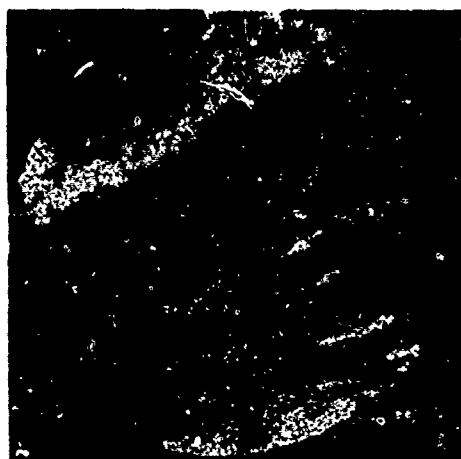


Figure 8.69 Fracture Surfaces of Failed Fatigue Specimens Series W6-Multiple-Bond/3-Axis Diffusion Bonded with 304 S.S. Powder Contamination

110 KSI

Mag 10X

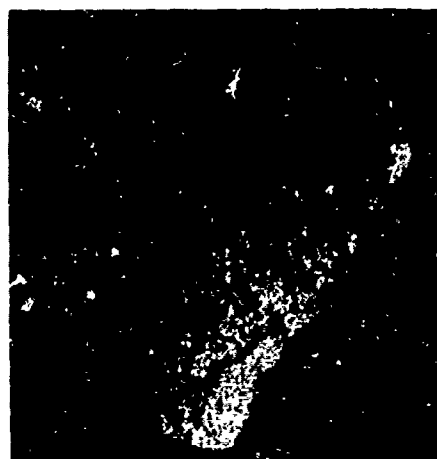
80 KSI



X6A2

68.

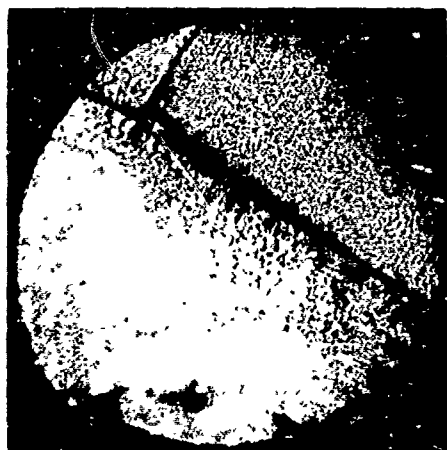
2 KC



X6A1

160.

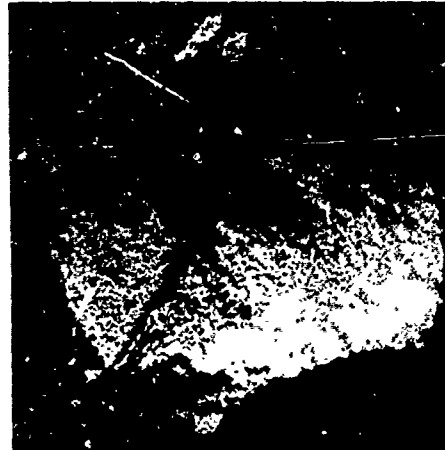
7 KC



X6A3

180

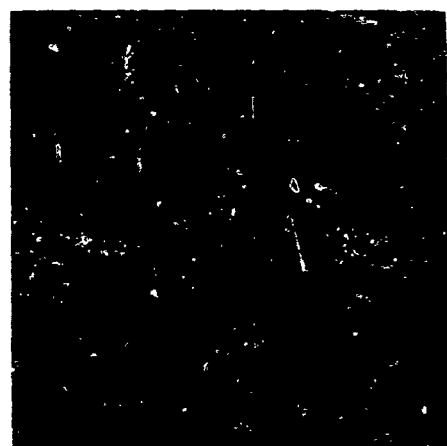
1 KC



X6B1

190.

22 KC



X6B3

147.

1 KC



X6B2

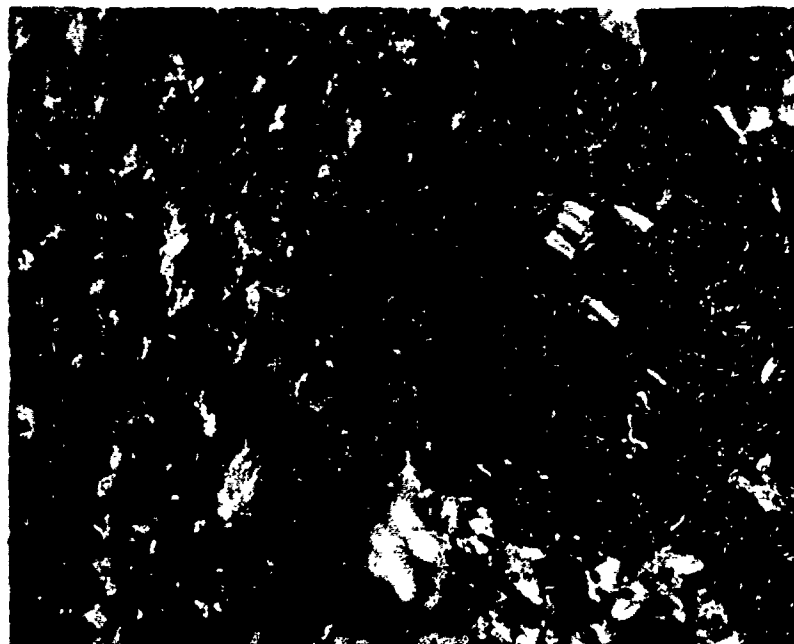
83.

25 KC

Figure 8.70 Fracture Surfaces of Failed Fatigue Specimens Series X6-Multiple-Bond/3-Axis Diffusion Bonded with  $\text{SiO}_2$  Powder Contamination

### 8.3.3 Microstructural Analysis of Intentional Defect-Initiated Fatigue Failures

Photomicrographs showing microstructures surrounding the various types of intentional defects in fracture fatigue specimens are shown in Figures 8.71 through 8.75. In Figures 8.71 and 8.72, surface voids at the diffusion bonded interface are shown while in Figures 8.73 through 8.75, surface contamination is displayed. In Figures 8.74 and 8.75, the different effects of stainless steel and  $\text{SiO}_2$  powder on the surrounding titanium can be observed. In addition, Figure 8.76 shows the results of microprobe X-ray analysis performed in the defect area of specimen W3B2 (stainless steel powder inclusion). Distances of diffusion for the elements involved along with changes in microstructure around the defect are dramatically displayed.



275X

Darkfield



200X

Etch:

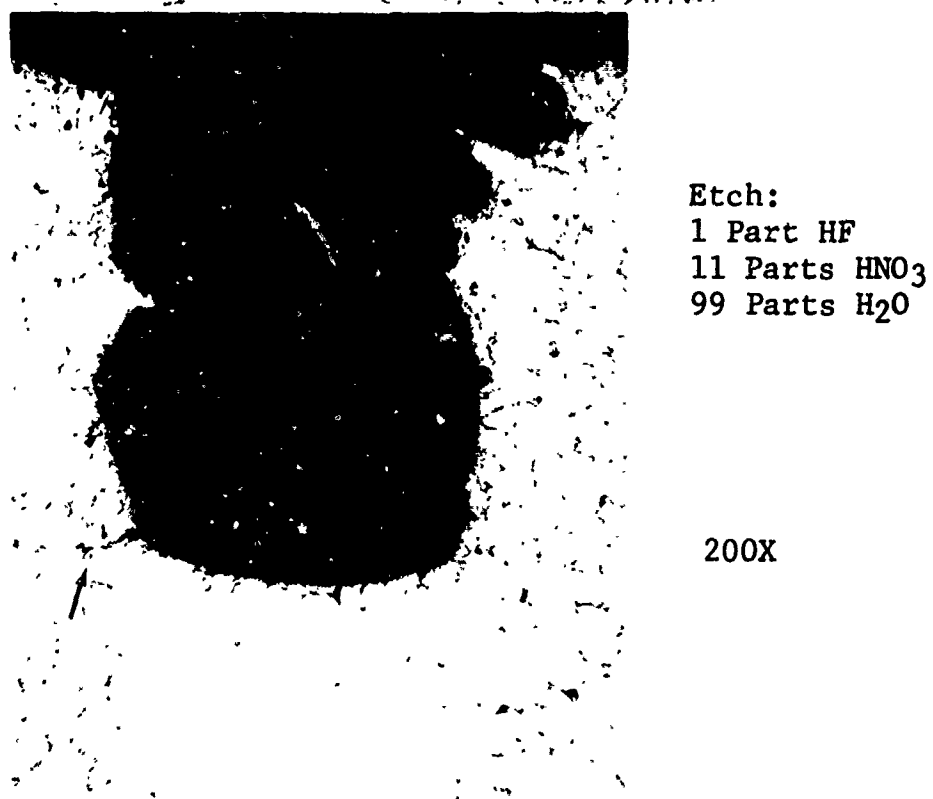
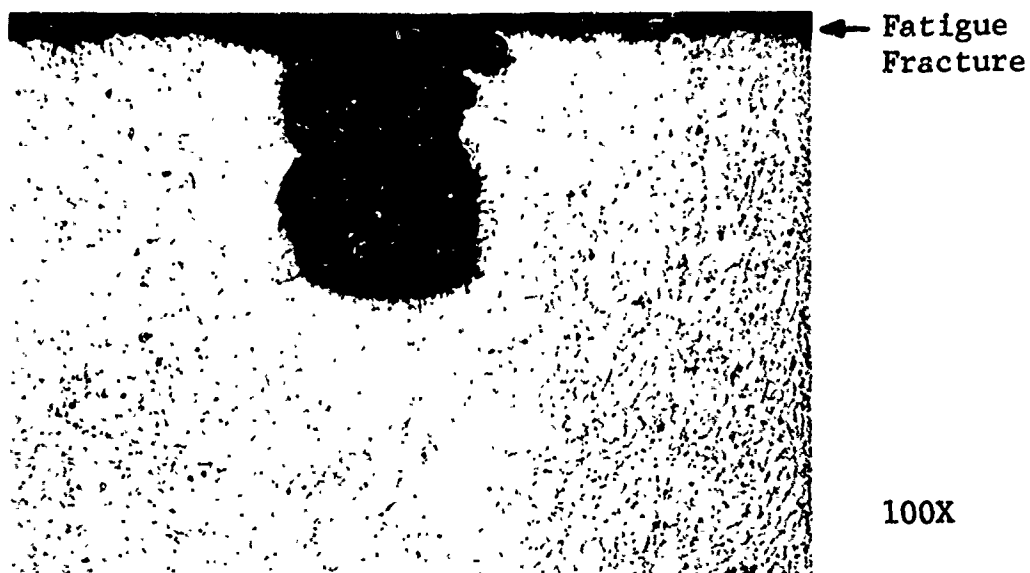
1 Part HF

11 Parts HNO<sub>3</sub>

99 Parts H<sub>2</sub>O

Top photo was taken of the fracture looking down into the hole. Cubic grain growth and slip planes can be seen inside hole. Photomicrograph shows that metallic growth has occurred from diffusion bonding temperatures and pressures.

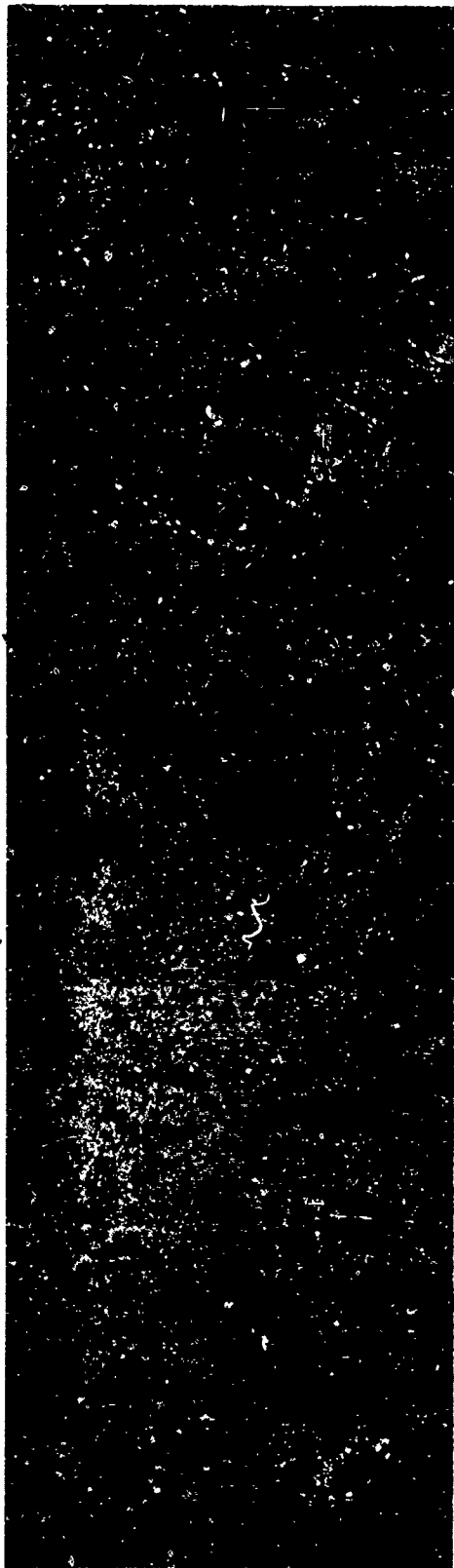
Figure 8.71 Microstructure of Diffusion Bonded Ti-6Al-4V Specimen S3B2 Containing a .0065" Dia Electric Discharge Formed Hole



Although fatigue failure occurred at top of hole at diffusion bonded interface, a fatigue crack can be seen to have formed at bottom of drilled hole. Microsection not thru hole center-line.

Figure 8.72 Microstructure of Diffusion Bonded Ti-6Al-4V Fatigue Specimen U3B1 Containing Drilled .020" Dia. Void

← Alpha Layer → ← Fatigue Fracture Surface →



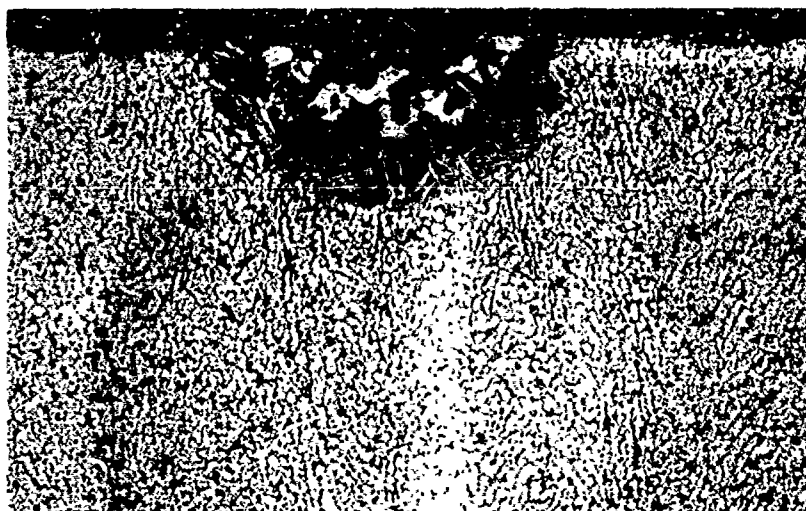
A. 0.01" Deep Alpha Case is Detectable by Lesser Amount of Dark Etching Beta Around Alpha Equiaxed Grains. (100X)

← Fatigue Fracture Surface →

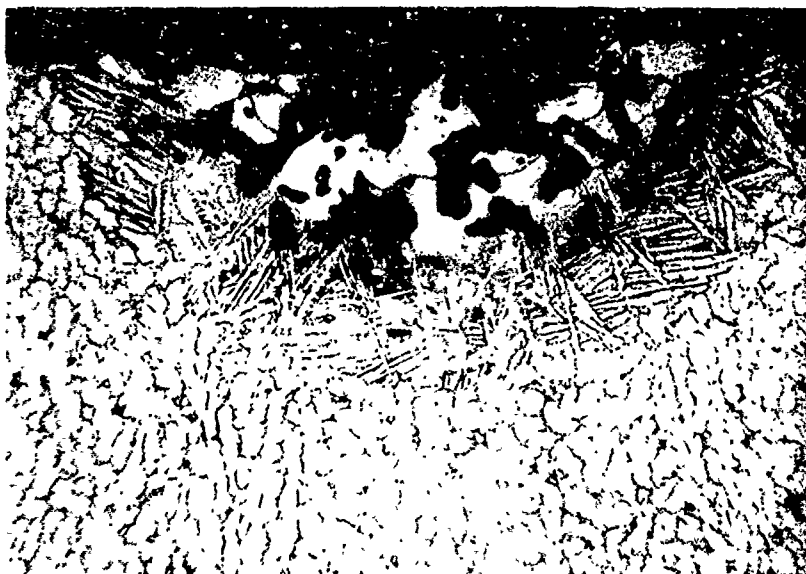


B. Mating Surface to Microsection of (A). Normal Equiaxed Alpha Grains in Beta Matrix. (200X)

Figure 8.73 Microstructure of Diffusion Bonded Ti-6Al-4V Fatigue Specimen V3A3 Containing an Alpha Case Defect



100X

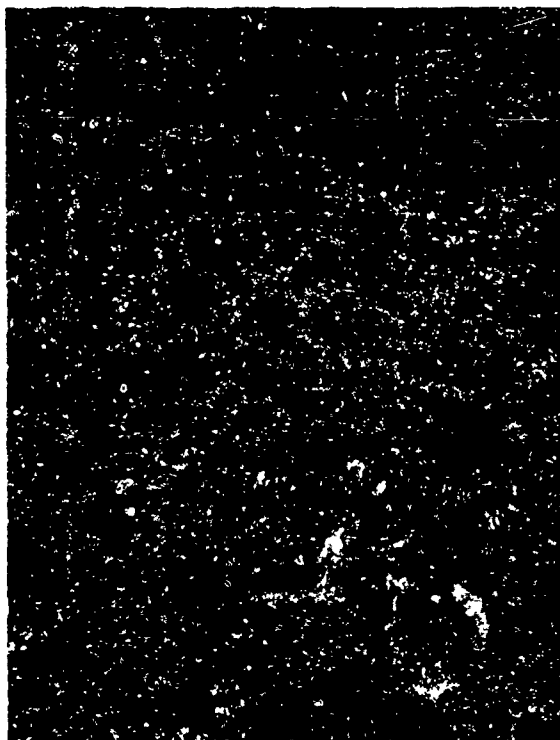


Etch:  
1 Part HF  
11 Parts HNO<sub>3</sub>  
99 Parts H<sub>2</sub>O

200X

The defect resulted from filling an original .013" dia x .006" deep drilled hole with 304S.S. powder and bonding 6 hours at 1700F with 5% deformation. The 19% Cr and 58% Fe in the 304 diffusing into the Ti-6Al-4V lowered the beta transus, allowing transformation of the equiaxed alpha to beta at the 1700F bonding temperature. On cooling, part of this beta was retained (dark etching constituent) adjacent to the coalesced 304 powders. The remainder of the converted beta transformed to acicular alpha forming the .004" deep layer shown above.

Figure 8.74 Microstructure of Diffusion Bonded Ti-6Al-4V Specimen W3B2 Containing 304S.S. Powder Defect at the Bond Plane



A. View of Defect in Fatigue Failed Fracture Surface (175X)



B.  $\text{SiO}_2$  in Hole Reacted Very Slightly with Ti to Form More Beta (200X)



C. Overexposed Photos Show  $\text{SiO}_2$  in Hole and on Mating Fracture Surface with Very Little Reaction with Titanium. Failure Started at Diffusion Bonded Interface (100X)

Figure 8.75 Microstructure of Diffusion Bonded Ti-6Al-4V Specimen X3A1 Containing  $\text{SiO}_2$  Powder in Drilled .013" Dia. Hole



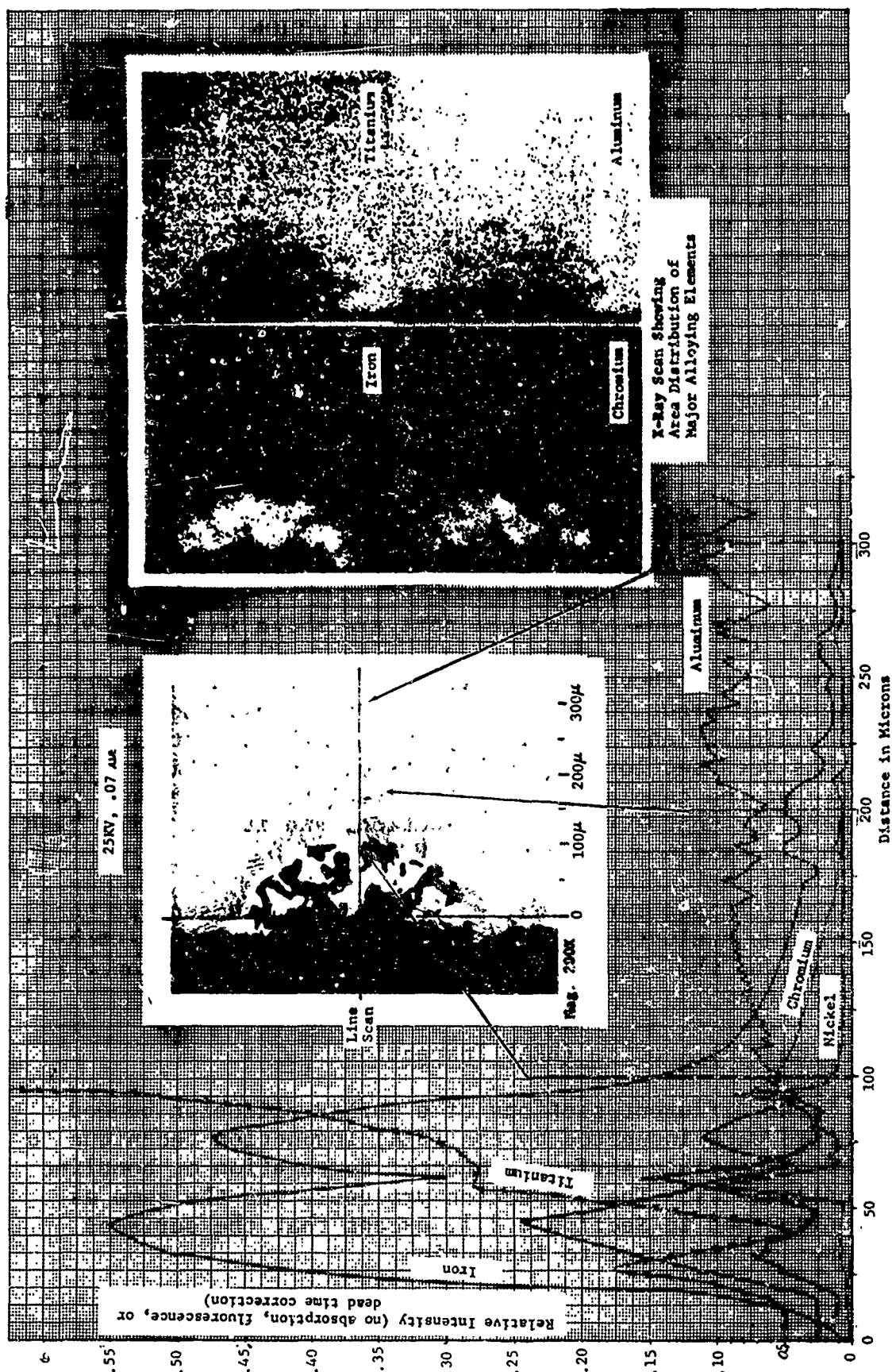


Figure 8.76 microprobe X-Ray Analysis of Diffusion Bonded Ti-6Al-4V Containing 304 S.S. Powder Defect Specimen W382

## 9. LARGE STRUCTURE EVALUATION

In 1968 (Ref. 17), North American Rockwell was selected as a subcontractor to General Dynamics/Fort Worth to fabricate a demonstration structure of diffusion bonded titanium (6Al-4V). In order to evaluate the fabrication process thoroughly, a structure was built that included as many facets of manufacturing as could be conceived. The specific details included:

- . Two hundred inch radius on the bottom plate;
- . Long edge taper on that radius;
- . Both radius and 45-degree fillets;
- . A reinforced hole;
- . Grid stiffening.

The original dimensions of the part are shown in Figure 9.1.

Two of the above structures were fabricated. One was sectioned in about 50 parts and extensively examined both metallurgically and mechanically (Ref. 18). The other structure has been sectioned into 5 parts as shown in Figure 9.2. Because of the complexity of this structure, it presents many problems for nondestructive evaluation, and it has never been thoroughly examined for defects.

The sections marked #1, #2, and #3 were chosen for non-destructive evaluation by fluorescent penetrant, blue-etch-anodize, and the advanced ultrasonic techniques developed in this program.

### 9.1 Blue-Etch-Anodize (BEA) Inspection

Three different sections of a GD/NAR diffusion bonded structure were inspected by the (BEA) inspection technique to determine possible surface connected segregation or bondline discontinuities. The inspection procedure was the same as that described in Section 6.2.1, except that the surfaces were not milled prior to inspection.

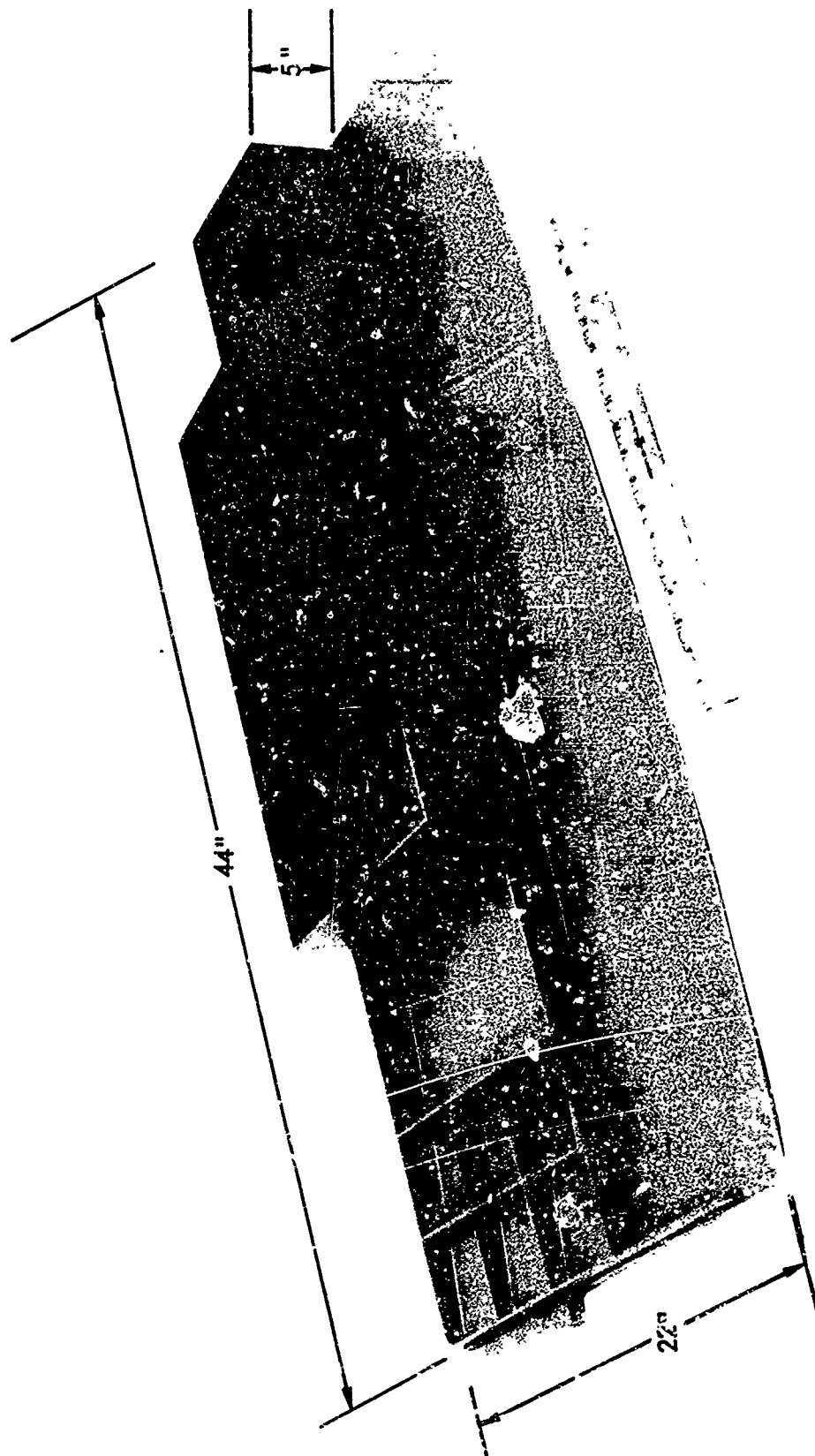


Figure 9.1 Large Diffusion Bonded Structure Details

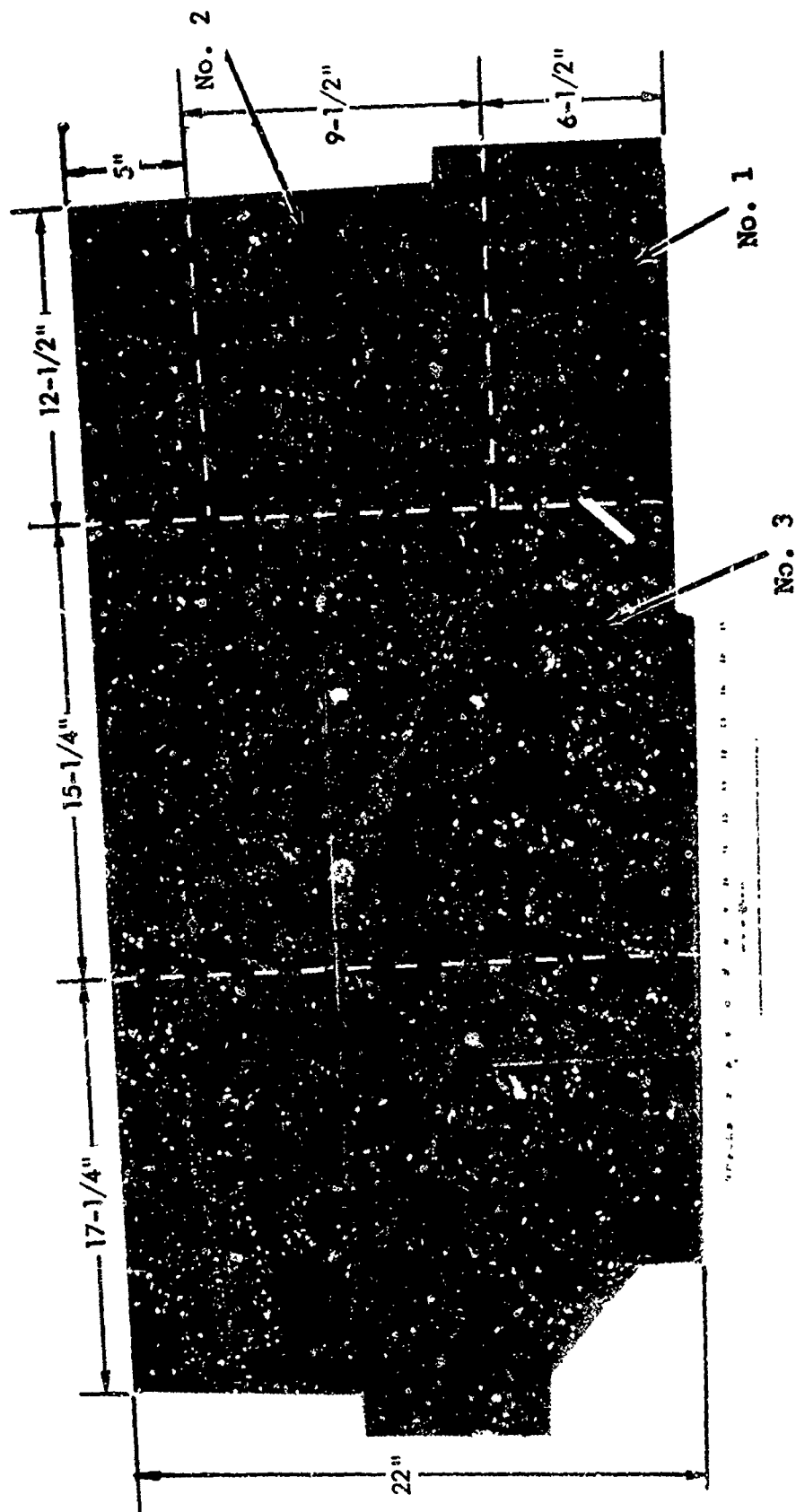


Figure 9.2 Sectioning and Numbering Diagram

### 9.1.1 Inspection Results

Part #1 - Several dark blue areas were detected in this part. Most of these areas can be seen in Figure 9.3. These segregated areas could be due to either tooling reactions with the titanium or air contamination. No dark blue lines which would be associated with bondlines were detected.

Part #2 - Several dark blue areas were detected. Most of the dark blue areas found were associated with fillets located close to the thin wall in the middle of the specimen. One of the most pronounced dark blue areas is shown in Figure 9.4.

Part #3 - Several dark blue areas were detected. However, only one dark blue line was observed which seemed to be related to a bondline or fillet. This line is shown in Figure 9.5.

### 9.1.2 Verification of Defects

One of the areas on Part #1 (Location 1, Figure 9.3) having a darker blue color relative to the rest of the part was analyzed using X-ray diffraction and hardness measurements. X-ray diffraction results showed the alpha titanium phase primarily present with an expanded lattice constant  $C$ . This is indicative of interstitials dissolved in the alpha titanium structure. Hardness readings on this same sample gave a value of  $R_C = 38.3$  as compared to the average parent material value of  $R_C = 33.5$ , again indicative of interstitial contamination.

A section from another portion of Part #1 (Location 2, Figure 9.3) containing a blue area was sectioned and photographed. This area is shown in Figure 9.6. This area was found to contain a contaminated surface layer.

## 9.2 Fluorescent Penetrant Inspection

The procedure used for inspection of the three GD/NA2 diffusion bonded parts was the same as described previously in Section 6.2.2 specimens. However, the diffusion bonded parts received no surface treatment prior to inspection.

### 9.2.1 Inspection Results

Part #1 - No flaw indications were found in this part.

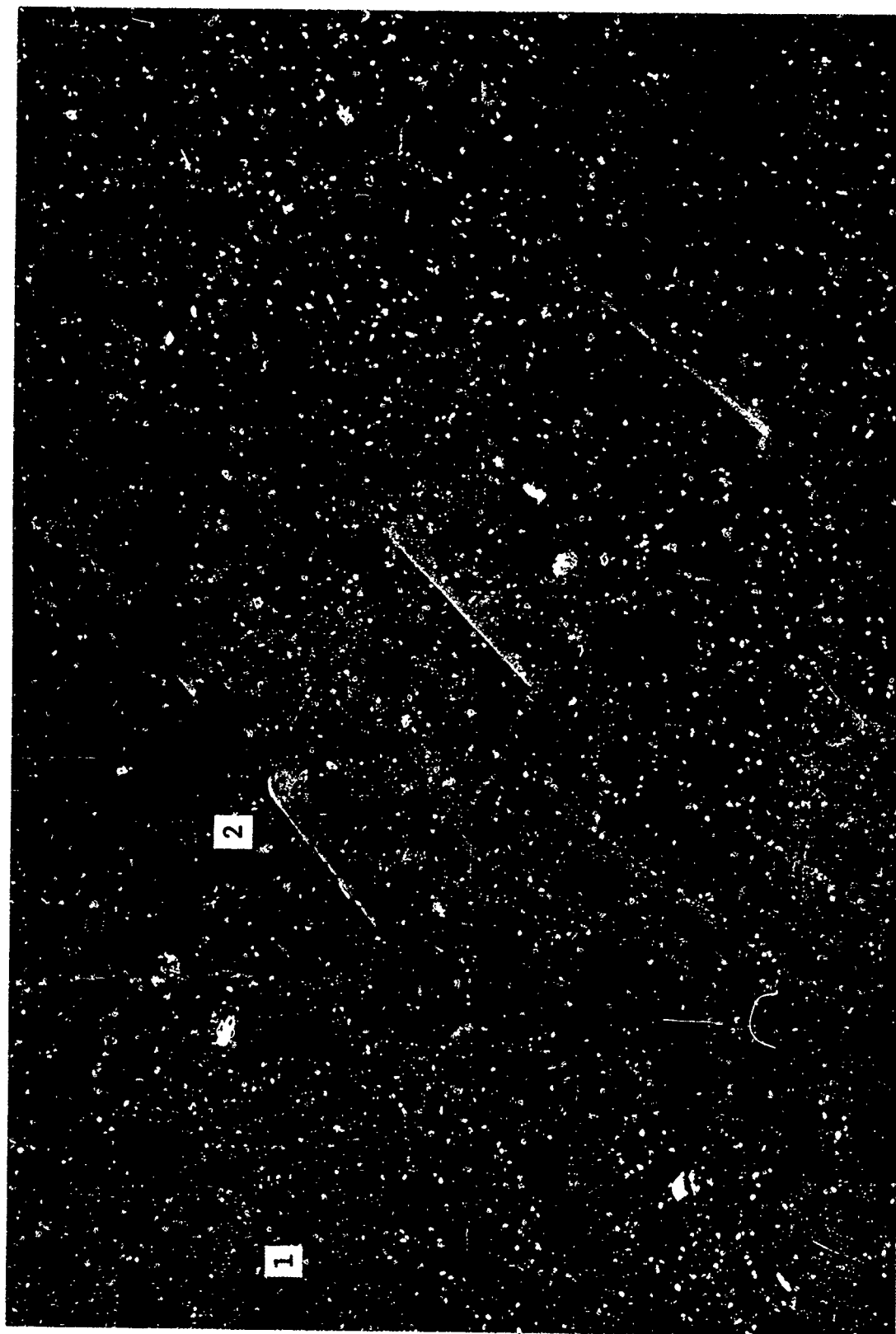
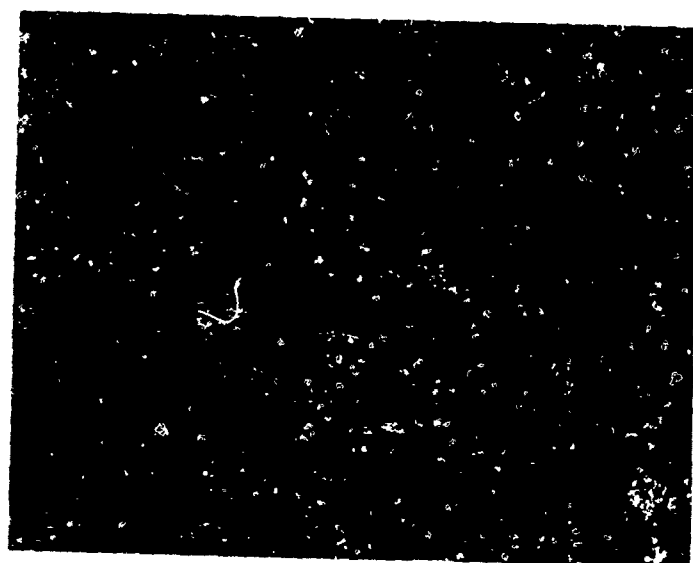


Figure 9.3 Blue Etch-Anodize Record of Part #1 Showing Surface-Connected Segregation



Figure 9.4 Blue Etch-Anodize Record of Part #2 Indicating Color Dis-  
continuities at Fillets



**Figure 9.5** Blue Etch-Anodize Record of Part #3 Showing Surface-Connected Segregation



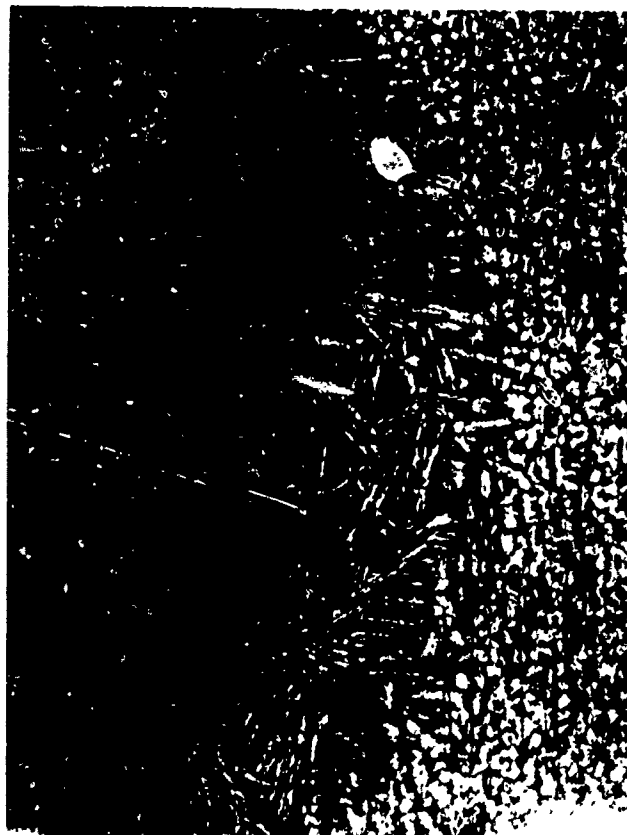


Figure 9.6 Photomicrograph of Contaminated Surface  
Layer in Part #1 (80X)

Part #2 - A small flaw indication was detected in a fillet area close to the thin wall in the middle of the specimen (see Figure 9.7). This flaw indication was sufficiently small that no further diagnostics were attempted.

Part #3 - Two major flaw indications were found in this part. They are shown in Figure 9.8.

### 9.2.2 Verification of Defects

The corner section of Part #3 which included the defects shown in Figure 9.8 was sectioned such that the flaws could be inspected more closely. The corner was then etched. The crack as detected is shown in Figure 9.9.

### 9.3 Ultrasonic Inspection

Part #1 (Figure 9.3) was selected for inspection by optimized Delta-Scan, variable tilt/multiple scan pulse-echo and contact signal averaged pulse echo. Three reference defects were fabricated in the fillet area of an upstanding stiffener. The reference flaws were (a) flat bottom holes (FBH) of 3/64-in. and 5/64-in. dia. and (b) 3/64-in. diameter drilled hole with unintentional metallic inclusion (drill tip).

The holes were fabricated  $30^{\circ}$  off-vertical and 0.18 in. deep per Figure 9.10.

#### 9.3.1 Delta-Scan

The C-scan system with a 5 MHz Delta-Scan head as described in Section 6.2.3 was utilized. Operating parameter optimization on the 5/64-in. FBH resulted in a transducer-transducer distance of separation of 0.55 in. and a transducer-to-specimen distance of 0.5 in. The diffusion bonded structure was oriented smooth side up (rib side down) with the stiffeners parallel to the X-Y coordinates of the scanner. Signal level was set at 50% of the response from the 5/64-in. FBH. Two scans were made with the structure rotated  $90^{\circ}$  between scans. This was done to obtain perpendicular and parallel alignment of the Delta-Scan head with each rib. The scan records are given in Figures 9.11 and 9.12. Rib locations and thereby diffusion bond areas are shown by the dotted lines.

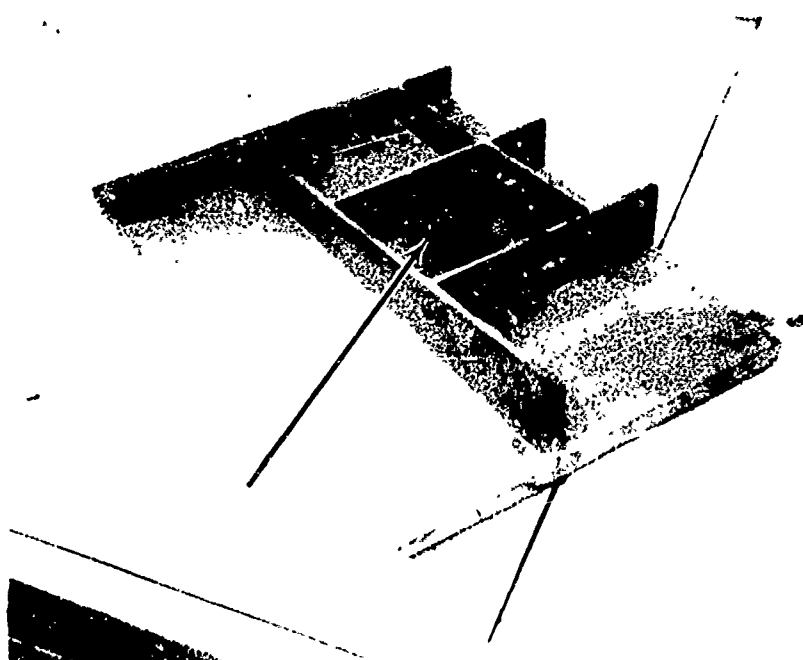


Figure 9.7 Fluorescent Penetrant Record of Part #2 with Location of Flaw Indication

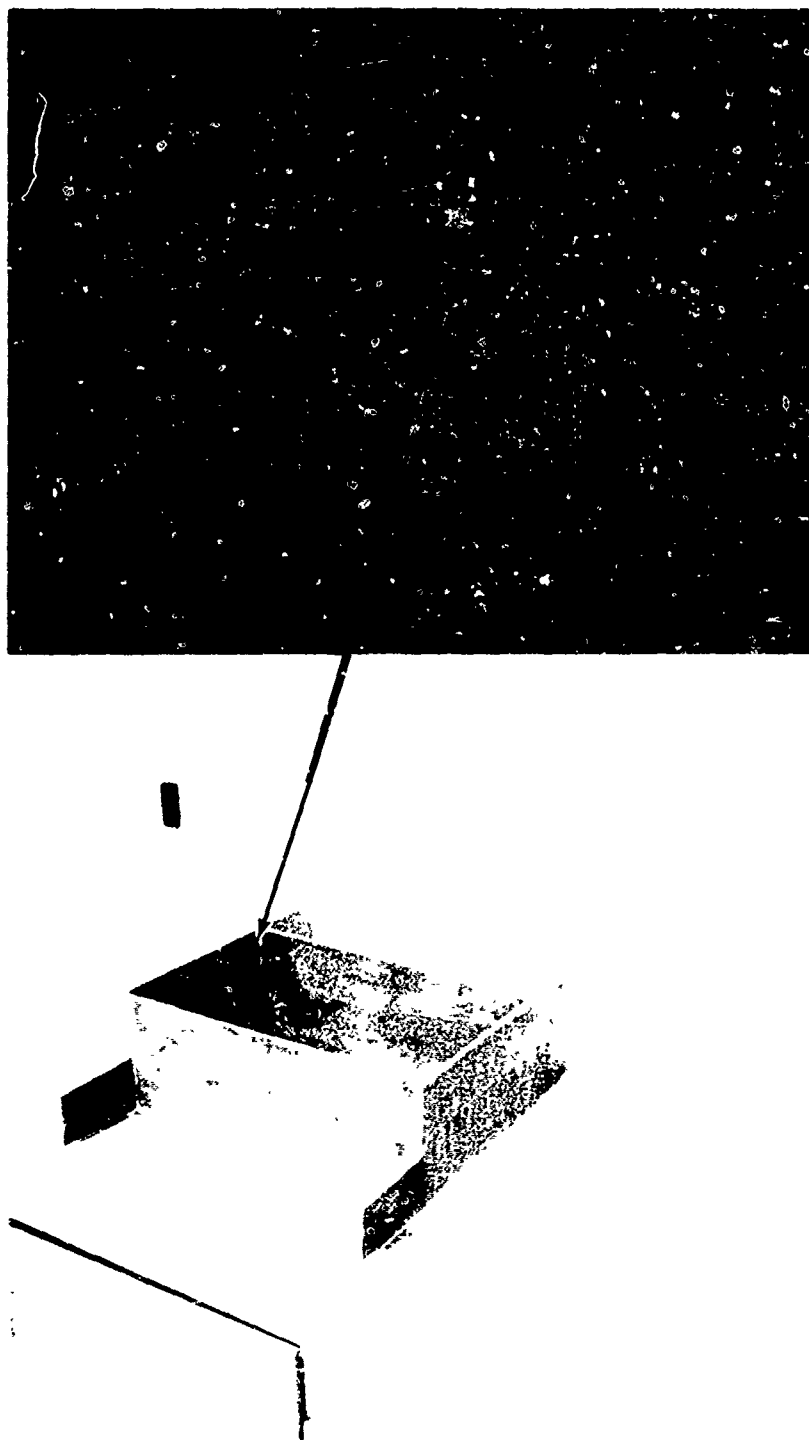


Figure 9.8 Fluorescent Penetrant Records of Part #3 Showing Flaw Indications and Locations



12X Mag

Figure 9.9 Photographs of Flaw in Fillet of Part #3 Detected by  
Fluorescent Penetrant Inspection

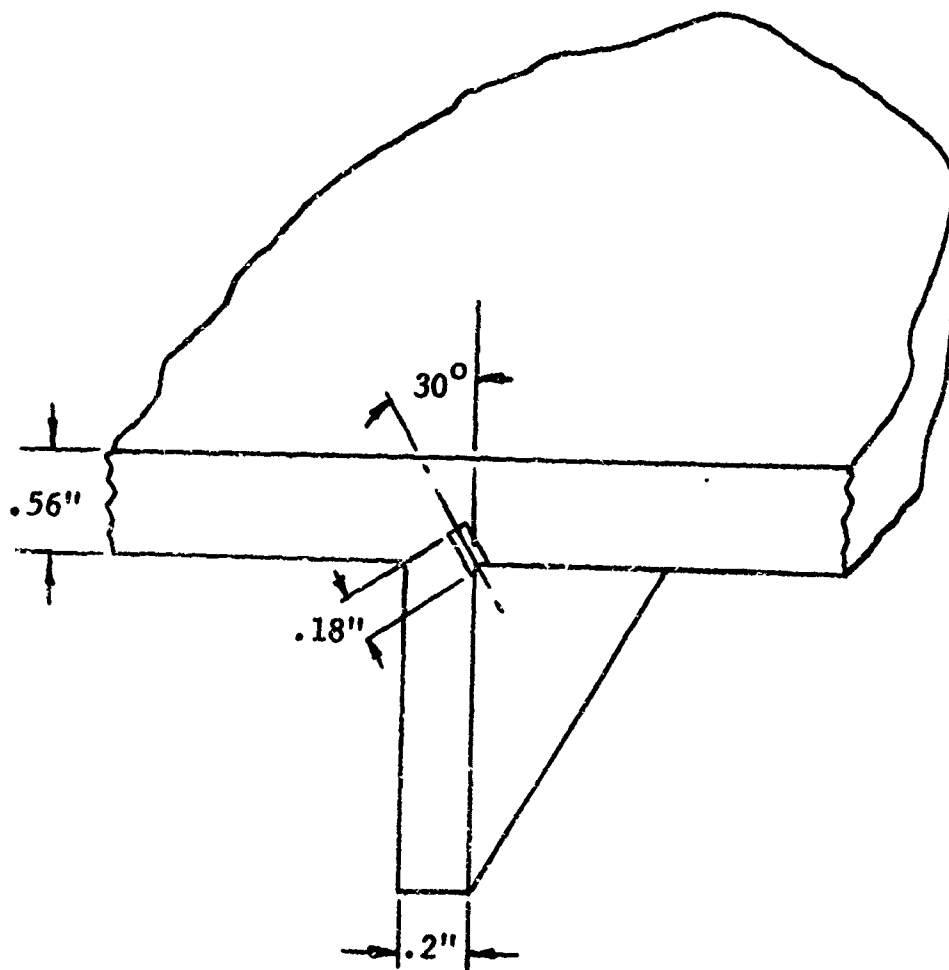


Figure 9.10 Orientation of Reference Holes in Part #1

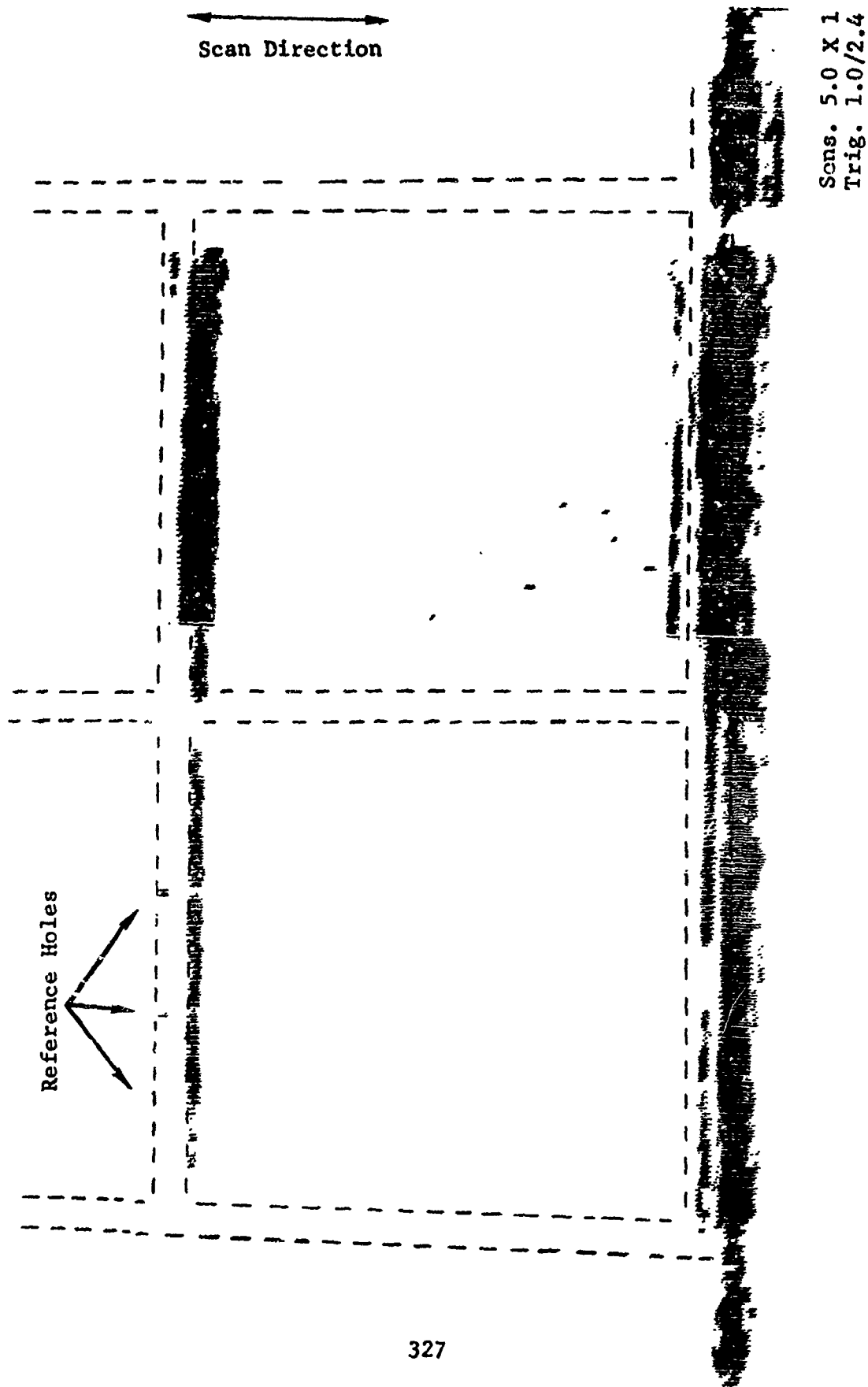


Figure 9.11 Delta/C-Scan Record of Part #1

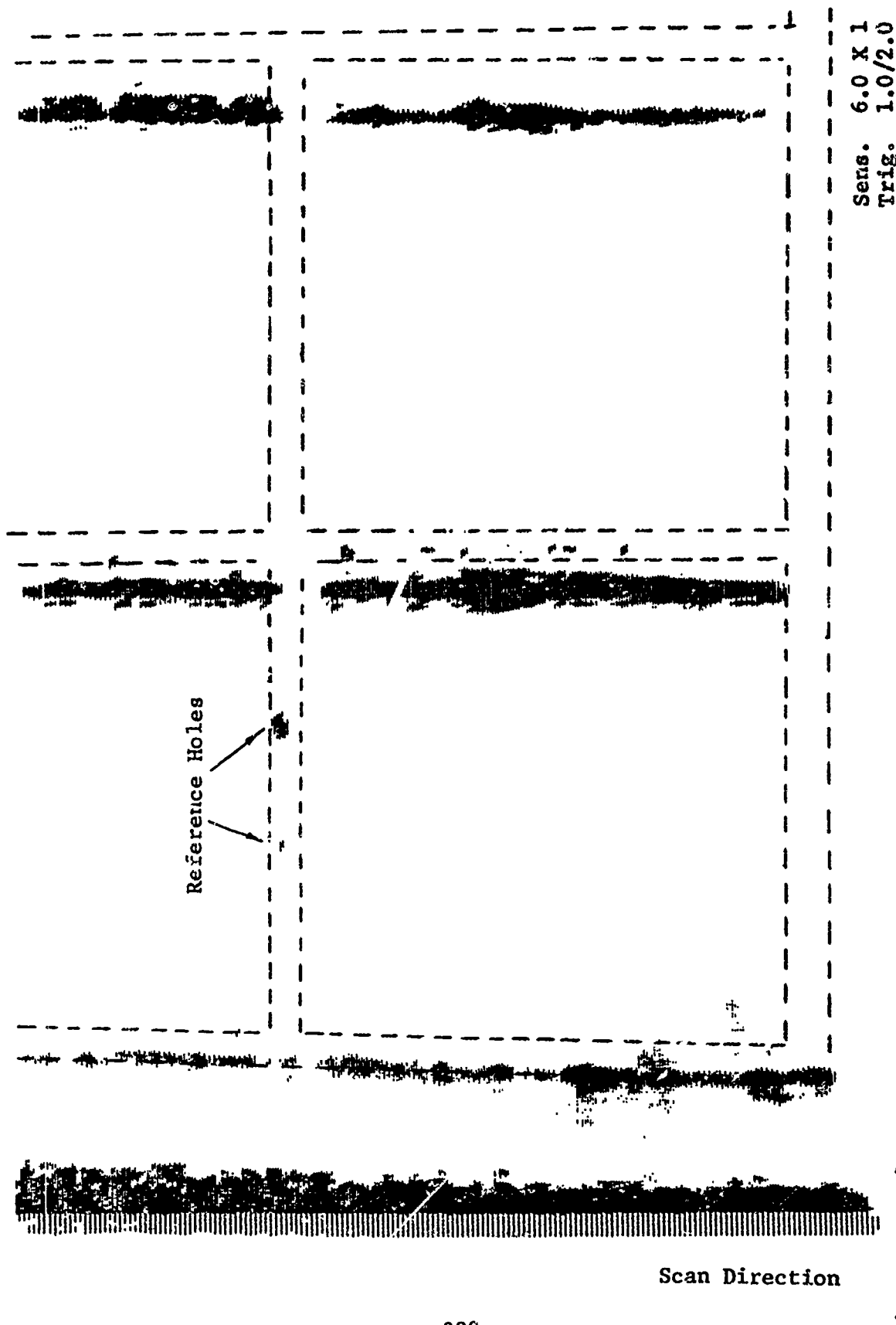


Figure 9.12 Delta/C-Scan Record of Part #1 (90° Rotation)



The linear indications aligned with the ribs are returns from the fillet radii. Indications in the bond areas will be correlated with the results of the other modes of ultrasonic inspection described in the next sections.

### 9.3.2 Variable Tilt-Multiple Scan

The AFML Computer-Automated Ultrasonic Inspection System described in Section 4.2 was used to evaluate Part #1 from the large diffusion bonded structure. The part was oriented with respect to the X, Y, and Tilt axes of the scanner, as shown in Figure 9.13.

Inspection was carried out at 10 MHz using a Panametrics Model A311, 10/0.5I S/N 998 transducer (flat-faced). Signal level was set at 30% of screen saturation using the maximized response from the inclined 5/64 FBH. This maximized response occurred at a transducer tilt angle of  $-8^{\circ}$ . This value agrees with Snell's Law for a water-titanium system and a reflecting surface within the titanium whose normal is inclined at  $30^{\circ}$  to the vertical.

A preliminary set of scans was made over the reference holes at tilt angles of  $-8^{\circ}$  to  $+8^{\circ}$  in  $2^{\circ}$  increments. The hole indications were distinct and separate at  $\theta = -8^{\circ}$ , but became less so at  $\theta = -6^{\circ}$  (see Figure 9.14). The flaw depth data were called from the computer disc storage file to interpret the indications at  $\theta = -6^{\circ}$ .

Table 9.1 presents these data which indicate that signals from outside the FBH location were returned from a depth corresponding to the fillet radius between the rib and plate. This ability to discriminate between legitimate and extraneous indications based on the data in disc memory is clearly a valuable feature of the AFML Computer-Automated Inspection System.

The scan records at  $-2^{\circ}$  and  $0^{\circ}$  (Figure 9.15) indicate the presence of the 3/64-in. dia. drilled hole between the two flat-bottom holes which do not appear. This re-emphasizes that conventional C-scan ( $\theta = 0^{\circ}$ ) is inadequate for inspecting displaced and angularized bond planes.

The remaining scans from  $+2^{\circ}$  to  $+8^{\circ}$  contained no relevant indications and are not included for brevity.

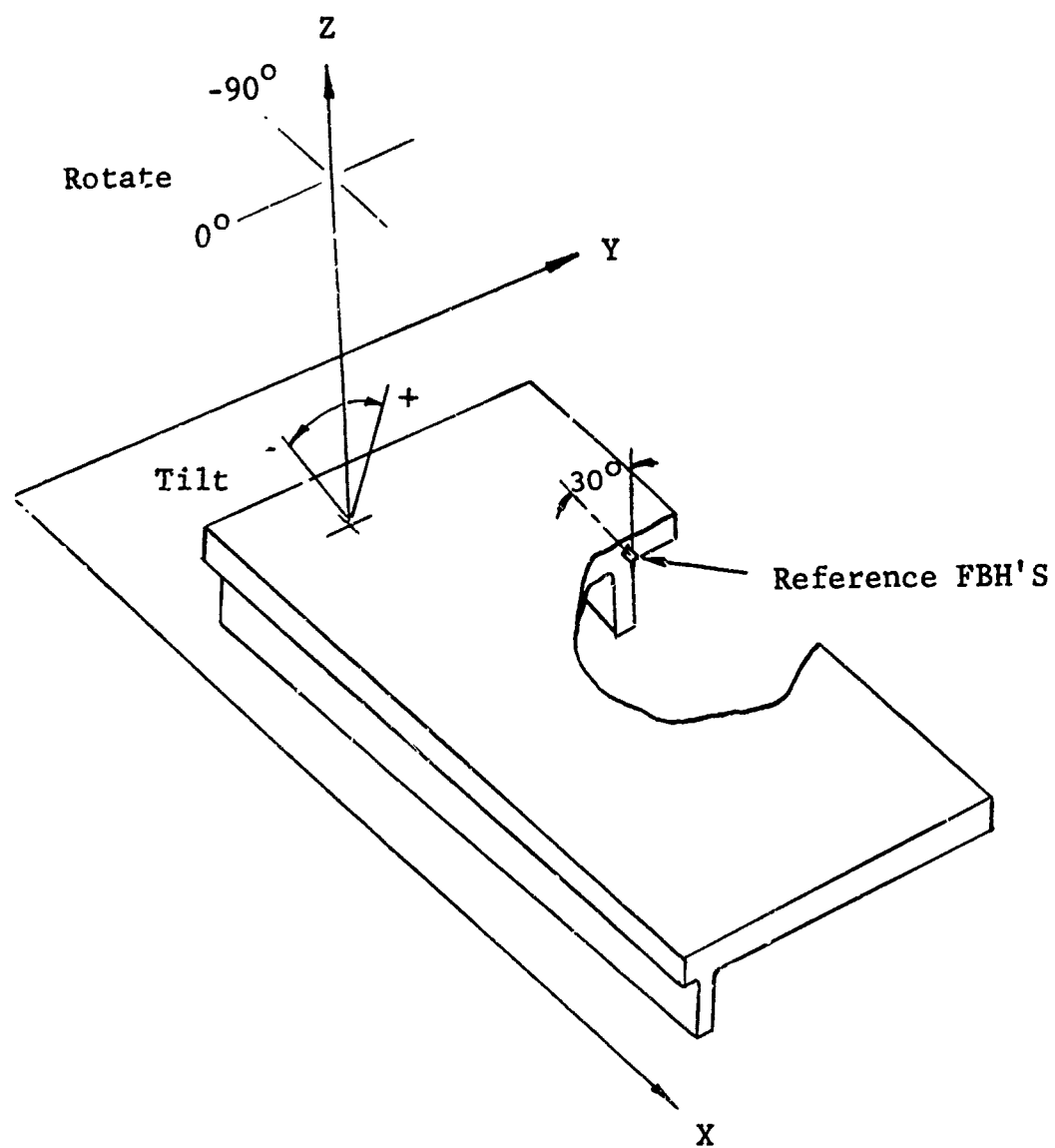
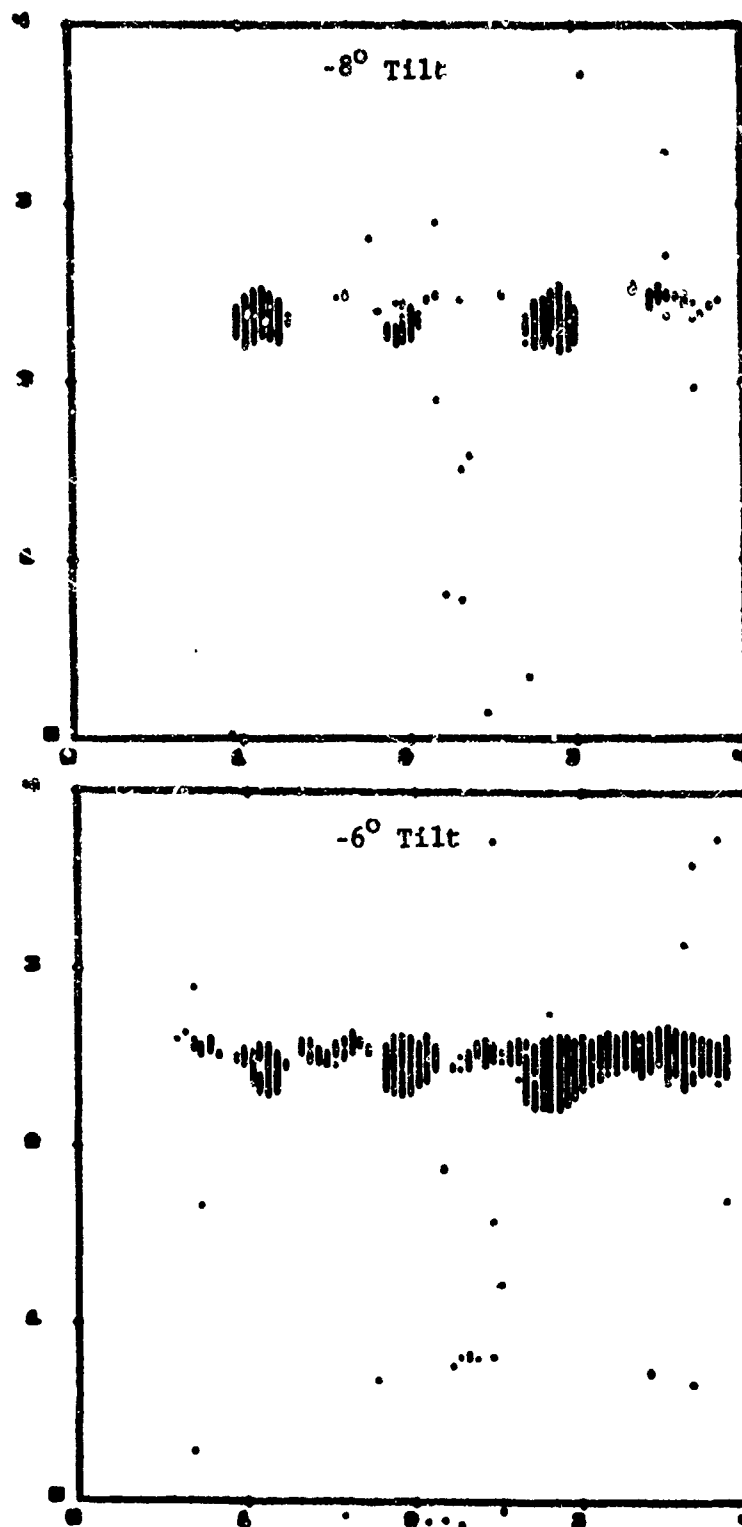


Figure 9.13 Orientation of Part #1 with Respect to Scanner Coordinate System



REFLECTION MODE FLAW DISPLAY

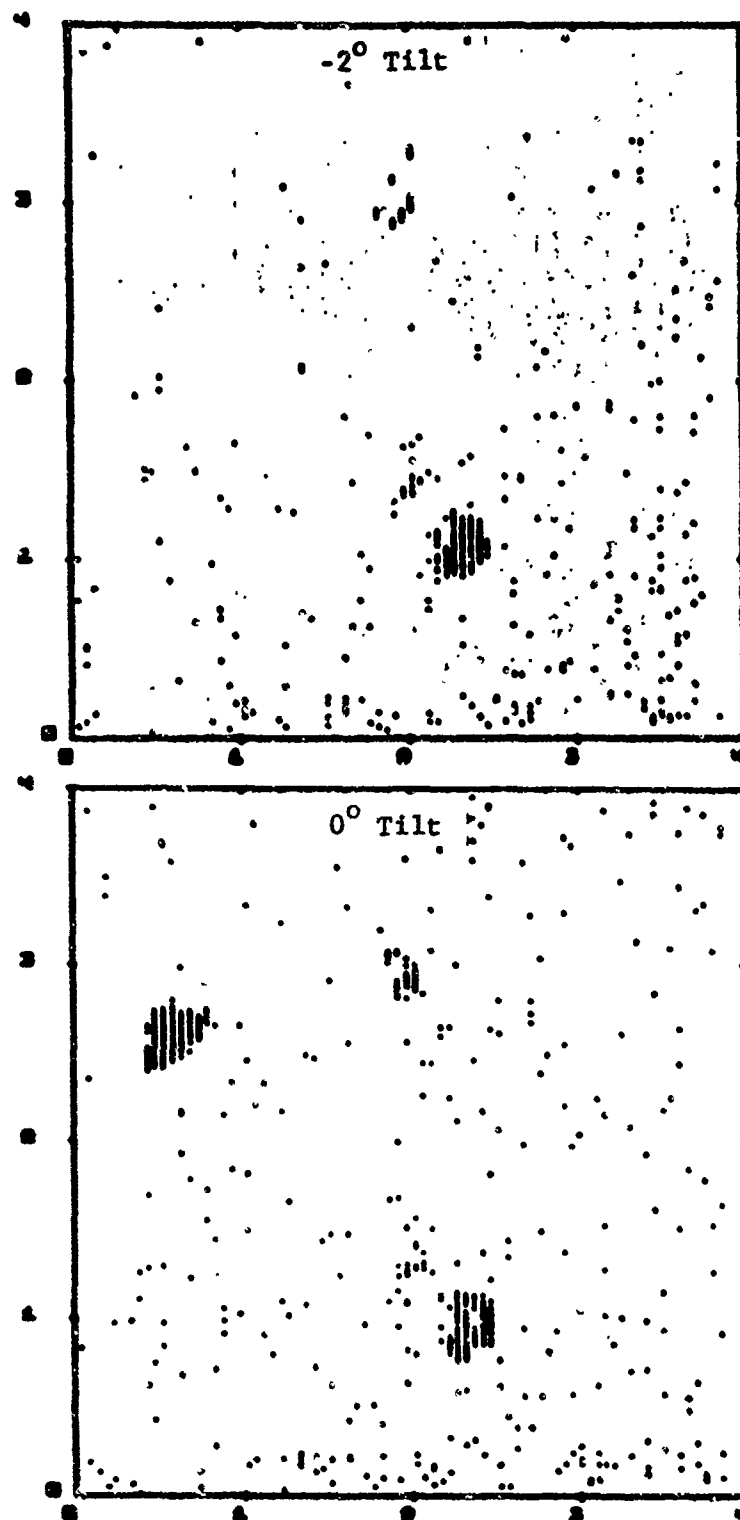
OPERATOR : TCM  
PART : TI BLK

DATE : 18-JUN-74 TIME : 10:54:23  
ATTEN : 0 DB

Figure 9.14 Flaw Display in Reference Hole Area of Part #1  
(Transducer Inclination,  $-8^\circ$  and  $-6^\circ$ )

Table 9.1 Reflection Mode Data Report

REFLECTION MODE DATA REPORT			18-JUN-74	10:29:57	PAGE	3	
X	Y	Z	ROTATE	TILT	THICK	FLW DP	FLW AM
2.89	2.50	0.00	0.0	-5.8	19.54	0.44	4095
2.89	2.50	0.00	0.0	-5.8	19.51	0.43	4095
2.89	2.50	0.00	0.0	-5.8	19.53	0.43	4095
2.89	2.51	0.00	0.0	-5.8	19.51	0.43	4095
2.89	2.51	0.00	0.0	-5.8	19.50	0.43	4098
2.89	2.51	0.00	0.0	-5.8	19.93	0.43	4092
2.89	2.51	0.00	0.0	-5.8	19.51	0.43	4069
2.89	2.51	0.00	0.0	-5.8	19.93	0.43	4054
2.89	2.52	0.00	0.0	-5.8	19.53	0.43	4036
2.89	2.52	0.00	0.0	-5.8	19.68	0.43	4014
2.89	2.52	0.00	0.0	-5.8	19.93	0.42	3997
2.89	2.52	0.00	0.0	-5.8	19.53	0.42	3938
2.89	2.52	0.00	0.0	-5.8	19.53	0.43	3917
2.89	2.53	0.00	0.0	-5.8	19.91	0.43	3858
2.89	2.53	0.00	0.0	-5.8	19.51	0.42	3830
2.89	2.53	0.00	0.0	-5.8	19.51	0.41	3776
2.89	2.53	0.00	0.0	-5.8	19.92	0.41	3731
3.29	2.49	0.00	0.0	-5.8	19.51	0.59	3695
3.29	2.49	0.00	0.0	-5.8	19.70	0.59	3730
3.29	2.49	0.00	0.0	-5.8	19.50	0.59	3746
3.29	2.50	0.00	0.0	-5.8	19.52	0.59	3760
3.29	2.50	0.00	0.0	-5.8	19.52	0.59	3778
3.29	2.50	0.00	0.0	-5.8	19.66	0.60	3791
3.29	2.50	0.00	0.0	-5.8	19.93	0.60	3796
3.29	2.50	0.00	0.0	-5.8	19.51	0.59	3808
3.29	2.50	0.00	0.0	-5.8	19.52	0.59	3827
3.29	2.51	0.00	0.0	-5.8	19.53	0.59	3820
3.29	2.51	0.00	0.0	-5.8	19.66	0.59	3826
3.29	2.51	0.00	0.0	-5.8	19.95	0.59	3823



REFLECTION MODE FLAW DISPLAY

OPERATOR : TCM  
PART : TI BLK

DATE : 18-JUN-74 TIME : 14:51  
ATTEN : 20 DB

Figure 9.15 Flaw Display in Reference Hole Area of Part #1  
(Transducer Inclination,  $-2^\circ$  and  $0^\circ$ )

Inspection of the entire Part #1 was done at (a) tilt angles of  $-8^{\circ}$  to  $+8^{\circ}$  in  $2^{\circ}$  increments,  $0^{\circ}$  rotate angle, i.e., the transducer tilted about the scanner X-axis and (b) tilt angles of  $-8^{\circ}$  to  $+8^{\circ}$  in  $2^{\circ}$  increments,  $-90^{\circ}$  rotate angle, i.e., the transducer tilted about the scanner Y-axis. This is equivalent to a 17-transducer array.

Selected scan records are given in Figure 9.16 through 9.18. As before, the  $-8^{\circ}$  tilt,  $0^{\circ}$  rotate record shows the reference holes, while the  $0^{\circ}$  tilt record does not.

Interpretation of the scan records for defect verification was accomplished by (a) spatial discrimination in the X-Y plane, (b) flaw depth vs. part thickness, and (c) frequency of occurrence as a function of tilt angle. A further check was correlation with the Delta/C-Scan records.

A site for sectioning and defect verification, based on these criteria, was a rib intersection located at  $X = 8.3$  in.,  $Y = 4.8$  in.

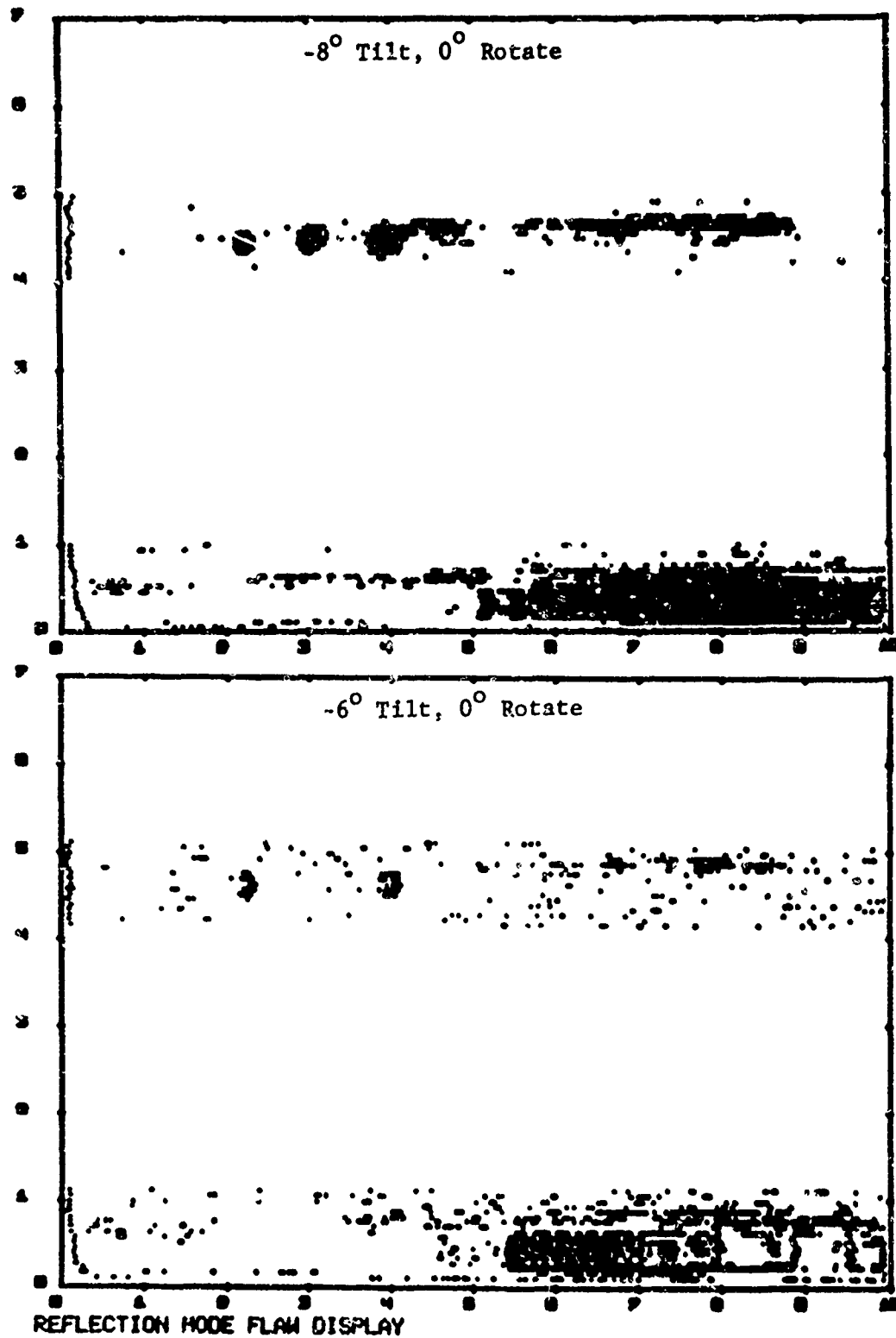
#### 9.3.3 Contact Signal-Averaged Pulse-Echo

The signal-averaging system described in Section 4.1 was utilized to selectively evaluate areas on Part #1 identified as potential defect sites by the previous two inspection techniques.

Inspection was done at 10 MHz from the rib side with the gate set to include the rib-plate diffusion bond plane. Figures 9.19 and 9.20 are typical records which correspond to locations  $X = 5.5$  in.,  $Y = 4.6$  in., and  $X = 1.1$  in.,  $Y = 1.5$  in. per Figure 9.17. Correspondence of flaw indications from all three ultrasonic techniques was obtained at the location  $X = 8.3$  in.,  $Y = 4.8$  in. This location was therefore selected for defect verification.

#### 9.3.4 Defect Verification

Part #1 was sectioned at location  $X = 8.3$  in.,  $Y = 4.8$  in. Two sections  $1/8$ -in. apart in the Y-Z plane were polished and etched. Figure 9.21 shows the sections related to Part #1 and the corresponding microstructural features. Connected grain boundaries generally perpendicular to the Z-axis are visible in Section A. Section B in Figure 9.21 exhibited a clearly defined elliptic area with major and minor axis dimensions of 0.24 in. and 0.15 in., respectively.



OPERATOR : TCM  
PART : TI BLK

DATE : 19-JUN-74 TIME : 14:35.28  
ATTEN : 0 DB

Figure 9.16 Flaw Display of Part #1 (-8° and -6° Tilt; 0° Rotate)

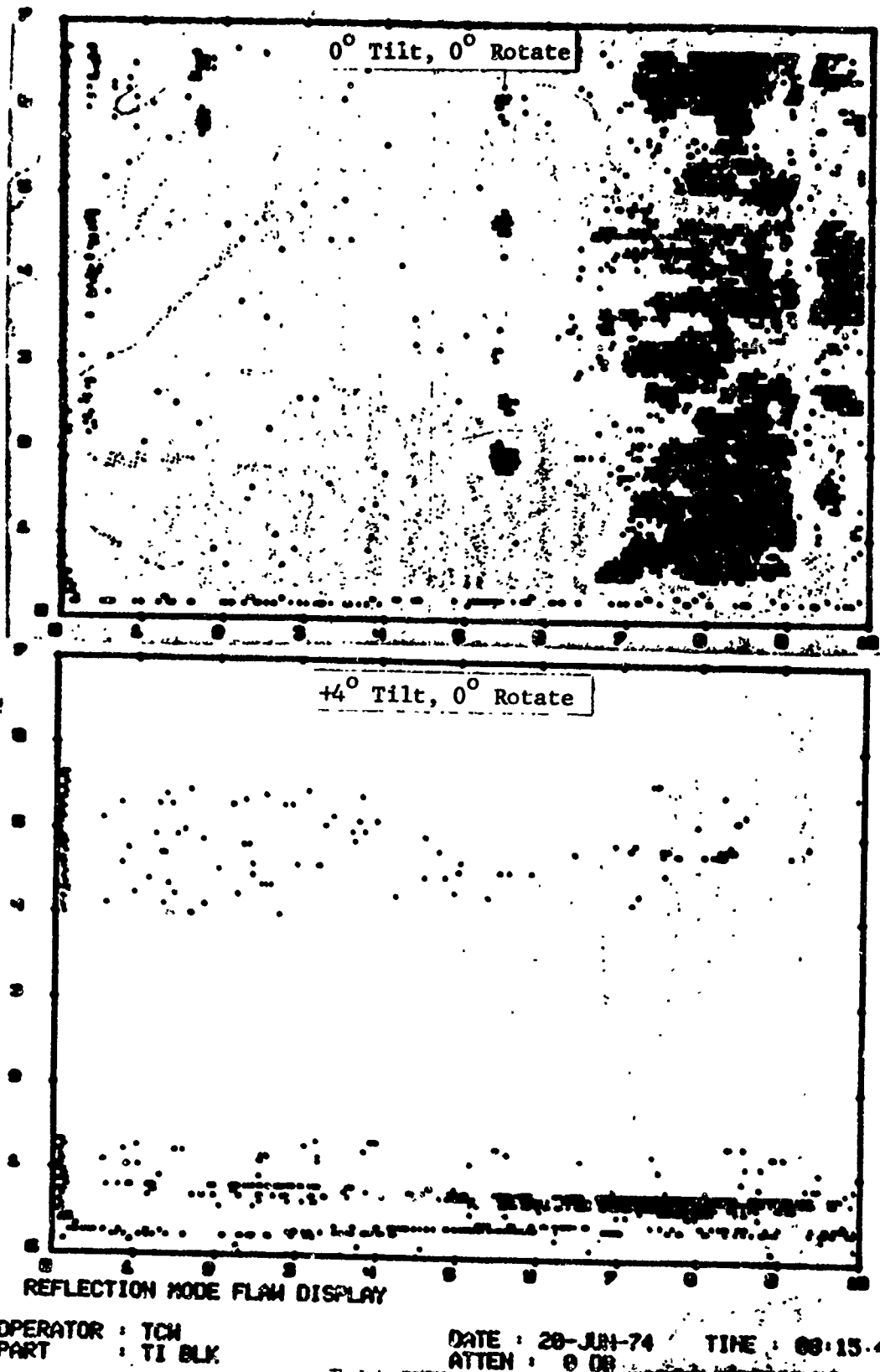
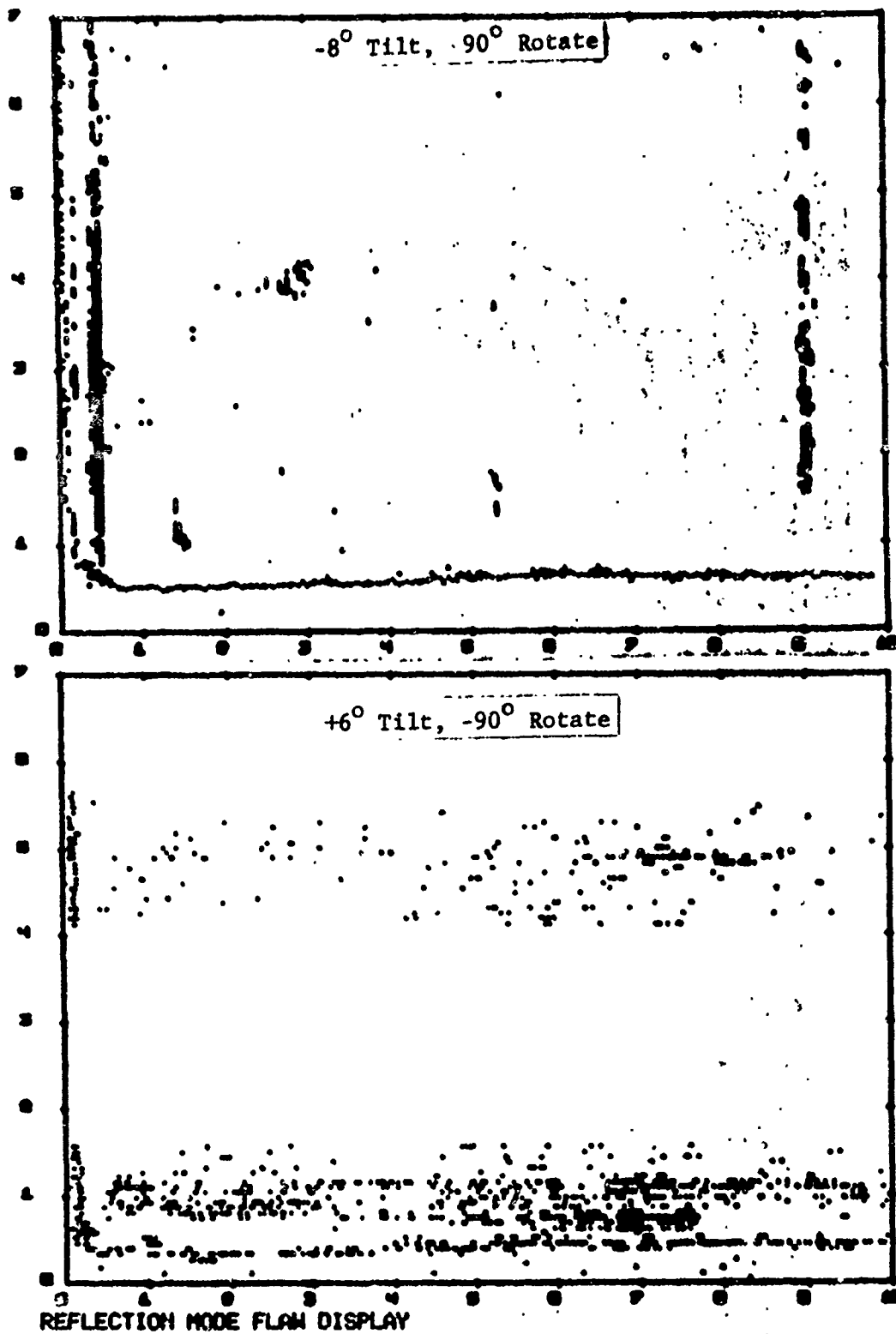


Figure 9.17 Flaw Display of Part #1 (0° and +4° Tilt; 0° Rotate)





OPERATOR : TCM  
PART : TI BLK

DATE : 20-JUN-74 TIME : 08:15:43  
ATTEN : 0 DB

Figure 9.18 Flaw Display of art #1 (-8° and +6° Tilt; -90° Rotate)

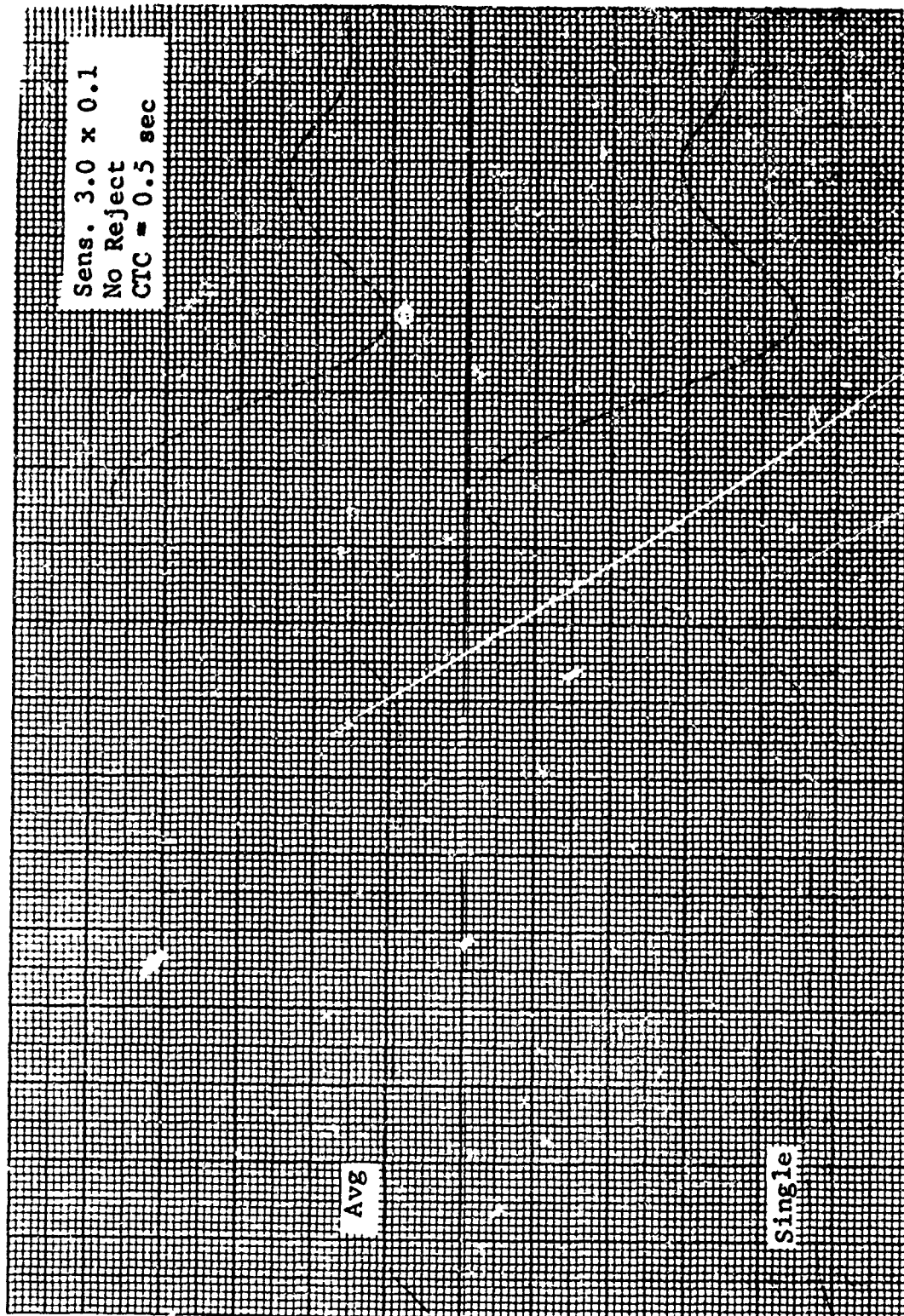


Figure 9.19 Signal-Averaged Pulse-Echo Record (X = 5.5 in.,  
Y = 4.6 in.)

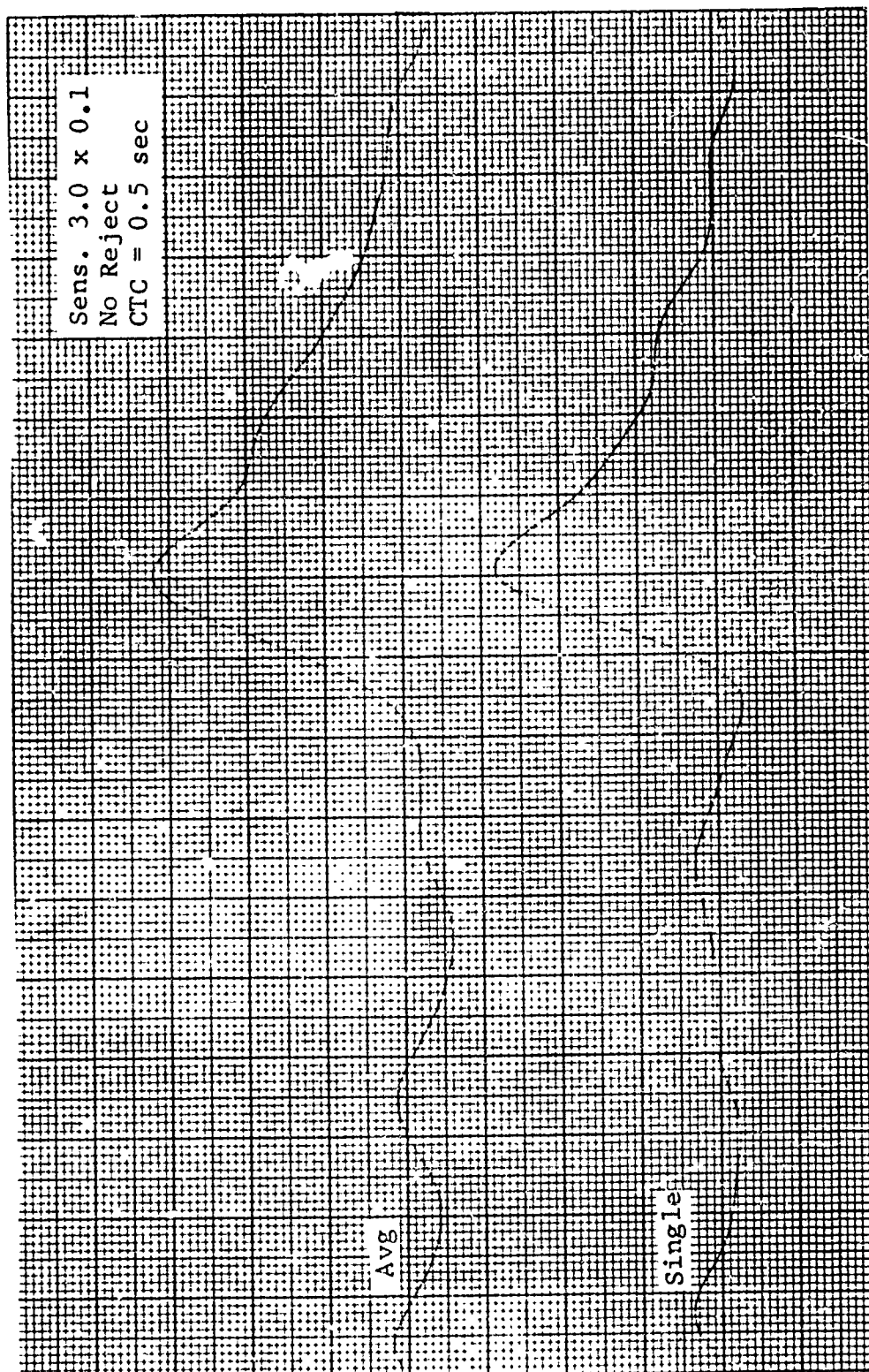
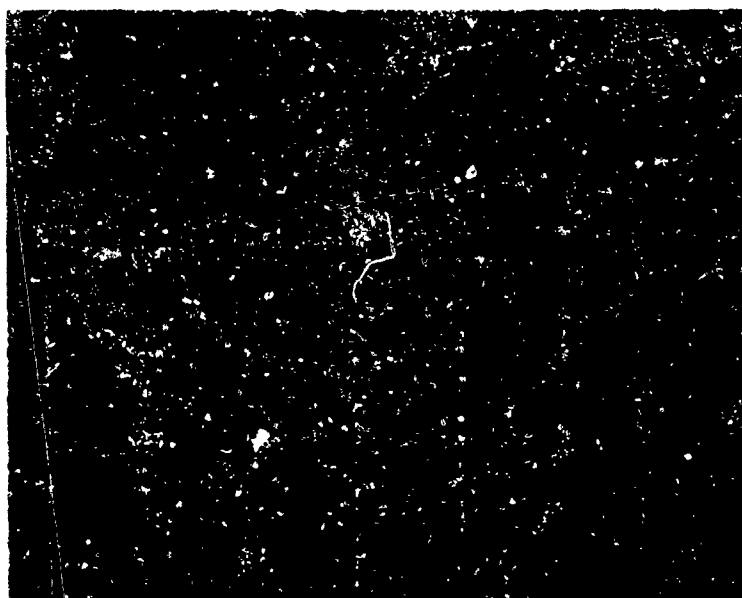


Figure 9.20 Signal Averaged Pulse-Echo Record ( $X = 1.1$  in.,  
 $Y = 1.5$  in.)



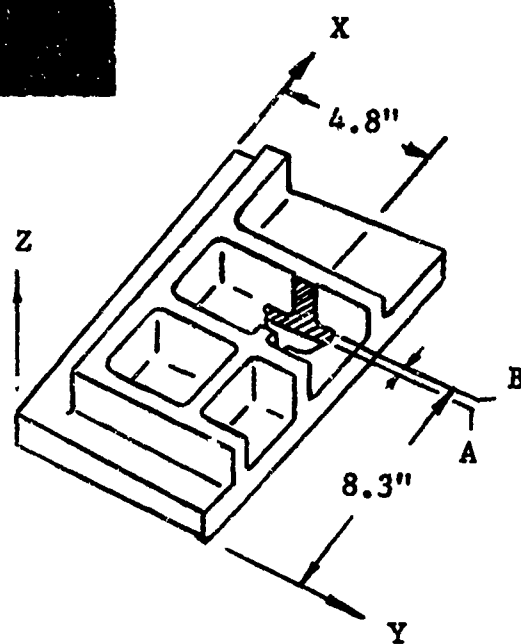
100X

Section A



12X

Section B



Locations of  
Sections A and B

Figure 9.21 Photomicrographs of Microstructural Anomalies in Bond Plane of Part #1 at  $X = 8.3$  in.,  $Y = 4.8$  in.

The results of microhardness traverses across the elliptic area are given in Figure 9.22. A maximum point-to-point difference of over 200 Knoop Hardness numbers was observed. This ranged from 452 KHN (Rockwell C44) in an alpha case area to 235 KHN (Rockwell C20) in the elliptic area. Hardness in the parent material is 335 KHN (Rockwell C33).

While hardness in titanium alloys is more difficult to relate to tensile strength than in steel alloys, the observed difference in ultrasonic response implies a difference in acoustic impedance and ultimately elastic modulus.

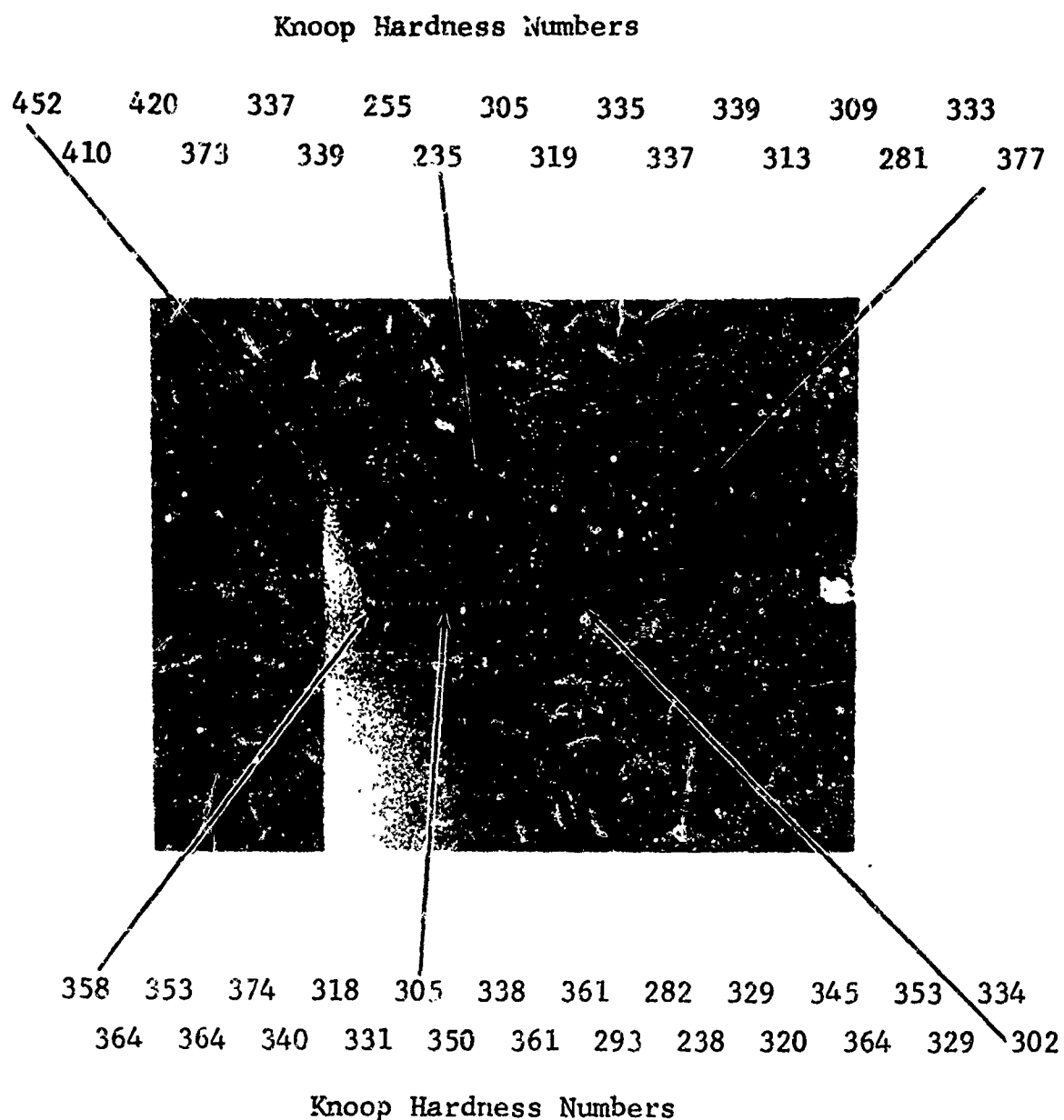


Figure 9.22 Microhardness Variations Across Elliptic Area in Rib Intersection of Part #1.

## 10. CONCLUSIONS AND RECOMMENDATIONS

The results reported herein allow the following conclusions:

1. The inspection systems developed in this study generated and processed a large mass of data to obtain increased sensitivity to small randomly-oriented defects. Future efforts must reduce and interpret these data before display to a greater degree than accomplished heretofore in order to make production line accept/reject decision making feasible.
2. The AFML Computer Automated Inspection system can operate efficiently in the variable tilt mode at transducer tilt angles up to  $10^{\circ}$  off vertical. The use of variable transducer tilt is very desirable for inspections of displaced and angularized bond planes.
3. Acoustic Emission Monitoring can detect flaws, debonding and inclusions before failure and to some extent before reaching the yield point.
4. Attenuation measurements verify that the bonding cycle effectively eliminates differences in texture. Grain size variations and the amount of beta processing are readily detectable by attenuation measurements indicating the potential for identifying localized changes in grain structure due to excessive temperature or contaminants.
5. The Blue Etch-Anodize process is especially effective in detecting alpha case layers in diffusion bond planes. Alpha case specimens exhibited lower reduction of area in tension and generally poorer fatigue life.
6. Fluorescent penetrant was effective only for

extremely low deformation across a bond plane resulting in a surface-connected deficiency.

7. Optimized Delta/C-scan proved effective for inspecting bond planes in thin sections (e.g., 1" thick) and for evaluation of displaced and angularized bond planes. Defects in the form of voids, silica and stainless steel (inclusions with major dimensions of .010" and greater were detected by this technique.
8. Signal-Averaged Pulse-Echo measurements as accomplished by the system developed herein provided an increase in low level defect signal detection by collecting and processing 24 times the data per point as conventional pulse echo techniques. The increase in defect-signal-to-grain noise ratio does not approach the theoretical value from random noise theory since the variation of grain noise with transducer rotation was found to be non-random and in fact a relatively smooth function.

The arithmetic average of grain structure noise waveforms can be used to effectively normalize defect signal amplitudes for correlation with tensile and fatigue properties.

The work reported herein suggests fruitful areas for further investigation and immediate applications as recommended below:

1. The use of statistical functions affected by phase rather than amplitude should be pursued for defect discrimination (e.g., cross correlation).
2. The data generated in this effort on defect size type and geometry should be further analyzed from the view point of the effect of defects on fatigue life. This would be an important step in defining defect acceptability limits.
3. Blue etch-anodize should be included as a



diffusion bond inspection requirement.

4. Greater emphasis must be placed on computer algorithms for ultrasonic data processing, interpretation and decision making as opposed to display of minimally processed data and subsequent operator interpretations.
5. Evaluation of real diffusion bonded structures should use correlation between ultrasonic techniques like those reported here as a means of defect discrimination.

## REFERENCES

1. Ashton, J. H., et al, "Solid State Diffusion Bonding - III: Vacuum Hot-Press Parameter Study," General Dynamics Report FZM-12-13108, 22 September 1970.
2. Roth, W., "Scattering of Ultrasonic Radiation in Polycrystalline Metals," Jour. Appl. Phys., Vol. 19, pp. 901-911, October 1948.
3. Mitchell, D. K., et al, "Investigation and Development of a Technique to Enhance Ultrasonic Flaw Response in Metals," Battelle Final Technical Report, Contract No. N00024-71-C-5360, Naval Ship Engineering Center, Dept. of the Navy, 27 July 1972.
4. Ermolov, I. N., and Pilin, B. P., "Possible Ways of Improving the Sensitivity of Ultrasonic Inspection of Parts with a Large-Grain Structure," Soviet Jour. of Nondestructive Testing, Vol. I, pp 46-49, Jan.-Feb. 1969.
5. Kennedy, J. C., and Woodmansee, W. E., "Electronic Signal Processing Techniques, Phase III - Nondestructive Testing," Order No. 1246, January 1972.
6. Regalbuto, J. A., "1st Annual Tech. Report, "Nondestructive Testing of Diffusion Bonded Titanium Alloys for Engine and Airframe Components," FZM-6170, (30 June 1972-31 May 1973).
7. Martin, G., Moore, J. F., and Coate, F. M., "Exploratory Development of Nondestructive Testing Techniques for Diffusion Bonded Interfaces," AFML-TR-70-188, September 1970.
8. Mason, W. P., and McSkimin, J. H., "Attenuation and Scattering of High Frequency Sound Waves in Metals and Glasses," Jour. Acoustical Soc. of Amer., Vol. 19, pp 464-473 (1947).
9. Papadakis, E. M., "Buffer Rod System for Ultrasonic Attenuation Measurements," Jour. Acous. Soc. Amer., Vol. 44, No. 5, pp. 1437-1441, 1968.

10. ASTM Designation E112-63, "Standard Methods for Estimating the Average Grain Size of Metals," 1963.
11. Bacon, D. J., and Snell, W. A., "Blue Etch Anodize - An Improved Method for Nondestructive Detection of Surface Connected Segregation in Titanium Alloys," Pratt and Whitney, Hartford, Conn., MERL Report No. 1944, 8 February 1971.
12. Lord, R. J., "Evaluation of the Reliability and Sensitivity of NDT Methods for Titanium Alloys," Interim Report No. 2, Report MDC A2394, McDonnell Douglas Corp., 20 July 1973.
13. Novak, S. R., and Rolfe, S. T., "Modified WOL Specimen for K<sub>I</sub>sec Environmental Testing," Jour. of Materials, Vol. 4, No. 3, 701-728, 1969.
14. Owczarski, W. A., King, W. H., and O'Connor, J. W., "The Tensile Properties and Fracture Characteristics of Titanium Diffusion Welds," Welding Journal, Welding Research Supplement, pp 377-383, 1969.
15. Lucas, J. J., "Improvements in the Fatigue Strength of Ti-6Al-4V Forgings," 2nd Int. Titanium Conference, Titanium Science and Technology, Proceedings, Vol. 3, pp 2081-2096 (1972).
16. Gunderson, A., Gegel, H. L., and Lyon, S. R., "Fatigue Behavior of Diffusion Bonded Ti-6Al-4V Having Very Small Defects," 2nd Int. Titanium Conference, Titanium Science and Technology, Proceedings, Vol. 1, pp 649-664 (1972).
17. Jones, E. J., Lewellen, T. E., and Studer, V. J., "Diffusion Bonding Evaluation (Annealed 6Al-4V Titanium)," General Dynamics Report MR-D-348, January 1970.
18. Witzell, W. E., "Evaluation of Diffusion Bonded Titanium 6Al-4V," General Dynamics Report 22L-69-028, MP-S72-1-682, July 1969.

## APPENDIX A

### Material Characterization

The material for this program is Ti 6Al4-V Plate obtained from the RMI Company, Niles, Ohio, to North American Rockwell Specification ST0170LB0032 Rev. E Cond. A (annealed). Plate sizes are 1 x 40 x 90-in. and  $\frac{1}{2}$  x 40 x 90-in. The producers' chemistry and tensile properties (verified at General Dynamics) are given in Table A-1.

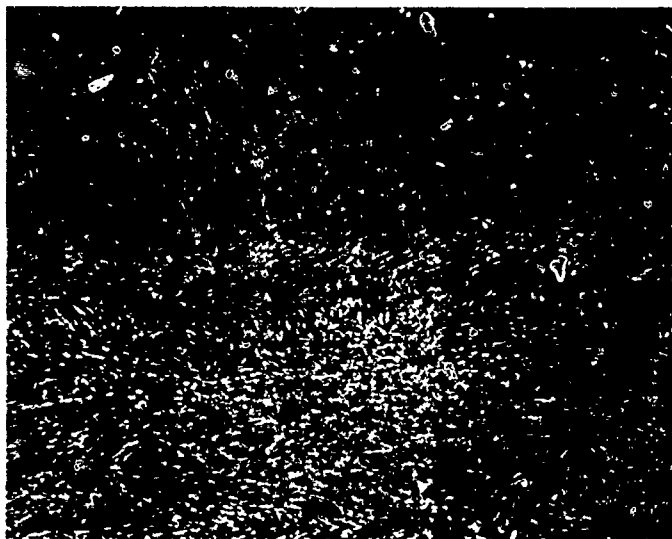
Table A-1

Ti 6Al-4V PLATE CHEMISTRY AND PROPERTIES

Ingot Number		890225 ( $\frac{1}{2}$ in.)	890284 (1 in.)
Chemistry			
C%		0.01	0.02
N		0.009	0.008
Fe		0.17	0.19
Al		6.1	6.0
V		4.0	4.0
O		0.117	0.115
H (ppm)		80	121
Properties Ultimate (KSI)	L	141.9	140.3
	T	138.0	138.0
Yield (KSI) (0.2%) Offset	L	132.5	131.3
	T	130.0	129.5
% Elongation	L	15.0	14.0
	T	15.0	14.0

The titanium plate material was ultrasonically C-scanned to Class A specifications at both the producer and General Dynamics facilities.

Microstructural features of the  $\frac{1}{2}$ -in. and 1-in. plates are given in Figures A.1 through A.9. The  $\frac{1}{2}$ -in. plate exhibits more nearly equi-axed grain structure than the 1-in. plate.

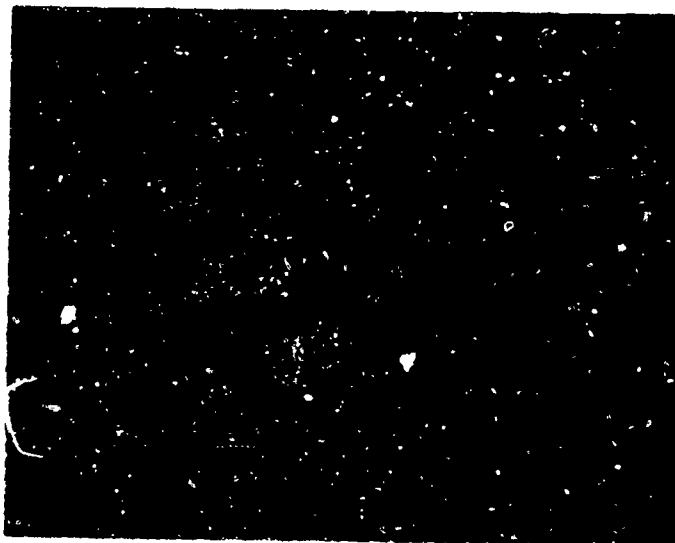


RMI MATERIAL  
H.T. 890204-02-1A  
SURFACE OF MATERIAL  
AS-RECEIVED  
100X MAG

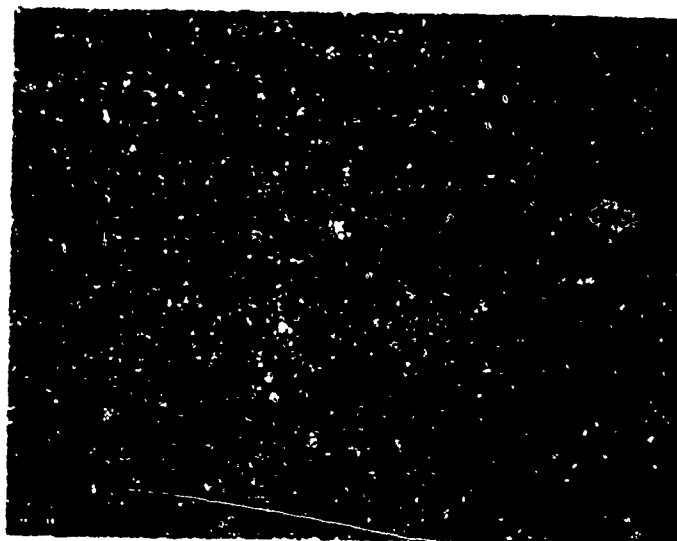


RMI MATERIAL  
H.T. 890204-02-1A  
CENTER OF MATERIAL  
AS-RECEIVED  
100X MAG

Figure A.1 Photomicrographs of 1-inch Ti 6Al-4V Plate, Annealed  
(RMI Photos)



RMI MATERIAL  
H.T. 890225-03-1A  
SURFACE OF MATERIAL  
AS-RECEIVED  
100X MAG

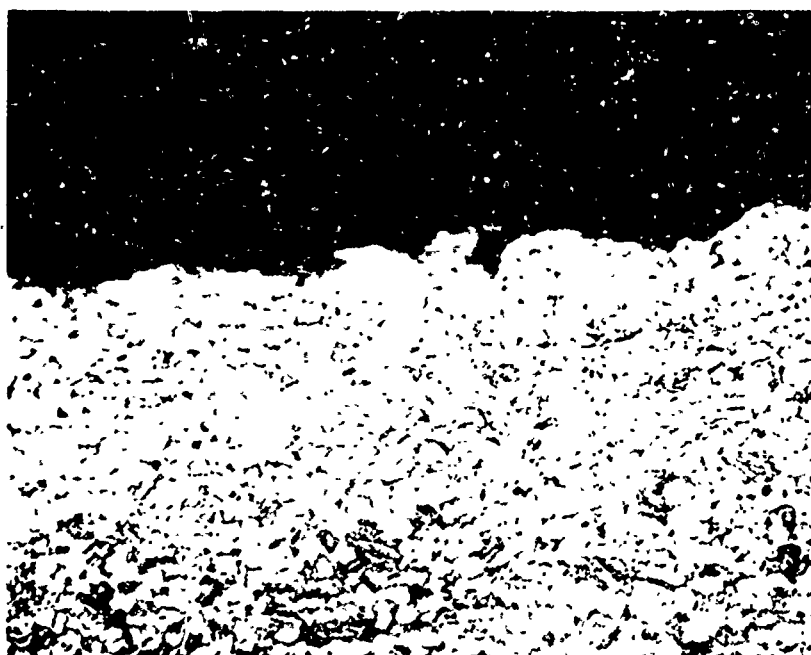


RMI MATERIAL  
H.T. 890225-03-1A  
CENTER OF MATERIAL  
AS-RECEIVED  
100X MAG

Figure A.2 Photomicrographs of  $\frac{1}{2}$ -inch Ti 6Al-4V Plate, Annealed  
(RMI Photos)



RMI MATERIAL  
H.T. 890204-02-1A  
SURFACE OF CENTER SEC-  
TION OF MATERIAL  
AS-RECEIVED  
100X MAG

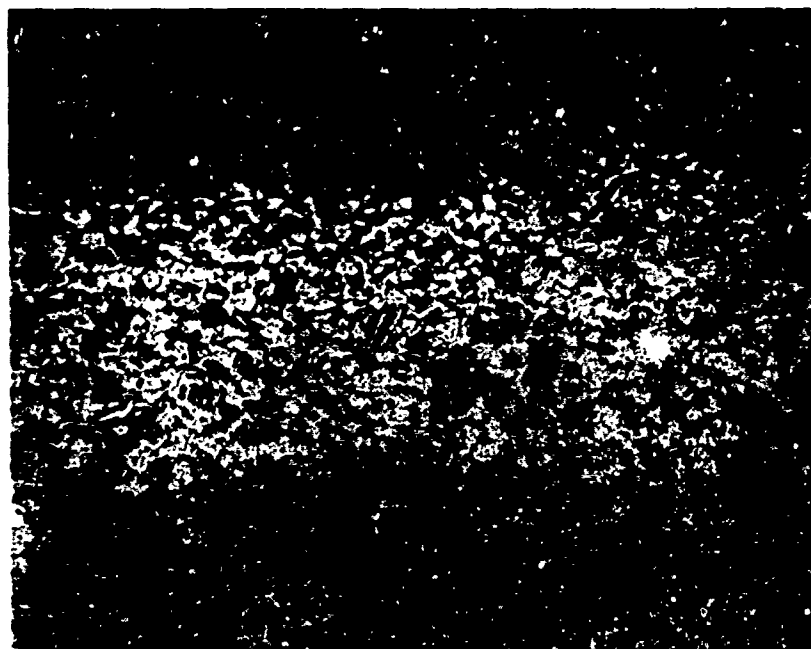


RMI MATERIAL  
H.T. 890204-02-1A  
SURFACE OF CENTER SEC-  
TION OF MATERIAL  
AS-RECEIVED  
500X MAG

Figure A.3 Photomicrographs of Outer Edge Surface of  $\frac{1}{2}$ -inch Ti  
6Al-4V Plate, Annealed (CAD Process Control Photos)



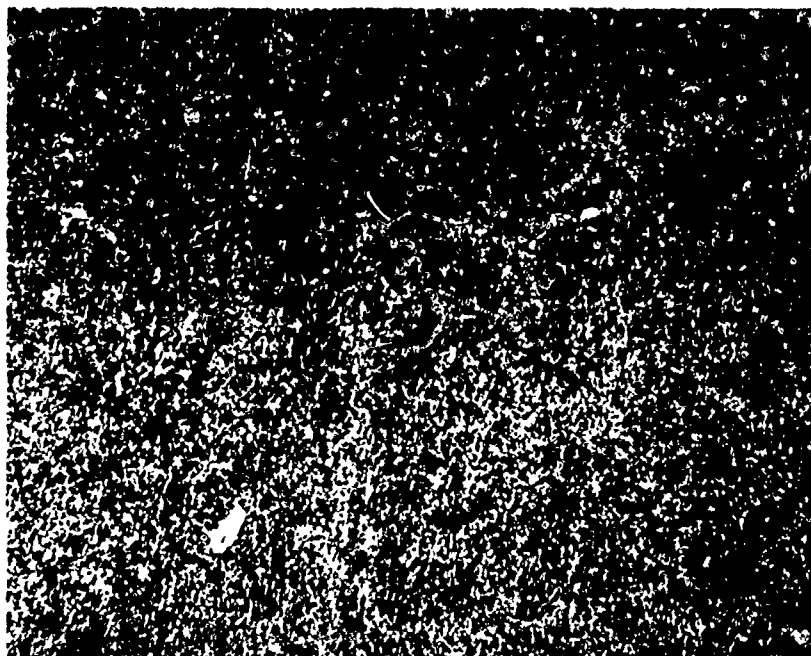
RMI MATERIAL  
H.T. 890204-02-1A  
SURFACE OF END SECTION  
OF MATERIAL  
AS-RECEIVED  
100X MAG



RMI MATERIAL  
H.T. 890204-02-1A  
SURFACE OF END SECTION  
OF MATERIAL  
AS-RECEIVED  
500X MAG

Figure A.4 Photomicrographs of Central Surface of  $\frac{1}{2}$ -inch T1 6Al-4V Plate, Annealed (CAD Process Control Photos)



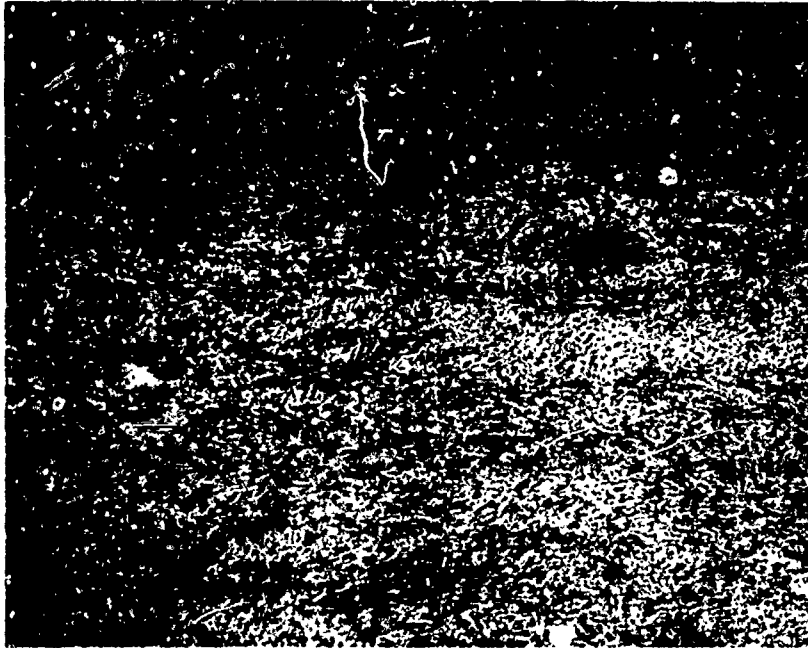


RMI MATERIAL  
H.T. 890204-02-1A  
CENTER OF MATERIAL  
AS-RECEIVED  
100X MAG



RMI MATERIAL  
H.T. 890204-02-1A  
CENTER OF MATERIAL  
AS-RECEIVED  
500X MAG

Figure A.5 Photomicrographs of Central Interior of 1/2-inch Ti 6Al-4V Plate, Annealed (CAD Process Control Photos)

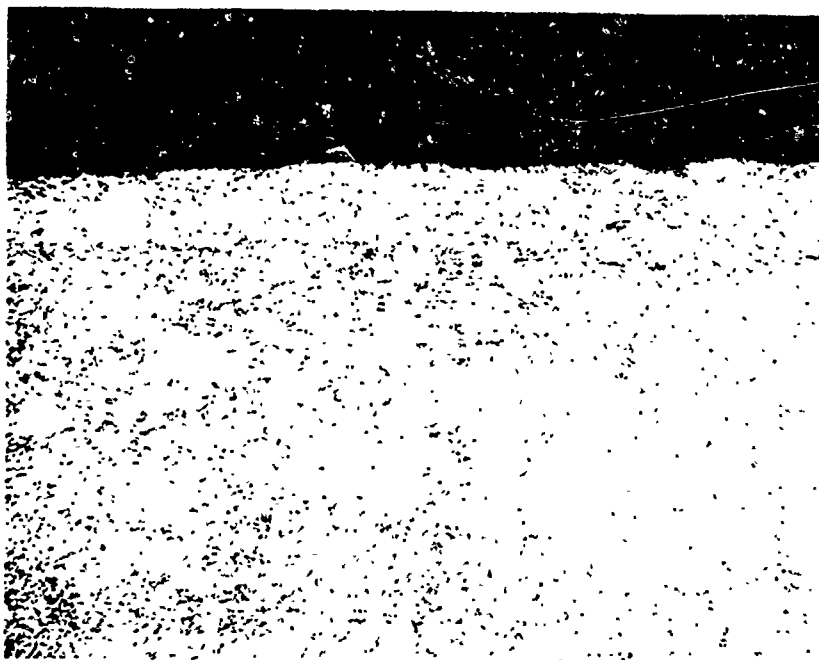


RMI MATERIAL  
H.T. 890204-02-1A  
SURFACE OF MATERIAL  
AS-RECEIVED  
100X MAG

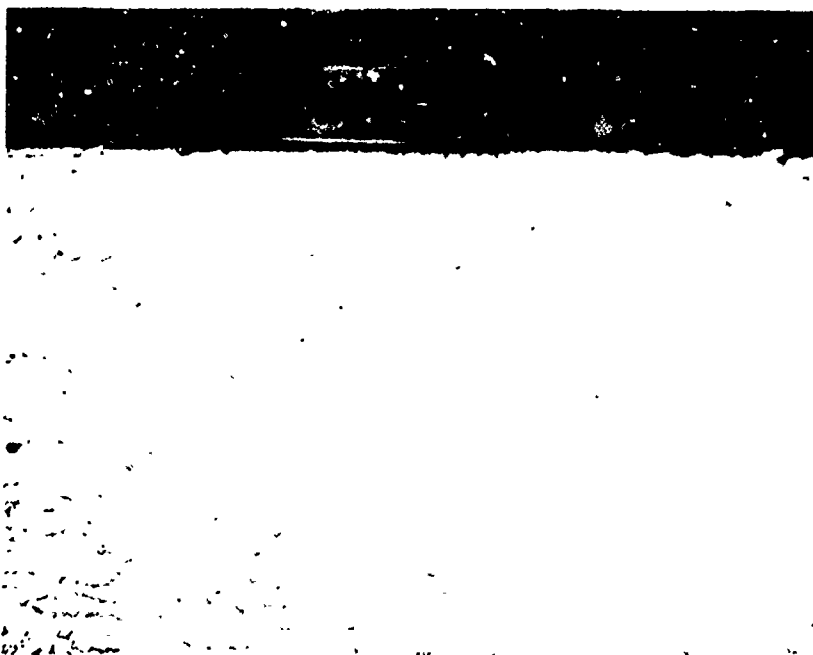


RMI MATERIAL  
H.T. 890204-02-1A  
SURFACE OF MATERIAL  
AS-RECEIVED  
500X MAG

Figure A.6 Photomicrographs of Surface of 1-inch Ti 6Al-4V Plate, Annealed, Longitudinal Direction (CAD Process Control Photos)



RMI MATERIAL  
H.T. 890204-02-1A  
SURFACE OF MATERIAL  
AS-RECEIVED  
100X MAG



RMI MATERIAL  
H.T. 890204-02-1A  
SURFACE OF MATERIAL  
AS-RECEIVED  
500X MAG

Figure A.7 Photomicrographs of Surface of 1-inch Ti 6Al-4V Plate, Annealed, Longitudinal Transverse Direction (CAD Process Control Photos)



RMI MATERIAL  
H.T. 890204-02-1A  
CENTER OF MATERIAL  
AS-RECEIVED  
100X MAG



RMI MATERIAL  
H.T. 890204-02-1A  
CENTER OF MATERIAL  
AS-RECEIVED  
500X MAG

Figure A.8 Photomicrographs of Center of 1-inch Ti 6Al-4V Plate,  
Annealed, Longitudinal Transverse Direction (CAD Process  
Control Photos)

## APPENDIX B

### BLUE ETCH-ANODIZE PROCEDURE\*

Parts must be free of cleaning or buffing compounds and other foreign materials. Proper anodizing requires that the current fall to zero after the initial surge that takes place upon the application of the 30 v. Continued amperage indicates foreign material or unmasked protective coatings on the part and/or exposed metal other than titanium on the processing fixture. Any of these faults will result in an unsatisfactory blue color and a poor color contrast between normal material and the segregation.

All steel parts of anodizing fixtures should be masked with a hard permanent material, such as Microsol E1003. All identification markings must be masked with plastic tape to assure their retention:

The test comprises 15 steps, as follows:

1. Vapor degrease part.
2. Immerse part in heavy-duty alkali cleaner for 1 to 2 min. at 120 to 180° F.
3. Rinse part in clean cold water, and inspect for water breaks. Repeat cleaning and rinsing until part is clean.
4. Hang part on titanium alloy hook and immerse in agitated solution of a dry acid salt, such as MacDermid Metex Acid Salt M-629 (16 oz per gal), at room temperature for 1.5 min. Agitate part upon immersion.
5. Rinse etched part thoroughly in clean cold water, removing loosely adhering smut by pressure spraying (compressed air-water).
6. Attach anodizing fixture to part as quickly as possible with a minimum of handling.
7. Rinse fixtured part in clean cold water.
8. Immerse fixtured part in a 15 oz. per gal. solution of trisodium phosphate at  $70 \pm 10$ ° F, agitating part upon immersion. Anodize at 30 v for 30 sec., being sure not to turn on the current until the part is completely immersed.

\* Procedure as outlined in Reference 11

- Do not agitate fixtured part during anodizing.
9. Remove fixtured part and rinse in clean water.
  10. Detach part from anodizing fixture, attach to a titanium alloy hook, and rinse in clean cold water. Avoid unnecessary handling.
  11. Immerse part in aqueous nitric-hydrofluoric acid solution. Use 35% (by volume) technical grade nitric acid and 2.5% (by volume) technical grade hydrofluoric acid. The purpose of this step is to remove most of the blue color from the background to develop maximum color contrast between the segregation and the background. Immersion periods: Ti-6Al-4V, 2 to 10 sec.; Ti-8Al-1V-Mo, 15 to 25 sec.; and Ti-6Al-2Sn-4Zr-2Mo, 10 to 20 sec.
  12. Remove part from acid, immerse in clean cold water as rapidly as possible and rinse thoroughly.
  13. Rinse in hot water (190 to 210°F).
  14. Blow dry with clean compressed air.
  15. Inspect.

Processing tanks may be unlined, except for the two acid tanks which must be lined with rigid PVC or its equivalent. We recommend temperature indicators for the alkali cleaner, anodizing and hot water tanks. Mechanical stirrers are required in the alkali cleaner, both acid tanks and the anodizing tank. The rinse tank adjacent to the dry acid salt tank must have pressure spraying equipment, and timers are used on both acid tanks and the anodizing tank.

The rectifier must be rated at a maximum of 6% ripple at 30 v, no load. It should also allow the voltage to be raised to 30 v rapidly (1 to 3 sec.), preferably with automatic control. Finally, the rectifier should have a time-actuated switch which will cut out a 1.2 ohm resistor (installed in series with the load) after 3 sec. This resistor limits the initial surge of current, reducing chances of arcing.